Isotope Systematics of Gypsum and its Hydration Water

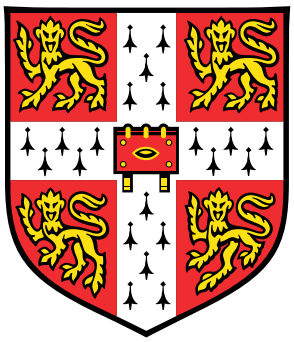

Nicholas Philip Evans

The Godwin Laboratory for Palaeoclimate Research,
Department of Earth Sciences

University of Cambridge

This dissertation is submitted for the degree of

Doctor of Philosophy

Clare College

September 2018

To my parents

&

to my brother

***

It may be that the gulfs will wash us down:
It may be we shall touch the Happy Isles,
And see the great Achilles, whom we knew.
Tho' much is taken, much abides; and tho'
We are not now that strength which in old days
Moved earth and heaven, that which we are, we are;
One equal temper of heroic hearts,
Made weak by time and fate, but strong in will
To strive, to seek, to find, and not to yield.

Alfred, Lord Tennyson

Declaration

I hereby declare that except where specific reference is made to the work of others, the contents of this dissertation are original and have not been submitted in whole or in part for consideration for any other degree or qualification in this University, or any other. This dissertation is the result of my own work and includes nothing which is the outcome of work done in collaboration, except where specifically indicated in the text. This dissertation contains fewer than 275 numbered pages of which not more than 225 pages are text, illustrations and bibliography.

Nicholas Philip Evans
September 2018

Acknowledgements

First and foremost, I would like to thank my supervisor, David Hodell. He has allowed me the freedom to pursue any research ideas that I wanted to investigate. His drive to step on untouched ground and to explore new ideas has been inspiring, and has taught me a lot about how to approach both scientific problems and life.

Secondly, I want to thank Fernando Gázquez and Thomas Bauksa. Experiencing their passion for science has been particularly motivating, and our collaboration in the lab has provided hours of fun. They have both been important mentors to me, and their guidance has been been invaluable.

I also thank Rachel Flecker and Edward Tipper for evaluating this thesis.

Finally, want to thank my family, to whom I dedicate this book. Without their support, this work would be a castle in the sky. I will be eternally grateful for their love.

Publication List

Chapter 2

- Gázquez, F., Evans, N. P., Hodell, D. A., 2017. Precise and accurate isotope fractionation factors (α^{17}O, α^{18}O and αD,) for water and $CaSO_4 \cdot 2H_2O$ (gypsum). Geochimica et Cosmochimica Acta 198, 259–270.

- Gázquez, F., Mather, I., Rolfe, J., Evans, N. P., Herwartz, D., Staubwasser, M., Hodell, D. A., 2015. Simultaneous analysis of $^{17}O/^{16}O$, $^{18}O/^{16}O$ and $^{2}H/^{1}H$ of gypsum hydration water by cavity ring-down laser spectroscopy. Rapid Communications in Mass Spectrometry 29 (21), 1997–2006.

Chapter 3

- Evans, N. P., Bauska, T. K., Gázquez-Sánchez, F., Brenner, M., Curtis, J. H., Hodell, D. A., 2018. Quantification of drought during the collapse of the classic Maya civilization. Science 361 (6401), 498–501.

Chapter 5

- Evans, N. P., Turchyn, A. V., Gázquez, F., Bontognali, T. R., Chapman, H. J., Hodell, D. A., 2015. Coupled measurements of δ^{18}O and δD of hydration water and salinity of fluid inclusions in gypsum from the Messinian Yesares Member, Sorbas Basin (SE Spain). Earth and Planetary Science Letters 430, 499–510.

Collaborations

Outside of the remit of this thesis, contributions have been made to a number of different projects. These include:

1. geochemical analysis of carbonate veins in the oceanic crust (*Turchyn, A.V.*);

2. reconstruction of the palaeohydrologic changes in lakes of the Bolivian Altiplano (*Bauska, T. K.; Gázquez-Sánchez, F; Baker, P. A.*);

3. investigating the potential on-going subsurface dolomite formation at DSDP Leg 42A site 374 (*McKezsie, J. A.*), and;

4. using stable isotopes of gypsum hydration water to ascertain the role of water condensation in the formation of subaerial gypsum speleothems (*Gázquez-Sánchez, F*).

Abstract

Triple oxygen and hydrogen isotope analysis of the structurally-bound water in gypsum can provide a direct measure of past hydrologic variability. This thesis presents the development of the water extraction and isotopic measurement procedures, the calculation of the gypsum-water isotope fractionation factors, and the application of the method to constrain the palaeo-hydrologic conditions in two temporally and geographically disparate sites.

Measurement of the isotopic composition of gypsum hydration water is used to examine the hydrological changes that occurred during the Terminal Classic Drought of the Maya lowlands (~800-1000 CE), coincident with the period when the Classic Maya Civilization of Mesoamerica collapsed. The data provide a complete and direct archive of hydrological conditions that have previously been limited to ice core records. Mean annual rainfall is shown to have decreased by between 41% and 54%, with intervals of up to 70%, compared to present-day conditions. This study has also shown for the first time that relative humidity was 2%-7% lower during the Terminal Classic Drought compared to today.

The methodology is also applied to the massive gypsum deposits in the marginal and deep basins of the Mediterranean to interpret the chemical evolution of parent water bodies during the Messinian Salinity Crisis (5.97-5.3 Ma). By combining the measurement of gypsum hydration water with other traditional (e.g. strontium) and novel (e.g. calcium and barium) isotope tracers, the hydrological changes during the deposition of Primary Lower Gypsum units of the Sorbas Basin in southeastern Spain, the Upper Gypsum units of Sicily, and deep basin deposits have been constrained. The results indicate that all deposits experienced a significant freshwater contribution to the mother fluids from which they formed. It is proposed that obliquity-controlled sea level and eccentricity-modulated precession, superimposed on longer-term tectonic restriction of the Mediterranean-Atlantic exchange, together controlled the varying depositional environments during the formation of the Messinian Salt Giant.

This thesis demonstrates that the analysis of gypsum hydration water is a powerful tool for palaeoclimate reconstruction. The methodology can be applied to gypsum (and other hydrated minerals) in a wide range of settings across geological space and time, providing a rich source of information about the environmental conditions under which they formed.

Nicholas P. Evans
Isotope Systematics of Gypsum and its Hydration Water

Contents

List of Figures

List of Tables

List of Abbreviations, Nomenclature and Units

List of Abbreviations

AMOC	Atlantic meridional overturning circulation
BSE	bulk silicate Earth
CE	common (or current) era
CIESM	Mediterranean Science Commission (Commission Internationale pour l'Exploration Scientifique de la Méditerranée)
CP	chemically pure
CRDS	cavity ring-down laser spectroscopy
CRM	confocal Raman microscopy
DSC	differential scanning calorimetry
DSDP	Deep Sea Drilling Project
E/I	evaporation/inflow
E/P	evaporation/precipitation
EDX	energy-dispersive X-ray spectroscopy
EPS	extracellular polymeric substance
E	east
FIM	fluid inclusion microthermometry

GC	gas chromatography
GHW	gypsum hydration water
GRA	gamma-ray attenuation
HR-ICP-MS	high resolution inductively-coupled plasma mass spectrometry
IAEA	International Atomic Energy Agency
ICP-OES	inductively-coupled plasma optical emission spectroscopy
ICSD	Inorganic Crystal Structure Database
IRMS	isotope ratio mass spectrometry
IR	infra-red
LN_2	liquid nitrogen
LE	Lower Evaporites
LLNL	Lawrence Livermore National Laboratory
LMWL	local meteroric water line
MC-ICP-MS	multiple-collector inductively-coupled plasma mass spectrometry
MCM	micro-combustion module
MES	Messinian Erosion Surface
MOW	Mediterranean outflow water
MSA	methyl-sulfonic acid
MSC	Messinian Salinity Crisis
MWL	meteroric water line
NARR	North American regional reanalysis
ND	neutron diffraction
NMR	nuclear magnetic resonance
N	north

ODP	Ocean Drilling Program
OD	outer diameter
P/E	precipitation/evaporation
PLG	primary lower gypsum
RH_n	normalised relative humidity
RLG	resedimented lower gypsum
RS	Raman spectroscopy
SC	supercone
SEM	scanning electron microscopy
SE	south-east
SRM	standard reference material
S	south
TC/EA	high temperature conversion elemental analyzer
TCP	Terminal Classic Period
TGA	thermogravimetric analysis
TIMS	thermal ionisation mass spectrometry
Tm_{ice}	final melting temperature of ice
T	temperature
UA	Upper Abad
UE	Upper Evaporites
UG	Upper Gypsum
VCDT	Vienna-Canyon Diablo Troilite
VPDB	Vienna Pee Dee Belemnite
VSMOW	Vienna Standard Mean Ocean Water

WASP	water analyser sample preparation
W	west
XRD	X-ray diffraction

Nomenclature

α	fractionation factor
α_{eq}	equilibrium fractionation
α_{kin}	kinetic fractionation
Δ	gross change in a variable
δ	incremental change in a variable
ε	transformed fraction as a function of total mass loss
$\lambda_{1/2}$	half life
Ω	electrical resistance
θ	the triple-isotope exponent; $\ln\left(\alpha^{17}\mathrm{O}\right) / \ln\left(\alpha^{18}\mathrm{O}\right)$
$mbsf$	metres below sea floor
R^2	correlation coefficient
D	Deuterium (^{2}H)
d-excess	Deuterium-excess
SI_{gyp}	saturation index of gypsum
F	flux
V	atmospheric water vapour
w	wind-induced turbulence
Xe	fraction of water loss by evaporation with respect to the inflow of a system (0 = no evaporation, 1 = all water is lost to evaporation)

Prefixes

M	mega (10^6)
k	kilo (10^3)
c	centi (10^{-2})
m	milli (10^{-3})
μ	micro (10^{-6})
n	nano (10^{-9})
p	pico (10^{-12})

List of Units

Å	angstrom (0.1 nanometer)
A	ampere
$^{\circ}C$	temperature in degrees centigrade
a	annum
g	gram
h	hour
J	joule
l	litre
M	Molar
mol	mole
m	metre
mbar	unit of pressure; standard atmospheric pressure at sea level is defined as 1013.25 mbar
min	minute
N	normality

pH	logarithm to the base 10 of the reciprocal of the hydrogen ion concentration
ppm	parts per million
ppt	parts per thousand
rpm	revolutions per minute
S	Siemens
s	second
V	volt
wt%	weight percent
yr	year
φ	porosity
%	per cent
‰	per mille, parts per thousand

Chapter 1

Introduction

1.1 Stable water isotopologues

Measurements of stable water isotopologues (e.g. $H_2{}^{16}O$, $H_2{}^{17}O$, $H_2{}^{18}O$, and $HD^{16}O$) have been utilised since the 1950s with the aim of improving our understanding of the hydrological cycle and its links to climate (Urey et al., 1951; Epstein and Mayeda, 1953; Friedman, 1953; Emiliani, 1955; Craig, 1961; Dansgaard, 1964). Water isotopologues differ by their mass and molecular symmetry, resulting in slightly different behaviours during phase transitions. Fractionation processes that lead to the enrichment or depletion of the heavy isotopes (i.e. ^{18}O and D) during phase changes can be quantified if isotope ratios are expressed relative to a standard. The isotopic composition is traditionally given as a deviation from the ocean reservoir, and the delta (δ) notation is used to quantify stable isotopes as relative ratios expressed in parts per thousand (‰):

$$\delta = \left(\frac{R_{Sample}}{R_{Standard}} - 1 \right) \times 1000$$

R_{Sample} and $R_{Standard}$ are the molar ratio of the heavy to light isotopes in the sample and in the Vienna Standard Mean Ocean Water (VSMOW) standard, respectively (Craig, 1961; Dansgaard, 1964).

At first order, variations in oxygen ($\delta^{17}O, \delta^{18}O$) and hydrogen ($\delta D$) isotope ratios occur due to the difference in saturation vapour pressures between the light and heavy isotopes, resulting in an *equilibrium fractionation*. The larger diffusivity of light isotopes with respect to heavy isotopes during evaporation can also results in a *kinetic (non-equilibrium) fractionation* (Gat, 1996). There is an added value in combining $\delta^{18}O$ and δD measurements because kinetic effects have a larger influence on $\delta^{18}O$ than on δD (Merlivat, 1978; Merlivat and Nief, 1967; Risi et al., 2010). The effects of non-equilibrium fractionation are quantified

as the Deuterium excess (d-excess) (Dansgaard, 1964):

$$d\text{-}excess = \delta\mathrm{D} - 8 \cdot \delta^{18}\mathrm{O}$$

where 8 is the reference slope of the meteoric water line (MWL) worldwide. Non-equilibrium fractionation during evaporation causes the fractionation ratio of the two molecules to deviate from the ~1:8 ratio observed under equilibrium conditions. The extent of this deviation is influenced by factors including the relative humidity gradient above the water surface, air and water temperature, and evaporative cooling and turbulence on the water surface (Merlivat and Jouzel, 1979; Cappa, 2003; Gázquez et al., 2018) (Fig. 1.1 A-E).

The measurements of triple oxygen isotopes (^{18}O, ^{17}O, ^{16}O) allows derivation of the parameter ^{17}O-excess (Barkan and Luz, 2007; Luz and Barkan, 2010; Steig et al., 2014), expressed in per meg (10^{-3} ‰):

$$^{17}\mathrm{O}\text{-}excess = \left(\ln\left[\delta^{17}\mathrm{O} + 1\right] - 0.528 \ln\left[\delta^{18}\mathrm{O} + 1\right]\right)$$

The value of 0.528 has been proposed to describe the δ^{17}O and δ^{18}O global MWL relationship (Luz and Barkan, 2010). The trajectory of δ^{18}O and ^{17}O-excess in evaporated water is relatively insensitive to temperature and salinities below 100 g l^{-1} (Luz and Barkan, 2010; Passey et al., 2014); however, it is significantly affected by other parameters such as atmospheric relative humidity (Fig. 1.1 F-I) (Gázquez et al., 2018). As δ^{17}O, δ^{18}O and δD show different sensitivities to equilibrium and kinetic fractionation processes, the simultaneous measurement of triple oxygen and hydrogen isotopes (and utilisation of the derived d-excess and ^{17}O-excess parameters) in climatic archives can provide detailed information on climate conditions of the past.

1.2 Statement of the problem

Geochemical proxies derived from climatic archives are used to reconstruct past climatic variations. To this end, examination of the mineral chemistry of substrates that derive a common atom with the water from which they form should be directly linked to the changes in water balance of the regional environment during formation. An ideal proxy should vary quantitatively and with respect to variations in the climatic parameter of interest. Derived palaeoclimatic interpretations from traditional climate proxy archives are often under-constrained, however, due to a combination of (i) assumptions that must be made to isolate the parameter of interest, and (ii) analytical constraints. Below, the limitations of the traditional methodologies used to reconstruct palaeoclimate variations are described, and

a new method that permits the simultaneous measurements of triple oxygen and hydrogen isotopes in hydrated minerals is proposed.

1.2.1 Limitations of traditional proxy archives

The majority of studies that attempt to quantify past climate changes use either oxygen-bearing proxies (such as carbonate) or hydrogen-bearing proxies (such as plant waxes and alkenones). Few studies to date have combined the two isotope systems, because the materials used for analysis preclude simultaneous measurement of the multiple isotopologues of water. Indeed, the relative influence of climatic variables such as temperature, relative humidity and wind turbulence on a water body are impossible to deconvolve from the individual analysis of δ^{18}O or δD (Fig. 1.1). Even when δ^{18}O and δD are combined, the relationship between the isotope pairs is complicated if two or more of the climate variables are unknown, preventing a unique, quantitative interpretation of the environmental parameters influencing the water body. Additionally, in evaporative systems such as marine sabkhas, the isotope 'salt effect' affects the activity ratios between free water and water in ionic hydration shells, thus producing different hydrogen and oxygen isotope fractionations (Feder and Taube, 1952; Taube, 1954; Sofer and Gat, 1972; Driesner et al., 2000; Herwartz et al., 2017).

The isotopic content of the proxies themselves may also be controlled by:

i. Temperature-dependent fractionation factors (Urey, 1947; Epstein et al., 1953; Epstein and Mayeda, 1953; Friedman and O'Neil, 1977; Chappell and Shackleton, 1986);

ii. Mineralogy (e.g. Tarutani et al., 1969);

iii. The pH of the solution (Deuser et al., 1968; Zeebe and Wolf-Gladrow, 2001);

iv. Any kinetic effects manifested during mineral precipitation (McConnaughey, 1989) and, in the case of carbonate minerals, additional biochemical 'vital' effects (Gat, 1996).

Because both palaeoclimatic archives and the water from which they form are sensitive to several climatic and non-climatic processes and conditions, some of which may be unknown, isotopic datasets can often be underdetermined.

Combined analysis of δ^{17}O, δ^{18}O and δD is a powerful method to estimate hydrologic changes quantitatively because hydrogen and triple oxygen isotopes each undergo slightly different fractionation during evaporation, leading to changes in the derived d-excess and ^{17}O-excess parameters (Surma et al., 2015; Herwartz et al., 2017; Gázquez et al., 2017b,

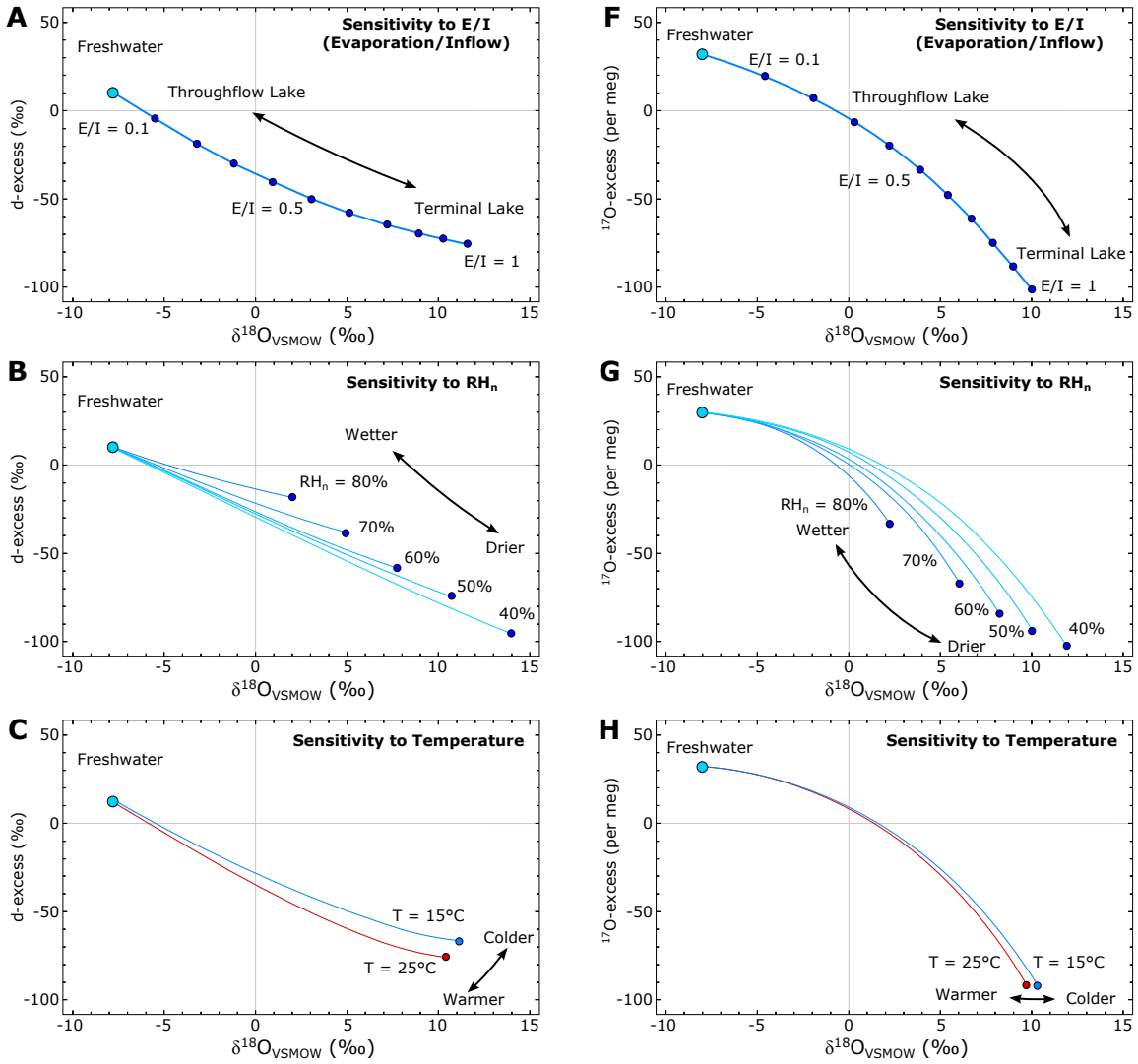

Fig. 1.1a. Sensitivity of d-excess vs. $\delta^{18}O$ (A-E) and ^{17}O-excess vs. $\delta^{18}O$ (F-J) to different environmental parameters during the evaporation of a water body in partial equilibrium with atmospheric vapour (after Gázquez et al. 2018). The isotopic composition of the freshwater endmember is $\delta^{18}O$ = −8‰; δD = −54‰; d-excess = 10‰; ^{17}O-excess = 30 per meg. When all parameters remain constant, the isotopic compositions of water pools with different ratios of Evaporation/Inflow (E/I) are also represented in figures A and F. The isotopic composition of a terminal lake has then been modelled under different conditions of normalised relative humidity (RH_n) (B and G), temperature (C and H), boundary layer turbulence (created by wind) (D and I), and the degree of equilibrium between the atmospheric vapour and the freshwater input (E and J).

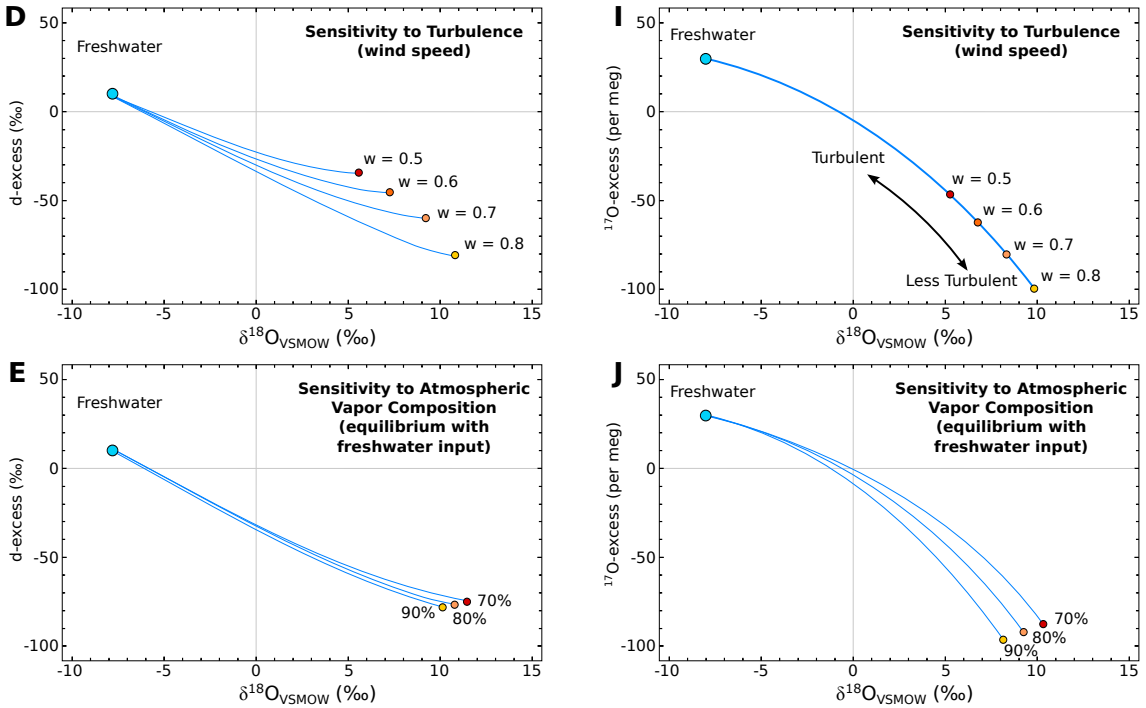

Fig. 1.1b. Continuation of Fig. 1.1a. See left.

2018). The differing sensitivities of $\delta^{17}O$ and $\delta^{18}O$ to equilibrium and kinetic fractionation processes means that the ^{17}O-excess parameter provides a greater constraint on hydrological conditions than does the analysis of $\delta^{18}O$ and/or δD alone (Barkan and Luz, 2007) (Fig. 1.1 F-J). The main advantages of the ^{17}O-excess parameter over d-excess are:

i. The ratio of the triple-isotope exponent, θ ($\ln {}^{17}\alpha / \ln {}^{18}\alpha$), is almost identical within a 30°C temperature range, making ^{17}O-excess largely temperature-independent (Barkan and Luz, 2005; Cao and Liu, 2011; Surma et al., 2015); and

ii. ^{17}O-excess is insensitive to elevated salt concentrations; while both cations and anions affect the $^{2}H/^{1}H$ salt effect (Driesner et al., 2000), making d-excess a function of the salt composition, the activity ratios of $^{18}O/^{16}O$ and $^{17}O/^{16}O$ are both controlled by the cations and thus ^{17}O-excess should remain unaffected (Sofer and Gat, 1972; Herwartz et al., 2017).

The significant benefits of the triple oxygen isotope system have resulted in its recent application to reconstruct evaporative processes, such as the effect of evapotranspiration photosynthesis on atmospheric O_2 (Landais et al., 2006; Li et al., 2017b), glacial-interglacial hydrologic conditions at the ocean surface (e.g. Landais et al., 2008), and the parent waters

of carbonates (e.g. Benedix et al., 2003; Clayton and Mayeda, 1984; Farquhar, 1998; Passey et al., 2014), as well as being employed as a tracer of biosphere productivity (e.g. Luz et al., 1999) and to examine water-rock interactions (Pack and Herwartz, 2014). To date, however, analysis of the full suite of water isotopologues has been limited to polar ice cores (e.g. Risi et al., 2010; Landais et al., 2012; Winkler et al., 2013) and modern environments such as lakes (e.g. Surma et al., 2015, 2018) where the material analysed is the water substance itself. Because the predicted trends of both d-excess and ^{17}O-excess in evaporating waters display different responses to climate variables, they can be evaluated individually using iterative computer models to deconvolve individual hydrological parameters (e.g. Gázquez et al., 2018). If analysed together, triple oxygen and hydrogen isotopes and their derived parameters provide a powerful constraint on the hydrological conditions during proxy formation.

1.2.2 Analytical limitations

Despite the benefits of measuring all water isotopologues, analytical challenges have prevented the widespread application of ^{17}O-excess to date. Firstly, ^{17}O comprises less than 0.04% of all naturally occurring stable oxygen, resulting in small signal variability. Measuring ^{17}O therefore requires instrumentation capable of extremely high precision (better than 0.01‰, or 10 per meg). Secondly, traditional isotope ratio mass spectrometry (IRMS) does not permit the direct measurement of ^{17}O-excess from water or via conversion to CO_2 (often used for measuring δ^{18}O in water) due to isobaric interferences; the ^{17}O-containing CO_2 isotopologue, $^{12}C^{17}O^{16}O$ (~760 ppm), is masked by the more abundant $^{13}C^{16}O_2$ isotopologue (~11,000 ppm) of the same nominal mass (Passey et al., 2014). Fluorination chemistry (e.g. using cobalt fluorine) has therefore been used to convert H_2O to O_2 for measurement via IRMS:

$$2\,H_2O + 4\,CoF_3 \longrightarrow O_2 + 4\,CoF_2 + 4\,HF$$

with the resultant O_2 measured for long time periods to produce the required precision. The conversion of H_2O to O_2 also precludes the simultaneous measurement of oxygen and hydrogen isotopic ratios, thereby requiring multiple instrumental calibrations and increasing potential for isotopic fractionation during sample preparation. These analytical difficulties, coupled with the numerous safety risks associated with the fluorination method, have resulted in only a small number of laboratories measuring δ^{17}O in water.

Recent developments in cavity ring-down laser spectroscopy (CRDS) have now made it possible to measure water isotopes directly as H_2O vapour at a precision comparable to or better than IRMS. CRDS is a time-based measurement system that uses a laser to

quantify spectral absorption lines unique to $H_2{}^{16}O$, $H_2{}^{17}O$, $H_2{}^{18}O$, and $HD^{16}O$ in an optical cavity. Unlike IRMS, CRDS allows simultaneous measurement of oxygen and hydrogen isotopic ratios without the need to convert the water into another gas, thereby minimising the opportunity for isotopic fractionation (Gázquez et al., 2015). Measuring all isotopologues on a single phase (H_2O vapour) also simplifies calibration, resulting in greater precision and accuracy than is achievable by IRMS, especially for hydrogen isotopes.

1.3 Novel approach

Many minerals found in nature and in the geological record incorporate molecular water (H_2O) or hydroxyl (OH) into their crystal structures during formation, theoretically providing a vector to simultaneously analyse triple oxygen and hydrogen isotopes through the geological record. Examples of hydrated (or hydoxylated) minerals include iron oxides (goethite), phyllosilicates, and evaporitic minerals. While phyllosilicates and goethite are both predominantly the product of chemical weathering reactions, evaporites are water-soluble mineral sediments (Goldschmidt, 1937) that form from the concentration and crystallisation of ions from an aqueous solution (Hardie and Eugster, 1980). The isotopic composition of the crystallisation water of these hydrated minerals has the potential to provide information on the isotopic composition of waters from which they formed (Horita, 1989; Hodell et al., 2012).

The oxygen and hydrogen isotopes of the original fluid from which a hydrated mineral precipitated can be determined if:

i. isotopic equilibrium is achieved between the mother and hydration water;

ii. the fractionation factors (α) during mineral formation are known (and temperature-independent or the temperature dependence is known);

$$\alpha = \frac{\left({}^{18}O/{}^{16}O\right)_{crystal\text{-}water}}{\left({}^{18}O/{}^{16}O\right)_{mother\text{-}water}} \quad or \quad \frac{\left({}^{17}O/{}^{16}O\right)_{crystal\text{-}water}}{\left({}^{17}O/{}^{16}O\right)_{mother\text{-}water}} \quad or \quad \frac{\left(D/H\right)_{crystal\text{-}water}}{\left(D/H\right)_{mother\text{-}water}}$$

iii. and no isotope exchange has occurred between environmental and hydration water after mineral deposition (Hodell et al., 2012).

If all conditions are met, the measurement of oxygen and hydrogen isotopes and their derived parameters (d-excess and ^{17}O-excess) could provide quantitative hydrological information, including changes in atmospheric relative humidity, wind velocity and water source, which have been difficult to achieve and calibrate in traditional archives (e.g. Gázquez

et al., 2018). Additionally, hydrated minerals have a greater occurrence, both geographically and throughout time, compared to all other archives that yield triple oxygen and hydrogen isotope data (e.g. Warren, 2016).

Theoretically, gypsum ($CaSO_4 \cdot 2\,H_2O$) is a favourable mineral for the study of hydration water systematics both because of its widespread occurrence (e.g. Warren, 2016), and because the structurally bonded water in gypsum is thought to form in equilibrium with the ambient gypsum mother water during gypsum formation (e.g. Sofer, 1978; Hodell et al., 2012; Herwartz et al., 2017). The corresponding isotope fractionation factors for $D/^{1}H$ and $^{18}O/^{16}O$ have been traditionally viewed as temperature- (Gonfiantini and Fontes, 1963; Hodell et al., 2012) and salinity- (Sofer and Gat, 1972; Horita, 1989) independent, but the $^{17}O/^{16}O$ fractionation factor has not been determined.

Despite the abundance of gypsum in the sedimentary record, relatively few studies have utilised gypsum hydration water (GHW) for palaeoenvironmental reconstruction. Concerns that the isotopic composition of GHW can be modified by post-depositional recrystallisation (i.e. dissolution and reprecipitation) or isotopic exchange with environmental water have limited the use of GHW as a palaeoenvironmental proxy to date (e.g. Pierre and Fontes, 1978; Sofer, 1978), although other studies have indicated gypsum displays relatively low rates of exchange (e.g. Charola et al., 2007; Hodell et al., 2012). The post-depositional isotopic exchange of GHW can be examined via exchange and dehydration experiments (see Section 2.5) and by comparison to other climatic proxy datasets (e.g. Hodell et al., 2012; Grauel et al., 2016; Li et al., 2017a). Additionally, positive correlation between proxy and GHW indicates that, at least in some cases, the primary isotopic composition of GHW is preserved in time (Hodell et al., 2012; Grauel et al., 2016; Gázquez et al., 2017a).

As well as the potential derivation of all isotopes of the water from which gypsum precipitated, it is also possible to use GHW to derive palaeo-water temperatures in environments where gypsum and carbonate co-precipitate. The $\delta^{18}O$ of calcite ($\delta^{18}O_{cal}$) or aragonite ($\delta^{18}O_{arag}$) is dependent upon both the temperature (T) and the $\delta^{18}O$ of the water ($\delta^{18}O_{water}$) from which the carbonate was precipitated (Urey et al., 1951; Epstein et al., 1953). Tandem measurements of both GHW and carbonate $\delta^{18}O$ that were deposited concurrently permit the deconvolution of the $\delta^{18}O$ carbonate signal into its temperature and $\delta^{18}O$-water components via carbonate palaeo-temperature equations (Hodell et al., 2012). For example, calculation of the temperature at which the calcitic shells form can be conducted using the equation of Anderson and Arthur (1983):

$$T\,(^{\circ}C) = 16 - 4.14 \cdot \left(\delta^{18}O_{cal\,(PDB)} - \delta^{18}O_{water\,(SMOW)}\right) + 0.13 \cdot \left(\delta^{18}O_{cal\,(PDB)} - \delta^{18}O_{water\,(SMOW)}\right)^{2}$$

and calculation of the temperature at which the aragonitic shells form can be conducted

using the equation of Grossman and Ku (1986):

$$\mathrm{T}\,(^{\circ}C) = 21.8 - 4.59 \cdot \left(\delta^{18}\mathrm{O}_{arag\,(PDB)} - \delta^{18}\mathrm{O}_{water\,(SMOW)}\right)$$

This method provides a powerful constraint for oxygen isotope palaeothermometry (Hodell et al., 2012; Grauel et al., 2016).

1.4 Objectives and thesis outline

The advent of novel analytical methods such as CRDS coupled with the ability to extract and simultaneously analyse all isotopes of water from a geologically abundant mineral such as gypsum provides an exciting new direction for palaeoclimatological research. The opportunity to pioneer novel methods for palaeoclimatic reconstruction led Professor D. A. Hodell to bring together a multidisciplinary team of scientists in geochemistry, mineral physics, and *ab initio* molecular dynamics to study hydration water in minerals.

The primary objective of this thesis is to understand how the chemistry of the fluids from which gypsum formed is reflected in the geochemistry and the mineralogy of deposits in geologic space and time. This research specifically provides quantitative and semi-quantitative information to establish criteria for the reconstruction of the palaeoenvironmental conditions during the deposition of gypsum in marine and non-marine environments. To achieve this, this thesis examines the triple oxygen and hydrogen isotopic composition of GHW, and the isotopic and elemental variations of both traditional and novel tracers (including calcium and barium isotopes) to deduce the origin of ancient gypsum deposits. The work presented in this thesis would not have been possible without the assistance of the multiple members of the 'Water Isotopes in Hydrated Minerals' team. To provide clarity, the work carried out by Nicholas P. Evans is highlighted at the beginning of each chapter or section.

This thesis is structured as follows:

Chapter 2 outlines the mechanisms of gypsum formation and water incorporation upon precipitation. The chapter includes a description of the methods that have been developed over the course of this research to extract and analyse GHW, as well as the calculation of the fractionation factors between gypsum and free water. The conditions under which gypsum's structurally-bound water can undergo exchange with secondary waters are subsequently discussed, including primary research into the thermal dehydration mechanics of gypsum at elevated temperatures. This work provides a basis on which to study GHW as a proxy of the actual isotopic composition of palaeo-waters, and to provide quantitative information

about the relative effects of climatic factors, such as humidity, precipitation, and temperature change at the time of gypsum formation in evaporative environments.

Chapter 3 describes the application of the novel geochemical method to reconstruct the triple oxygen and hydrogen isotopes of palaeo-lake water, specifically to gypsum that was deposited during peak drought conditions that occurred between 600 and 1100 AD on the Yucatán Peninsula, Mexico. This period included the Terminal Classic Period when the Classic Maya Civilisation of Mesoamerica collapsed (Hodell et al., 1995; Kennett et al., 2012). Our data provide a complete and direct archive of hydrological conditions that have previously been limited to ice core records.

The measurement of all isotopes of water permits the application and use of numerical models, previously limited to modern lakes, to constrain palaeo-lake hydrology, thus providing robust, quantitative estimates of past changes in rainfall and relative humidity. In contrast to a previous estimate that inferred a 'modest drought' based on a less robust method using a speleothem proxy (Medina-Elizalde and Rohling, 2012), mean annual rainfall was found to have decreased between 41% and 54%, with intervals of up to 70%, compared to today. It has also been shown for the first time that relative humidity was between 2-7% lower than present-day conditions during the Terminal Classic Drought.

Chapter 4 outlines the current understanding, discoveries and controversies of the period known as the 'Messinian Salinity Crisis' (MSC; 5.97-5.33 Ma). Interpretation of the depositional environments of the Mediterranean's evaporite facies is critical to producing a reliable interpretation of the MSC. The contribution of continental and marine source waters to Mediterranean brines during precipitation of the 'Primary Lower Gypsum' and 'Upper Gypsum' units are poorly constrained, however, and the factors that trigger the appearance of different evaporite facies are largely unknown. The isotope tracers used to interpret the hydrological history during gypsum deposition are outlined, and the methodologies used in the subsequent chapters are described.

Chapter 5 describes a single-cycle study of Primary Lower Gypsum unit in the Sorbas Basin, South-eastern Spain. The objective was to reconstruct the changing environment of deposition and its relation to astronomically-forced climate change. The $\delta^{18}O$ and δD of GHW and salinity of fluid inclusions were measured in the same samples to test if they record the composition of the mother fluid from which gypsum was precipitated. Water isotopes are highly correlated with fluid inclusion salinity suggesting the hydration water has not exchanged after formation. The relatively low water isotope values and fluid inclusion salinities indicate a significant influence of meteoric water, whereas $\delta^{34}S$, $\delta^{18}O_{SO_4}$ and $^{87}Sr/^{86}Sr$ support a dominantly marine origin for the gypsum deposits. The discrepancy between water and elemental isotope signatures can be reconciled if meteoric

water dissolved previously deposited marine sulfates supplying calcium and sulfate ions to the basin which maintained gypsum saturation. This recycling process accounts for the marine $\delta^{34}S$, $\delta^{18}O_{SO_4}$ and $^{87}Sr/^{86}Sr$ signatures, whereas the low $\delta^{18}O$ and δD values of gypsum hydration water and fluid inclusion salinities reflect the influence of freshwater.

Chapter 6 builds on the methods used in Chapter 5. Here, a high-resolution, multi-isotope approach is utilised to reconstruct the paleo-hydrological dynamics of the Sorbas Basin and the wider Mediterranean region during the first stage of the Messinian Salinity Crisis. Measurements of GHW from 12 cycles of the Primary Lower Gypsum are combined with salinity inferred from gypsum fluid inclusions, $^{87}Sr/^{86}Sr$, $\delta^{44/40}Ca$, $\delta^{34}S$, and $\delta^{18}O_{SO_4}$ in the same samples, as well as isotopic analysis $\delta^{44/40}Ca$, $^{87}Sr/^{86}Sr$, $\delta^{18}O_{carb}$, $\delta^{13}C$ of the interbedded carbonate marls. Results indicate that obliquity-controlled sea level and eccentricity-modulated precession, superimposed on longer-term tectonic restriction of the Mediterranean-Atlantic exchange, together played a significant role in modulating gypsum-marl deposition in the Sorbas Basin. Strontium isotopes in gypsum display a gradual, but non-unidirectional, divergence from the seawater curve up-section, with slight reversals in the general trend of decreasing $^{87}Sr/^{86}Sr$ at ~5.84 Ma and 5.72 Ma. Maximum divergence of $^{87}Sr/^{86}Sr$ from the seawater curve, as well as anomalous authigenic carbonate mineralogy (dolomite) and high $\delta^{18}O_{carb}$ is coincident of glacial stage TG20 and an eccentricity minimum at ~5.75 Ma. Calcium isotopes track the variability in $^{87}Sr/^{86}Sr$, overprinted by Rayleigh fractionation effects. The non-unidirectional changes in strontium and calcium isotopes in combination with the patterns of the expression (i.e. thickness and facies) of the cycles in the Sorbas section indicate that sea level variability influenced basin hydrology.

Chapter 7 investigates the origin of gypsum deposition of both onshore and deep basin deposits in the Mediterranean basin during the last stage of the MSC (5.55-5.33 Ma). Strontium, calcium and barium isotope data obtained from the onshore Upper Gypsum have significantly lower values than data obtained from the Primary Lower Gypsum deposits, whereas oxygen and hydrogen isotopes of GHW display higher values. These data demonstrate that the onshore Upper Gypsum deposits formed from the intense evaporation of a dominantly freshwater fluid, during a period where the connection to the Atlantic was periodic and highly restricted. The deep-basin 'Upper Evaporites' from Deep Sea Drilling Project (DSDP) / Ocean Drilling Program (ODP) sites 372 and 654 are characterised by similar strontium, calcium and sulfate isotope values to those of the onshore Upper Evaporites. The deep basin water isotope data deviates from the majority of the onshore deposits, however, indicating that variable and heterogeneous hydrologic conditions characterised the deep basins during evaporite formation.

Chapter 2

Calcium Sulfate Systematics

2.1 Introduction

The isotopic composition of the crystallisation water of gypsum can potentially be utilised as a palaeoclimatic proxy to trace geological and hydrogeological processes (e.g. Fontes and Gonfiantini, 1967; Matsubaya and Sakai, 1973; Sofer, 1978). To examine the potential for gypsum and its structural hydration water to accurately record the oxygen and hydrogen isotopic signature of the fluid from which it formed, it is important to understand the mechanisms of gypsum formation and how water is incorporated into the mineral during crystallisation. Knowledge of the associated gypsum-water fractionation factors (α) is particularly crucial, as small deviations in assumed $\alpha^{18}O_{gypsum\text{-}water}$, $\alpha^{17}O_{gypsum\text{-}water}$, and $\alpha D_{gypsum\text{-}water}$ result in variability that impacts the derived d-excess and ^{17}O-excess parameters, thus affecting the quantitative calculation of environmental conditions during formation. To interpret the water isotope signatures, the complete extraction and accurate measurement of the gypsum hydration water (GHW) and the isotopic ratios is fundamental in providing reliable information about the conditions under which the gypsum formed and any subsequent interaction with other fluids after deposition.

In this chapter, the mechanisms of calcium sulfate formation are outlined to provide a framework to understand the conditions under which gypsum forms (Section 2.2). Subsequently, the development of a semi-automated procedure to extract GHW and measure the evolved water by cavity ring-down laser spectroscopy (CRDS) is discussed (Section 2.3). The methodology presents several analytical advantages over earlier methods, including better long-term precision, higher sample throughput, reduced sample size and less memory effect between consecutive samples. Using this methodology, precise and accurate isotope fractionation factors for gypsum and water ($\alpha^{18}O_{gypsum\text{-}water}$, $\alpha^{17}O_{gypsum\text{-}water}$ and $\alpha D_{gypsum\text{-}water}$) are calculated (Section 2.4). Finally, the dehydration of gypsum and sub-

sequent ion exchange mechanisms are examined to ascertain the ability of gypsum to record the isotopic signature of the fluid from which it formed and the range of environmental conditions over which it is stable (Section 2.5).

2.2 Calcium sulfate formation

2.2.1 Calcium sulfate solubility and thermodynamic stability

Calcium sulfate can exist in various structural forms and the $CaSO_4$-H_2O system has been classically characterised into the three main groups:

i. calcium sulfate dihydrate, *gypsum* ($CaSO_4 \cdot 2H_2O$) with 20.9 wt% water;

ii. calcium sulfate hemihydrate, *bassanite* ($CaSO_4 \cdot 0.5H_2O$) with ~6.2 wt% water, and;

iii. *anhydrite* ($CaSO_4$) (Fig. 2.1).

Other intermediate and complimentary crystalline phases of calcium sulfate have also been reported. These include differing forms of hemihydrate (α and β $CaSO_4 \cdot 0.5H_2O$ and $CaSO_4 \cdot nH_2O$ where $0 < n < 1.0$, $n \neq 0.5$), distinguished on the basis of their specific surface area, crystal sizes, habit and surface topography (Freyer and Voigt, 2003; Ballirano and Melis, 2009; Hildyard et al., 2011), whereas anhydrite can be subcategorised into soluble (AIII$-CaSO_4$ or γ-$CaSO_4$) and insoluble phases (AI$-CaSO_4$ or α-$CaSO_4$ and AII$-CaSO_4$ or β-$CaSO_4$) (Christensen et al., 2008; Lou et al., 2011; Prieto-Taboada et al., 2014). Soluble anhydrite (γ-$CaSO_4$) derives its name from its metastable nature, and hydrates to bassanite under normal atmospheric conditions (e.g. Harrison, 2012). When exposed to temperatures above ~300°C, γ-anhydrite transforms into the insoluble β-anhydrite and no longer rehydrates (Prieto-Taboada et al., 2014).

The direct precipitation of the different calcium sulfate phases is thought to be dependent on the temperature, salinity and the supersaturation of calcium and sulfate in the mother solution (e.g. Ostroff, 1964; Hardie, 1967; D'Ans, 1968; Billo, 1987; Freyer and Voigt, 2003; Ossorio et al., 2014) (Fig. 2.2). At a given temperature, salinity and supersaturation, the solid phase with the lowest solubility should represent the stable phase (Freyer and Voigt, 2003). Early solubility measurements and thermodynamic calculations indicated that gypsum should precipitate from pure calcium sulfate aqueous solutions below temperatures of ~50°C (D'Ans, 1968; Hardie, 1967), whereas anhydrite should directly precipitate above this temperature. Determination of the stability region of each of the calcium sulfate phases has proved elusive, however, due to inconsistencies between solubility measurements and

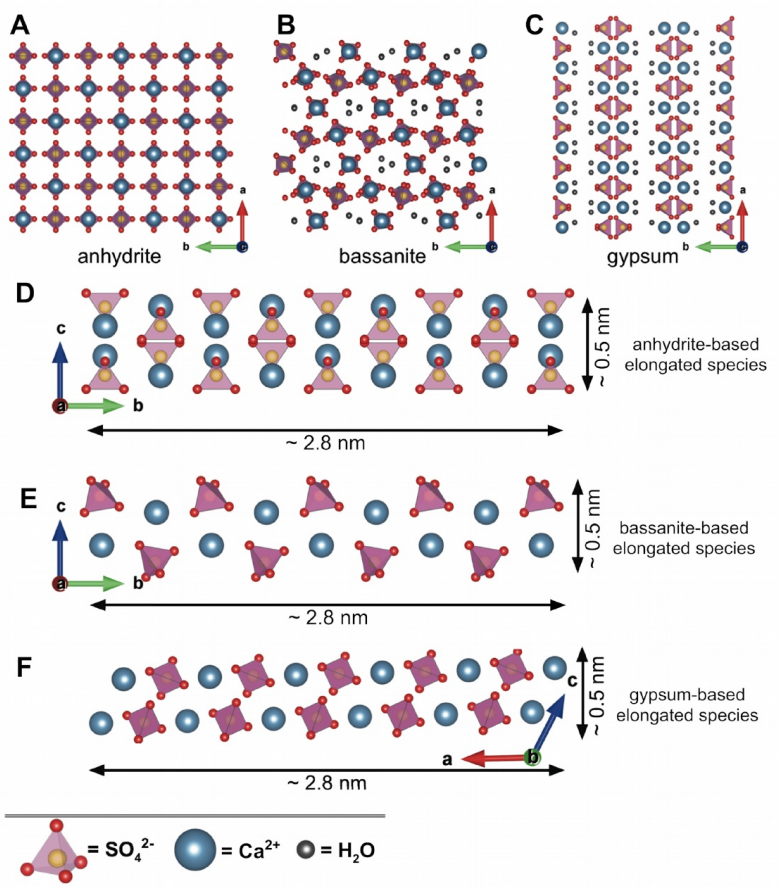

Fig. 2.1. Structural projections (along the c-axis) of the three main calcium sulfate phases: anhydrite (AII form) (**A**), bassanite (**B**), and gypsum (**C**). Tetrahedra are sulfate ions, large spheres are Ca^{2+} ions, and small spheres are water molecules. Structural projection (along the a-axis) of anhydrite (AII form) (**D**), bassanite (**E**), and gypsum (**F**) (from Stawski et al., 2016).

thermodynamic predictions of stability, and data obtained in laboratory precipitation studies (e.g. Billo, 1987; Freyer and Voigt, 2003; Ossorio et al., 2014). Experimental data indicates that γ-anhydrite does not directly precipitate within its predicted stability field, and that gypsum forms at temperatures above its theoretical equilibrium (Ossorio et al., 2014). The intrinsic slow growth dynamics of γ-anhydrite mean that even when stable microscopic anhydrite nuclei are formed in an aqueous solution, a longer time period is required for volumetrically significant amounts of anhydrite to form (Ossorio et al., 2014).

Direct gypsum formation from aqueous solutions was originally assumed to occur via a single-step process following the classical nucleation and growth mechanism (e.g. Packter, 1974). Recent work using synchrotron-based in situ X-ray techniques has shown that gypsum precipitation occurs via a predictable four-stage solution-based nucleation and growth

pathway (Stawski et al., 2016). During this process, amorphous calcium sulfate and/or nano-crystalline bassanite forms as a precursor to gypsum (Saha et al., 2012; Van Driessche et al., 2012; Wang et al., 2012). If the water volume available during formation is limiting, the reaction will be directly halted at the intermediate point and bassanite will emerge as the bulk crystalline phase (Stawski et al., 2016). Low water activity also increases the residence time of the bassanite precursor: in highly saline solutions (e.g. water activity ~0.8), bassanite is the primary precipitate for up to 2 months at 80°C before turning into γ-anhydrite (Ossorio et al., 2014; Rapin et al., 2016). At higher water activities and lower temperatures, bassanite is unstable and will fully hydrate to gypsum (Badens et al., 1998) (Fig. 2.3). Due to the instability bassanite and and slow growth kinetics of γ-anhydrite formation, gypsum is the major primary precipitate in natural environments on Earth.

In summary, the major and volumetrically most important gypsum deposits worldwide are formed from direct deposition from a solution saturated with respect to gypsum at temperatures below ~60°C, while smaller volumes of gypsum may form via the hydration of γ-anhydrite.

2.2.2 Natural ion sources for calcium sulfate formation

The formation of calcium sulfate in natural environments is dependent on both the proportion of specific dissolved ions in a water body, and the mechanism that results in the separation of dissolved calcium sulfate from the water solute (i.e. promoting precipitation). The evaporation of waters in (semi-) enclosed environments is the most common mechanism that results in a rise in concentration of dissolved ions in a water solution. 'Freshwater', containing >1 $g\,l^{-1}$ total dissolved solids, can be evaporatively concentrated so that the waters become brackish, saline, brine, and finally a bittern (Bąbel and Schreiber, 2014). While these terms are not defined unequivocally, brackish commonly refers to the transitional zone between marine and freshwater, saline waters have salinities similar to or greater than seawater (35 $g\,l^{-1}$ total dissolved solids), brines are waters that contain sodium chloride and are significantly more saline than seawater, and bitterns are usually defined as brines that are stripped of their sodium chloride content (Bąbel and Schreiber, 2014).

The ion source for all evaporite deposits originate from soluble chemical compounds (salts) dissolved in natural waters on Earth. There are many natural types of salt-containing waters, including lakes, rivers, and groundwater; the ocean, however, is the volumetrically largest source (~47.6×10^{18} kg of salts; Hay et al., 2006). Of the many elements dissolved in seawater, Na^+ (30.5), Cl^- (55.1), $SO_4{}^{2-}$ (7.7), Mg^{2+} (3.7), Ca^{2+} (1.2), K^+ (1.1), and $HCO_3{}^-$ (0.4) (proportion of total salts by weight, in %, is given in brackets; Hay et al., 2006) create the stable and volumetrically significant salts as the product of seawater evaporation

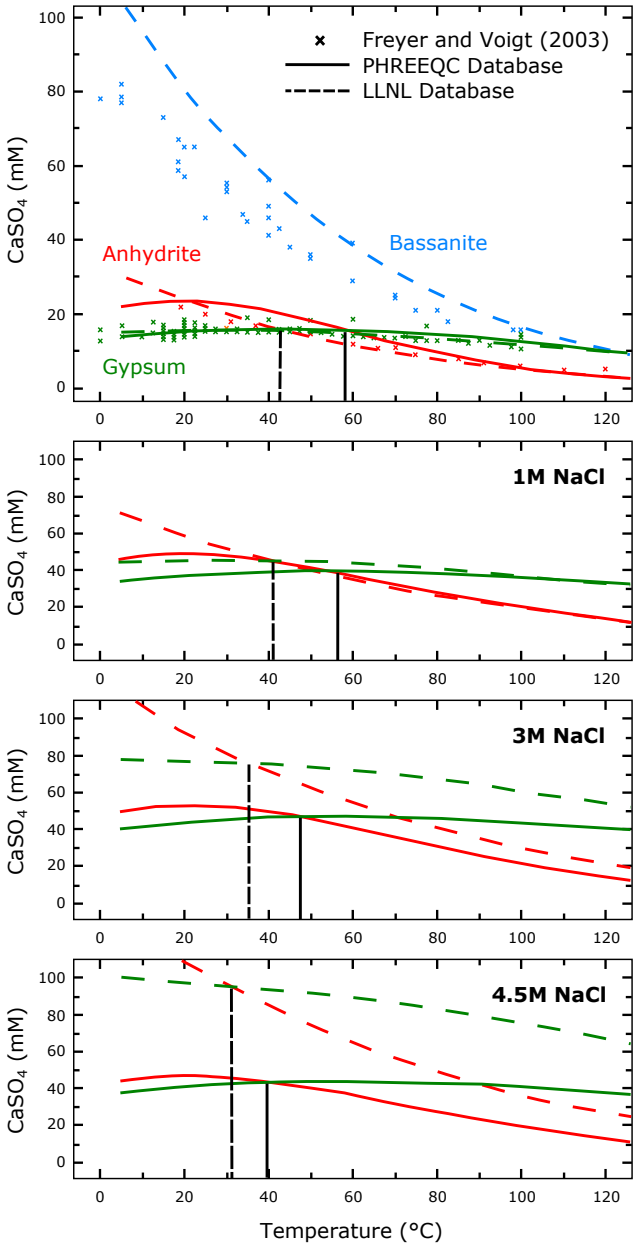

Fig. 2.2. Solubility curves of gypsum, bassanite and anhydrite as a function of temperature (0°C to 120°C) and salinity (0 M, 1 M, 3 M and 4.5 M NaCl) calculated from experimental and modelled data (after Ossorio et al., 2014). Solubility data (crosses) were obtained from Freyer and Voigt (2003) and the references therein. Calculated solubility curves of the calcium sulfate phases were obtained from the PHREEQC database (solid lines) and the Lawrence Livermore National Laboratory (LLNL) database within operated within PHREEQC (dashed lines) (Parkhurst and Appelo, 2013). Black vertical lines mark the gypsum-anhydrite transition temperature obtained with the PHREEQC (solid lines) and LLNL (dashed lines) databases.

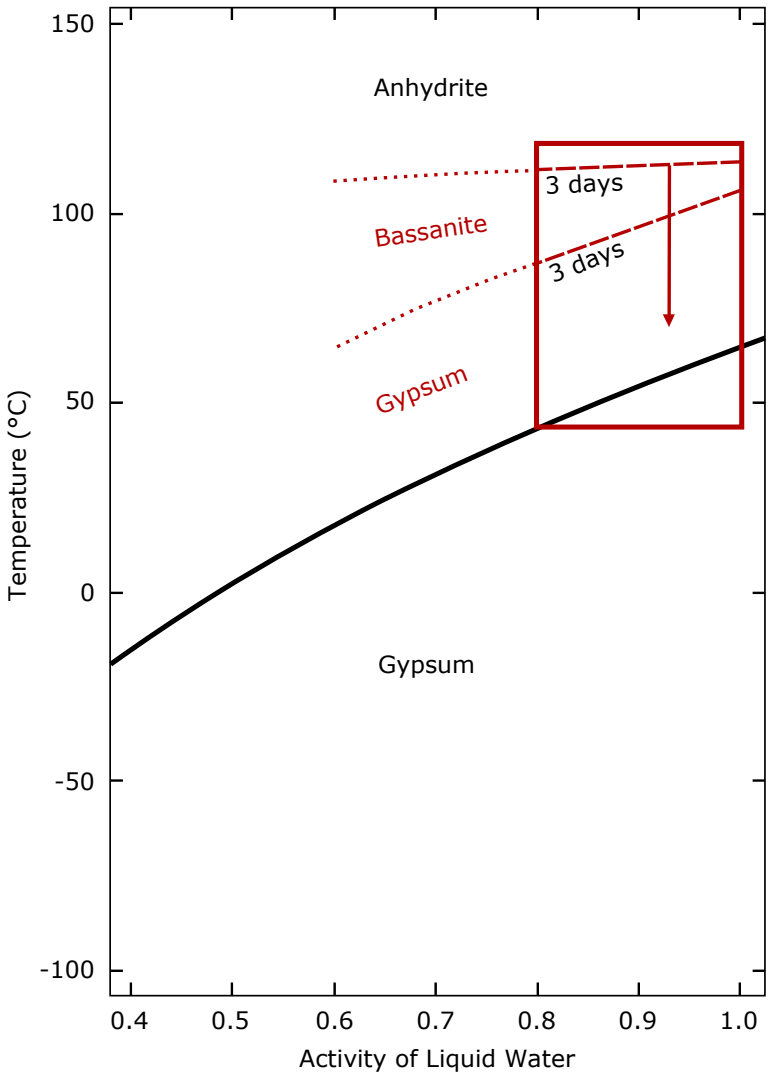

Fig. 2.3. Calcium sulfate stability as a function of temperature and water activity in aqueous solution (after Rapin et al., 2016). The solid black line represents the gypsum-anhydrite transition (Freyer and Voigt, 2003). Kinetic boundaries (i.e. boundaries delimiting the phases found in solution after a specific timing) from Ossorio et al. (2014) are reported (red dashed lines) and represent the precursor phases found in solution after 3 days, with subsequent evolution path leading to the formation of anhydrite (red arrow). The red box denotes the range covered by the experiments of Ossorio et al. (2014). Extrapolated trends to lower water activities are shown in dotted red lines, and are only indicative.

(see Bąbel and Schreiber, 2014).

The precipitation of evaporitic minerals induced by the evaporative concentration of seawater results in the modification of the ionic composition of the mother fluid due to the combined constraints of equilibrium and mass balance (Eugster, 1980; Bąbel and Schreiber, 2014). During equilibrium crystallisation, both the ion activity product of the solution must remain constant (at constant pressure and temperature), and the appropriate molar proportions of ions must be removed from the solution (Hardie and Eugster 1971; Eugster and Hardie, 1978). Thus, during the evaporation of modern seawater, the concentrations of major ions systematically change in a predictable way and result in three stages of mineral precipitation (Usiglio, 1849);

$$calcium\,carbonate \longrightarrow calcium\,sulfate \longrightarrow sodium\,chloride$$

This sequence is also well known from geochemical studies in both solar saltworks (Fig. 2.4) and laboratory seawater evaporation experiments (e.g. Schreiber and Kingsman, 1975; Warren, 1982; Ortí et al., 1984; McCaffrey et al., 1987).

Calcium carbonate: Evaporitic alkaline earth carbonates are the first to precipitate at elevated salinities (>35‰) induced by evaporation of seawater due to their relatively low solubility in water. Calcium carbonate precipitation eliminates $HCO_3{}^-$ ions from the solution according to the reaction:

$$Ca^{2+} + 2\,HCO_3{}^- \longrightarrow CaCO_3 + H_2O + CO_2$$

The greater the disparity between the initial concentration of Ca^{2+} and $HCO_3{}^-$ ion in solution, the more rapid the enrichment-depletion process will be (Eugster, 1980; Holland et al., 1996; Bąbel and Schreiber, 2014). Thus, fluids that are initially rich in carbonate will experience a relative enrichment of carbonate and depletion of calcium and vice versa. As modern seawater contains a relatively high $Ca^{2+}/HCO_3{}^-$ ratio, the evaporated seawater brine will experience a relative depletion of carbonate and enrichment of calcium after calcite precipitation (Eugster, 1980; Bąbel and Schreiber, 2014).

During the precipitation of calcium carbonate the Mg/Ca ratio in the solution also increases, first producing low-Mg calcite or aragonite ($CaCO_3$) (Sandberg, 1983), and eventually high-Mg calcite $(Ca, Mg)CO_3$ and protodolomite ($CaMg(CO_3)_2$) (Eugster, 1980). In natural environments, several other nonevaporite-driving mechanisms commonly induce $CaCO_3$ deposition within a basin (e.g. Decima et al. 1988). Evaporation-driven precipitation of carbonate occurs up to the salinity characterising the precipitation of gypsum (i.e. ~140‰).

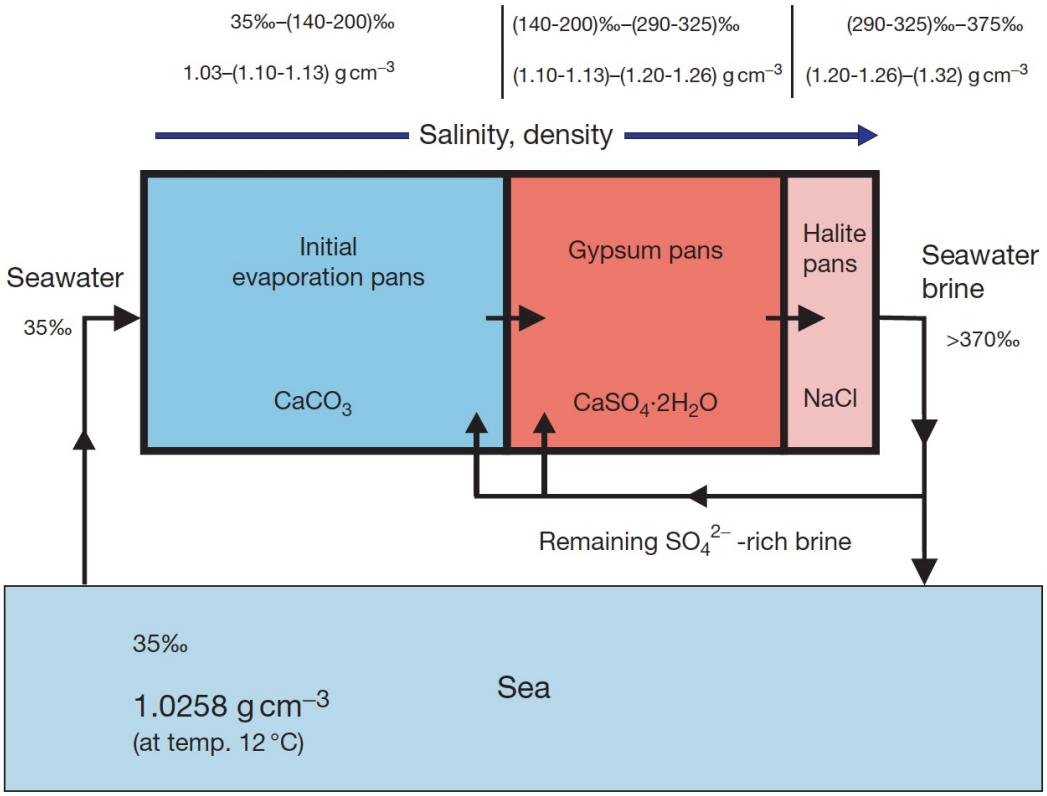

Fig. 2.4. Schematic of a marine saltwork, displaying the evaporation pathway of seawater with increasing salinity and water density, modified after Ortí (2011) and Bąbel and Schreiber (2014). Remaining sulfate-rich brine flows back to the ocean or, in some saltworks, back to the concentration pans to promote more precipitation of gypsum, which crystallises due to a mixture of brines (Bąbel and Schreiber, 2014).

Calcium Sulfate: Modern seawater contains relatively high Ca^{2+}/HCO_3^- and SO_4^{2-}/HCO_3^- ratios. As such, Ca^{2+} is not fully consumed during the prior precipitation of $CaCO_3$, resulting in the supersaturation of the brine for gypsum during evaporation. Gypsum saturation occurs at salinities of ~140‰ when ~80% of the original seawater has evaporated (Ortí, 2011; Rossi et al., 2015). The resultant deposits of gypsum precipitation can be divided into two major facies groups:

i. Fine-grained gypsum facies are characterised by fine-grained laminae in thin beds, often found in deep basins and in association with fine- to coarse-grained slope clastics (e.g. gypsum turbidites and gypsum breccias). On platforms, gypsum cumulates often display more distinct lamination, and the clastic facies are mainly composed of disorganised gypsum blocks (Ortí, 2011). This facies also includes microcrystalline laminated gypsum microbialites (stromatolites), an organo-sedimentary deposit

formed by the interaction of a microbial community (Bąbel, 2004) that often show vertically stratified coloured zones (white, green, brown and black) of a few mm to ~1 cm thick.

ii. Selenite facies are autochthonous, coarse-grained (>2 mm), massive deposits that display euhedral crystal structures. Selenite can occur as tabular, reticular, and columnar crystals or develop twins or intergrowths along the (001) plane. Crystals commonly display upward competitive growth and exhibit zonation due to the presence of matrix inclusions (Ortí, 2011). The term selenite also includes other 'crystalline varieties' of gypsum such as satin spar, desert rose, and gypsum flower. Individual selenite crystals can reach up to several tens of centimetres or even metres in length (Warren, 2016).

Because $Ca^{2+} < SO_4{}^{2-}$ in seawater, gypsum precipitation ceases when Ca^{2+} ions are exhausted.

Sodium chloride: Halite (NaCl) begins to crystallise when seawater is evaporated to ~10% of the original volume. Minor amounts of gypsum form during the early stages of halite crystallisation due to the overlap of the crystallisation fields (Bąbel and Schreiber, 2014). Halite is a cubic structure and displays three perfect cleavage directions at right angles. Millimetre-scale zoning, often arranged into chevron-like pattern, is often seen in halite crystals growing in bottom crusts. The rapid rate of growth results in trapped fluid inclusions within the crystalline structure (Lowenstein et al., 2001; Rigaudier et al., 2011).

Unlike seawater brines, the evaporative concentration of typical continental waters does not draw on the near iso-geochemical reservoir of the open ocean (Warren, 2016). Continental waters have a more variable suite of dissolved ions derived from the weathering of local material, resulting in a larger and less predictable range of minerals that precipitate during evaporation. For example, flow through of limestone aquifers produces waters rich in Ca^{2+} to $HCO_3{}^-$, dolomite dissolution generates Mg^{2+}, and erosion of igneous and metamorphic matrixes often yields fluids containing Ca^{2+}, Na^+ and $HCO_3{}^-$ (e.g. Hardie, 1991; Warren, 2016).

In typical freshwater environments, the anionic content is often dominated by bicarbonate (Eugster and Hardie, 1978). Therefore as the Ca^{2+} present in the fluid is removed during the evaporative $CaCO_3$ phase of precipitation, further evaporation cannot result in the precipitation of Ca-bearing evaporites such as gypsum (Hardie and Eugster, 1971). To increase the Ca^{2+} to $HCO_3{}^-$ ratio of freshwaters to facilitate gypsum precipitation, fluids need to be enriched in calcium and/or sulfate, either via mixing with seawater, or from surrounding lithologies that are leached in the drainage basin (e.g. marine-derived evaporites) around the evaporative system (Rossi et al., 2015). Equally, in marginal marine

environments, the input of differing continental waters may result in the alteration of the ion ratios and salinity thresholds to reach mineral saturation. Whereas high salinities are required to saturate evaporated seawater (a $Na-Cl-SO_4-Mg$ brine) with gypsum (~140‰; Warren, 2016), gypsum saturation can be reached at low salinities (~5‰) when additional calcium and sulfate are added from non-marine sources (Rossi et al., 2015).

In summary, the geochemistry of calcium sulfate is linked to the process of evaporation of a water body leading to salinity increase and concentration of calcium and sulfate ions. As water incorporation into calcium sulfate occurs via a predictable pathway (e.g. Stawski et al., 2016), the triple oxygen and hydrogen isotope composition of the GHW should provide reliable and reproducible information regarding the isotope composition of the fluid at the time of mineral precipitation. While the volumetrically most abundant gypsum precipitates forms from these major reservoirs, a small percentage of gypsum also forms from hydrothermal fluids (e.g. Gázquez et al., 2013), volcanic vapours (e.g. Zimbelman et al., 2005), and during brine freezing (e.g. Marion, 1997; Stark et al., 2003). It is therefore important to extract and analyse GHW precisely, and investigate gypsum-water fractionation factors as a function of the large range of environmental conditions (i.e. variable temperatures and salinities) under which gypsum may form.

2.3 Simultaneous analysis of $^{17}O/^{16}O$, $^{18}O/^{16}O$ and $^{2}H/^{1}H$ of gypsum hydration water by cavity ring-down laser spectroscopy

Adapted from the publication: *Fernando Gázquez, Ian Mather, James Rolfe,* ***Nicholas P. Evans****, Daniel Herwartz, Michael Staubwasser and David A. Hodell (2015). Rapid Commun. Mass Spectrom, 29, 1997–2006.*

The modification of the extraction procedure introduced by Hodell et al. (2012) is described. F.G., I.M., J.R., and D.A.H. designed and built the vacuum assembly. F.G. and N.P.E. conducted the extraction of GHW from a synthetic gypsum standard and a variety of natural gypsum minerals, as well as the subsequent triple oxygen and hydrogen isotope measurements using a new generation CRDS analyser (Picarro L2140-i). To validate the ^{17}O-excess values obtained by CRDS, D.H. and M.S. measured the $\delta^{17}O$ and $\delta^{18}O$ of GHW by fluorination followed by isotope ratio mass spectrometry (IRMS) of O_2. The procedure presents several analytical advantages over earlier methods, including better long-term precision, higher sample throughput and reduced sample size.

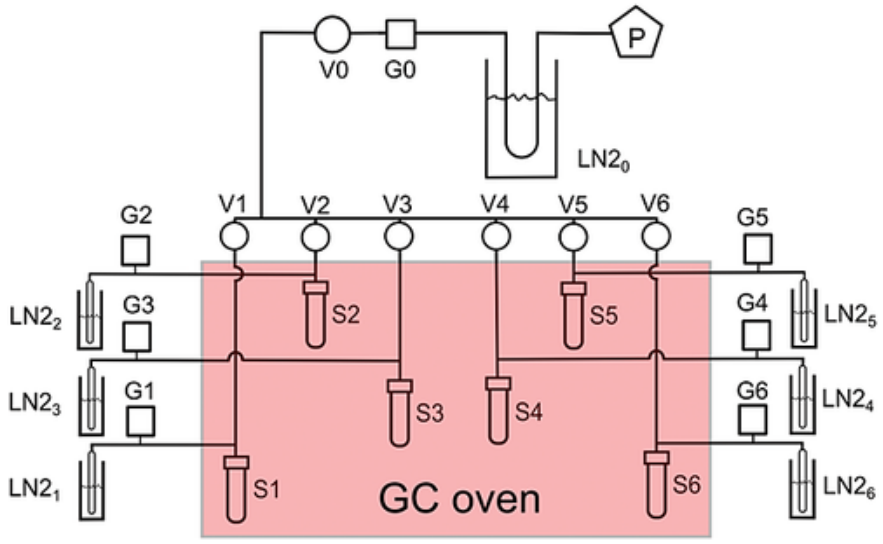

Fig. 2.5. Schematic of the WASP (Water Analyser Sample Preparation) device developed for the extraction of gypsum hydration water. P: Two-stage rotation pump; G: Pirani gauges; V: Swagelok® valves; S: 12 mm Pyrex tubes for samples; LN_2: Cryogenic traps and 6 mm OD tubes for freezing GHW.

2.3.1 The vacuum assembly

A semi-automated procedure is developed for extracting hydration water from gypsum by slowly heating the sample to 400°C in vacuo and cryogenically trapping the evolved water. The Water Analyser Sample Preparation (WASP) system comprises an adapted, programmable gas chromatography (GC) oven and six individual extraction lines attached to a common backing line, coupled to a two-stage rotary pump (Edwards® E2M2, Crawley, UK) (Fig. 2.5). A liquid nitrogen (LN_2) trap is fitted before the vacuum pump to improve pumping efficiency and avoid backstreaming of pump oil.

Each line is ~1 m in length and composed of ¼-inch outer diameter (OD) stainless steel tubing with an internal diameter of ~4 mm (Fig. 2.5). The six lines can be isolated individually by means of Swagelok valves (Swagelok SS-DSS4, London, UK). Samples are loaded into disposable 12 mm Pyrex tubes located in the GC oven (ThermoFinnigan TRACE GC; Thermo Scientific, Bremen, Germany). The programmable oven provides complete control over heating steps and rapid cooling following the analysis; this permits several consecutive runs of the apparatus per day. The hydration water is recovered outside the oven in 6 mm break-seal tubes by cryogenic trapping in LN_2 (Fig. 2.5). The Pyrex and break-seal tubes are connected to the stainless steel tubing via ¼-inch Swagelock Ultra-torr unions fitted with VitonTM O-rings, which are replaced after every five or six runs of the apparatus. All the stainless steel lines outside the GC oven are wrapped in heating tape and held at 70°C to prevent condensation of water in the extraction lines.

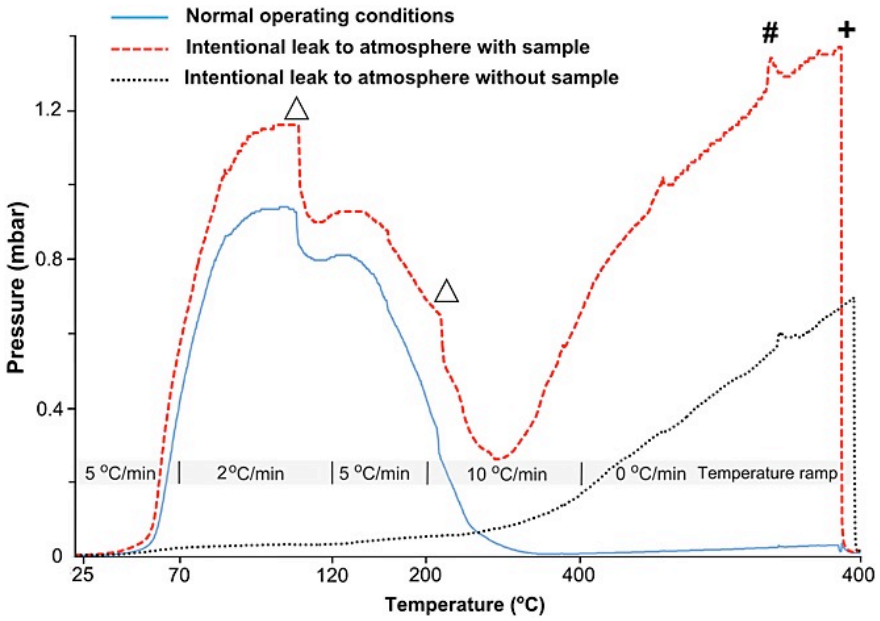

Fig. 2.6. Typical pressure profile recorded during the extraction of GHW. The temperature ramp used along the dehydration process is given. The final pressure differs depending on whether the line is leaking or functioning properly. Vacuum leaks can affect the isotopic composition of the extracted GHW. Δ = raise LN_2 trap; # = heat cold spots; + = pump non-condensable gases.

A Pirani gauge (Edwards® APG100 Active Pirani vacuum gauge) is fitted to each of the six lines for monitoring pressure via an Edwards TIC 6 head instrument controller. The pressure in each line is continuously monitored during the extraction using a computer interface to the WASP system. The change in pressure as a function of time allows identification of any abnormalities (e.g. leaks) during the GHW extraction procedure (Fig. 2.6).

2.3.2 Extraction of GHW

Prior to GHW extraction via the WASP system, gypsum samples (~200 mg) are ground to a homogenous powder in an agate mortar. Powders are loaded into 12 mm OD Pyrex tubes, topped with 3 cm of quartz wool (to prevent loss of gypsum powder during dehydration) and dried at 45°C for 24 h. To remove adsorbed water, samples are then either inserted into the vacuum lines in the WASP and placed under vacuum to a pressure of ~5×10^{-3} mbar for at least 3 h at room temperature, or pumped offline for 3 h in a desiccator connected to a two-stage rotary pump (Edwards) and a LN_2 trap fitted in-line between the pump and the desiccator. This low vacuum pumping (10^{-2} mbar to 10^{-3} mbar) is effective at removing adsorbed water with no detectable loss of hydration water (Playà et al., 2005). No difference has been found in the isotopic results between the two pumping methods. This allows up

to 18 gypsum samples (15 unknowns and 3 standards) to be extracted each day, thereby considerably increasing the sample throughput compared with earlier methods (e.g. Hodell et al., 2012). An analytical-grade powdered gypsum standard (C/2360/50; Fisher Scientific, Hemel Hempstead, UK), denoted as the NEWGYP standard hereafter, is utilised in all experimental runs to evaluate the external precision of the method.

After the lines have been completely evacuated (pressure ~5×10^{-3} mbar), each branch is isolated from the vacuum and the glass 6 mm break-seal tubes at the end of each of the lines are immersed in LN_2 for water trapping. GHW is exhumed by slowly heating the sample to 400°C (Fig. 2.6). The temperature ramp is 5°C min^{-1}, between 25°C and 70°C, and 2°C min^{-1} between 70°C and 120°C. In the temperature range of 70°C and 120°C, gypsum dehydration occurs under low-to-medium vacuum conditions (McConnell et al., 1987). The slower heating during the second step is required to avoid rapid dehydration of the sample that can lead to gypsum powder blowing through the line. At 110°C, the cryogenic traps are raised (~3 cm) to increase the surface area for freezing the water. The ramp is increased to 5°C min^{-1} between 120°C and 200°C. At 200°C, the cryogenic traps are again raised (~5 cm). After this step, the temperature ramp is increased to 10°C min^{-1} between 200°C and 400°C. Once the oven reaches 400°C, this temperature is held constant for 40 min to ensure complete recovery of all water in the lines by the cryogenic traps. Finally, non-condensable gases are pumped away for 30 s before the 6 mm break-seal tubes are flame sealed. The GHW extraction process takes approximately 2 h per run. The pressure in the lines typically reaches 1.2 mbar at 130°C (after 30 min) and then gradually decreases to ~10^{-2} mbar at the end of the heating stage (Fig. 2.6).

After water extraction, the 6 mm OD tubes containing 40-60 µl of hydration water are stored until ready for analysis. Prior to analysis, water is frozen into the base of the break-seal tube by immersion in LN_2. Subsequently, the tube is scored with a diamond cutter, broken to a fixed height of 25 mm, and then quickly inserted into the 2 ml septum-capped vials used by an A0325 autosampler (Picarro).

2.3.3 Isotopic measurement of GHW by CRDS

Triple oxygen and hydrogen isotopes of water are measured simultaneously by CRDS using a L2140-i Picarro water isotope analyser (Steig et al., 2014), interfaced with an A0211 high-precision vaporiser (both from Picarro, Santa Clara, CA, USA). A Picarro micro-combustion module (MCM®), comprising of an 8 cm-long cylindrical cartridge filled with metallic wool coated with a proprietary catalyst, is placed in-line between the vaporiser and the water isotope analyser. The MCM has been shown to remove combustible compounds from water samples (Brand et al., 2009; Saad et al., 2013). For experiments that utilised the

MCM (denoted as 'MCM On' hereafter), the cartridge was held at a constant temperature of 200°C. For experiments that did not utilise the accessory (denoted as 'MCM Off' hereafter), the WARM mode (~80°C) configuration was used. This configuration avoids water vapour condensation in the MCM transfer line, thereby reducing the memory effect between injections; however, this MCM mode does not remove organics from the vapour stream. Both the MCM On and MCM Off analyses use dry air (containing 21% O_2) as the carrier gas. Each sample is injected ten times into the vaporiser, which is heated to 110°C.

2.3.4 Internal and external precision of the CRDS/WASP system

Internal precision of the CRDS is calculated from the repeat analysis of an in-house water standard (SPIT). Memory effects from previous water samples are avoided by rejecting the first three analyses of the ten injections into the vaporiser. The values for the final seven injections are averaged with a typical in-sample precision ($\pm 1\sigma$) of ±0.02‰ for $\delta^{17}O$ values, ±0.04‰ for $\delta^{18}O$ values, and ±0.19‰ for δD values (n = 23). The ^{17}O-excess and d-excess were calculated for each injection using the corrected $\delta^{17}O$, $\delta^{18}O$ and δD values. The ^{17}O-excess and d-excess from the seven repeated analyses were then averaged. Typical in-sample ^{17}O-excess and d-excess precisions ($\pm 1\sigma$) in water standards (SPIT, n = 23) were 13 per meg and 0.2‰, respectively. This agrees with the guaranteed precision given by the manufacturer (15 per meg for ^{17}O-excess). No ^{17}O-excess or d-excess values were rejected.

Results of CRDS analysis are normalised against the VSMOW standard by analysing internal standards before and after each set of 12 to 15 samples. To this end, four internal water standards (JRW, BOTTY, SPIT and ENR-15) were calibrated against VSMOW, using $\delta^{17}O$ and $\delta^{18}O$ values of 0.0‰, respectively, SLAP using $\delta^{17}O$ of -29.6986‰ and $\delta^{18}O$ values of -55.5‰ (Lin et al., 2010; Schoenemann et al., 2013), and the GISP standard water was analysed as an unknown. GISP yielded an average ^{17}O-excess value of 25 ± 12 per meg. This value is in good agreement with the results reported by Schoenemann et al. (2013) (22 ± 11 per meg). The in-run drift of the instrument was corrected (when necessary) by the analysis of an internal standard every 3 or 4 samples.

The long-term precision of the method, including GHW extraction using the WASP system and sample preparation, was ±0.07‰ for $\delta^{17}O$ values, ±0.13‰ for $\delta^{18}O$ values, and ±0.49‰ for δD values (n = 37, 7 injections each, $\pm 1\sigma$) for analyses of NEWGYP ($\delta^{17}O$ = 0.18‰, $\delta^{18}O$ = 0.31‰ and δD = -51.02‰). No significant differences (within analytical errors) in the value of the in-house water standard, NEWGYP, were found and no systematic drift has been observed in the $\delta^{17}O$, $\delta^{18}O$ and δD measurements of the standard over time (Fig. 2.7). In principle, any long-term drift can be monitored and corrected as the gypsum standard is extracted with each five unknown samples. No such drift was observed. If a drift

is observed, a correction could be applied to improve the long-term reproducibility of the method.

The WASP system was tested for memory effects by extracting the hydration water of isotopically depleted and enriched gypsum in two consecutive runs of the apparatus. These gypsum standards (DPL-gyp and ENR-gyp) were produced by hydrating anhydrous $CaSO_4$ with isotopically depleted (-6.1‰, -8.6‰, and -131.4‰ for $\delta^{17}O$, $\delta^{18}O$ and δD values, respectively) and enriched (11.2‰, 21.7‰ and 57.8‰ for $\delta^{17}O$, $\delta^{18}O$ and δD, respectively) waters, following the procedure of Conley and Bundy (1958). Prior to the first extraction, the lines were evacuated to a pressure of ~5×10^{-3} mbar for 4 days before the first experiments to remove potential adsorbed water remaining from previous samples. The system was evacuated for 30 min between the two consecutive runs. The samples extracted in the first run were found not to influence the $\delta^{17}O$, $\delta^{18}O$ and δD values of the samples extracted in the second run of the apparatus. The values for the isotopically enriched gypsum ($\delta^{17}O$ = 13.05‰, $\delta^{18}O$ = 25.10‰ and δD = 34.83‰, n = 3, 7 injections each) showed analytical errors ($\pm1\sigma$) of ±0.08‰, ±0.16‰ and ±0.24‰ for the $\delta^{17}O$, $\delta^{18}O$ and δD values, respectively, and the errors for the isotopically depleted gypsum ($\delta^{17}O$ = -6.81‰, $\delta^{18}O$ = -12.86‰, and δD = -150.39‰, n = 4, 7 injections each) were ±0.06‰, ±0.12‰ and ±0.53‰, respectively (Appendix A; Table A.2). These results show that there is no measurable memory effect in the WASP system with the pumping protocol.

The presence of organic matter and other contaminants in gypsum, including gases derived from microbial activity such as H_2S and CH_4 trapped in the mineral lattice, may produce spectral interferences in the CRDS measurements when GHW is analysed, as has also been reported for the analysis of water extracted from the xylem of plants (Brand et al., 2009; Saad et al., 2013). Such contamination is likely to be greater in gypsum deposited in environments associated with organic matter degradation, such as lakes and marine settings. To evaluate gypsum formed in a wide variety of depositional environments, the natural sample set included gypsum formed by evaporation in a lake (PI 6A-13H-2 8 cm and PI 6C-7H-2 26 cm; Hodell et al. 2012), gypsum derived from seawater evaporation in a coastal setting (Salina 1; Evans et al., 2015), gypsum speleothems generated by drip water evaporation in a gypsum cave (SBL-2.3 and SBL-8; Gázquez and Calaforra, 2014), and two samples of natural gypsum formed in hydrothermal environments (CRI-01 and BG-10; García-Guinea et al., 2002; Gázquez et al., 2013).

For natural gypsum samples, CRDS using the MCM produced values ranging from -1.00‰ to 5.61‰ for $\delta^{17}O$, from -1.93‰ to 10.74‰ for $\delta^{18}O$ and from -53.36‰ to 13.21‰ for δD (Appendix A; Table A.3). The in-sample reproducibility ($\pm1\sigma$) of the CRDS analyser for the analysis of natural gypsum samples was typically ±0.03‰ for $\delta^{17}O$ values,

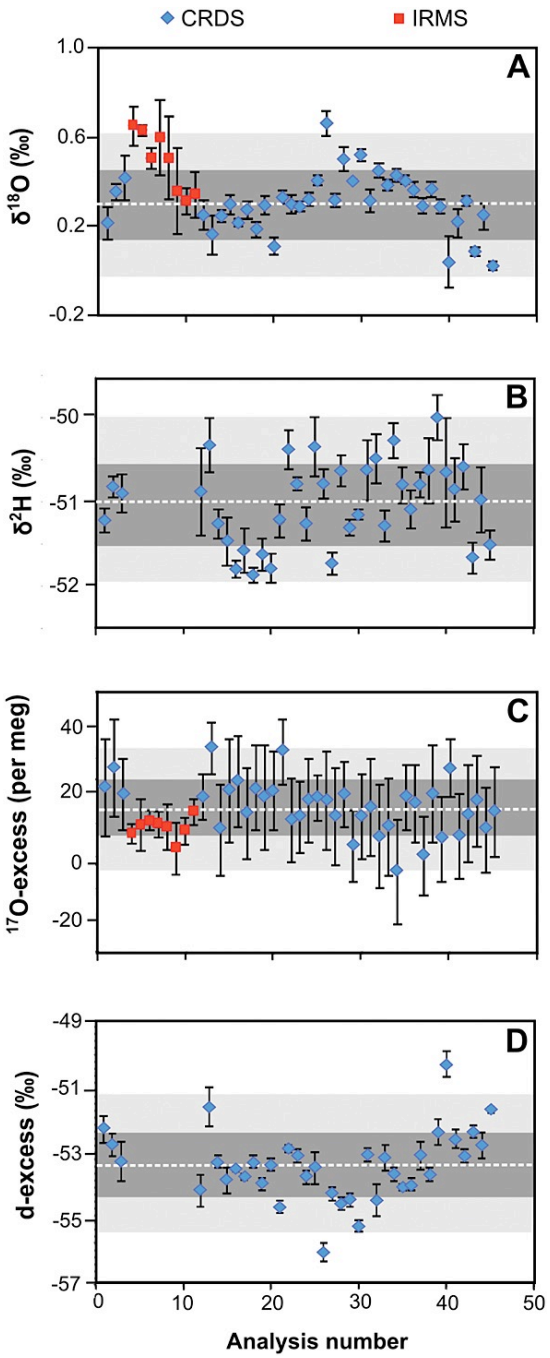

Fig. 2.7. The δ^{18}O (**A**), δD (**B**), ^{17}O-excess (**C**) and d-excess (**D**) values of GHW from the repeated analysis of a gypsum standard (NEWGYP), extracted using the WASP and analysed by CRDS (n = 37) and IRMS (n = 8). δ^{17}O displayed a similar trend to δ^{18}O. Data are displayed following the order in which the samples were extracted using the WASP. Error bars refer to the internal error ($\pm 1\sigma$ obtained from the repeated analysis of the same hydration water (7 injections for CRDS and 3-4 for IRMS). The long-term means (dashed line) and external errors are shown for $\pm 1\sigma$ (deep-grey shade) and $\pm 2\sigma$ (light-grey shade).

±0.04‰ for $\delta^{18}O$ values, and ±0.24‰ for δD values, found by taking the average of seven consecutive injections for each GHW sample. These results are similar to those observed for the analysis of water standards. Regarding the long-term reproducibility of natural samples, the replicate GHW extraction and subsequent analysis in different runs of sample Salina 1 (n = 3, 7 injections each) gave an error ($\pm 1\sigma$) of ±0.02‰ for $\delta^{17}O$ values, ±0.03‰ for $\delta^{18}O$ values, and ±0.16‰ for δD values (Appendix A; Table A.3). This demonstrates the long-term precision obtainable for the hydration water of natural gypsum samples using the method.

To validate the values obtained by CRDS, D. Herwartz and M. Staubwasser measured the GHW $\delta^{17}O$ and $\delta^{18}O$ of the NEWGYP standard and the natural gypsum samples by fluorination followed by IRMS of O_2 at the University of Cologne (Cologne, Germany). ~800 mg of sample was loaded into the WASP, and the subsequent water samples (2.8 µl) were injected via an autosampler into a CoF_3 reactor held at 375°C which converts H_2O into O_2 and HF, following the method developed by Barkan and Luz (2005). Helium carries the products through a double cold trap immersed in LN_2 to freeze out the HF. The O_2 is then trapped using 5 Å molecular sieve held at LN_2 temperature. Helium is pumped away after disconnecting the oxygen trap from the He stream and sample O_2 is transferred to one tube in a 12-fold sample manifold immersed in LN_2. For this study a manifold typically contained four reference water extractions, leaving eight sample tubes for O_2-extractions from two or three unknown water samples. To minimize memory effects at least three sample injections were discarded when switching between waters of different isotopic values. The CoF_3 line is LabView (National Instruments, Austin, TX, USA) controlled and runs fully automated overnight. The sample O_2 was then analysed on a MAT253 IRMS (Thermo Scientific) in dual-inlet mode at m/z 32, 33 and 34. Each measurement comprises 66 samples to reference comparisons divided into 3 blocks of 22 cycles each. Each block begins with a peak centre and adjustment of bellow pressure, such that the ion beam intensity at m/z 32 is 8.5 V. The idle time was set to 17 s and the integration time to 12 s. The baseline was measured for 240 s prior to the first sample. The $\delta^{17}O$ sample and $\delta^{18}O$ sample values were normalised to VSMOW via internal lab standards that were measured with the samples. As for the CRDS data, SLAP of $\delta^{17}O$ = -29.6986‰ and $\delta^{18}O$ = -55.5‰ was used for SMOW-SLAP scaling (Schoenemann et al., 2013). Analysis of SMOW (n = 15) and SLAP (n = 15) during the course of this study gave -28.699 ± 0.011‰ (1σ) and -53.622 ± 0.024‰ (1σ) for the $\delta^{17}O$ measured-SLAP and $\delta^{18}O$ measured-SLAP values, respectively. This slightly contracted scale relative to the IAEA-scale appears to be typical for MAT253 instruments (Schoenemann et al., 2013).

The IRMS analysis of NEWGYP (n = 8, 3 or 4 analyses each) yielded mean values and

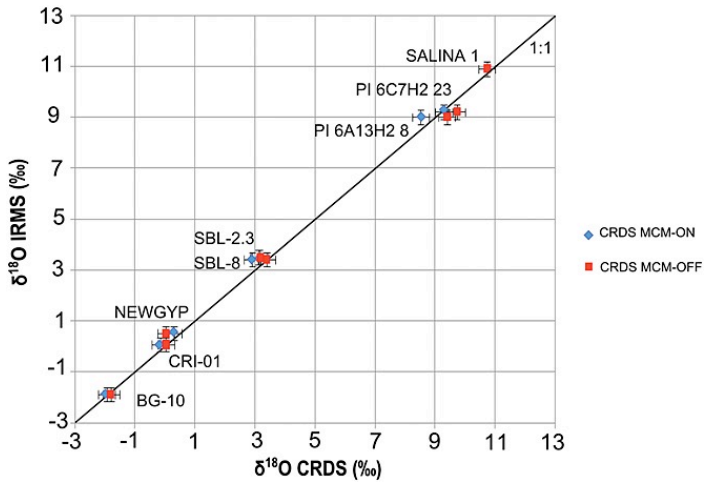

Fig. 2.8. Cross-plot of δ^{18}O values in GHW of natural samples analysed by CRDS/MCM compared with measurements of the same samples by IRMS. The long-term $\pm 2\sigma$ error of the method (0.26‰ for the δ^{18}O values from the CRDS measurements and 0.28‰ for the δ^{18}O values from the IRMS analyses) is given for all samples. The in-sample $\pm 2\sigma$ errors (7 injections for CRDS and 3-4 for IRMS) are smaller than the data symbols.

reproducibility ($\pm 1\sigma$) of 0.28 ± 0.07‰ and 0.51 ± 0.14‰ for the δ^{17}O and δ^{18}O values, respectively, which are within the 2σ error of the CRDS measurements. For most natural samples, the δ^{17}O, δ^{18}O and δD values of GHW did not differ significantly whether or not the MCM was used (within the 2σ error) from the results obtained by IRMS (Fig. 2.8). However, the ^{17}O-excess of both the NEWGYP standard and natural samples differed considerably between CRDS and IRMS when the MCM was not used. The ^{17}O-excess values measured by CRDS were considerably higher than those obtained by IRMS when the MCM was turned off. By contrast, the ^{17}O-excess results from CRDS were similar to those achieved by IRMS when the MCM was used (Appendix A; Table A.3), resulting in a close 1:1 relationship (Fig. 2.9). The difference in ^{17}O-excess values with MCM On and Off reflects the degree of spectral interference caused by contamination.

Using the MCM, the long-term precision ($\pm 1\sigma$) of the method for ^{17}O-excess determination by CRDS of NEWGYP was ±8 per meg (n = 37) (Appendix A; Table A.1). In addition, no systematic drift in the ^{17}O-excess of the standard has been observed with time (Fig. 2.7). Remarkably, this reproducibility is better than the typical in-sample precision obtained from seven consecutive injections (±13 per meg) observed in both water standards and GHW. Similar precision (typically ±15 per meg) is also obtained by randomly choosing the ^{17}O-excess of injections from NEWGYP samples, extracted on different days and analysed in different CRDS analyser runs. This is a consequence of the minimised importance of drift, memory effect and potential isotopic fractionation occurring during the ^{17}O-excess

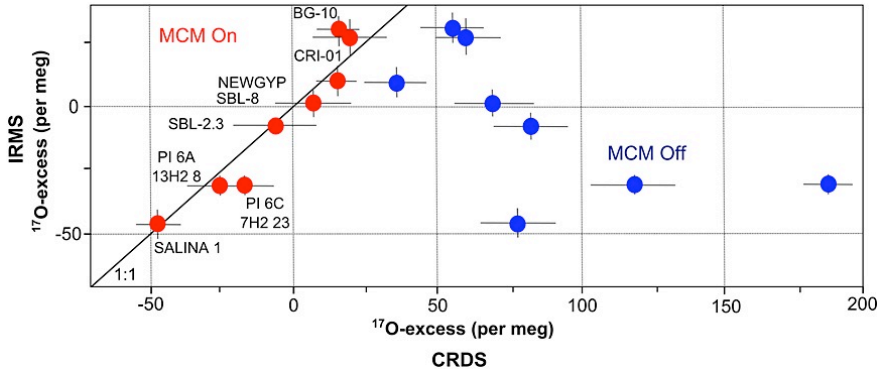

Fig. 2.9. Cross-plot of ^{17}O-excess in synthetic and natural gypsum analysed by CRDS and IRMS. The analyses by CRDS that used the MCM yielded results similar to those obtained by IRMS. Error bars refer to the consecutive analyses (7 injections for CRDS and 3-4 analyses for IRMS) of the same hydration water.

measurements, compared with the measurement of the δ^{17}O and δ^{18}O values. The repeated extraction and measurement (n = 3, 7 injections each) of one natural gypsum sample (Salina 1) by CRDS using the MCM produced an analytical error ($\pm 1\sigma$) of ±7 per meg. This indicates that the long-term ^{17}O-excess precision of the method using CRDS is similar for synthetic and natural gypsum when the MCM is powered on. The long-term precision is also similar to that obtained for the analysis of water standards, as observed from the repeated measurement of an internal water standard (SPIT, ±8 per meg, n = 23) in different runs over the period of this study.

2.3.5 Discussion of the WASP/CRDS setup

A distinct advantage of CRDS over IRMS is the possibility of simultaneously determining D/^{1}H, along with ^{17}O/^{16}O and ^{18}O/^{16}O, on the same hydration water sample. This enables the calculation of both d-excess and ^{17}O-excess in GHW. The long-term d-excess of the NEWGYP standard (n = 37) was -53.4 ± 1.1‰ (Fig. 2.7). This reproducibility is comparable with the long-term precision observed from the repeated measurement of the SPIT water standard (±0.9‰, n = 23). No systematic drift in the d-excess of the NEWGYP standard has been observed with time (Fig. 2.7). As for the natural gypsum samples, the d-excess in GHW analysed by CRDS using the MCM ranged from -39.7‰ to -71.9‰. As expected, the values are positively correlated with those of the ^{17}O-excess across the dataset.

Use of the MCM removes impurities that affect the ^{17}O-excess determination. The differences in ^{17}O-excess in natural samples in the MCM On/Off experiments are greater in the case of gypsum samples generated in organic- and microbe-rich environments (e.g. lake sediments). This, as expected, points to higher concentration of contaminants in these

types of material and suggests that the cause of the spectral interferences could be H_2S or organic compounds released by natural gypsum samples during dehydration. Further evidence for the presence of impurities in GHW is given by a strong smell of H_2S in water after extraction, especially in water from lacustrine gypsum samples.

Results reveal that the use of the MCM accessory is crucial for accurate determination of the ^{17}O-excess in GHW by CRDS. In earlier work, this device was found to be necessary for isotopic analysis of water samples with high concentrations of organic compounds, such as water extracted from the xylem of plants that usually contains alcohols that spectroscopically interfere with the CRDS analysis (Brand et al., 2009; Saad et al., 2013). To date, the efficiency of the MCM has been demonstrated for the removal of alcohols and other organic compounds from water (Saad et al., 2013). However, catalytic oxidation of other substances also occurs, such as H_2S, volatile organic compounds and long-chain compounds, and this is important for the analysis of GHW samples. Although this accessory removes most impurities, we suspect that organic-rich gypsum samples (e.g. those from lake sediments) may require additional pre-treatment to remove organic compounds (H_2O_2, sodium hypochlorite, etc.). However, any pre-treatment procedure will require testing to ensure that it does not alter the δ^{18}O and δD values of the hydration water.

The WASP system also offers distinct advantages over previous methodologies. One critical advance is the ability of the WASP extraction line to monitor internal pressure during GHW extraction, thus detecting vacuum leaks in individual lines (Fig. 2.6). When operating correctly, the pressure in the lines displayed similar profiles, first increasing up to 1 mbar at around 120°C, and then decreasing to below 5×10^{-2} mbar at the end of the extraction process. When O-rings are compromised, profiles showed slightly greater pressures (up to 1.2 mbar) at 120°C (Fig. 2.6). The pressure decreased by as much as 0.2 mbar when the LN_2 trap was raised for a second time, but subsequently increased to around 1.4 mbar by the end of the run. In the line run as a blank with no sample, the pressure increased constantly to reach a final value of 0.7 mbar, and no drop in pressure occurred during the run (Fig. 2.6).

The isotopic composition of the NEWGYP standard extracted in the leaky line showed no difference within error (0.03‰ for the δ^{17}O value, 0.03‰ for the δ^{18}O value and -51.24‰ for the δD value) from that obtained from the properly functioning line (0.07‰ for the δ^{17}O value, 0.09‰ for the δ^{18}O value, and -51.39‰ for the δD value). However, slight differences were observed in the results of the ENR-gyp samples. The enriched gypsum extracted in the leaking line showed slightly lower isotope values (12.78‰ for the δ^{17}O value, 24.58‰ for the δ^{18}O value, and 33.56‰ for the δD value) than those from the properly functioning line in the same run (12.96‰ for the δ^{17}O value, 24.93‰ for the δ^{18}O value, and 34.63‰ for the δD value). This suggests that vacuum leaks can alter the

isotopic ratio values of samples extracted using the WASP, especially for hydration waters with an isotopic composition significantly different from that of the ambient water vapour in the laboratory atmosphere. Therefore, it is vital to monitor the pressure in the WASP during GHW extraction to ensure that no leaks occur during extraction.

2.3.6 Conclusions

The method presented provides precise and simultaneous isotopic measurements of $\delta^{17}O$, $\delta^{18}O$ and δD values. The derived d-excess and ^{17}O-excess, can be obtained from GHW using the new extraction apparatus and subsequent measurement by CRDS.

2.4 Precise and accurate isotope fractionation factors ($\alpha^{17}O$, $\alpha^{18}O$ and αD) for water and $CaSO_4 \cdot 2H_2O$ (gypsum)

Adapted from the publication: *Fernando Gázquez,* ***Nicholas P. Evans*** *and David A. Hodell (2017). Geochimica et Cosmochimica Acta, 198, 259–270.*

Isotope fractionation factors ($\alpha^{17}O$, $\alpha^{18}O$ and αD) between GHW and free water of the mother solution were determined in the temperature range from 3°C to 55°C at different salinities and precipitation rates. F.G. and D.A.H. designed the experimental setup and F.G. conducted the experiments. F.G. and N.P.E. extracted and analysed GHW and N.P.E. performed all other analytical procedures.

2.4.1 Introduction

The isotopic fractionation factor (α) between the mother water and GHW is defined as:

$$\alpha_{gypsum\text{-}water} = \frac{\alpha_{gypsum} + 1000}{\alpha_{water} + 1000}$$

where α_{gypsum} and α_{water} denote the isotopic ratio (i.e. $^{17}O/^{16}O$, $^{18}O/^{16}O$ and $^{2}H/^{1}H$) of the hydration water and mother water, respectively, relative to VSMOW.

Calculating the $\alpha^{18}O_{gypsum\text{-}water}$ requires measurement of the relative difference in the isotopic composition of GHW and the free water of the mother solution. Multiple methods of gypsum precipitation have been employed, including evaporation of solutions saturated in $CaSO_4$ (e.g. Gonfiantini and Fontes, 1963), the hydration of γ-$CaSO_4$ (e.g. Hodell et

al., 2012), and mixing of $CaCl_2$ and Na_2SO_4 solutions (e.g. Gonfiantini and Fontes, 1963; Fontes and Gonfiantini, 1967; Tan et al., 2014).

The first stable isotopic measurement of GHW was made by Baertschi (1953), who reported an $\alpha^{18}O_{gypsum\text{-}water}$ of 1.0035. Seminal papers by Gonfiantini and Fontes (1963) and Fontes and Gonfiantini (1967) investigated gypsum-water fractionation factors over the temperature range of 17°C to 57°C. Gonfiantini and Fontes (1963) argued that their rehydration experiments gave a precise $\alpha^{18}O_{gypsum\text{-}water}$ = 1.0040, although two 'steady state' evaporation experiments produced an $\alpha^{18}O_{gypsum\text{-}water}$ = 1.0031. Overall, $\alpha^{18}O_{gypsum\text{-}water}$ and $\alpha D_{gypsum\text{-}water}$ were reported as 1.0037 (±0.0005) and 0.985, respectively. Within analytical uncertainty, both $\alpha^{18}O_{gypsum\text{-}water}$ and $\alpha D_{gypsum\text{-}water}$ were found not to be sensitive to temperature variability across the range investigated (Gonfiantini and Fontes, 1963; Fontes and Gonfiantini, 1967). Fractionation factors produced by Matsubaya (1971) and Sofer (1975) apparently confirmed $\alpha^{18}O_{gypsum\text{-}water}$ = ~1.0040 and $\alpha D_{gypsum\text{-}water}$ = 0.980 although, because the datasets are not accessible, the precision and accuracy of these experiments remain unclear. More recently, Hodell et al. (2012) found $\alpha^{18}O_{gypsum\text{-}water}$ = 1.0039±0.0004 and $\alpha D_{gypsum\text{-}water}$ = 0.981 ± 0.002, which did not differ significantly from previous values. As the majority of the reported gypsum-water fractionation factors are within analytical error, most investigations that utilise $\alpha_{gypsum\text{-}water}$ use rounded values of $\alpha^{18}O_{gypsum\text{-}water}$ = 1.004 and $\alpha D_{gypsum\text{-}water}$ = 0.98 (e.g. Sofer, 1978; Bath et al., 1987; Khademi et al., 1997; Kasprzyk and Jasinska, 1998; Farpoor et al., 2004; Buck and Van Hoesen, 2005; Hodell et al., 2012; Chen et al., 2016).

The opposite signs of $\alpha^{18}O_{gypsum\text{-}water}$ and $\alpha D_{gypsum\text{-}water}$ mean that the oxygen isotopic composition GHW is enriched by ~4‰ compared to the isotopic composition of mother water, whereas ^2H is depleted by ~20‰ (e.g. Gonfiantini and Fontes, 1963; Fontes and Gonfiantini, 1967). The enrichment of the oxygen isotope can be explained if the GHW is related to the water of the hydration sphere of Ca^{2+}, which is likely to be enriched in ^{18}O because of the difference in vibration frequencies of the two isotopic forms of water along the bonds formed between water and cation (Taube, 1954; Gonfiantini and Fontes, 1963; Longinelli, 1979; Oi and Morimoto, 2013). In contrast, the depletion of GHW in ^2H by ~20‰ may be ascribed to the fact that the hydration sphere of SO_4^{2-} in solution is depleted in ^2H with respect to the free water (Oi and Morimoto, 2013).

Although the fractionation factors from different studies are in general agreement, the reason for the slight scatter in reported $\alpha_{gypsum\text{-}water}$ values and temperature/salinity effects on the gypsum-water isotopic fractionation remains poorly understood. Firstly, the slight scatter in reported $\alpha_{gypsum\text{-}water}$ values may imply that full equilibrium between GHW and the mother fluid are not always reached in experiments (possibly due to sluggish exchange

between the solution and GHW; Herwartz et al., 2017), or that $\alpha_{gypsum\text{-}water}$ differs due to the different methods of gypsum precipitation employed (which have traditionally been thought of as equivalent). Alternatively, the drying process prior to GHW extraction may differ between studies, and thus adsorbed water on the surface of the crystals may not have been not effectively removed. Secondly, Hodell et al. (2012) found a slight positive temperature dependence (0.00012 per °C) for $\alpha D_{gypsum\text{-}water}$ between 12°C and 37°C, although the full extent of this temperature dependence was not fully investigated. Any temperature dependence will impact investigations of hydrothermal gypsum that use the accepted $\alpha^{18}O_{gypsum\text{-}water}$ and $\alpha D_{gypsum\text{-}water}$ of 1.004 and 0.98 (e.g. Matsuyaba and Sakai, 1973), as $\alpha_{gypsum\text{-}water}$ may differ at the higher temperatures of hydrothermal gypsum precipitation (e.g. 55°C; Garofalo et al., 2010; Gázquez et al., 2012, 2013). Finally, the derived uncertainty of $\alpha_{gypsum\text{-}water}$ measurements is also unsatisfactory for many geological and palaeoclimate applications. Standard errors of ±0.0004 and ±0.002 for $\alpha^{18}O_{gypsum\text{-}water}$ and $\alpha D_{gypsum\text{-}water}$ reported by Hodell et al. (2012) result in a derived mother fluid error of ~0.4‰ and ~2‰ for $\delta^{18}O$ and δD, respectively.

Here the fractionation factors for gypsum are calculated by measuring the relative difference in the isotopic composition of the hydration water and the free water of the mother solution. Gypsum precipitation experiments were conducted at a range of temperatures (3°C to 55°C) and salinities (0 to 300 $g\,l^{-1}$). The effect of precipitation rate on isotope fractionation factors was evaluated by changing the initial concentration of $CaCl_2$ and Na_2SO_4.

2.4.2 Methods

2.4.2.1 Hydration of anhydrous $CaSO_4$

100 ml of 0.5 M Na_2SO_4 solution was added to 1.5 g of analytical grade powdered anhydrite (Acros, UK) to induce hydration to gypsum (Conley and Bundy, 1958). Sodium sulfate acts a catalyst during the hydration reaction of anhydrite, and acceleration of the reaction takes place through the medium of transient surface complexes that are unstable in dilute solution and finally evolve to gypsum (Conley and Bundy, 1958). Importantly, the hydration sphere of Na^+ does not isotopically affect the activity of water in dilute solutions; thus, the addition of Na_2SO_4 does not interfere with isotopic fractionation during gypsum precipitation (Taube, 1954; Gonfiantini and Fontes, 1963). The conversion of anhydrite to gypsum occurs in two steps via the intermediate hemihydrate of calcium sulfate (i.e. bassanite) (Van Driessche et al., 2012; Wang et al., 2012).

Prior to the experiment, anhydrite was heated to 400°C for 3 h to completely remove all hydration and adsorbed water. Subsequent analysis by ATR-FTIR (Attenuated Total

Reflectance, Bruker Platinum accessory, coupled to a Fourier Transformation Infrared Spectrometer instrument, Bruker, Tensor II; Department of Earth Sciences, University of Cambridge, UK) detected only anhydrite, with no traces of gypsum or bassanite. X-ray diffraction (XRD) analysis of the same material showed insignificant amounts of bassanite (0.5%) and gypsum (0.4%).

Experiments were performed in duplicate or triplicate in a conical flask with a greased ground glass stopper and joint to prevent evaporation. Before mixing, the anhydrite and the Na_2SO_4 solutions were temperature equilibrated in an oven at 20°C, 25°C, 30°C, 35°C and 40°C for at least 2 h. Anhydrite was added to the solution and then constantly stirred at 700 rpm for 24 h using a wireless magnetic stirrer. After mixing, the flasks containing the solution and the anhydrite were placed again in the oven and temperature was maintained to a precision of ±0.1 °C (1σ).

Experiments at the lower temperatures of 8°C and 3°C were conducted in a refrigerator and cold room, respectively, in which temperatures were monitored for the duration of the experiments and varied by less than 0.5°C.

At temperatures greater than 45°C, the conversion of anhydrite to gypsum was incomplete (e.g. 42 wt% of gypsum at 45°C or 0 wt% at 60°C) because of the greater stability of anhydrite relative to gypsum at temperatures above ~42°C (Ostroff, 1964; D'Ans, 1968). Thus, we only consider the experiments in which the hydration of anhydrous $CaSO_4$ resulted in over 98 wt% conversion to gypsum (i.e. experiments performed at temperature below 40°C). A water sample (200 μl) from each experiment was stored for subsequent isotopic analysis. We found that during temperature equilibration in the experiments at 3°C, Na_2SO_4 precipitation occurred because of a rapid decrease in solubility at temperatures below 10°C. For this reason, experiments at 3°C used a 0.05 M Na_2SO_4 solution.

After 24 h, the solutions were vacuum filtered using Millipore nitrocellulose filters (0.45 μm φ pore). Samples were then dried at 45°C for 48 h. Thermogravimetric analysis (Netzsch STA 449 F1 Jupiter) showed that this drying method removed all adsorbed water, but did not result in the loss of hydration water. The mineralogy of the dry precipitates was analysed by XRD.

2.4.2.2 Mixing $CaCl_2$ and Na_2SO_4 solutions

Gypsum saturation was achieved by mixing solutions of $CaCl_2 \cdot 6H_2O$ and Na_2SO_4 of varying concentrations to control the rate of precipitation. Experiments with three different initial Ca^{2+} and $SO_4{}^{2-}$ concentrations (0.5 M, 0.33 M and 0.125 M) were conducted by diluting mother solutions of 0.5 M $CaCl_2 \cdot 6H_2O$ (analytical grade, Sigma–Aldrich) and 0.5 M Na_2SO_4 (analytical grade, Fisher Scientific).

Experiments were conducted at 5°C, 20°C, 25°C, 45°C and 55°C using a water bath (±0.1°C) and solutions were temperature equilibrated for 2 h prior to mixing. A sample of each solution was collected after mixing. In order to promote slower gypsum precipitation, no stirring or shaking of these gypsum precipitation experiments occurred (referred to as free-drift experiments hereafter). Experiments at 25°C and 55°C were repeated by setting the shaking mode of the bath at 110 rpm to promote solution homogenisation and fast gypsum precipitation (referred to as shaking experiments hereafter). Both sets of experiments lasted 10 days. Subsequently, solutions were filtered and the precipitate was dried and analysed by XRD using the same method employed in the anhydrite hydration experiments (Section 2.4.2.1). A sample of each solution was stored after filtering. The saturation index of gypsum (SI_{gyp}) in the initial solution was calculated using PHREEQC (3.1.7) (Parkhurst and Appelo, 2013).

2.4.2.3 Gypsum precipitation in brines

Experiments examining gypsum precipitation from brines of varying salinity used the same methodology described in Section 2.4.2.1, but varying amounts of NaCl were added to the initial 0.5 M Na_2SO_4 solutions. The NaCl concentrations in the final solution were 30 g l^{-1}, 80 g l^{-1}, 150 g l^{-1}, 200 g l^{-1} and 300 g l^{-1}. All the experiments were conducted in duplicate at 20°C and used the same procedure for filtering, drying, and mineralogical analysis described in Sections 2.4.2.1 and 2.4.2.2.

2.4.2.4 Isotopic analyses and calculation of fractionation factors

The GHW was extracted and water isotopes were analysed using the same methods described in Section 2.3. The mother waters collected from each experiment and the corresponding hydration water extracted from the gypsum were measured consecutively by CRDS under the same instrument conditions. This direct comparison minimises the effect of drift and provides precise and accurate estimates of the fractionation factor that is calculated as the isotopic difference between the sequential samples of the mother water and GHW. By analysing the waters before and after gypsum precipitation, we found that the isotopic composition of the solution did not change over the course of the experiments within error (Appendix B; Table B.1); therefore, the values of the initial solutions were used for the calculation of the isotope fractionation factors.

Temperature (°C)	$\alpha^{17}O^{*}$	1σ	$\alpha^{18}O^{*}$	1σ	θ	1σ	n*	$\alpha^{18}O^{\#}$	1σ	$\alpha D^{\#}$	1σ	n$^{\#}$
3	1.00197	0.00005	1.00372	0.0001	0.53	0.0011	4	1.0037	0.0001	0.9788	0.0003	4
8	1.00201	0.00009	1.0038	0.00016	0.5293	0.0014	4	1.0037	0.0002	0.9801	0.0006	6
20	n.a	-	n.a	-	-	-	-	1.0034	0.0001	0.9814	0.0011	4
25	1.00181	-	1.00341	-	0.5298	-	1	1.0035	0.0001	0.981	0.0006	5
30	1.00174	0.000	1.00329	0.00001	0.5289	0.0014	1	1.0033	0.0001	0.9803	0.0009	2
35	n.a	-	n.a	-	-	-	-	1.0034	0.000	0.9812	0.0003	4
40	1.00169	-	1.00318	-	0.5314	-	1	1.0034	0.0002	0.9821	0.0009	5

Table 2.1. Isotope fractionation factors ($\alpha^{17}O_{gypsum\text{-}water}$, $\alpha^{18}O_{gypsum\text{-}water}$ and $\alpha D_{gypsum\text{-}water}$) between GHW and its mother solution obtained experimentally by the hydration of anhydrite. See Appendix B for complete report. (*Analyses conducted with Picarro L-2140i analyser; $^{\#}$averaged results of samples analysed by Picarro L-1102i and L-2140i analysers).

2.4.3 Results

2.4.3.1 Hydration of anhydrite at low salinities

The $\alpha^{18}O_{gypsum\text{-}water}$ values of the anhydrite hydration experiments varied from 1.0033 ± 0.0001 to 1.0037 ± 0.0001 in the temperature range from 3°C to 40°C, with the lowest values at 30°C and the highest values at 3-8°C. There was no statistically significant trend over this temperature range given the analytical uncertainty of the measurements (R^2 = 0.56; p-value >0.05). In contrast, $\alpha D_{gypsum\text{-}water}$ increased with temperature from 0.9788 ± 0.0003 at 3°C to 0.9821 ± 0.0009 at 40°C and showed significant dependence with temperature (R^2 = 0.89; p-value <0.05) (Table 2.1, Fig. 2.10, Appendix B; Table B.1).

The $\alpha^{17}O_{gypsum\text{-}water}$ was determined in the experiments of hydration of $CaSO_4$ and varied in the same manner as $\alpha^{18}O_{gypsum\text{-}water}$ reflecting mass-dependent fractionation in the triple oxygen isotope system (Cao and Liu, 2011), with minimum value of 1.0017 ± 0.0001 in the temperature range from 25°C to 40°C and maximum of 1.0020 at 8°C (Table 2.1). The relationship between $\alpha^{17}O_{gypsum\text{-}water}$ and $\alpha^{18}O_{gypsum\text{-}water}$ is given by the parameter θ (Mook, 2000):

$$\alpha^{17}O_{gypsum\text{-}water} = \alpha^{18}O_{gypsum\text{-}water}{}^{\theta}$$

where $\theta = \ln\left(\alpha^{17}O_{gypsum\text{-}water}\right) / \ln\left(\alpha^{18}O_{gypsum\text{-}water}\right)$.

θ was found to be 0.5297 ± 0.0012 (n = 11) and displayed no correlation with temperature (Table 2.1). All gypsum samples yielded a weight loss of hydration water of

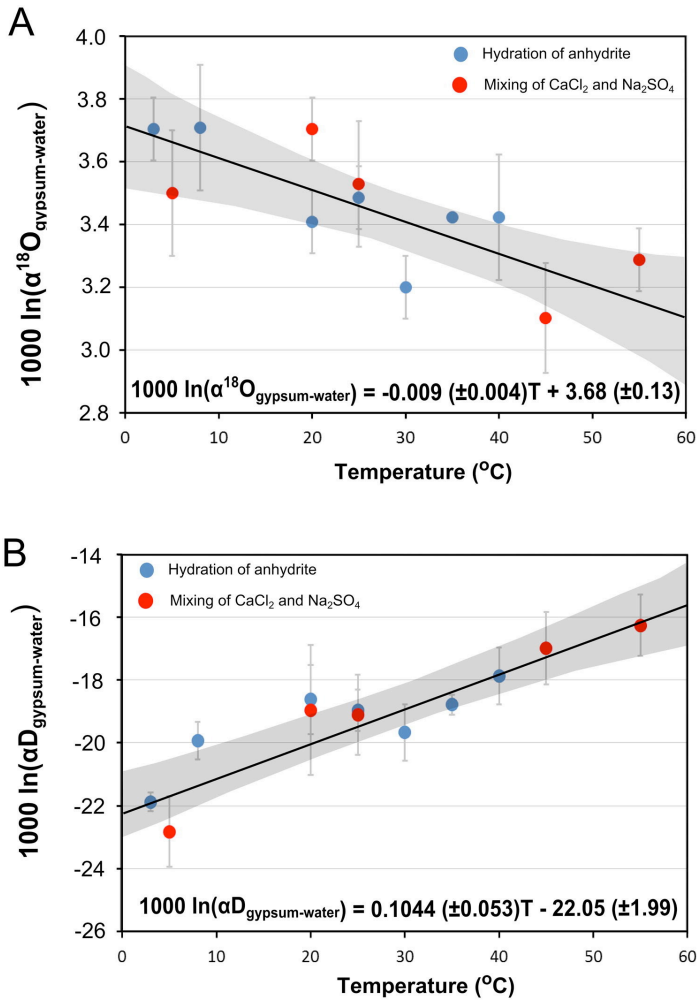

Fig. 2.10. Isotope fractionation factors (**A**: $\alpha^{18}O_{gypsum\text{-}water}$; **B**: $\alpha D_{gypsum\text{-}water}$) between GHW and its mother solution at different temperatures obtained experimentally by hydration of anhydrite and mixing of $CaCl_2$ and Na_2SO_4 solutions. Note that mixing experiment results are averaged values of gypsum precipitation at different initial SI_{gyp} of the solution (see Table 2.2 and Appendix B). Error bars denote 1σ. Grey shades represent the 95% confidence limits.

Temperature (°C)	0.25 Ca^{2+}/0.25 SO_4^{2-} ($mol\,l^{-1}$)				0.166 Ca^{2+} /0.166 SO_4^{2-} ($mol\,l^{-1}$)				0.065 Ca^{2+} /0.065 SO_4^{2-} ($mol\,l^{-1}$)			
	$\alpha^{18}O$	1σ	αD	1σ	$\alpha^{18}O$	1σ	αD	1σ	$\alpha^{18}O$	1σ	αD	1σ
5	1.0035	0.0001	0.978	0.001	1.0035	0.0002	0.977	0.003	1.0035	0.0003	0.976	0.000
20	1.0038	0.0001	0.983	0.001	1.0036	-	0.98	-	1.0037	0.000	0.979	0.000
25	1.0036	0.0001	0.982	0.000	1.0035	0.0001	0.981	0.000	1.0035	0.000	0.98	0.001
45	1.0032	0.0001	0.984	0.000	1.0029	0.000	0.983	0.000	1.0032	-	0.982	-
55	1.0034	0.0001	0.984	0.001	1.0033	0.0001	0.984	0.001	1.0031	0.000	0.983	0.001

Table 2.2. Isotope fractionation factors ($\alpha^{17}O_{gypsum\text{-}water}$, $\alpha^{18}O_{gypsum\text{-}water}$ and $\alpha D_{gypsum\text{-}water}$) between GHW and its mother solution obtained experimentally by mixing of $CaCl_2$ and Na_2SO_4 solutions at different initial concentrations of Ca^{2+} and SO_4^{2-} and different temperatures. Initial Ca^{2+} and SO_4^{2-} concentrations are given. SI_{gyp} ranged from 0.66 to 1.50 (Appendix B). Analyses were conducted with a Picarro L-1102i analyser.

over 20%, similar to that of the gypsum standard (20.5 ± 0.3%). This suggests that there was complete hydration of anhydrite to gypsum and complete mineral dehydration in the extraction procedure for GHW. Insignificant amounts of bassanite and anhydrite (less than 1 wt%) were detected in all samples (Appendix B; Table B.4).

2.4.3.2 Gypsum precipitation from mixing of $CaCl_2$ and Na_2SO_4 solutions

Experiments of gypsum precipitation from mixing of $CaCl_2$ and Na_2SO_4 solutions produced a mean $\alpha^{18}O_{gypsum\text{-}water}$ value of 1.0034 ± 0.0003 in the temperature range from 5°C to 55°C. No measurable differences were found between the free-drift gypsum precipitation and the shaking experiments. No significant relationship was observed with temperature considering the analytical uncertainty of the measurements ($R^2 = 0.73$; p-value >0.05). The $\alpha^{18}O_{gypsum\text{-}water}$ value was unaffected by the different initial SI_{gyp} of the solution within the analytical error (Figs 2.10 and 2.11 and Table 2.2).

Unlike the oxygen isotope fractionation factor, $\alpha D_{gypsum\text{-}water}$ was affected by changes in both temperature and initial SI_{gyp}. The average $\alpha D_{gypsum\text{-}water}$ was 0.9815 ± 0.0025 between 5°C and 55°C. No measurable differences were found between the free-drift gypsum precipitation and the shaking experiments. The experiments conducted at 55°C produced the highest values of $\alpha D_{gypsum\text{-}water}$ (0.984 ± 0.001) compared with gypsum precipitation at lower temperatures (e.g. 0.977 ± 0.001 at 5°C). Hydrogen isotope fractionation shows a clear increasing trend with temperature by 0.0001 units per °C ($R^2 = 0.94$; p-value <0.05; taking the average of the experiments at different initial SI_{gyp}). The $\alpha D_{gypsum\text{-}water}$ was affected by the SI_{gyp} of the initial solution, increasing by 0.0033 for each increase of 1 unit

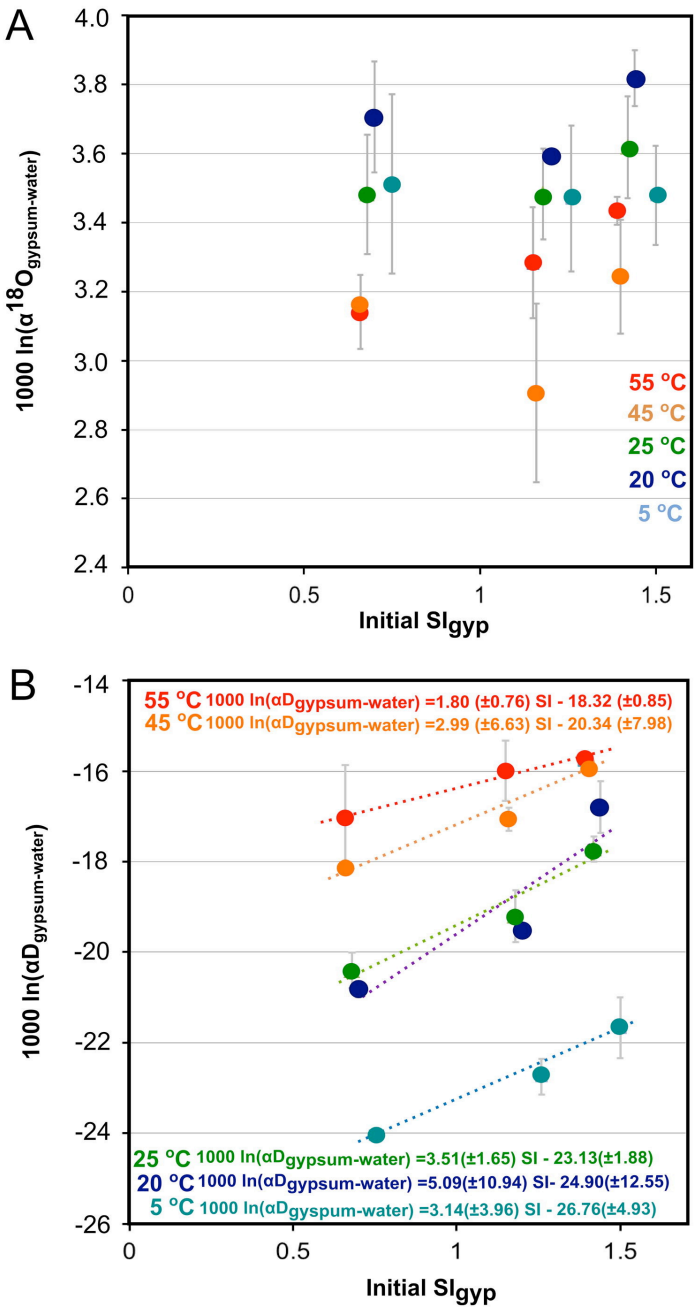

Fig. 2.11. Isotope fractionation factors (**A**: $\alpha^{18}O_{gypsum-water}$; **B**: $\alpha D_{gypsum-water}$) between GHW and its mother solution obtained experimentally by mixing of $CaCl_2$ and Na_2SO_4 solutions at different initial concentrations of Ca^{2+} and SO_4^{2-} and temperatures. Error bars denote 1σ.

in the SI_{gyp}. This linear trend is similar (±0.0012, 1σ) at different temperatures. Less than 1 wt% of bassanite and anhydrite has been detected in all samples (Appendix B; Table B.4).

2.4.3.3 Gypsum precipitation from brines

The addition of NaCl to the solution does not affect $\alpha^{18}O_{gypsum\text{-}water}$ (1.0033 ± 0.0001) below 150 g l^{-1} of NaCl, and results were similar to gypsum precipitation at 20°C when no NaCl was added (1.0034 ± 0.0001) (Table 2.3 and Fig. 2.12). In contrast, $\alpha^{18}O_{gypsum\text{-}water}$ increased to 1.0038 ± 0.0002 at a salinity of 200 g l^{-1} and to 1.0047 ± 0.0003 at 300 g l^{-1}. The $\alpha D_{gypsum\text{-}water}$ increased linearly with salinity from 0 to 300 g l^{-1} NaCl by 0.00003 units per gram of NaCl in solution and showed the greatest value of 0.9893 ± 0.0002 at 300 g l^{-1} (Table 2.3). The water content of the solids was 20.7 ± 0.3% in experiments performed at salinities between 30 and 150 g l^{-1} of NaCl, whereas the water yield was slightly lower (19.7 ± 0.1%) in the experiments at 200 g l^{-1} and 300 g l^{-1}. Mineralogical analyses by XRD detected only gypsum in the experiments at NaCl concentrations below 150 g l^{-1} and small amounts of bassanite and unconverted anhydrite of up to 2.5% and 4.6% respectively at 300 g l^{-1}(Appendix B; Table B.3).

2.4.4 Discussion

2.4.4.1 Effect of temperature and precipitation rate on the isotope fractionation factors in gypsum hydration water

Most equilibrium fractionation factors between the solution and the solid phase approach unity (i.e. no fractionation between the solution and the mineral, α = 1) with increasing temperature (Friedman and O'Neil, 1977). In the experiments, $\alpha D_{gypsum\text{-}water}$ increases with temperature in the gypsum formed using two methods (conversion of anhydrite to gypsum and mixing of $CaCl_2$ and Na_2SO_4 solutions). These methods produce similar results for $\alpha^{18}O_{gypsum\text{-}water}$ and $\alpha D_{gypsum\text{-}water}$ in the range of temperature studied within analytical uncertainties (Fig. 2.10). In the case of $\alpha^{18}O_{gypsum\text{-}water}$, no significantly statistical relationship with temperature was observed when examining separately the results from each method of gypsum precipitation (p-value >0.05 in both cases). However, when combining the results from both methods, a slight dependence of $\alpha^{18}O_{gypsum\text{-}water}$ with temperature becomes significant (R^2 = 0.70; p-value <0.05; Fig. 2.10) because of the increased number of observations. The equation for $\alpha^{18}O_{gypsum\text{-}water}$ (expressed as 1000 ln($\alpha^{18}O_{gypsum\text{-}water}$)), as a function of temperature (°C) is:

$$1000 \ln\left(\alpha^{18}O_{gypsum\text{-}water}\right) = -0.009\,(\pm 0.004)\,T + 3.68\,(\pm 0.13)$$

whereas the temperature dependence of $\alpha D_{gypsum\text{-}water}$ is given by:

$$1000 \ln(\alpha D_{gypsum\text{-}water}) = -0.104\,(\pm 0.053)\,T - 22.05\,(\pm 1.99)$$

This very small dependence of $\alpha^{18}O_{gypsum\text{-}water}$ on temperature is not relevant for many geological and palaeoclimate applications; however, the greater sensitivity of $\alpha D_{gypsum\text{-}water}$ to temperature has implications for the calculation of δD of the mother solution, especially when gypsum forms in hydrothermal environments from hydration of anhydrite (e.g. Matsuyaba and Sakai, 1973; Bath et al., 1987). For example, using the revised fractionation factor value at 55°C (1.0033 ± 0.0002), the inferred value of $\delta^{18}O$ in the mother water increases by 0.7‰ compared to using the fractionation factor of 1.004 (Gonfiantini and Fontes, 1963; Sofer, 1978). δD value decreases by ~4‰ using the revised fractionation factor (0.984) instead of the accepted value (0.980; Sofer, 1978). Hence, the temperature of gypsum formation should be considered when choosing which fractionation factors to apply.

At lower temperatures (i.e. from 20°C to 40°C), the two methods of gypsum precipitation produce slightly lower values for $\alpha^{18}O_{gypsum\text{-}water}$, but similar $\alpha D_{gypsum\text{-}water}$ values (within analytical error) compared to previously proposed values (Gonfiantini and Fontes, 1963; Fontes and Gonfiantini, 1967; Sofer, 1978; Hodell et al., 2012). For $\alpha^{18}O_{gypsum\text{-}water}$, we obtained a value of 1.0034 ± 0.0001 from 20°C to 40°C, which is within the error reported previously (i.e. 1.0037 ± 0.0005 in Gonfiantini and Fontes, 1963; 1.0039 ± 0.0004 in Hodell et al., 2012), but mostly closer to the lower range of values and more precise. For $\alpha D_{gypsum\text{-}water}$, obtained values from 20°C to 40°C (0.9812 ± 0.0007) are within error of previous measurements (0.981 ± 0.002 between 12 and 37°C; Hodell et al., 2012), but are also more precise.

By using the proposed $\alpha^{18}O_{gypsum\text{-}water}$ value of 1.0034 ± 0.0001, any calculation of mother water in the range from 20°C to 40°C produces a $\delta^{18}O$ of water that is ~0.6‰ higher than if the fractionation factor of 1.004 is used instead (Appendix B; Table B.5). This results in significant differences for quantitative isotopic studies using GHW, such as the tandem carbonate-GHW palaeothermometer (Hodell et al., 2012). Values of $\delta^{18}O$ of mother water that are 0.6‰ greater will lead to water temperatures that are approximately 2°C higher than those calculated using a fractionation factor of 1.004.

$CaCl_2/Na_2SO_4$ mixing experiments at different initial SI_{gyp} were performed to calculate the effect of precipitation rate on the isotope fractionation factors. Results show that, at different initial SI_{gyp}, within the studied range of saturations (SI_{gyp} = 0.66-1.50) there are no measurable differences in $\alpha^{18}O_{gypsum\text{-}water}$ (Table 2.2), independent of gypsum formation temperature. Unlike $\alpha^{18}O_{gypsum\text{-}water}$, the hydrogen fractionation factor, however, increases

at a constant rate with SI_{gyp} at all temperatures by 0.003 ± 0.001 per unit of SI_{gyp}.

The studied range of supersaturation is ~5 to ~20 times greater than gypsum saturation under equilibrium conditions (e.g. 0.014 M of dissolved $CaSO_4$ at 25°C). Equilibrium or near-equilibrium conditions are expected during the precipitation of most natural gypsum deposits. However, the experiments at relatively elevated saturations are useful to ascertain the role of kinetic effects on isotopes fractionation during gypsum precipitation.

The fractionation factors between GHW and free water obtained experimentally are the net result of equilibrium and kinetic effects for oxygen and hydrogen isotopes. The relative importance of the two is governed by the rate of gypsum precipitation. Pure equilibrium-controlled fractionation may occur during slow gypsum precipitation, whereas kinetic isotopic fractionation is more likely at higher precipitation rates. This is demonstrated by the increase in $\alpha D_{gypsum\text{-}water}$ with increasing saturation (SI_{gyp}). This suggests that the equilibrium fractionation (i.e. SI_{gyp} = 0) for hydrogen isotopes may be lower than the values obtained from $CaCl_2/Na_2SO_4$ mixing experiments at different temperatures, in which $\alpha D_{gypsum\text{-}water}$ is partially controlled by kinetic effects.

The fact that $\alpha^{18}O_{gypsum\text{-}water}$ does not show measurable trends with SI_{gyp} may indicate that kinetic effects are minimal for oxygen isotopes. The $\alpha^{18}O_{gypsum\text{-}water}$ is controlled by isotopic fractionation between the free solution and the hydration sphere of Ca^{2+} in solution (Taube, 1954; Gonfiantini and Fontes, 1963; Oi et al., 2013). The results suggest that different calcium concentrations in the solution and SI_{gyp} do not affect the isotopic values of the hydration sphere of Ca^{2+}, within the range of experimental conditions investigated.

No measurable differences in $\alpha^{18}O_{gypsum\text{-}water}$ and $\alpha D_{gypsum\text{-}water}$ were observed between the free-drift and the shaking experiments performed at the same SI_{gyp} and temperature. This is because the initial saturations used in the experiments are relatively far from the gypsum precipitation equilibrium. At these saturation levels, there is little difference in the rate of gypsum nucleation and precipitation between both types of experiments, as gypsum crystallisation occurs immediately after mixing the initial $CaCl_2$ and Na_2SO_4 solutions.

The relative difference in $\alpha D_{gypsum\text{-}water}$ between the experiments conducted at lower initial SI_{gyp} (0.66-0.70) and those at higher SI_{gyp} (1.39-1.44) is 0.0024 ± 0.0010. This suggests that holding all other parameters constant (isotopic composition of the solution, temperature, etc.), faster precipitation of gypsum causes enrichment of hydrogen isotopes in GHW by ~2.4‰ with respect to the experiments with the lowest initial SI_{gyp} (and therefore the slowest rates of precipitation), within the studied range of SI_{gyp}. Unlike the insignificant effect of different initial SI_{gyp} and calcium concentrations on the hydration sphere of Ca^{2+}, the isotopic values of the hydration sphere of SO_4^{2-} are affected by different ionic concentrations and gypsum precipitation rates, within the range of experimental conditions

investigated. Although more experiments are needed to explore $\alpha D_{gypsum\text{-}water}$ closer to the saturation point of gypsum, we assume that the relationship between $\alpha D_{gypsum\text{-}water}$ and SI_{gyp} follows the same linear relationship at lower saturations. The $\alpha D_{gypsum\text{-}water}$ values are extrapolated to for $SI_{gyp} = 0$ and to estimate the expression of pure equilibrium fractionation, with application to cases when gypsum precipitates under near-equilibrium conditions.

The results indicate that at $SI_{gyp} = 0$, the value of $\alpha D_{gypsum\text{-}water}$ should be 0.0046 ± 0.0019 lower than in the experiments with faster gypsum precipitation (i.e. SI_{gyp} = 1.39–1.50). Therefore, at the slowest gypsum growth rates, δD in GHW is depleted by ~4.6‰ when compared with the gypsum formed at the faster precipitation rates in the experiments at any given temperature.

This finding has potentially important implications for accurate calculations of δD of the fluid from GHW (particularly for determining d-excess values), especially in gypsum crystals formed at low saturation state. This is the case for the megacrystals of the caves in the Naica mine (Chihuahua, Mexico) (García-Ruiz et al., 2007; Gázquez et al., 2012, 2013), where gypsum speleothems grew from a solution with SI_{gyp} close to 0 and temperature around 47-55°C.

2.4.4.2 Effect of salinity on the isotope fractionation factors in gypsum hydration water

The initial salinity (NaCl concentration) of the solution also controls the fractionation factor between water and gypsum. Results suggest that a $\alpha^{18}O_{gypsum\text{-}water}$ is not affected by NaCl concentrations below 150 g l^{-1}. Above 150 g l^{-1}, the fractionation of oxygen isotopes increases gradually from 1.0034 below 150 g l^{-1} to 1.0047 ± 0.0003 at 300 g l^{-1}. For hydrogen, the $\alpha D_{gypsum\text{-}water}$ increases linearly with salinity from 0.9806 to 0.9893 between 0 g l^{-1} and 300 g l^{-1} (Table 2.3 and Fig. 2.12). Therefore, gypsum that precipitates from a 300 g l^{-1} NaCl solution has a δD that is ~10‰ lower than gypsum precipitated from freshwater with the same isotopic composition (when all other variables are held constant). Given that gypsum formed from evaporated seawater starts to precipitate when the solution reaches a salinity of ~130 g l^{-1}, the effect of salinity on $\delta^{18}O$ hydration water is small for most gypsum precipitates. However, the hydrogen isotopes fractionate by 3‰ less at a salinity of 130 g l^{-1} compared to freshwater. This implies that when the conventional fractionation factors are applied to gypsum formed from evaporated seawater (i.e. ~130 g l^{-1}), the values of d-excess are 10‰ more positive than when the revised fractionation factors are used instead (assuming no salinity effect on $\delta^{18}O$).

The effect of NaCl concentration on the fractionation factor between water and gypsum

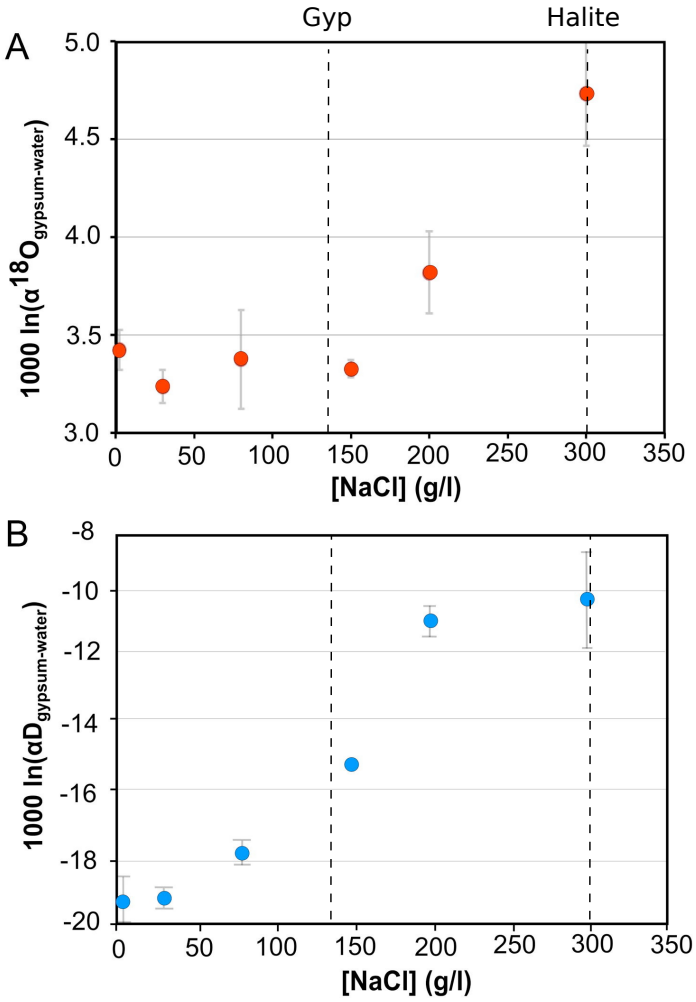

Fig. 2.12. Isotope fractionation factors (**A**: $\alpha^{18}O_{gypsum\text{-}water}$; **B**: $\alpha D_{gypsum\text{-}water}$) between GHW and its mother solution at different salinities obtained experimentally by hydration of anhydrite in solutions with different amounts of NaCl. Error bars denote 1σ. The vertical dashed lines indicate the approximate salinities at which gypsum and halite begin to precipitate during the evaporation of seawater.

NaCl concentration ($g\,l^{-1}$)	$\alpha^{18}O$	1σ	αD	1σ	n
0	1.0034	0.0001	0.9806	0.001	4
30	1.0032	0.0001	0.9807	0.0003	2
80	1.0034	0.0003	0.9824	0.0004	2
150	1.0033	0.0001	0.9846	0.0001	3
200	1.0038	0.0002	0.9886	0.0004	2
300	1.0047	0.0003	0.9893	0.0002	2

Table 2.3. Isotope fractionation factors ($\alpha^{18}O_{gypsum\text{-}water}$ and $\alpha D_{gypsum\text{-}water}$) between GHW and its mother solution obtained experimentally by hydration of anhydrite from solutions with different concentrations of NaCl at 20°C. See Appendix B for complete data report. Measurements were made using a Picarro L-1102i analyzer.

can be attributed mainly to decreases in the activity of water as salinity increases, which is related to the effect of Cl^- on the hydration spheres of Ca^{2+} and $SO_4{}^{2-}$ (Di Tommaso et al., 2014). As a consequence, the activity and isotopic ratios of water in brines are not the same as for freshwater (Sofer and Gat, 1975). Another explanation of the effect of NaCl on the fractionation factor is that the precipitation of intermediate hydrated calcium sulfate phases (e.g. bassanite) could affect the fractionation factors between water and gypsum at high salinities. Indeed, the stability of bassanite increases with increasing NaCl concentration (Ostroff, 1964; Ossorio et al., 2014). Considering these results, the salinity of the solution from which gypsum precipitated should be considered for calculations of the original $\delta^{18}O$, δD, and derived d-excess from gypsum precipitated from brines (i.e. evaporative marine gypsum).

2.4.4.3 Triple oxygen isotope fractionation in gypsum hydration water

The parameter θ, which describes the relationship between $\alpha^{17}O$ and $\alpha^{18}O$ ($\alpha^{17}O_{gypsum\text{-}water} = \alpha^{18}O_{gypsum\text{-}water}{}^{\theta}$), has been determined for water-GHW. We observed $\theta = 0.5297 \pm 0.0012$ (1σ) in the experiments of hydration of anhydrite and θ is independent of temperature. The observed θ value is close to the greatest theoretical values of this parameter in any mass-dependent fractionation process of triple oxygen isotope, which ranges from 0.52 to 0.5305 (Matsuhisa et al., 1978; Cao and Liu, 2011; Bao et al., 2016). This θ value agrees with that given by Barkan and Luz (2005) in vapour-liquid water equilibrium ($\theta = 0.529 \pm 0.001$), as well as other equilibrium mass-dependent reactions for the triple oxygen isotope system (Miller, 2002; Cao and Liu, 2011; Bao et al., 2016). Although no dependence of θ with temperature has been detected in the experiments, this parameter increases with

temperature in most water–mineral systems during oxygen isotope fractionation. However, in the temperature range from 0°C to 50°C no measurable trends (within analytical uncertainties of the current methods) are expected for most geochemical systems, including CO_2-water, quartz-water and calcite-water (Cao and Liu, 2011), agreeing with observations in the GHW-water system.

2.4.5 Conclusions

The $\alpha D_{gypsum\text{-}water}$ is 0.9812 ± 0.0007 at 20°C. Between 3°C and 55°C and salinities <150 g l^{-1} of NaCl, $\alpha D_{gypsum\text{-}water}$ was found to increase by 0.0001 units per °C. The $\alpha^{18}O_{gypsum\text{-}water}$ displays a very small decrease with temperature of 0.00001 per °C, which is not significant over much of the temperature range considered for palaeoclimate applications. Between 3°C and 55°C, $\alpha^{18}O_{gypsum\text{-}water}$ averages 1.0035 ± 0.0002. Precipitation of gypsum in NaCl concentrations below 150 g l^{-1} did not significantly affect $\alpha^{18}O_{gypsum\text{-}water}$, but $\alpha D_{gypsum\text{-}water}$ increases linearly with NaCl concentrations even at relatively low salinities. It is necessary, therefore, to apply a salt correction for gypsum formed from brines. Fractionation factors for ^{17}O and ^{18}O were found to follow the theoretical mass-dependent fractionation on Earth (θ = 0.529 ± 0.001). Specific examples of the importance of using the revised fractionation factors when calculating the isotopic composition of the fluids are given in Gázquez et al. (2017).

2.5 Gypsum-water isotopic exchange

Once accurate and precise gypsum-water fractionation factors are known, it is necessary to understand the conditions under which gypsum's structurally-bound water can undergo exchange with secondary waters. GHW can only be used for accurate palaeoenvironmental reconstruction if gypsum deposits are both primary and have not undergone (i) dehydration or (ii) recrystallisation and isotope exchange, thus retaining the original water isotopic composition (Hodell et al., 2012). Knowledge of the mechanisms of gypsum dehydration, recrystallisation and exchange is needed in ascertain the extent to which GHW is retained within the crystalline structure, and thus for the subsequent interpretation of hydration water signatures.

2.5.1 Gypsum dehydration

Gypsum may dehydrate due to elevated temperatures during sediment burial and exhumation cycles or hydrothermal processes (e.g. Warren, 2016). Numerous studies have ex-

amined the thermally induced dehydration of gypsum, focusing on the dehydration mechanisms from gypsum through to α-anhydrite, the associated empirical activation energies, and the occurrence and duration of the intermediate phases during the dehydration (see Ballirano and Melis, 2009). There is a currently a consensus that the thermal dehydration of gypsum occurs in a two-step process (e.g. McAdie, 1964; Abriel et al., 1990; Christensen et al., 2008; Paulik et al., 1992; Deutsch et al., 1994; Chang et al., 1999; Robertson and Bish, 2013; Prieto-Taboada et al., 2014), the final dehydrated product being reached via the formation of the intermediate hemihydrate, bassanite:

$$CaSO_4 \cdot 2H_2O \longrightarrow CaSO_4 \cdot 0.5H_2O + 1.5H_2O \longrightarrow \gamma\text{-}CaSO_4 + 0.5H_2O$$

During the analysis of large, single crystals, however, it is reported that γ-anhydrite can be directly produced without the appearance of a hemihydrate intermediate (e.g. Badens et al., 1998; Sarma et al., 1998; Prasad et al., 2005). Reported activation energies of the dehydration reaction also range from 60 kJ mol^{-1} to 500 kJ mol^{-1} between studies (e.g. Strydom et al., 1995; Ballirano and Melis, 2009), and inconsistencies in experimental analysis have resulted in a wide range of reported initial dehydration temperatures (~57°C to ~100°C; Prasad et al., 2001; Prieto-Taboada et al., 2014).

Discrepancies between previous studies have been attributed to multiple factors that include the rate at which gypsum is heated, atmospheric relative humidity and/or water vapour pressure, crystalline size and sample purity (e.g. Khalil, 1982; Paulik et al., 1992; Badens et al., 1998; Harrison, 2012; Robertson and Bish, 2013). Results may also be affected by the nature of the samples analysed; the majority of previous studies examine powdered gypsum samples, while some utilise polycrystalline samples but with very small mean grain sizes (e.g. between 45 μm and 123 μm; Fusseis et al., 2012). The samples previously analysed are often not applicable to gypsum seen in natural environments, such as the mm to cm scale crystals examined in palaeoclimatological studies of Hodell et al. (2012), Gázquez et al. (2013), and Grauel et al. (2016) (among others).

Here, in situ confocal Raman spectroscopy (RS) and tandem thermogravimetric (TGA) and differential scanning calorimetry (DSC) measurements were made on different crystalline grain sizes of gypsum to both determine the stability of the intermediate bassanite phase during the thermal dehydration of gypsum, and to understand the timing of the dehydration and rehydration reactions.

2.5.2 Thermal dehydration of gypsum monitored by in situ Raman spectroscopy and TGA/DSC

A systematic study was conducted to determine (1) the timing of the dehydration of gypsum as a function of temperature and grain size of the starting material, and (2) to investigate the stability of the intermediate bassanite phase during the dehydration reaction. *in situ* confocal RS and TGA and DSC measurements were made on four different crystalline grain sizes of gypsum. To minimise intra-method variability, TGA/DSC and RS experiments were conducted at the same internal conditions – this included the same sample housing, gas flow (and thus water vapour pressure) and heating rates. Experiments were conducted at both isothermal temperatures and at continuous incremental temperature ramps (e.g. 1°C min^{-1}, 5°C min^{-1} etc.). Experiments were designed by N.P.E. and carried out by N.P.E. and Gernot Nehrke at the Alfred Wegener Institute, Bremerhaven.

2.5.2.1 Methods

An analytical-grade synthetic gypsum powder, NEWGYP (Fisher Scientific, C/2360/50; Gazquez et al., 2015), was used for experimental analysis. Differing grain size fractions were obtained by sieving the powder so that the sample grain sizes were within the range of two mesh diameters; 38 to 64 μm, 64 to 125 μm, and 125 to 300 μm. Gypsum with larger grain sizes (>500 μm) was obtained from fragments of a natural gypsum sample obtained from the Messinian deposits of the Sorbas Basin (Evans et al., 2015). The individual crystals were examined under a confocal microscope prior to analysis. Only crystals that contained a negligible volume of fluid inclusions were used. Hereafter, the differing grain sizes are referenced respect to their mean grain size (rounded to the nearest 50 μm), and are therefore referred to as '50 μm gypsum', '100 μm gypsum' '200 μm gypsum', and '500 μm gypsum', respectively.

Isothermal experiments were conducted at 60°C, 70°C, 80°C, 90°C, 100°C and 120°C, where a ramp rate of 1°C min^{-1} was used to reach the desired temperature. Non-isothermal experimental conditions implemented during individual runs using TGA, DSC and RS are outlined in Table 2.4. To maintain constant relative humidity between analyses, all experiments were performed under a dry N_2 atmosphere.

The dehydration of gypsum was investigated by means of a Mettler Toledo TGA/DSC instrument equipped with an auto sampler. Data was collected and processed using the Mettler Toldeo Star software version 11. The gas flow was set to 40 ml min^{-1} N_2 (20 ml sample gas, and 20 ml protective gas).

RS measurements were made using a WITec alpha 300 R (WITec GmbH, Germany)

Experiment ID	Temperature Ramp (°C min^{-1})	T_{max} (°C)	Crucible lid on/off
1	1	200	Off
2	5	200	Off
3	10	200	Off
4	20	200	Off
5	1	200	On
6	5	200	On
7	10	200	On
8	20	200	On

Table 2.4. Reference table of experimental conditions used for TGA, DSC and RS analysis.

CRM housed at the BioGeosciences section at the Alfred Wegener Institute, Bremerhaven. A 488 nm diode laser was used for all Raman measurements. Spectra were acquired using an UHTS 300 spectrometer equipped with an EMCCD camera. Raman spectra have been obtained using a grid with 600 lines and for high spectral resolution with 2400 lines. A Linkam THMSG600 temperature controlled stage connected to an LNP95 LN_2 cooling system was placed under the microscope and a Zeiss objective (LD Plan-Neofluar 20x / NA 0.4 corr) was used for all CRM measurements. The chamber of the temperature-controlled stage was sealed with a thin cover glass and the N_2 flow inside the chamber adjusted to the same flow used in the TGA runs (40 ml min^{-1}). The gas flow was determined using an Agilent Technologies, ADM1000 universal gas flowmeter connected to the outflow of the temperature-controlled stage. A wash bottle could also be fitted to the inlet N_2 flow to allow for controlled changes in relative humidity of the chamber.

Prior to TGA/DSC and CRM analysis, 10 mg (±0.5 mg) of gypsum was placed in 30 ml alumina crucibles (Mettler Toledo material no.: 51140843). The same 30 μl alumina crucibles used in the TGA were housed inside the chamber of the temperature-controlled stage of the CRM.

The addition of a lid to the crucible that houses the gypsum in all experiments is known to increase the partial pressure of water exerted on the sample (e.g. Lou et al., 2011). This is a result of the restriction to the removal of water from the boundary layer around the gypsum as it is expelled from the structure upon dehydration, thus causing an increase in pressure in the local environment. An alumina lid (Mettler Toledo material no.: 51140477) that has a hole of diameter ~1 mm was utilised in 'lid on' experiments, whereas no lid was applied in 'lid off' experiments (Table 2.4).

When the lids of crucibles were on in CRM experiments, the laser was focused onto the gypsum through the hole in the lid. As the crucible that houses the gypsum is heated from its base in the temperature-controlled stage and the Raman laser is focused onto the top of the sample, there is minor lag between the reference temperature and the real temperature of the sample when measured. Modelling of this transient condition demonstrates that this lag is on the order of 3°C min^{-1} at a heating rate of 20°C min^{-1}, becoming negligible at a heating rate of 1°C min^{-1}. The reference temperature is reported without correction.

Fig. 2.13A shows the Raman spectra obtained from analysis gypsum, bassanite and soluble γ-anhydrite. The 300 to 4000 cm^{-1} spectra can be split into sulfate (300–1300 cm^{-1}) and water (3400–3700 cm^{-1}) peak regions. The flexion vibrations have been further subdivided into $\nu 1$, $\nu 2$, $\nu 3$, and $\nu 4$ (SO_4) and an H_2O region (Fig. 2.13C) (e.g Prieto-Taboada et al., 2014).

Black body radiation causes growth of the baseline at elevated temperatures, especially to the higher Raman shift frequencies. This results in partial masking of the spectra in the H_2O region. This effect was increased during slower heating profiles, as well as when the lid of the crucible was added. Therefore, the Raman band of the $\nu 1$ (SO_4) region was selected for analysis. The majority of other studies employ deconvolution analysis to separate the relative contribution of the individual peaks in the 1008 cm^{-1} to 1025 cm^{-1} range (e.g. Prieto-Taboada et al., 2014). Here, a high resolving grid was employed between 900 cm^{-1} and 1200 cm^{-1} so that the individual peaks representing gypsum, bassanite, and soluble γ-anhydrite at 1008 cm^{-1}, 1015 cm^{-1}, and 1025 cm^{-1}, respectively, can be fully separated (Fig. 2.13B).

2.5.2.2 Results

Transformation experiments monitored by TGA/DSC – Non-isothermal analysis

TGA determines the mass loss of a sample over the course of thermal dehydration, and is represented as a curve displaying percentage weight loss over time (e.g. Fig. 2.14). DSC is a measurement of the difference in heat flow between the sample and a reference, thus providing a measure of the heat absorbed or released during phase transitions. The resultant output of DSC experiments is a curve of heat flux over time, where exothermic reactions are shown by a divergence of the curve below the baseline. Experiments are compared when the lid of the crucible that houses the gypsum is omitted (Fig. 2.14A) and applied (Fig. 2.14B).

Fig. 2.14A shows the TGA and DSC curves of the dehydration of 100 μm gypsum at heating ramps of 1 min^{-1}, 5 min^{-1}, 10 min^{-1} and 20°C min^{-1} when the lid of the crucible that houses the sample is omitted (experiments 1-4; Table 2.4). A comparison of the TGA

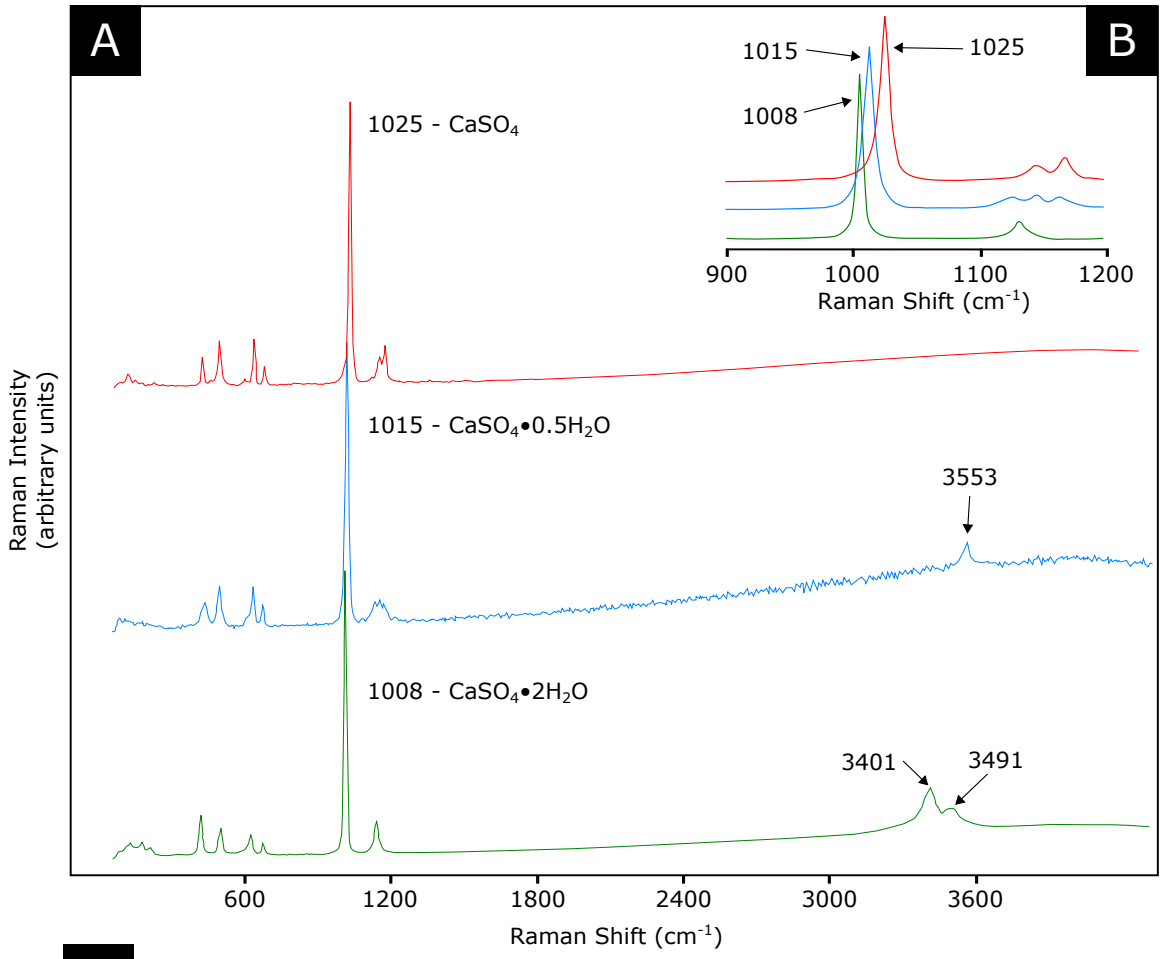

C

Compound	$v_2(SO_4)$		$v_4(SO_4)$			$v_1(SO_4)$	$v_3(SO_4)$			(H_2O)	
Gypsum	415	495		620	673	1008		1134		3401	3491
Bassanite	428	489		627	669	1015		1128			2553
γ-Anhydrite	420	490		630	673	1025			1167		
β-Anhydrite	417	499	609	628	675	1017	1111	1128	1160		
α-Anhydrite	417	497	609	628	676	1017	1108	1127	1158		

Fig. 2.13. **A**: Raman spectra (0 cm^{-1} to 4200 cm^{-1}) identified during the analysis of gypsum, bassanite, and soluble γ-anhydrite. **B**: Raman spectrum of the v1(SO_4) stretching region (900 cm^{-1} to 1200 cm^{-1}) produced using a high resolving grid. **C**: Suggested Raman Spectra in the $CaSO_4$–H_2O System (Prieto-Taboada et al., 2014).

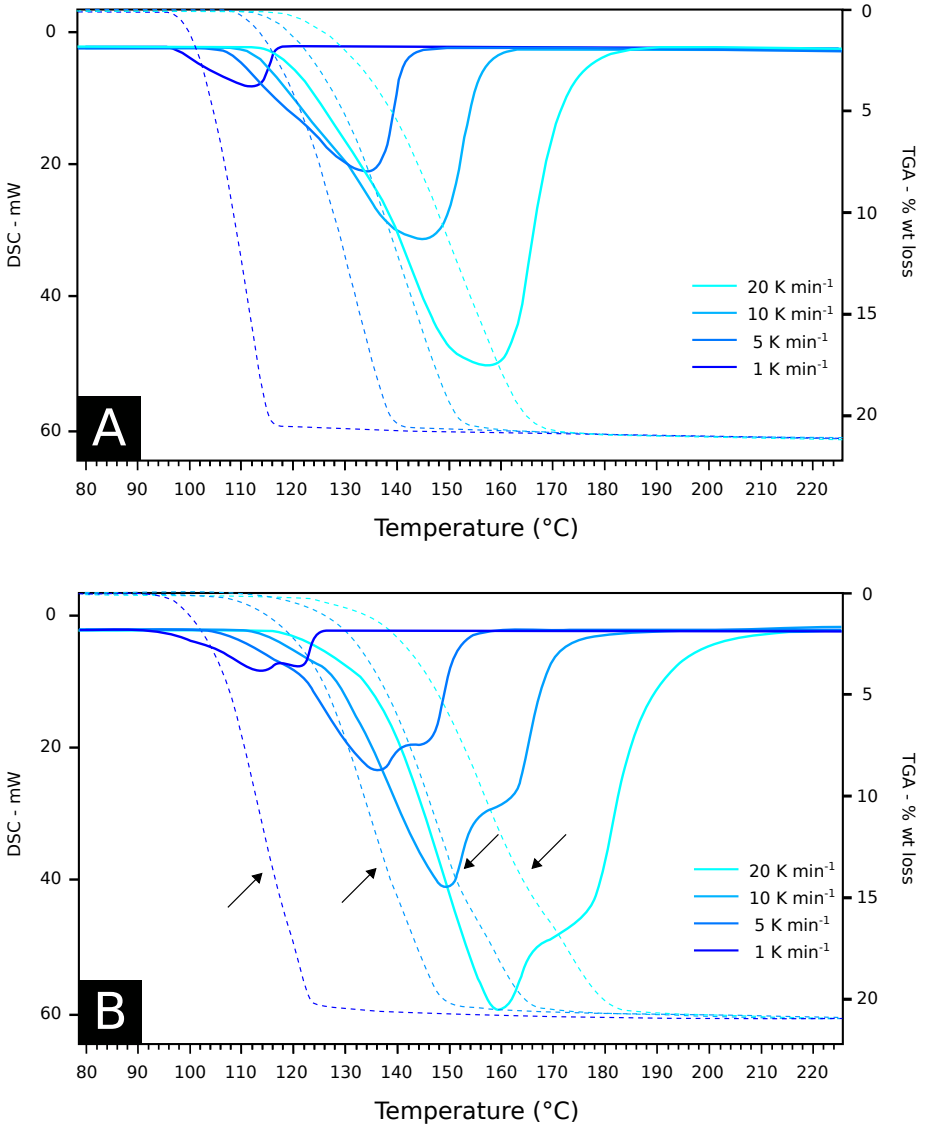

Fig. 2.14. Thermogravimetric analysis (TGA; dashed lines) and differential scanning calorimetry (DSC; solid lines) profiles of 100 μm gypsum at heating rates of 1°C min^{-1}, 5°C min^{-1}, 10°C min^{-1} and 20°C min^{-1}: **A**: Lid of the crucible is not applied. **B**: Lid of the crucible is applied. Black arrows denote points on the TGA curve where the rate of mass loss changes.

curves obtained for 100 μm gypsum at all heating rates shows that the onset of dehydration, represented by the initial reduction in mass, occurred at lower temperatures when lower heating rates are used and at higher temperatures when heating rates are higher. The rate of mass loss appeared to gradually increase from the onset until the termination of dehydration. Over all experiments, the total mass loss was found to be 20.9%, indicating all water had been removed from the crystal structure. All DSC curves display a single peak.

Fig. 2.14B shows the TGA and DSC results of the dehydration of 100 μm gypsum when the crucible lid is applied, but all other conditions remain constant (i.e. experiments 5-8; Table 2.4). 'Lid on' experiments display three observable differences to 'lid off' experiments: Firstly, DSC curves displayed two distinct peaks. Secondly, a reduction in the gradient of the TGA curve was observed, indicating that the rate of mass loss was retarded at ~75% of the total mass loss (black arrows; Fig. 2.14B). Thirdly, the termination of the dehydration reaction in experiments 5 to 8 occurred at higher temperatures compared to experiments 1 to 4 (Fig. 2.14A).

To compare the effect of grain size on the dehydration profiles, Fig. 2.15 displays 50 μm, 100 μm and 500 μm gypsum at a heating ramp of 10°C min^{-1} with both crucible lid off and on (experiments 3 and 7, respectively). The DSC curves of 50 μm gypsum show two distinct peaks, both when the crucible lid is on and off, and the TGA of both profiles show a step at ~75% of the total mass loss. 500 μm gypsum shows a single DSC peak and continuous weight loss in both experiments, however. Results from these analyses show that the onset of dehydration occurs at lower temperatures for smaller grain sizes. Analysis of 50 μm, 100 μm and 500 μm gypsum at heating rates of 1°C min^{-1}, 5°C min^{-1} and 20°C min^{-1} all produce similar profiles to those observed at a heating rate of 10°C min^{-1} (i.e. Fig. 2.15), but the onset of dehydration occurs at lower temperatures when heating rates are lower and vice versa.

Transformation experiments monitored by RS – Non-isothermal analysis

To compare the effect of grain size on the dehydration profiles with TGA/DSC analysis, all experiments (i.e. Table 2.4; experiments 1 to 8) were conducted on 50 μm, 100 μm and 500 μm gypsum. Fig. 2.15 displays the temperatures over which the $\nu 1$ (SO_4) modes of 1008 cm^{-1}, 1015 cm^{-1} and 1028 cm^{-1} were observed during the dehydration of 50 μm, 100 μm and 500 μm gypsum at ramp rate of 10°C min^{-1} with crucible lid off (experiment 3; dashed line) and on (experiment 7; solid line). During the dehydration of 50 μm and 100 μm gypsum, the $\nu 1$ (SO_4) mode shifted from 1008 cm^{-1} to 1015 cm^{-1} and 1028 cm^{-1} over different timescales. Lid-on experiments showed a systematic increase in the time period over which the 1015 cm^{-1} mode was observed. As observed in TGA/DSC experiments,

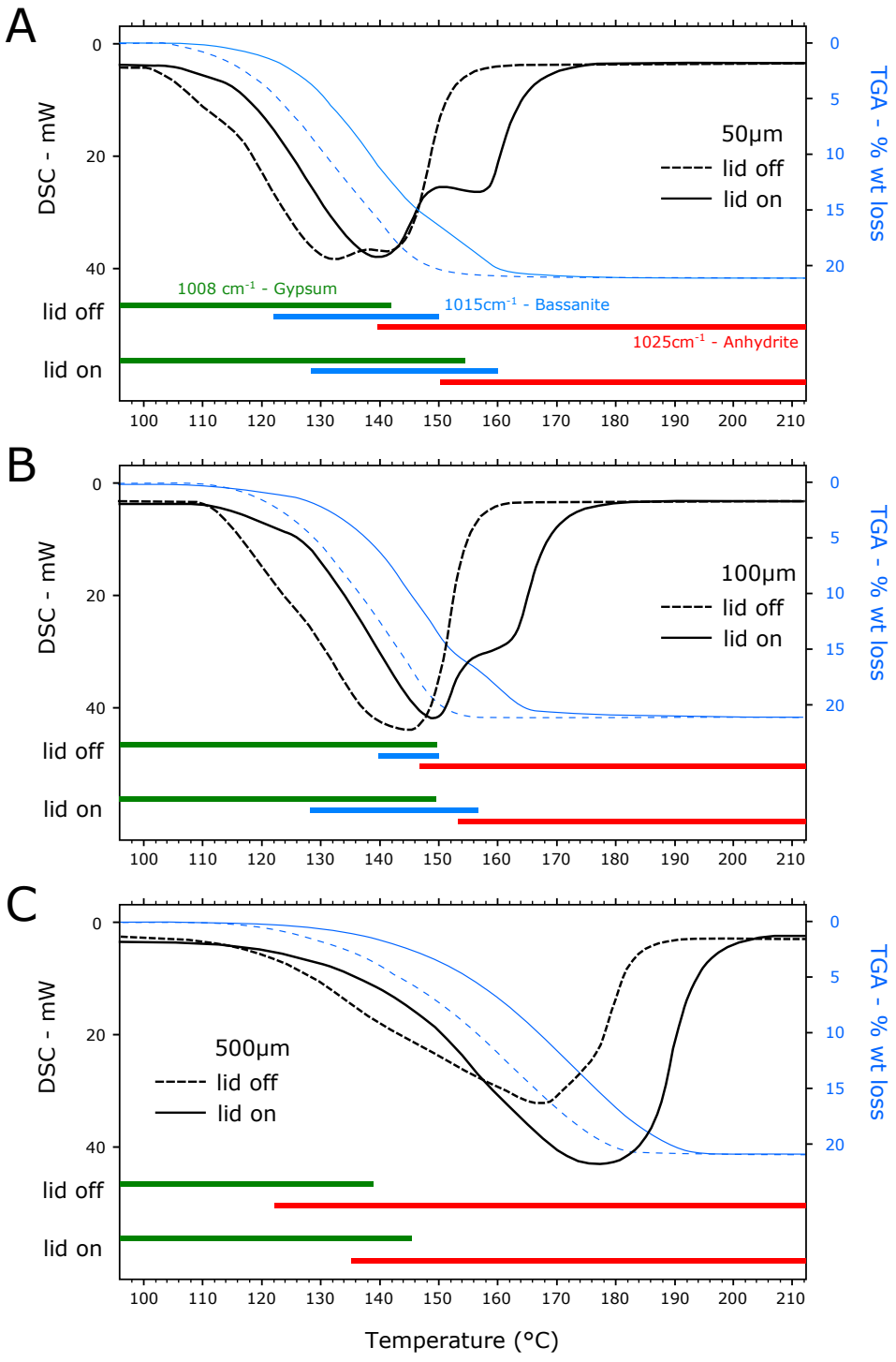

Fig. 2.15. Thermogravimetric (TGA) and differential scanning calorimetry (DSC) profiles of (**A**) 50 μm, (**B**) 100 μm, and (**C**) 500 μm gypsum at a heating rates of 10 °C min^{-1}. Horizontal bars indicate presence of raman spectra at 1008 cm^{-1}(green), 1015 cm^{-1} (blue), and 1025 cm^{-1}(red), representing gypsum, bassanite, and soluble γ-anhydrite, respectively.

analysis of gypsum at heating rates of 1°C min^{-1}, 5°C min^{-1} and 20°C min^{-1} all produce similar profiles to those observed at a heating rate of 10°C min^{-1}, where the transition to each phase occurred at lower temperatures for lower heating rates and visa versa. Notably, during the dehydration of 500 μm gypsum at all ramp rates and during both lid-on and lid-off experiments, the $\nu 1$ (SO_4) mode shifts directly from 1008 cm^{-1} to 1028 cm^{-1}, omitting the intermediate $\nu 1$ (SO_4) mode at 1015 cm^{-1}.

Transformation experiments monitored by TGA/DSC – Isothermal analysis

Experimental data obtained from isothermal analysis of 50 μm, 100 μm, 200 μm and 500 μm gypsum at 60°C, 70°C, 80°C, 90°C, 100°C and 120°C displayed continuous weight loss and one DSC peak for all grain sizes in both lid-on and lid-off experiments. The transformed fractions (ε) were calculated as a function of the total mass loss:

$$\varepsilon = \frac{W_i - W_t}{W_i - W_f}$$

where W_i = initial gypsum sample weight; W_t = sample weight after heating for time t; and W_f = sample weight corresponding to complete water loss (Khalil, 1982). Representative $\varepsilon\%$ values of the investigated gypsum materials at different isothermal temperatures are shown in Fig. 2.16 as a function of time. The termination of dehydration reaction (i.e. $\varepsilon = 1$) occurred after a shorted time period for both higher temperatures and in lid-off experiments. Dehydration of 50 μm, 100 μm, 200 μm and 500 μm gypsum at 60°C and 70°C (both lid-on and lid-off experiments) was incomplete after 3 days (i.e. ε did not reach 1).

Transformation experiments monitored by RS – Isothermal analysis

1008 cm^{-1}, 1015 cm^{-1} and 1028 cm^{-1} modes were visible simultaneously during the dehydration of 50 μm and 100 μm gypsum, while only the 1008 cm^{-1} and 1028 cm^{-1} modes were present during the dehydration of 500 μm gypsum. Dehydration of 50 μm and 100 μm gypsum at 60°C only displayed the 1008 cm^{-1} modes after 3 days, while dehydration reactions at 70°C displayed both 1008 cm^{-1}and 1015 cm^{-1} modes after 3 days.

2.5.2.3 Discussion

Timing of gypsum dehydration:

An accurate understanding of the isotopic modification of GHW due to dehydration and rehydration induced by exposure to elevated temperatures is needed for the accurate

interpretation of GHW signatures. Isothermal TGA/DSC experiments show that the onset of the dehydration of gypsum (represented by the initial mass loss of a sample) occurs earlier both at higher temperature and with decreasing grain size (Fig. 2.16). While the partial dehydration of finer grain sizes (e.g. 50 μm and 100 μm gypsum) occurs at temperatures of 60°C, larger grain sizes (i.e. 500 μm gypsum) do not show weight loss over the time period studied. Therefore, assuming a normal geothermal gradient, massive, crystalline gypsum should be the stable phase at depths up to ~2 km.

The heterogeneity of dehydration temperature with grain size has not been discussed in detail previously. It has been hypothesised that the differing phases produced during the dehydration process require different reaction energies, accounting for both the separation of water molecules from the crystal structure as well as evaporation of the released dehydration water (e.g. van der Heijden et al., 2011). Changes to parameters such as the vapour pressure and temperature will therefore influence the dehydration kinetics, changing the efficiency of dehydration (e.g. McAdie, 1964; Badens et al., 1998; Ballirano and Melis, 2009; Lou et al., 2011; Fusseis et al., 2012). During gypsum dehydration, the local environment is associated with a net volume increase as water exhumed has a greater volume than the pore spaces that develop. If water expulsion is restricted (e.g. due to crystalline size), the fluid pressure will increase, slowing the dehydration reaction (Bedford et al., 2017). The increased stability of larger grain sizes of gypsum may therefore be linked to the increased stabilisation of the inner domain of the crystalline structure caused by the increased pressures during heating. The timing and rate of dehydration of differing crystalline grain sizes of gypsum is therefore likely controlled by a feedback of pressure release and pore formation on the grain scale.

Stability of the intermediate bassanite phase:

The presence of two peaks within a DSC profile during the dehydration of powdered gypsum has previously been interpreted as the two-step dehydration process of gypsum through the bassanite intermediate ($CaSO_4 \cdot 2H_2O \longrightarrow CaSO_4 \cdot 0.5H_2O + 1.5H_2O \longrightarrow CaSO_4 + 0.5H_2O$), while the 3:1 mass loss in the TGA curve is consistent with the stoichiometry of this dehydration reaction (Paulik et al., 1992; Lou et al., 2011) (Fig. 2.15). A single DSC peak and no change in the rate of mass loss is interpreted to represent a single step transition (i.e. $CaSO_4 \cdot 2H_2O \longrightarrow CaSO_4 + 2H_2O$), as observed in isothermal experiments below 100°C and non-isothermal experiments when the crucible lid was omitted (e.g. van der Heijden et al., 2011; Lou et al., 2011). During the dehydration of 100 μm gypsum at a heating ramp of 10°C min^{-1} (lid off), the CRM detected multiple phases of calcium sulfate coexisting simultaneously at the same temperature (i.e. at 147°C; Fig. 2.15B).

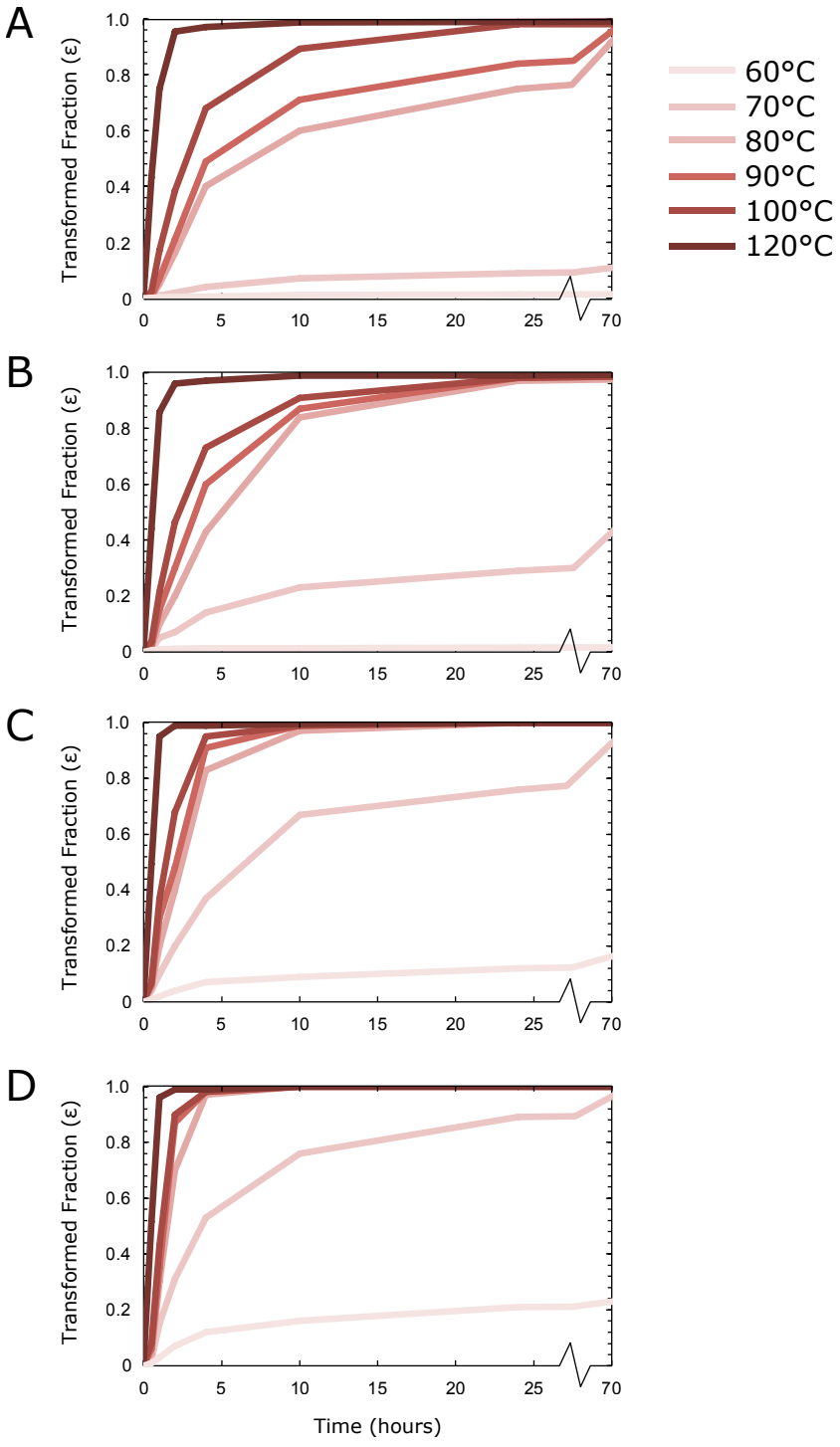

Fig. 2.16. Isothermal analysis of (**A**) 500 μm, (**B**) 200 μm, (**C**) 100 μm and (**D**) 50 μm gypsum over the temperature range 60˚C to 120°C with the crucible lid applied. Transformed fractions (ε), a function of the total mass, loss versus time curves for the dehydration (gypsum to γ-anhydrite). Note broken x-axis between 25 h and 70 h.

Direct comparison with the DSC curve shows this temperature coincides with the crest of the single DSC peak. The existence of intermediate phases can therefore be concealed in the TGA/DSC analysis (Putnis et al., 1990). It can be concluded that the stability of the bassanite intermediate is dependent on the rate of moisture release in the local environment, which may be due to increased temperatures (increasing the rate of moisture expulsion), and/or restricted removal of the expelled water due to the application of a lid.

During the dehydration of 500 μm gypsum at all temperatures (Fig. 2.15C), the $\nu 1$ (SO_4) mode shifts directly from 1008 cm^{-1} to 1028 cm^{-1}, while the 1015 cm^{-1} mode is suppressed beyond detectible limits. This $\nu 1$ (SO_4) mode shift (in both lid on and lid off experiments) occurs at only ~5% total weight loss. As the Raman laser only samples the surface of the crystal, the transition in the internal crystal structure is still in progress. The timing of the Raman shift and the lack of 1015 cm^{-1} mode is consistent with the observation of a sharp dehydration front that propagates inward from the margin of polycrystalline samples in time-series synchrotron X-ray micro-tomography experiments (Fusseis et al., 2012). Gypsum breakdown across the dehydration front of larger crystals is therefore very efficient and most likely controlled by the orientation of the gypsum lattice with respect to the advancing front (Fusseis et al., 2012). Dehydration of smaller grain sizes (< 200 μm), however, produces a prolonged bassanite phase due to both the reduced stability of smaller crystalline lattice and the increased efficiency of fluid drainage, lowering the internal crystalline water pressure. The presence of the bassanite intermediate is therefore likely controlled by a feedback of pressure release on the grain scale.

2.5.2.4 Conclusions

The initial temperature of dehydration increases with increasing grain size. Isothermal temperature experiments (up to 3 days in duration) conducted on crystalline grain sizes larger than 500 µm did not result in weight loss at temperatures below 65°C. In contrast, powdered gypsum with crystalline grain sizes less than 200 µm experienced partial weight loss between 60°C and 70°C, but did not fully dehydrate. Above 70°C, all gypsum fully dehydrated over differing timescales, where increasing temperature resulted in an increase in the rate of dehydration.

RS demonstrated that gypsum with crystalline grain sizes less than 200 µm dehydrated to γ-$CaSO_4$ via an observable bassanite intermediate during all isothermal temperatures and ramped temperatures experiments. The observed duration of bassanite was increased at both smaller grain sizes and increased partial pressure. At grain sizes larger than 500 µm, bassanite was undetectable by RS and TGA/DSC during the dehydration process. Overall, results suggest that stable isotopes of GHW can be used to reconstruct the isotopic

composition of palaeo-waters in environments where large (>500 μm) crystals are present, burial/exhumation of the sample has not exceeded ~2 km depth and recrystallisation has not occurred.

2.5.3 Gypsum recrystallisation and isotope exchange

Post-depositional isotope exchange of GHW may occur if gypsum is in contact with water that is isotopically different from its hydration water. The isotopic exchange reactions for oxygen and hydrogen isotopes between gypsum hydration water and pore water are:

$$CaSO_4 \cdot 2H_2{}^{16}O + H_2{}^{18}O \longrightarrow CaSO_4 \cdot 2H_2{}^{18}O + H_2{}^{16}O$$

$$CaSO_4 \cdot 2H_2{}^{16}O + HD{}^{18}O \longrightarrow CaSO_4 \cdot 2DH{}^{18}O + H_2{}^{16}O$$

The kinetics governing the rate of exchange via these reactions are not well understood, but are likely mediated by factors such as temperature, pressure, humidity, crystal size, and disequilibrium time (Hodell et al., 2012). Equally, the rate of oxygen versus hydrogen isotope exchange is likely to differ due to the differing rates of diffusion of the $H_2{}^{18}O$ and $DH{}^{16}O$ isotopologues into and out of the crystal structure. Thus, if isotope exchange were to occur, the $\Delta\delta D/\Delta\delta^{18}O$ relationship would deviate from its original value (Hodell et al., 2012).

Long-term isotope exchange experiments were set up in the Godwin Laboratory, Cambridge, to investigate the rate of GHW exchange (Fig. 2.17). Gypsum from the Cabezo de Maria, southeastern (SE) Spain, of 1 mm-2 mm grain size was placed in $CaSO_4$-saturated waters at 45°C with significantly differing isotopic composition (enriched: $\delta^{18}O$ = 21.6‰, δD = 58‰; depleted: $\delta^{18}O$ = -19.5‰, δD = -151‰) to that of the original GHW ($\delta^{18}O$ = -0.89‰, δD = -55.08‰). After two years, no exchange was found to occur. Results suggest that gypsum of mm-sized grain size will retain the isotopic composition of the water from which they form in most natural settings.

The isotopic composition of GHW can also be altered by dissolution in under-saturated waters and secondary precipitation of gypsum in sediment pore waters, however (Hodell et al., 2012; Pierre, 2018). Gypsum may undergo diagenetic transformations due to gypsum's relatively high solubility in water (2.0 g l^{-1} to 2.5 g l^{-1}) and halokinetic properties, making deposits somewhat mobile, both physically and chemically, in sedimentary environments (Orti, 2011; Bąbel and Schreiber, 2014). If dissolution and secondary precipitation were to occur, the hydration water of the recrystallised gypsum will have an isotopic composition in equilibrium with sediment pore waters (Hodell et al., 2012). The isotopic signature of

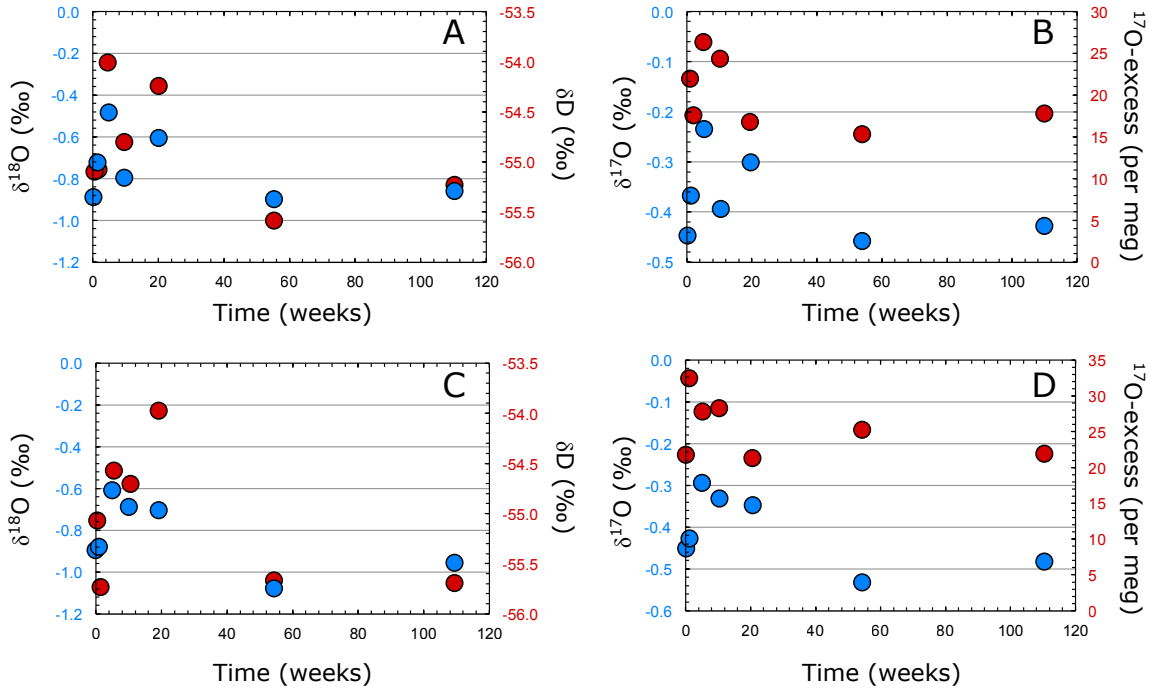

Fig. 2.17. Gypsum exchange experiments. 1 mm to 2 mm gypsum crystals (from the Cabezo de Maria, SE Spain) are placed in $CaSO_4$-saturated waters at 45°C. Initial GHW composition is -0.89‰, -55.08‰ and 22 per meg for $\delta^{18}O$, δD and ^{17}O-excess, respectively. Enriched water (**A** and **B**) has the isotopic composition $\delta^{18}O$ = 21.6‰, δD = 58‰; depleted water (**C** and **D**) has the isotopic composition $\delta^{18}O$ = -19.5‰, δD = -151‰. No isotopic exchange between the gypsum hydration water and the solution water is seen after >2 years.

GHW after recrystallisation is easily recognisable, and multiple samples will display no evaporative slope (Sofer, 1978). Equally, extensive recrystallisation results in recognisable changes to crystalline morphology, where primary features, i.e. clear, euhedral crystals with swallow-tail twinning, are replaced by gypsum entombing sediments and secondary diagenetic features (e.g. Hodell et al., 2012; Warren, 2016).

GHW is also believed to be free of 'vital effects' that influence standard $\delta^{18}O$ measurements of carbonates (e.g. Herwartz et al., 2017). In carbonates, vital effects generally result in lighter isotope compositions than expected for equilibrium fractionation (McConnaughey, 1989) due to the rate limiting step inducing the kinetic effect is conversion of $CO_2 \longrightarrow HCO_3^-$ and slow re-equilibration with water, especially at elevated pH (Herwartz et al., 2017). Thus a similar 'vital effect' is not expected for GHW (Herwartz et al., 2017). Additionally, biological effects have not been observed to impact GHW in environments where gypsum precipitation was likely mediated by microorganisms, such as the moderately saline (<100 g l^{-1}) ponds of Atacama Desert, Chile, where gypsum displayed variable

coloration (black, white, brown and greenish) and a friable structures (Thompson and Ferris, 1990; Vogel et al., 2009; Vogel et al., 2010; Farías et al., 2014; Herwartz et al., 2017).

Overall, the triple oxygen and hydrogen isotopic composition of GHW may serve as a useful palaeoenvironmental proxy, given that the isotopic composition of GHW is stable over a wide range of natural conditions. Analysis of GHW permits the actual isotopic composition of palaeo-waters to be determined with little to no effect of temperature, and thus GHW may be used as a tool for quantitative palaeohydrological reconstructions.

Chapter 3

Quantification of drought during the collapse of the classic Maya civilisation

Adapted from the manuscript: ***Nicholas P. Evans**, Thomas K. Bauska, Fernando Gázquez, Mark Brenner, Jason H. Curtis, and David A. Hodell. Science 361, 498-501 (2018).*

The demise of Lowland Classic Maya civilisation during the Terminal Classic Period (TCP, ~800-1000 CE) is a well-cited example of how past climate may have impacted ancient societies. Attempts to estimate the magnitude of hydrologic change, however, have met with equivocal success because of the qualitative and indirect nature of available climate proxy data. The past isotopic composition (δ^{18}O, δD, ^{17}O-excess and d-excess) of water in Lake Chichancanab, Mexico, was reconstructed by analysing the structurally-bound water in sedimentary gypsum, which was deposited under peak drought conditions. The triple oxygen and hydrogen isotope data provide a direct measure of past changes in lake hydrology. We modelled the data and conclude that annual precipitation decreased between 41% and 54% (with intervals of up to 70% rainfall reduction during peak drought conditions) and that relative humidity declined by between 2% and 7% compared to present-day conditions. Our modelling results provide robust, quantitative estimates of the magnitude of hydrologic change during the TCP that can be used to assess how drought affected agriculture in the northern Maya Lowlands.

D.A.H., N.P.E., and F.G. developed the analytical method and designed the study; M.B., J.H.C., and D.A.H. collected the original sediment cores from Lake Chichancanab; N.P.E. sampled the cores; N.P.E. and F.G. performed all isotopic analyses; T.K.B. designed the

transient model and performed drought simulations; and N.P.E. wrote the paper with contributions from all other authors.

3.1 Introduction

More than two decades ago, a sediment core from Lake Chichancanab (Yucatán Peninsula, Mexico; Fig. 3.1) provided the first physical evidence of a temporal correlation between drought and the sociopolitical transformation of the Classic Maya civilisation during the TCP (Hodell et al., 1995). Presence of gypsum horizons and a concomitant increase in the oxygen isotope ratio ($^{18}O/^{16}O$) in shells of ostracods and gastropods suggested the TCP was among the driest periods of the Holocene in northern Yucatán. Paleoclimate records produced subsequently provided additional evidence for drought during the TCP (Curtis et al., 1996; Hodell et al., 2001; Haug, 2003; Medina-Elizalde et al., 2010; Kennett et al., 2012; Wahl et al., 2013; Douglas et al., 2015), but the magnitude of hydro-climate change and its influence on Maya agricultural and sociopolitical systems remains controversial (Douglas et al., 2016a). The qualitative nature of most climate proxy archives, combined with dating uncertainties, has prevented detailed assessment of the relationship between past climate and cultural changes (Yaeger and Hodell, 2009; Douglas et al., 2016a,b).

Recent attempts to quantify estimates of past changes in rainfall amount and assess the impact on ancient Maya agriculture have utilised isotopes of either oxygen ($\delta^{18}O$) (Medina-Elizalde et al., 2010; Medina-Elizalde and Rohling, 2012) or hydrogen (δD) (Douglas et al., 2014, 2015, 2016a). No study to date has combined the two isotope systems because materials used for analysis (i.e. carbonates and leaf waxes) preclude simultaneous measurement of the multiple isotopologues of water. Combined analysis of $\delta^{18}O$, $\delta^{17}O$ and δD is a powerful method to estimate past hydrologic changes quantitatively because hydrogen and triple oxygen isotopes each undergo slightly different fractionation during evaporation, leading to changes in the derived d-excess and ^{17}O-excess parameters (see Chapter 1). In an effectively closed hydrological basin such as Lake Chichancanab, the primary controls on the isotopic fractionation of lake water during evaporation include: the fractional loss of precipitation to evaporation (P/E), normalised relative humidity (RH_n), temperature, and changes in the precipitation source (Hodell et al., 1995, 2001, 2005a; Gázquez et al., 2018). The d-excess is largely dependent on RH_n and temperature, whereas ^{17}O-excess is controlled mainly by RH_n (Surma et al., 2015; Herwartz et al., 2017; Gázquez et al., 2018). Because the predicted trends of d-excess and ^{17}O-excess in evaporating waters display different responses to climate variables, they can be evaluated individually using an iterative model (see Section 3.4).

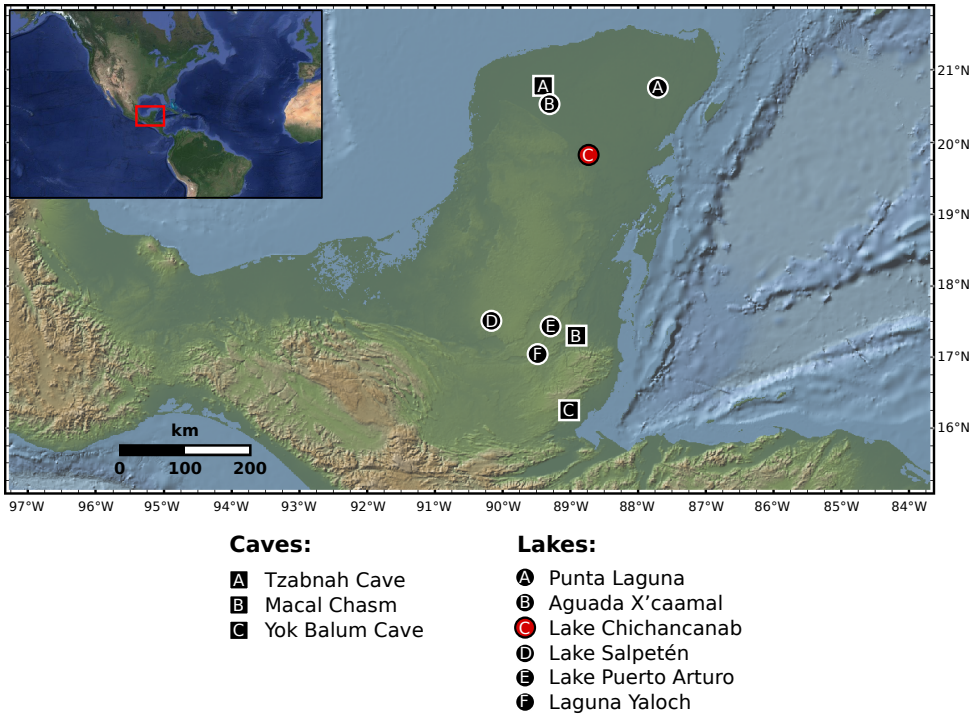

Fig. 3.1. Map of the Maya Lowlands displaying the locations of proxy climate archives (north to south); the Chaac speleothem of Tzabnah Cave (Medina-Elizalde et al., 2010); Punta Laguna (Curtis et al., 1996); Aguada X'caamal (Hodell et al., 2005b); Lake Chichancanab (this study) (Hodell et al., 2005a, 2001, 1995; Douglas et al., 2014); Lake Puerto Arturo (Wahl et al., 2014); Laguna Yaloch (Wahl et al., 2013); Macal Chasm (Webster et al., 2007); Lake Salpetén (Douglas et al., 2015); the Yok I speleothem of Yok Balum Cave (Kennett et al., 2012).

We took advantage of the benefits of using all isotopologues of water and their derived parameters (d-excess and ^{17}O-excess) by measuring triple oxygen and hydrogen isotopes in the hydration water of gypsum ($CaSO_4 \cdot 2\,H_2O$) in sediment cores from Lake Chichancanab (Hodell et al., 2005). Today, the lake water is near saturation for gypsum and during past periods of drier climate, when the lake volume shrank, gypsum precipitated from the lake water and was preserved as distinct layers within the accumulating sediments (Hodell et al., 1995, 2001, 2005a). When gypsum forms, water molecules are incorporated directly into its crystalline structure and this GHW records the isotopic composition of the parent fluid, with known isotopic fractionations (Sofer, 1978; Hodell et al., 2012; Herwartz et al., 2017; Gázquez et al., 2017a,b, 2018). Unlike oxygen isotope fractionation during formation of carbonate minerals (Lachniet, 2009; Kluge and Affek, 2012), fractionation during gypsum crystallisation is practically independent of temperature (Chapter 2), biological or kinetic

(non-equilibrium) effects (Herwartz et al., 2017). Additionally, isotopes of GHW that are measured in the sedimented gypsum inherently record the driest periods, offering a distinct advantage over other traditional climate archives such as speleothems or mollusk shells, which may fail to register peak drought conditions because of growth hiatuses. Absolute differences in the δ^{18}O, δD, ^{17}O-excess and d-excess, between modern and paleo-lake water, provide an estimate of differences between the lake hydrologic budget during the TCP and today (Fig. 3.2). Results were evaluated using a numerical isotope mass balance model that must satisfy all isotope variables, and thus provide a more robust constraint on past hydrology than does modelling δ^{18}O or δD alone.

3.2 Materials and methods

3.2.1 Sediment cores and sampling

Lake Chichancanab is located at ~19°51'21"N 88°45'49"W, Yucatán Peninsula, SE Mexico (Fig. 3.1). In March 2004, core CH1 7-III-04 was collected from Lake Chichancanab with a piston corer in 14.7 m of water (Hodell et al., 2005). Shortly after collection, cores were split, wrapped in plastic film and stored at 4°C. Core sections were measured for bulk density by gamma-ray attenuation (GRA) by Hodell et al. (2005), and contain high-density gypsum bands interbedded with low-density organic layers (Fig. 3.3). Gypsum was sampled at 0.5 cm intervals – individual crystals were picked from the >350 μm size fraction and ground to a powder. Powdered samples were dried in an oven at 45°C for 15 h to 20 h and placed under vacuum (~10^{-3} mbar) for ~3 h to remove adsorbed water prior to hydration water extraction (Playà et al., 2005).

3.2.2 Gypsum Hydration Water (GHW)

GHW was extracted from each sample (150-200 mg) by heating to 400°C and trapping the evolved water, in vacuo, using a bespoke offline extraction system described in Chapter 2. 1σ was ±0.07‰ for δ^{17}O, ±0.12‰ for δ^{18}O, ±0.63‰ for δD, ±0.8‰ for d-excess and ±6 per meg (±0.006‰) for ^{17}O-excess.

We suggest the gypsum in Lake Chichancanb preserves the isotopic composition of the lake water at the time of deposition and has not undergone post-depositional diagenesis or exchange with modern lake water. After applying fractionation factors, the isotopic values of the palaeo-lake waters are considerably enriched compared to the modern lake (Fig. 3.2; Fig. 3.3). If the GHW had exchanged with sediment pore water, a relatively homogeneous

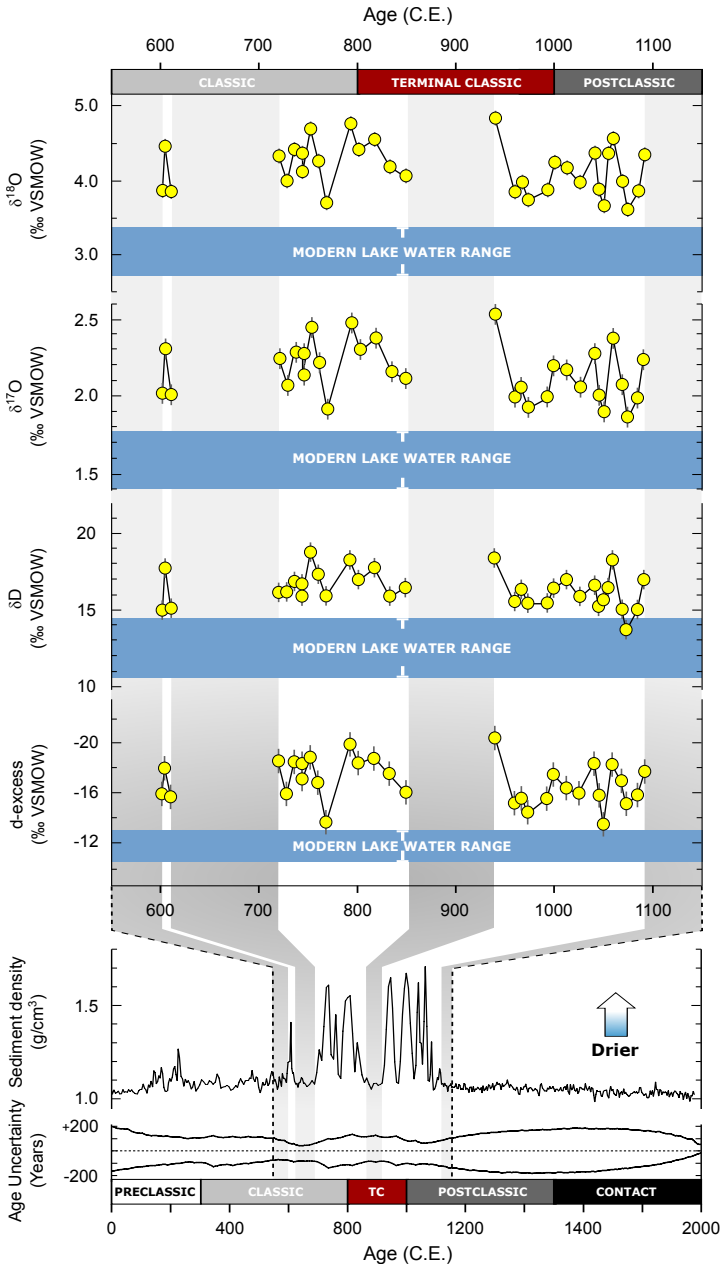

Fig. 3.2. Water isotopes during drought periods compared to modern water isotopes of Lake Chichancanab. (**Lower**) Sediment density record of core CH1 7-III-04 from 0 CE to 2000 CE (shown relative to Maya chronology) (Hodell et al., 2005). Periods of gypsum precipitation are indicated by density values >1.1 g cm^{-3}. Age uncertainty (95% confidence intervals) are derived from Bayesian age-depth analysis and normalised to the best-fit age model (Fig. 3.11). (**Upper**) δ^{18}O, δ^{17}O, δD and d-excess (δD–8 $\cdot$ δ^{18}O) of palaeo-lake water data (yellow circles) from 550 to 1150 CE shown after correction of measured GHW for known fractionation factors at 26°C. Horizontal blue band defines the mean ($\pm 1\sigma$) isotopic composition recorded in the modern lake. Positive δ^{18}O, δ^{17}O and δD values and negative d-excess values reflect periods of drought. Note d-excess axis is reversed.

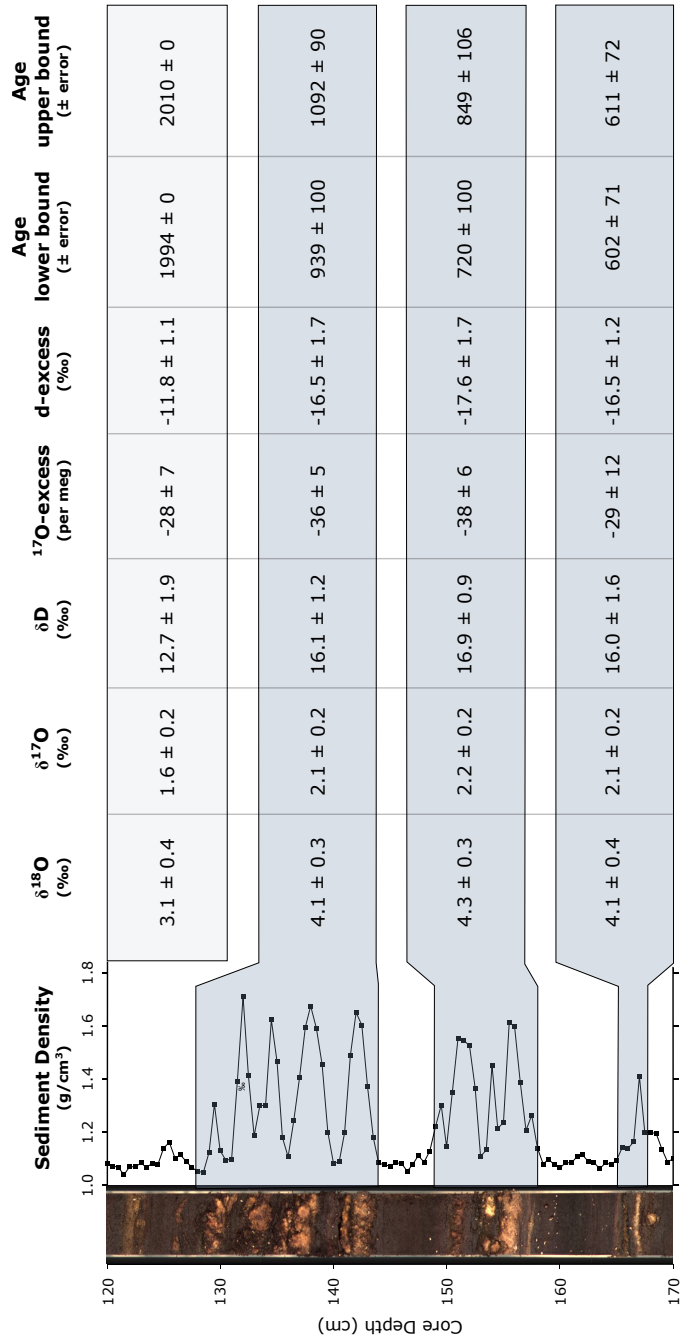

Fig. 3.3. Image of split core CH1 7-III-04 (Hodell et al., 2005). Sediments are composed of interbedded gypsum- and organic-rich strata containing abundant shell material. Solid black line represents the GRA bulk density record measured on core CH1 7-III-04 (Hodell et al., 2005). Periods of gypsum precipitation are indicated by positive density excursions >1.2 g cm^{-3}. The δ^{18}O, δ^{17}O, δD and d-excess (‰, VSMOW) and ^{17}O-excess (per meg, VSMOW) ($\pm 1\sigma$) of the modern lake water and measured GHW during each of the three periods of gypsum deposition (after correction for known fractionation factors at 26°C) are displayed.

isotopic profile, with values similar to the current lake water, would be expected. Furthermore, the burial depth of the gypsum is shallow (< 2 m) and the sediments are porous, thus isotopic gradients in pore water would be strongly attenuated by diffusion and advection with overlying lake water (Gázquez et al., 2018).

3.2.3 Precipitation, meteoric and lake water samples

The triple oxygen and hydrogen isotopic measurement of lake water (n = 156), river and ground water (n = 92), and rainwater (n = 31) samples from stations across the Yucatán Peninsula are reported from a collection period of 1994 to 2010 (Fig. 3.4; Appendix C; Tables C.5, C.6 and C.7). Measurements were made using an L2140-i Picarro CRDS water isotope analyser. The majority of rainwater samples were collected at 20°00'59"N 89°01'13"W, ~30 km west of Lake Chichancanab (Hodell et al., 2012). All water samples were collected and stored in Qorpak bottles with Polyseal cone-lined caps to prevent evaporation.

3.2.4 Biogenic carbonate measurements

Shells and shell fragments of the gastropod Pyrgophorus coronatus were picked from 0.5 cm intervals of core CHI 7-III-04. Shells were cracked and sonicated in methanol to remove contaminant debris. Subsequently, samples were treated with 10% H_2O_2 for 30 min to remove organic matter, dried and ground to a fine powder. Stable oxygen isotopes of carbonate were measured using a ThermoScientific GasBench II, equipped with a CTC autosampler coupled to a MAT253 mass spectrometer (Spötl and Vennemann, 2003). Samples were flushed with CP grade helium then acidified with 104% H_3PO_4 and reacted at 70°C for 1 hour. Repeat analysis of the Carrara Marble standard yielded a 1σ analytical precision of ±0.1‰ for $\delta^{18}O$. Results are reported relative to the Vienna Pee Dee Belemnite (VPDB). Small sample fragments were run on a Kiel III carbonate preparation device interfaced with a Finnigan MAT 252 mass spectrometer. Analytical precision was estimated at ±0.08‰ for $\delta^{18}O$.

3.3 Results

The modern regional climate around Lake Chichancanab is characterised by a mean annual precipitation of ~1200 mm, a mean annual surface water temperature of ~26°C and a net annual water deficit of 300–400 mm yr^{-1} (Hodell et al., 2005). Large changes in precipitation and RH_n occur between the dry (November to May) and rainy seasons (June to October) (Wassenaar et al., 2009; Medina-Elizalde and Rohling, 2012). Measured $\delta^{18}O$ and δD of

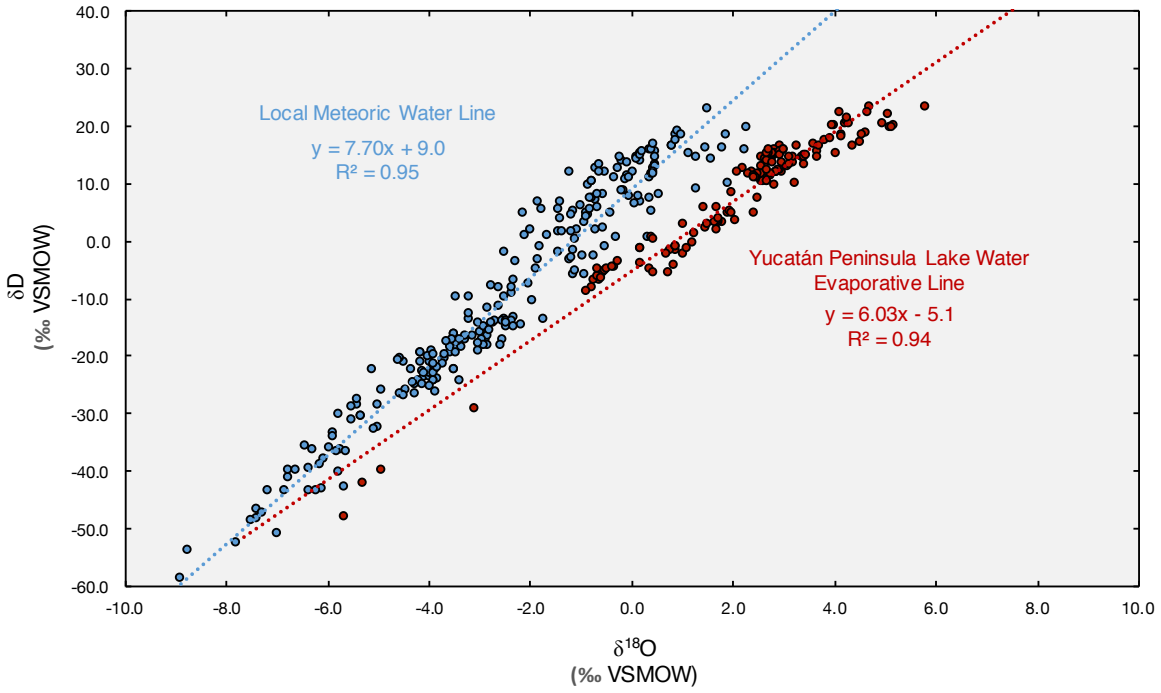

Fig. 3.4. δ^{18}O and δD of rain, surface water, and ground water (blue squares). Solid blue line represents the local meteoric water line estimated by least-squares linear regression through rain, surface and groundwater data. Red squares indicate measurements made on lakes with varying hydrologic budgets and evaporative losses across the Yucatán Peninsula. Solid red line represents the evaporative line (with slope = 5.8) estimated by least-squares linear regression using lake data. Note that this slope is comparable to the slope of modern data from Lake Chichancanab alone (slope = 5.1), and is significantly different from that of the slope of measured GHW data (slope = 3.1) (Fig. 3.5).

precipitation and groundwater samples from the Yucatán Peninsula, collected from 1994 to 2010, define a local meteoric water line (LMWL) with slope 7.7 (Fig. 3.4). Evaporation enriches the lake in the heavier isotopes of oxygen and hydrogen in water (2.6‰ < δ^{18}O < 3.8‰ and 10.1‰ < δD < 17.2‰), evolving along an evaporative line defined by δD = 5.1 · δ^{18}O – 3.1. This evaporation line intersects the LMWL at δ^{18}O = -4.7(±1.2)‰ and δD = -27.5(±10.7)‰, which is within error of the mean oxygen and hydrogen isotope values recorded in local rivers and groundwater from the International Atomic Energy Agency's (IAEA) regional Global Network of Isotopes in Precipitation stations (δ^{18}O = -4.1‰; δD = -24.3‰) (Wassenaar et al., 2009) and this study (δ^{18}O = -4.0‰; δD = -23.5‰).

The gypsum deposited during the droughts of the Terminal Classic and early Postclassic Periods (~720 to 1100 CE) was used to calculate the δ^{18}O, δ^{17}O and δD of the palaeo-lake water, which ranged from 3.6‰ to 4.9‰ for δ^{18}O, 1.9‰ to 2.5‰ for δ^{17}O, and 13.7‰ to 18.8‰ for δD (Fig. 3.5). Mean values of the palaeo-lake waters (δ^{18}O = 4.2‰; δ^{17}O = 2.2‰; δD = 16.4‰) during drought episodes are significantly greater than modern lake values (δ^{18}O = 3.1‰; δ^{17}O = 1.6 ‰; δD = 12.7‰). Age uncertainty associated with the lake record and periods of gypsum precipitation was calculated using Bayesian age-depth analysis of radiocarbon ages obtained from the sediment cores (see Section 3.4.4). High drought probabilities are found specifically during the onset (~750 and ~850 CE) and the end (~950 to ~1050 CE) of the TCP (P > 0.85 and P > 0.95, respectively). Multiple proxy climate records across the Maya Lowlands also provide evidence of drought synchronicity, with only slight temporal variations across the region (Douglas et al., 2016a).

3.4 Modelling

3.4.1 Transient model details

To estimate quantitatively the magnitude of drought during the TCP, we employed a transient model that explicitly simulates the evolution of the isotopic and chemical composition of the lake water, including the gypsum flux to the lake sediments (Fig. 3.6).

The transient box model presented here is a lake basin with a surface and deep box (Fig. 3.7A). The volume (4.57×10^7 m^3), surface area (1.02×10^7 m^2), and surface area to depth relationship conform to data presented in Hodell et al. (2005) (Fig. 3.7B). This geometry equates to a mean depth of 4.5 m in the model with the modern deepest area of the basin equal to ~15 m.

The basin is fed by a precipitation flux determined by North American Regional Reanalysis (NARR) data (~1 m water equivalent/m^2/a; Fig. 3.8) with a constant catchment size

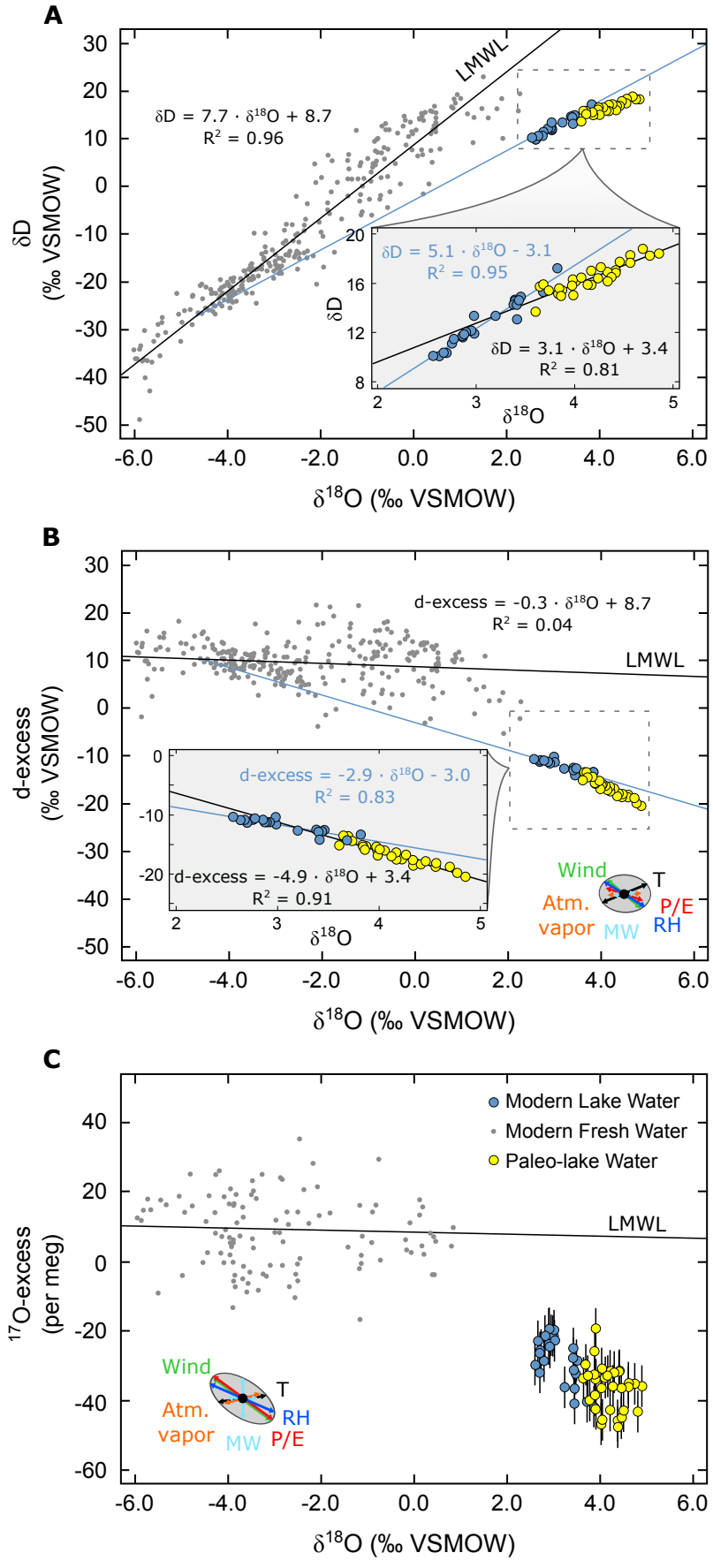
A
LMWL
δD = 7.7 · δ18O + 8.7
R2 = 0.96
δD = 5.1 · δ18O - 3.1
R2 = 0.95
δD = 3.1 · δ18O + 3.4
R2 = 0.81
δD (‰ VSMOW)
δ18O (‰ VSMOW)
B
d-excess = -0.3 · δ18O + 8.7
R2 = 0.04
LMWL
d-excess = -2.9 · δ18O - 3.0
R2 = 0.83
d-excess = -4.9 · δ18O + 3.4
R2 = 0.91
Wind
T
Atm. vapor
P/E
MW
RH
d-excess (‰ VSMOW)
δ18O (‰ VSMOW)
C
Modern Lake Water
Modern Fresh Water
Paleo-lake Water
LMWL
Wind
T
Atm. vapor
RH
MW
P/E
17O-excess (per meg)
δ18O (‰ VSMOW)

Fig. 3.5. **Left**: (**A**) Comparison of measured local meteoric water, modern lake water, and palaeo–lake water data. Paleo–lake water data (yellow circles) are shown after correction of measured GHW for known fractionation factors at 26°C. (**A**) δ^{18}O versus δD space. (**B**) δ^{18}O vs d-excess space. (**C**) δ^{18}O versus ^{17}O-excess space. Local meteoric water measurements (grey circles) define the local meteoric water line (LMWL). Relative to modern lake waters (blue circles), paleo–lake water displays greater δ^{18}O and δD values along an evaporative trend. The grey ellipses define the relative influence of variables that can affect the isotopic composition of water in δ^{18}O vs d-excess and δ^{18}O vs ^{17}O-excess; the effects of precipitation/evaporation (P/E), normalised relative humidity (RH_n), temperature (T), changes to source composition (MW), the degree of equilibrium between atmospheric vapour and fresh water (Atm. vapour), and turbulence created by wind are indicated. The size of each arrow is derived from the tolerance given for each input parameter in Table 3.2.

through time. The basin hydrology is effectively closed (Perry et al., 2002). Groundwater flux to and from the lake (equivalent to ~10% of precipitation) delivers Ca^{2+}, $SO_4{}^{2-}$, Na^{2+}, K^+, Mg^{2+} and Cl^- and maintains the lake near the modern salt balance, with gypsum near saturation. Water is lost via evaporation, which is held constant at a rate of 1.07 m water equivalent/m^2/a with the absolute flux evolving through time, depending on the surface area of the lake.

The saturation state of gypsum was calculated offline with the PHREEQC model for a wide range of solutions, starting at modern conditions. The lake model incorporates these solutions in a look-up table to calculate the gypsum saturation at every time step. If the lake exceeds saturation, Ca^{2+} and $SO_4{}^{2-}$ are removed by gypsum precipitation at a rate that maintains the lake below saturation, with a response time of 1 year. Combining the mass of gypsum precipitated and surface area of the lake at a given time-step allows us to calculate the gypsum accumulation in the lake sediment. This is then used to calculate a synthetic core log of density, assuming the density of accumulating gypsum is 2.31 g cm^{-3} and that the accumulation of other sediments is constant at 0.941 mm yr^{-1}, with a density of 1.06 g cm^{-3} based on the mean sediment accumulation that brackets the drought periods (Fig. 3.9).

3.4.2 Transient model isotope and ionic mass balance

The isotope mass balance model employs a Craig-Gordon evaporation scheme as formulated in Criss (1999). The overall isotopic fractionation during evaporation (α_{evp}) depends on the equilibrium fractionation (α_{eq}), kinetic fractionation (α_{kin}), relative humidity (h) and the isotopic ratio of water vapour (R_v) and the evaporating surface of the basin (R_b), whereby:

$$\alpha_{evp} = \alpha_{eq}\alpha_{kin}\left(\frac{1-h}{1-\alpha_{eq}h\frac{R_v}{R_b}}\right) \tag{3.1}$$

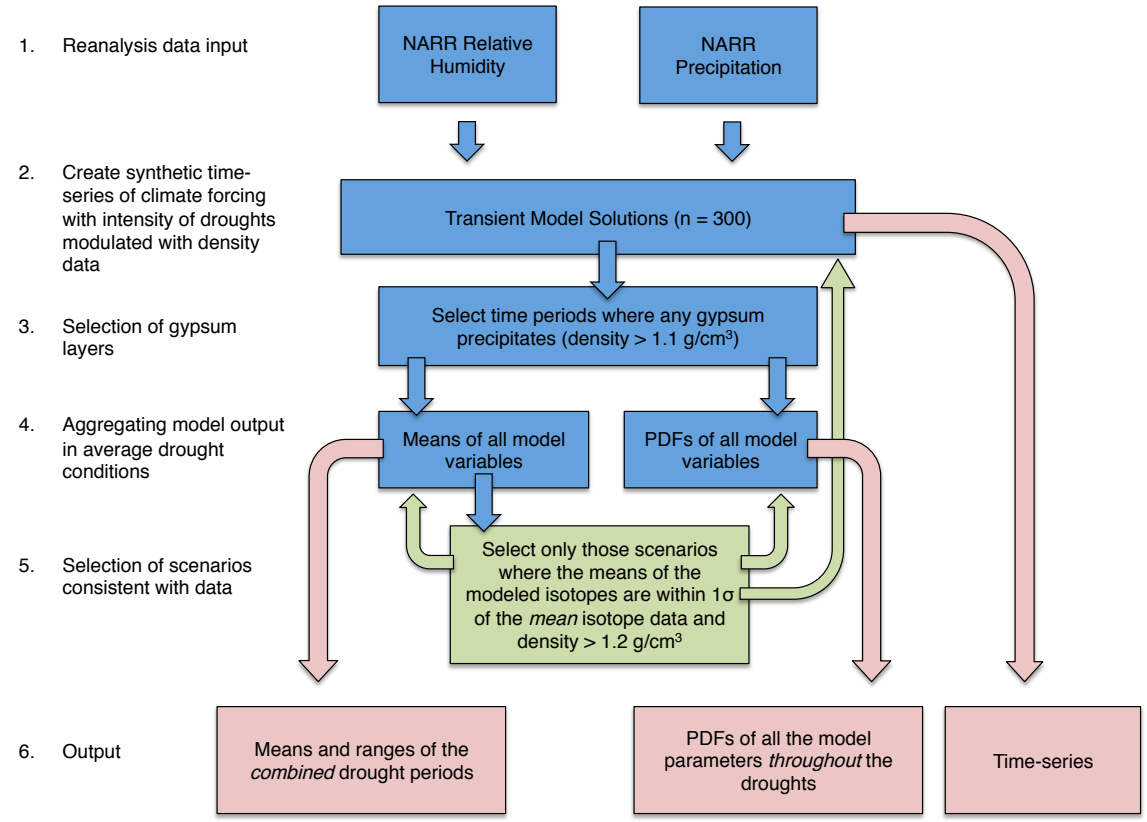

Fig. 3.6. Transient model summary of forcing (blue boxes and arrows), scenario selection by model/data comparison (green boxes and arrows), and model output (red boxes and arrows).

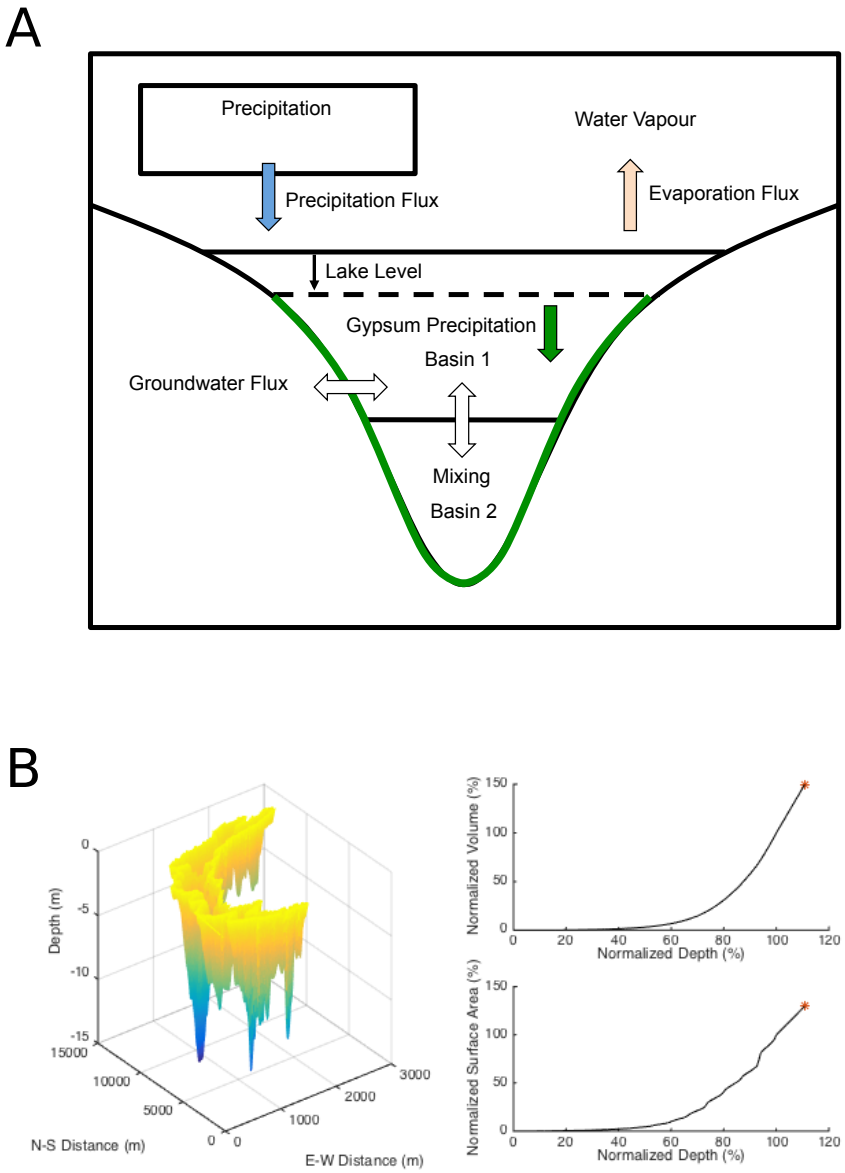

Fig. 3.7. (**A**) Diagrammatic representation of the two-box model used in transient model scenarios. (**B**) The bathymetry of Lake Chichancanab used in the transient model (Hodell et al., 2005), and generated normalised surface area and volume vs normalised depth.

α_{eq} for $H_2{}^{18}O$ ($\alpha^{18}O_{eq}$) and DHO (αD_{eq}) are calculated using an assumed lake surface temperature of 25°C and the equations of Horita and Wesolowski (1994). The equilibrium fractionation for $H_2{}^{17}O$ is then a function $\alpha^{18}O_{eq}$, where:

$$\alpha^{17}O_{eq} = \alpha^{18}O_{eq}^{\theta_{eq}}$$

and the equilibrium fractionation parameter between ^{18}O and ^{17}O (θ_{eq}) is 0.529 (Barkan and Luz, 2005).

Kinetic fractionation factors for all three minor isotopes are calculated as a function of wind-induced turbulence (w), lake surface temperature (T) and the kinetic fractionation parameter between ^{18}O and ^{17}O (θ_{kin}):

$$\begin{aligned}\alpha^{18}O_{kin} &= 1.0283^{w}\\ \alpha D_{kin} &= (1.25 - 0.02T)(\alpha^{18}O_{kin} - 1) + 1\\ \alpha^{17}O_{kin} &= \alpha^{18}O_{kin}^{\theta_{kin}}\end{aligned}$$

We assume R_v depends on the degree to which the atmospheric water vapour (V_{eq}) is in equilibrium (Gibson et al., 2016) with isotopic ratio of precipitation (R_p) where:

$$R_v = R_p\left(\alpha_{eq(p-v)}V_{eq}\right)$$

The general form of the mass-balance equation for the mass of a given species (mX) of either isotope or ion in basin box 1 ($b1$) is:

$$\frac{dmX_{b1}}{dt} = F_pR_p - F_{evp}R_{evp} + F_{gb1}R_g - F_{b1g}R_{b1} + F_{b2b1}R_{b2} - F_{b1b2}R_{b1}$$

Similarly the mass balance for basin box 2 ($b2$) is:

$$\frac{dmX_{b2}}{dt} = F_{b1b2}R_{b1} - F_{b2b1}R_{b2}$$

In this set of equations F represents the various fluxes of water in terms of mass of the major water isotope ($^1H_2{}^{16}O$) and R represents the ratio of minor isotope or ionic species relative to $^1H_2{}^{16}O$. As examples, the ratio of deuterium in box 1 is:

$$R_{\mathrm{DHO},b1} = \frac{\mathrm{mDHO}_{b1}}{\mathrm{m}^1\mathrm{H}_2{}^{16}\mathrm{O}_{b1}}$$

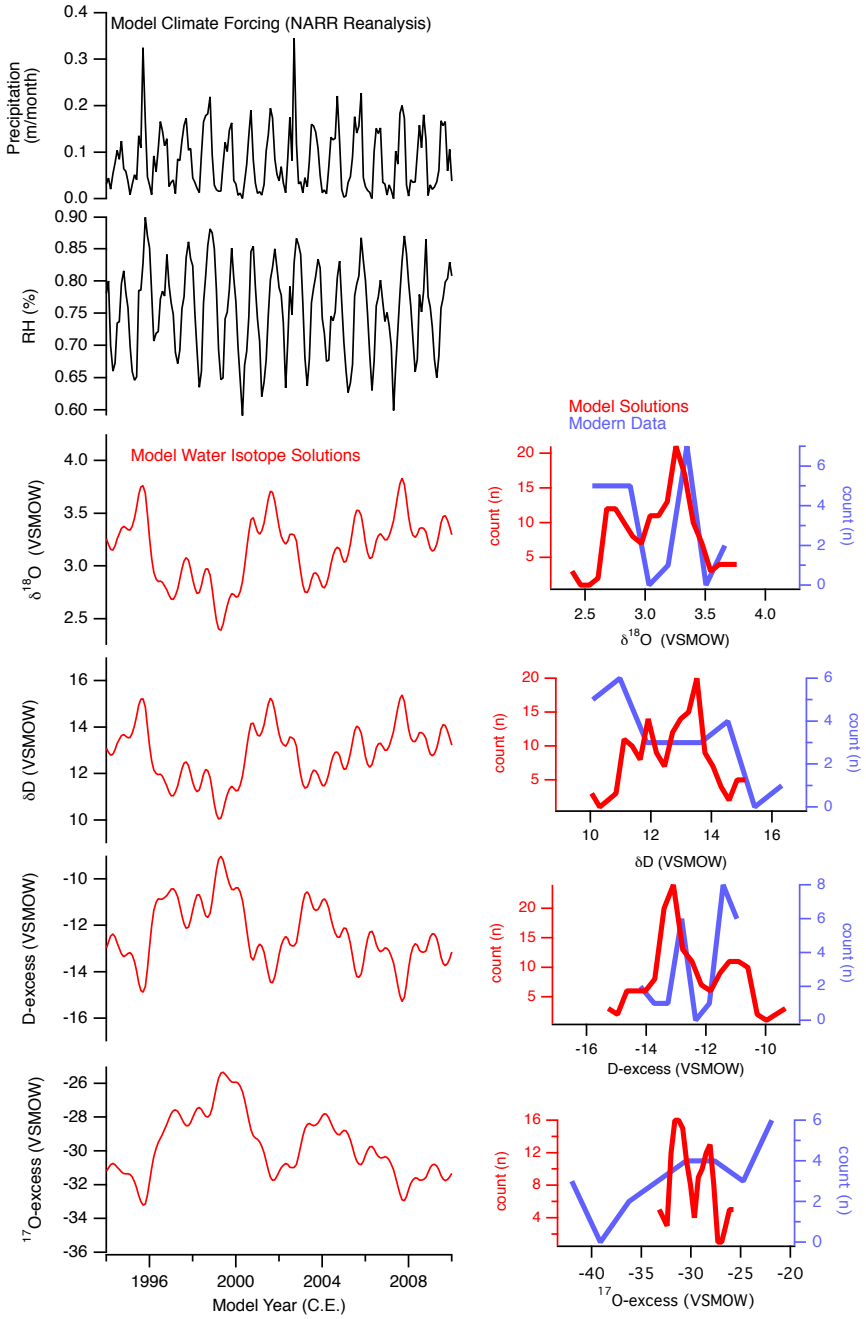

Fig. 3.8. Transient model climate forcing. The transient model is forced with North American Regional Reanalysis (NARR) data for local precipitation and relative humidity (RH_n) across the modern sampling period from 1994 to 2010 (black lines). Modelled water isotope solutions (red lines) are then compared to measured modern data (blue lines) as histograms (right panel). The model successfully reproduced the mean of modern isotope data, with insignificant gypsum precipitation. The time interval from 1994 to 2010 is subsequently used as the baseline for comparison to palaeo-simulations.

The concentration of Ca in box 1 is:

$$R_{[\mathrm{Ca}],b1} = \frac{\mathrm{Ca}_{b1}}{\mathrm{m}^{1}\mathrm{H}_{2}{}^{16}\mathrm{O}_{b1}}$$

When the overall water mass balance is calculated (i.e. the variation in volume):

$$R_{1\mathrm{H}_{2}{}^{16}\mathrm{O}_{b1}} = 1$$

Ratios for external isotopes such as the precipitation and groundwater fluxes are referenced relative to VSMOW such that:

$$R_{\mathrm{DHO},p} = \left(\frac{\delta \mathrm{D}}{10^{3}} + 1\right) R_{\mathrm{DHO},VSMOW}$$

The isotopic ratios of the evaporation flux (R_{evp}) are determined from Equation 3.1 and the isotopic ratios of the basin surface (R_{b1})

$$R_{evp} = \frac{R_{b1}}{\alpha_{evp}}$$

3.4.3 Transient model parameterisation

When modelling the isotopic composition of the palaeo-lake, the (i) lake surface temperature (T), (ii) wind-induced turbulence (w), (iii) isotopic composition of the atmospheric vapour, (iv) salinity effect on isotope fractionation, (v) the isotopic composition of the freshwater input, and (vi) any variability caused by the amount effect must be known or assumed (Table 3.1).

i. To constrain water temperature changes at Lake Chichancanab during the TCP, tandem measurements of both GHW and carbonate $\delta^{18}\mathrm{O}$ that were deposited concurrently permit the deconvolution of the $\delta^{18}\mathrm{O}$ carbonate signal into its temperature and $\delta^{18}\mathrm{O}$-water components via the carbonate palaeo-temperature equation (Hodell et al., 2012). To calculate the temperature at which the aragonitic shells of Pyrgophorus coronatus formed, we used the equation of Grossman and Ku (1986) that is based on analysis of foraminifera (*Hoeglundina elegans*) and gastropods:

$$T\,^{\circ}C = 21.8 - 4.59\left(\delta^{18}\mathrm{O}_{arag\,(PDB)} - \delta^{18}\mathrm{O}_{water\,(SMOW)}\right)$$

The $\delta^{18}\mathrm{O}$ of gastropod aragonite and GHW is used to estimate $\delta^{18}\mathrm{O}_{arag}$ and $\delta^{18}\mathrm{O}_{water}$,

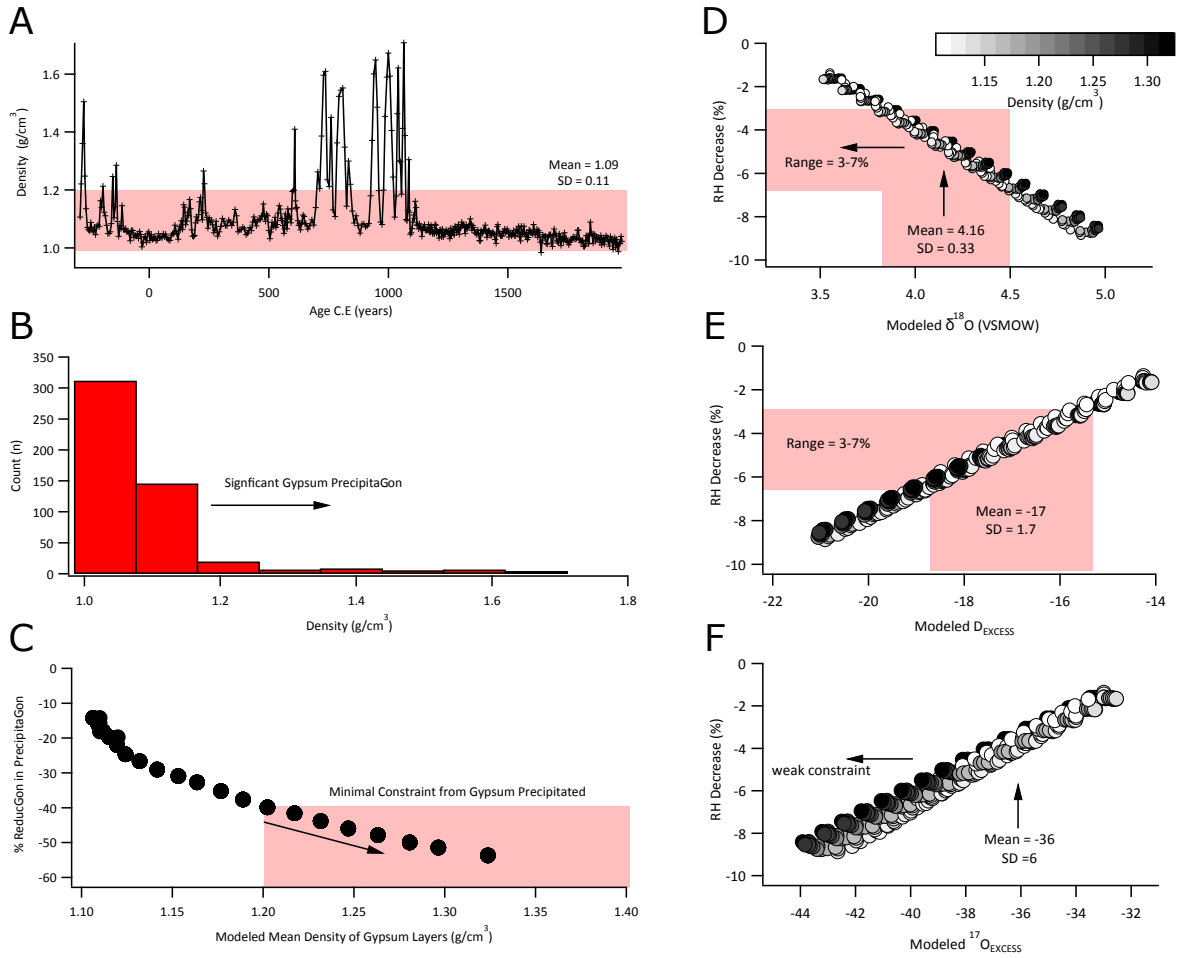

Fig. 3.9. Transient model precipitation and relative humidity scenarios. (**A**) GRA bulk density record of core CH1 7-III-04 (5). From 500 CE to 2000 CE, mean ($\pm 1\sigma$) sediment density = 1.09±0.11 g cm^{-3} (red horizontal band). (**B**) Histogram of counts from GRA bulk density record from 500 CE to 2000 CE (**C**) Example of the relationship between modelled mean core density (g cm^{-3}) and the modelled reduction in precipitation (%). Varying the minimum cut-off point from which modelled data are compared to GHW data changes the baseline precipitation reduction estimate. Example of modelled δ^{18}O (**D**), d-excess (**E**), and ^{17}O-excess (**F**) data plotted as a function of modelled densities. Mean GHW ($\pm 1\sigma$) data are then compared to modelled runs to derive %RH$_n$ decrease.

Category	Parameter	Units	Value
Lake Evaporation	Lake Temperature	°C	25
	w	-	0.5
	V_{eq}	-	0.6
	Vapour Temperature	°C	25
	θ_{eq}	-	0.529
	θ_{kin}	-	0.518
Precip.	$\delta^{18}O$	(‰, VSMOW)	-4.5
	d-excess		10
	^{17}O-excess		2.5
Groundwater	$\delta^{18}O$	(‰, VSMOW)	-4.5
	d-excess		10
	^{17}O-excess		2.5
	Ca	g kg^{-1}	0.607
	SO_4		2.455
	Na		0.2
	Mg		0.2
	K		0.011
	Cl		0.234
Fluxes	F_p	m water equivalent/m^2/a	Reanalysis data = ~1
	F_e		1.07
	F_{gb}	kg (~m water equivalent/m^2/a)	1.02e9 (~0.1)
	F_{bg}		1.02e9 (~0.1)
	F_{b1b2}		1.02e10 (~1.0)
	F_{b2b1}		1.02e10 (~1.0)

Table 3.1. Transient model parameters. See text for details of parameters.

respectively. Gypsum and gastropod samples were only used if they were in direct contact with each other, or the shell fragments were found embedded within gypsum. The derived temperature from Pyrgophorus coronatus and gypsum from the same bed averaged 25.9 ± 1.7°C (Appendix C; Table C.2). This temperature is indistinguishable from the mean annual temperature of the lake today (Hodell et al., 2012). Equally, because ^{17}O-excess is minimally affected by temperature changes, moderate variations in mean temperature result in insignificant effects on the trajectories of the evaporated waters. For example, 5°C of temperature change has a small effect on the model results for ^{17}O-excess (up to ~±2 per meg in a terminal lake), whereas d-excess changes by as much as ~3‰ in a terminal lake, when all other parameters remain constant (Gázquez et al., 2018). Thus, the model sensitivity to temperature changes is low.

ii. It is known that the proportion of $\alpha^{18}O_{kin}$ may be suppressed by turbulent flow induced by wind (Uemura et al., 2010), and therefore wind could alter isotope mass balance, especially for d-excess and ^{17}O-excess. The exponent 'w' is set between 0.5 (pure turbulence) and 1 (no wind). Measured wind speeds in the region of Lake Chichancanab are ~3 m s^{-1} and relatively constant over the year (Soler-Bientz et al., 2010), resulting in a well-mixed lake-surface layer. When turbulence is not considered, the model yields d-excess and ^{17}O-excess values that are systematically too low compared to the analytical data for some modern periods. We also tested this variable by analysing modern and palaeo-lake water data using previously published Monte Carlo models (Gázquez et al., 2018) (Section 3.5.1). These tests provide the best fit to modelled data when w is kept constant at ~0.5 when modelling both the modern and the TCP GHW data.

iii. The isotopic composition of modern atmospheric vapour is not well constrained in the Yucatán Peninsula, nor are there estimates available for how this variable has changed in the past. Assuming equilibrium with local meteoric water, the isotopic composition of atmospheric water vapour can be approximated (Gázquez et al., 2018). Gibson et al. (2016), however, suggested that the isotopic composition of atmospheric vapour is often only in partial equilibrium with that of local freshwater. We assumed a degree of equilibrium of 60%, a reasonable estimate for most tropical and intertropical regions (Gibson et al., 2016). Note that Gázquez et al. (2018) show that the triple oxygen and hydrogen system is relatively sensitive to the isotopic composition of the vapour, especially for coastal lakes affected by advection of marine vapour masses. In coastal lakes, the isotopic composition of the modern atmospheric vapour is in

equilibrium with seawater rather than freshwater. This is probably not the case at Lake Chichancanab, which is located ~140 km inland.

iv. High concentrations of NaCl and other salts within a lake can cause the water isotopic activity ratios to diverge from the corresponding concentration ratios, as a consequence of isotopic fractionation between free water and water in ionic hydration shells (Sofer and Gat, 1975; Herwartz et al., 2017). This 'salt effect' is different for hydrogen and oxygen isotope fractionation, resulting in complications when interpreting the relationship between δ^{18}O and δD at salt concentrations >100,000 mg l^{-1} (Sofer and Gat, 1975; Herwartz et al., 2017). The total dissolved salt concentration in Lake Chichancanab today is ~4000 mg l^{-1} (Hodell et al., 2005). Substantial oxygen and hydrogen isotope fractionation effects caused by high salinity would not be expected at these low concentrations (Sofer and Gat, 1975; Criss, 1999). During periods of lake drawdown, the transient model displays elevated salt concentrations, but concentrations that approach 100,000 mg l^{-1} are never experienced in model runs.

v. The mean ($\pm 1\sigma$) modern isotopic composition of regional groundwater is -4.0 ±1.7‰ for δ^{18}O, -2.10 ±0.9‰ for δ^{17}O and -23.5 ±12.8‰ for δD. We use δ^{18}O = -4.5 and δD = -26 (so that d-excess = 10‰) and set ^{17}O-excess = 2.5 per meg to model present-day conditions. These variables are held constant throughout the transient model runs, although they can be systematically varied to reflect isotope effects such as the amount effect (see below and Section 3.5). We tested the effect of non-systematic variability on the isotopic composition of meteoric water (using bounds of ±0.5‰ for δ^{18}O, ±5‰ for d-excess, and ±9.5 per meg for ^{17}O-excess), using the steady state Monte Carlo model of Gázquez et al. (2018) to quantify derived uncertainty (Section 3.5.1).

vi. The amount effect (i.e. correlation between depletion of heavy isotopes in rainfall with greater amount of rain) is thought to play a role in the Yucatán Peninsula and thus the isotopic composition of meteoric water may vary over the timescales modelled (Medina-Elizalde et al. 2010; Medina-Elizalde and Rohling, 2012). The amount effect and its perturbation in the δ^{18}O of precipitation (P) over a seasonal cycle was calculated from isotopic composition of precipitation collected at Hobonil, 20°00'59"N 89°01'13"W (Hodell et al., 2012), and rainfall amounts from the proximal metrological station of Dziuche, 19°54'00"N 88°48'40"W, from 2006 to 2009. The linear regression ($\delta^{18}\mathrm{O} = -0.0176(\mathrm{P}) - 0.1204$; R^2 = 0.92) is very similar to that found by Medina-Elizalde et al. (2010) from the IAEA station in Veracruz, México ($\delta^{18}\mathrm{O} = -0.0118(\mathrm{P}) - 0.64$; R^2 = 0.80). We compiled data from Veracruz between 1969 and 1985 (omitting years with poor data coverage) and the records

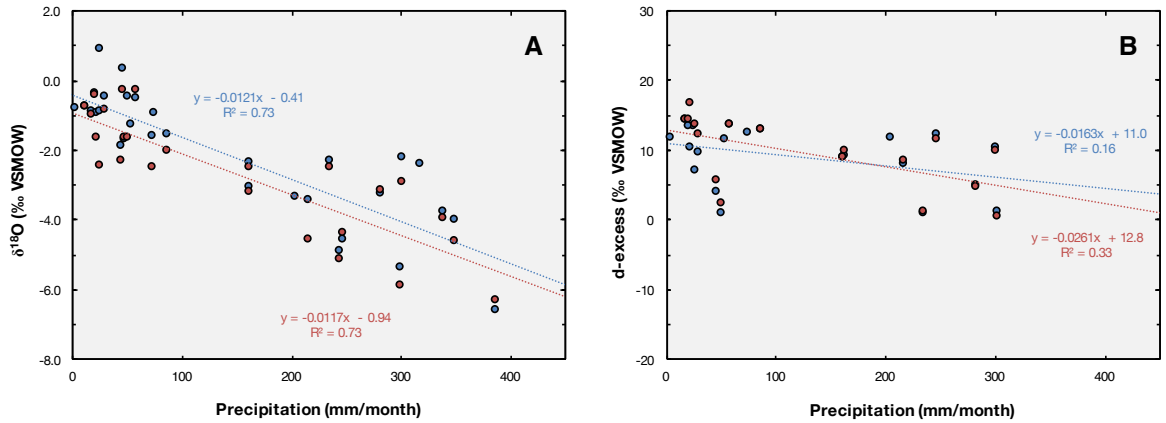

Fig. 3.10. The amount effect relationship between monthly precipitation amount and monthly mean rainfall (**A**) δ^{18}O and (**B**) d-excess during the dry (November to May) and rainy seasons (June to October) from the IAEA station in Veracruz, México (years 1969 to 1985) and Hobonil (20°00'59"N 89°01'13"W; 2006 to 2009). Both raw (blue squares) and amount-weighted (red squares) show that rainfall δ^{18}O is negatively correlated to the amount of precipitation on seasonal time scales, whereas there is no significant amount effect displayed by d-excess.

from Chichancanab between 2006 and 2009 (Hodell et al. 2012). The compiled linear regression for δ^{18}O ($\delta^{18}\mathrm{O} = -0.0121(\mathrm{P}) - 0.41$) displays a significant correlation ($R^2 = 0.73$), whereas there was no significant amount effect displayed by d-excess or ^{17}O-excess (Fig. 3.10).

3.4.4 Age models

Age uncertainty associated with the lake record and periods of gypsum precipitation was calculated using Bayesian age-depth analysis of radiocarbon ages obtained from the sediment cores (Hodell et al., 2005). We estimated calendar ages with 95% confidence intervals using the Bayesian Age–Depth Modelling software 'BACON' in R (Fig. 3.11; Appendix C; Table C.3) (Blaauw and Christen, 2011). Derived age-depth error (95% confidence intervals) was normalised to the best-fit line to produce age-depth errors for the Chichancanab density record (Fig. 3.2). To quantify age uncertainty in relation to the timing of dry intervals, we inverted the density record of core CH1-III-04 and identified data outside one standard deviation of the mean sediment density from core CH1-III-04. This would be equivalent to selecting sediment densities >1.2 g cm^{-3}, equivalent to the periods from which GHW was extracted. The BACON function 'Events' was then used to quantify the probability of arid conditions at any calendar age. 50-year window widths were used, with the windows moving at 10-year steps from the core's bottom ages to its top (Blaauw and Christen, 2011).

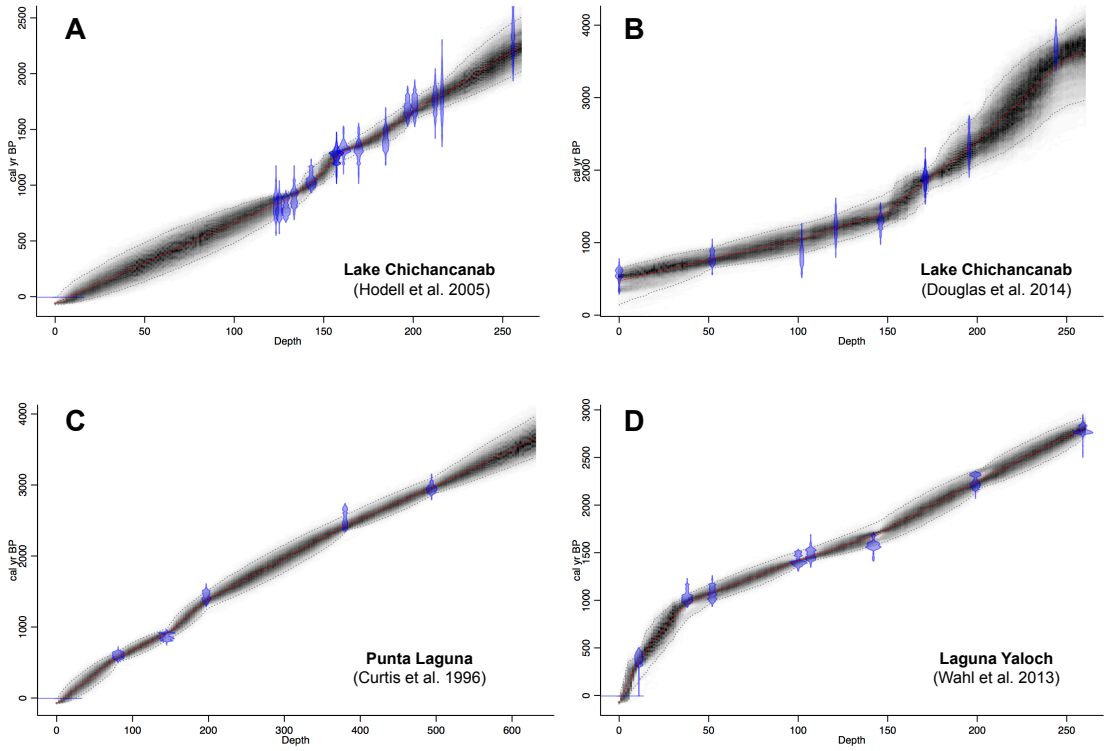

Fig. 3.11. Bayesian age models produced for (**A**) core CHI 7-III-04 of Lake Chichancanab (Hodell et al., 2005), (**B**) Plant waxes of Lake Chichancanab (Douglas et al., 2014), (**C**) Punta Laguna (Curtis et al., 1996) and (**D**) Laguna Yaloch (Wahl et al., 2013) by the program BACON. Dark shading indicates age uncertainty at each depth and the red lines indicate the best-fit age model.

The probabilities of drought occurring specifically during the onset (~750 to ~850 CE) and the end (~950 to ~1050 CE) of the TCP are high (Probability > 0.85 and Probability > 0.95, respectively). Multiple proxy climate records across the Maya Lowlands also provide evidence of drought synchronicity, with only slight temporal variations across the region (Fig. 3.12) (e.g. Douglas et al., 2016a).

We also used Bayesian age modelling techniques to synthesise the regional proxy records of Curtis et al. (1996), Wahl et al. (2013) and Douglas et al. (2014) (Fig. 3.12). To quantify age uncertainty in relation to the timing of dry intervals, we inverted the records and identified the lowest 10th percentile of the raw data for Wahl et al. (2013) and Douglas et al. (2014), and the 5-point smooth of the δ^{18}O *Cytheridella ilosvayi* record from Curtis et al. (1996).

All proxy records dated using radiometric techniques yielded a significant age uncer-

tainty. Overall, although individual records show subtle variations in drought timing, the age uncertainty results in the chance of drought occurring any time between 500 and 1300 CE (Bhattacharya et al., 2017). Gypsum deposition at Lake Chichancanab displays a significant chance of occurring from ~750 to ~850 CE (Probability of drought at 800 CE = 0.85), coinciding with the onset of the collapse of Terminal Classic Maya Civilisation (Fig. 3.12).

3.5 Discussion

To estimate quantitatively the magnitude of drought during the TCP, we employed a transient model that explicitly simulates the evolution of the isotopic and chemical composition of the lake water, including the gypsum flux to the lake sediments. The modelled gypsum flux can be compared to observed variations in the gypsum content of the sediments, as expressed by variations in sediment bulk density (Hodell et al., 2005). Changes in lake surface-area-to-volume ratio were obtained from the lake bathymetry (Fig. 3.7). The model was run at sub-monthly resolution in a series of millennial-duration experiments, forced with NARR data for local precipitation and RH_n. The model was first tested using the climate forcing across the modern sampling period from 1994 to 2010 (Fig. 3.8). It successfully reproduced the mean of modern isotope data, with insignificant gypsum precipitation. This time interval, which was fortuitously one of the driest of recent decades, was then used as the baseline for comparison to palaeo-simulations.

To provide scenarios that are directly comparable to the GHW data, long transient simulations were performed in which rainfall and RH_n were reduced by variable amounts to simulate a series of multi-decadal-scale droughts. The use of a model allows us to compare, directly and quantitatively, climate conditions affecting the modern lake with those of plausible drought conditions. Precipitation and/or RH_n forcings are directly modulated by the density record of core CH1-III-04 (Hodell et al., 2005); the maximum variability during a run was set to the maximum density point over time, and precipitation and/or RH_n were reduced linearly across all months. Absolute reductions in P/E and RH_n were referenced relative to mean NARR data over the period from 1994 to 2010. In other words, a 50% reduction in precipitation and a 5% reduction in RH_n would equate to 50% less rainfall in each month and a 5% reduction in RH_n each month (e.g. 75% to 70%) during a modelled time period compared to the 1994 to 2010 baseline.

First, only the intervals over which the model produced gypsum deposition (modelled sediment density >1.1 g cm^{-3}) were selected. The periods of modelled gypsum accumulation were then aggregated into drought conditions for a given scenario via two pathways: (i) all model variables were averaged across all of the droughts, and (ii) probably density

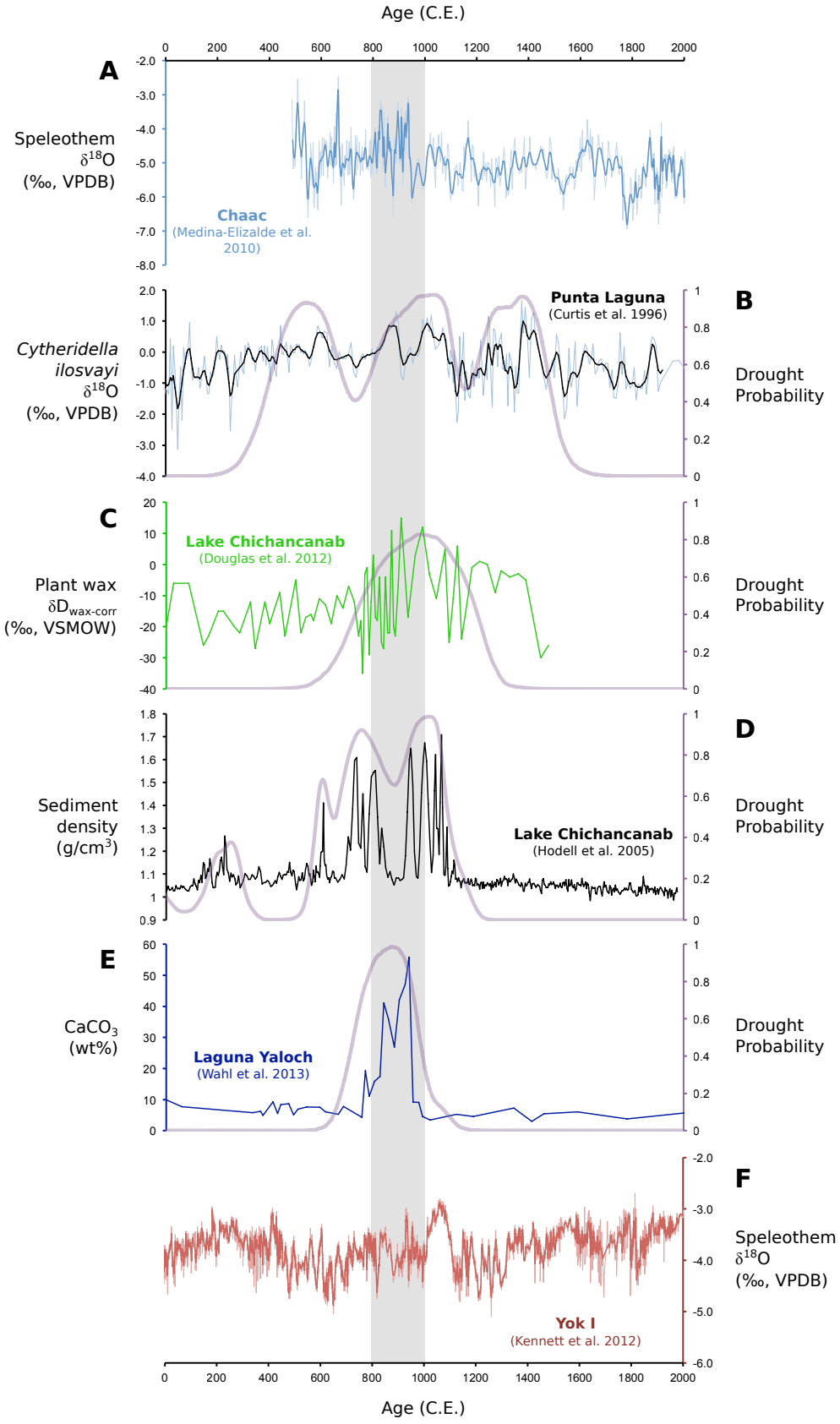
Age (C.E.)
A
Speleothem
$\delta^{18}O$
(‰, VPDB)
Chaac
(Medina-Elizalde et al. 2010)
B
Punta Laguna
(Curtis et al. 1996)
Cytheridella ilosvayi
$\delta^{18}O$
(‰, VPDB)
Drought Probability
C
Lake Chichancanab
(Douglas et al. 2012)
Plant wax
$\delta D_{wax\text{-}corr}$
(‰, VSMOW)
Drought Probability
D
Lake Chichancanab
(Hodell et al. 2005)
Sediment density
(g/cm^3)
Drought Probability
E
$CaCO_3$
(wt%)
Laguna Yaloch
(Wahl et al. 2013)
Drought Probability
F
Yok I
(Kennett et al. 2012)
Speleothem
$\delta^{18}O$
(‰, VPDB)
Age (C.E.)

Fig. 3.12. **Left**: Selection of palaeoclimate records from the Maya Lowlands, arranged from north to south: (**A**) Chaac speleothem (Tzabnah Cave) δ^{18}O (Medina-Elizalde et al., 2010); (**B**) Punta Laguna δ^{18}O (Curtis et al., 1996); (**C**) Lake Chichancanab δDwax-corr (Douglas et al., 2014); (**D**) Lake Chichancanab sediment density (Hodell et al., 2005) (**E**) Laguna Yaloch weight percent calcium carbonate ($CaCO_3$) (Wahl et al., 2013); (**F**) Yok I speleothem (Yok Balum Cave) δ^{18}O (Kennet et al., 2012). Age uncertainty analysis for proxy sites displays drought probabilities in given time intervals for the proxy data. All age models were calculated using Bayesian age analyses. The vertical grey bar indicates the TCP between 800 and 1000 CE. δDwax-corr values indicate δD_{wax} values corrected for the influence of vegetation change (Douglas et al., 2014).

functions were constructed incorporating the variability within and between each decadal-length drought (Fig. 3.6). Data consistent scenarios were then selected by excluding those model runs that fell outside the 1σ range of the isotope data and where, on average, the model failed to produce significant gypsum accumulation (cut-off of average density <1.2 g cm^{-3} based on 1σ range; Fig. 3.9A).

A major constraint on the modelled P/E variability is the sediment density range from which the modelled data is selected. As displayed in Fig. 3.9, if the modelled sediment density threshold is changed from 1.2 g cm^{-3}, the lower bound of P/E and RH_n estimates will vary systematically. Importantly, increasingly conservative estimates for periods of gypsum precipitation (i.e. modelled sediment density >1.2 g cm^{-3}) produce increasingly more severe reductions in baseline P/E and RH_n.

Two possible scenarios were tested subsequently: (i) a reduction in precipitation with accompanying shifts in the isotopic composition of rainwater (i.e. the amount effect) and, (ii) a reduction in precipitation with accompanying decreases in RH_n (Fig. 3.13).

In the first scenario, precipitation δ^{18}O was reduced according to the amount effect relationship (i.e. $\delta^{18}O_{precipitation}/\Delta Precipitation_{volume}$ = –0.0121 mm^{-1}; Fig. 3.10) with associated changes in δD and δ^{17}O that track the Global MWL (i.e. no changes in d-excess or ^{17}O-excess). No scenarios with these assumptions are able to reproduce the relationship between δ^{18}O, d-excess and ^{17}O-excess observed in the data. If the constraints provided by d-excess and ^{17}O-excess are removed and only δ^{18}O and gypsum precipitation are employed, our model permits reductions in precipitation that average 50% over all drought intervals (Fig. 3.13, blue lines). This estimate is in broad agreement with previous work that relied on carbonate δ^{18}O-derived precipitation estimates (using the local amount effect), which predicted reductions of up to 40% (Medina-Elizalde et al., 2010; Medina-Elizalde and Rohling, 2012). Our greater estimate of 50% is in part a consequence of the peak drought δ^{18}O values recorded by gypsum, as well as the integration of simulated gypsum formation and true lake bathymetry in the model. Crucially, however, the added information from the d-excess and ^{17}O-excess data suggests that multi-decadal shifts in

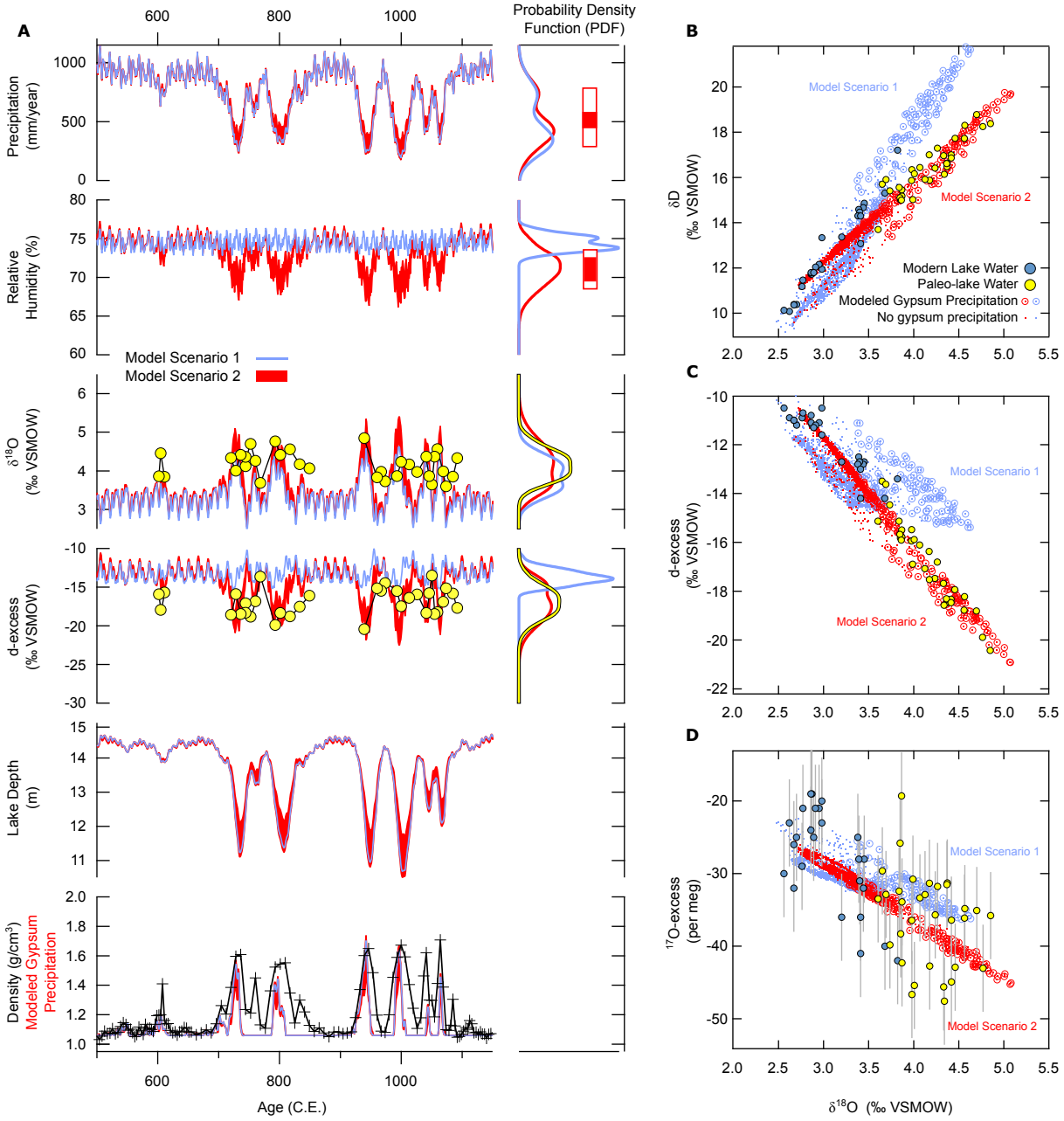
A
B
C
D
Probability Density Function (PDF)
Precipitation (mm/year)
Relative Humidity (%)
δ18O (‰ VSMOW)
d-excess (‰ VSMOW)
Lake Depth (m)
Density (g/cm3)
Modeled Gypsum Precipitation
Model Scenario 1
Model Scenario 2
Age (C.E.)
δD (‰ VSMOW)
Modern Lake Water
Paleo-lake Water
Modeled Gypsum Precipitation
No gypsum precipitation
17O-excess (per meg)
δ18O (‰ VSMOW)

Fig. 3.13. **Left**: (**A**) Transient model of the lake system from 550 to 1200 CE GHW data (yellow circles) and core density are plotted against sampling ages derived from Bayesian age-depth analysis. Multi-decadal-scale droughts were simulated by forcing (1) a reduction in precipitation with accompanied shifts in the isotopic composition of rainwater (i.e. the amount effect, $\delta^{18}O_{precipitation}/\Delta Precipitation_{volume}$ = –0.0121‰/mm; Scenario 1, blue line) and (2) reductions in precipitation with accompanied decreases in RH_n (Scenario 2, red field). Probably density functions incorporate the variability within and between each decadal-length drought (GHW data = yellow line; scenario 1 = blue line; scenario 2 = red line). Scenario 1 fails to match the d-excess data derived from GHW. Scenario 2 successfully reproduces all and d-excess data. When all model variables were averaged across all droughts, the mean precipitation and reduction (closed red boxes adjacent to PDFs) is 47% (with a 1σ level of 41-54%) and 4% (1σ level 2-7%), respectively. The $1\pm\sigma$ range determined from probability density functions (open red boxes adjacent to PDFs) shows the variability of precipitation and throughout the droughts. Scenarios 1 and 2 are also plotted as (**B**) $\delta^{18}O$ vs δD, (**C**) $\delta^{18}O$ vs d-excess and (**D**) $\delta^{18}O$ vs ^{17}O-excess. Open circles indicate points in the model at which gypsum is precipitating; dots indicate modelled data points when gypsum is not precipitating. Error bars ($\pm1\sigma$) are shown or are smaller than the symbols.

the $\delta^{18}O$ of precipitation (caused by the amount effect) were not the dominant factor that affected the isotope budget of Lake Chichancanab during the TCP.

In the second scenario, precipitation was reduced without changes in the $\delta^{18}O$ of precipitation, but instead with concurrent changes in RH_n. In this case excellent agreement between the modelled evolution of all isotopic data is observed, with increases in $\delta^{18}O$ accompanied by decreases in d-excess and ^{17}O-excess (Fig. 3.13, red lines). This analysis yielded plausible scenarios of precipitation reduction that average 47% across all droughts (with a 1σ level of 41% to 54%) accompanied by RH_n reductions of 4% (1σ level 2% to 7%). This result provides a robust, quantitative estimate of the mean annual hydrological conditions of the combined drought periods during the TCP at Lake Chichancanab.

It should also be noted that a combination of RH_n reduction and the amount effect could potentially reproduce the observed data during the TCP. Although a combination of RH_n reduction and the amount effect cannot be definitively ruled out, given the great number of possible outcomes when modelling three variable parameters, our experiments show that the amount effect does not dominate the isotopic budget of the lake. Thus, any influence of the amount effect (in combination with RH_n reductions) at Lake Chichancanab during the TCP will have little effect on modelled outcomes because of the dominance of RH_n in the ^{17}O-excess and d-excess signal.

Although the time evolution of our model is not a direct reconstruction of climate conditions, the model permits heterogeneity within and between each decade-long drought. The $\pm1\sigma$ range determined from the probability density functions indicates that the precipitation reduction could vary from 20% to 70% throughout the modelled droughts (Fig. 3.13). This variability represents the transition into and out of drought phases and demonstrates that

the severity of the droughts could be intense (up to a 70% reduction in precipitation), while maintaining the isotope balance and without desiccating the lake. Although variability in the seasonal delivery of rainfall (or lack thereof) is difficult to constrain because the residence time of the lake water is greater than an annual cycle, our results provide quantitative estimates for the total annual reduction in the water available to the ancient Maya for agricultural and domestic use. Note that recorded Colonial-period accounts of later droughts (e.g. 1535-1560 and 1765-1773), during which high mortality, famines, and population displacement were reported (Hoggarth et al., 2017), are not manifest as intervals of gypsum precipitation in Lake Chichancanab. The lack of gypsum formation is likely a result of shorter duration and/or lower severity of these droughts, providing further evidence that the TCP was an unusually dry period for the Holocene on the Yucatán Peninsula.

3.5.1 Monte Carlo modelling scenarios

In addition to transient model experiments described above, a previously described steady state model of the lake was used in a series of Monte Carlo experiments to determine the range of climatological conditions that simultaneously satisfy all stable isotope results of GHW, in combination with statistical estimates of uncertainty (Gázquez et al., 2018). In these scenarios, the parameter 'Xe' represents the hydrologic balance of the lake. A scenario in which all water is lost by outflow and no evaporation occurs is represented as Xe = 0, whereas a scenario in which all water is lost to evaporation (i.e. a terminal basin) is represented as Xe = 1. The Xe of Lake Chichancanab is not believed to have changed over the last ~1500 years and near-terminal conditions are expected (Perry et al. 2002). Equally, Gázquez et al. (2018) show that when Xe ranges from 0.75 to 1, changes in this parameter barely affect the RH_n values derived from this Monte Carlo model. Here, conservative estimates of Xe were chosen between 0.8 and 0.9 to cover all likely variability (Table 3.2).

Modelled GHW data suggest there was a reduction in RH_n of between 2% and 9% during the TCP, compared to the period when modern lake water was sampled (1994-2010), in good agreement with our transient experiments (2% to 7%) (Appendix C; Table C.8). Estimated errors for RH_n are smaller than 4% (1σ) when all variables listed in Table 3.2 are considered. The slightly greater estimates for reductions in RH_n relative to the transient model arise because the steady-state assumption in the Monte Carlo model precludes an accurate simulation of isotopic balance during lake level fluctuations. Because the model does not account for the additional isotopic enrichment in the lake due to decreased P/E during a lake-level drawdown, it is slightly biased towards higher estimates of RH_n reduction.

Category	Parameter	Units	Values [Range]
Lake Evaporation	Lake Temperature	°C	[22 to 28]
	w	-	[0.5 to 0.6]
	V_{eq}	-	[0.6 to 0.7]
	Xe	-	[0.8 to 0.9]
	Vapour Temperature	°C	25
	θ_{eq}	-	0.529
	θ_{kin}	-	0.518
Precip.	$\delta^{18}O$	(‰, VSMOW)	[-5 to -4]
	d-excess		[5 to 15]
	^{17}O-excess		[-7 to 12]

Table 3.2. Steady-state parameters for Monte Carlo simulations. See text for details of parameters.

3.6 Conclusions

Using triple oxygen and hydrogen isotope data to independently deconvolve climate variables precipitation, RH_n and the amount effect, the changing hydrological conditions at Lake Chichancanab have been constrained. This approach provides a significant advance over previous attempts to estimate the magnitude of rainfall reduction during the TCP droughts (e.g. Medina-Elizalde and Rohling, 2012). Furthermore, these quantitative estimates of past rainfall and RH_n can serve as input variables in crop models, to better understand how drought affected agriculture (e.g. maize production) in the northern Maya Lowlands during the TCP (Yaeger and Hodell, 2009).

Chapter 4

The Messinian Salinity Crisis and methods of study

4.1 Introduction

'Saline giants', extensive accumulations of evaporitic salts of up to several kilometres in thickness (Hsü et al., 1973), have formed throughout the Phanerozoic, but have no modern equivalent. The largest Quaternary evaporite basins (e.g. Salar de Uyuni, 9654 km^2, ~120 m thick; Salar de Atacama, 3064 km^2, >900 m thick) are largely insignificant in scale when compared to ancient evaporative systems such as the Cretaceous Aptian salt basins of the southern Atlantic (741,000 km^2, >900 m thick) and the Triassic Hith Formation of the Middle East (1,107,000 km^2, ~100 m thick) (Evans, 2006; Warren, 2010). Saline giants are commonly the focus of applied research by the petroleum industry because of the sealing capacity of salt rock and the association hydrocarbon fluids. In the absence of modern analogues, however, there are major difficulties in establishing a comprehensive understanding of the hydrological, sedimentological, and geochemical processes that may operate in such extensive evaporative basins (Bąbel, 2007; Bąbel and Schreiber, 2014).

The geologically most recent of the known saline giants was deposited in the Mediterranean region during the late Miocene. Plate tectonic convergence of Africa and Eurasia formed the various Mediterranean basins, and subduction dynamics in the Alborán region resulted in a reduction of the hydrological exchange between the Mediterranean and the Atlantic (Flecker et al., 2015). A combination of this tectonic forcing (e.g. Garcia-Castellanos and Villaseñor, 2011), eustatic factors (e.g. Manzi et al., 2013), and astronomically-forced climate change (e.g. Krijgsman et al., 1999; Hilgen et al., 2007; Lugli et al., 2010) is thought to have driven fluctuation in Mediterranean salinity, resulting in the precipitation

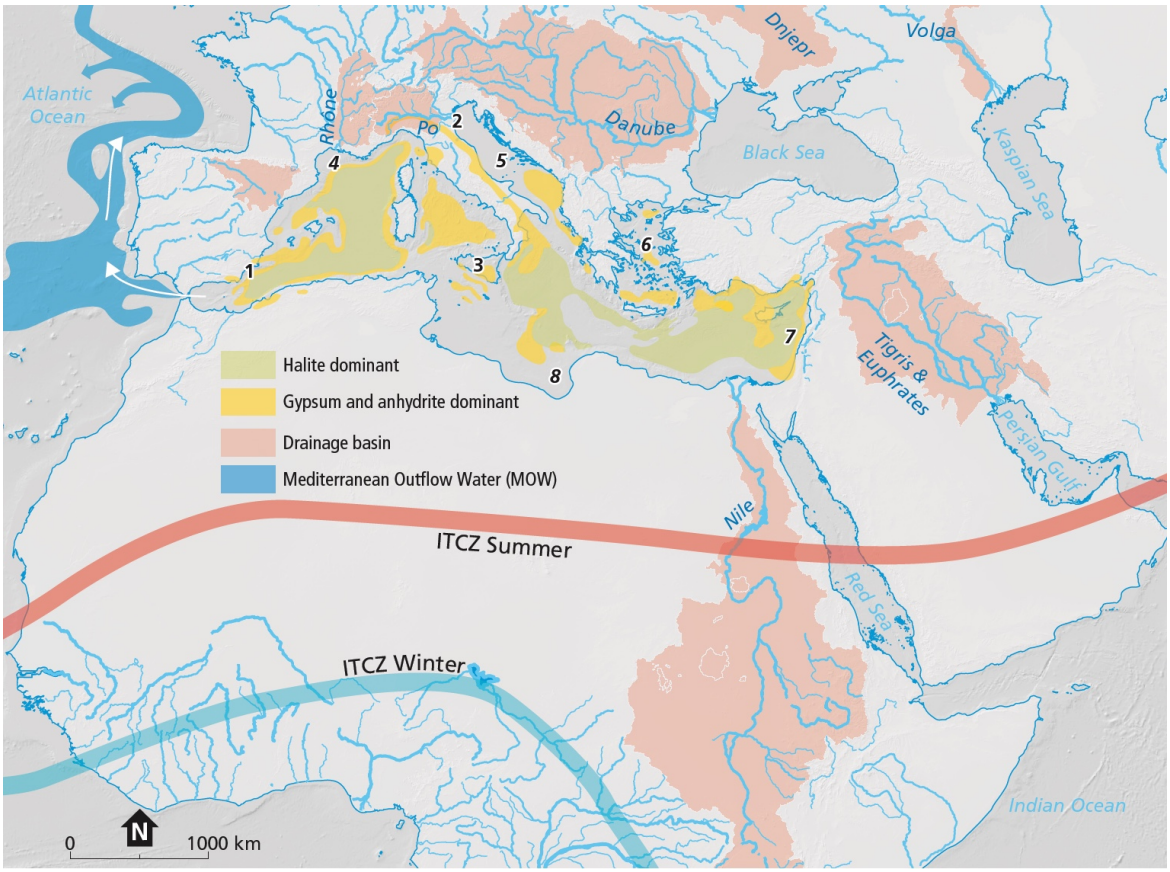

Fig. 4.1. Modern topographical map of the Mediterranean region. Messinian evaporite deposits, the major rivers/drainage basins are indicated. White arrows show Mediterranean outflow water (MOW). Numbers refer to Messinian and modern marginal and intermediate basins. From Simon (2017).

of over one million cubic kilometres of evaporite deposits during the period known as the Messinian Salinity Crisis (MSC; 5.97-5.33 Ma) (Hsü et al., 1973; Krijgsman et al., 1999; Rouchy and Caruso, 2006; Roveri et al., 2014a).

The concept of a late Miocene 'salinity crisis' (Selli, 1960) was first formulated from onshore studies, while the deep basin extent of the Messinian salt was only recognized after seismic investigations carried out during the 1960s and 1970s were confirmed by the discovery of evaporites during Deep Sea Drilling Project (DSDP) Leg 13 (Hsü et al., 1977, 1973). The deposits of the Mediterranean have been subsequently recognised as unique amongst the saline giants due to their relatively young age and relative lack of significant tectonic modification (Warren, 2010; Roveri et al., 2014b). It has also been suggested that the MSC impacted global climate systems and ocean chemistry by contributing warm, saline water to northern latitudes (white arrows, Fig. 4.1), influencing the Atlantic Meridional Overturning Circulation (AMOC) (Hernandez-Molina et al., 2014), in addition to seques-

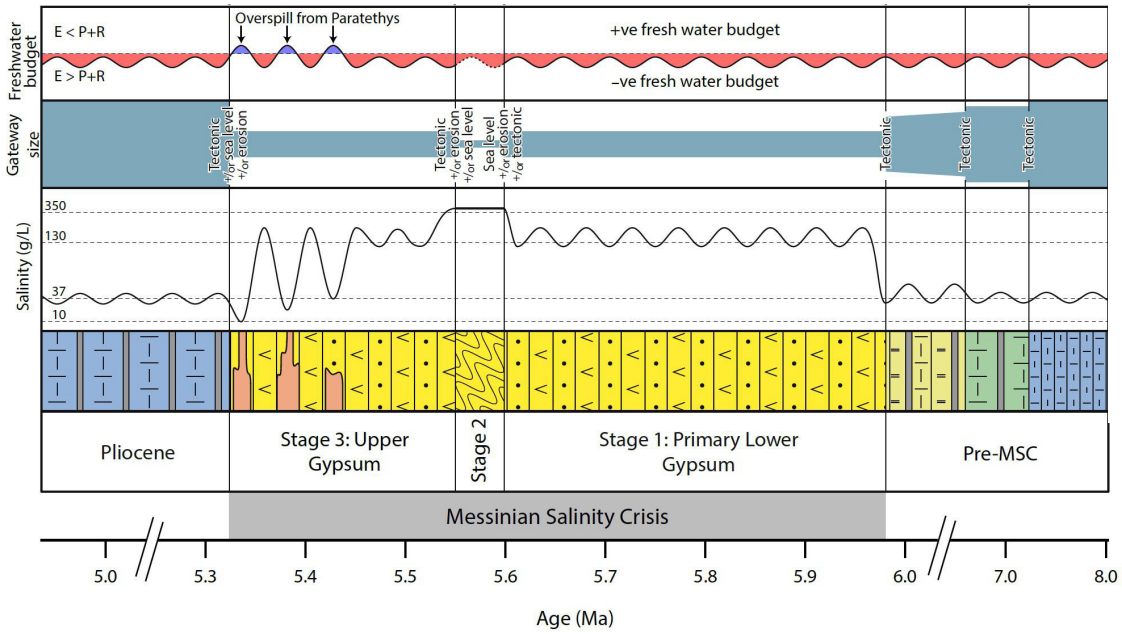

Fig. 4.2. Illustration of the main features of the MSC and Mediterranean's exchange history including lithology, Mediterranean salinity, a qualitative representation of gateway size and the probable drivers (tectonics, erosion, sea level) of changing dimensions and the Mediterranean's freshwater budget (E = evaporation; P = precipitation over the Mediterranean; R = river discharge into the Mediterranean Sea). From Simon (2017), modified from Flecker et al. (2015).

tering 5% (Ryan, 2009) to 10% (Garcia-Castellanos and Villaseñor, 2011) of the global salt content into the Mediterranean. The age and scale of this single, giant evaporite system has resulted in its repeated use as a cornerstone for the investigation of evaporite deposition (Meilijson et al., 2018).

As with the other saline giants that developed episodically over geological time, the causes of and mechanisms by which large volumes of gypsum, anhydrite and halite accumulated on the Mediterranean seafloor over a relatively brief period of ~640 ka are controversial. This is in part because of the absence of modern evaporitic systems comparable in terms of both size and mineralogy (Evans, 2006; Warren, 2010). Moreover, the absence of a complete cored succession from the deep basinal Mediterranean prevents a complete synthesis of onshore and offshore records (Roveri et al., 2014a). Thus, the evolution of the MSC has been traditionally explained by using observations and data from uplifted marginal areas (Fig. 4.1). In onshore successions, a stratigraphic consensus model has been proposed comprising of three sedimentary units characterised by distinct evaporitic associations (see CIESM, 2008 and Roveri et al., 2014a). In stratigraphic order, these units can be broadly categorised as: the Primary Lower Gypsum (Lower Evaporites), followed by halite with

clastic gypsum, ending in either brackish deposits (Lago Mare) or gypsum sequences (Upper Evaporites) (Fig. 4.2). Because the related deposits are mostly hidden from scrutiny in the deep basin, correlation between onshore and offshore sediments is difficult, hampering the development of a comprehensive stratigraphic model (Simon and Meijer, 2017).

The subsequent chapters are individually focused on the interpretation of the two time-distinct periods of gypsum deposition - The Primary Lower Gypsum (Chapters 5 and 6) and the Upper Gypsum (Chapter 7) - to provide a robust framework to interpret the causes of and mechanisms by which large volumes of gypsum accumulated on the Mediterranean sub-basins during the MSC. In order to give clear stratigraphic context for this subdivision, the currently accepted stratigraphy of the MSC is outlined in this chapter (Section 4.2). Subsequently, both traditional and novel isotope tracers, and their potential to interpret the hydrological variability during gypsum deposition, are described (Section 4.3). These methods provide new insights into the conditions under which gypsum forms, and help distinguish changes in Mediterranean-Atlantic connectivity from the regional freshwater budget during the generation and evolution of evaporite formation across the MSC.

4.2 Stratigraphy of the MSC

In 2008, the CIESM (Mediterranean Science Commission) defined a stratigraphic consensus model consisting of three main stages during the MSC (Fig. 4.3). Although this consensus model can explain most (currently available) data, knowledge of the MSC sedimentary evolution is heavily biased by onshore exposures. Within the CIESM (2008) framework, we outline new offshore and modelling data that potentially calls for a revaluation of the commonly accepted stratigraphic models for the MSC (e.g. Simon and Meijer, 2017; Meilijson et al., 2018).

4.2.1 Mediterranean onshore successions

In marginal basins of the circum-Mediterranean, onshore pre-evaporite successions consist of cyclic alternations of homogeneous marls, sapropels and diatomites. The pre-evaporite carbonate-marls sediments were deposited in response to astronomically-driven climate oscillations (e.g. Krijgsman et al., 1999; Sierro et al., 2001, 1999) and have been correlated and cyclostratigraphically tuned across the Mediterranean basin (e.g. Hilgen et al., 2007). The lowermost gypsum bed marks the onset of the MSC (Krijgsman et al., 1999; Manzi et al., 2013), which was originally dated at 5.96 Ma by Krijgsman et al., (1999) using the same integrated high-resolution stratigraphy. This age was later redefined to 5.971 Ma by

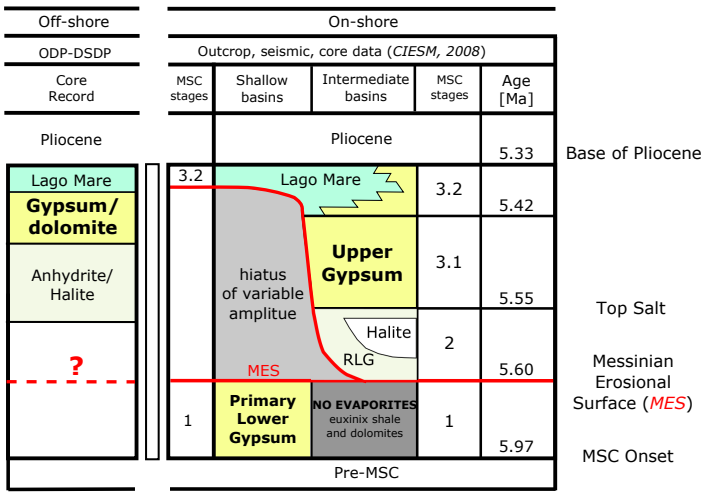

Fig. 4.3. Late Miocene chronostratigraphy of the Mediterranean (modified after Roveri et al., 2014a). Messinian Salinity Crisis (MSC) Stage 1 is marked by the deposition of the Lower Evaporites or Primary Lower Gypsum in the shallow basins and euxinic conditions in the deep basins. MSC Stage 2 is characterised by erosion on the shelves, and halite deposition in the deep basins. MSC Stage 3 is subdivided in the Upper Evaporites or Upper Gypsum (3.1) and the brackish to fresh Lago Mare facies (3.2).

Manzi et al. (2013), based on a reinterpretation of the lowermost gypsum bed in the Sorbas basin, south-eastern Spain.

Stage 1 (~5.97-5.61 Ma) – *Primary Lower Gypsum* The first period of evaporite deposition, known as the Primary Lower Gypsum (PLG), comprises up to 16 beds of massive gypsum (1 m to 35 m in thickness), interbedded with thin layers (~0.5 m to 5 m in thickness) of finely laminated marls or shale (Roveri et al., 2009; Lugli et al., 2010). The deposition of these evaporate-marl cycles is also reported to be controlled by the variations of Earth's orbital parameters, mainly the ~21 kyr precession cycle (Krijgsman et al., 2001, 1999; Lugli et al., 2010; Manzi et al., 2013). According to this interpretation, evaporite deposition occurred at the precession maxima (i.e. minimum summer insolation when summer solstice and aphelion coincided) when evaporation exceeded precipitation during periods of dry climate, and marl deposition occurred at precession minima (maximum summer insolation when summer solstice and perihelion coincided) when rainfall increased (Krijgsman et al., 2001, 1999) (Fig. 4.4). Assuming precession does control the periodicity of gypsum deposition, the top of Stage 1 Lower Evaporites has been determined to be 5.61 Ma by cyclostratigraphy (Krijgsman et al., 2001; Hilgen et al., 2007; CIESM, 2008). In situ PLG deposits are well preserved in the western and central Mediterranean regions such as the Betic Cordillera and the Apennines (Roveri et al., 2014a). In other locations, the develop-

ment of PLG evaporites can be deduced from their occurrence as isolated blocks (e.g. Zakynthos, Aegean Sea; Bąbel, 2004; Lugli et al., 2010) or within resedimented deposits (e.g. Cyprus, Levant margin; Lugli et al., 2013). The lower ~5 cycles of all PLG sections consist of massive, vertically-elongated, twinned selenite crystals described as 'arrow-headed' or 'swallow-tailed' (Bąbel, 2004; Lugli et al., 2010) (Fig. 4.4). The crystals have a preferred vertical orientation and produce a 'palisade'-like structure (Dronkert, 1985). The crystalline size of gypsum is generally large (up to 50 cm in length) and homogenous, although a slight reduction in crystal size is seen up-section in some cycles. The massive aspect of these selenite beds is thought to indicate that the brine concentration did not drop to carbonate saturation (e.g. Lugli et al., 2010). The lower contact between the overlying gypsum and underlying carbonate marls is often undulating, and contains structures interpreted to be 'nucleation cones' (Dronkert, 1985). These load structures consist of conical clusters of crystals that occur at the base of the gypsum beds, representing the initial nucleation points of gypsum that sank into the relatively soft marls (Lugli et al., 2010). The occurrence of the branching 'supercones' (Dronkert, 1985) from the sixth cycle upwards (Lugli et al., 2010) is of particular importance as it provides a marker bed for correlation to other sections across the Mediterranean (Roveri et al., 2014a). Indeed, PLG sections across the Mediterranean are sufficiently similar in terms of vertical facies distribution and cycle stacking pattern that they have been used for basin-wide correlation of individual cycles (Lugli et al., 2010; Roveri et al., 2014a). These basin-wide stratigraphic similarities, combined with measured strontium isotope values which have been reported to be 'within error' of, or close to, open ocean values (see section 4.3.5), suggest that the PLG precipitated from a relatively homogeneous Atlantic-fed water body (Lugli et al., 2007, 2010; Roveri et al., 2014a; García-Veigas et al., 2018).

From the sixth cycle upwards, there is a significant change in facies across all PLG sections (Fig. 4.4). While the base of the gypsum beds in each individual cycle generally consist of the largest crystals (up to ~30 cm in length), the crystal size becomes progressively smaller (up to a few centimetres) up section (Fig. 4.5). Massive palisade gypsum often gives way to a 'banded selenite' facies, consisting of finer (~1 cm to 10 cm) crystals that are separated by thin carbonate laminae (Lugli et al., 2010). According to Bąbel (2007), such features reflect characteristic fluctuations of the pycnocline (i.e. the gypsum-saturation interface) that repeatedly interrupts selenite growth. Above the banded selenite, the gypsum grades into giant cauliflower-shaped supercones (SC) in some cycles. Supercone structures are created from clusters of small gypsum crystals creating curved, horizontal branches up to ~2 m in length. The branches originate from a central nucleation region and gradually increase in length towards the top of the section, thus forming the inverted cauliflower-shaped

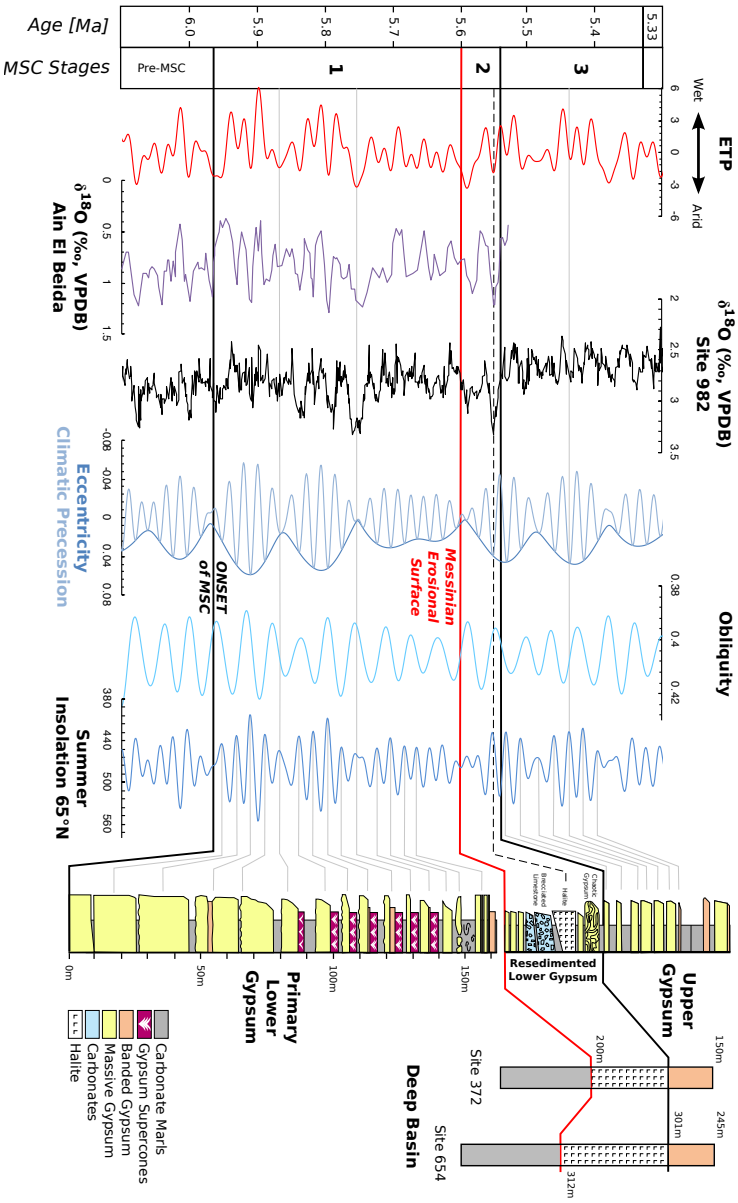

Fig. 4.4. Messinian MSC chronostratigraphy and astronomical tuning of the Mediterranean Messinian Lower Gypsum (Yesares Member, Sorbas basin, SE Spain), halite and Upper Gypsum (Eraclea Minoa, Sicily). Schematic representation of the vertical facies arrangement of an ideal PLG and UG section orbitally tuned, with gypsum beds calibrated with the aridity peak of the insolation curve. The revised benthic δ^{18}O record of site 982 from Drury et al. (2018) is also compared to the benthic δ^{18}O record from Ain El Beida (van der Laan et al., 2005). The Primary Lower Gypsum unit was deposited during stage 1 of MSC. During stage 3 of the MSC, the Upper Gypsum was deposited in Sicily and Eastern Mediterranean, while the Northern Apennines and the Betics are characterised by deposition of terrigenous units. Proposed correlation between the onshore sections and the offshore deposits recovered from DSDP/ODP cores are also shown (see Roveri et al., 2014a).

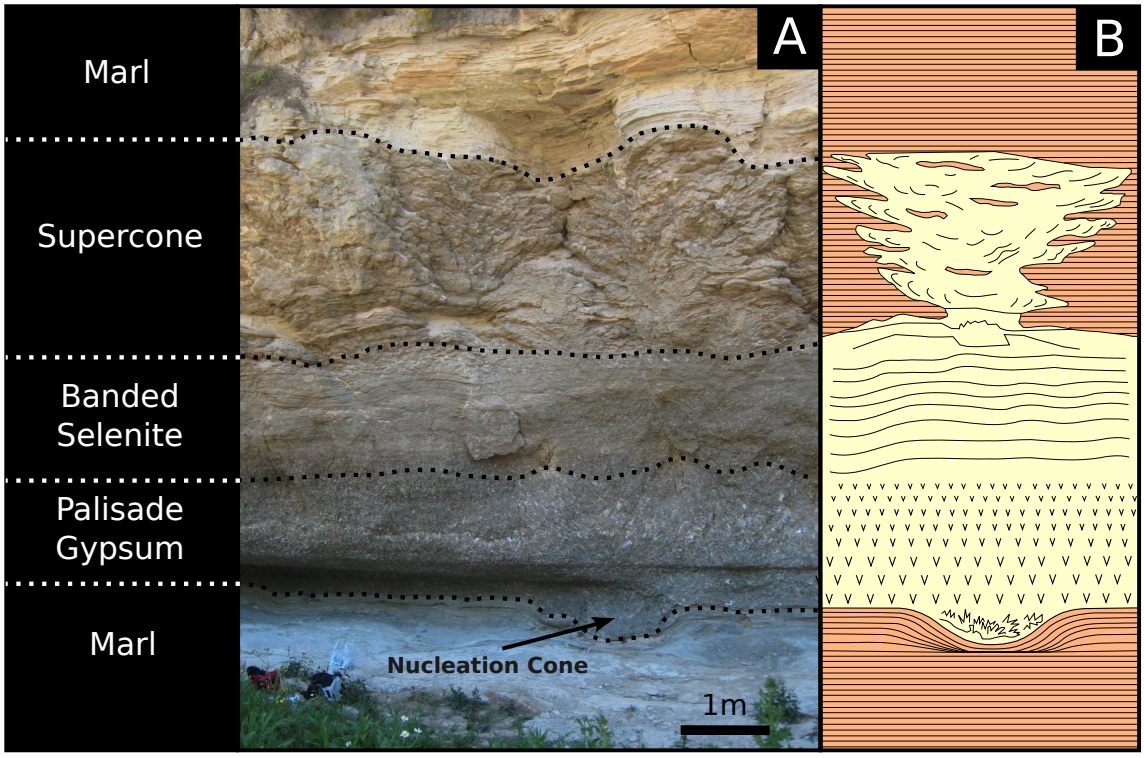

Fig. 4.5. Cycle 10 of the PLG (Yesares Member, Río de Aguas section, SE Spain), displaying the differing crystal morphology and structures (**A**) relative to a schematic diagram (**B**) (after Dronkert, 1985). Carbonate marls occur at the onset and termination of the cycle. Nucleation cones represent the onset of gypsum precipitation. Palisade gypsum directly above the nucleation cones contains large, vertically orientated selenite crystals. Selenite palisade is overlain by banded selenite that are, in turn, overlain by asymmetric conical structure (supercones) juxtaposed to carbonate marls.

cones (Dronkert, 1977; Lugli et al., 2010). Laminated marls can occur in pods between the branches of the supercones and carbonate minerals are composed almost entirely of dolomite (Evans et al., 2015; Chapter 5). Some of the carbonate laminae can be traced into the gypsum crystals where they thin and disappear, indicating the gypsum and marl are syndepositional.

Stage 2 (~5.61-5.55 Ma) – *resedimented gypsum and halite* While the halite phase of Stage 2 only developed in the deep basins, the upper boundary of the PLG in some marginal basins is incised by a major erosive event known as the Messinian Erosion Surface (MES). The marginal erosion surface was caused by a sea level drop, which resulted in reworking and transport of sediments to the Mediterranean basin centre (see Roveri et al., 2014a and references therein). Glacial stages TG14 and TG12 occurred during this interval and may have caused further restriction of the Mediterranean-Atlantic exchange (e.g. Hilgen et al.,

2007). The total sea level fall during this period is uncertain. The drop in sea level is thought to have promoted slope instability and gravity failure around the basin margins, resulting in the Resedimented Lower Gypsum (RLG) unit (Roveri et al., 2008).

Stage 3 (~5.55-5.33 Ma) – *Upper Evaporites and Lago Mare* Stage 3 deposits developed in the deep basins, which have been subsequently uplifted into marginal settings. Sub-basins of the southern and eastern Mediterranean (i.e. Sicily and Cyprus; Rouchy and Caruso, 2006; Manzi et al., 2013, 2009) contain both selenite and cumulate gypsum facies (the 'Upper Evaporites' or 'Upper Gypsum' (UG); Manzi et al., 2009), while in the northern and western areas, evaporite-free 'Lago Mare' (e.g. Orszag-Sperber, 2006) units are comprised of grey-to-white marls interbedded with deltaic or fluvial conglomerates (Fortuin and Krijgsman, 2003). These sediments contain fauna that live in brackish water (Bassetti et al., 2004; Orszag-Sperber, 2006). The development of potential shallow-water environments during this period is also implied from strontium isotope values (measured on both evaporites and fossils) that diverge away from the global oceanic water value, indicating a substantial dilution of surface waters, locally punctuated by episodic, precession-driven, evaporitic events (e.g. Flecker et al., 2002; Flecker and Ellam, 2006; Roveri et al., 2014b).

The Upper Evaporites of Stage 3 consist of repeated gypsum-carbonate marl beds that, similar to PLG evaporitic cycles, represent a response to precession-driven climate oscillations (see Manzi et al., 2009 and references therein). Exposures on Sicily and Cyprus show alternations of gypsum beds (3 m to 8 m thick) and marl horizons (5 m to 20 m thick) containing typical Lago-Mare flora and fauna (e.g. Rouchy et al., 2001; Gliozzi et al., 2007; Londeix et al., 2007). The most complete stage 3 succession occurs at Eraclea Minoa, Sicily, where 10 sedimentary cycles (7 with gypsum) have been recognised and correlated regionally between the top of the stage 2 deposits and the base of the Pliocene (Van Der Laan et al., 2006; Hilgen et al., 2007; Manzi et al., 2009) (Fig. 4.4).

The UG shows different facies and cycles thickness with respect to stage 1 PLG deposits (Manzi et al., 2009) (Fig. 4.6). Much of the Eraclea Minoa section, for example, consists of marl and thinly-bedded sandstone packages that are tens of metres thick, showing a slight coarsening and thickening up-section. Before the onset of gypsum beds, the marl and sandstone deposits are overlain sharply by decimetre-thick tabular graded sandstone beds (unit S1). The first gypsum consists of decimetre-thick, fine-grained gypsum (<5 mm) and grey marl graded beds (unit G1a) that sit conformably on the underlying marl and sandstone layers. This unit is characterised by traction and fallout sedimentary structures indicating deposition from high-density to low-density gravity flows (Manzi et al., 2009). Fine-grained laminar gypsum beds (unit G1b) overlie unit G1a, each bed up to a few tens

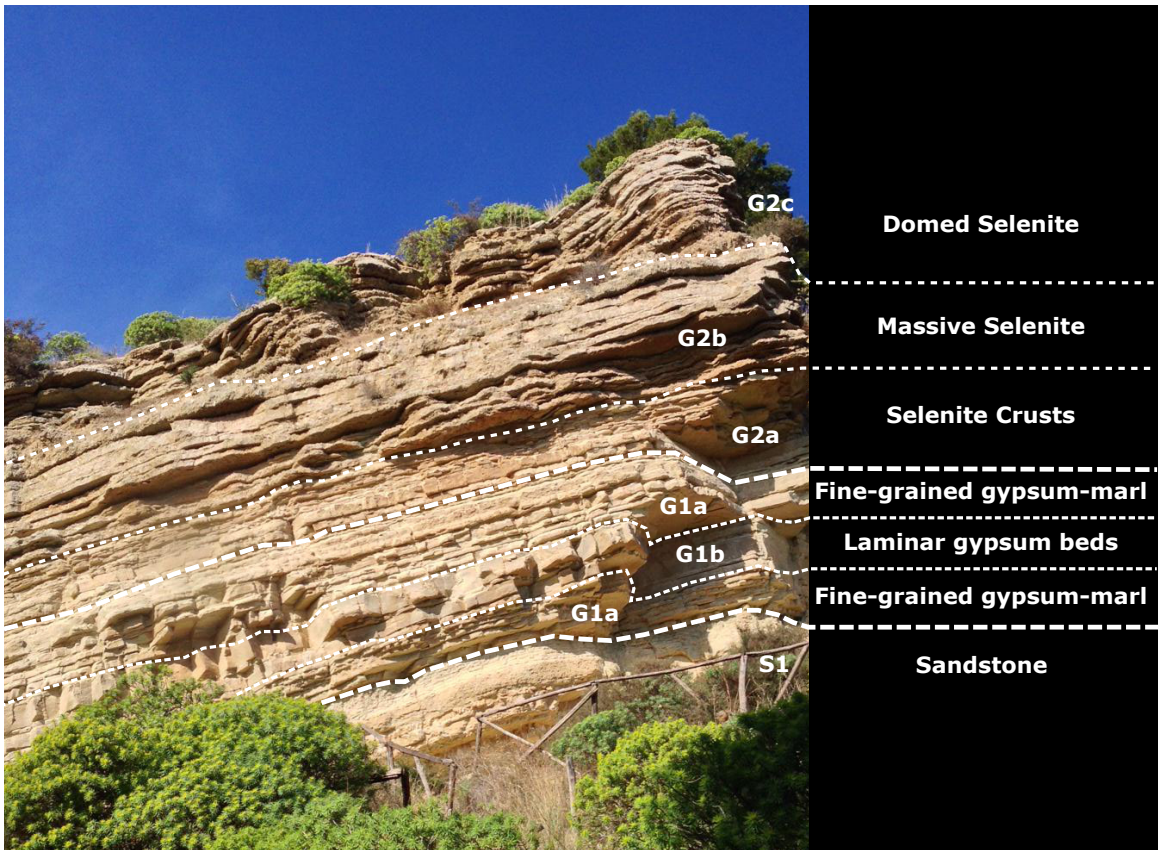

Fig. 4.6. Cycle 4 of the UG (Eraclea Minoa section, Sicily), displaying the main recognised facies and facies associations after Manzi et al. (2009). See text description for description.

of centimetres thick. Above, the laminar gypsum transitions into centimetre-thick, selenite crusts (unit G2a), likely formed as bottom growth primary evaporites. Unit G2a is followed by decimetre-thick massive selenite beds (each bed up to ~1 m thick), which are separated by thin marl horizons (up to ~30 cm thick) (unit G2b). At the top of the gypsum sections, domed structures (unit G2c) are present. These selenite domes have been compared to the dome-like features found in modern marine salinas and marine-fed lakes (Warren, 1982). Locally, reworked selenite beds up to a few centimetres in thickness can be found at the tops of the domes (Manzi et al., 2009). While these features have been traditionally interpreted as erosional surfaces (e.g. Rouchy and Caruso, 2006), Schreiber (1997) interprets these truncations as the point at which gypsum growth stops at the saturation water interface (i.e. the pycnocline).

4.2.2 Mediterranean offshore successions

In the deep basin, seismically-imaged evaporite bodies have been subdivided into three units characterised by different seismic facies. From oldest to youngest, they are labelled as the Lower Unit, Mobile Unit, and Upper Unit. These seismic units have been historically correlated with the PLG, Halite and UG of the onshore record, respectively (Roveri et al., 2014a). The offshore and onshore Messinian units are physically disconnected, however, and establishing reliable correlations is difficult.

Stage 1 (~5.97-5.61 Ma) Little is known about the deposition of the offshore sedimentary units coeval to the onshore PLG, but evidence from the Apennines and geochemical relationships suggest that organic-rich shales and dolomites accumulated in the deep basins (De Lange and Krijgsman, 2010; Flecker et al., 2015). De Lange and Krijgsman (2010) argued that the possible lack of gypsum in these deep environments is because sulfate acts as an oxidant for organic matter mineralisation in deep water. In hypersaline settings, water masses become anoxic due to high-density stratification and lack of ventilation. Sustained sulfate consumption results in a diminished deep water sulfate concentrations and thus undersaturation with respect to gypsum (De Lange et al., 1990; Torfstein and Turchyn, 2017). The balance between organic matter remineralisation-related sulfate consumption and the supply of sulfate from shallow-water gypsum formation may therefore determine if the deep-water sulfate concentration becomes too low to permit gypsum formation and preservation (De Lange and Krijgsman, 2010).

Stage 2 (~5.61-5.55 Ma) The primary evaporitic deposits during this phase include the thick and extensive halite and K–Mg salts (mainly represented by kainite, $MgSO_4KCl \cdot 3\,H_2O$, but also; carnallite, $KMgCl_3 \cdot 6\,H_2O$; bischofite, $MgCl_2 \cdot 6\,H_2O$; and sylvite, KCl) (see Yoshimura et al., 2016 and references therein). The presence of K-Mg salt minerals reflects extreme hypersaline environments during this stage. This extreme stage is often linked to a desiccated Mediterranean (e.g. Hsü et al., 1973).

In the present stratigraphic scenario, the deposition of halite and K-Mg salts occurs in a short period of ~50 ka during the MSC acme (CIESM, 2008; Roveri et al., 2014a). Recent analysis from cuttings and well-log data from industry drilling in the eastern Mediterranean Levant Basin, however, has shown that halite may have started to precipitate in the deep basins around the onset of the PLG deposition at 5.97 Ma (Meilijson et al., 2018). A box model developed by Simon and Meijer (2017) has recently suggested the possibility of synchronous deposition of deep-basin halite and shallower deposition of gypsum during Atlantic connectivity. Indeed, while the MES at the top of the PLG can be traced off-

shore in seismic lines, it splits into several surfaces, not all of which are erosional (Lofi et al., 2011; Flecker et al., 2015). The cores from the Levant Basin contradict a 'chaotic' sedimentation and unconformity scenario for the base of the MSC in the deep basins because of the consistent recovery of the drilled record, lack of any indication of truncation in the seismic section, and no sedimentary evidence indicating substantial reworked or transported deposits in this interval (Meilijson et al., 2018). A coeval initiation of basinal halite and marginal PLG precipitation would therefore call for a revaluation of the commonly accepted stratigraphic model for the MSC (CIESM, 2008). Additionally, it would necessitate the revaluation of global-scale climatic and oceanographic models of the MSC, taking into account the possibility of an increase in the duration of halite precipitation and the older age for the initiation of halite deposition (Meilijson et al., 2018).

Stage 3 (~5.55-5.33 Ma) ODP and DSDP holes have recovered material that correlates to the offshore seismic unit labelled as the 'Upper Unit', and indicate that Lago Mare sediments overlie deep-sea evaporites (Hsü et al., 1973; Roveri et al., 2014b). The correlative relationship between these offshore deposits and the marginal sediments remains unclear, however (Flecker et al., 2015). To avoid a possible hydrocarbon blowout in the Mediterranean, only the upper surfaces of the deep evaporites were sampled. With drilling penetration in evaporites at 80 m or less, 95% of the Messinian salts are unsampled beneath the deep Mediterranean basin and its continental margins. Deep offshore Messinian successions that have been cored, such as site 654 in the Tyrrhenian Sea, display a cyclical stacking pattern in the Upper Unit that could be tentatively correlated with the onshore succession of the UG (Roveri et al., 2014a). Preliminary strontium isotope measurements for this section imply that the correlation of the 'Upper Unit' with the onshore UG succession may be not correct, however (Roveri et al., 2014b). In a scenario proposed by Roveri et al. (2014b), the 'Upper Unit' would largely correlate to stage 2 (including onshore RLG and halite) rather than the previously assumed stage 3. Only the uppermost part of the Upper Unit, often not detectable from seismic data because of its limited thickness (<50 m), may be considered the offshore counterpart of stage 3 onshore deposits.

The 'Zanclean flooding' at the end of the MSC saw the return of the Mediterranean basin to fully and stable marine conditions. This substantial palaeoceanographic change is typically recorded by a sharp lithological and palaeontological boundary, suggesting a geologically instantaneous event (Roveri et al., 2014a). This event has been used to define the Zanclean/Pliocene stage GSSP in the Eraclea Minoa section (Sicily; Van Couvering et al., 2000).

Across stages 1 to 3 of the MSC, questions remain regarding both the contribution of

continental and marine source waters to Mediterranean brines during precipitation of the PLG and UG (Flecker and Ellam, 2006; Lugli et al., 2010; Natalicchio et al., 2014), and the origin of the hydrological change that triggers the appearance of different carbonate, chlorite and sulfate facies (e.g. the branching selenite facies from the 6th cycle upwards of the PLG units; Lugli et al., 2010). Indeed, numerical models that simulate the formation of Messinian evaporites (e.g. Garcia-Castellanos and Villaseñor, 2011; Topper and Meijer, 2013) are currently limited by the lack of reliable geochemical constraints for both the onshore and offshore evaporitic sequences, and a lack of knowledge about their spatial dimensions and heterogeneity. An integrated approach that combines external factors that force Mediterranean hydrology, e.g. tectonics, climate, eustatic sea level change, with an accurate understanding basin level hydrological variability is critical for developing a unified theory that explains the formation of the Mediterranean Salt Giant. In order to address these open questions, we present an overview of current and novel geochemical methods that may, in conjunction, provide an integrated understanding of the Upper and Lower Gypsum of the MSC.

4.3 Differentiation of ancient gypsum deposits – major / trace elements and isotopic tracers

In order to precipitate gypsum in natural environments such as the late Miocene Mediterranean basin, supersaturation with respect to gypsum must be achieved by the concentration of calcium and sulfate ions within a basin. Supersaturation can occur if evaporation in a basin exceeds the inflow, thus creating a negative water balance, or by the inflow being concentrated in calcium and/or sulfate ions (or a combination of both). For marine-sourced gypsum to form, an evaporative basin is usually restricted from the open ocean by a topographic barrier inducing a negative water balance. Such a barrier can either emerge or subside (e.g. due to sea level rise/fall or tectonic activity) and maintain a connection to the open ocean, or the barrier may sporadically restrict open water connections between the basin area and the ocean (e.g. a salt lagoon) (Bąbel and Schreiber, 2014). By definition, therefore, the majority of 'marine' evaporative basins are fundamentally 'marginal marine' basins, surrounded by land and thus always under some influence of non-marine sources of water. Thus, a marginal marine basin can contain fluids that range from strictly marine, to a mixture of marine and non-marine (hybrid), to brackish (during intervals of wetter climate) (Bąbel and Schreiber, 2014). Methods to interpret and distinguish the geological and hydrogeochemical character of (i) marine/marginal marine or (ii) continental/non-marine gypsum

deposits are therefore fundamental to the understanding evolution of ancient gypsum for palaeo-climatic and palaeo-environmental reconstructions.

Environmental tracers provide an important tool for understanding the source, flow and mixing dynamics of water in both the terrestrial and oceanic realm. Tracers, such as ion ratios, fluid inclusion analysis, and the isotopic compositions of minor/trace elements and incorporated water molecules, can be utilised individually or together to reconstruct the hydrogeochemical processes operating within a system. The degree of sensitivity of an isotopic geochemical tracer is dependent on both the isotopic and concentration contrast between oceanic and freshwater inputs. The isotopic compositions of such binary mixtures are therefore related to their end-member compositions in simple ways that can be expressed by relatively straightforward algebraic expressions (i.e. mixing lines).

Here I describe the various tracers and the analytical methods employed to measure the trace element concentrations, isotopic ratios, and fluid inclusion- based salinity estimates that will be utilised in Chapters 5, 6 and 7. This section describes the preparation of the gypsum and carbonate samples and the methods developed over the course of this research to produce data that can be utilised to interpret the evolution of the environment of gypsum precipitation during the deposition of the Upper and Lower Gypsum units of the MSC.

4.3.1 Gypsum Hydration Water

The measurement of triple oxygen and hydrogen isotopes of GHW provides independent information that may be used to disentangle the competing effects of fractionation during evaporation, transport, and precipitation (as discussed in Chapter 1 and in Gázquez et al., 2018). GHW also provides an excellent marker to record the derivation of H_2O in brines; with SMOW taken as a reference standard (and its oxygen and hydrogen isotopes values equal to zero), fluids dominated by meteoric waters generally display depleted isotopic values (Craig, 1961; Dansgaard, 1964). Evaporated seawater brines mixed with meteoric or other waters may have distinct $\delta^{18}O$, $\delta^{17}O$ and δD values due to mixture of H_2O with different isotopic characteristics.

Although the GHW of many freshwater gypsum deposits have lower $\delta^{18}O$, $\delta^{17}O$ and δD values than their marine equivalents, this is not always the case. Freshwater gypsum from highly evaporative freshwater environments may lead to brines that are enriched in ^{18}O and ^{2}H even above that of marine gypsum. For example, gypsum from the marine salt works of the Cabo de Gata, SE Spain, display a maximum $\delta^{18}O$ value of 8.8‰, whereas the GHW of freshwater gypsum from Lake Estanya, Southern Pyrenees, reach values of 10.6‰. While a distinction between marine and non-marine gypsum is no longer possible based on isotopic analysis of the GHW alone, triple oxygen isotopes can be used to examine basin recharge

(e.g. Surma et al., 2018). This provides important information regarding the hydrological evolution of palaeo-basins.

Methodology: The extraction and analysis of GHW was conducted using the methods described in Chapter 2.

Sampled gypsum crystals were initially divided into two parts: whole crystals were preserved for fluid inclusion analysis, while crystals for GHW, trace element and isotope analysis were ground to a powder and dried for 24 h at 45°C to remove adsorbed water. Approximately 200 mg of dried powder was used for GHW extraction, while the excess powder was homogenised and stored trace element and isotope analysis.

4.3.2 Fluid Inclusions Analysis

During the precipitation of gypsum, the crystal growth surface inevitably contains imperfections. Typically, continued growth of the crystal will engulf such imperfections, thus producing a vacuole containing the fluid present at the moment of sealing. The trapped fluids that are enclosed during the growth of the crystal are termed primary, and contain a sample of the fluid responsible for the precipitation of the diagenetic phase (Goldstein and Reynolds, 1994). Primary fluid inclusions in gypsum are identified by a relationship to growth surfaces, where elongate inclusions in gypsum occur along the (001) plane and more equidimensional inclusions occur normal to $(\bar{1}03)$ plane (Goldstein and Reynolds, 1994). A careful distinction must be made between primary and secondary fluid inclusions in gypsum, where the latter display prismatic to elongated shape up to 100 μm in length. Secondary inclusions are arranged along the (010) cleavage plane, with the major axis parallel to the (100) plane (Natalicchio et al., 2014), lack a zonal arrangement, are present on different planes than primary fluid inclusions, and are unrelated to growth bands of host selenite crystals (Attia et al., 1995).

Chemical analysis of fluid inclusions in gypsum and other saline minerals is a powerful tool for the estimation of brine composition (e.g. Knauth and Beeunas, 1986; Lowenstein et al., 2001; Rigaudier et al., 2011). A second technique, fluid inclusion microthermometry (FIM), can be used to deduce the salinity of the parent fluid. Fluids that contain dissolved salts depress the freezing temperature of water and the melting temperature of ice; thus, the melting temperature of frozen fluid inclusions is related to the salinity of the parent brine. To date, only a few studies have used this technique on fluid inclusions in modern and ancient gypsum to determine brine salinities (e.g. Attia et al., 1995; Natalicchio et al., 2014). This reticence likely stems from concerns about the lack of knowledge regarding secondary fluid inclusion formation and how interaction with secondary fluids may impact the chemistry

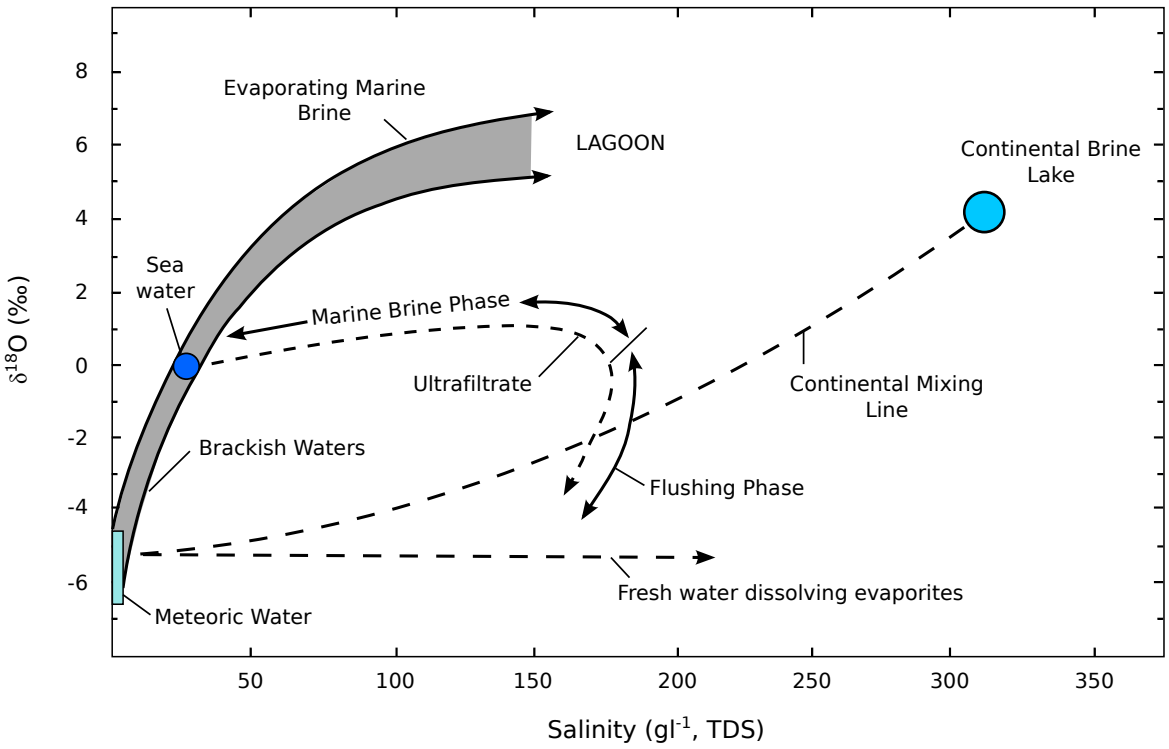

Fig. 4.7. Schematic of changes in salinity and isotopic composition of formation waters in δ^{18}O-salinity space, illustrating evaporation, continental mixing and freshwater dissolution of evaporites. After Gat (1996).

of primary inclusions. Equally, FIM is limited to mm-sized selenite crystals where growth zonation is clearly defined, and thus cannot be performed on microcrystalline gypsum.

A combination of water isotopes deduced from GHW and salinity deduced from gypsum fluid inclusions provide information on the composition of formation waters and fluid behaviour during evaporation. Together, changes in the salinity and water isotopic composition allow derivation of the processes of evaporation, continental water mixing, and freshwater dissolution/reprecipitation cycles (Fig. 4.7). Additionally, coupling of gypsum water isotopes and salinity of fluid inclusions in the same samples can be used to test if they record the composition of the mother fluid from which gypsum was precipitated (Chapter 5).

Methodology: The method for microthermometric analysis closely followed that described by Attia et al. (1995). Thin (<1 mm) samples of gypsum were obtained by cleaving the mineral along 010 planes using a razor blade. The fragments were placed in a Linkam THMSG600 heating-freezing stage attached to a Zeiss Axio Scope.A1 microscope equipped with a 100× objective.

Primary inclusions in modern and Messinan gypsum crystals are all single phase, con-

taining only liquid. By freezing the inclusions to −70°C and then heating to 30°C at a rate of 20°C min^{-1}, vapour bubbles were formed due to the stretching of the inclusion during ice formation. The first melting temperature of fluid inclusions and the final melting temperature of ice (Tm_{ice}) were observed by cooling to −70°C and subsequently heating at a rate of 5°C per minute to −50°C, 2°C per minute to −15°C and at 0.3°C per minute to 0°C. Ice crystals were identified by their low birefringence, low relief and a rounded shape near Tm_{ice} (Attia et al., 1995). At Tm_{ice}, ice crystals decreased in size until no longer visible. Tm_{ice} was recorded to within 0.1°C and reproduced at least twice for each inclusion with an error of ±0.2°C. Salinities of the Messinian and modern fluid inclusions were calculated from the final melting temperatures of ice and expressed as both wt% NaCl equivalent (Bodnar, 1993) and parts per thousand (Goldstein and Reynolds, 1994).

4.3.3 Sulfur isotopes and oxygen isotopes of sulfate

Sulfur isotopes have previously been used to study the origin of gypsum and other sulfur containing minerals in sedimentary systems (Fontes et al., 1973; Longinelli, 1979; Pierre and Rouchy, 1990; Lu et al., 2001). Modern seawater has a $\delta^{34}S$ of ~21‰ and a $\delta^{18}O$ of ~8‰ (Turchyn and Schrag, 2004). Gypsum precipitates with a negligible sulfur isotope fractionation, but with as much as a 3‰ offset for oxygen isotopes (Lloyd, 1968). The oxygen isotope fractionation factor remains poorly constrained, however, and is often considered negligible (e.g. Torfstein and Turchyn, 2017). The oxygen isotope composition of the precipitating sulfate depends on the variable contribution of oxygen atoms from water and from atmospheric oxygen (Calmels et al., 2007). Abiotic oxygen isotope exchange between aqueous sulfate and water does not occur over geologically relevant timescales (Lloyd, 1968; Rennie and Turchyn, 2014). If the sulfate from seawater trapped in a basin was quantitatively precipitated, then, by mass conservation, the $\delta^{34}S$ and $\delta^{18}O_{SO_4}$ of the bulk precipitated gypsum should reflect that of seawater.

The multiple valence states of sulfur results in its frequent use in biological processes, and the sulfur isotopic composition is often utilised as a primary tracer of the redox dynamics in lacustrine environments both in the modern environment and over geological time (Claypool et al., 1980; Canfield et al., 2004 and references therein). The microbially-mediated reduction of sulfate to sulfide, termed 'microbial sulfate reduction', involves a sulfur isotopic fractionation where the light isotope (^{32}S) is preferentially distilled into the product sulfide relative to the heavier isotope (^{34}S) (Torfstein and Turchyn, 2017). Microbial sulfate reduction coupled to organic carbon oxidation is described through the simplified equation:

$$2\,CH_2O + {SO_4}^{2-} \longrightarrow 2\,{HCO_3}^{-} + H_2S$$

The rate at which the $^{34}S/^{32}S$ ratio in the residual sulfate increases is mainly controlled by factors such as the rate of microbial sulfate reduction, temperature, sulfate concentration, and organic carbon supply (e.g. Torfstein and Turchyn, 2017). Microbial sulfate reduction also fractionates the sulfate-bound oxygen isotopes, whereby the residual sulfate is preferentially enriched in the heavy isotope (^{18}O). The relative change in the sulfur and oxygen isotope composition of sulfate over the onset of microbial sulfate reduction has been shown to reflect the degree of recycling of sulfur within cells (over the amount which is unidirectionally reduced). The $\delta^{18}O_{SO_4}$ therefore reflects the latest oxidation pathway of the reduced sulfur, plus any equilibration with water along the oxidation or reduction pathway (Torfstein and Turchyn, 2017). Thus, the oxygen isotope ratio of sulfate has become a powerful tool for exploring sedimentary and aqueous sulfur redox dynamics.

The $\delta^{34}S$ and $\delta^{18}O_{SO_4}$ isotopes also provide a possible means of distinguishing whether gypsum was deposited in a marine, non-marine, or hybrid brine. The $\delta^{34}S$ and $\delta^{18}O_{SO_4}$ of marine dissolved sulfate in reservoirs are globally uniform (20‰ ±0.5‰ for $\delta^{34}S$; 9.5‰ ±0.5‰ for $\delta^{18}O_{SO_4}$) without significant change from the Tertiary to present (Thode and Monster, 1965; Lloyd, 1968; Turchyn and Schrag, 2004). Thus, the sulfur isotopic composition of aqueous sulfate (and therefore the gypsum that precipitates) in a marine system influenced by continental waters reflects the balance between runoff (generally with depleted values compared to seawater) and the amount of water column microbial sulfate reduction, which is controlled by the stability and length of water column stratification leading to deep-basin anoxia (Torfstein and Turchyn, 2017). The oxygen isotopic composition of sulfate is controlled by the same processes, but is particularly sensitive to the incorporation of oxygen atoms during sulfide oxidation, and the degree of intracellular equilibration between intermediate valence state sulfur species and water (Torfstein and Turchyn, 2017). Sulfate concentrations in most terrestrial waters are low, with most rivers containing three orders of magnitude less sulfate than seawater (Lu and Meyers, 2003). Because of the much higher sulfate concentration in marine brines than in freshwater, the $\delta^{34}S$ and $\delta^{18}O_{SO_4}$ of marine gypsum are relatively insensitive to non-marine contributions.

Methodology: Powdered gypsum was initially dissolved in deionised water, and a supersaturated barium chloride solution (~30 g l^{-1}) was subsequently added to the solution to precipitate the aqueous sulfate from gypsum dissolution as barite ($BaSO_4$). Prior to analysis the barite was cleaned in 6 N HCl and rinsed in deionised water to purify it from any co-precipitating minerals. The barite was weighed into tin and silver capsules and analysed for sulfur and oxygen isotopes, respectively. For oxygen isotopes of sulfate, barite was pyrolysed at 1450°C in a High Temperature Conversion Elemental analyser (TC/EA), and

the resulting carbon monoxide (CO) was measured by continuous flow IRMS with a ThermoFisher Delta V Plus. For sulfate isotope analysis, the barite was combusted at 1030°C in a Flash Element analyser (EA), and the resulting sulfur dioxide (SO_2) was measured by continuous flow IRMS (Delta V Plus). Samples were run in triplicate for $\delta^{18}O_{SO_4}$ and the average and standard deviation of these replicate analyses are presented. Samples were bracketed by NBS127, IAEA-SO5 and IAEA-SO6, international barite standards, which were corrected to $\delta^{34}S$ of 20.3‰, 0.5‰ and -34.1‰, respectively (1σ = 0.2‰). $\delta^{18}O_{SO_4}$ was bracketed by NBS127, IAEA-SO5 and IAEA-SO6 which were corrected to 8.6‰, 12.1‰ and -11.4‰, respectively, and reported uncertainties reflect the average and standard deviation of triplicate analyses of each $\delta^{18}O_{SO_4}$ sample ($1\sigma < 0.5$‰).

4.3.4 Strontium Isotopes

Strontium isotopes provide a natural fingerprint of rock-water interactions and have been widely utilised in studies of weathering and hydrology (e.g. Hodell et al., 1989; Muller et al., 1990; Müller and Mueller, 1991; Palmer and Edmond, 1992; McArthur et al., 2001; Flecker and Ellam, 2006). Many biogenic carbonate, phosphate and evaporitic minerals (including gypsum) incorporate strontium isotopes during precipitation without fractionation at low temperatures or modification due to biotic processes. Thus, unless post-depositional diagenesis has altered the primary strontium isotopic signature, measurement of these materials can provide a record of the strontium isotopic composition of the fluids from which they formed.

The abundance of ^{87}Sr is expressed relative to the abundance of stable ^{86}Sr (i.e. $^{87}Sr/^{86}Sr$). $^{87}Sr/^{86}Sr$ is commonly measured by multiple-collector inductively-coupled plasma mass spectrometry (MC-ICP-MS) or thermal ionisation mass spectrometry (TIMS). TIMS instrumental mass fractionation effects are overcome by linear normalisation of measured isotopic ratios to constant values of stable isotope pairs; by convention, $^{87}Sr/^{86}Sr$ ratios are normalised to $^{86}Sr/^{88}Sr$ = 0.1194 (Elderfield, 1986).

Heterogeneity in $^{87}Sr/^{86}Sr$ ratios of dissolved strontium across geologically diverse environments provides a useful tool quantifying end-member mixing processes over time. At the global scale, temporal variation in the $^{87}Sr/^{86}Sr$ ratio of seawater occurs due to the variable input of strontium derived from two main sources: (i) the continental crust and (ii) the upper mantle. Continental crust supplies dissolved strontium to the oceans dominantly through the chemical weathering of old silicate lithologies, and thus provide waters with high $^{87}Sr/^{86}Sr$ ratios (>0.720), but with low strontium concentrations. Upper mantle sources supply strontium principally through hydrothermal activity at mid-oceanic ridges, submarine weathering of basalts and chemical weathering of continental basalts (Elderfield, 1986). Weathering of such atypical continental crust result in low $^{87}Sr/^{86}Sr$ ratios (0.706-

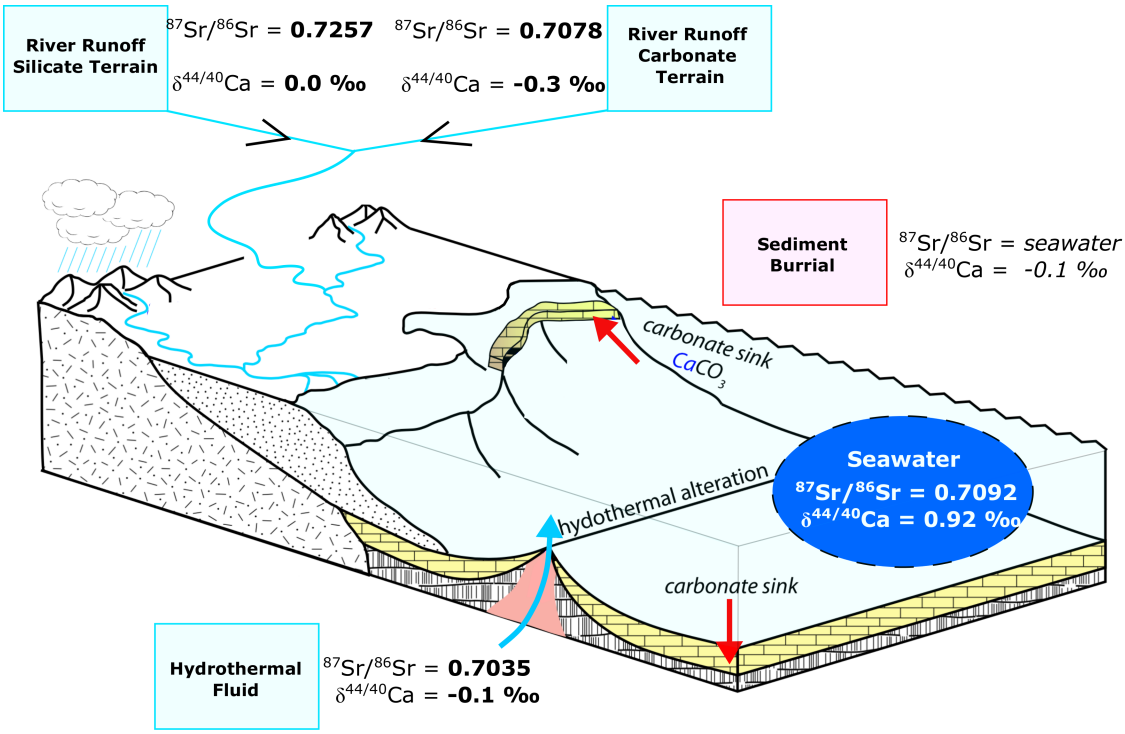

Fig. 4.8. Schematic of calcium and strontium cycling in the modern surface environment, with sources labelled in bold and sinks italicised. Isotopic data from Fantle and Tipper (2014) and Palmer and Edmond (1992). For calcium and strontium, major sources include riverine calcium sourced from continental weathering and hydrothermal fluids at mid-ocean ridge systems. $CaCO_3$ formation and burial is the major sink. Modified after Husson et al. (2015).

0.709) but high strontium concentrations (up to 1000 ppm) (Palmer and Edmond, 1992). The residence time of strontium is significantly longer than the mixing time of the ocean (~10,000 years), and thus the seawater $^{87}Sr/^{86}Sr$ ratio is the homogenous at any one point in time, resulting in a single temporal strontium isotope record (Elderfield, 1986).

At the local scale, the $^{87}Sr/^{86}Sr$ ratio of water in a semi-enclosed basin connected to the global ocean is controlled by a simple mixing between seawater and other strontium-bearing water sources feeding the basin (e.g. river run-off and groundwater) (Flecker and Ellam, 2006) (Fig. 4.8). Importantly, average global river waters have strontium concentrations ~40 times lower than that of seawater (Palmer and Edmond, 1992).

In the Mediterranean today, the $^{87}Sr/^{86}Sr$ values of the Rhone (~0.70872) and the Nile (~0.70600) are lower than the global seawater average, and make up >80% of the total Mediterranean riverine input (McArthur et al., 2001; Flecker et al., 2002; Topper et al., 2014). During the MSC, river input was likely largely made up by North African rivers that are dry today (Simon et al., 2017). On the marginal basin scale, the strontium characteristics of the river input are also dependent on locally outcropping rocks in small catchments (Topper

et al., 2014). While previous studies conducted on marginal Mediterranean basins, such as the Sorbas Basin (SE Spain), have inferred a higher $^{87}Sr/^{86}Sr$ (~0.70910) riverine value than that of coeval ocean water values (~0.70900) on the basis of $^{87}Sr/^{86}Sr$ measurements of ostracods from the lacustrine Zorreras Member (located two units above gypsum deposited during the MSC; Modestou et al., 2017) and secondary gypsum veins (Lu and Meyers, 2003), only ~0.1% of the river discharge into the Mediterranean flows directly into marginal basins (Topper et al., 2014). The Mediterranean freshwater budget was therefore dominated by rivers with low $^{87}Sr/^{86}Sr$.

Methodology: Contamination and its potential effect on strontium (and calcium) isotope signatures was tested in our samples by leaching gypsum in three steps under clean laboratory conditions. Lu et al. (1997) demonstrated that a leaching process involving treating the sample with alcohol, deionised water, and HNO_3 washes significantly reduced certain elemental contaminations. Here, samples were washed in methanol to mechanically separate clays, followed by two deionised water washes to remove ions liberated from fluid inclusions during the grinding process. This was followed with three washes in 10% ammonium hydroxide to remove adsorbed ions from any remaining clays and three washes with 0.001 M HCl to dissolve any carbonates present. Finally, the sample was exposed to three washes of deionised water to remove any traces of the leaching reagents. Approximately 30 samples that were treated via this process were compared to gypsum samples directly dissolved in deionised water. The concentrations of contaminant elements (such as aluminium and sodium) were very low (below detection) in both sample sets, and isotopic measurements made on both leached and non-leached samples were all within analytical error.

An aliquot of sample solution containing approximately 300 ng of strontium was dried down and dissolved in 200 μl 3 M HNO_3. Strontium was separated using Eichrom Sr Spec resin with 100 μm to 150 μm mesh particle size in clean lab conditions. $^{87}Sr/^{86}Sr$ measurements were made by TIMS (Thermo-Scientific Triton Plus MC-TIMS). The separated Sr was dried down, refluxed in 2 N HNO_3 and subsequently dried down once again. Samples were then loaded onto degassed single Re filaments together with 1 μl of tantalum phosphate activator. A current of ~0.8 A was continuously applied during the loading. The evaporation filament is heated manually until a stable signal between 4 V and 6 V of ^{88}Sr on a 1011 Ω resistor is reached. Data acquisition was comprised of 10 blocks of 20 measurements with a ~8 s integration time in static mode. Results were normalised to $^{88}Sr/^{86}Sr$ 0.1194 with an exponential fractionation correction. Runs were bracketed with the NBS 987 standard. The 11 analyses of NBS 987 during the course of this study gave a mean value of 0.710253 (2σ = 0.000007). Blanks were <350 pg and negligible for the Sr concentration of these samples.

A small number of samples (n = 6) were analysed with a VG Sector 54 TIMS. In this case, separated strontium was dried down, refluxed in HCl to ensure crystallisation in a chloride form, and subsequently dried down once again. The resultant crystals were loaded and analysed on a VG Sector TIMS to determine the $^{87}Sr/^{86}Sr$ ratio. Runs were bracketed with an internal NBS 987 standard. NBS 987 gave 0.710262 ($2\sigma = 0.000016$) on 45 separate measurements over the last two years. Procedural blanks for strontium were negligible.

4.3.5 Calcium Isotopes

Calcium is one of the major dissolved components of seawater (~400 ppm) and the most abundant cation in rivers (~20 ppm, but may constitute up to ~100 ppm in carbonate catchments; Fantle and Tipper, 2014). The high abundance of calcium is related to the stability of its nucleus, forming six naturally occurring stable or quasi-stable isotopes, ^{40}Ca (96.94%), ^{42}Ca (0.65%), ^{43}Ca (0.14%), ^{44}Ca (2.09%), ^{46}Ca (0.01%) and ^{48}Ca (0.19%), where ^{48}Ca is treated as stable because of its long half-life of 6×10^{18} years (Fantle and Tipper, 2014). The isotopic composition of calcium in minerals may vary over long timescales as ^{40}Ca can be produced via natural β decay of ^{40}K ($\lambda_{1/2} = 1.27 \times 10^{9}$) (Marshall and DePaolo, 1982). For most samples, enrichments in ^{40}Ca due to radiogenic decay of ^{40}K will be minimal owing to its long half-life and usually limited to less than the range of current analytical uncertainty (DePaolo, 2004).

The stable isotopic composition of Ca is expressed in the δ-notation notation relative to a normalisation standard using parts per thousand (‰) units. There are four reference standards that have been used to date: CaF_2, 'bulk silicate Earth' (BSE), seawater, and SRM-915a (Fantle and Tipper, 2014). Here, $\delta^{44/40}Ca$ values are referenced against BSE, which gives modern seawater $\delta^{44/40}Ca$ as 0.92‰. The $^{44}Ca/^{40}Ca$ ratio is measured by TIMS, while the $^{44}Ca/^{42}Ca$ ratio (expressed as $\delta^{44/42}Ca$) is measured by MC-ICP-MS because of large interferences on ^{40}Ca from $^{40}Ar^{+}$. Assuming $^{44}Ca/^{40}Ca$ and the $^{44}Ca/^{42}Ca$ ratios follow mass-dependent behaviour, a simple correction can be made to compile values into a single database on a uniform scale (Fantle and Tipper, 2014). Analytical fractionation of calcium isotopes during measurement via TIMS is corrected for via the addition of enriched ^{42}Ca-^{48}Ca double spike.

Calcium fractionates isotopically during mineral precipitation, where calcite, aragonite and barite incorporate isotopically light calcium into their structure (e.g. Gussone et al., 2005, 2003). The degree of this fractionation varies with mineralogy (calcite vs. aragonite; Gussone et al., 2005), temperature (Gussone et al., 2005), and precipitation rate. Calcium isotope fractionation during mineral precipitation is believed to be kinetically controlled, and related to aqueous ion-mineral surface interactions (Fantle and DePaolo, 2007; DePaolo,

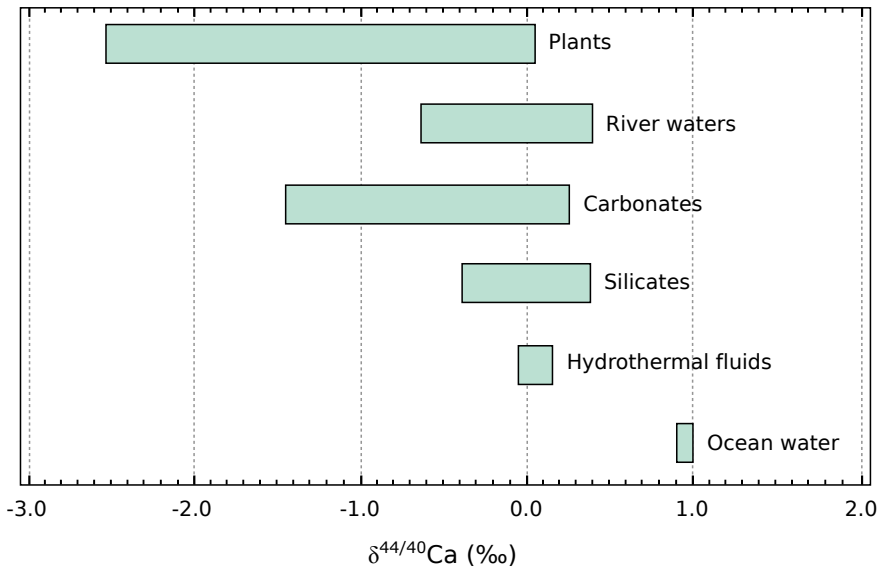

Fig. 4.9. Compilation of calcium isotope data from seawater, hydrothermal fluids, silicates, carbonates, rivers and plants (after Fantle and Tipper, 2014). Values are referenced against BSE.

2011). The calcium isotopic fractionation associated with gypsum precipitation is close to equilibrium and unity for some natural systems over long time scales (Fantle and DePaolo, 2007). The fractionation factor close to chemical equilibrium over short experimental time scales is in the range of ~0.9995 (Harouaka et al., 2014), a value that is in agreement with predictions based on surface reaction kinetic model of calcite precipitation (e.g. DePaolo, 2011). Thus, during the evaporation of a fluid such as seawater, calcium isotopes should follow a Rayleigh fractionation path, where the light isotope is preferentially incorporated into precipitated calcium minerals and the heavy isotope is relegated to the concentrating brine (e.g. Hensley, 2006).

The sizes of the main surficial calcium reservoirs and their calcium isotope composition are given in Fig. 4.9, displaying a total range of $\delta^{44/40}$Ca values of ~4‰ (Fantle and Tipper, 2014). Calcium in the modern ocean is isotopically homogenous (0.92 ±0.20‰ 2σ), owing to its long residence time of 1 Ma (Fantle and Tipper, 2014). Calcium inputs to the ocean system are mainly from riverine and hydrothermal sources. Because of mass-dependent fractionation during terrestrial calcium cycling, interpreting the proportion of riverine calcium derived from carbonate, silicate, and evaporite lithologies is more complex than interpretations of radiogenic isotopes (e.g. ^{87}Sr/^{86}Sr), where all process-related mass-dependent fractionation is removed by normalisation during data reduction (Tipper et al., 2010, 2008; Fantle and Tipper, 2014) (Fig. 4.8). While there are no coherent spatial trends in riverine $\delta^{44/40}$Ca, this can be beneficial to elucidate marine-freshwater mixing profiles, as riverine inputs to a local system will always drive calcium isotopes towards lower values.

The only quantitatively significant calcium output to the ocean system is $CaCO_3$ precipitation and burial (Fantle and Tipper, 2014; Fig. 4.8). $CaCO_3$ minerals are fractionated from seawater, where ^{40}Ca is preferentially taken up into the solid, leaving seawater enriched in ^{44}Ca. At steady state, the average $\delta^{44/40}Ca$ composition of the $CaCO_3$ output flux must equal the $\delta^{44/40}Ca$ value of the input flux (~-0.1‰), which is thought to be stable over geologic timescales (Tipper et al., 2010). Unlike other trace isotopic systems (e.g. $^{87}Sr/^{86}Sr$), calcium species are major constituents of carbonates and gypsum, and thus are not subject to the same concerns regarding diagenesis and isotopic resetting (Husson et al., 2015).

Methodology: Calcium isotope ($^{44}Ca/^{40}Ca$) analysis was conducted using a Thermo Scientific Triton Plus MC-TIMS, closely following the method of Bradbury and Turchyn (2018). Sample aliquots containing 6 μm of calcium were combined with a ^{42}Ca-^{48}Ca double–spike at a ratio of 10:1 (sample-to-spike) in acid-cleaned Teflon vials. The 48:42 ratio of the double–spike is 1:1, similar to the optimum ratio of 3:2 for a ^{42}Ca-^{48}Ca double-spike (Rudge et al., 2009). Dissolved gypsum and carbonate samples were dried down, refluxed in ultra-pure nitric acid to ensure crystallisation in a nitric form, and then combined with the double spike. The samples were then dried and re-dissolved in 0.5% nitric acid and calcium was separated using a Dionex ICS-5000+ IC system coupled with a Dionex AS-AP fraction collector. The samples were run through a high-capacity carboxylate-functionalised column (Dionex CS-16) using 30 mM methyl-sulfonic acid (MSA) at a flow rate of 1 ml min^{-1}. The conductivity of the samples is continuously measured during the separation, and a minimum peak slope of 0.003 μS/s determines the sample collection during a set time window (Bradbury and Turchyn, 2018). The procedural blank on the Dionex as determined independently by Inductively Coupled Plasma Optical Emission Spectroscopy (ICP-OES) is 96 ng of calcium, when 7 ml of eluent was collected from the Dionex. During the collection of 4.4 μg of calcium using the Dionex, this represents ~2% of the collected calcium.

The collected calcium was subsequently dried down before being re-eluted in 1 μl of 2 M nitric acid and 4 μg of calcium was loaded on an outgassed 0.7 mm Re filament with 0.5 μl of 10% trace metal purity phosphoric acid as an activator. A current of ~0.8 A was continuously applied during the loading. The samples are run using a double filament method, with the ionisation filament being heated to 1400˚C (as measured on a pyrometer), and the evaporation filament is heated manually until a stable signal between 5 V and 10 V of ^{40}Ca on a 1011 Ω resistor is reached. The method consists of a dynamic collection routine (40-44 and 42-48) with an integration time of 8.389 s. 10 blocks of 20 cycles are collected, with peak centring and baseline being run at the start of the run, and lens focusing occurring

every 2nd block. Total run-time not including heating is 1.5 h. The average external 2σ standard deviation over 9 months on the standard NIST915B was 0.10‰ (mean = -0.28, n = 82).

4.3.6 Barium Isotopes

Naturally occurring barium is a mix of six stable isotopes, ^{132}Ba (0.10%), ^{134}Ba (2.42%), ^{135}Ba (6.59%), ^{136}Ba (7.85%), ^{137}Ba (11.23%), ^{138}Ba (71.70%) and one long-lived radioactive primordial isotope, ^{130}Ba (0.11%), was recently identified as being unstable by geochemical means. Barium has been used as a water-mass tracer of riverine input to the coastal ocean by directly measuring seawater concentrations (Guay and Falkner, 1997) or Ba/Ca ratios in corals (McCulloch et al., 2003) and foraminifera (Lea and Boyle, 1989), but barium isotopes have never been applied to constrain endmember-mixing systems. Ba-isotope data of samples are reported in the δ-notation ($\delta^{138/134}$Ba) using parts per thousand (‰) units relative to the Ba standard NIST3104a.

Previous studies have reported Ba isotopic compositions variously as $\delta^{137/134}$Ba normalised to the Fluka $Ba(NO_3)_2$ standard (e.g. Cao et al., 2016) or $\delta^{138/134}$Ba as normalised to NIST3104a (e.g. Horner et al., 2015). Horner et al. (2015) and Pretet et al. (2015) have both demonstrated that the differences between the Fluka and NIST Ba standards in their Ba isotopic compositions are within the analytical uncertainty. Therefore, one can be simply converted to the other directly by multiplying by ~1.33 (Hsieh and Henderson, 2017).

Compiled global upper-ocean barium data show relatively constant concentrations (35-45 nM) in near-surface waters, with the exception of areas near river inputs or strong upwelling (Hsieh and Henderson, 2017). The relatively uniform barium concentrations in the upper ocean indicate that barium removal is slow relative to supply and mixing, implying that near-surface Ba isotope values are controlled by basin-scale balances rather than by regional or short-term processes (Hsieh and Henderson, 2017). Measured seawater $\delta^{138/134}$Ba values vary from 0.24‰ to 0.65‰ (Hsieh and Henderson, 2017; Bridgestock et al., 2018).

Riverine input of barium to the surface ocean is the major external source, with potential to influence surface-water compositions near the input source, and to control the global barium isotope composition of the oceans on long timescales (Hsieh and Henderson, 2017). Cao et al. (2016) measured barium in eight rivers, recording low $\delta^{138/134}$Ba values (relative to typical seawater) between -0.1‰ and 0.4‰. Importantly, barium concentrations in rivers range from 100 nM to 500 nM (Cao et al. 2016), which is higher than seawater (30 nM to 170 nM). The combination of distinct marine and non-marine isotopic signatures and higher barium concentrations in riverine waters suggest that barium isotopes could potentially provide a powerful tracer for riverine inputs in marginal oceanic settings.

Methodology: Barium isotope ($^{138}Ba/^{134}Ba$) analysis was conducted using a Thermo Scientific Triton Plus MC-TIMS at the University of Oxford by Luke Bridgestock. Between 0.1 g and 0.4 g of powdered gypsum was leached in deionised water (~4 ml water, per 1 g of gypsum) over a period of 24 h with regular treatments in an ultrasonic bath. The supernatant was separated from the residual solid material and evaporated to dryness, before re-dissolving in 10 ml to 15 ml of 7.5 M HNO_3. Samples contained between 25 ng and 1283 ng of Ba. Samples were equilibrated with appropriate quantities of a Ba double spike solution (Hsieh and Henderson, 2017) prior to purification by a 2 stage cation exchange chromatography procedure (adapted from Bridgestock et al., 2018), utilising 2 ml of AG50-X8 resin (200 μm to 400 μm mesh size) (Table 4.1).

Spiked sample solutions were evaporated to dryness and re-dissolved in 5 ml to 15 ml of 3 M HCl, depending on the quantity of solid residue. To maximise the separation efficiency of Ba from Ca and Sr, sample solutions were split into two aliquots (2.5 ml to 7.5 ml) that were processed through the cation exchange chromatography procedure separately (Table 4.1; stages 1A and 1B). The volume of 3 M HCl used to elute the matrix was adjusted based on the volume sample solution loaded onto the column to give a total volume of 18 ml. The Ba elutions from stages 1A and 1B were then recombined and processed through the chromatography procedure again (Table 4.1; stage 2). Organics leached from the cation exchange resin were oxidised by the sequential addition and evaporation of 60 μl 15 M HNO_3 and 9.8 M H_2O_2. The procedural blank was assessed to be <0.48 ng of Ba (n = 2), representing <1.95% of the sample Ba processed though the procedure.

Ba isotope measurements were made using TIMS featuring a double Re filament assembly. The purified Ba was loaded onto the evaporation filament in 2 M HCl without an activator gel. Ba ionisation was achieved by applying currents of 2000 mA to 2500 mA to the ionisation filament and 50 mA to 300 mA to the evaporation filament. Ion beam intensities of between 4 V to 12 V were achieved for ^{138}Ba. Ba isotope ratios were measured following the protocol described by Hsieh and Henderson (2017).

Isotopic analyses of the Ba standard (NIST3104a) were conducted every measurement session, alongside analyses of the samples. The long-term reproducibility of $\delta^{138/134}Ba$ values determined for NIST3104a was between ±0.02‰ and ±0.03‰ (2σ) over a period of 3 months. This level of agreement (±0.03‰) is taken to represent the analytical uncertainty of the sample analyses (Bridgestock et al., 2018). A higher level of uncertainty (±0.05‰) is assigned for the samples 'BdI C15 5 cm' and 'EM4 Dome 30 cm' due to the lower ion beam intensities (~4 V for ^{138}Ba) achieved during TIMS analyses. A single measurement of the barite standard NBS-127 yielded $\delta^{138/134}Ba$ = -0.30 ± 0.03‰, in agreement with the values published by Horner et al. (2017) ($\delta^{138/134}Ba$ = -0.27 ± 0.02 ‰; 2σ, n = 4).

Procedure	Stages 1A and 1B	Stage 2
1. Clean resin	20 ml H_2O & 20 ml 6 M HCl	20 ml H_2O & 20 ml 6 M HCl
2. Condition resin	20 ml 3 M HCl	20 ml 3 M HCl
3. Load sample	2.5-7.5 ml 3 M HCl	1 ml 3 M HCl
4. Elute matrix	11.5-15.5 ml 3 M HCl	18 ml 3 M HCl
5. Elute Ba	10 ml 4 M HNO_3	10 ml 4 M HNO_3

Table 4.1. Cation exchange chromatography procedure employed for purification of Ba from gypsum samples, conducted using AG50-X8 resin (200-400 mesh) and Teflon shrink fit columns with a resin bed volume of 2 ml and aspect ratio (diameter: length) of 0.05.

4.3.7 Trace element chemistry

Major and trace element concentrations of gypsum and carbonate samples were determined by ICP-OES after dilution in 0.1 M HNO_3 to a constant calcium concentration of between 10 ppm and 50 ppm. Samples were run on a Varian Vista Axial ICP-OES using the 315.887 nm Ca emission line. In-house calibration standards were prepared to closely match the concentration matrix of the media solutions.

Trace element chemistry was also determined using a Thermo Element XR, a single collector sector field high-resolution inductively-coupled plasma mass spectrometry (HR-ICP-MS), using the process described by Misra et al. (2014). An aliquot of each sample solution was taken and diluted with sufficient 0.1 M HNO_3 and 0.5% HF matrix such that the calcium concentration was 10 ppm and the total volume of the resultant solution was 300 μl.

4.3.8 Carbonate sample preparation

Carbonate samples were prepared for isotope analysis by treating the samples with methanol, ammonia and water washes, each performed in triplicate. Unlike the leaching process for gypsum, the acid wash was omitted for carbonate samples to prevent the dissolution of calcite, which could affect the dolomite-calcite ratio of the sample and potentially cause isotopic fractionation. After leaching, the samples still possessed a small percentage of contaminants (e.g. clays). To isolate the carbonate phase and prevent the samples from being excessively contaminated during dissolution, the solid sample was dried, weighed and placed in a volume of 0.1 M HCl containing 110% of the acid required for complete dissolution of the carbonate, calculated to avoid elemental variation generated by incomplete dissolution. Samples that were not treated via this process displayed significant clay contamination and isotope values varied by more than 2σ in some cases.

4.3.9 X-ray diffraction (XRD) of carbonates

XRD analysis was conducted on carbonates primarily to estimate the relative proportion of calcite to dolomite in the sample. Samples were ground to <5 μm particles, slurry mounted onto glass slides with acetone, and analysed with a D8 Bruker diffractometer equipped with primary Gobbel mirrors for parallel Cu Ka X-rays and a Vantec position sensitive linear detector. Collection conditions were: 10° to 70° in 2θ, 0.02 step size, 450 s/step, divergence slit 0.2 mm. Rietveld refinements were performed with software Topas 4.0 (Cohelo, 2007). Crystal structures of all phases were retrieved from the inorganic crystal structure database (ICSD) (Allmann and Hinek, 2007).

Rietveld quantitative analysis is known to be unreliable for minor phases (<5 wt %). The accuracy is considered to be ±1-2% relative for major phases. As the estimated standard deviations from the Rietveld calculation are related to the mathematical fit of the model, they have no bearing on the accuracy or quantification itself (Madsen and Scarlett, 2008).

4.3.10 Total inorganic carbon, $\delta^{18}O_{carb}$ and $\delta^{13}C$ of bulk carbonates

Carbonate samples were digested in 50% H_3PO_4 for 20 h at 70°C and total inorganic carbon was measured using an AutoMateFX autosampler coupled to a UIC (Coulometrics) 5011 CO_2 coulometer (Engleman et al., 1985). Analytical precision was estimated by analysis of reagent-grade $CaCO_3$ (100%) and $MgCa(CO_3)_2$ (100%) and yielded a mean and 1σstandard deviation of 99.5 ±0.4% and 94.6 ±0.8% for calcite and dolomite, respectively. The dolomite is likely underestimated because of incomplete reaction even after 20 h. Wt% calcite and dolomite of samples were calculated using the dolomite/calcite ratio obtained by XRD multiplied by the total inorganic carbon measured by coulometric titration. Results are expressed as wt% $CaCO_3$ and wt% $MgCa(CO_3)_2$ assuming typical stoichiometry.

For stable isotope analysis, bulk sediment samples were ground to a fine powder, flushed with CP grade helium then acidified with 104% H_3PO_4 and left to react for 1 h at 70°C. Stable carbon and oxygen isotopes of carbonate were measured using a ThermoScientific GasBench II, equipped with a CTC autosampler coupled to a MAT253 mass spectrometer (Spötl and Vennemann, 2003). Analytical precision was estimated at ±0.08‰ for $\delta^{13}C$ and ±0.1‰ for $\delta^{18}O_{carb}$ by repeated analysis of the Carrara Marble standard. Results are reported relative to the VPDB.

4.3.11 Scanning electron microscopy (SEM)

SEM analyses of carbonate samples were performed with a Zeiss Supra 50 VP equipped with an energy dispersive X-ray detector for element analysis (EDX). SEM images and EDX analysis were obtained with a secondary electron detector, a working distance of 9 mm to 10 mm, and an accelerating voltage of 15 kV. In order to reduce the possibility of misinterpreting recent microbial contamination with fossilised biological structure, only the surface of freshly broken samples is investigated. Prior to analysis, the samples were coated with 10 nm of platinum. SEM analysis was carried out by T.R.R. Bontognali at ETH, Zurich.

4.4 Summary

Trace elements, isotopes, and salinity measurements deduced from fluid inclusions provide a useful means to determine the origin of gypsum precipitated during the MSC. Most information on MSC brine chemistry to date has been inferred from the analysis of gypsum using traditional tracers such as strontium concentrations, $^{87}Sr/^{86}Sr$, $\delta^{34}S$ and $\delta^{18}O_{SO_4}$. Taking into account secular variation of oceanic $^{87}Sr/^{86}Sr$ and $\delta^{34}S$ during the Phanerozoic (McArthur et al., 2001), $^{87}Sr/^{86}Sr$ and $\delta^{34}S$ of gypsum that are close to expected oceanic values supports a marine origin (e.g. Cendón et al., 2004). This criterion is particularly useful where the isotopic composition of weathered continental material is markedly different from the expected oceanic value (Rossi et al., 2015). This is the case in many Tertiary circum-Mediterranean basins, for example, where continental sulfate is mainly recycled from Triassic marine evaporites, thus being markedly different in $^{87}Sr/^{86}Sr$ and $\delta^{34}S$ from marine Tertiary sulfate (e.g. Rossi et al., 2015). $^{87}Sr/^{86}Sr$, $\delta^{34}S$ and $\delta^{18}O_{SO_4}$ isotopes of gypsum are, however, insensitive to minor non-marine contributions due to the large concentration differences between marine and continental fluids, and consequently near-marine $^{87}Sr/^{86}Sr$, $\delta^{34}S$ and $\delta^{18}O_{SO_4}$ isotopes do not necessarily indicate pure marine depositional environments.

Coupling traditional tracers to novel tracers such as $\delta^{44/40}Ca$, $\delta^{138/134}Ba$ and triple oxygen and hydrogen isotopes of GHW can provide additional constraints on the relative continental contribution, redox processes and reservoir effects influencing the deposition of gypsum during the MSC. Increasing the number of isotopic tracers employed with differing endmember mixing sensitivities delimits the number of endmember sources that can be partitioned. By directly comparing trace elements, isotopes, and salinities deduced from fluid inclusions in the same sample, it is possible to test to see if all tracers agree as to the origin of the sample, or whether certain systems have undergone post-depositional resetting.

Importantly, this method provides a significant advance over previous attempts to constrain the hydrological budget of the MSC as continental contributions, redox processes and reservoir effects can be individually examined in each sample, and subsequently deconvolved on both a local and regional scale.

Chapter 5

Coupled measurements of δ^{18}O and δD of hydration water and salinity of fluid inclusions in gypsum from the Messinian Yesares Member, Sorbas Basin (SE Spain)

Adapted from the publication: ***Nicholas P. Evans**, Alexandra V. Turchyn, Fernando Gázquez, Tomaso RR Bontognali, Hazel J. Chapman, and David A. Hodell. (2015). Earth and Planetary Science Letters, 430, 499-510.*

One cycle (cycle 10) of gypsum–marl deposition from the Messinian Yesares Member in Sorbas Basin, Spain was studied with the objective of reconstructing the changing environment of deposition and its relation to astronomically-forced climate change. The δ^{18}O and δD of gypsum hydration water ($CaSO_4 \cdot 2H_2O$) and salinity of fluid inclusions were measured in the same samples to test if they record the composition of the mother fluid from which gypsum was precipitated. Water isotopes are highly correlated with fluid inclusion salinity suggesting the hydration water has not exchanged after formation. The relatively low water isotope values and fluid inclusion salinities indicate a significant influence of meteoric water, whereas δ^{34}S, $\delta^{18}O_{SO_4}$ and ^{87}Sr/^{86}Sr support a dominantly marine origin for the gypsum deposits. The discrepancy between water and elemental isotope signatures can be reconciled if meteoric water dissolved previously deposited marine sulfates supplying calcium and sulfate ions to the basin which maintained gypsum saturation. This recycling

process accounts for the marine δ^{34}S, $\delta^{18}O_{SO_4}$ and $^{87}Sr/^{86}Sr$ signatures, whereas the low δ^{18}O and δD values of gypsum hydration water and fluid inclusion salinities reflect the influence of freshwater.

The cyclic deposition of gypsum and marl in the Yesares Member has previously been interpreted to reflect changing climate related to Earth's precession cycle. The δ^{18}O, δD and salinity of the parent brine increased from low values at the base of the cycle to a maximum in the massive gypsum palisade, and decreased again to lower values in the supercones at the top of the cycle. This pattern, together with changes in mineralogy (calcite–dolomite–gypsum), is consistent with a precession-driven change in climate with wettest conditions (summer insolation maxima) associated with the base of the calcium carbonate marls and driest conditions (summer insolation minima) during formation of the gypsum palisade.

5.1 Introduction

During the Messinian salinity crisis (MSC), the Mediterranean Sea was transformed into a giant brine pool where more than one million cubic kilometres of salt was deposited in ~640 ka (Krijgsman et al., 1999; Rouchy and Caruso, 2006). Most of the deposits in the deep basins have remained unsampled thus studies have relied upon onshore Messinian deposits in marginal basins to infer the stratigraphic history of the MSC (Roveri et al., 2014a) (Fig. 5.1).

In marginal basins of the circum-Mediterranean, the lowermost gypsum bed marking the onset of the MSC is dated at ~5.97 Ma (Krijgsman et al., 1999; Manzi et al., 2013). The overlying unit known as the Primary Lower Gypsum (PLG) comprises up to 16 beds of massive gypsum interbedded with finely laminated marls or shale (Roveri et al., 2009; Lugli et al., 2010). The deposition of these evaporite-marl cycles is reported to be controlled by the variations of Earth's orbital parameters, mainly the ~21 kyr precession cycle (Krijgsman et al., 2001, 1999; Manzi et al., 2009; Lugli et al., 2010). According to this interpretation, evaporite deposition occurred at the precession maxima (i.e. minimum summer insolation when summer solstice and aphelion coincided) when evaporation exceeded precipitation during periods of dry climate and marl deposition occurred at precession minima (maximum summer insolation when summer solstice and perihelion coincided) when rainfall increased (Krijgsman et al., 2001, 1999).

Whereas orbital forcing may explain the observed large-scale lithological cyclicity, the composition and salinity of the brines from which large volumes of sulfate minerals formed are still debated. Most information on brine chemistry has been inferred using strontium ($^{87}Sr/^{86}Sr$), sulfur (δ^{34}S), and oxygen isotopes in sulfate ($\delta^{18}O_{SO_4}$) (e.g. Longinelli, 1979;

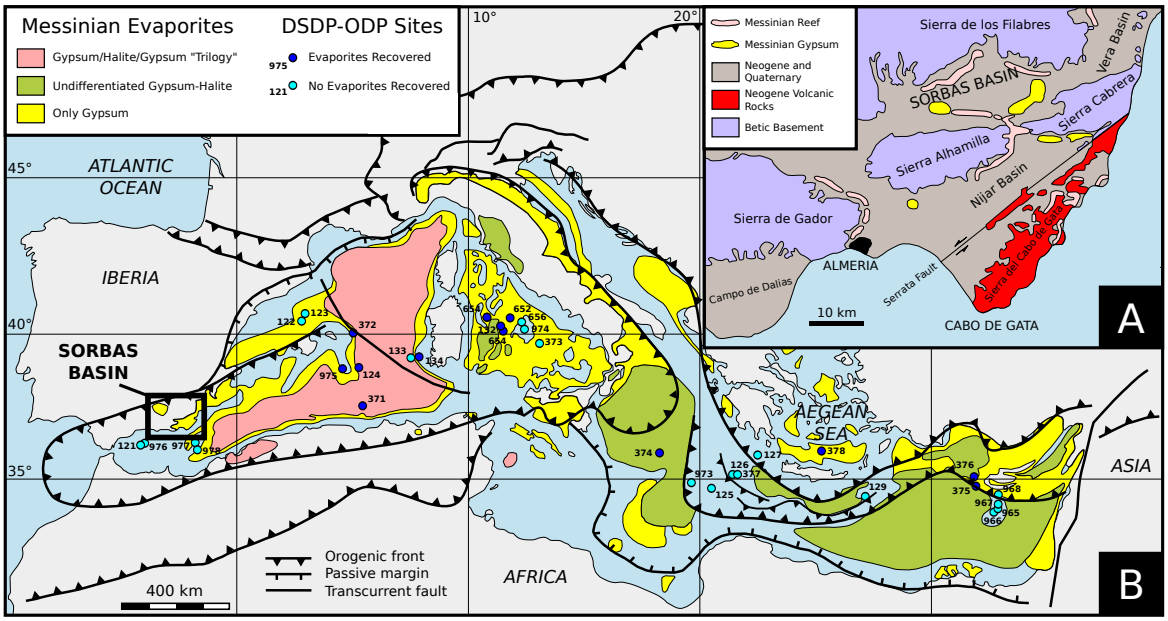

Fig. 5.1. (**A**) Location map of the Sorbas Basin and surrounding areas modified after Krijgsman et al. (2001). Indicated are the distributions of the outcropping marginal Messinian reefs (Cantera Member) and gypsum deposits (Yesares Member). (**B**) Map of the Messinian evaporites in the Mediterranean modified after Rouchy and Caruso (2006) and Roveri et al. (2014a). Also shown is the location of the DSDP-ODP boreholes in which Messinian evaporites were recovered.

Müller and Mueller, 1991; Lu and Meyers, 2003; Lugli et al., 2010). Here the traditional isotope tracers are combined with the measurement of GHW and fluid inclusions to reconstruct the chemical composition of the parent brine solution.

The measurement of oxygen and hydrogen isotopes in GHW is a potentially powerful tool for studying the nature of the parent water from which gypsum was precipitated (Sofer, 1978; Longinelli, 1979; Hodell et al., 2012). An assumption of the method is that once formed, gypsum hydration water retains its isotope composition and does not undergo postdepositional isotopic exchange (Sofer, 1978). To test this assumption, we compare the isotope composition of the hydration with the salinity of fluid inclusions in gypsum estimated by microthermometry (Goldstein and Reynolds, 1994; Attia et al., 1995; Natalicchio et al., 2014). We expect the $\delta^{18}O$ and δD of hydration water to be well correlated with the salinity of primary fluid inclusions if it has retained the isotopic signature of the mother water.

In addition to $^{87}Sr/^{86}Sr$, $\delta^{34}S$, and $\delta^{18}O_{SO_4}$ isotope analysis of gypsum, oxygen and hydrogen isotopes in gypsum hydration water and salinity of fluid inclusions were measured in gypsum from the sixth cycle of gypsum deposition from the Río de Aguas section, Sorbas Basin. We also measured modern gypsum deposits from the Cabo de Gata Salina, Almería,

Spain, to provide a comparison to Messinian gypsum. We demonstrate that the hydration water in Messinian gypsum of Sorbas Basin has retained its original isotopic composition and can be used to infer paleoenvironmental conditions of gypsum deposition. We also show a well-defined cyclicity in the mineralogy and δ^{18}O and δD of gypsum hydration water and fluid inclusion salinity over a single gypsum cycle that is consistent with astronomical forcing of Messinian climate.

5.2 Geological setting

The Neogene Sorbas Basin in SE Spain is an elongated intra-montane depression surrounded by basement highs of the Betic Internal Zone (Fig. 5.1). The deposition of evaporites begins with gypsum/marl cycles of the basal Yesares Member. These evaporites consist of gypsum deposits that are interbedded with laminated marls. The Yesares Member consists of a total of 15 gypsum cycles and is best exposed in the Río de Aguas section in the Sorbas Basin (Krijgsman et al., 2001; Roveri et al., 2009). The facies description for cycle 10 is given in Section 4.2.1.

5.3 Methods

5.3.1 Field locations and sample collection methods

We sampled gypsum cycle 10 that is exposed at the base of the Río de Aguas section (37°05'23.2" N 002°06'54.2" W) in Sorbas Basin, SE Spain (Dronkert, 1985; Krijgsman et al., 2001). Samples were collected in April 2013 and March 2014. The zero depth reference was taken as the horizontal base of the palisade gypsum layer; therefore, gypsum crystals sampled in nucleation cones have a negative depth reference. Marl samples were obtained from the base of the section and from marls juxtaposed to the supercones.

5.3.2 Geochemical methodology

All geochemical methodology is given in Section 4.3.

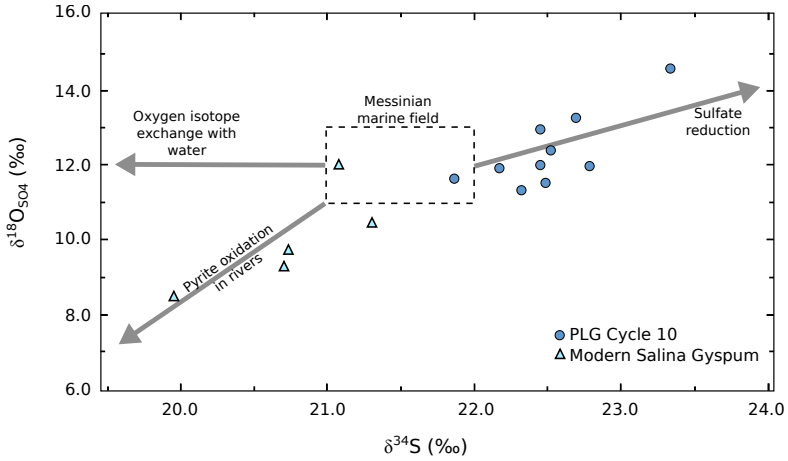

Fig. 5.2. δ^{34}S versus δ^{18}O of sulfate of the Yesares Gypsum. Open box defines Messinian seawater range (Paytan, 1998; Turchyn and Schrag, 2004).

5.4 Results

5.4.1 δ^{34}S and δ^{18}O of sulphate

Ten samples were analyzed for sulfur and oxygen isotopes of sulfate (Appendix D; Table D.6). These data are shown in Fig. 5.2 relative to the expected range of gypsum precipitated from Miocene seawater. δ^{34}S varies between 21.9 and 23.3‰ VCDT and $\delta^{18}O_{SO_4}$ between 11.3 and 14.5‰ VSMOW. There are negligible differences in the isotope composition among the nucleation cone, palisade, banded selenite, and supercone samples and δ^{34}S and $\delta^{18}O_{SO_4}$ display no systematic changes with depth in the section.

5.4.2 Sr isotopes

Eleven samples from cycle 10 were measured for Sr isotopic analysis (Appendix D; Table D.4). The range of $^{87}Sr/^{86}Sr$ is small (29 ppm), varying between 0.708941 and 0.708970. These values fall slightly below the range of strontium isotope seawater expected for the Messinian (McArthur et al., 2001) (Fig. 5.3).

5.4.3 XRD, wt% calcite and wt% dolomite of bulk carbonates

Thirty one marl samples were analysed by XRD (Appendix D; Table D.8). The results are semi-quantitative and indicative of the relative abundances of common mineralogical components only. In addition to clay, the major phases are gypsum, calcite, and dolomite and each occurs in varying proportions in cycle 10. The marls at the base of the section

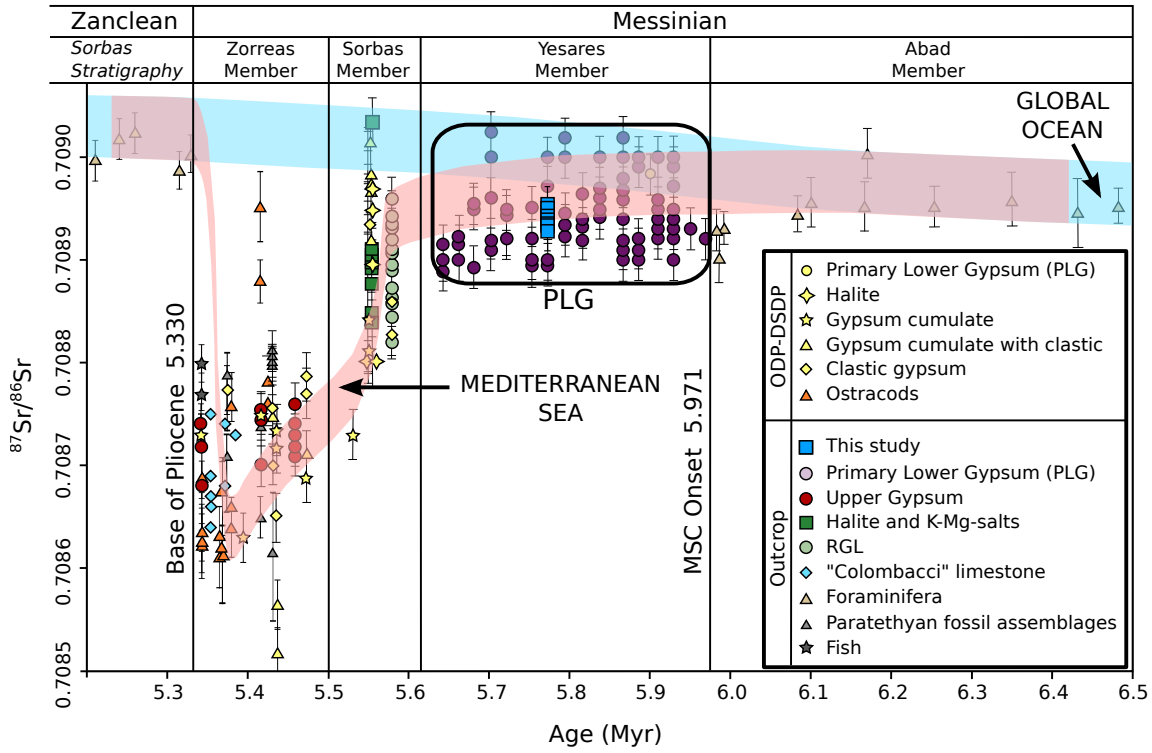

Fig. 5.3. Sr isotope curve during the Messinian in the Mediterranean Sea and Global Ocean. The progressive change in the isotopic composition of Mediterranean waters during the MSC occurred because of the restricted exchange with the global ocean due to closure of the gateways as well as a contribution of freshwater with low $^{87}Sr/^{86}Sr$ from rivers (e.g. Nile and Rhone) or from the Paratethys (Roveri et al., 2014a). $^{87}Sr/^{86}Sr$ data from this study are plotted at 5.795 Ma in accordance with the cyclostratigraphic dating of cycle 10. Sorbas Basin stratigraphy after Krijgsman et al. (2001). Figure modified after Roveri et al. (2014b).

contain both calcite and dolomite. The ratio of calcite to dolomite in the lower marls decreases up-section such that dolomite becomes more dominant toward the gypsum–marl contact (Fig. 5.4). Fine-grained gypsum within the marl is abundant in the upper marl from 8 cm below the marl-gypsum contact. Marls juxtaposed to supercones are purely dolomitic and contain varying proportions of gypsum.

5.4.4 δ^{18}O and δ^{13}C of bulk carbonates

The oxygen and carbon isotope composition of thirty-seven carbonate samples vary widely from -3.7‰ to 3.5‰ for $\delta^{18}O_{carb}$ and from -4.9‰ to 1.5‰ for $\delta^{13}C$ (Appendix D; Table D.8; Fig. 5.5). The carbon and oxygen isotope composition of the carbonates are within the range of other Messinian carbonates associated with evaporites in the Mediterranean

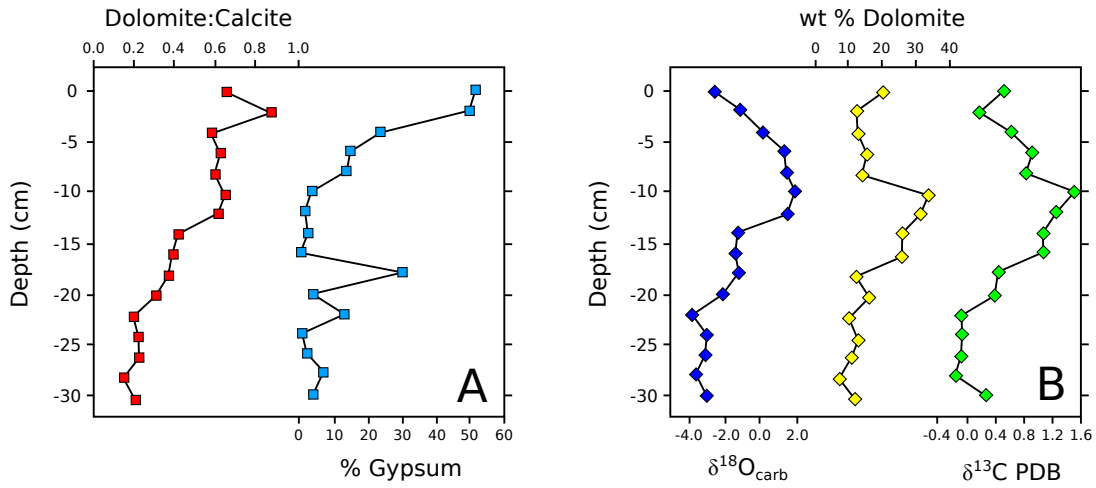

Fig. 5.4. (**A**) The ratio of dolomite to calcite of the marls at the base of the section. % gypsum is obtained from XRD data; (**B**) $\delta^{18}O_{carb}$, $\delta^{13}C$ and % dolomite in the marls at the base of the section. 0 cm is the gypsum–marl contact.

(Longinelli, 1979). Marls at the base of cycle 10 ranged from −3.7‰ to 1.9‰ for $\delta^{18}O_{carb}$ and between −0.1‰ and 1.5‰ for $\delta^{13}C$. In contrast, marls juxtaposed with the super-cones show relatively high $\delta^{18}O_{carb}$ ($2.8 < \delta^{18}O_{carb} < 3.5$‰) and low $\delta^{13}C$ values ($-4.9 < \delta^{13}C < -3.8$‰).

5.4.5 Gypsum hydration waters

Twenty-six samples representing massive, banded and branching selenite were analysed for their GHW (Appendix D; Table D.1). The measured $\delta^{17}O$, $\delta^{18}O$ and δD values of GHW gypsum from cycle 10 range from 1.38‰ to 3.38‰, 2.02‰ to 6.32‰, and -37.71‰ to -6.23‰, respectively. Eleven modern gypsum samples were also analysed from the Salina at Cabo de Gata, Almería, Spain. The measured $\delta^{17}O$, $\delta^{18}O$ and δD values of GHW range from 5.50‰ to 6.27‰, 12.05‰ to 10.25‰, and 9.57‰ to 19.71‰, respectively.

The oxygen and hydrogen isotope composition of the parent water in which the gypsum formed is calculated by correcting for gypsum-water fractionation factors (Chapter 2). Fractionation factors were assumed to be 1.0035 and 0.981 for oxygen and hydrogen isotopes, respectively. The fractionation factors were selected based on water temperature (~15˚C to 20°C; Section 5.5.8) and salinity (<150 g l^{-1}; Section 5.5.2) estimates at the time of formation. Following correction, the $\delta^{17}O$ of the gypsum mother water for gypsum from cycle 10 is estimated to have ranged between -0.47‰ to 1.52‰, the $\delta^{18}O$ from -1.47‰ to 2.81‰, and δD from -13.97‰ to 13.01‰. The calculated d-excess values of the mother

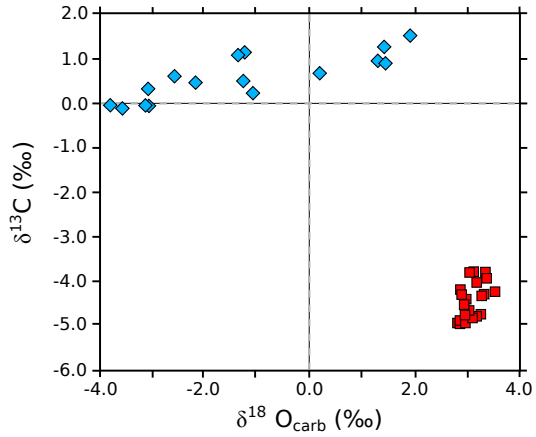

Fig. 5.5. δ^{18}O and δ^{13}C of carbonates from the marl intervals within the Yesares Formation. Diamonds are marls taken from the base of Cycle 10; squares are marls taken from beds juxtaposed to supercones.

water range from -11.2‰ to -2.2‰, whereas the ^{17}O-excess ranges from -37 per meg to -10 per meg. The d-excess and ^{17}O-excess values are negatively correlated with those of the δ^{18}O across the dataset. The calculated gypsum mother water δ^{17}O, δ^{18}O and δD of the modern Salina samples ranged from 3.68‰ to 4.45‰, 6.82 to 8.81‰, and 29.12‰ to 39.46‰, respectively. The calculated d-excess values of the mother water range from -29.7‰ to -23.0‰, and the ^{17}O-excess ranges from -82 per meg to -51 per meg (Fig. 5.6).

The δ^{18}O and δD of gypsum mother water show a systematic change through cycle 10 (Fig. 5.7). The most negative δ^{18}O and δD values are found at the base of the section in the nucleation cone, which represents the first gypsum to precipitate above the marl. δ^{18}O and δD increase up section into the gypsum palisade reaching maximum values of 2.8‰ and 13.0‰, respectively, at 56 cm. Above this peak, δ^{18}O and δD fall to average values of 0.6‰ and -1.0‰, respectively, in the banded selenite above 130 cm. Isotope values in the supercones are lower than those below with average values of 0.0 for δ^{18}O and -6.4‰ for δD. The top of the supercone has the lowest δ^{18}O and δD values of -0.7‰ and -11.5‰, respectively. Thus, the entire section displays a systematic change from low isotopic values at the base (nucleation cone), to maximum values in the middle (palisade gypsum), and a return to low isotopic values near the top (supercone).

5.4.6 Microthermometric analysis

Eleven samples from the Messinian gypsum of the Sorbas Basin and two samples from the modern Salina at Cabo de Gata, Almería, Spain, were selected for microthermometric analysis (Appendix D; Table D.6). Primary inclusions in Messinian gypsum froze at temperatures be-tween -40˚C and -60°C, with simultaneous shrinkage of the vapour bubble.

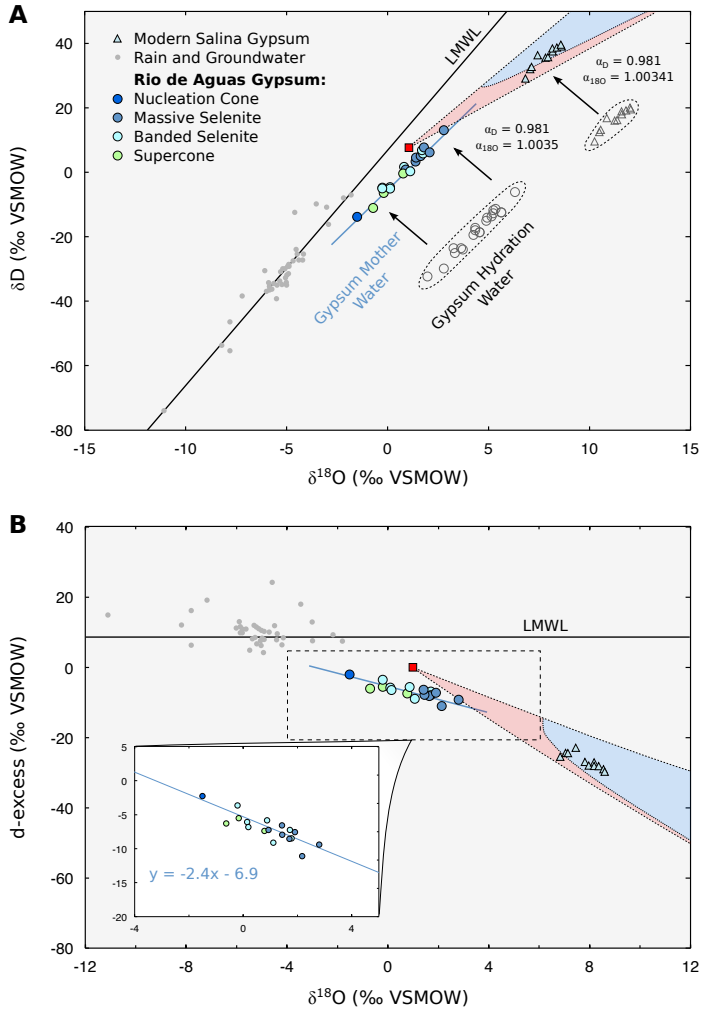

Fig. 5.6. Comparison of measured local meteoric water (grey circles) and predicted Messinian brine mother water values for the differing facies of the Yesares Gypsum after correction for fractionation factors (coloured diamonds) (Chapter 2). In (A) δ^{18}O vs δD and (B) δ^{18}O vs d-excess space, local meteoric water measurements define the local meteoric water line (LMWL). The blue line represents the evaporative line estimated by least-squares linear regression using mother-water data of Messinian gypsum (in panel A, δD = 6.3 · δ^{18}O – 5.4; R^2 = 0.97). Light blue triangles are modern gypsum data from the Cabo de Gata Salina. Red square is modern Mediterranean Seawater. The trajectories for the evaporation of Mediterranean seawater for high (90%; slope ~7) and low (40%; slope ~3) humidities are shown, defining a range of possible δ^{18}O and δD values (pink field). Gypsum precipitation takes place at 3 to 7 times concentrated seawater; gypsum saturation (blue field) is calculated using the Rayleigh Distillation equation, assuming initial δ^{18}O and δD values of ~1‰ and 8‰, respectively, 75% equilibrium between atmospheric vapour and fresh water, and gypsum saturation occurring at an evaporation ratio of 3.8× (evaporation ratio = weight of H_2O of original seawater divided by weight of H_2O in residual evaporated brine). Errors (1σ) are less than the width of the symbols.

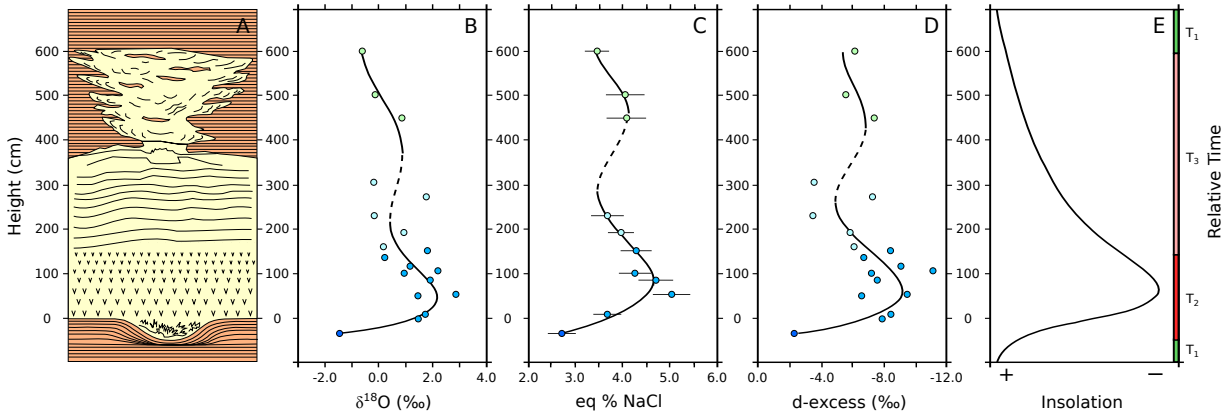

Fig. 5.7. (**A**) Schematic diagram of Cycle 10 scaled to height of the section, showing carbonate marls at the base and top, a nucleation cone at the base of the gypsum, gypsum palisade, banded selenite and supercone. Data points in B, C and D are plotted relative to the height from which the samples were taken. (**B**) δ^{18}O (VSMOW) of gypsum mother water vs. height in section; 1σ is the width of the symbol. (**C**) wt% NaCl eq vs height in section. Wt% NaCl calculated from the final melting temperatures of ice using the equation of Bodnar (1993). Error bars denote 1σ. (**D**) d-excess vs. height in section; note that the d-excess axis is reversed. 1σ is the width of the symbol. All trend lines are 5th Order Polynomial Regressions. (**E**) Hypothetical insolation curve, where T1 denotes the humid period during marl deposition, T2 denotes the period of gypsum palisade formation at the peak of the cycle, and T3 denotes the time period during banded selenite and supercone growth; T1+T2+T3 is equal to approximately 21 ka, although the relative duration of T1, T2 and T3 is unknown.

During heating, first melting was observed between -42˚C and -32°C, but this transition is easily missed.

The Tm_{ice} of 206 primary Messinian inclusions ranged between -0.2°C and -6.0°C. The average Tm_{ice} was -2.71°C. Using the revised equation and table for determining the freezing point depression of H_2O-NaCl solutions of Bodnar (1993), salinities estimates range from 0.35% to 9.21% (average 4.45 wt% NaCl equivalent). Tm_{ice} of modern gypsum from the Cabo de Gata Salina ranged between -6.5˚C and -10.1°C (average -8.0°C), corresponding to an average salinity of 11.7%.

The Tm_{ice} of fluid inclusions show a systematic change during cycle 10. When Tm_{ice} values are converted to wt% NaCl equivalent, the curve co-varies with the δ^{18}O and δD of gypsum hydration water data (Fig. 5.7). Nucleation cone samples at the base of the section display the highest melting temperatures (averaging a Tm_{ice} of -1.7°C) and lowest salinities. Moving up into the palisade gypsum, the lowest Tm_{ice} and greatest salinity values occur at 56 cm, averaging -3.6°C and 5.9 wt% NaCl equivalent, respectively. Above this maximum,

values increase throughout the banded selenite to average Tm_{ice} values of -2.5°C at 231 cm. Supercone Tm_{ice} values are collectively very similar to the banded selenite, averaging a Tm_{ice} of -2.6°C.

5.5 Discussion

An outstanding question regarding the depositional environment of Messinian gypsum in marginal basins of the Mediterranean is whether the gypsum was precipitated directly from seawater or was influenced by meteoric water (e.g. Longinelli, 1979; Müller and Mueller, 1991; Attia et al., 1995; Playà et al., 2000; Flecker et al., 2002; Lu and Meyers, 2003; Lugli et al., 2010; Natalicchio et al., 2014). Strontium and sulfur isotope results favour a dominantly marine origin whereas hydration water and fluid inclusion data support a significant contribution by meteoric water. Below, these seemingly contradictory interpretations are discussed and an explanation is proposed to reconcile the geochemical data.

5.5.1 Strontium, sulfur and oxygen isotopes of gypsum

Our measured $\delta^{34}S$ of gypsum of the Sorbas Basin ranges between 21.9‰ and 23.3‰ VCDT (Fig. 5.2), which agrees with those measured in other Messinian evaporite deposits (e.g. Longinelli, 1979; Lu et al., 2001; Lugli et al., 2007), and is similar to Miocene seawater as reconstructed through pelagic marine barite from the equatorial Pacific (~21‰). This suggests that the Mediterranean Sea in the Miocene was connected, and isotopically similar, to the global ocean. Similarly, the measured $\delta^{18}O_{SO_4}$ of Yesares gypsum (11.3‰ to 14.5‰) is similar to the $\delta^{18}O_{SO_4}$ of Miocene seawater sulfate, reconstructed from pelagic marine barite (~12‰; Turchyn and Schrag, 2004). The fact that near-seawater values are measured for sulfur and sulfate-oxygen isotopes in the gypsum of the Yesares Member suggest that deposition was dominantly in a marine environment (e.g. Müller and Mueller, 1991; Lu and Meyers, 2003).

It has been suggested that gypsum precipitates with a negligible sulfur isotope fractionation, but as much as a 3‰ offset for oxygen isotopes (Lloyd, 1968). However, this oxygen isotope fractionation factor remains poorly constrained, and the isotope composition of a multiply evaporated basin may evolve over time. If the sulfate from Miocene seawater trapped in the Mediterranean were quantitatively precipitated, then, by mass conservation, the $\delta^{34}S$ and $\delta^{18}O_{SO_4}$ of the bulk precipitated gypsum should reflect Miocene seawater. Subsequent solution-reprecipitation of the gypsum in water with a similar $\delta^{34}S$ or $\delta^{18}O_{SO_4}$ will not alter the $\delta^{34}S$ or $\delta^{18}O_{SO_4}$ of the gypsum significantly. Abiotic oxygen isotope

exchange between aqueous sulfate and water does not occur over geologically relevant timescales (Lloyd, 1968; Rennie and Turchyn, 2014).

The sulfur and sulfate-oxygen isotope composition of meteoric water that could have been supplied to the site of gypsum formation would largely reflect the isotope composition of sulfur-bearing minerals that are being locally weathered. Measurements of the δ^{34}S and $\delta^{18}O_{SO_4}$ in Spanish rivers today are heavily biased towards evaporite values (high δ^{34}S and $\delta^{18}O_{SO_4}$) owing to the ongoing weathering of the Messinian evaporites. However, underneath these evaporites exist sedimentary deposits containing shale beds that plausibly bear pyrite, and it is possible that oxidative pyrite weathering could have dominated the terrestrial sulfate–isotope signal during the MSC. Oxidative weathering of pyrite produces river sulfate that is enriched in the ^{32}S isotope and typically with a $\delta^{18}O_{SO_4}$ similar to the δ^{18}O of the water (e.g. ~-5‰) (Calmels et al., 2007). Thus, it is hypothesised that if a significant amount of sulfate used to make the Yesares gypsum was derived from terrestrial sources, then the δ^{34}S and $\delta^{18}O_{SO_4}$ of the gypsum would be significantly lower than the measured values.

^{87}Sr/^{86}Sr of a semi-enclosed marginal basin is similarly a function of the balance between ocean and riverine input, both of which are characterised by different strontium concentrations and ^{87}Sr/^{86}Sr. Because of the long residence time of strontium relative to the mixing time of the ocean, ^{87}Sr/^{86}Sr is homogeneous in the global ocean. The ^{87}Sr/^{86}Sr of Messinian seawater is well established with values varying between 0.70900 and 0.70903 during the MSC (McArthur et al., 2001). There is no fractionation of strontium isotopes during gypsum precipitation; thus, a direct comparison can be made between the ^{87}Sr/^{86}Sr of gypsum and the parent solution.

Measured ^{87}Sr/^{86}Sr of the gypsum samples in cycle 10 of the Río de Aguas section vary between 0.708941 and 0.708970. The values fall slightly below the range of the strontium isotope curve for seawater (McArthur et al., 2001), suggesting that continental waters with a lower ^{87}Sr/^{86}Sr than contemporaneous Miocene seawater may have modified the brine within the Sorbas Basin. The values are within the range given by Roveri et al. (2014b) for the ^{87}Sr/^{86}Sr isotopic composition of Mediterranean seawater values between 5.97 Ma and 5.60 Ma (Fig. 5.3), who interpret the near global ocean values as a dominantly marine formation environment. If the interpretation of Roveri et al. (2014b) is correct, the ^{87}Sr/^{86}Sr data, coupled with δ^{34}S and $\delta^{18}O_{SO_4}$ data, imply there was little contribution of meteoric water to the brine that formed the Yesares Gypsum.

5.5.2 Gypsum hydration water and microthermometry

The observed range of δ^{18}O and δD of gypsum mother water (-1.47‰ to 2.81‰; -13.97‰ to 13.01‰, respectively) is significantly lower than the expected range from gypsum formed solely from the evaporation of seawater. Assuming a starting point of seawater with modern δ^{18}O and δD values, Fig. 5.6A shows the possible trajectories of δ^{18}O and δD for evaporative concentration under conditions of high and low humidity. Modern gypsum measured from the Salina at Cabo de Gata falls in the region of predicted gypsum saturation for evaporated seawater. If the gypsum precipitated in the Sorbas Basin were solely of marine origin, we would expect the values to fall along a mixing line within this zone of gypsum saturation. Instead all δ^{18}O and δD values from cycle 10 fall well below the saturation point for gypsum on the evaporative line. This implies that the Yesares Gypsum was precipitated from a hybrid brine, consisting of a mixture of seawater and meteoric water.

An alternative explanation of the low δ^{18}O and δD of hydration water is that the values do not reflect the original brine but have undergone postdepositional isotopic exchange of the crystallisation water with meteoric water. The kinetics of the isotopic exchange of GHW is not well studied, but Sofer (1978) concluded GHW only retains its isotopic composition under dry conditions (e.g. Negev Desert) and exchanges isotopically under humid conditions. Sofer suggested the GHW method can only be applied to primary gypsum that has not undergone dehydration, exchange, or recrystallisation, and thus has retained its original water isotopic composition. To test if the isotope composition of GHW is reliable in the Sorbas Basin, GHW isotopic results were directly compared with microthermometric analysis of primary fluid inclusions from the same samples in cycle 10.

Primary fluid inclusions trap the parent brine and reflect the composition of the solution from which the gypsum precipitated (Attia et al., 1995). Microthermometric data show that no Messinian fluid inclusions have salinities high enough to be within the range of gypsum saturation if evaporated from seawater. Gypsum first precipitates during the evaporation of seawater at a wt% NaCl equivalent of ~11%, which should correspond to a Tm_{ice} of −7˚C to −8°C (Attia et al., 1995; Natalicchio et al., 2014). In comparison, the fluid inclusions from the modern Salina samples melted at −8.0°C corresponding to 11.7 wt% NaCl equivalent, and are above the point of gypsum saturation. In contrast, Messinian fluid inclusions from cycle 10 have average wt% NaCl equivalent ranging from 2.87% to 5.76% (averaging 4.5 wt% NaCl equivalent), indicating that the fluids from which gypsum precipitated were moderately saline to brackish (Attia et al., 1995; Natalicchio et al., 2014). Additionally, the average strontium contents of selenite from cycle 10 samples range from 506 ppm to 989 ppm, whereas the gypsum from the Cabo de Gata Salina also have an average strontium concentration of 1730 ppm. As the partition coefficient of strontium into gypsum is less

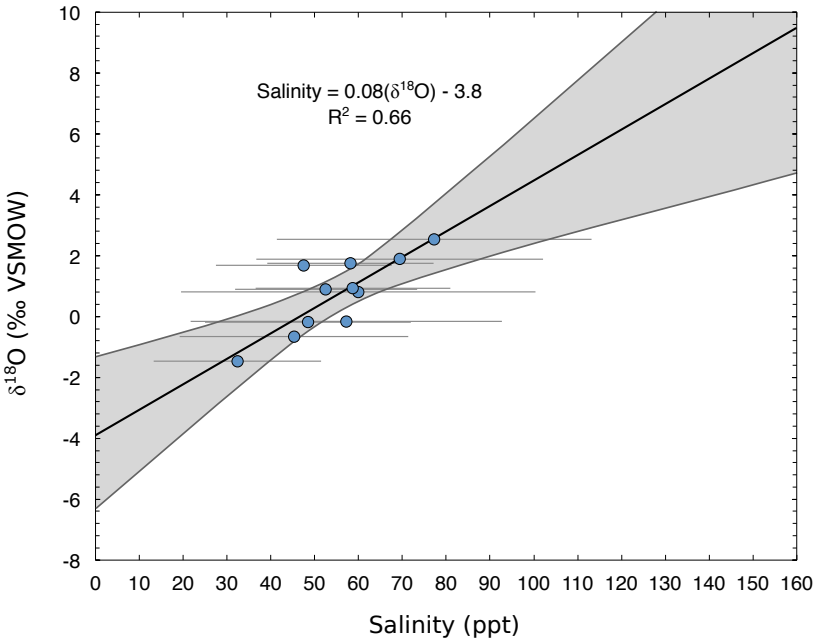

Fig. 5.8. Coupled measurements of δ^{18}O of hydration water and salinity of fluid inclusions in Messinian Gypsum. Salinities calculated from the final melting temperatures of ice using the equation of Goldstein and Reynolds (1994). The dark grey band denotes 95% confidence limits. The y intercept at zero salinity defines the freshwater δ^{18}O endmember. Error bars denote 1σ. 1σ in δ^{18}O space is the edge of the symbol.

than unity (Kushnir, 1980), the strontium concentration of gypsum precipitated directly from seawater after evaporative enrichment should correspond to ~1500 ppm to 4000 ppm (Rosell et al., 1998; Rossi et al., 2015).

Using the equation of Goldstein and Reynolds (1994), we converted wt% NaCl equivalent to salinity in parts per thousand (ppt) seawater. The salinity of primary Messinian fluid inclusions is correlated with δ^{18}O and δD of gypsum mother water, yielding an R^2 of 0.66 and 0.65, respectively (Fig. 5.8). The intercepts of the regression equations and salinity are -3.8 ±2 for δ^{18}O and -30.2 ±15 for δD. These values define the isotope composition of the freshwater endmember and are within error of the average isotope values of precipitation and groundwater data from the local region of Almería today (δ^{18}O = -4.3‰ and δD = -22.2‰; IAEA, 2005). These results provide strong evidence that both the fluid inclusion and gypsum hydration water are representative of the mother brines in which the gypsum formed and postdepositional isotopic exchange has not occurred. These results also imply that the mother fluid from which the gypsum was precipitated was influenced by meteoric water.

5.5.3 Decoupling of the source of ions and water during gypsum formation

An inconsistency exists between the marine origin of gypsum implied by sulfur and oxygen isotopes of sulfate and the significant meteoric influence inferred from the $\delta^{18}O$ and δD of gypsum hydration water and the salinities of fluid inclusions. The formation of the PLG is most commonly attributed to the evaporation from brines produced by continuous inflow of seawater from the Atlantic Ocean, providing the ion supply necessary for gypsum precipitation, coupled with episodes of reduced outflow under drier climate conditions (Krijgsman and Meijer, 2008; Topper and Meijer, 2013). A non-marine origin of Messinian gypsum in marginal basins raises questions concerning the marine signatures sulfur and oxygen isotopes in sulfate. An alternate mechanism is needed to explain the lower salinities inferred from fluid inclusion and isotopic results in the Sorbas PLG.

One interpretation is that strontium isotopes, sulfur and oxygen isotopes in sulfate are relatively insensitive to freshwater inputs and are therefore not recording the dilution of seawater by non-marine fluids. Even if this is the case, a mechanism is needed to explain the source of the ion required to reach gypsum saturation. A plausible explanation is sulfate molecules are decoupled from the source of the water for the gypsum hydration water, which was a mixture of marine and terrestrial sources. The source of the sulfate and strontium may come from dissolution of previously deposited marine gypsum that recharged the basin and maintained gypsum saturation. Evaporation of this fluid would produce a brine with the observed $\delta^{18}O$ and δD values and salinities, while retaining marine $\delta^{34}S$ and $\delta^{18}O_{SO_4}$ values and near-marine $^{87}Sr/^{86}Sr$ values, because of low concentrations of these elements in meteoric water. In addition, the dissolution of marine gypsum (with a strontium content of ~1500 ppm to 4000 ppm) in meteoric water will result in molar Sr/Ca ratios lower than seawater. Subsequent gypsum precipitation will reflect the low Sr/Ca ratios of the hybrid fluid, which is indicative of the low strontium concentrations observed in the majority of the Sorbas PLG sample. This recycling mechanism has been proposed previously by Natalicchio et al. (2014) to explain salinity inferred from fluid inclusions in gypsum from the Piedmont Basin (Italy).

5.5.4 Deposition of the lower marl unit

A change to the isotopic composition of the carbonate can be seen at the base of cycle 10, which is made up of a mixture of calcite and dolomite (Fig. 5.4). There is an increase in the proportion of dolomite/calcite towards the top of the marl where it transitions into the gypsum unit above. The proportion of gypsum in the marls increases in the 8 cm below the

transition into the massive gypsum above the marl. This progression of calcite to dolomite to gypsum is indicative of fractional crystallisation of minerals by evaporative enrichment (Eugster, 1980).

The $\delta^{18}O_{carb}$ and $\delta^{13}C$ values of bulk carbonate in the lower marl unit of cycle 10 increase from -3.7‰ and -0.1‰, respectively, at the base to a maximum of 1.9‰ and 1.5‰ at 10 cm below the transition into the massive gypsum before decreasing in the top of the lower marl unit (Fig. 5.4). The $\delta^{18}O_{carb}$ and $\delta^{13}C$ of bulk carbonate is expected to be higher in the marls dominated by dolomite because of the different isotope fractionation factor for oxygen and carbon isotopes between calcite and water, and dolomite and water; the oxygen and carbon isotope composition of dolomite is ~2.6‰ and ~2.4‰ greater than calcite when formed in equilibrium (Sheppard and Schwarcz, 1970; Vasconcelos et al., 2005). This indicates that a good correlation exists between the percent dolomite and bulk $\delta^{18}O_{carb}$ and $\delta^{13}C$. The relatively positive $\delta^{13}C$ in the marls at the base of the section suggest there is not significant oxidation of organic carbon, which would drive the $\delta^{13}C$ lower (Fig. 5.4). SEM investigations show that both calcite and dolomite present in the lower unit are authigenic (Fig. 5.9). Indeed, no angular or fractured mineral surfaces indicative of transport and mechanical erosion were observed. The elongated, almost acicular, morphology of the calcite crystal as well as the rhombohedral habit of the dolomite is commonly observed in carbonate minerals that form in the peritidal and supratidal zone of modern evaporitic environments (Bontognali et al., 2010). We found no clear morphological evidence (i.e. dissolution/re-crystallisation structures, hybrid mineral shapes) suggesting that the dolomite formed through a penecontemporaneous replacement of calcite. Therefore, the progressive enrichment in dolomite versus calcite observed in the studied sequence may have been caused by an environmental change from fresher peritidal hybrid-waters to more evaporated intertidal/supratidal conditions.

5.5.5 Formation of the supercone-marl unit

The origin of the supercone structures and associated laminated marls in the Río de Aguas section have prompted much speculation since their initial description by Dronkert (1985). We have identified important differences in the mineralogical and isotopic composition of the marl at the base of the cycle and the marl associated with the supercones near the top. The carbonate in the marl of the supercone unit is entirely dolomite and display higher $\delta^{18}O_{carb}$ and lower $\delta^{13}C$ values than those in the lower marl unit (Fig. 5.4).

The supercone selenite and the associated marl are considered to be syndepositional as individual lamina thin and disappear into gypsum crystals. Some laminae wrap around the supercone branches and can be traced above and below (Fig. 5.10). The syndepositional

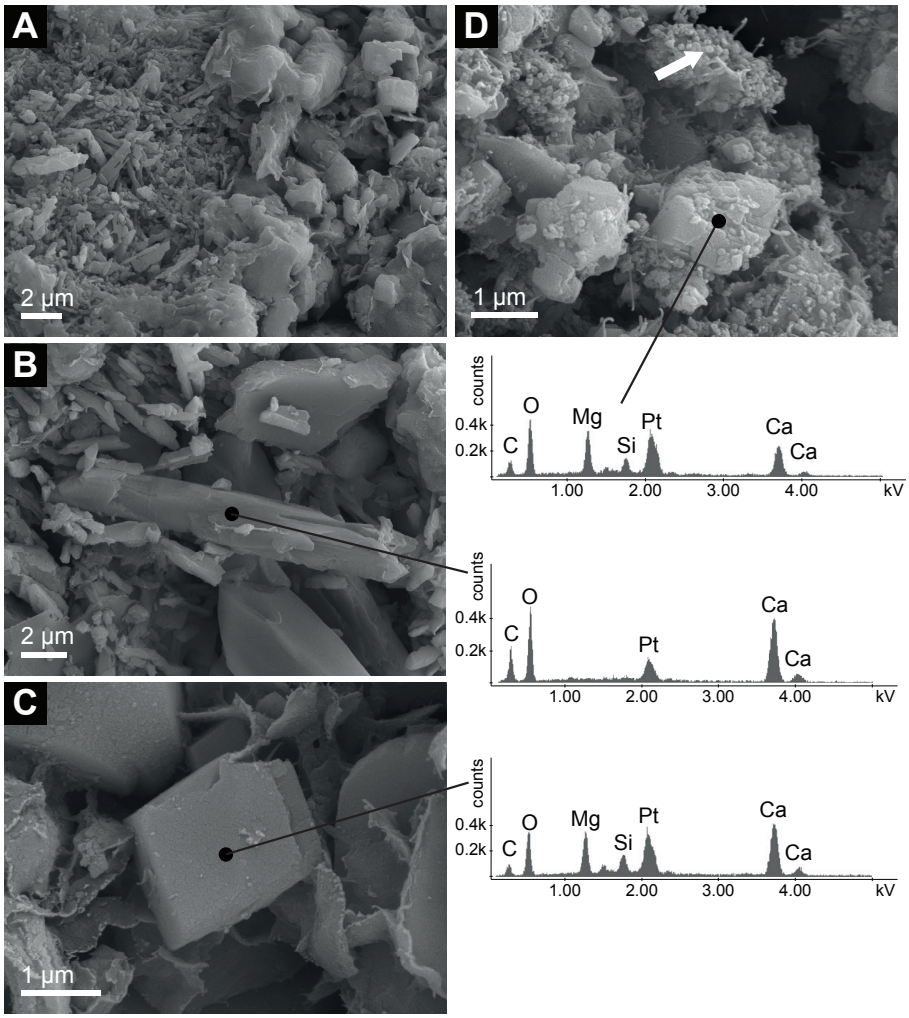

Fig. 5.9. Scanning electron microscopy (SEM) photomicrographs and energy dispersive X-ray (EDX) analyses of the carbonate minerals present in the studied samples. (A) Image of a representative sample of the lower marl unit (i.e., RdA1 -25 cm). Calcite crystals are characterized by an elongated, almost acicular morphology, while dolomite crystals display a rhombohedral habit. No morphological evidence indicates that dolomite formed through a diagenetic replacement of calcite or whether it is a primary precipitate. Both calcite and dolomite are authigenic. (B) Typical calcite crystal present in the lower unit and corresponding EDX spectrum, which is consistent with a Ca-carbonate. (C) Typical dolomite crystal present in the lower unit and corresponding EDX spectrum, which is consistent with dolomite. (D) Image of representative dolomite crystals present in the upper unit (i.e., SC marl 100) and corresponding EDX spectrum. Rhombohedral crystals of dolomite seem to form through aggregation of dolomite nanoglobules (white arrow), which suggests that dolomite in the 'supercone unit' is a primary precipitate. Dolomite crystals that form through aggregation of nanoglobules are typically observed in microbially mediated dolomite. Pt peaks in all EDX spectra are due to the metal coating used for sample preparation. Si peaks in the spectra measured from dolomite are interpreted as a contamination from the surrounding authigenic silicate minerals.

nature of the dolomitic marl and gypsum permits palaeotemperature to be estimated if the gypsum and dolomite were formed in isotopic equilibrium with the same water. The δ^{18}O of the gypsum hydration water provides the δ^{18}O of the water whereas the $\delta^{18}O_{carb}$ of the dolomite provides the carbonate value (Hodell et al., 2012). Marl sample SC50-10 ($\delta^{18}O_{dolomite}$ = 3.05‰) is directly juxtaposed to gypsum sample SC50B (δ^{18}O = 1.08‰), and together yield a temperature of 19.2°C using the dolomite–water palaeotemperature equation of Vasconcelos et al. (2005). This temperature is close to the average sea surface temperature from the local region of Almería today (15°C to 25°C). It also agrees with Messinian sea surface temperatures (17°C to 18°C) obtained from fluid inclusion analyses in Messinian halite (Speranza et al., 2013). These reasonable temperature estimates provide support that the dolomite and gypsum of the marl-supercone beds were formed at the same time from water with similar δ^{18}O values.

The marls associated with the supercones are very finely laminated and lack any evidence of bioturbation indicating anoxic conditions, and are reminiscent of the anoxic dolomite found in the Messinian Tripoli Formation in the deep basin (McKenzie et al., 1979). The δ^{13}C of the dolomite is low and varies between -3.8‰ and -4.9‰, indicating a source of dissolved inorganic carbon at least partially derived from the oxidation of organic matter; thus, the formation of the dolomite may be microbially mediated (Vasconcelos et al., 1995; Vasconcelos and McKenzie, 1997). This interpretation is also supported by the morphology of the dolomite crystals, which form through aggregation of spherical/amorphous nanoglobules (Fig. 5.9). In a study conducted with sulfate reducing bacteria capable of mediating dolomite formation, Bontognali et al. (2008) demonstrate that such nanoglobules represent the early stage of mineral nucleation within microbially produced extracellular polymeric substances (EPS). Nanoglobules that merge to form rhombohedral dolomite have also been observed in microbial mats that occur in the intertidal and supratidal zone of the sabkha of Abu Dhabi (Bontognali et al., 2010). In this modern evaporitic environment, dolomite can co-occur with gypsum crystals. As the sediment ages, only the dolomite (and not the microbial mat) is preserved, similar to observations in the marls juxtaposed to supercones.

5.5.6 Climate control of gypsum–marl deposition

The gypsum-marl cycles of the PLG are purported to represent climatic changes paced by precession with gypsum deposited during more arid conditions and sapropelic marl during more humid conditions (Krijgsman et al., 2001, 1999; Krijgsman and Meijer, 2008). The mineralogical and isotopic trends support this interpretation for cycle 10:

i. The peak wet conditions occurred at the precession minimum (maximum summer

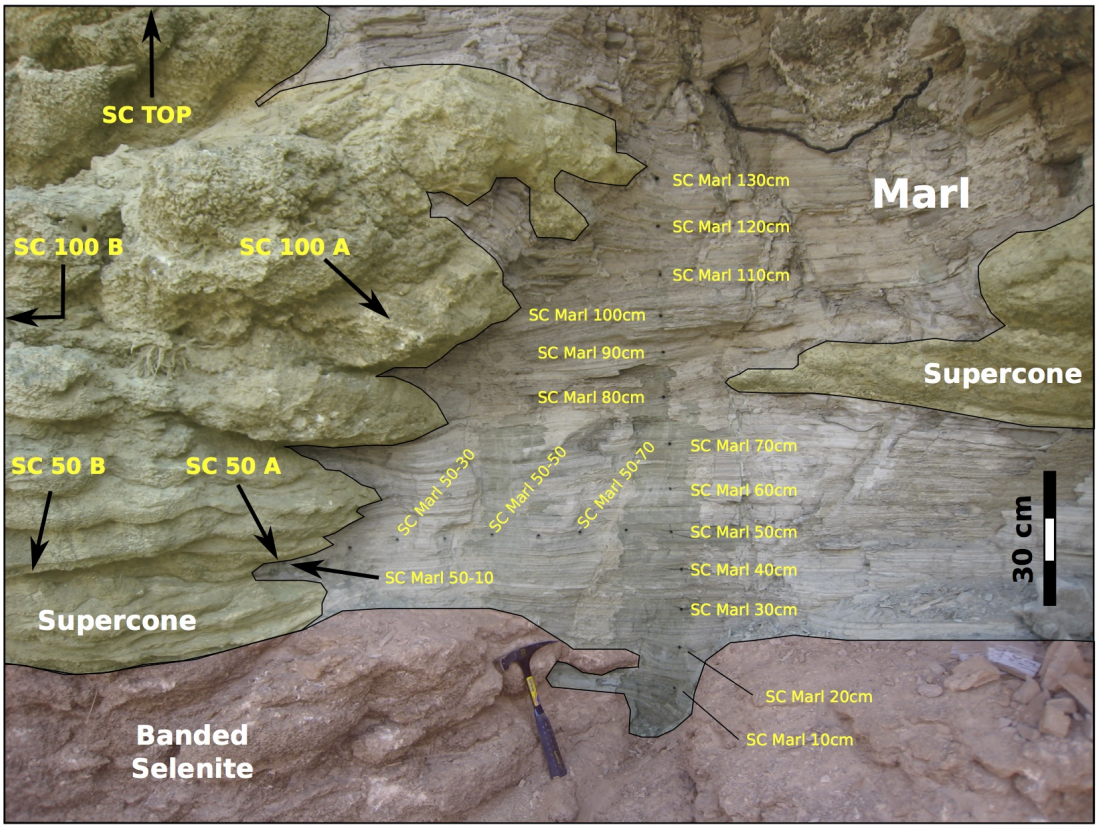

Fig. 5.10. Sample locations of Supercone ('SC') gypsum and marls juxtaposed to supercones ('SC Marls'), cycle 10, Río de Aguas section.

insolation) and is represented by the deposition of the laminated marl at the base of the studied section. Climate conditions became progressively drier promoting the formation of dolomite, and finally gypsum towards the top of the lower marl unit (Fig. 5.4).

ii. As climate became progressively drier, detrital input declined and pure gypsum began to precipitate in nucleation cones. The hydration water of the gypsum in the nucleation cones has relatively low δ^{18}O and δD and the fluid inclusions indicate relatively low salinity compared to the gypsum above (Fig. 5.7).

iii. Salinity, δ^{18}O and δD progressively increased above the nucleation cones reaching a maximum in the massive selenite palisade unit, marking peak aridity associated with the precession maxima (summer insolation minimum). A highly stratified brine, which in relation to total water depth produces a high and stable pycnocline (the gypsum saturation interface), creates the condition necessary for massive selenite growth (Bąbel, 2007). The δ^{18}O and δD and salinity of the palisade gypsum support

formation at a low saturation state needed for slow crystal growth (Bąbel, 2007).

iv. After formation of the gypsum palisade, the trend in aridity reversed indicating a progressive decrease in salinity related to increased freshwater input as recorded by decreasing salinity, δ^{18}O and δD values of the banded selenite unit.

v. As precipitation increased with increasing summer insolation, the supercones and associated dolomitic marls began to be deposited. The salinity of fluid inclusions and δ^{18}O and δD of gypsum in the supercones are lower than the banded and massive selenite units below. Detrital input also increased and led to the deposition of the dolomitic marls juxtaposed to the supercones (Section 5.5.5). Above the supercone the basal clay unit of Cycle 10 was deposited, marking the return of wetter climate conditions associated with the precession minimum.

5.6 Conclusions

We made tandem measurements of the isotopic composition of GHW and the salinity of fluid inclusions to test whether Messinian gypsum retained the original isotopic composition and salinity of the mother water. After correction of oxygen and hydrogen isotopes of GHW for known fractionation factors, we show that the δ^{18}O and δD of the mother water is highly correlated with salinity of fluid inclusions in gypsum deposits of cycle 10 within the Yesares Member. The intercepts of the regression equations (i.e. at zero salinity) define the isotope composition of the freshwater endmember. These values are within error of the average isotope composition of precipitation and groundwater data from the local region of Almería today. This agreement provides strong evidence that the GHW has retained its isotope composition and has not undergone postdepositional exchange.

The isotope and salinity values indicate a significant contribution of meteoric water during formation of Messinian gypsum in the Sorbas Basin. This observation contrasts with sulfur and oxygen isotopes in sulfate ($21.9 < \delta^{34}S < 23.3$‰; $11.3 < \delta^{18}O_{SO_4} < 14.5$‰) and strontium isotopes ($0.708942 < {}^{87}Sr/{}^{86}Sr < 0.708971$) that are similar to those measured in other Messinian evaporites of the Mediterranean. We suggest the source of the ions for gypsum formation is recycled from previously deposited units, whereas the source of the water is a mixture of marine and meteoric sources. The ${}^{87}Sr/{}^{86}Sr$, $\delta^{34}S$, and $\delta^{18}O_{SO_4}$ retain the signature of the parent sulfate deposits because of low concentrations of these elements in meteoric water, whereas the δ^{18}O and δD and salinity reflect a mixed signal of marine and freshwater. The recycling of solutes explains the discrepancies between strontium, sulfur

and water isotopes by decoupling the geochemical signatures of the ions and water during gypsum formation.

Lastly, we demonstrate that the patterns displayed by the δ^{18}O and δD and salinity of the gypsum, together with the overall changes in mineralogy (calcite–dolomite–gypsum) in cycle 10, are consistent with a precession-driven change in climate. Additional studies are needed to determine whether the patterns observed here for cycle 10 apply to other cycles in the Yesares Member.

Chapter 6

Geochemical evidence for meteoric water, orbital and eustatic control of basin hydrology during the first stage of the Messinian Salinity Crisis

***Nicholas P. Evans**, Fernando Gázquez, Thomas K. Bauska, Harold J. Bradbury, Alexandra V. Turchyn, José María Calaforra, and David A. Hodell.*

Twelve cycles of gypsum-marl deposition from the Messinian Yesares Member in the Sorbas Basin, Spain were examined using a high-resolution, multi-isotope approach to reconstruct the palaeo-hydrological dynamics of the basin and the wider Mediterranean region during the first stage of the Messinian Salinity Crisis (MSC). The past isotopic composition (δ^{18}O, δD, ^{17}O-excess and d-excess) of basin waters during evaporite formation were determined by analysing the structurally bound water in sedimentary gypsum ($CaSO_4 \cdot 2H_2O$). These measurements are combined with salinity inferred from gypsum fluid inclusions, strontium (^{87}Sr/^{86}Sr), calcium ($\delta^{44/40}$Ca), sulfur (δ^{34}S), and oxygen isotopes of sulfate ($\delta^{18}O_{SO_4}$) in the same samples, as well as isotopic analysis ($\delta^{44/40}$Ca, ^{87}Sr/^{86}Sr, $\delta^{18}O_{carb}$, δ^{13}C) of the interbedded carbonate marls, to determine the changing environment of deposition and its relation to astronomically-forced climate change.

This study provides data to show that obliquity-controlled sea level and eccentricity-modulated precession, superimposed on longer-term tectonic restriction of the Mediterranean-Atlantic exchange, together played a significant role in modulating gypsum-marl deposition in the Sorbas Basin. Strontium isotopes in gypsum display a gradual, but non-unidirectional

divergence from the seawater curve up-section, with slight reversals in the general trend of decreasing $^{87}Sr/^{86}Sr$ at ~5.84 Ma and 5.72 Ma. Maximum divergence of $^{87}Sr/^{86}Sr$ from the seawater curve, as well as anomalous authigenic carbonate mineralogy (dolomite) and high $\delta^{18}O_{carb}$ is coincident of glacial stage TG20 and an eccentricity minimum at ~5.75 Ma. Calcium isotopes track the variability in $^{87}Sr/^{86}Sr$, overprinted by Rayleigh fractionation effects. The non-unidirectional changes in strontium and calcium isotopes in combination with the patterns of the expression (i.e. thickness and facies) of the cycles in the Sorbas section indicate that sea level changes influenced basin hydrology.

6.1 Introduction

During the first stage of the Late Miocene Messinian Salinity Crisis (MSC, 5.97 Ma to 5.60 Ma), large volumes of sulfates and interbedded carbonate marls (the Primary Lower Gypsum, PLG) were deposited in silled sub-basins of the Mediterranean. The Sorbas Basin (SE Spain) has become a type-locality for this first stage of cyclic evaporite deposition, and is important in the study of the oceanographic evolution of the Miocene Mediterranean Sea owing to its proximity to the Atlantic gateway. Questions remain, however, about the factors that mediated the precipitation of gypsum and carbonate during each of the 15 gypsum-marl cycles, as well as the primary ion source during each depositional episode.

Previous studies that utilised traditional isotope tracers, such as strontium ($^{87}Sr/^{86}Sr$), sulfur ($\delta^{34}S$), and oxygen isotopes in sulfate ($\delta^{18}O_{SO_4}$), suggest that the deposition of the PLG occurred under a permanent open-ocean connection between the Mediterranean and the Atlantic, driven by astronomically controlled climatic oscillations (e.g. Longinelli, 1979; Müller and Mueller, 1991; Krijgsman et al., 1999; Lu and Meyers, 2003; Lugli et al., 2010; Manzi et al., 2013; Roveri et al., 2014a). The average freshwater budget in the Mediterranean remains largely unconstrained, however, because of the insensitivity of the traditional isotope tracers to continental water input. There is also evidence suggesting Mediterranean salinity may have been lower than the saturation horizon at which gypsum precipitation occurs (~130 $g\,l^{-1}$) during the evaporation of only seawater (e.g. Rosell et al., 1998; Natalicchio et al., 2014; Dela Pierre et al., 2014; Rossi et al., 2015; Evans et al., 2015). Because of difficulties reconstructing both palaeosalinity and the relative influence of continental water contributions on the PLG gypsum-carbonate cycles (e.g. Lu and Meyers, 2003; Rossi et al., 2015), neither the amplitude nor the phasing of salinity changes in the Mediterranean basin are clear (Flecker et al., 2015). Additionally, the correlation between isotopic variations, eustatic sea-level changes and orbital oscillations has remained tentative owing to the relatively low sampling resolution in the majority of previous studies.

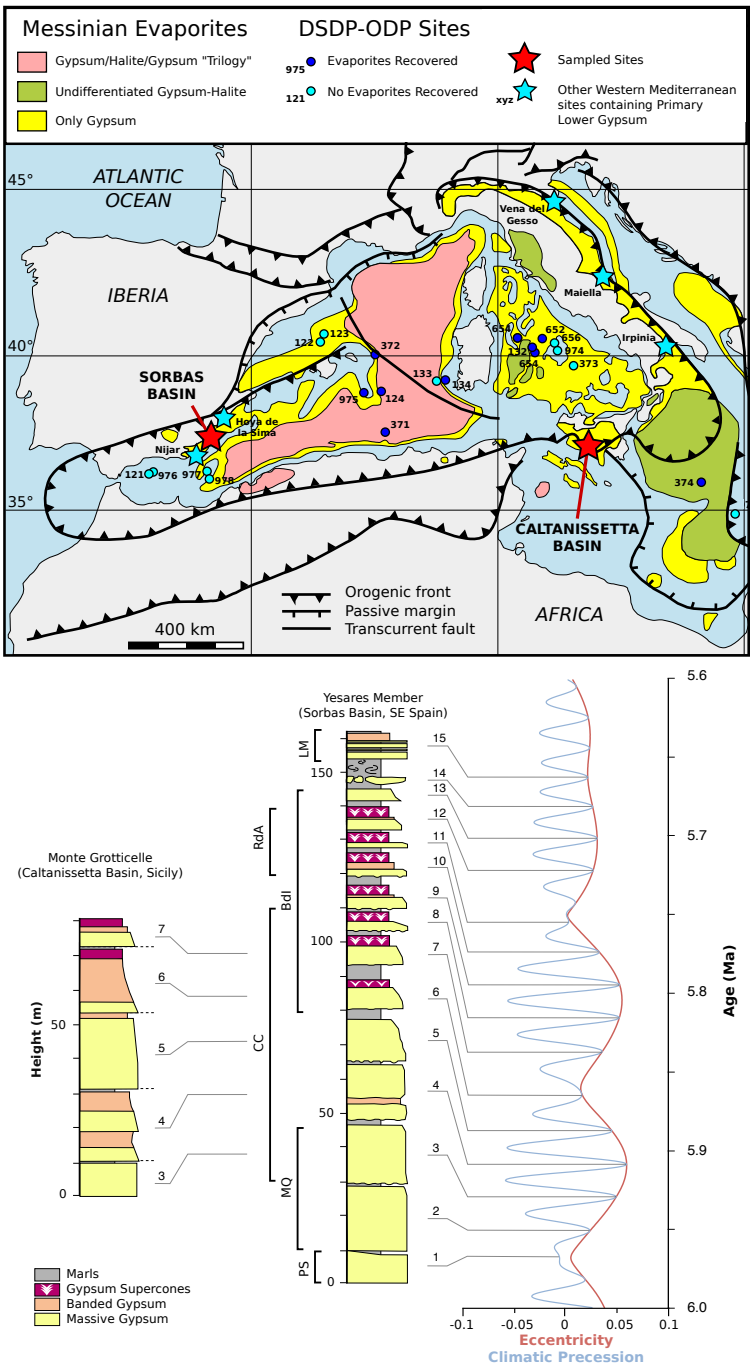

Fig. 6.1. (**Upper**) Map of the Messinian evaporites in the Mediterranean and the sampled basins. Also shown is the location of the DSDP-ODP boreholes in which Messinian evaporites were recovered, as well as other PLG sections found in marginal basin settings. Modified after Rouchy and Caruso (2006) and Roveri et al. (2014a). (**Lower**) Astronomical tuning of the PLG units in the Sorbas and Caltanissetta Basins. Also shown are the localities of the sampled sections relative to the Sorbas Basin log: PS (the Perales section); MQ (the Majadas Viejas quarry); CC (Covadura Cave); BdI (the Barranco del Infierno section); RdA (the Río de Aguas section); LM (the Los Molinos section). See text for details.

A unified theory that explains the formation of the Mediterranean Salt Giant requires an accurate understanding of the ion source and underlying mechanism by which the PLG formed. Here, a high-resolution (sub-precessional scale), multi-isotope study of 12 cycles of the Yesares Member, Sorbas Basin, is performed to constrain the hydrological variability during the first stage of the MSC. In addition to $^{87}Sr/^{86}Sr$, $\delta^{34}S$, and $\delta^{18}O_{SO_4}$ isotope analysis of gypsum, we measured the triple oxygen and hydrogen isotopes in GHW, calcium isotopes ($\delta^{44/40}Ca$), and salinity deduced from fluid inclusions. Together, these measurements provide detailed information on the parent water from which gypsum and carbonate were precipitated and offer high-resolution, independent evidence for the relative influence of basin stratification, sea-level variability and continental influences in marginal basins. We demonstrate that the Messinan PLG formed from evaporation of seawater that was strongly influenced by abundant freshwater input. We also show non-unidirectional changes in intra-cycle strontium and calcium isotope values are consistent with eustatic sea-level variability, and suggest that the appearance of the differing selenite facies can be linked to periods of increased northern hemisphere glaciation.

6.2 Geological setting

The Sorbas Basin, SE Spain: The Sorbas Basin (Fig. 6.1) preserves the transitional interval between the marine marls of the Upper Abad (UA) Member to the stage 1 evaporites of the Yesares Formation (Krijgsman et al., 2001). This area was likely part of the Betic Corridor that connected the Atlantic and the Mediterranean during the Late Miocene (Sierro et al., 2001, 1999). It therefore represents a key area for understanding the Western Mediterranean palaeoceanographic evolution during the onset of the MSC (Reghizzi et al., 2017).

The karstified Yesares Member occurs within a ~140 m thick sequence consisting of gypsum-carbonate cycles that have been astronomically tuned to precession (e.g. Krijgsman et al., 2001, 1999; Roveri et al., 2009; Lugli et al., 2010). The selenitic gypsum units are up to 30 m thick. The facies description is given in Section 4.2.1.

Dronkert (1985) was the first to describe the sedimentary cycles of the Yesares Member of the Sorbas Basin, reporting 12 cycles of alternating gypsum and carbonate-marl. In subsequent studies, however, the reported stacking pattern and number of cycles of the Yesares Member differs significantly from this original interpretation. Rosell et al. (1998) described 13 cycles in their stratigraphic log of the Los Molinos section, whereas Krijgsman et al. (2001) described 14 cycles in the same section. Lugli et al. (2010) and Roveri et al. (2009) reported 15 and 16 cycles, respectively, although these studies interpret the basal

cycle of the Los Molinos section to be cycle 2. This is because 'cycle 1', a carbonate-sapropel couplet that occurs at the base of this locality, has been correlated with a recently discovered gypsum cycle at the base of the Perales section (Manzi et al., 2013). As well as the addition of this cycle at the bottom of the PLG, the variable number of total cycles described is likely related to the differing interpretation of the upper half of the Los Molinos section where outcropping gypsum units are obscured.

We reinvestigated the cyclicity and stacking pattern of the Yesares Member in the Sorbas Basin (Fig. 6.1). We focus our study on gypsum and carbonates from the passages of Covadura Cave (Bosque branch; 37°07'21"N 002°04'8"W); the Majadas Viejas quarry (37°04'41"N, 002°05'51"W); the Perales section (37°06'24" N 002°02'33" W); the Río de Aguas section (37°05'23.2" N 002°06'54.2" W); the Los Molinos section (37°06'19" N 002°04'44" W); and the Barranco del Infierno section (37°04'58" N 002°07'07" W). Our field surveys concluded that twelve distinct gypsum-carbonate cycles are present in the wider basin, whereas an additional three gypsum-carbonate cycles are present in uppermost part of the Los Molinos section.

The lowermost gypsum bed is located at the Perales section. Manzi et al. (2013) recognized this highly discontinuous gypsum bed within the 'transitional interval' at the Abad-Yesares boundary (Sierro et al., 2001) below the lowermost continuous gypsum layer (i.e. cycle 2). The subsequent two cycles are exposed at the Majadas Viejas quarry, displaying massive selenite with little crystal variation. Cycles 3-8 can be observed in the passages of Covadura Cave. The sixth cycle marks the first appearance of branching selenite supercones, and the stacking pattern in the Covadura Cave is generally recognizable in the lower half of the Los Molinos section.

The upper part of the Yesares Member is best exposed in the Rio de Aguas and Barranco del Infierno sections, where the transition into the lowermost Sorbas Member is also exposed (Krijgsman et al., 2001). Eight distinct gypsum cycles are present in the Barranco del Infierno section; the uppermost gypsum cycle is a relatively discontinuous layer consisting of massive selenite, whereas the lower seven cycles in this section display both massive selenite and supercone structures. The presence of seven cycles containing supercones allows us correlate the lowermost cycle of the Barranco del Infierno section to cycle 6 in the Covadura Cave. Thus, the eight cycles of the Barranco del Infierno section correspond to cycles 6-13. The three cycles exposed at the base of the Rio de Aguas section also contain supercone structures and are overlain by a discontinuous gypsum/carbonate unit. These cycles at Rio de Aguas are recognizable as the lateral equivalent of the upper part of the Barranco del Infierno section, thus corresponding to evaporite cycles 10-12. Dronkert (1985) observed a similar correlation between the Rio de Aguas and Barranco del Infierno

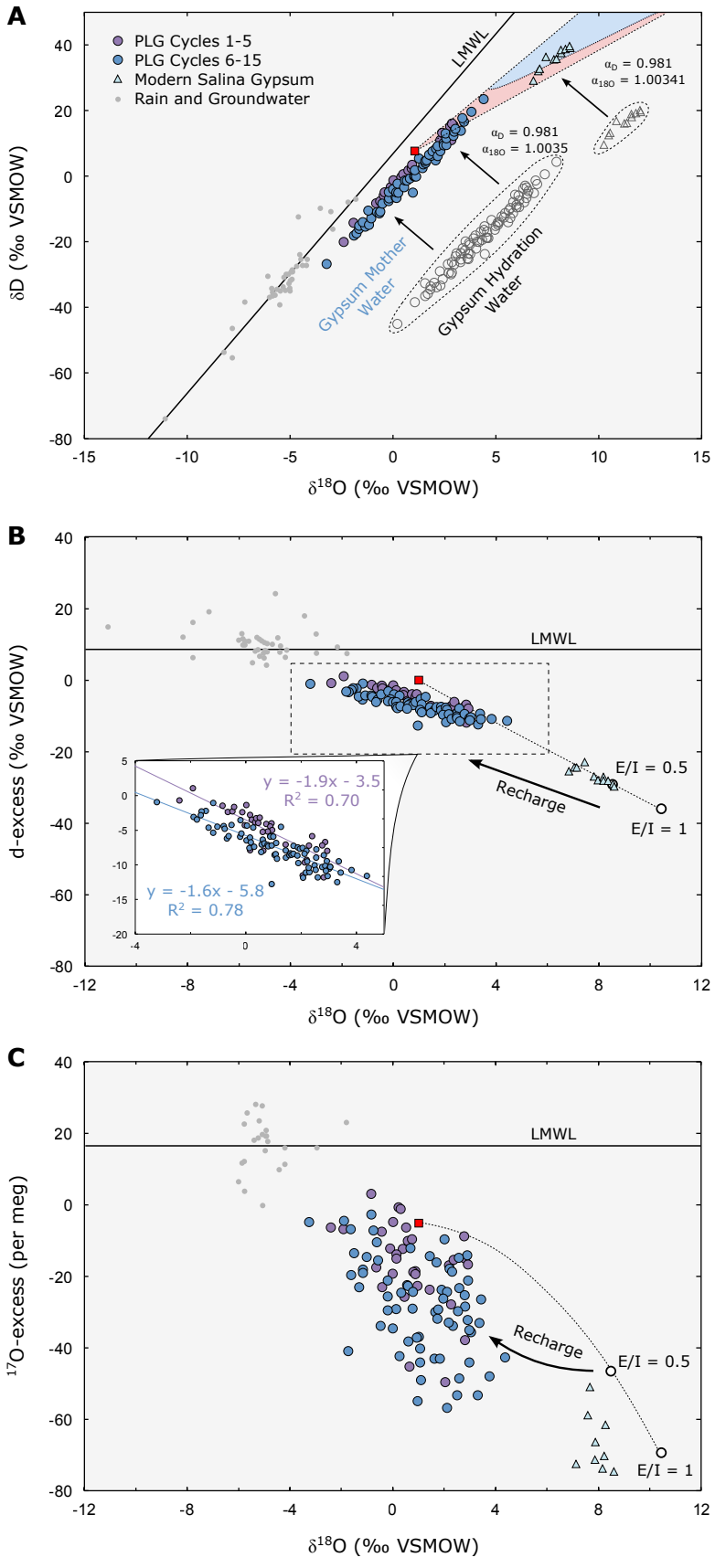
A
PLG Cycles 1-5
PLG Cycles 6-15
Modern Salina Gypsum
Rain and Groundwater
LMWL
α_D = 0.981
α_{18O} = 1.00341
α_D = 0.981
α_{18O} = 1.0035
Gypsum Mother Water
Gypsum Hydration Water
δD (‰ VSMOW)
δ18O (‰ VSMOW)
B
LMWL
E/I = 0.5
E/I = 1
Recharge
y = -1.9x - 3.5
R2 = 0.70
y = -1.6x - 5.8
R2 = 0.78
d-excess (‰ VSMOW)
δ18O (‰ VSMOW)
C
LMWL
Recharge
E/I = 0.5
E/I = 1
17O-excess (per meg)
δ18O (‰ VSMOW)

Fig. 6.2. **Left**. Comparison of measured local meteoric water (grey circles) and predicted mother water values after correction for fractionation factors (Gázquez et al., 2017). In (**A**) δ^{18}O vs δD, (**B**) δ^{18}O vs d-excess and (**C**) δ^{18}O vs ^{17}O-excess space, local meteoric water measurements define the local meteoric water line (LMWL). Light blue triangles are modern gypsum data from the Cabo de Gata Salina. Red square is Modern Mediterranean Seawater. The trajectories for the evaporation of Mediterranean seawater for high (90%; slope ~7) and low (40%; slope ~3) humidities are shown in A, defining a range of possible δ^{18}O and δD values (pink field). Gypsum precipitation takes place at 3 to 7 times concentrated seawater; gypsum saturation (blue field) is calculated using the Rayleigh Distillation equation, assuming initial δ^{18}O and δD values of ~1‰ and 8‰, respectively, 75% equilibrium between atmospheric vapour and fresh water, and gypsum saturation occurring at an evaporation ratio of 3.8× (evaporation ratio = weight of H_2O of original seawater divided by weight of H_2O in residual evaporated brine). Mixing lines in B and C are derived from the model of Gázquez et al. (2018) at a humidity of 75% and a starting point of modern Mediterranean seawater. The mixing curve does not match the data, indicating that basin recharge with freshwaters was dominant. Errors (1σ) are less than the width of the symbols, and ±6 for ^{17}O-excess.

sections, although he incorrectly correlated the cycles to the Los Molinos section and does not log the discontinuous gypsum layer above the uppermost supercone cycle.

The uppermost part of the Los Molinos section contains two further gypsum-carbonate cycles. The carbonate-marls below the uppermost gypsum layer display signs of slumping. The uppermost cycle contains massive, metre-thick intervals of selenite interbedded with distinct layers of carbonate marls (up to 30 cm thick), whereas the two gypsum layers below are composed of discontinuous gypsum beds, often interbedded with limestone. As the two uppermost cycles of the Los Molinos section are not present in the Rio de Aguas and Barranco del Infierno sections, the beds are unlikely to be laterally continuous across the basin.

The Caltanissetta Basin, Sicily: We compare our samples from the Sorbas Basin to the samples collected from the PLG units of the Caltanissetta Basin (Fig. 6.1). The PLG units occur as large disarticulated units that are detached from their original substratum, but still preserve most of their original sedimentary features (Caruso et al., 2015). The chaotic nature of the blocks has been interpreted either as redeposition of previously intact PLG units from small northern sub-basins in the central foredeep via gravity flows (Roveri et al., 2006a), or the result of the combined effects of the salt deformation under regional compressive events and halokinesis followed by collapse dissolution (Rouchy and Caruso, 2006). The Monte Banco (37°26'30"N 13°29'00"E), Monte Grotticelle (37°26'10"N 13°29'30"E) and Santa Elisabetta sections display differing numbers of cycles and limited interbedded carbonates owing to the reworking. The stacking pattern is discussed in Section 4.2 and can be correlated with the PLG of the Sorbas basin (e.g. Lugli et al., 2010).

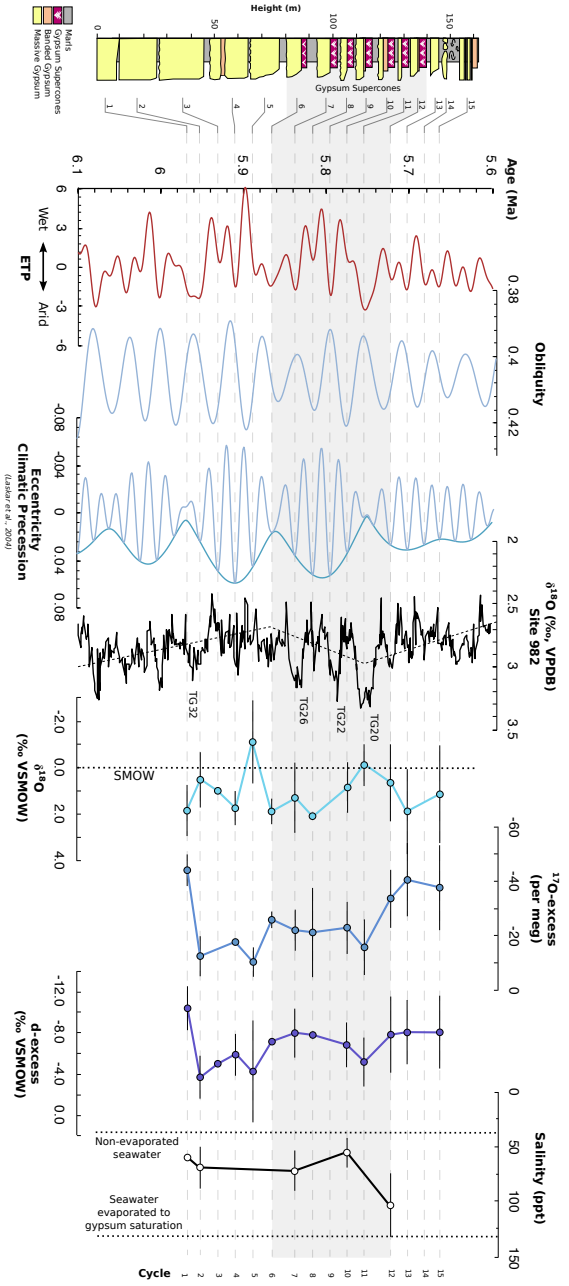

Fig. 6.3. Mean intra-cycle $\delta^{18}O$, ^{17}O-excess and d-excess data (calculated from measurement of GHW) and salinity data (deduced from fluid inclusions and calculated using the equation of Goldstein and Reynolds, 1994) are plotted against their designated cycle. Error bars define $\pm 1\sigma$ of the data in each cycle. Each gypsum bed of the Yesares Member is plotted in relation to its proposed orbital tuning (Laskar et al., 2004; Lugli et al., 2010; Manzi et al., 2013), where gypsum precipitation correlates with insolation minima. The benthic $\delta^{18}O$ (Hodell et al., 2001; modified by Drury et al., 2018) is also shown, and the major glacial stages are indicated. The horizontal grey band indicates the appearance of gypsum supercone cycles (cycles 6-12).

6.3 Sample collection methods

In the Sorbas Basin, individual in situ gypsum crystals (n = 135) were removed with a hammer and chisel. Cycles 2, 7, and 10 were subject to high-resolution sampling, where >22 discrete, evenly spaced gypsum samples were analysed in each cycle. Carbonate samples (n = 129) were taken using a battery-powered drill fitted with a coring drill bit. The corer was inserted parallel to the bedding plane after removal of the outer 5 cm of marl to avoid contamination. In the Caltanissetta Basin, gypsum samples (n = 24) were collected from Monte Grotticelle and Monte Banco using the same techniques.

6.4 Results

6.4.1 Gypsum Hydration Water (GHW)

One hundred and fifty-nine samples representing massive, banded and branching selenite were analysed (Appendix D; Table D.1). The oxygen and hydrogen isotope composition of the parent water in which the gypsum formed is calculated by correcting the measured values for the gypsum-water fractionation factors (Chapter 2). Fractionation factors were assumed to be 1.0035 and 0.981 for oxygen and hydrogen isotopes, respectively, which represents a water temperature of ~15°C to 20°C and salinity of <150 g l^{-1} (Chapter 5). The sensitivity of the fractionation factors to temperature is low, especially for oxygen isotopes (Gázquez et al., 2017). Following correction, the $\delta^{17}O$, $\delta^{18}O$ and δD of the gypsum mother water for the Sorbas Basin PLG are shown in Fig. 6.2.

Inter-cycle trends: The range of $\delta^{18}O$ and δD does not vary greatly among gypsum cycles, with little change up-section (Fig. 6.3). Mean ($\pm\sigma$) $\delta^{18}O$ and δD values across the entire section are 0.99 (±1.5) ‰ and 1.1 (±9.6) ‰, respectively. The lowest mean $\delta^{18}O$ and δD values occur in cycle 5 ($\delta^{18}O$ = -1.1‰; δD = -13.3‰) and cycle 11 ($\delta^{18}O$ = -0.1‰; δD = -6.2‰). The highest mean intra-cycle values occur in cycle 8 ($\delta^{18}O$ = 2.1‰; δD = 9.0‰) and cycle 13 ($\delta^{18}O$ = 1.9‰; δD = 7.1‰).

Deuterium excess is also relatively constant across all gypsum cycles with a mean ($\pm\sigma$) value of -6.8 (±3.0) ‰ (Fig. 6.3). ^{17}O-excess is -44 (±6) per meg at the base of cycle 1, but rises to a mean value of -19 (±9) per meg over cycles 2 to 11. In cycles 12 to 15, ^{17}O-excess returns to lower values (-37 (±13) per meg), similar to cycle 1. d-excess and ^{17}O-excess are also negatively correlated with $\delta^{18}O$ and δD; the most positive mean intra-cycle values occur in cycle 5 (d-excess = -1.1‰; ^{17}O-excess = -13 per meg) and cycle 12 (d-excess = -0.1‰; ^{17}O-excess = -16 per meg).

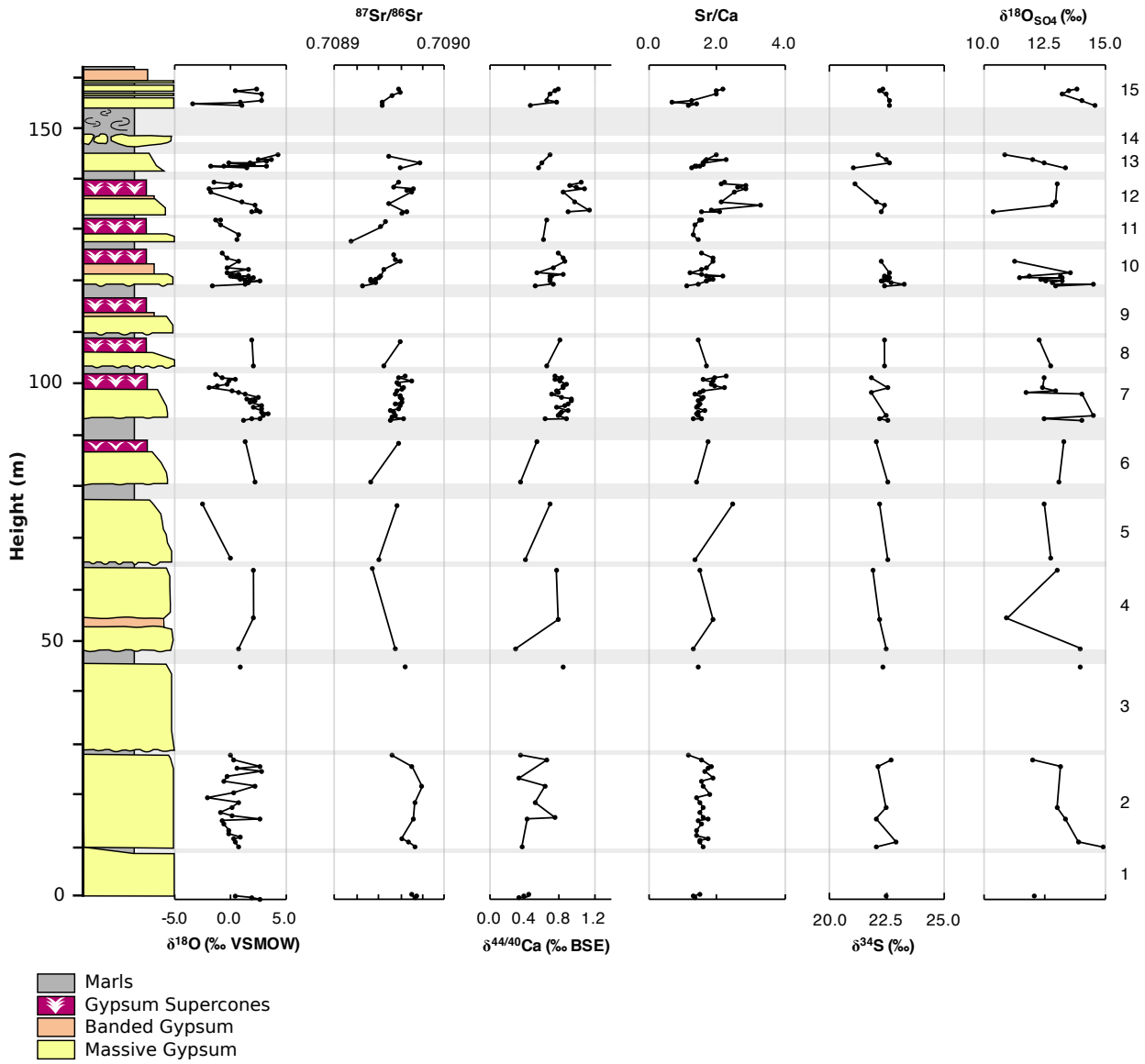

Fig. 6.4. The $\delta^{18}O$ deduced from GHW, strontium isotopes, calcium isotopes, bulk Sr/Ca ratio, sulfur and oxygen isotopes of sulfate of individual samples are shown relative to their sample location in relation the Yesares section.

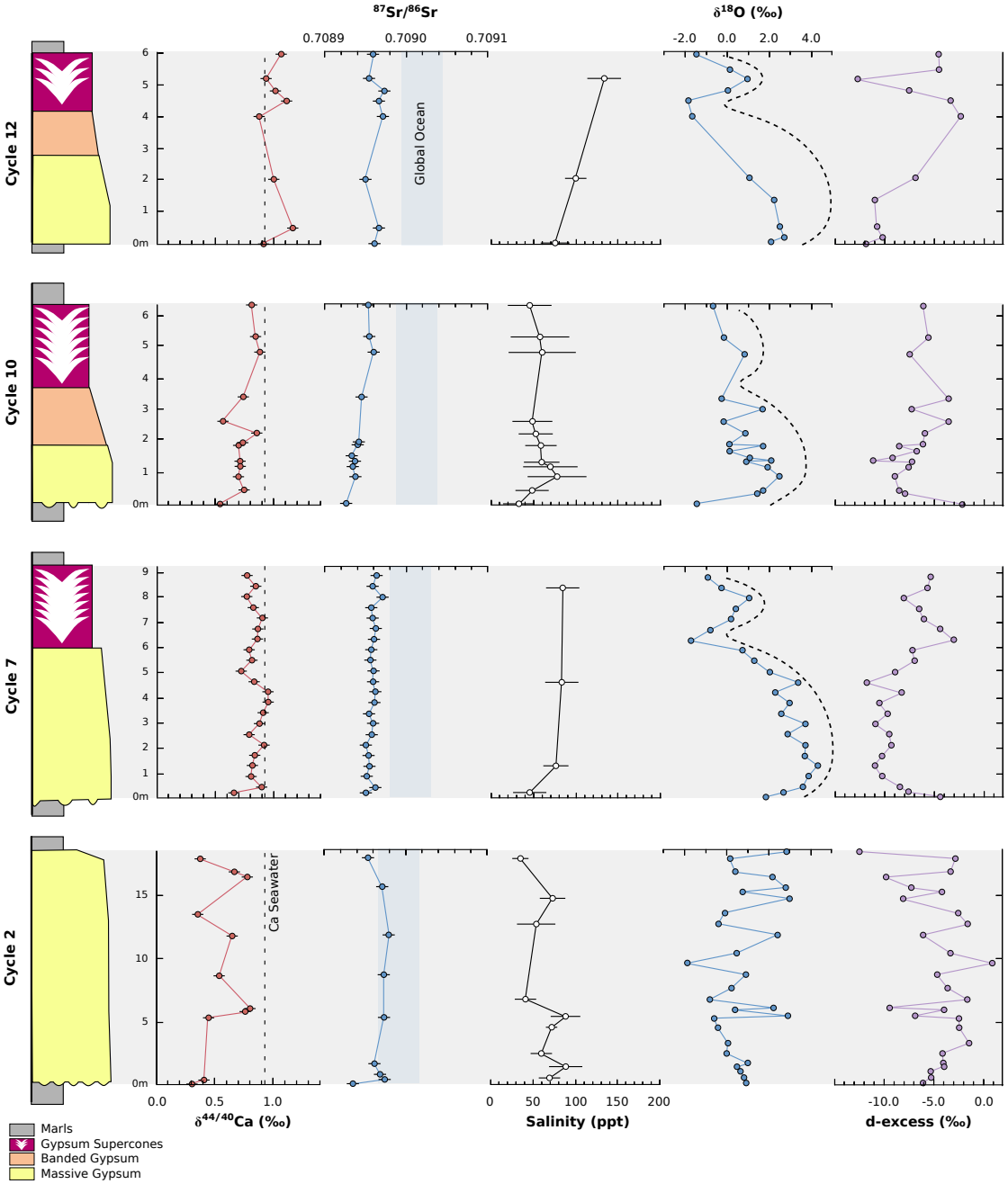

Fig. 6.5. Schematic diagram of cycles 2, 7, 10 and 12 scaled to height of each of the sections. Calcium isotope data, strontium isotope data, salinity data (deduced from fluid inclusions and calculated using the equation of Goldstein and Reynolds, 1994), δ^{18}O and d-excess data deduced from GHW are plotted relative to the height from which the samples were taken. Dashed lines are a guide for the eye, highlighting the similarity in δ^{18}O values in cycles 7, 10 and 12.

Intra-cycle trends: On the basis of oxygen and hydrogen isotope compositions, the Sorbas section can be divided into three parts: (i) a lower section (cycles 1 to 4) with homogeneous isotope trends within cycles, (ii) a middle section beginning with cycle 5, where cycles display systematic, decreasing upward trends of δ^{18}O and δD values, and (iii) an upper section beginning with cycle 13, where cycles display systematic, increasing upward trends of δ^{18}O and δD values (Fig. 6.4). The middle section coincides with the appearance of banded selenite and branching supercone structures within the cycles.

The δ^{18}O, δD, ^{17}O-excess and d-excess of gypsum mother water within cycles 1 to 4 exhibit low amplitude oscillations, with no clear intra-cycle trends (Fig. 6.4; Fig. 6.5). These beds consist of massive selenite with little change in facies.

Cycles 7, 10, 11 and 12 display a clear and systematic inter-cycle change in δ^{18}O and δD values (Fig. 6.4; Fig. 6.5). The δ^{18}O and δD values increase upwards from the base of the section to maximum values in the gypsum palisade at ~50 cm to 100 cm. Above this peak, δ^{18}O and δD fall to their lowest values at the base of the supercone structures. Isotope values in the supercones are more variable, but a small cyclic trend is apparent where the δ^{18}O and δD increase to more positive values ~150 cm above the base of the supercones, and then fall to lower values at the top of the cycle. Overall, these cycles display a systematic change of increasing δ^{18}O and δD from the base of the section that reach maximum values in the lower-middle (palisade gypsum), and a fall to low isotopic values near the top (supercone). These trends are also apparent in cycles 5 and 6, despite the comparatively low sampling resolution.

Cycles 13 and 15 show a general trend towards higher δ^{18}O and δD values towards the top of each cycle (Fig. 6.4). Cycle 13 is composed of a discontinuous bed of massive selenite, whereas cycle 15 is composed of massive, metre-thick intervals of selenite interbedded with distinct layers of carbonate marls (up to 30 cm thick) and topped by domed gypsum layers.

6.4.2 Sr isotopes

Seventy-one samples from Messinian gypsum and 12 samples from the interbeded carbonates from the Sorbas Basin were processed for strontium isotopic analysis (Appendix D; Table D.4). For gypsum samples, the ^{87}Sr/^{86}Sr ranged between 0.708916 and 0.708979. These values fall slightly below the strontium isotope range expected for Messinian seawater, which varies from ~0.708989 at 5.971 Ma to ~0.709014 and 5.6 Ma relative to a NIST SRM 987 value of 0.710248 (McArthur et al., 2001).

Inter-cycle trends: The lowermost gypsum cycle (cycle 1) has $^{87}Sr/^{86}Sr$ values that are indistinguishable from seawater (difference in mean $^{87}Sr/^{86}Sr$ from seawater = 0.000016), but the difference increases up-section to a maximum departure from the global seawater curve in cycles 10 and 11 (difference in mean $^{87}Sr/^{86}Sr$ from seawater = 0.000068) (Fig. 6.6). Overall, mean $^{87}Sr/^{86}Sr$ values decrease away from the seawater curve up-section, but this trend reverses at cycles 7 and 12 with a slight recovery towards the global ocean seawater curve. This defines a ~100 ka cyclicity within the $^{87}Sr/^{86}Sr$ profile, and transition from cycles 6 to 7 and 11 to 12 correlate temporally with periods of eccentricity minima.

Intra-cycle trends:

The $^{87}Sr/^{86}Sr$ values of gypsum analysed of cycles 1 through 4 display very little intra-cycle variation; isotope values display a slight variance throughout the gypsum bed, but there is no significant correlation towards higher or lower values up-section within each layer (Fig. 6.4; Fig. 6.5). Cycles 5 through 15 display a significant and systematic change in $^{87}Sr/^{86}Sr$ within each cycle; the lowest Sr isotope ratios are recorded at the base of each gypsum layer, and values increases up-section toward maximum values the top of each cycle. No sharp changes in the Sr isotopic composition of the gypsum are observed at the transition between gypsum facies.

The range of $^{87}Sr/^{86}Sr$ for the interbedded carbonates (n = 9) varies between 0.708936 and 0.708423, with an average value of 0.708720 (Appendix D; Table D.8). These values are significantly lower than $^{87}Sr/^{86}Sr$ of the massive gypsum layers. The $^{87}Sr/^{86}Sr$ for the carbonate marls juxtaposed to supercones (n = 3) ranges from 0.709025 to 0.708991, with an average value of 0.709011, which is within the range of the Sr isotopic composition of the surrounding gypsum.

6.4.3 Ca isotopes

The results of Ca isotope analysis are reported in Appendix D (Table D.4). For gypsum samples (n = 75), the range of $\delta^{44/40}Ca$ varies between 0.30‰ and 1.16‰.

Inter-cycle trends: The lowest $\delta^{44/40}Ca$ values are found in gypsum cycles 1 to 5, where mean ($\pm\sigma$) values of all 5 cycles are 0.53 (±0.13) ‰ (Fig. 6.6). A step change in Ca isotopes occurs at cycle 7. Mean $\delta^{44/40}Ca$ of cycles 7 to 11 are 0.79 (±0.10) ‰. Up-section, Ca isotope values of cycle 12 also display a stepped increase compared to the lower cycles, with mean $\delta^{44/40}Ca$ values of 1.01 (±0.10) ‰. Calcium isotope values of cycles 13 to 15 (0.68 ± 0.10 ‰) return to similar values as cycles 7 to 11. Overall, $\delta^{44/40}Ca$ of gypsum

increases up-section, with step changes defining a ~100 ka cyclicity similar to those seen in $^{87}Sr/^{86}Sr$ results.

The range of $\delta^{44/40}$Ca for the interbedded carbonates (n = 19) varies between -0.35‰ and 0.46‰, and average intra-cycle $\delta^{44/40}$Ca decreases up-section (Appendix D; Table D.8). The $\delta^{44/40}$Ca for the carbonate marls juxtaposed to supercones ranges from 0.18‰ to 0.21‰.

Intra-cycle trends: The lowest Ca isotope values in each cycle are observed at the base of the bed. In general, all cycles display a trend towards higher $\delta^{44/40}$Ca toward the top of the bed, but this correlation is weak. Ca isotopes exhibit low amplitude oscillations in all cycles. There is no correlation between Ca isotope variability and gypsum facies or grain size (Fig. 6.4).

6.4.4 δ^{34}S and δ^{18}O of sulfate

Fifty-two samples were analysed for sulfur isotopes and oxygen isotopes of sulfate (Appendix D; Table D.6). δ^{34}S of gypsum from the Sorbas Basin show a narrow range of values between 21.1‰ and 23.3‰ VCDT, and $\delta^{18}O_{SO_4}$ varies between 10.4 and 14.9‰ VSMOW. These values fall on or slightly above the δ^{34}S and $\delta^{18}O_{SO_4}$ isotope range expected for sulfate minerals precipitated from evaporated Late Miocene seawater (i.e. δ^{34}S ~22‰ and $\delta^{18}O_{SO_4}$ ~12‰, relative to NBS-127 values of 21.1‰ and 8.6‰ for δ^{34}S and $\delta^{18}O_{SO_4}$, respectively) (Fig. 6.7).

Inter-cycle trends: Gypsum δ^{34}S values remain homogenous across the entire section, with mean ($\pm\sigma$) values of 22.4 ($\pm$0.4) ‰ (Fig. 6.7). The $\delta^{18}O_{SO_4}$ is also relatively unchanging across the section, displaying mean ($\pm\sigma$) values of 12.9 ($\pm$1.0) ‰. From cycles 1 to 12, there is a slight trend toward lower $\delta^{18}O_{SO_4}$ values up-section, although cycle 15 reverses this trend and displays anomalously high values of 13.9 ($\pm$0.5) ‰.

Intra-cycle trends: Sulfate isotope compositions are also relatively homogenous within individual cycles of the Sorbas Basin (Fig. 6.4). There are negligible differences in the isotope composition among the nucleation cone, palisade, banded selenite, and supercone facies, and changes in δ^{34}S and $\delta^{18}O_{SO_4}$ with depth are not repeatable between cycles.

The δ^{34}S and $\delta^{18}O_{SO_4}$ of gypsum from the Caltanissetta Basin show similar values to those found in the Sorbas Basin, where δ^{34}S and $\delta^{18}O_{SO_4}$ vary between 22.6‰ and 22.9‰ VCDT and 12.7‰ and 14.6‰ VSMOW, respectively.

6.4.5 Microthermometric analysis

Thirty-four samples from the Messinian gypsum of the Sorbas Basin, 4 samples from the Caltanissetta basin, and 2 samples from the modern Salina at Cabo de Gata, Almería, Spain, were selected for microthermometric analysis (Appendix D; Table D.6).

The final melting temperature (Tm_{ice}) of 405 primary Messinian inclusions ranged between -0.2°C and -6.1°C, with an average Tm_{ice} of -3.2°C (Fig. 6.8). Using the revised equation and table for determining the freezing point depression of H_2O–NaCl solutions of Bodnar (1993), average salinity estimates of individual samples range from 2.9% to 8.5% (average 5.3 wt% NaCl equivalent). Tm_{ice} of modern gypsum from the Cabo de Gata Salina ranged between -6.5°C and -10.1°C (average -8.0°C), corresponding to an average salinity of 11.7%.

Within the section, the average wt% NaCl equivalent of gypsum from cycles 1 to 9 is 5.1 (±1.1) % (Fig. 6.3). These values are well below the threshold for gypsum precipitation from the evaporation of seawater alone. The mean wt% NaCl of cycle 11 is 7.2 (±1.2) %, representing a significant increase compared to the lower cycles.

6.4.6 XRD, wt% calcite and wt% dolomite of bulk carbonates

Eighty five marl samples were analysed by XRD (Appendix D; Table D.8). The results are semi-quantitative and indicative of the relative abundances of common mineralogical components only. In addition to clay, the major phases are gypsum, calcite, and dolomite.

The marls interbedded with the lower 7 cycles contain dominantly calcite. The marls at the base of cycle 10 contain both calcite and dolomite (Fig. 6.6). The ratio of calcite to dolomite in the lower marls of cycle 10 decreases up-section such that dolomite becomes more dominant toward the gypsum–marl contact. Fine-grained gypsum within the marl is abundant in the upper marl from 8 cm below the marl-gypsum contact. Between cycles 10 and 11, marls are dominantly composed of dolomite with minor amounts of calcite. Marls juxtaposed to supercones in cycles 10 and 11 are purely dolomitic and contain varying proportions of gypsum.

6.4.7 $\delta^{18}O_{carb}$ and $\delta^{13}C$ of bulk carbonates

The oxygen and carbon isotope composition of 129 carbonate samples vary from -8.3‰ to 5.8‰ for $\delta^{18}O_{carb}$ and from -4.9‰ to 2.0‰ for $\delta^{13}C$ (Appendix D; Table D.8; Fig. 6.6 and Fig. 6.9). The carbon and oxygen isotope composition of the carbonates are within the range of other Messinian carbonates associated with evaporites in the Mediterranean (Longinelli,

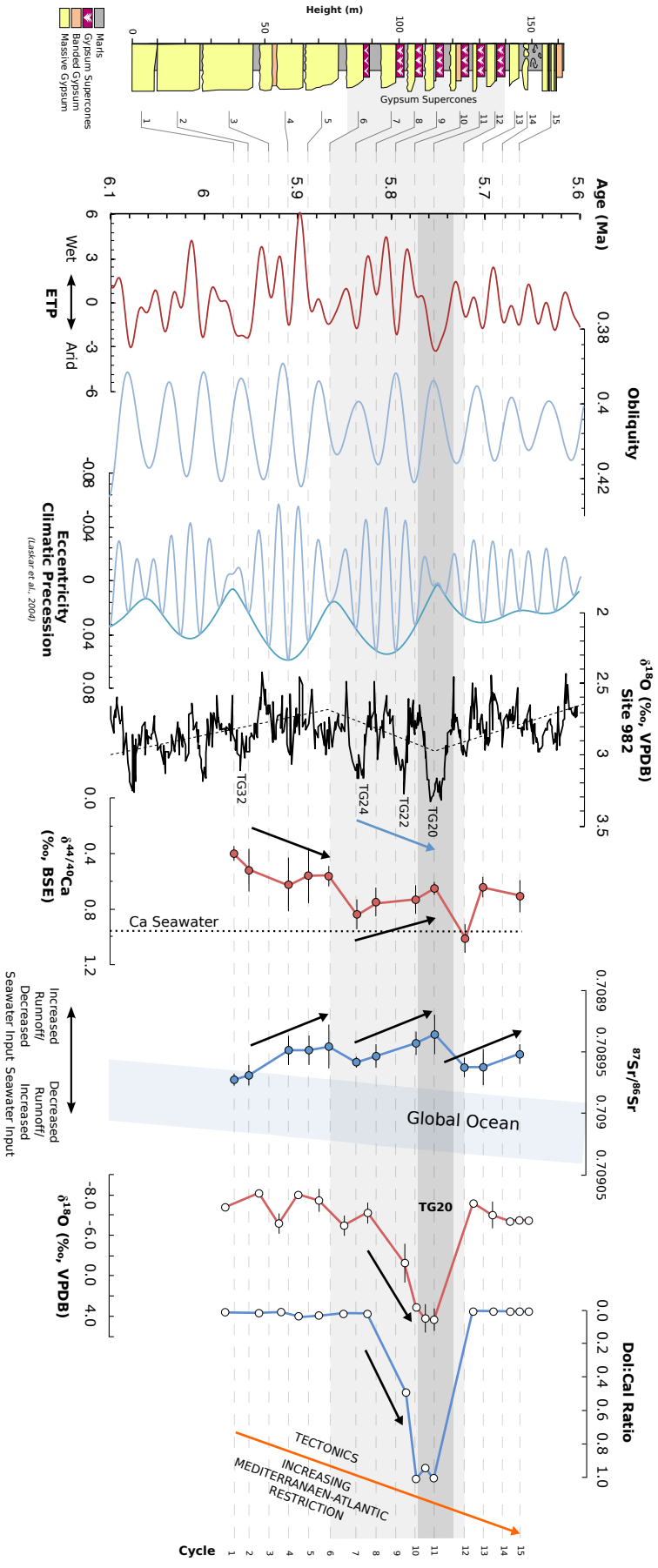
Marls
Gypsum Supercones
Banded Gypsum
Massive Gypsum
Height (m)
Gypsum Supercones
Age (Ma)
Obliquity
Wet
ETP
Arid
Eccentricity
Climatic Precession
(Laskar et al., 2004)
δ18O (‰, VPDB)
Site 982
TG32
TG24
TG22
TG20
δ44/40Ca
(‰, BSE)
Ca Seawater
Increased Runnoff/ Decreased Seawater Input
Decreased Runnoff/ Increased Seawater Input
87Sr/86Sr
Global Ocean
δ18O (‰, VPDB)
TG20
Dol:Cal Ratio
TECTONICS
INCREASING MEDITERRANAEN-ATLANTIC RESTRICTION
Cycle

Fig. 6.6. **Left**. Mean intra-cycle $^{87}Sr/^{86}Sr$ and $\delta^{44/40}Ca$ data from gypsum beds, and $\delta^{18}O_{carb}$ and dolomite-calcite ratio of the interbedded carbonates are plotted against their designated cycle. Error bars define $\pm 1\sigma$ of the data in each cycle. Note that carbonate data plotted between the dashed lines denote carbonate samples located between gypsum beds, whereas carbonate samples that are plotted on the dashed lines denote carbonate samples that are located in supercones. Each gypsum bed of the Yesares Member is plotted in relation to its proposed orbital tuning (Laskar et al., 2004; Lugli et al., 2010; Manzi et al., 2013), where gypsum precipitation correlates with insolation minima. The benthic $\delta^{18}O$ (Hodell et al., 2001; modified by Drury et al., 2018) is also shown, and the major glacial stages are indicated. The light grey horizontal grey band indicates the appearance of gypsum supercone cycles (cycles 6-12). The dark grey horizontal band highlight the glacial period TG20. The blue arrow highlights the period of increased cooling and global sea-level fall through TG24, TG22 and TG20. The orange arrow indicates the expected, gradual influence of the tectonic restriction of the Mediterranean-Atlantic exchange of the isotope systems shown. The black arrows highlight key trends in $^{87}Sr/^{86}Sr$, $\delta^{44/40}Ca$, $\delta^{18}O_{carb}$ and dolomite-calcite data. Note that there is significant correlation between shifts in $^{87}Sr/^{86}Sr$, $\delta^{44/40}Ca$, $\delta^{18}O_{carb}$ and dolomite-calcite data and glacial TG24, TG22 and TG20.

1979). The $\delta^{18}O_{carb}$ of the marls from cycles 1 to 7 average -6.1 (±1.4) ‰, whereas the $\delta^{13}C$ averages -0.8 (±1.4) ‰. At the base of cycle 10, mean ($\pm\sigma$) $\delta^{18}O_{carb}$ and $\delta^{13}C$ increase to -1.2 (±1.9) ‰ and 0.6 (±1.9) ‰, respectively. Marls juxtaposed to supercones in cycles 10 and 11 show the highest $\delta^{18}O_{carb}$ values, but the lowest $\delta^{13}C$ values, averaging 3.1 (±0.2) ‰ and -4.4 (±0.4) ‰, respectively. Additionally, the marls between cycle 10 and 11 show high $\delta^{18}O_{carb}$ and low $\delta^{13}C$ values, averaging 4.1 (±1.4) ‰ and -1.6 (±2.1) ‰, respectively. In this cycle, negative excursions in the $\delta^{18}O_{carb}$ are well correlated with an increase in the calcite:dolomite ratio. Above cycle 12, the $\delta^{18}O_{carb}$ and $\delta^{13}C$ return to values similar to those of cycles 1 to 7, averaging -5.8‰ and -1.1‰, respectively.

6.5 Discussion

The causes and mechanisms leading to deposition of the PLG remain controversial. Outstanding problems include (i) the composition and salinity of brines that formed the gypsum and carbonate layers, and (ii) the relative influence of orbital forcing, Mediterranean-Atlantic exchange dynamics, and eustatic sea-level variability during evaporate deposition. The majority of previous studies have utilised strontium and sulfur isotopes to constrain the water budget during evaporate formation; however, because these tracers are relative insensitive to meteoric input, the multiple factors that can influence basin hydrology have been difficult to deconvolve. Below we discuss our multi-isotope approach to address the outstanding questions of PLG formation and propose an explanation to reconcile the geochemical data.

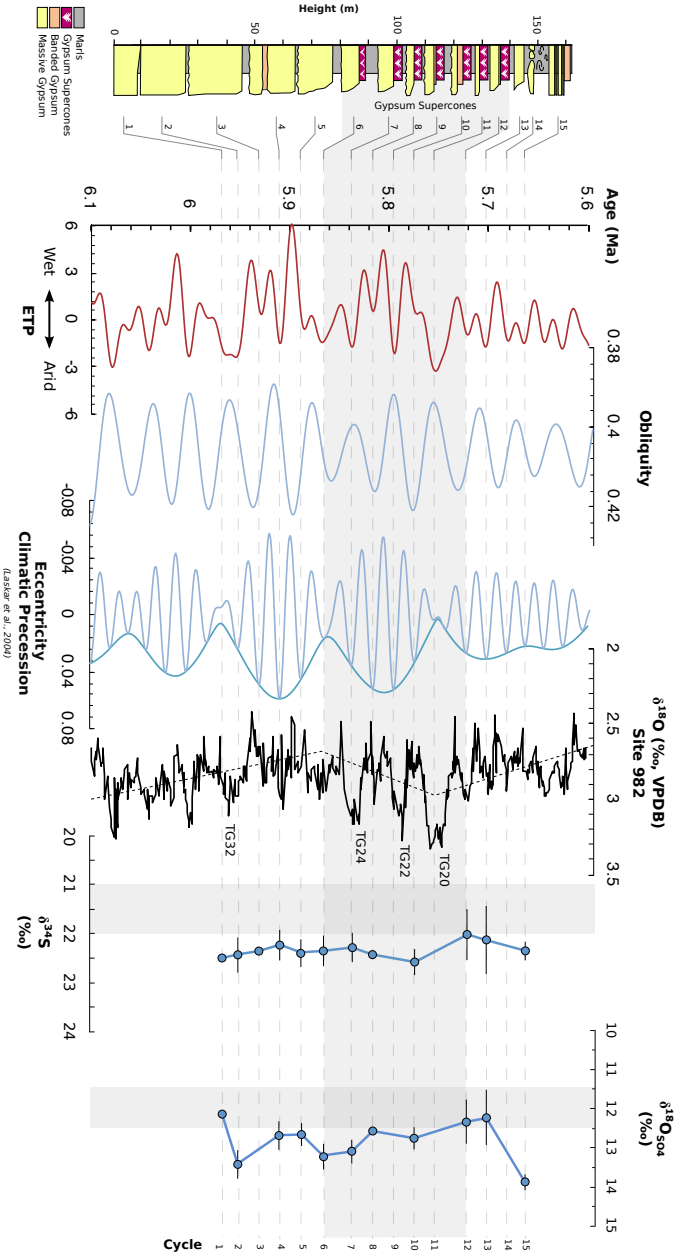

Fig. 6.7. Mean intra-cycle $\delta^{34}S$ and $\delta^{18}O_{SO_4}$ data are plotted against their designated cycle. Error bars define $\pm 1\sigma$ of the data in each cycle. Each gypsum bed of the Yesares Member is plotted in relation to its proposed orbital tuning (Laskar et al., 2004; Lugli et al., 2010; Manzi et al., 2013), where gypsum precipitation correlates with insolation minima. The benthic $\delta^{18}O$ (Hodell et al., 2001; modified by Drury et al., 2018) is also shown, and the major glacial stages are indicated. The horizontal grey band indicates the appearance of gypsum supercone cycles (cycles 6-12). The vertical grey band denotes the range of Late Miocene marine sulfates (Paytan et al., 1998).

6.5.1 Brine composition during PLG deposition

The commonly accepted palaeo-hydrologic models for the formation of the PLG suggest that gypsum precipitated from the evaporation of brines formed by continuous inflow of seawater from the Atlantic Ocean, providing the necessary ion supply (Krijgsman and Meijer, 2008; Topper and Meijer, 2013). Water isotopes of GHW (e.g. Evans et al., 2015) and salinities determined from fluid inclusions (e.g. Natalicchio et al., 2014) suggest that gypsum precipitation may have occurred at lower salinities than those expected during the evaporation of only seawater (~130 g l^{-1}). We applied the approach of Evans et al. (2015) to 12 of the 15 Sorbas PLG cycles.

The $\delta^{18}O$, $\delta^{17}O$ and δD of the water from which gypsum formed ranges between -1.71‰ to 2.27‰, -3.23‰ to 4.38‰ and -26.76‰ to 23.48‰, respectively. If the Yesares Gypsum were to have formed directly from the evaporation of seawater, the expected results would be significantly higher than those measured, probably similar to the evaporated seawater that formed the Salinas gypsum (Fig. 6.2). Additionally, microthermometric salinity data indicate that Messinian fluid inclusions do not have salinities high enough to be within the range of gypsum saturation if derived from the evaporation of seawater alone. This implies that all cycles of the Yesares Gypsum were precipitated from a hybrid brine, consisting of a mixture of seawater and meteoric water. Analysis of the evaporation trajectories (i.e. $\delta^{18}O$ vs d-excess and $\delta^{18}O$ vs ^{17}O-excess) and isotope mass-balance (Gázquez et al., 2018) demonstrates that the recorded isotopic composition cannot be formed from the simple evaporation of water in a closed basin, where evaporating water evolves along a trajectory towards the isotopic end-point (Surma et al., 2018). Basin recharge (mixing) drives the water's isotopic composition along a trajectory below the expected evaporation trend (Fig. 6.2), as has been demonstrated to occur in other modern hydrologic systems (Herwartz et al., 2017; Surma et al., 2018). Basin recharge by meteroric water is the only mechanism that can produce the observed water isotope variability for the Sorbas PLG, suggesting that gypsum formed at a steady state with continuous inflow of freshwater.

The significant freshwater contribution to the mother brines recorded by GHW and salinity deduced from fluid inclusions is confirmed by strontium isotope data obtained from the same samples. Our results from the PLG of the Sorbas Basin show that $^{87}Sr/^{86}Sr$ values are significantly lower than global seawater values, with an increasing departure from global ocean $^{87}Sr/^{86}Sr$ values up-section (Fig. 6.6). Given the uncertainties on both the riverine strontium concentration and isotopic ratio during the Messinian, early studies concluded that these near-oceanic $^{87}Sr/^{86}Sr$ values required the PLG to precipitate from water dominated by seawater (e.g. Flecker et al., 2002; Lu and Meyers, 2003; Flecker and Ellam, 2006; Lugli et al., 2007). Indeed, Evans et al. (2015) argued that if a significant amount of strontium and

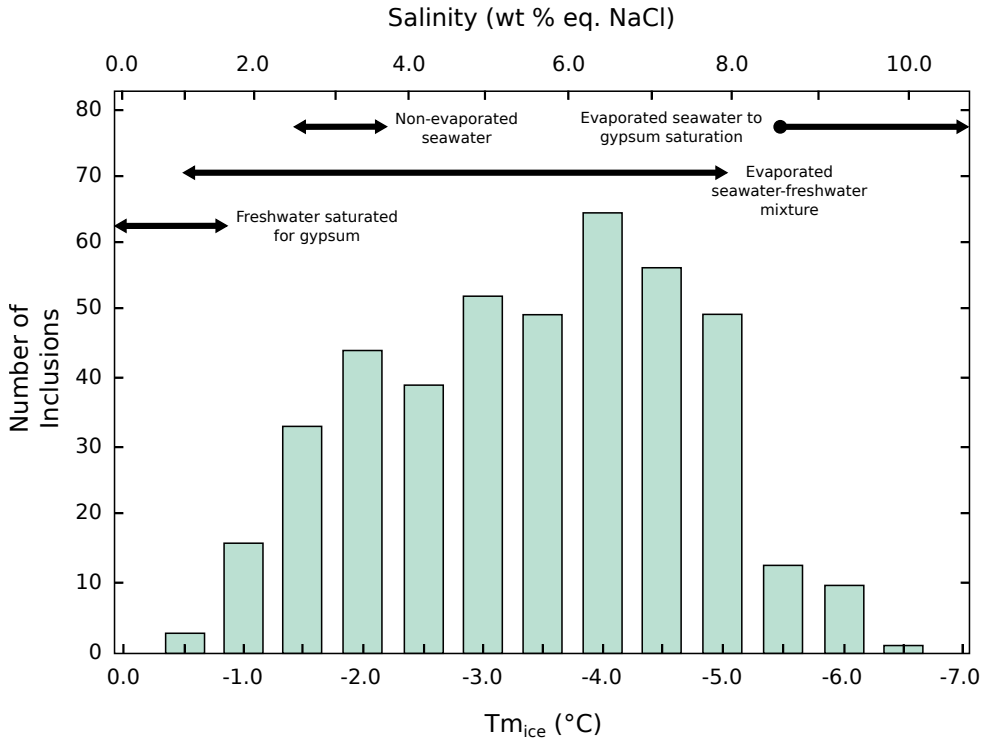

Fig. 6.8. Histogram of Tm_{ice} measured in PLG fluid inclusions.

sulfate used to make the PLG were derived from terrestrial sources, the $^{87}Sr/^{86}Sr$, $\delta^{34}S$ and $\delta^{18}O_{SO_4}$ composition of the gypsum would fall toward lower riverine values (Chapter 5). Simple mixing simulations using the Messinian marine $\delta^{34}S$ (~22‰, 2600 ppm sulfate) and the weighted modern major Mediterranean river inputs (~0‰, ~30 ppm sulfate) (Longinelli and Cortecci, 1970) indicate that a dilution of over 90-95% of the Mediterranean Sea is required to shift the $\delta^{34}S$ away from the marine value. Sulfate isotopes are therefore highly insensitive to continental contributions. Additionally, Topper (2013) demonstrated that when Mediterranean river discharge constitutes around 40% of the water fluxes into a basin, the basinal $^{87}Sr/^{86}Sr$ value will deviate measurably from relatively high oceanic values (~0.70900) toward lower riverine values of the Rhone (~0.70872) and the Nile (~0.70600) (Flecker and Ellam, 2006). The high precision of our Sr isotope results allow us to confirm that gypsum precipitation occurred in a water body strongly influenced by freshwater input. The increased departure of measured $^{87}Sr/^{86}Sr$ from global ocean values indicates a progressive reduction of marine inflow and the increasing influence of continental input up-section.

The high proportion of freshwater inflow into the Mediterranean combined with surface evaporation leading to a denser fluid that flowed towards the deeper parts of the basin

would have led to significant water column stratification (Simon and Meijer, 2017). Indeed, homogenous $\delta^{34}S$ and $\delta^{18}O_{SO_4}$ of gypsum of both the Yesares Member (21.1‰ < $\delta^{34}S$ < 23.3‰; 10.4‰ < $\delta^{18}O_{SO_4}$ < 14.9‰) and Caltanissetta Basin (22.4‰ < $\delta^{34}S$ < 23.2‰; 12.7‰ < $\delta^{18}O_{SO_4}$ < 14.6‰) are higher than expected for Late Miocene seawater ($\delta^{34}S$ ~ 21‰; $\delta^{18}O_{SO_4}$ ~ 12‰), likely driven to higher values by cyclic bacterial sulfate reduction in a stratified water column (Fig. 6.7) (De Lange and Krijgsman, 2010; García-Veigas et al., 2018). A scenario of freshwater inflow resulting in water column stratification is further supported by evidence of a changing carbon source in the Sorbas Basin: low $\delta^{13}C$ values in some interbedded carbonates indicate that freshwater inputs resulted in an increase in primary production in the surface water supplying the primary carbon source for microbial sulfate reduction in the water column (Torfstein and Turchyn, 2017) (Fig. 6.9).

6.5.2 Orbital, tectonic and glacio-eustatic control on basin hydrology

Our high resolution, multi-isotope approach allows us to more accurately link isotopic variations to the climate-driven hydrological changes within a single precessional cycle. Within the Sorbas Basin PLG, oxygen and hydrogen isotopes of GHW, $^{87}Sr/^{86}Sr$ and $\delta^{44/40}Ca$ display distinctive patterns of isotopic variability both (i) within individual gypsum-marl cycles, related to the arid-humid climate oscillations controlled by precessional forcing, and (ii) over longer time scales in relation to eustatic sea-level changes superimposed on longer-term tectonic restriction and the amplitude modulation of precession by eccentricity.

6.5.2.1 Precessional scale orbital and tectonic control on basin hydrology

Gypsum deposition in the PLG is thought to occur at the precession maxima (i.e. minimum summer insolation when summer solstice and aphelion coincided) when evaporation exceeded precipitation during periods of dry climate, whereas marl deposition is assumed to have occurred at precession minima (maximum summer insolation when summer solstice and perihelion coincided) when rainfall increased (Krijgsman et al., 1999, 2001). Within a depositional cycle, variations in water isotopes (Evans et al., 2015) and $^{87}Sr/^{86}Sr$ (e.g. Flecker and Ellam, 2006; Lugli et al., 2010; Topper et al., 2014; Reghizzi et al., 2018) have been shown to correlate with the changing freshwater budget forced by orbital precession. Wide sampling intervals and lack of results from the interbedded carbonate layers from previous studies have resulted in tenuous links between measured isotopic variations and climatic forcing.

Firstly, we are able to confirm the inference that carbonate marl deposition occurred at precession minima when rainfall increased (Krijgsman et al., 1999, 2001; Lugli et al.,

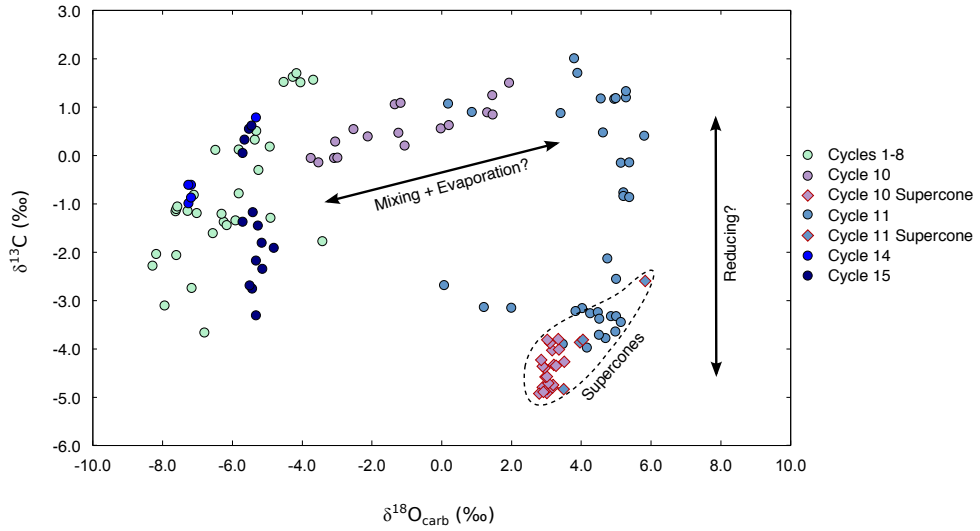

Fig. 6.9. Cross-plot of δ^{18}O vs δ^{13}C of carbonates from the marl intervals within the Yesares Formation.

2007; Roveri et al., 2014a). By isolating the carbonate phase from the surrounding clays (see Chapter 4), we could subsequently measure the Sr and Ca isotopes to identify the isotopic composition of the mother fluids from which they formed. The ^{87}Sr/^{86}Sr results of the carbonate marls demonstrate that these horizons are always lower than those of the interbedded gypsum layers. These data agree with Sr isotope analysis of mollusc shells that, with one exception, yield values equal to or lower than that of gypsum measured in the same section (Reghizzi et al., 2017). Additionally, $\delta^{44/40}$Ca values of the interbedded carbonates are generally lower than the $\delta^{44/40}$Ca of the gypsum (both before and after correction for fractionation factors), strongly suggesting that the freshwater flux to the basin was greater during the deposition of the carbonate marls (Fig. 6.10).

During the climatic transition from precession minimum to precession maximum, river input is expected to decrease while E/P increases, leading to the precipitation of gypsum horizons. In Chapter 5, it was shown that, in a gypsum single cycle, δ^{18}O and δD of GHW increased from low values at the base of the cycle to a maximum in the massive gypsum palisade, and decreased again to lower values in the supercones at the top of the cycle. This pattern, together with changes in mineralogy in the carbonates at the base of the cycle (calcite–dolomite–gypsum), is consistent with a precession-driven change in climate. Additionally, box modelling has shown that ^{87}Sr/^{86}Sr is expected to increase toward global ocean values during the arid phase as the inflow from the riverine input of Sr decreases during the precession maximum phase (Topper et al., 2014).

We have identified important differences in the thickness and isotopic composition of the gypsum in relation to the appearance of differing facies within the PLG. Cycles 1-5

are composed of thick homogenous massive selenite deposits; our GHW data show that $\delta^{18}O$ and δD display no trends within the cycles and do not mirror the cyclic trend observed previously in cycle 10 (Chapter 5; Evans et al., 2015). From the first occurrence of branching supercones in cycle 6, however, the cyclic trends in $\delta^{18}O$ and δD become regular and highly consistent (Fig. 6.4). Strontium concentrations (e.g. Rosell et al., 1998) and salinity deduced from fluid inclusions in gypsum (Fig. 6.3) also show relatively uniform values in the lower beds (i.e. cycles 1 to 4), but more variable values that often increase upwards in the sixth gypsum cycle and above.

The $\delta^{44/40}Ca$ and $^{87}Sr/^{86}Sr$ values obtained from the PLG also display consistent variability within each gypsum layer. The lowest $\delta^{44/40}Ca$ and $^{87}Sr/^{86}Sr$ values are usually found at the base of each gypsum bed, although the standard deviation of both $\delta^{44/40}Ca$ and $^{87}Sr/^{86}Sr$ within each cycle is low (Fig. 6.4 and Fig. 6.5). Importantly, there is no significant relationship between $\delta^{44/40}Ca$ and crystal size, and thus the growth kinetics cannot be considered as the main controlling factor of $\delta^{44/40}Ca$ in the selenitic gypsum facies. The low intra-cycle isotopic variability in the lower gypsum beds (i.e. cycles 1 to 4) results in a weak correlation between $\delta^{44/40}Ca$ and $^{87}Sr/^{86}Sr$ within each cycle. This lack of correlation suggests that the slight increase in $\delta^{44/40}Ca$ from the base to the top of individual cycles could reflect ongoing Rayleigh fractionation in the brine during gypsum precipitation, rather than changes to the meteoric and/or marine input. This indicates that a steady state was achieved after sufficient calcium was removed from the brine such that the input flux was equivalent to the output precipitation. Thus, crystallisation took place beneath a stable and protective pycnocline in marginal Mediterranean water bodies, resulting in near-constant $\delta^{44/40}Ca$ and $^{87}Sr/^{86}Sr$ values within each cycle.

The upper cycles containing supercones (i.e. cycles 6 to 12) show a stronger correlation between $\delta^{44/40}Ca$ and $^{87}Sr/^{86}Sr$ ($R^2 = 0.53$), where low isotope values are usually found at the base of each gypsum bed that increase to higher values at the top. These data suggest that gypsum precipitation at the base of each cycle started from a water body strongly influenced by freshwater input with a progressive weakening of riverine input towards the top of each cycle. Isotopes of GHW, however, are relatively high in the massive selenite at the base of the gypsum cycles and fall towards lower values in the supercone structures. This indicates that the freshwater-dominated fluid that formed the massive gypsum at the base of each cycle required relatively high levels of evaporation to reach gypsum saturation, resulting in increased $\delta^{17}O$, $\delta^{18}O$ and δD values. The supercone structures likely formed from fluids that were composed of less meteoric input compared to the base of the cycle, but were more enriched in calcium and sulfate ions, requiring less evaporative enrichment to reach gypsum saturation. The necessary ionic input may have resulted from evaporite recycling

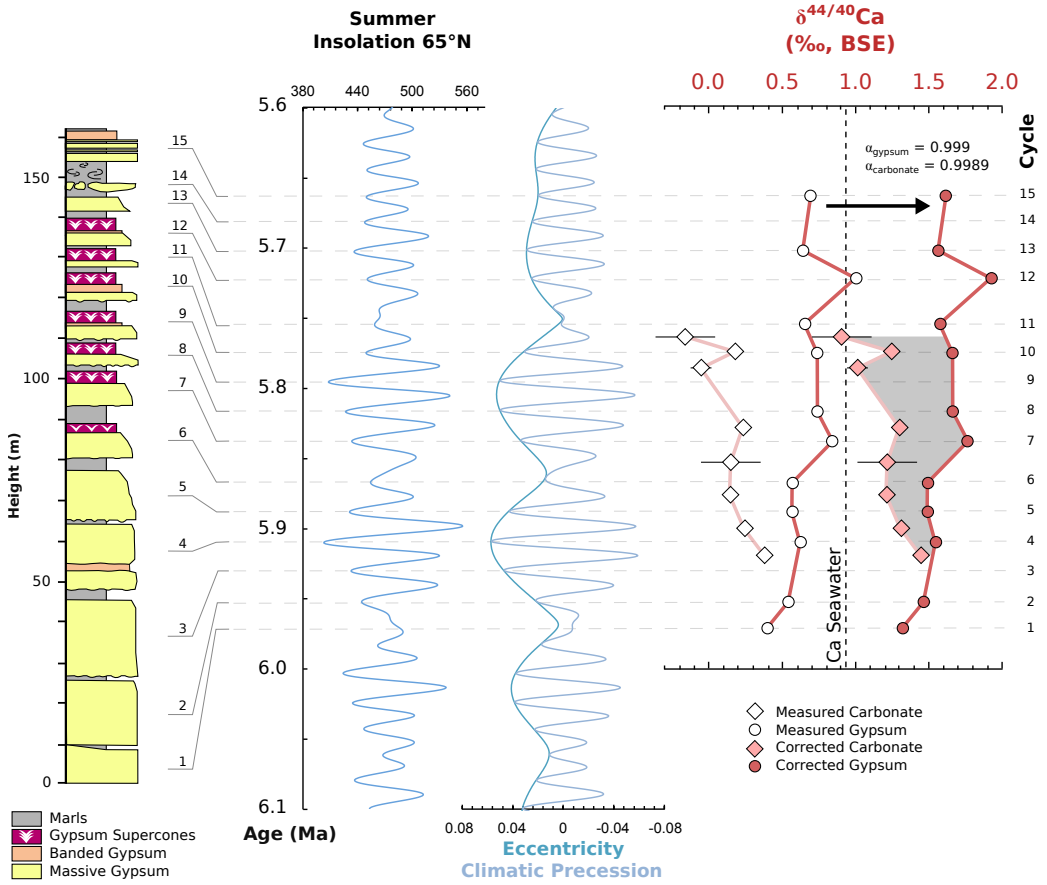

Fig. 6.10. Mean intra-cycle $\delta^{44/40}$Ca data of the gypsum and interbedded carbonates are plotted against their designated cycle. Error bars define $\pm 1\sigma$ of the data in each cycle. Note that carbonate data plotted between the dashed lines denote carbonate samples located between gypsum beds, whereas carbonate samples that are plotted on the dashed lines denote carbonate samples that are located in supercones. Measured values (open diamonds) are corrected for calcium fractionation factors (Tipper et al., 2010; Harouaka et al., 2014). Note that the relative difference in gypsum and carbonate $\delta^{44/40}$Ca increases up-section.

from the lower cycles (Evans et al., 2015; Rossi et al., 2015), and confirms that gypsum crystallisation was likely controlled by the oscillating level of a pycnocline (Manzi et al., 2009; Lugli et al., 2010).

The influence of decreasing Mediterranean-Atlantic exchange driven by tectonic restriction can largely explain the intra-cycle isotopic profiles and changes in gypsum bed thickness observed in the Sorbas section. The lower 4 cycles display relatively homogenous isotopic profiles and massive gypsum deposits, reflecting deposition under conditions of hydrological stability and relatively deep (~200 m) waters, whereas the more variable results from the upper cycles and thinner gypsum beds result from a shallowing of the basin. Tectonic modification of the Atlantic gateway directly controlled the seawater input to the Mediterranean (Simon et al., 2017; Krijgsman et al., 2018), resulting in a reduction in seawater input, and thus the reduction in gypsum bed thickness, up-section. If tectonics were the only cause of the decrease in Mediterranean-Atlantic exchange and the patterns of the expression (i.e. thickness and facies) of the gypsum cycles, however, a uni-directional trend in facies and geochemical profile reflecting uplift and the gradual constriction of the Mediterranean-Atlantic gateways would be expected. This is not observed: strontium isotopes in gypsum, for example, display a gradual, but non-unidirectional divergence from the seawater curve up-section, with slight reversals in the general trend of decreasing $^{87}Sr/^{86}Sr$ at ~5.84 Ma and 5.72 Ma (Fig. 6.6). Step changes in calcium isotopes track the variability in $^{87}Sr/^{86}Sr$. Additionally, the gypsum supercones facies are deposited during periods of both high low eccentricity, indicating that their formation cannot be unilaterally related to long-term changes in precession forcing. Thus, factors other than tectonics and precessional scale orbital dynamics must be involved in the formation of the differing gypsum facies.

6.5.2.2 Glacio-eustatic control on basin hydrology

Global eustatic sea-level changes, as recorded by deep-sea benthic $\delta^{18}O$ variations, potentially influenced the connection between the Atlantic and Mediterranean (Hodell et al., 2001). A comparison of $\delta^{44/40}Ca$ and $^{87}Sr/^{86}Sr$ in gypsum cycles and $\delta^{18}O$ of the carbonate marls with the benthic $\delta^{18}O$ record of ODP Site 982 (Hodell et al., 2001; Drury et al., 2018) provides information on sea-level control of the Mediterranean-Atlantic water exchange during the time of PLG deposition (Fig. 6.6). We suggest that glacio-eustatic changes, superimposed on longer-term tectonic restriction of the Mediterranean-Atlantic exchange, were together responsible for some of the facies and geochemical changes observed in the Sorbas Basin sequence.

A eustatic sea-level influence on PLG deposition was suggested by Manzi et al. (2013), after re-correlation of the MSC-onset to an eccentricity minimum roughly coincident with

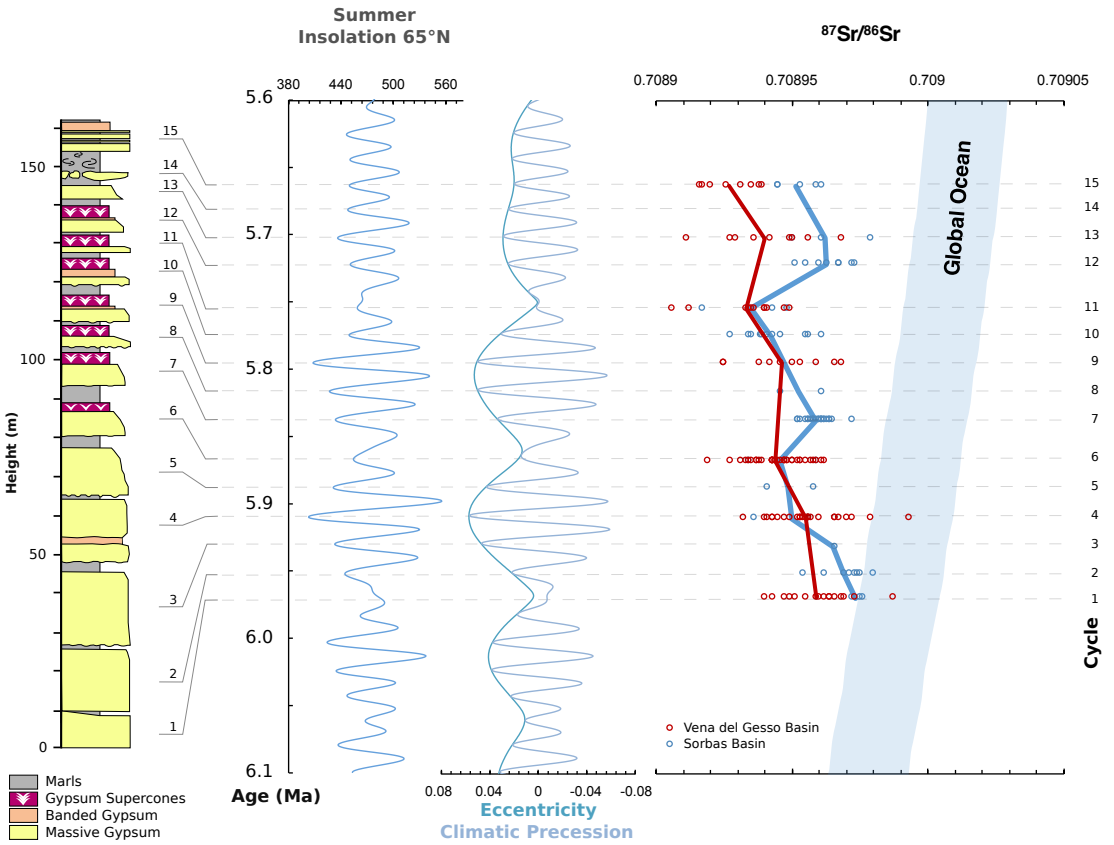

Fig. 6.11. Sr isotope data of the PLG from Vena del Gesso Basin, Northern Italy (Reghizzi et al., 2018), and the Sorbas Basin (this study) are calibrated with the orbital eccentricity and precession curves (Laskar et al., 2004). Note that the data from the Vena del Gesso Basin displays a progressive divergence from the oceanic curve up-section, whereas data from the Sorbas Basin show shifts returning towards the seawater curve in PLG cycles 7 and 12.

glacial stage TG32. It is interesting to note that TG32 is weakly expressed in the Site 982 record, potentially indicating that tectonic restriction was the main driving force that initiated the start of the MSC (Fig. 6.6). However, the appearance of gypsum supercone facies in cycle 6 and a stepped increase in $\delta^{44/40}$Ca and ^{87}Sr/^{86}Sr during the transition from cycle 6 to 7 can be linked to the start of a cooling phase, characterised by glacial conditions in the northern hemisphere and global sea-level fall recorded by increasing benthic δ^{18}O at Site 982 (Lugli et al., 2010; Dela Pierre et al., 2011; Manzi et al., 2013). The step change in our $\delta^{44/40}$Ca and ^{87}Sr/^{86}Sr data is coincident with glacial stages TG 26 and TG24 and the transition out of an eccentricity minimum phase, indicative of a reduction in both seawater and freshwater input due to the modulation of precession by eccentricity. The resultant change in sea level governed by both eustatic variability and eccentricity modulation of precession likely resulted in the fluctuation of the pycnocline and the formation of branching gypsum units.

The $\delta^{44/40}$Ca and ^{87}Sr/^{86}Sr in both the gypsum and the interbedded carbonates progressively diverge from global ocean values from cycle 7 to 11, during the period of increased cooling and global sea-level fall through TG24, 22 and 20. The strong correlation between $\delta^{44/40}$Ca and ^{87}Sr/^{86}Sr in the upper part of the PLG (i.e. cycles 6 to 12) indicate that both systems are reposing to changes in water source and an increase in the freshwater fraction up-section. The departure of the ^{87}Sr/^{86}Sr from the global oceanic curve over these cycles in the Sorbas PLG is also characterised by a similar evolution of ^{87}Sr/^{86}Sr in PLG deposits from the Vena del Gesso basin (northern Italy; Reghizzi et al., 2018) (Fig. 6.11). Due to gaps in the Vena del Gesso cycle analysis, however, the Sr profile does not display the slight reversals in the general trend of decreasing ^{87}Sr/^{86}Sr up-section.

Glacial stage TG20, the largest glaciation during the deposition of the PLG, is expressed both in variations in the isotopic composition of gypsum in cycles 9 to 11, as well as a change in carbonate mineralogy during this period (Fig. 6.6). The ^{87}Sr/^{86}Sr of cycle 9 to 11 displays the greatest divergence away from the global ocean curve. Additionally, the progressive increase in carbonate δ^{18}O and transition from calcite- to dolomite-dominated carbonate marls from cycle 9 to 11 indicate an highly restricted oceanic inflow during this period, providing clear evidence that global sea-level variability influenced the mineralogy and geochemistry of the gypsum-marl cycles. The terminal supercone cycle and the final step change in $\delta^{44/40}$Ca and ^{87}Sr/^{86}Sr coincides with the termination of TG20, indicating the occurrence slight seawater incursion after this phase (Fig. 6.6). Thus, the non-unidirectional divergence of $\delta^{44/40}$Ca and ^{87}Sr/^{86}Sr confirms that glacio-eustatic changes, superimposed on longer-term tectonic restriction of Mediterranean-Atlantic exchange and orbital forcing, were responsible for the differing geochemical profiles observed in the

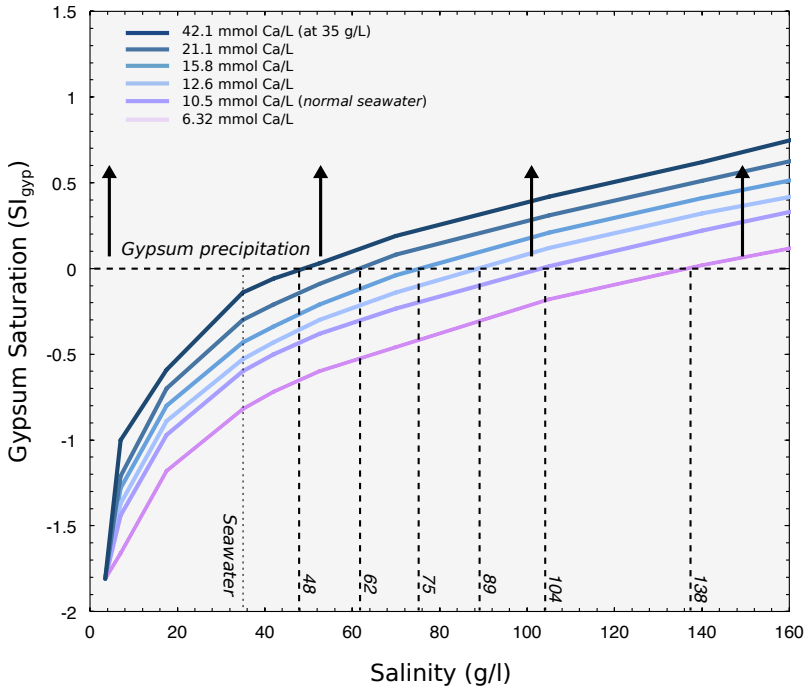

Fig. 6.12. Graph showing the salinity at which the gypsum saturation (SI_{gyp}) is reached during the evaporation seawater containing different calcium [Ca^{2+}] and sulfate [$SO_4{}^{2-}$] concentrations. Evaporation of normal seawater is represented by curve with 10.5 mmol l^{-1} Ca at normal seawater salinity and shows that gypsum will precipitate at salinities of ~104 g l^{-1}. Other curves represent an addition or removal of calcium relative to the starting seawater concentration, where the stated ratio of [Ca^{2+}] to [$SO_4{}^{2-}$] (i.e. x mmol l^{-1} Ca^{2+}: 28.9 mmol l^{-1} $SO_4{}^{2-}$]) increases/decreases at the same rate.

Yesares Member.

After cycle 12 and TG20, global sea-level was likely higher, but the continued tectonic uplift likely reduced the exchange to a point whereby thick gypsum deposits were prevented from forming in the sequence. As tectonic restriction continued, the gypsum facies disappear form the upper sequence and are replaced by freshwater limestone beds.

6.5.3 A mechanism for PLG formation: an orbitally forced dissolution flux

An inconsistency exists between the large proportion of freshwater implied from Sr and GHW isotopes during the formation of the PLG, and the source of calcium and sulfate ions needed for the formation of such large gypsum deposits. A mechanism other than simple evaporation of seawater is needed to explain the lower salinities inferred from fluid inclusion and isotopic results in the PLG.

Natalicchio et al. (2014) and Evans et al. (2015) proposed that gypsum formed from a mix of seawater and Ca^{2+}- and $SO_4{}^{2-}$-enriched freshwaters derived from partial dissolution and recycling of coeval marginal evaporite deposits. The recycling of carbonate and gypsum deposits would have occurred in marginal areas of the basin where evaporites were deposited previously. Alternatively, recycling could also occur via in situ early recrystallisation, which will not affect the $\delta^{34}S$ or $\delta^{18}O_{SO_4}$ values, but will change the isotopic composition of the GHW, salinity and strontium concentration (e.g. Longinelli, 1979). To date, a late Miocene gypsum deposit that formed solely from the evaporation of seawater has not been found in the Mediterranean, and the consistent $^{87}Sr/^{86}Sr$ profiles between differing circum-Mediterranean basins indicate that the original fluids were composed of a large percentage of freshwater. While recycling processes likely enhanced ionic input at a local scale, basin-wide recycling without evidence for evaporative marine gypsum (either due to physical absence or lack of discovery) is harder to justify.

Measurement of both Ca and Sr isotopes in PLG sections provide clues to the origin of the ion source for gypsum formation. The $\delta^{44/40}Ca$ values generally track the variations in $^{87}Sr/^{86}Sr$ of the gypsum layers up-section, suggesting that the same mechanism of enhanced continental runoff is impacting both isotope systems. The low $^{87}Sr/^{86}Sr$ on the freshwater input is indicative of the weathering of carbonate rocks, and weathering of carbonate with low $\delta^{44/40}Ca$ (~-0.1‰) would also result in a lowering of $\delta^{44/40}Ca$ during increased fluvial discharge. The dissolution of carbonate and addition of calcium to the Mediterranean basin may provide the additional ion source needed to form gypsum at lower than predicted salinities.

The increased weathering of carbonates inferred from fluctuations in calcium and strontium isotopes provides a potential explanation for the unexpectedly low salinities found within many of the PLG of many Mediterranean marginal basins. Both the solubility of gypsum (K_{sp}) and the product of dissolved calcium [Ca^{2+}] and sulfate [$SO_4{}^{2-}$] determines gypsum precipitation. If $\left[Ca^{2+}\right] \times \left[SO_4{}^{2-}\right] > K_{sp}$, then gypsum super-saturation is reached and will precipitate. Because normal seawater (0.01 mol/l [Ca^{2+}], 0.028 mol/l [$SO_4{}^{2-}$]; $K_{sp}{}^{CaSO_4 \cdot 2H_2O} =\sim 0.28 \times 10^{-3}$) is under-saturated for gypsum (~2.6×10^{-3}) (Broecker, 1982), evaporation is needed to increase the concentration of dissolved [Ca^{2+}] and [$SO_4{}^{2-}$]. Seawater salinities are required to rise from ~35 ppt to ~130 ppt (Warren, 2016) before gypsum saturation is reached, requiring the loss of ~70% of the starting volume. By adding [Ca^{2+}] and/or [$SO_4{}^{2-}$] to the system, the product of $\left[Ca^{2+}\right] \times \left[SO_4{}^{2-}\right]$ will rise without the need for large amounts of evaporation (Fig. 6.12). The addition of calcium ions from the large scale weathering of the African continent will mean that the gypsum saturation level can be reached at lower salinities. Additionally, unlike the weathering of ancient evaporites

that could potentially alter the $\delta^{34}S$ or $\delta^{18}O_{SO_4}$ of the gypsum, the dissolution of carbonates would only alter the calcium and strontium isotopic signatures.

6.5.4 Conclusions

Multi-isotope analysis of 12 of the 15 cycles of the Yesares Member indicate that PLG deposition was influenced by hydrologic dynamics that were governed by precessional-scale climate oscillations, tectonics and eustatic sea-level change. The homogeneous isotopic contents recorded in the lower cycles of the sequence suggest hydrological stability and relatively deep waters, whereas these conditions are progressively modified upwards and greater isotopic variability is seen in the upper part of the section, suggesting a shallowing trend driven by tectonic restriction. Critically, reversals of the general trend of decreasing in Sr isotopes up-section together with step changes in Ca isotopes, as well as high $\delta^{18}O_{carb}$ and anomalous mineralogy of the co-occurring marls, indicates eustatic sea level variability also controlled the seawater input by affecting the rate of Mediterranean-Atlantic exchange. The gypsum of all cycles was formed in a hybrid brine consisting of a seawater body strongly influenced by abundant freshwater input that increased up-section. The freshwater input likely enhanced the dissolved carbonate ion flux and stratification of the Mediterranean basin, facilitating gypsum precipitation.

Chapter 7

Upper Evaporites of the Messinian Salinity Crisis

***Nicholas P. Evans**, Fernando Gázquez, Thomas K. Bauska, Luke Bridgestock, Harold J. Bradbury, Alexandra V. Turchyn, and David A. Hodell.*

This chapter aims to address fundamental questions related to mechanisms responsible for the salinity fluctuations experienced by the Mediterranean basin during the terminal stages of the Messinian Salinity Crisis (MSC). Analysis of gypsum hydration water (GHW) from both onshore and deep basin deposits is conducted to obtain the δ^{18}O, δD, ^{17}O-excess, and d-excess of the mother fluids from which they formed. The measurements are combined with salinity deduced from fluid inclusion melting temperatures, strontium, calcium, barium and sulfate isotopes in order to reconstruct the hydrological changes in the Mediterranean basin during the late stage of the MSC. The results from the Upper Gypsum (UG) are compared with those of the Primary Lower Gypsum (PLG) deposits (Chapter 6) to contrast the different environments of deposition.

Strontium, calcium and barium isotope data obtained from the onshore UG are significantly lower than results of the PLG deposits, whereas oxygen and hydrogen isotopes of measured gypsum hydration water display higher values. These data demonstrate that the onshore UG deposits formed from intense evaporation of a dominantly freshwater fluid, with a periodic and highly restricted connection to the Atlantic. The deep-basin 'Upper Evaporites' from DSDP/ODP sites 372 and 654 are characterised by similar strontium, calcium and sulfate isotope values to those of the onshore Upper Evaporites. The deep basin water isotope data deviates from the majority of the onshore deposits, however, indicating that variable and heterogeneous hydrologic conditions characterised the deep basins during

evaporite formation.

7.1 Introduction

The reduction of the hydrological exchange between the Mediterranean Sea and Atlantic Ocean during late Miocene ultimately culminated in the deposition of large volumes of sulfate and chloride minerals in the Mediterranean basin during the event known as the Messinian Salinity Crisis (MSC; 5.97 Ma to 5.33 Ma) (Roveri et al., 2014a). According to the consensus model of the MSC (CIESM, 2008), the acme of evaporite precipitation was associated with the deposition of halite between 5.60 Ma and 5.55 Ma (stage 2) coupled with the incision of deep canyons at the basin margins, both a result of a significant sea level drop of greater than 1500 m. The subsequent deposits include the Upper Evaporites (stage 3.1; 5.55 Ma to 5.42 Ma) and brackish-water 'Lago-mare' (stage 3.2; 5.42 Ma to 5.33 Ma) units in marginal to intermediate settings. The Upper Evaporites typically consist of gypsum-marl alternations that represent a response to precession-driven climate oscillations (e.g. Manzi et al., 2009), similar to stage 1 PLG evaporitic cycles (Chapter 6). An evaporite layer in the deep Mediterranean basin has also been identified from seismic data and is thought to be coeval to the onshore Upper Evaporates (see Roveri et al., 2014a). The topmost part of these basinal units were sampled during DSDP Leg 13 in 1970, DSDP Leg 42A in 1975, ODP Leg 107 in 1986, and Legs 160 and 161 in 1995.

Debate is still ongoing regarding the palaeoenvironmental and hydrological conditions that prevailed during stage 3 of the MSC, and how they differ from the conditions that occurred during the formation of the older PLG. The occurrence of brackish water fauna such as ostracods with Black Sea affinity (Gliozzi et al., 2007; Stoica et al., 2016) suggest that shallow, brackish lake environments existed both at the bottom of a desiccated Mediterranean and around its margins (e.g. Hsü et al., 1973; Orszag-Sperber, 2006). The discovery of marine fish remains (e.g. Carnevale et al., 2006), however, indicates a continuous or episodic flux of Atlantic waters into the Mediterranean during deposition of the stage 3 evaporites.

Here, the hydrological history of the last stage of the MSC from both onshore (Caltanissetta Basin, Eraclea Minoa section, Sicily) and offshore (DSDP Leg 42A site 372 and ODP Leg 107 site 654) deposits are determined. To estimate the composition of the fluids that formed the Upper Evaporites in stage 3, triple oxygen and hydrogen isotopes of GHW, strontium ($^{87}Sr/^{86}Sr$) and calcium ($\delta^{44/40}Ca$), barium ($\delta^{138/134}Ba$), sulfur ($\delta^{34}S$), oxygen isotopes of sulfate ($\delta^{18}O_{SO_4}$) and salinity (deduced from fluid inclusion melting temperatures) were measured. The $^{87}Sr/^{86}Sr$, $\delta^{44/40}Ca$, $\delta^{138/134}Ba$ and GHW isotopes values are

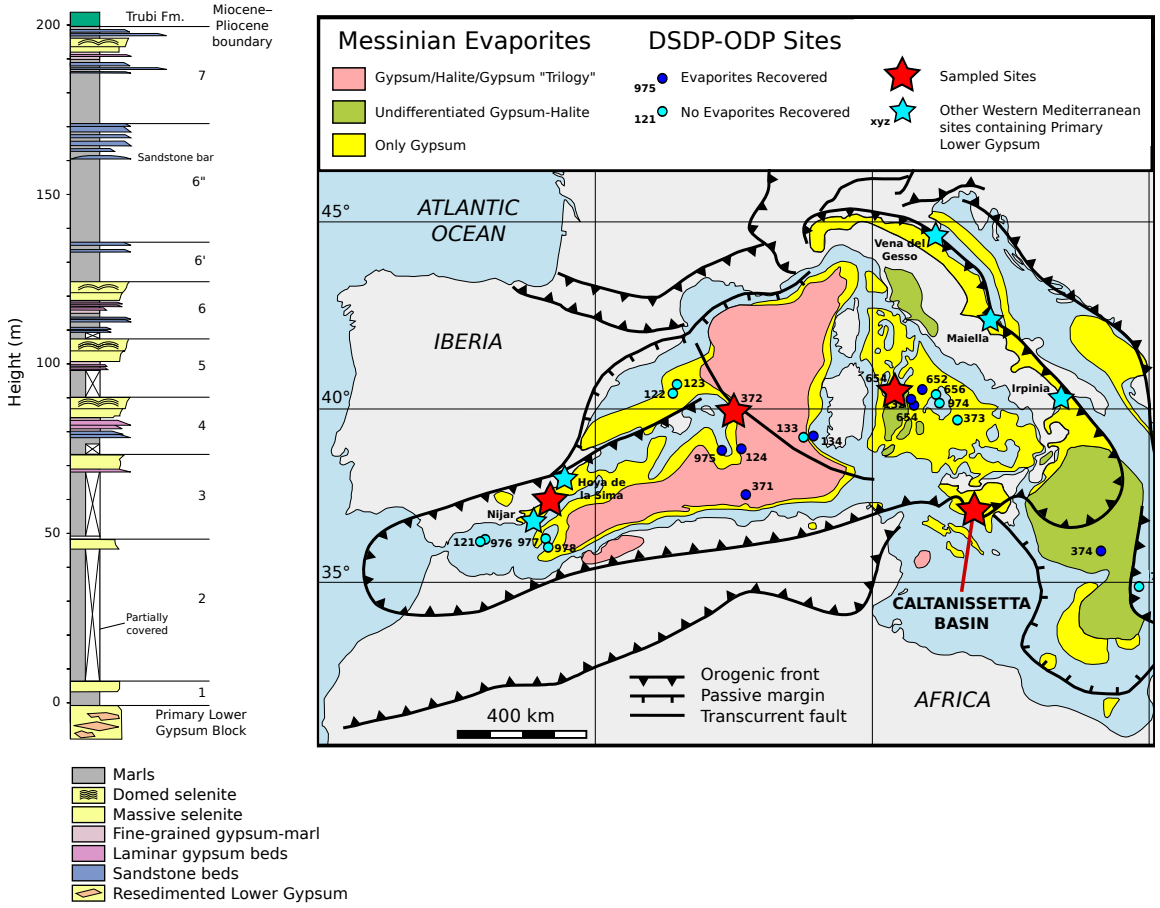

Fig. 7.1. (**Left**) Stratigraphic section of the 7 gypsum-marl cycles found at Eraclea Minoa, Caltanissetta Basin, Sicily (after Manzi et al., 2009). (**Right**) Map of the Messinian evaporites in the Mediterranean and the sampled sites including onshore basins, ODP Leg 107 site 654 and DSDP Leg 42A site 372. Also shown is the location of other DSDP-ODP boreholes in which Messinian evaporites were recovered, as well as other PLG sections found in marginal basin settings. Modified after Rouchy and Caruso (2006) and Roveri et al. (2014a).

significantly different from both the global ocean and PLG deposits. The data indicate that the proportion of oceanic water reaching the Mediterranean was significantly reduced during stage 3, and large variations in the hydraulic regime occurred during the gypsum-marl cycles.

7.2 Geological setting

7.2.1 Onshore deposits

The onshore record of the MSC is widely accepted to have originally formed in 'marginal' or 'peripheral' basins, i.e. sub-basins formed in the more proximal settings of the Mediterranean basins (Roveri et al., 2014a). Exposures on Sicily, for example, show alternations of gypsum and marl beds. The most complete stage 3 successions are found at Eraclea Minoa, Sicily, where 10 sedimentary cycles (7 with gypsum) have been recognized (Van der Laan et al., 2006; Hilgen et al., 2007; Manzi et al., 2009) overlaying a 'Resedimented Lower Gypsum' (RLG) block (Fig. 7.1).

According to Manzi et al. (2009) the UG facies include: marl and thin-bedded sandstone packages; graded sandstone beds (unit S1); fine-grained gypsum and grey marl graded beds (unit G1a); fine-grained laminar gypsum beds (unit G1b); selenite crusts (unit G2a); decimetre-thick massive selenite beds (which are separated by thin marl horizons up to ~30 cm thick) (unit G2b); and domed selenite structures (unit G2c) (Fig 4.6; Chapter 4).

Sixty-seven gypsum samples and 8 carbonate marl samples were chosen from cycles 3, 5 and 7 for isotopic analysis, and cycle 4 was chosen for high-resolution sampling. We also examined 4 samples taken from the RLG at the base of the section.

7.2.2 Offshore deposits

7.2.2.1 DSDP Site 372

We selected 14 gypsum samples of laminated gypsum from of core 8 (189 mbsf to 190 mbsf) of DSDP Site 372 (Fig. 7.2). The site is located at the East Menorca Rise in the Balearic Sea, western Mediterranean (40°01.86'N, 04°47.79'E). The major lithologies are nannofossil marls and clayey mudstones with extremely low coarse terrigenous clastic content, together with gypsum and dolomitic marls in the evaporitic sequence (Hsu and Montadert, 1978). Primary cumulative and clastic gypsum and dolomitic marls are found 150 mbsf to 199.5 mbsf. Lofi et al. (2011) report this unit as a pinch-out wedge of a seismic unit that is

ascribed to the 'Upper Evaporite', while Roveri et al. (2014a) separate the lower and upper halves of the unit into stage 2 and stage 3, respectively, based on $^{87}Sr/^{86}Sr$ stratigraphy.

7.2.2.2 ODP Site 654

Fifty-five samples were taken from cores 27-34 (242-291 mbsf) of ODP Site 654 (Fig. 7.2). Samples were mainly composed of regular laminar gypsum or wavy laminar gypsum (Fig. 6.3; Lugli et al., 2015). ODP Site 654 is located on the upper Sardinia margin of the Tyrrhenian Sea (40°34.76'N, 10°41.80'E) (Shipboard Scientific Party, 1987). Rhythmic alternation of clastic or cumulate gypsum and marls occurs between 242.7 and 313 mbsf (Borsetti et al., 1990). Similar to other deep basin sites, Roveri et al. (2014b) separate the upper and lower half of this unit and correlate the respective layers to MSC stages 3 and 2.

7.3 Results

7.3.1 Gypsum Hydration Water (GHW)

One hundred and thirty-six samples representing both onshore and offshore gypsum deposits were analysed (Appendix D; Table D.2). The oxygen and hydrogen isotope composition of the parent water in which the gypsum formed is calculated by correcting for gypsum-water fractionation factors. Fractionation factors were assumed to be 1.0035 and 0.981 for oxygen and hydrogen isotopes, respectively (Chapter 2). The fractionation factors used were selected based on estimated water temperature (~15°C to 20°C) and salinity (<150 g l^{-1}) at the time of gypsum formation, although the corrected values are relatively insensitive to the temperature and salinity chosen (Gázquez et al., 2017). Corrected results are displayed in Fig. 7.3.

Onshore Deposits: All cycles display significantly higher $\delta^{18}O$ and δD values and lower d-excess and ^{17}O-excess values compared to the PLG of the Sorbas Basin (Fig. 7.3 and Fig. 7.4). The $\delta^{18}O$ and δD values remain relatively constant through the section, averaging 4.5 (±1.5) ‰ and 21.5 (±10.9) ‰, respectively, while d-excess and ^{17}O-excess average -14.6 (±2.1) ‰ and -44 (±14) per meg, respectively.

The $\delta^{18}O$ and δD of gypsum mother water show a systematic change through cycle 4 of the UG in the Caltanissetta Basin (Fig. 7.5). The lowest $\delta^{18}O$ and δD values are found in the fine-grained laminar gypsum beds at the base of the cycle. The $\delta^{18}O$ and δD values steadily increase to maximum values of 6.49‰ and 37.24‰, respectively, in the gypsum palisade at ~6 m. The $\delta^{18}O$ and δD values maintain their high values into the dome structures above,

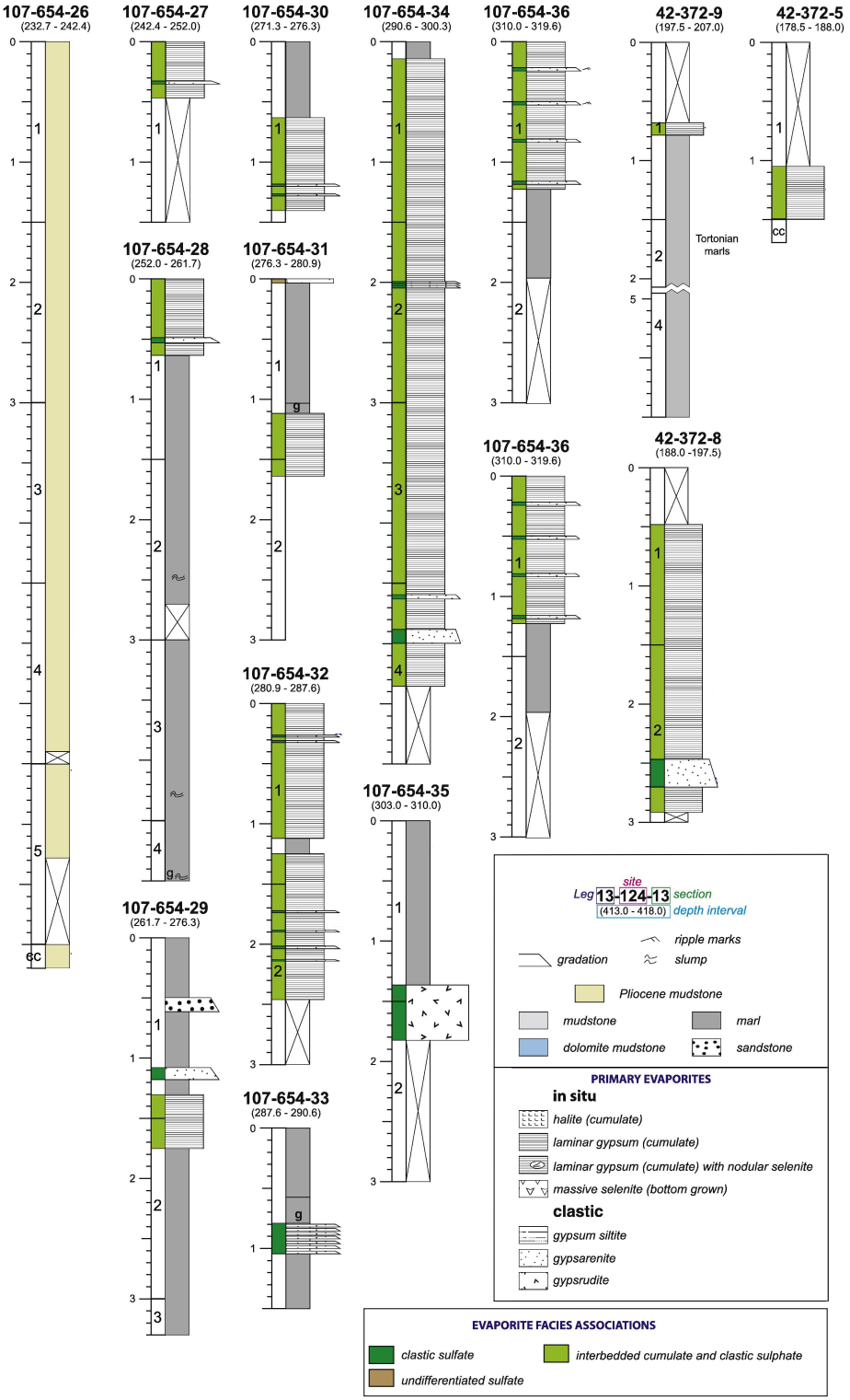

Fig. 7.2. Schematic depiction of the facies that were recovered from the cores of ODP Leg 107 site 654 and DSDP Leg 42A site 372 in the Eastern Mediterranean Sea (after Lugli et al., 2015).

although there is some variability as two samples display low values. Cycle 3 shows a similar trend, where δ^{18}O and δD increase up-section. The δ^{18}O and δD of Cycle 5 and 7 do not follow the same increasing trend up-section, but display relatively constant values over the cycle (δ^{18}O = 4.6 (±2.1) ‰ and 4.3 (±0.7) ‰, respectively).

Offshore Deposits: Mean δ^{18}O and δD from ODP Site 654 averages 1.0 (±0.8) ‰ and 4.9 (±4.2) ‰, respectively, similar to that of the onshore PLG (1.0 [±0.4] ‰ and 0.9 [±9.2] ‰, respectively), although the isotopic range of obtained from the PLG is greater. The δ^{18}O and δD range of gypsum from site 372 is $1.6 < \delta^{18}O < 3.0$‰ and $7.5 < \delta D < 12.2$‰ (Fig. 7.3 and Fig. 7.4). The δ^{18}O and δD also display relatively little variability down-core in both sites 654 and 372 (Fig. 7.5).

7.3.2 Microthermometric analysis

Six samples from the UG of the Caltanissetta Basin were selected for microthermometric analysis (Appendix D; Table D.7). The Tm_{ice} of 46 primary inclusions ranged between -1.2°C and -8.2°C, with an average Tm_{ice} of -4.4°C. Using the revised equation and table for determining the freezing point depression of H_2O–NaCl solutions of Bodnar (1993), average salinity estimates of individual samples range from 5.7% to 9.0% (average 7.1 wt% NaCl equivalent) (Fig. 7.5). Samples from the deep basin sites are composed of fine-grained laminar gypsum beds, and thus individual crystals could not be selected for microthermometric analysis.

7.3.3 Sr isotopes

Seventeen samples from the onshore UG, 7 samples from ODP site 654 and 4 samples from the RLG were processed for strontium isotopic analysis (Appendix D; Table D.5).

Onshore Deposits: For UG samples, the $^{87}Sr/^{86}Sr$ ranged between 0.708719 and 0.708795 (Fig. 7.6). These data show a strong divergence from the strontium isotope values expected for Messinian seawater, which varies from ~0.709015 at 5.55 Ma to ~0.709025 at 5.33 Ma (McArthur et al., 2001). Mean $^{87}Sr/^{86}Sr$ decreases up-section, with mean values in cycle 2 of 0.708783 to 0.708730 in cycle 7.

Within individual cycles of the onshore UG, there is a slight trend toward more positive $^{87}Sr/^{86}Sr$ values toward the top of each gypsum layer (Fig. 7.5). Within cycle 4, strontium concentrations increase from 595 ppm at the base of the cycle to 1333 ppm at the top.

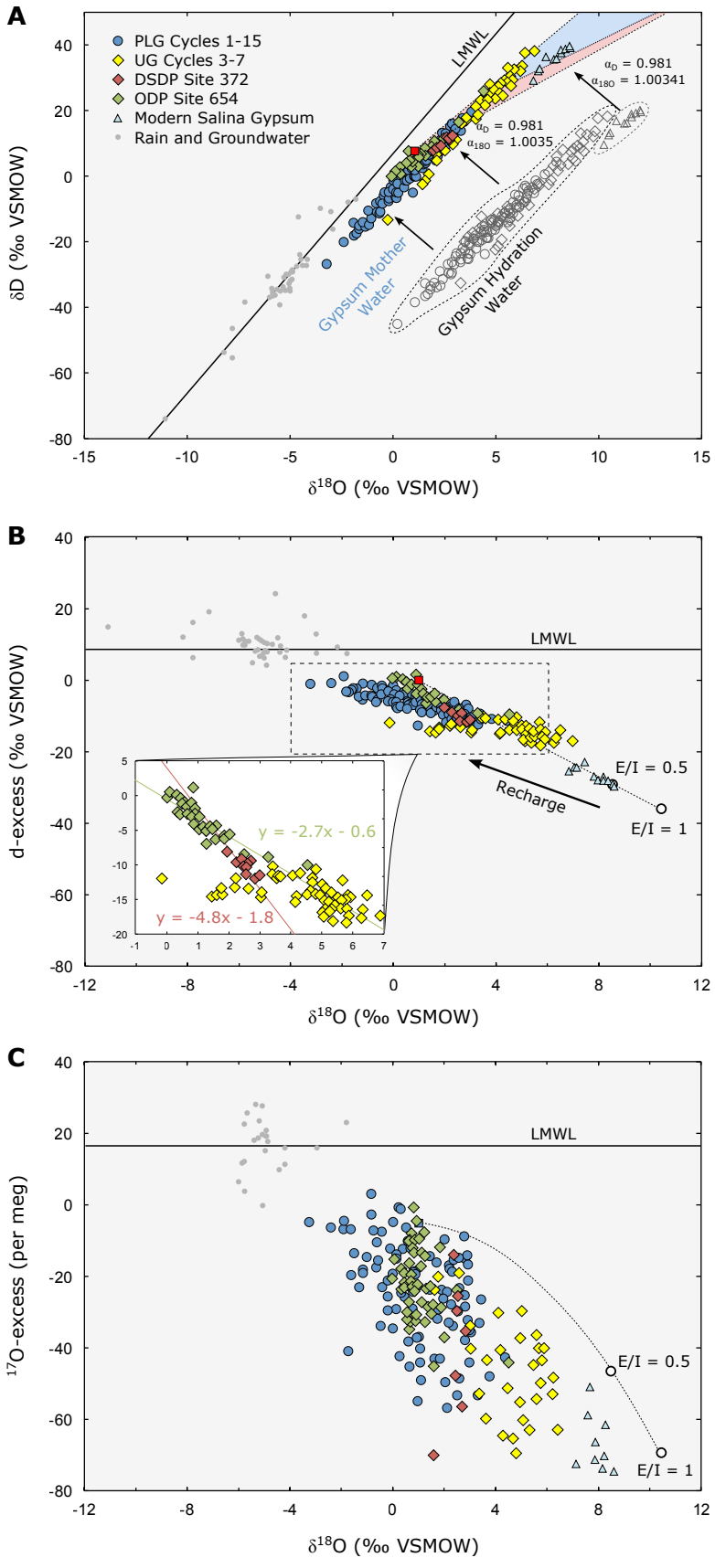
A
PLG Cycles 1-15
UG Cycles 3-7
DSDP Site 372
ODP Site 654
Modern Salina Gypsum
Rain and Groundwater
LMWL
α_D = 0.981
α_{18O} = 1.00341
α_D = 0.981
α_{18O} = 1.0035
Gypsum Mother Water
Gypsum Hydration Water
δD (‰ VSMOW)
δ18O (‰ VSMOW)
B
LMWL
E/I = 0.5
E/I = 1
Recharge
y = -2.7x - 0.6
y = -4.8x - 1.8
d-excess (‰ VSMOW)
δ18O (‰ VSMOW)
C
LMWL
E/I = 0.5
E/I = 1
17O-excess (per meg)
δ18O (‰ VSMOW)

Fig. 7.3. **Left**. Comparison of measured local meteoric water (grey circles) and predicted Messinian brine mother water values for the differing facies of the gypsum from sites 372 (red diamonds) and 654 (green diamonds), Upper Gypsum (yellow diamonds) and PLG (blue circles) after correction for fractionation factors (Gázquez et al., 2017). In (**A**) δ^{18}O vs δD, (**B**) δ^{18}O vs d-excess and (**C**) δ^{18}O vs ^{17}O-excess space, local meteoric water measurements define the local meteoric water line (LMWL). Light blue triangles are modern gypsum data from the Cabo de Gata Salina. Red square is Modern Mediterranean Seawater. The trajectories for the evaporation of Mediterranean seawater for high (90%; slope ~7) and low (40%; slope ~3) humidities are shown in A, defining a range of possible δ^{18}O and δD values (pink field). Gypsum precipitation takes place at 3 to 7 times concentrated seawater; gypsum saturation (blue field) is calculated using the Rayleigh Distillation equation, assuming initial δ^{18}O and δD values of ~1‰ and 8‰, respectively, 75% equilibrium between atmospheric vapour and fresh water, and gypsum saturation occurring at an evaporation ratio of 3.8× (evaporation ratio = weight of H_2O of original seawater divided by weight of H_2O in residual evaporated brine). Mixing lines in B and C are derived from the model of Gázquez et al. (2018) at a humidity of 75% and a starting point of modern Mediterranean seawater. The mixing curve does not match the data, indicating that basin recharge with freshwaters was dominant. Errors (1σ) are less than the width of the symbols, and ±6 for ^{17}O-excess.

Offshore Deposits: The ^{87}Sr/^{86}Sr variation of gypsum from ODP site 654 is large (0.708730 to 0.708806) and also significantly lower than late Miocene seawater. There is a slight decreases in ^{87}Sr/^{86}Sr values up-core (Fig. 7.5).

The ^{87}Sr/^{86}Sr of the RLG is very similar to mean PLG values (Fig. 7.6).

7.3.4 Ca isotopes

Six samples from the onshore UG and 11 samples from ODP site 654 were processed for calcium isotope analysis (Appendix D; Table D.5).

Onshore Deposits: The $\delta^{44/40}$Ca of the onshore UG is significantly lower than that of the PLG (Fig. 7.6). There are no trends in Ca isotopes up-section.

The $\delta^{44/40}$Ca of Cycle 4 of the UG varies between 0.03 and 0.54‰. $\delta^{44/40}$Ca generally increase from low values at the base to maximum values at the top of the cycle (Fig. 7.5).

Offshore Deposits: Calcium isotope values of gypsum from ODP Site 654 are significantly lower than both the onshore UG and the PLG, ranging between -0.13 and 0.46‰ (Fig. 7.6). The highest values occurred near the base of the sampled interval, and values decrease towards to the top of the core (Fig. 7.5).

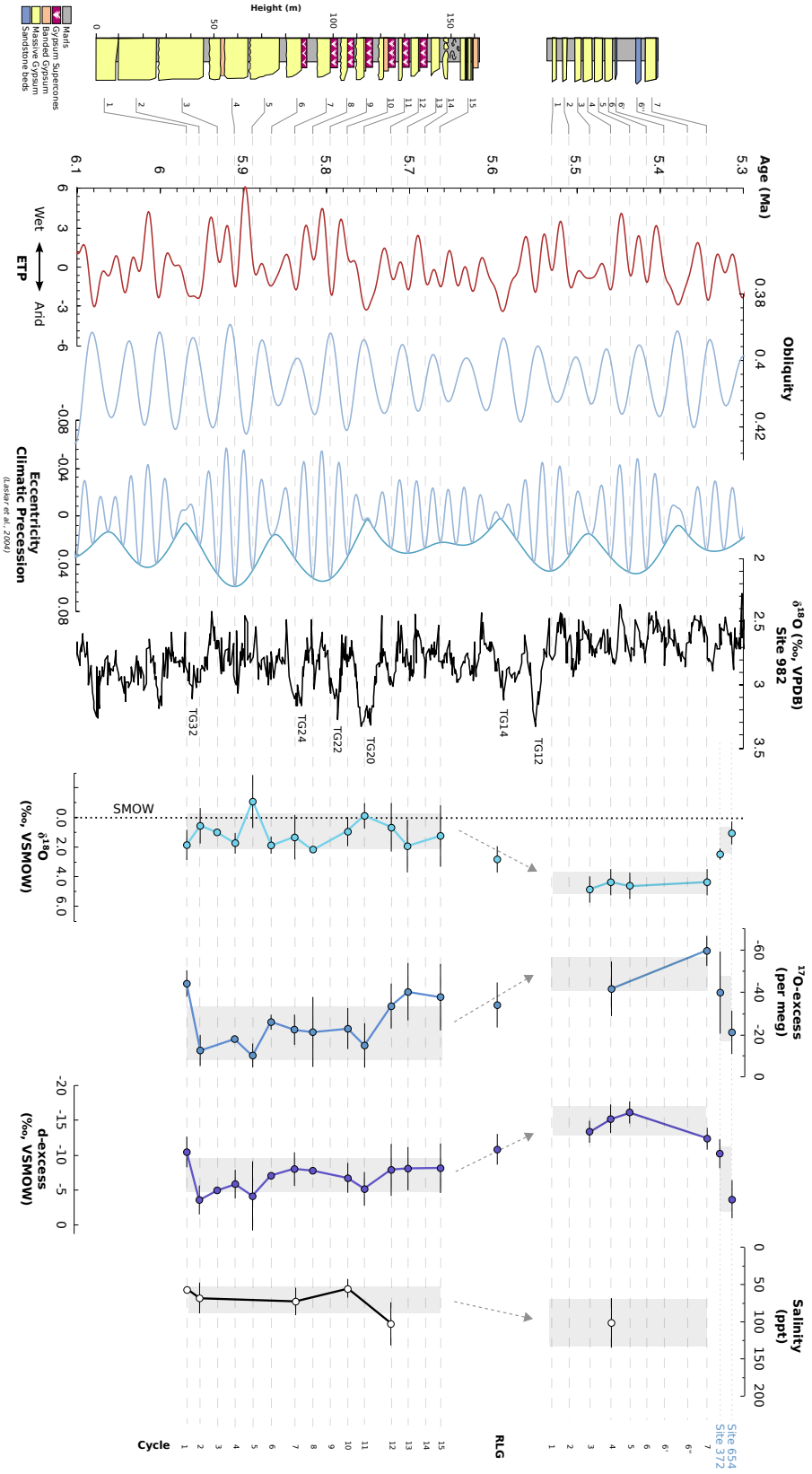
Marls
Gypsum Supercones
Banded Gypsum
Nodular Gypsum
Sandstone beds
Height (m)
Age (Ma)
Wet
Arid
ETP
Obliquity
Eccentricity
Climatic Precession
(Laskar et al., 2004)
δ18O (‰, VPDB)
Site 982
TG32
TG24
TG22
TG20
TG14
TG12
SMOW
δ18O
(‰, VSMOW)
17O-excess
(per meg)
d-excess
(‰, VSMOW)
Salinity
(ppt)
Site 654
Site 372
Cycle
RLG

Fig. 7.4. **Left**. Mean intra-cycle $\delta^{18}O$, ^{17}O-excess and d-excess data (calculated from measurement of GHW) and salinity data (deduced from fluid inclusions and calculated using the equation of Goldstein and Reynolds, 1994) are plotted against their designated cycle. Error bars define $\pm 1\sigma$ of the data in each cycle. The vertical grey bars indicate the $\pm 1\sigma$ range of the data from all PLG and all UG cycles, respectively. Each gypsum bed is plotted in relation to its proposed orbital tuning (Laskar et al., 2004; Lugli et al., 2010; Manzi et al., 2013), where gypsum precipitation correlates with insolation minima. Note that the the position of data from the RLG, ODP Leg 107 site 654 and DSDP Leg 42A site 372 is arbitrary and does not reflect the age of the deposit.

7.3.5 Ba isotopes

Four samples from the onshore UG, 17 samples from the PLG of Sorbas Basin (SE Spain), and 1 sample from the modern Cabo de Gata Salina, SE Spain, were processed for barium isotope analysis (Appendix D; Table D.5).

The $\delta^{138/134}$Ba of the PLG ranged from 0.00‰ to 0.23‰, with a mean value of 0.10‰ (Fig. 7.6). $\delta^{138/134}$Ba display no significant variability between different cycles, although similarities between mean values of $\delta^{138/134}$Ba and $\delta^{44/40}$Ca are apparent up-section. There is no defined variability in $\delta^{138/134}$Ba within any of the PLG cycles.

The $\delta^{138/134}$Ba of the UG ranged from -0.06 to 0.01, with a mean value of -0.01‰ (Fig. 7.6). Isotope values within cycle 4 show no trends with position in the cycle.

The $\delta^{138/134}$Ba of the sample from the Cabo de Gata Salina yielded a value of 0.08‰.

7.3.6 δ^{34}S and δ^{18}O of sulfate

Sixty two samples were analysed for sulfur isotopes and oxygen isotopes of sulfate (Appendix D; Table D.7). These data are shown in Fig. 7.7 relative to the expected range of gypsum precipitated from Miocene seawater and the PLG reported in Chapter 6.

Onshore Deposits: The δ^{34}S of gypsum from the onshore deposits of the Caltanissetta Basin varies between 20.8‰ and 22.6‰ VCDT and $\delta^{18}O_{SO_4}$ between 13.2‰ and 18.8‰ VSMOW. The δ^{34}S and $\delta^{18}O_{SO_4}$ of onshore UG are positively correlated with a slope of ~2.6 (Fig. 7.7).

Onshore UG deposits are characterised by similar δ^{34}S compositions the PLG (δ^{34}S ~22.5‰), although mean values are slightly lower and mean δ^{34}S decreases from 22.4‰ in cycle 3 to 21.1‰ in cycle 7 (Fig. 7.8). The $\delta^{18}O_{SO_4}$ values (15.9 ±1.8‰) are significantly higher than PLG ($\delta^{18}O_{SO_4}$ ~13‰), and above values expected from the precipitation of Late Miocene marine evaporites ($\delta^{18}O_{SO_4}$ ~12‰). Mean $\delta^{18}O_{SO_4}$ also decreases up-section from 18.5‰ in cycle 3 to 16.0‰ in cycle 7.

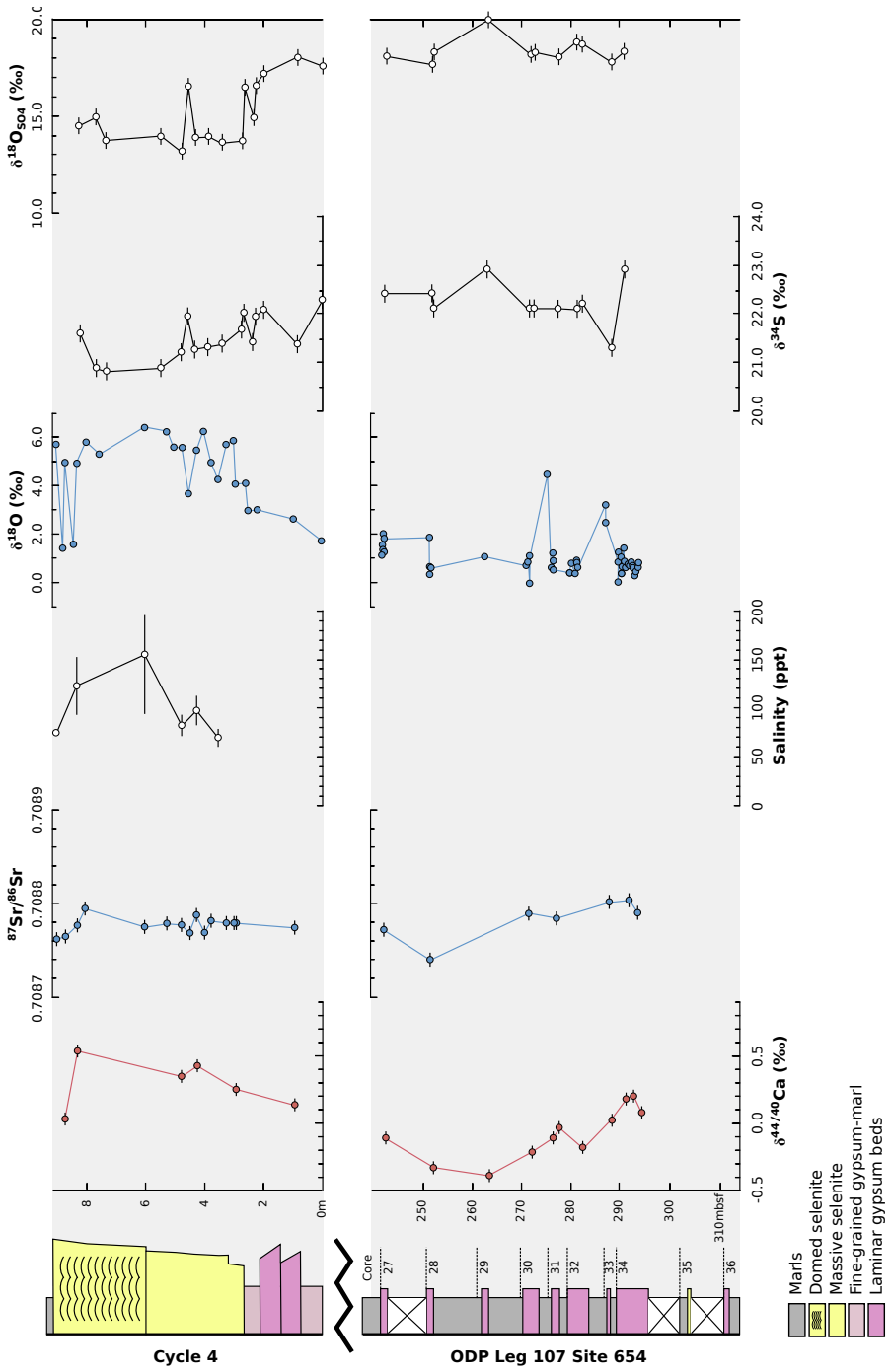

Fig. 7.5. Schematic diagram of UG cycle 4 and ODP Leg 107 site 654 scaled to height of each of the sections. Calcium isotope data, strontium isotope data, salinity data (deduced from fluid inclusions and calculated using the equation of Goldstein and Reynolds, 1994), δ^{18}O and d-excess data deduced from GHW are plotted relative to the height from which the samples were taken. Note there is no salinity data available from ODP Leg 107 site 654 due to the fine-grained nature of the gypsum present.

The $\delta^{34}S$ and $\delta^{18}O_{SO_4}$ show a systematic decrease with increasing height in cycle 4 (Fig. 7.5). The $\delta^{34}S$ and $\delta^{18}O_{SO_4}$ values decrease from ~21.0‰ and 14.0‰, respectively, at the base, to ~22.0 and 17.5‰, respectively, at the top.

Offshore Deposits: The $\delta^{34}S$ of gypsum from the offshore deposits from DSDP site 372 and ODP site 654 varies between 19.5‰ and 22.9‰ and $\delta^{18}O_{SO_4}$ between 15.3‰ and 20.3‰ (Fig. 7.8). Both $\delta^{34}S$ and $\delta^{18}O_{SO_4}$ show no correlations with depth (Fig. 7.5). Compared to the mean PLG values, the $\delta^{34}S$ and $\delta^{18}O_{SO_4}$ of the offshore deposits display lower and higher values, respectively. The $\delta^{34}S$ and $\delta^{18}O_{SO_4}$ of DSDP site 372 and ODP site 654 sulfates are positively correlated with a slope of ~1.2 (Fig. 7.7).

The $\delta^{34}S$ and $\delta^{18}O_{SO_4}$ RLG are in line with those of the PLG (22.3‰ and 12.8‰, respectively).

7.3.7 $\delta^{18}O_{carb}$ and $\delta^{13}C$ of bulk carbonates

The oxygen and carbon isotope composition of eight carbonate samples vary from -2.0 to 1.1‰ for $\delta^{18}O_{carb}$ and from -1.6 to -0.3‰ for $\delta^{13}C$ (Appendix D; Table D.8). The carbon and oxygen isotope composition of the carbonates are within the range of other Messinian carbonates associated with evaporites in the Mediterranean (Longinelli, 1979).

7.4 Discussion

The onshore UG unit of the Caltanissetta Basin (Sicily), and the offshore sulfate deposits recovered from DSDP and ODP sites are believed to record the last phase of the MSC, but the hydrological conditions under which the geographically disparate units formed are poorly understood. Our GHW and salinity data from the onshore deposits partially overlap with the range expected from the evaporation of seawater, but $^{87}Sr/^{86}Sr$, $\delta^{44/40}Ca$, $\delta^{138/134}Ba$ data support a significant contribution by meteoric water at both deep and shallow water sites. Below we discuss how the composition of PLG deposits differ from both the (i) onshore UG and (ii) deep basin units, and propose a mechanism that explains the geochemical data.

7.4.1 Isotopic comparison between the onshore Upper Gypsum and Primary Lower Gypsum

The corrected oxygen and hydrogen isotopic composition of GHW provide a record of the parent water from which gypsum precipitated (e.g. Evans et al., 2015; Herwartz et al., 2017;

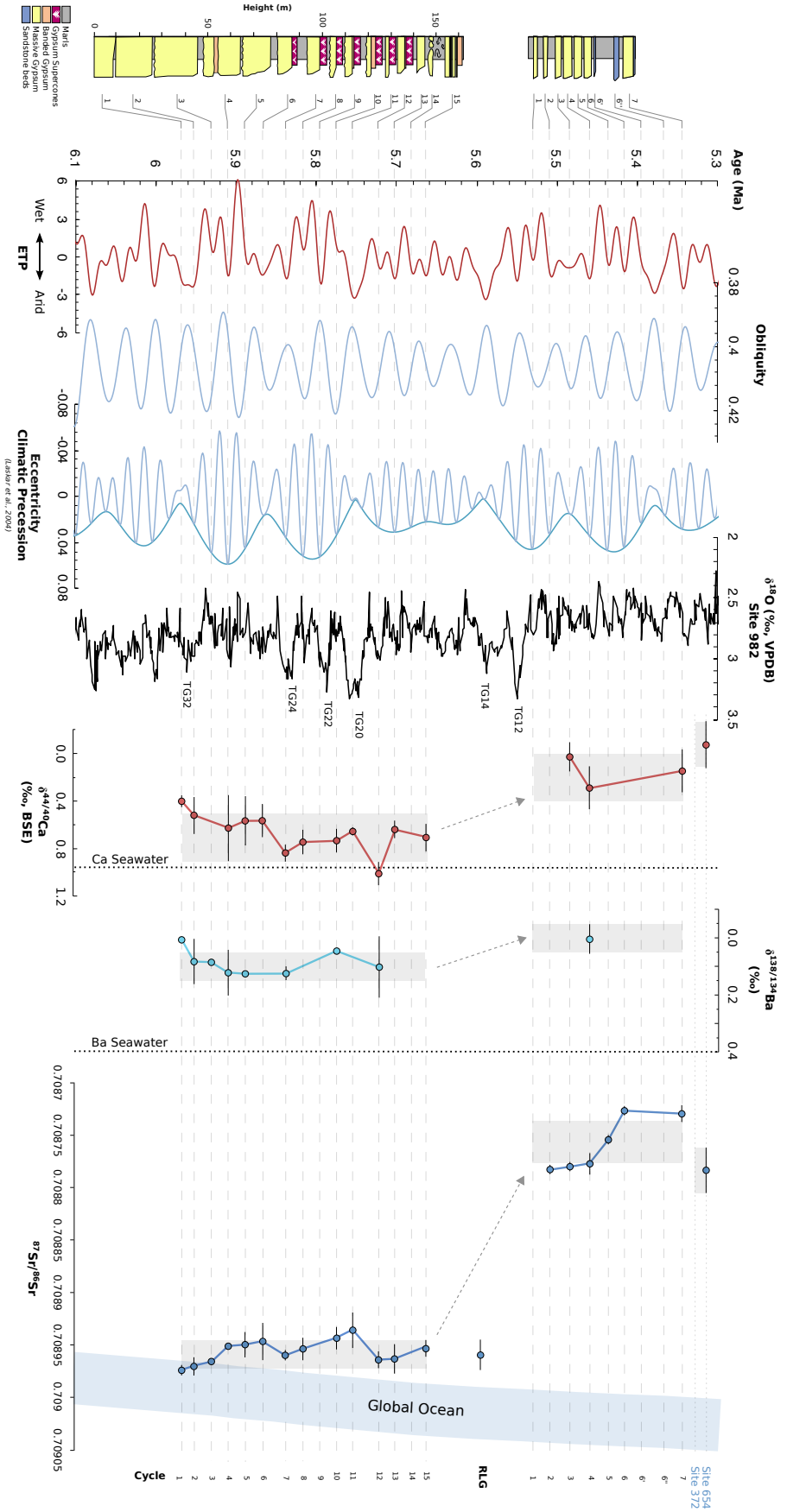
Marls
Gypsum Supercones
Banded Gypsum
Massive Gypsum
Sandstone beds
Height (m)
Age (Ma)
Wet
Arid
ETP
Obliquity
Eccentricity
Climatic Precession
(Laskar et al., 2004)
δ18O (‰, VPDB)
Site 982
TG32
TG24
TG22
TG20
TG14
TG12
δ44/40Ca
(‰, BSE)
Ca Seawater
δ138/134Ba
(‰)
Ba Seawater
87Sr/86Sr
Global Ocean
Cycle
RLG
Site 654
Site 372

Fig. 7.6. Left. Mean intra-cycle $\delta^{44/40}$Ca, $\delta^{138/134}$Ba and ^{87}Sr/^{86}Sr data plotted against their designated cycle. Error bars define $\pm 1\sigma$ of the data in each cycle. The vertical grey bars indicate the $\pm 1\sigma$ range of the data from all PLG and all UG cycles, respectively. Each gypsum bed is plotted in relation to its proposed orbital tuning (Laskar et al., 2004; Lugli et al., 2010; Manzi et al., 2013), where gypsum precipitation correlates with insolation minima. The benthic δ^{18}O (Hodell et al., 2001; modified by Drury et al., 2018) is also shown, and the major glacial stages are indicated. Note that the the position of data from the RLG, ODP Leg 107 site 654 and DSDP Leg 42A site 372 is arbitrary and does not reflect the age of the deposit. All isotope systems display a significant shift toward lower values in the UG compared to the PLG, indicative of an environment dominated by meteoric input.

Gazquez et al., 2018), whereas the ionic constituents of the mother fluid are preserved in primary fluid inclusions that trap the parent brine during gypsum precipitation (e.g. Attia et al., 1995). The δ^{18}O and δD of the UG units display values that are greater than results obtained from the PLG, and partially overlap with the isotopic range expected for evaporated seawater (Fig. 7.3). Salinity estimates deduced from the melting temperature of fluid inclusions from the UG (mean cycle 4 ($\pm\sigma$) = 102 ($\pm$34) ppt) partially overlap with the range of gypsum saturation expected if evaporated from seawater (> ~135 ppt) (Goldstein and Reynolds, 1994). Additionally, the δ^{34}S of the UG is similar to results obtained from the PLG and the range expected from sulfate minerals precipitated from normal Messinian seawater (~21‰) (Fig. 7.8). This may indicate that the sulfate molecule for gypsum formation may have been derived from a marine source, although simple mixing model calculations demonstrate that sulfur isotopes are highly insensitive to continental inputs, requiring >95% contribution from freshwater sources to cause a deviation in seawater δ^{34}S values (Chapter 6). Together, these results indicate that the UG formed from (predominantly) marine fluids that had undergone evaporation. However, the other isotopes systems suggest a different origin.

Strontium isotope data argues for a dominantly freshwater-sourced parent fluid. The onshore UG yields low ^{87}Sr/^{86}Sr values compared to the coeval global ocean. No significant overlap exists between the UG and the PLG (Fig. 7.6). The ^{87}Sr/^{86}Sr values of the Rhone (~0.70872) and Nile (~0.70600) are lower than the global seawater average during the Messinian (~0.709), and make up >80% of the total Mediterranean riverine input today (McArthur et al., 2001; Flecker et al., 2002; Topper et al., 2014). As the strontium isotope ratio of water in a marginal oceanic basin is a simple mixture between ocean water and meteoric sources feeding a basin, the strontium isotope data indicate that inflow from the global ocean was severely restricted and that continental waters dominated the Mediterranean during the precipitation of the UG.

Measurements of barium and calcium isotopes provide additional information regarding the relative freshwater flux to marginal settings. The evolution of both $\delta^{138/134}$Ba and

$\delta^{44/40}$Ca within a semi-enclosed marginal basin, similar to ^{87}Sr/^{86}Sr, is a function of the balance between ocean and riverine input. Riverine sources of barium constitute an important input to the surface ocean, where freshwater sources have lower isotope values ($\delta^{138/134}$Ba = -0.1‰ to 0.4‰; Cao et al., 2016) than typical seawater (0.4 ‰ to 0.6‰) (Hsieh and Henderson, 2017). The $\delta^{44/40}$Ca of ocean and riverine input are also characterised by different calcium concentrations and $\delta^{44/40}$Ca values (rivers ~-0.1‰; seawater = 0.92‰).

Both $\delta^{138/134}$Ba and $\delta^{44/40}$Ca measured in UG display lower values than PLG samples or Messinian seawater (Fig. 7.6), and display a significant correlation with measured ^{87}Sr/^{86}Sr in the Upper and Lower Gypsum (Fig. 7.9). The lower ^{87}Sr/^{86}Sr, $\delta^{138/134}$Ba and $\delta^{44/40}$Ca values in the UG are consistent with a dominant contribution of meteoric water to the fluids that formed Stage 3 deposits. Simple mixing simulations using the Messinian marine (0.70902, 8×10^{-3} kg m^{-3} Sr) and the weighted modern major river inputs of the Rhone and Nile Rivers (0.70763, 3×10^{-4} kg m^{-3} Sr) suggests a dilution of >80% of the Mediterranean Sea to reach the measured average of the UG (0.708771). Additionally, the influence of freshwater likely increased toward the top of the UG unit, as mean ^{87}Sr/^{86}Sr of cycle 7 is less (0.708725) than the cycles below in the section (e.g. cycle 4 = 0.708777).

The upper bound of the continental contribution can be constrained from the application of mixing models to the δ^{34}S values obtained from the gypsum deposits. This analysis yields results that suggest that the freshwater contribution did not exceed 95%. Volumes of freshwater input above this threshold would result in a lowing of the measured sulfur isotope results towards riverine values. Together, these data indicate that Mediterranean-Atlantic exchange persisted, although it was suppressed and episodic.

7.4.2 Semi-closed system behaviour during Upper Gypsum formation

The discrepancy between salinity, δ^{34}S and GHW signatures, and ^{87}Sr/^{86}Sr, $\delta^{138/134}$Ba and $\delta^{44/40}$Ca measurements made on the UG can be reconciled if significant evaporation occurred in a semi-closed system with large inputs of meteoric water. The isotopic composition of a mother fluid during the gypsum precipitation phase is a function of the mixing between seawater (δ^{17}O ~0‰; δ^{18}O ~0‰; δD ~0‰) and freshwater (e.g. Sicilian and Spanish freshwater; δ^{17}O = -2.79‰; δ^{18}O = -5.3‰; δD = -32.5‰) and the evaporative enrichment that is needed to reach gypsum saturation (dependent on the concentration calcium and sulfate ions in the fluid). During the evaporation of a brackish fluid, for example, a greater proportion of water needs to be lost during evaporation to reach gypsum saturation compared to the evaporation of seawater alone (e.g. Rossi et al., 2015). Using the method of Gázquez et al. (2018), we modelled the δ^{18}O, d-excess and ^{17}O-excess obtained from the GHW to estimate the hydrologic balance during gypsum precipitation.

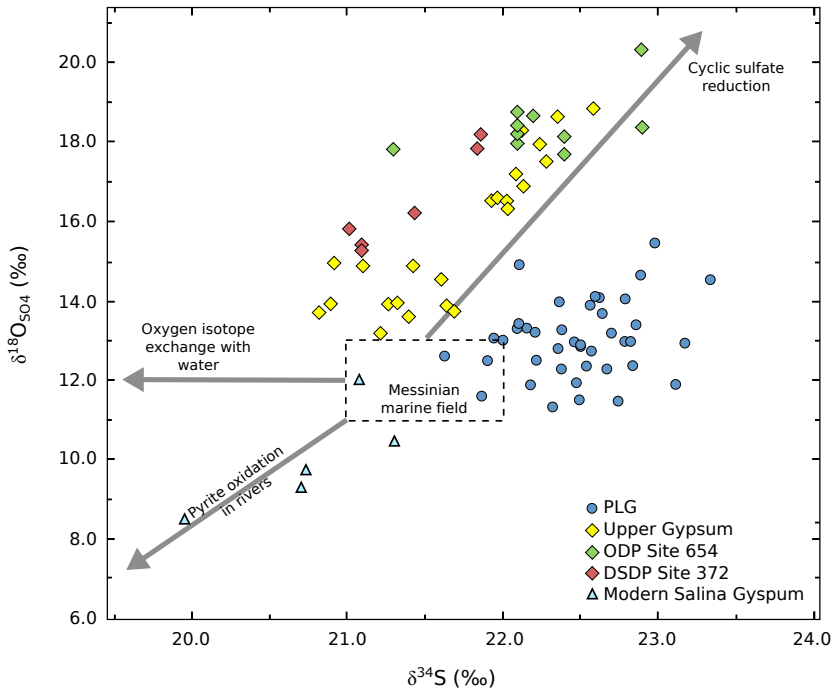

Fig. 7.7. Comparison of δ^{34}S vs. δ^{18}O of sulfate of the PLG and UG. Open box defines Messinian seawater range (Paytan, 1998; Turchyn and Schrag, 2004).

The Monte Carlo experiments are used to determine the range of climatological conditions that simultaneously satisfy all stable isotope results of GHW, in combination with statistical estimates of uncertainty. In these scenarios, the parameter 'Xe' represents the hydrologic balance. A scenario in which all water is lost by outflow and no evaporation occurs is represented as Xe = 0, whereas a scenario in which all water is lost to evaporation (i.e. a terminal basin) is represented as Xe = 1. Assuming (i) the isotopic composition of freshwater input and relative humidity (~75%) is similar to today, and (ii) the mother fluid was dominated by freshwater (80-95%) as evidenced by the ^{87}Sr/^{86}Sr, $\delta^{138/134}$Ba and $\delta^{44/40}$Ca results, we can estimate the hydrologic balance during UG formation.

Model results indicate that the UG was formed in a near-terminal basin (Xe ~ 0.8) with limited exchange with the wider Mediterranean water body during the evaporative phase. Open system behaviour (Xe > 0.5) would result in lower oxygen and hydrogen isotope values than those observed. The measured values also fall below a simple mixing line between Xe = 0 and Xe = 1 in δ^{18}O vs ^{17}O-excess space (Fig. 7.3). Constant evaporation in combination with recharge has been shown to drive the isotopic composition of the ambient brine water to a steady state value below pure evaporation mixing lines (e.g. Surma et al., 2018). It is therefore likely that freshwater basin recharge occurred during humid phases at

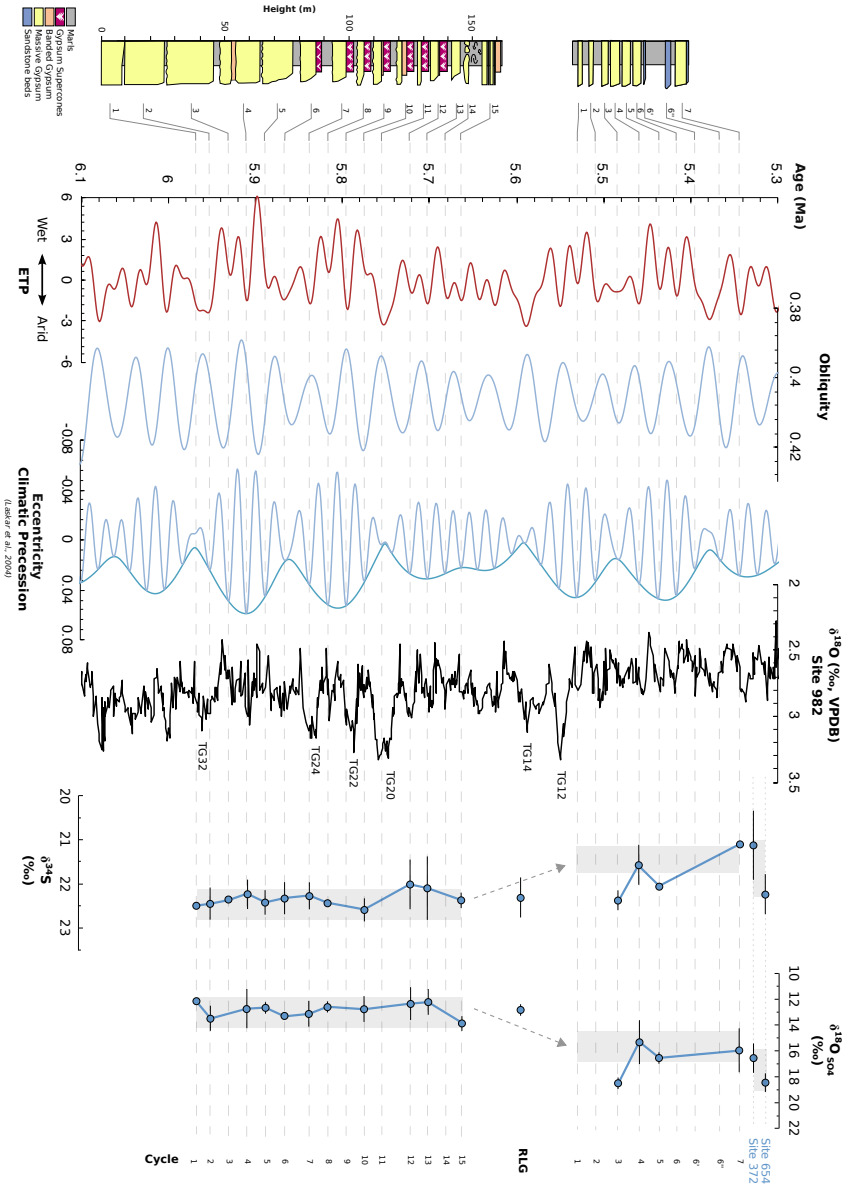

Fig. 7.8. Mean intra-cycle $\delta^{34}S$ and $\delta^{18}O_{SO_4}$ data are plotted against their designated cycle. Error bars define $\pm 1\sigma$ of the data in each cycle. The vertical grey bars indicate the $\pm 1\sigma$ range of the data from all PLG and all UG cycles, respectively. Each gypsum bed is plotted in relation to its proposed orbital tuning (Laskar et al., 2004; Lugli et al., 2010; Manzi et al., 2013), where gypsum precipitation correlates with insolation minima. The benthic $\delta^{18}O$ (Hodell et al., 2001; modified by Drury et al., 2018) is also shown, and the major glacial stages are indicated. Note that the the position of data from the RLG, ODP Leg 107 site 654 and DSDP Leg 42A site 372 is arbitrary and does not reflect the age of the deposit.

the sub-precessional scale, overprinting the large evaporative flux.

In semi-restricted settings where mother fluids are undergoing intense evaporative concentration, strontium and calcium isotopes of gypsum will be correlated if mixing of seawater and meteoric water occur, but uncorrelated if Rayleigh distillation predominates (Hensley, 2006). By directly comparing the calcium measurements with $^{87}Sr/^{86}Sr$ in the same sample, it is possible to distinguish if the shift toward higher values are related to the influx of seawater or Rayleigh distillation. In UG cycle 4, there is no measurable variance in $^{87}Sr/^{86}Sr$ results (Fig. 7.5), indicating a significant shift in the relative flux of meteoric and/or marine fluids to the basin is therefore unlikely. The $\delta^{44/40}Ca$, however, ranges from a low value of 0.14‰ at the base of the cycle to the greatest value of 0.54‰, found near the top (Fig. 7.5). The progressive increase in $\delta^{44/40}Ca$ values from the top of the cycle to the bottom is indicative of substantial Rayleigh distillation of calcium in a semi-enclosed basin. This is in contrast to PLG cycles that displayed limited isotopic variability (Fig. 6.5). The progressive increase in $\delta^{44/40}Ca$ from the base of cycle 4 to the top is also observed in the $\delta^{18}O$ and δD of the gypsum mother water and salinities deduced from fluid inclusions, driven by increased aridity associated with periods of precession maxima.

Variable Rayleigh distillation and isotope fractionation effects are also evidenced by the poor correlation between $\delta^{138/134}Ba$ and $\delta^{44/40}Ca$ results (Fig. 7.9). The $\delta^{44/40}Ca$ fractionation associated with gypsum formation results in an offset of between 0.5‰ and 2.2‰ in a closed system, leading to enrichment in $\delta^{44/40}Ca$ of the residual fluid (Harouaka et al., 2014; Blättler and Higgins, 2014). This fractionation may also vary due to additional factors such as temperature, precipitation rate, and crystal morphology (Harouaka et al., 2014). Similarly, the incorporation of the light isotope during mineral formation is expected to lead to enrichment of ^{138}Ba in the residual fluid. While stable barium isotope fractionation has been investigated in experimental materials and various minerals (e.g. von Allmen et al., 2010; van Zuilen et al., 2016), further study is needed to determine the isotope fractionation upon incorporation into gypsum. Barite, a well-known carrier for barium removal and remineralization (e.g. Griffith and Paytan, 2012), is a good candidate for a first order comparison owing to similar mineral structure (e.g. Böttcher et al., 2018). Laboratory precipitation of barite has indicated a fractionation of 1.00032 ±0.00005 (von Allmen et al., 2010), and Böttcher et al. (2018) found barite formed with a similar fractionation during the transformation of gypsum to $BaSO_4$. Thus, the variable nature of the gypsum-water fractionation during Ba and Ca incorporation likely results in the poor direct correlation between the $\delta^{138/134}Ba$ and $\delta^{44/40}Ca$ systems. When combined with $^{87}Sr/^{86}Sr$, however, they provide important information to confirm the freshwater influence in the parent fluids of the UG.

Finally, sulfur and oxygen isotopes of sulfate also show distinctive trends within gypsum beds. The sulfate isotope compositions are high at the base of each bed and decrease up-cycle (Fig. 7.5), and $\delta^{34}S$ and $\delta^{18}O_{SO_4}$ are systematically lower and higher compared to the PLG, respectively (Fig. 7.8). The range of $\delta^{34}S$ and $\delta^{18}O_{SO_4}$ values of the UG are positively correlated (Fig. 7.9) and vary considerably (20.8‰ to 22.3‰ for $\delta^{34}S$ and 13.2‰ to 17.9‰ for $\delta^{18}O_{SO_4}$) compared to expected normal marine values ($\delta^{34}S$ = ~21‰, $\delta^{18}O_{SO_4}$ = ~12.5‰), which is likely the result of sulfate-reducing bacteria increasing the ^{34}S and ^{18}O in the residual sulfur pool. Density-driven stratification during increased freshwater influx is known to enhance bacterial sulfate reduction (Torfstein and Turchyn, 2017), which potentially occurred during wet stages (at precession minima). During the transition from precession minima to precession maxima, the regional shift from wet to dry conditions may have caused sea level changes within the Mediterranean Basin, enhancing water column mixing and massive precipitation of gypsum. Indeed, García-Veigas et al. (2018) interprets the decreasing upwards $\delta^{34}S$ and $\delta^{18}O_{SO_4}$ trends within each of the UG cycles to reflect increased diffusion, or mixing, with an upper oxygenated water layer that increasingly occurs towards the top of each cycle.

Overall, the isotopic values indicate that the UG formed from a dominantly freshwater fluid that underwent intense evaporation. The evaporation likely occurred in a semi-enclosed environment, and led to significant Rayleigh distillation of the fluid as well as water column destabilisation during the precipitation of each of the gypsum cycles. These results differ from those of the PLG, where isotope results indicate deposition occurred at a steady state and under a greater influence of marine-sourced fluids.

7.4.3 Depositional environment of DSDP/ODP sites 654 and 372

Previous studies have compared the onshore units to those of the offshore deposits based on observations of crystal morphology and Sr isotope stratigraphy (e.g. Roveri et al., 2014b). Our measured $^{87}Sr/^{86}Sr$ values of gypsum from site 654 range from 0.708730 to 0.708806 and overlap the range of $^{87}Sr/^{86}Sr$ from the UG of Sicily (0.708719 and 0.708795), but are significantly lower than the values obtained from the PLG (Fig. 7.6). The trend in $^{87}Sr/^{86}Sr$ seen down-core from ~0.708750 at the top to ~0.708800 at the base (Fig. 7.5) is similar to the isotopic variability of the onshore UG from the top of the section to the base (mean $^{87}Sr/^{86}Sr$ of cycle 2 =0.708783; mean $^{87}Sr/^{86}Sr$ of cycle 7 = 0.708725) (Fig. 7.6). As both successions consist of similarly low strontium isotope values as well as similar cumulate gypsum laminites, Roveri et al. (2014b) concluded that evaporate deposits from onshore and offshore sites formed from a unified water body with a single, evolving isotopic composition.

Our $\delta^{44/40}$Ca, δ^{18}O and δD of gypsum mother water values show significant differences between the onshore and offshore deposits, questioning the singular evaporitic basin theory outlined by Roveri et al. (2014a). The range of gypsum mother water values from both site 372 ($1.6 < \delta^{18}O < 3.0$; $7.5 < \delta D < 12.2$‰) and site 654 ($0.0 < \delta^{18}O < 4.5$; $-0.4 < \delta D < 25.9$‰) overlap with those of the PLG and UG, but the total range is significantly smaller and values are greater than SMOW (Fig. 7.3). The slopes of the δ^{18}O and δD data from the two sites are also significantly different to the PLG and UG (site 654 = 5.3; site 372 = 2.8; PLG = 6.3; UG = 7.3), and the ^{17}O-excess and d-excess values fall below the evaporation trajectory expected from the simple evaporation of water. Similar to the onshore UG, these results can only be achieved from recharge driving the water's isotopic composition along a trajectory below the evaporation trend (e.g. Surma et al., 2018) (Fig. 7.3). The slopes of the evaporation trajectories intercept with SMOW, strongly suggesting that this recharge was composed of Atlantic waters.

Calcium isotope values at site 654 are measurably lower than those of the onshore UG (Fig. 7.6). Additionally, there is a progressive increase in $\delta^{44/40}$Ca down-core at site 654 (Fig. 7.5). The relatively high $\delta^{44/40}$Ca values at the base of the sampled interval are opposite to that expected from progressive enrichment up-section due to the Rayleigh distillation of calcium. This provides further evidence of basin recharge overprinting the process of evaporative enrichment during the period after major salt deposition (Blättler and Higgins, 2014).

The sulfur and oxygen isotope values of sulfate are also measurably different at site 654 compared to the onshore UG. The highest δ^{34}S values (22.1‰ to 23.4‰) and $\delta^{18}O_{SO_4}$ values (17.7‰ to 20.3‰) are measured in the laminated gypsum of site 654 (Fig. 7.8). The values are indicative of intense sulfate-reducing bacterial activity during gypsum deposition, resulting in an increase of both oxygen and sulfur isotope ratios of the remaining aqueous sulfate. These conclusions are supported by SEM observations which have revealed the abundance of bacteria trapped within the gypsum crystals (Pierre and Rouchy, 1990; Panieri et al., 2010).

The isotope data from the onshore UG and sites 654 and 372 can be reconciled if gypsum precipitated in an evaporitic system of coalescent units with differing degrees of hydrological restriction. In order to satisfy the isotopic variability at all sites, the Mediterranean Sea level was likely below the Atlantic connection, and strong fluctuations in the pycnocline due to intense evaporation was likely. Salinity fluctuations were also large over a precessional cycle (brackish to >150 g l^{-1}). This is confirmed by the presence of ostracod taxa such as Cyprideis, which tolerate much higher salinities (~2 g l^{-1}to 120 g l^{-1}; e.g. Gitter et al., 2015, and references therein) and have been recovered in deposits from both deep

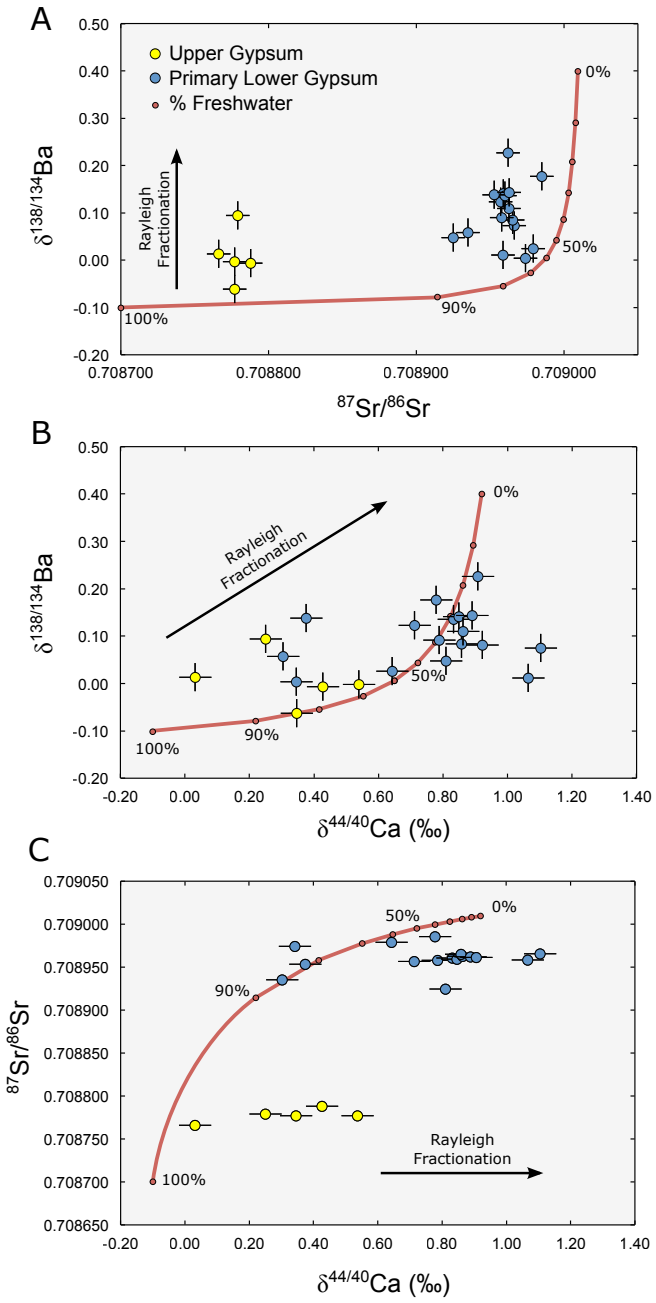

Fig. 7.9. Cross-plots of (**A**) $\delta^{138/134}$Ba vs ^{87}Sr/^{86}Sr, (**B**) $\delta^{138/134}$Ba vs $\delta^{44/40}$Ca, and (**C**) $\delta^{44/40}$Ca vs ^{87}Sr/^{86}Sr data measured in the same sample. Red lines define mixing between seawater (0%) and freshwater (100%). $\delta^{138/134}$Ba vs ^{87}Sr/^{86}Sr and $\delta^{44/40}$Ca vs ^{87}Sr/^{86}Sr display clear mixing trends between the PLG and UG samples, and $\delta^{138/134}$Ba and $\delta^{44/40}$Ca show differing degrees of Rayleigh fractionation. The combined effect of both Rayleigh fractionation and fractionation associated with gypsum formation results in a poor direct correlation between $\delta^{138/134}$Ba and $\delta^{44/40}$Ca.

and marginal settings (e.g. Stoica et al., 2016, and references therein). Oceanic inflow to the Mediterranean, while weakened, was persistent, as evidenced from near marine $\delta^{34}S$ and $\delta^{18}O_{SO_4}$ isotopes and the progressive decrease in $^{87}Sr/^{86}Sr$, both up-section in the UG and site 654. During periods of precession maxima, an increased ratio of evaporation to inflow resulted in mixing and partial drawdown of the Mediterranean water mass due to the highly restricted Mediterranean-Atlantic connection, resulting in gypsum precipitation both in deep and intermediate settings. Within each unit, large variations occurred in the hydraulic regime as evidenced by the changes in the redox potentials. In these semi-restricted basins, activity of sulfate reducing bacteria, evidenced by the variations values of sulfate, was likely conditioned by the amounts of organic material available (Pierre and Rouchy, 1990).

7.5 Conclusions

We investigated the hydrological history of Mediterranean Sea during the last stage of the MSC using isotopic compositions of sulfate and carbonate sediments recovered from three sites (Site 372 in Balearic Sea in the western Mediterranean, Site 654 in the Tyrrhenian Sea, and the onshore Upper Evaporites from the Caltanissetta basin, Sicily). We show that strontium, barium and calcium isotopes are indicative of a dominantly freshwater environment during the deposition of the upper evaporites, comprising stage 3 of the Messinian salinity crisis. Intense evaporation was needed to reach gypsum saturation, and gypsum precipitation occurred in heterogeneous, semi-restricted settings. Our results indicate that both marginal and deep basin deposits are sourced from similar fluids, although each site had specific depositional environments induced by local physiographic conditions.

References

Abriel, W., Reisdorf, K., Pannetier, J., 1990. Dehydration reactions of gypsum: A neutron and X-ray diffraction study. Journal of Solid State Chemistry 85 (1), 23–30.

Allmann, R., Hinek, R., 2007. The introduction of structure types into the Inorganic Crystal Structure Database ICSD. Acta Crystallographica Section A: Foundations of Crystallography 63, 412–417.

Anderson, T. F., Arthur, M. A., 1983. Stable isotopes of oxygen and hydrogen and carbon and their application to sedimentologic and paleoenvironmental problems. In: Stable Isotopes in Sedimentary Geology. SEPM (Society for Sedimentary Geology), Ch. 1, pp. 1–151.

Attia, O. E., Lowenstein, T., Wali, A., 1995. Middle Miocene Gypsum, Gulf of Suez: Marine or Nonmarine? SEPM Journal of Sedimentary Research Vol. 65A (4), 614–626.

Bąbel, M., 2004. Models for evaporite, selenite and gypsum microbialite deposition in ancient saline basins. Geologica Polonica Acta 54 (2), 313–337.

Bąbel, M., 2007. Depositional environments of a salina-type evaporite basin recorded in the Badenian gypsum facies in the northern Carpathian Foredeep. Geological Society, London, Special Publications 285 (1), 107–142.

Bąbel, M., Schreiber, B., 2014. Geochemistry of Evaporites and Evolution of Seawater. In: Treatise on Geochemistry. Vol. 9. Elsevier, pp. 483–560.

Badens, E., Llewellyn, P., Fulconis, J. M., Jourdan, C., Veesler, S., Boistelle, R., Rouquerol, F., 1998. Study of Gypsum Dehydration by Controlled Transformation Rate Thermal Analysis (CRTA). Journal of Solid State Chemistry 139 (1), 37–44.

Baertschi, P., 1953. Über die relativen Unterschiede im $H_2{}^{18}O$-Gehalt natürlicher Wässer. Helvetica Chimica Acta 36 (6), 1352–1369.

Ballirano, P., Melis, E., 2009. Thermal behaviour and kinetics of dehydration of gypsum in air from in situ real-time laboratory parallel-beam X-ray powder diffraction. Physics and Chemistry of Minerals 36 (7), 391–402.

Bao, H., Cao, X., Hayles, J. A., 2016. Triple Oxygen Isotopes: Fundamental Relationships and Applications. Annual Review of Earth and Planetary Sciences 44 (1), 463–492.

Barkan, E., Luz, B., 2005. High precision measurements of $^{17}O/^{16}O$ and $^{18}O/^{16}O$ ratios in H_2O. Rapid Communications in Mass Spectrometry 19 (24), 3737–3742.

Barkan, E., Luz, B., 2007. Diffusivity fractionations of $H_2^{16}O/H_2^{17}O$ and $H_2^{16}O/H_2^{18}O$ in air and their implications for isotope hydrology. Rapid Communications in Mass Spectrometry 21 (18), 2999–3005.

Bassetti, M. A., Manzi, V., Lugli, S., Roveri, M., Longinelli, A., Ricci Lucchi, F., Barbieri, M., 2004. Paleoenvironmental significance of Messinian post-evaporitic lacustrine carbonates in the northern Apennines, Italy. Sedimentary Geology 172 (1-2), 1–18.

Bath, A., Darling, W., George, I., Milodowski, A., 1987. and changes during progressive hydration of a Zechstein anhydrite formation. Geochimica et Cosmochimica Acta 51 (12), 3113–3118.

Bedford, J., Fusseis, F., Leclère, H., Wheeler, J., Faulkner, D., 2017. A 4D view on the evolution of metamorphic dehydration reactions. Scientific Reports 7 (1), 1–7.

Benedix, G., Leshin, L., Farquhar, J., Jackson, T., Thiemens, M., 2003. Carbonates in CM2 chondrites: constraints on alteration conditions from oxygen isotopic compositions and petrographic observations. Geochimica et Cosmochimica Acta 67 (8), 1577–1588.

Bhattacharya, T., Chiang, J. C., Cheng, W., 2017. Ocean-atmosphere dynamics linked to 800-1050 CE drying in mesoamerica. Quaternary Science Reviews 169, 263–277.

Billo, S. M., 1987. Petrology and kinetics of gypsum-anhydrite transitions. Journal of Petroleum Geology 10 (1), 73–85.

Blaauw, M., Christen, J. A., 2011. Flexible paleoclimate age-depth models using an autoregressive gamma process. Bayesian Analysis 6 (3), 457–474.

Blättler, C. L., Higgins, J. A., 2014. Calcium isotopes in evaporites record variations in Phanerozoic seawater SO_4 and Ca. Geology 42 (8), 711–714.

Bodnar, R., 1993. Revised equation and table for determining the freezing point depression of H_2O-NaCl solutions. Geochimica et Cosmochimica Acta 57 (3), 683–684.

Bontognali, T., Vasconcelos, C., Warthmann, R., Bernasconi, S., Dupraz, C., Strohmenger, C., McKenzie, J., 2010. Dolomite formation within microbial mats in the coastal sabkha of Abu Dhabi (United Arab Emirates). Sedimentology 57 (3), 824–844.

Bontognali, T. R., Vasconcelos, C., Warthmann, R. J., Dupraz, C., Bernasconi, S. M., McKenzie, J. A., 2008. Microbes produce nanobacteria-like structures, avoiding cell entombment. Geology 36 (8), 663.

Borsetti, A., Curzi, P., Landuzzi, V., Mutti, M., Ricci Lucchi, F., Sartori, R., Tomadin, L., Zuffa, G., 1990. Messinian and Pre-Messinian Sediments from ODP Leg 107 Sites 652 and 654 in the Tyrrhenian Sea: Sedimentologic and Petrographic Study and Possible Comparisons with Italian Sequences. In: Proceedings of the Ocean Drilling Program, 107 Scientific Results. Ocean Drilling Program.

Böttcher, M. E., Neubert, N., Escher, P., von Allmen, K., Samankassou, E., Nägler, T. F., 2018. Multi-isotope (Ba, C, O) partitioning during experimental carbonatization of a hyper-alkaline solution.

Chemie der Erde 78 (2), 241–247.

Bradbury, H. J., Turchyn, A. V., 2018. Calcium isotope fractionation in sedimentary pore fluids from ODP Leg 175: Resolving carbonate recrystallization. Geochimica et Cosmochimica Acta 236, 121–139.

Brand, W. A., Geilmann, H., Crosson, E. R., Rella, C. W., 2009. Cavity ring-down spectroscopy versus high-temperature conversion isotope ratio mass spectrometry; a case study on δ^2H and δ^{18}O of pure water samples and alcohol/water mixtures. Rapid Communications in Mass Spectrometry 23 (12), 1879–1884.

Bridgestock, L., Hsieh, Y. T., Porcelli, D., Homoky, W. B., Bryan, A., Henderson, G. M., 2018. Controls on the barium isotope compositions of marine sediments. Earth and Planetary Science Letters 481, 101–110.

Broecker, W. S., 1982. Tracers in the Sea. Eldigio.

Buck, B., Van Hoesen, J., 2005. Assessing the applicability of isotopic analysis of pedogenic gypsum as a paleoclimate indicator, Southern New Mexico. Journal of Arid Environments 60 (1), 99–114.

Calmels, D., Gaillardet, J., Brenot, A., France-Lanord, C., 2007. Sustained sulfide oxidation by physical erosion processes in the Mackenzie River basin: Climatic perspectives. Geology 35 (11), 1003–1006.

Canfield, D. E., Sorensen, K. B., Oren, A., 2004. Biogeochemistry of a gypsum-encrusted microbial ecosystem. Geobiology 2 (3), 133–150.

Cao, X., Liu, Y., 2011. Equilibrium mass-dependent fractionation relationships for triple oxygen isotopes. Geochimica et Cosmochimica Acta 75 (23), 7435–7445.

Cao, Z., Siebert, C., Hathorne, E. C., Dai, M., Frank, M., 2016. Constraining the oceanic barium cycle with stable barium isotopes. Earth and Planetary Science Letters 434, 1–9.

Cappa, C. D., 2003. Isotopic fractionation of water during evaporation. Journal of Geophysical Research 108 (D16), 4525.

Carnevale, G., Caputo, D., Landini, W., 2006. Late Miocene fish otoliths from the Colombacci Formation (Northern Apennines, Italy): Implications for the Messinian 'Lago-mare' event. Geological Journal 41 (5), 537–555.

Caruso, A., Pierre, C., Blanc-Valleron, M. M., Rouchy, J. M., 2015. Carbonate deposition and diagenesis in evaporitic environments: The evaporative and sulphur-bearing limestones during the settlement of the Messinian Salinity Crisis in Sicily and Calabria. Palaeogeography, Palaeoclimatology, Palaeoecology 429, 136–162.

Cendón, D., Peryt, T., Ayora, C., Pueyo, J., Taberner, C., 2004. The importance of recycling processes in the Middle Miocene Badenian evaporite basin (Carpathian foredeep): palaeoenvironmental implications. Palaeogeography, Palaeoclimatology, Palaeoecology 212 (1-2), 141–158.

Chang, H., Huang, P. J., Hou, S. C., 1999. Application of thermo-Raman spectroscopy to study dehydration of $CaSO_4 \cdot 2H_2O$ and $CaSO_4 \cdot 0.5H_2O$. Materials Chemistry and Physics 58 (1), 12–19.

Chappell, J., Shackleton, N. J., 1986. Oxygen isotopes and sea level. Nature 324, 137–140.

Charola, A. E., Pühringer, J., Steiger, M., 2007. Gypsum: a review of its role in the deterioration of building materials. Environmental Geology 52 (2), 339–352.

Chen, F., Turchyn, A. V., Kampman, N., Hodell, D., Gázquez, F., Maskell, A., Bickle, M., 2016. Isotopic analysis of sulfur cycling and gypsum vein formation in a natural CO_2 reservoir. Chemical Geology 436, 72–83.

Christensen, A. N., Olesen, M., Cerenius, Y., Jensen, T. R., 2008. Formation and Transformation of Five Different Phases in the $CaSO_4$-H_2O System: Crystal Structure of the Subhydrate β-$CaSO_4 \cdot 0.5H_2O$ and Soluble Anhydrite $CaSO_4$. Chemistry of Materials 20 (6), 2124–2132.

CIESM, 2008. The Messinian Salinity Crisis from mega-deposits to microbiology - A consensus report. In: In: Briand, F. (Ed.). Ciesm Workshop Monographs no. 33. p. 168.

Claypool, G. E., Holser, W. T., Kaplan, I. R., Sakai, H., Zak, I., 1980. The age curves of sulfur and oxygen isotopes in marine sulfate and their mutual interpretation.

Clayton, R. N., Mayeda, T. K., 1984. The oxygen isotope record in Murchison and other carbonaceous chondrites. Earth and Planetary Science Letters 67 (2), 151–161.

Cohelo, A., 2007. TOPAS-Academic. Coelho Software, Brisbane, Australia.

Conley, R., Bundy, W., 1958. Mechanism of gypsification. Geochimica et Cosmochimica Acta 15 (1-2), 57–72.

Craig, H., 1961. Isotopic Variations in Meteoric Waters. Science (New York, N.Y.) 133, 1702–1703.

Criss, R. E., 1999. Principles of Stable Isotope Distribution. Oxford University Press, Oxford.

Curtis, J. H., Hodell, D. A., Brenner, M., 1996. Climate Variability on the Yucatan Peninsula (Mexico) during the Past 3500 Years, and Implications for Maya Cultural Evolution. Quaternary Research 46 (01), 37–47.

D'Ans, J., 1968. Der Ubergangspunkt Gips-Anhydrit. Kali Steinsalz 5, 109–111.

Dansgaard, W., 1964. Stable isotopes in precipitation. Tellus.

De Lange, G. J., Boelrijk, N. A. I. M., Catalano, G., Corselli, C., Klinkhammer, G. P., Middelburg, J. J., Müller, D. W., Ullman, W. J., Van Gaans, P., Woittiez, J. R. W., 1990. Sulphate-related equilibria in the hypersaline brines of the Tyro and Bannock Basins, eastern Mediterranean. Marine Chemistry 31 (1-3), 89–112.

De Lange, G. J., Krijgsman, W., 2010. Messinian salinity crisis: A novel unifying shallow gypsum/deep dolomite formation mechanism. Marine Geology 275 (1-4), 273–277.

Decima, A., McKenzie, J. A., Schreiber, B. C., 1988. The origin of "evaporitive" limestones; an

example from the Messinian of Sicily (Italy). Journal of Sedimentary Research 58 (2), 256–272.

Dela Pierre, F., Bernardi, E., Cavagna, S., Clari, P., Gennari, R., Irace, A., Lozar, F., Lugli, S., Manzi, V., Natalicchio, M., Roveri, M., Violanti, D., 2011. The record of the Messinian salinity crisis in the Tertiary Piedmont Basin (NW Italy): The Alba section revisited. Palaeogeography, Palaeoclimatology, Palaeoecology 310 (3-4), 238–255.

Dela Pierre, F., Clari, P., Natalicchio, M., Ferrando, S., Giustetto, R., Lozar, F., Lugli, S., Manzi, V., Roveri, M., Violanti, D., 2014. Flocculent layers and bacterial mats in the mudstone interbeds of the Primary Lower Gypsum unit (Tertiary Piedmont basin, NW Italy): Archives of palaeoenvironmental changes during the Messinian salinity crisis. Marine Geology 355, 71–87.

DePaolo, D. J., 2004. Calcium Isotopic Variations Produced by Biological, Kinetic, Radiogenic and Nucleosynthetic Processes. Reviews in Mineralogy and Geochemistry 55 (1), 255–288.

DePaolo, D. J., 2011. Surface kinetic model for isotopic and trace element fractionation during precipitation of calcite from aqueous solutions. Geochimica et Cosmochimica Acta 75 (4), 1039–1056.

Deuser, W., Degens, E., Guillard, R., 1968. Carbon isotope relationships between plankton and sea water. Geochimica et Cosmochimica Acta 32 (6), 657–660.

Deutsch, Y., Nathan, Y., Sarig, S., 1994. Thermogravimetric evaluation of the kinetics of the gypsum-hemihydrate-soluble anhydrite transitions. Journal of Thermal Analysis 42 (1), 159–174.

Di Tommaso, D., Ruiz-Agudo, E., de Leeuw, N. H., Putnis, A., Putnis, C. V., 2014. Modelling the effects of salt solutions on the hydration of calcium ions. Phys. Chem. Chem. Phys. 16 (17), 7772–7785.

Douglas, P. M., Demarest, A. A., Brenner, M., Canuto, M. A., 2016a. Impacts of Climate Change on the Collapse of Lowland Maya Civilization. Annual Review of Earth and Planetary Sciences 44 (1), 613–645.

Douglas, P. M., Pagani, M., Eglinton, T. I., Brenner, M., Hodell, D. A., Curtis, J. H., Ma, K. F., Breckenridge, A., 2014. Pre-aged plant waxes in tropical lake sediments and their influence on the chronology of molecular paleoclimate proxy records. Geochimica et Cosmochimica Acta 141, 346–364.

Douglas, P. M. J., Brenner, M., Curtis, J. H., 2016b. Methods and future directions for paleoclimatology in the Maya Lowlands. Global and Planetary Change 138, 3–24.

Douglas, P. M. J., Pagani, M., Canuto, M. A., Brenner, M., Hodell, D. A., Eglinton, T. I., Curtis, J. H., 2015. Drought, agricultural adaptation, and sociopolitical collapse in the Maya Lowlands. Proceedings of the National Academy of Sciences 112 (18), 5607–5612.

Driesner, T., Ha, T.-K., Seward, T., 2000. Oxygen and hydrogen isotope fractionation by hydration complexes of Li^+, Na^+, K^+, Mg^{2+}, F^-, Cl^-, and Br^-: a theoretical study. Geochimica et Cosmochimica Acta 64 (17), 3007–3033.

Dronkert, H., 1977. The evaporites of the Sorbas basin. Instituto de Investigaciones Geológicas Diputación Provincial Universidad de Barcelona (32), 55–76.

Dronkert, H., 1985. Evaporite Models and Sedimentology of Messinian and Recent Evaporites. In: GUA Papers of Geology, Series 1, No. 24. p. 283.

Drury, A. J., Westerhold, T., Hodell, D., Röhl, U., 2018. Reinforcing the North Atlantic backbone: Revision and extension of the composite splice at ODP Site 982. Climate of the Past 14 (3), 321–338.

Elderfield, H., 1986. Strontium isotope stratigraphy. Palaeogeography, Palaeoclimatology, Palaeoecology 57 (1), 71–90.

Emiliani, C., 1955. Pleistocene Temperatures. The Journal of Geology 63 (6), 538–578.

Engleman, E. E., Jackson, L. L., Norton, D. R., 1985. Determination of carbonate carbon in geological materials by coulometric titration. Chemical Geology 53, 125–128.

Epstein, S., Buchsbaum, R., Lowenstam, H. A., Urey, H. C., 1953. Revised Carbonate-Water Isotopic Temperature Scale. Geological Society of America Bulletin 64, 1315–1326.

Epstein, S., Mayeda, T., 1953. Variation of ^{18}O content of waters from natural sources. Geochimica et Cosmochimica Acta 4 (5), 213–224.

Eugster, H. P., 1980. Geochemistry of Evaporitic Lacustrine Deposits. Ann. Rev. Earth Planet. 8, 35–63.

Eugster, H. P., Hardie, L. A., 1978. Saline lakes. In: Lerman, A. (Ed.), Chemistry. Geology, and Physics of Lakes. Springer, New York, pp. 237–293.

Evans, D. A., 2006. Proterozoic low orbital obliquity and axial-dipolar geomagnetic field from evaporite palaeolatitudes. Nature 444 (7115), 51–55.

Evans, N. P., Turchyn, A. V., Gázquez, F., Bontognali, T. R., Chapman, H. J., Hodell, D. A., 2015. Coupled measurements of δ^{18}O and δD of hydration water and salinity of fluid inclusions in gypsum from the Messinian Yesares Member, Sorbas Basin (SE Spain). Earth and Planetary Science Letters 430, 499–510.

Fantle, M. S., DePaolo, D. J., 2007. Ca isotopes in carbonate sediment and pore fluid from ODP Site 807A: The $Ca^{2+}_{(aq)}$-calcite equilibrium fractionation factor and calcite recrystallization rates in Pleistocene sediments. Geochimica et Cosmochimica Acta 71 (10), 2524–2546.

Fantle, M. S., Tipper, E. T., 2014. Calcium isotopes in the global biogeochemical Ca cycle: Implications for development of a Ca isotope proxy. Earth-Science Reviews 129, 148–177.

Farías, M. E., Contreras, M., Rasuk, M. C., Kurth, D., Flores, M. R., Poiré, D. G., Novoa, F., Visscher, P. T., 2014. Characterization of bacterial diversity associated with microbial mats, gypsum evaporites and carbonate microbialites in thalassic wetlands: Tebenquiche and La Brava, Salar de Atacama, Chile. Extremophiles 18 (2), 311–329.

Farpoor, M., Khademi, H., Eghbal, M., Krouse, H., 2004. Mode of gypsum deposition in southeastern Iranian soils as revealed by isotopic composition of crystallization water. Geoderma 121 (3-4), 233–242.

Farquhar, J., 1998. Atmosphere-Surface Interactions on Mars: ^{17}O Measurements of Carbonate from ALH 84001 . Science 280 (5369), 1580–1582.

Feder, H. M., Taube, H., 1952. Ionic Hydration: An Isotopic Fractionation Technique. The Journal of Chemical Physics 20 (8), 1335–1336.

Flecker, R., De Villiers, S., Ellam, R. M., 2002. Modelling the effect of evaporation on the salinity-$^{87}Sr/^{86}Sr$ relationship in modern and ancient marginal-marine systems: The Mediterranean Messinian Salinity Crisis. Earth and Planetary Science Letters 203, 221–233.

Flecker, R., Ellam, R. M., 2006. Identifying Late Miocene episodes of connection and isolation in the Mediterranean-Paratethyan realm using Sr isotopes. Sedimentary Geology 188-189, 189–203.

Flecker, R., Krijgsman, W., Capella, W., de Castro Martins, C., Dmitrieva, E., Mayser, J. P., Marzocchi, A., Modestu, S., Ochoa, D., Simon, D., Tulbure, M., van den Berg, B., van der Schee, M., de Lange, G., Ellam, R., Govers, R., Gutjahr, M., Hilgen, F., Kouwenhoven, T., Lofi, J., Meijer, P., Sierro, F. J., Bachiri, N., Barhoun, N., Alami, A. C., Chacon, B., Flores, J. A., Gregory, J., Howard, J., Lunt, D., Ochoa, M., Pancost, R., Vincent, S., Yousfi, M. Z., 2015. Evolution of the Late Miocene Mediterranean-Atlantic gateways and their impact on regional and global environmental change. Earth-Science Reviews 150, 365–392.

Fontes, J., Gonfiantini, R., 1967. Fractionnment isotopique de I'hydrogene dans I'eau de crystallization du gypse. Comptes Rendus de l'Académie des Sciences Paris 265, 4–6.

Fontes, J.-C., Letolle, R., Nesteroff, W., Ryan, W., 1973. Oxygen, Carbon, Sulfur, and Hydrogen Stable Isotopes in Carbonate and Sulfate Mineral Phases of Neogene Evaporites, Sediments, and in Interstitial Waters. In: Initial Reports of the Deep Sea Drilling Project, 13. U.S. Government Printing Office.

Fortuin, A. R., Krijgsman, W., 2003. The Messinian of the Nijar Basin (SE Spain): Sedimentation, depositional environments and paleogeographic evolution. Sedimentary Geology 160 (1-3), 213–242.

Freyer, D., Voigt, W., 2003. Crystallization and Phase Stability of $CaSO_4$ and $CaSO_4$- Based Salts. Monatshefte fur Chemie 134 (5), 693–719.

Friedman, I., 1953. Deuterium content of natural waters and other substances. Geochimica et Cosmochimica Acta 4 (1-2), 89–103.

Friedman, I., O'Neil, J., 1977. Compilation of stable isotope fractionation factors of geochemical interest. In: Fleischer, M. (Ed.), Data of Geochemistry. United States Geological Survey Professional Paper, p. 12.

Fusseis, F., Schrank, C., Liu, J., Karrech, A., Llana-Fúnez, S., Xiao, X., Regenauer-Lieb, K., 2012.

Pore formation during dehydration of a polycrystalline gypsum sample observed and quantified in a time-series synchrotron X-ray micro-tomography experiment. Solid Earth 3 (1), 71–86.

Garcia-Castellanos, D., Villaseñor, A., 2011. Messinian salinity crisis regulated by competing tectonics and erosion at the Gibraltar arc. Nature 480 (7377), 359–363.

García-Guinea, J., Morales, S., Delgado, A., Recio, C., Calaforra, J., 2002. Formation of gigantic gypsum crystals. Journal of the Geological Society 159 (4), 347–350.

García-Ruiz, J. M., Villasuso, R., Ayora, C., Canals, A., Otálora, F., 2007. Formation of natural gypsum megacrystals in Naica, Mexico. Geology 35 (4), 327.

García-Veigas, J., Cendón, D. I., Gibert, L., Lowenstein, T. K., Artiaga, D., 2018. Geochemical indicators in Western Mediterranean Messinian evaporites: Implications for the salinity crisis. Marine Geology 403 (October 2017), 197–214.

Garofalo, P. S., Fricker, M. B., Günther, D., Forti, P., Mercuri, A.-M., Loreti, M., Capaccioni, B., 2010. Climatic control on the growth of gigantic gypsum crystals within hypogenic caves (Naica mine, Mexico)? Earth and Planetary Science Letters 289 (3-4), 560–569.

Gat, J. R., 1996. Oxygen and hydrogen isotopes in the hydrological cycle. Annual Review of Earth and Planetary Sciences 24 (1), 225–262.

Gázquez, F., Calaforra, J. M., 2014. The Gypsum Karst of Sorbas, Betic Chain. In: F. Gutiérrez, M. G. (Ed.), Landscapes and Landforms of Spain. Springer, pp. 127–135.

Gázquez, F., Calaforra, J. M., Evans, N. P., Hodell, D. A., 2017a. Using stable isotopes (δ^{17}O, δ^{18}O and δD) of gypsum hydration water to ascertain the role of water condensation in the formation of subaerial gypsum speleothems. Chemical Geology 452, 34–46.

Gázquez, F., Calaforra, J.-M., Forti, P., Rull, F., Martínez-Frías, J., 2012. Gypsum-carbonate speleothems from Cueva de las Espadas (Naica mine, Mexico): mineralogy and palaeohydrogeological implications. International Journal of Speleology 41 (2), 211–220.

Gázquez, F., Calaforra, J. M., Stoll, H., Sanna, L., Forti, P., Lauritzen, S.-E., Delgado, A., Rull, F., Martínez-Frías, J., 2013. Isotope and trace element evolution of the naica aquifer (Chihuahua, Mexico) over the past 60,000 yr revealed by speleothems. Quaternary Research 80 (03), 510–521.

Gázquez, F., Evans, N. P., Hodell, D. A., 2017b. Precise and accurate isotope fractionation factors (α^{17}O, α^{18}O and αD) for water and $CaSO_4 \cdot 2H_2O$ (gypsum). Geochimica et Cosmochimica Acta 198, 259–270.

Gázquez, F., Mather, I., Rolfe, J., Evans, N. P., Herwartz, D., Staubwasser, M., Hodell, D. A., 2015. Simultaneous analysis of ^{17}O/^{16}O, ^{18}O/^{16}O and ^{2}H/^{1}H of gypsum hydration water by cavity ring-down laser spectroscopy. Rapid Communications in Mass Spectrometry 29 (21), 1997–2006.

Gázquez, F., Morellón, M., Bauska, T., Herwartz, D., Surma, J., Moreno, A., Staubwasser, M., Valero-Garcés, B., Delgado-Huertas, A., Hodell, D. A., 2018. Triple oxygen and hydrogen isotopes of gypsum hydration water for quantitative paleo-humidity reconstruction. Earth and

Planetary Science Letters 481, 177–188.

Gibson, J., Birks, S., Yi, Y., 2016. Stable isotope mass balance of lakes: a contemporary perspective. Quaternary Science Reviews 131, 316–328.

Gitter, F., Gross, M., Piller, W. E., 2015. Sub-Decadal Resolution in Sediments of Late Miocene Lake Pannon Reveals Speciation of Cyprideis (Crustacea, Ostracoda). PLOS ONE 10 (4), 1–21.

Gliozzi, E., Ceci, M. E., Grossi, F., Ligios, S., 2007. Paratethyan Ostracod immigrants in Italy during the Late Miocene. Geobios 40 (3), 325–337.

Goldschmidt, V. M., 1937. The principles of distribution of chemical elements in minerals and rocks. The seventh Hugo Müller Lecture, delivered before the Chemical Society on March 17th, 1937. J. Chem. Soc., 655–673.

Goldstein, R. H., Reynolds, T. J., 1994. Systematics of fluid inclusions in diagenetic minerals. In: SEPM Short Course 31, Society for Sedimentary Geology. p. 199.

Gonfiantini, R., Fontes, J. C., 1963. Oxygen isotopic fractionation in the water of crystallization of gypsum. Nature 200, 644–646.

Grauel, A.-L., Hodell, D. A., Bernasconi, S. M., 2016. Quantitative estimates of tropical temperature change in lowland Central America during the last 42 ka. Earth and Planetary Science Letters 438, 37–46.

Griffith, E. M., Paytan, A., 2012. Barite in the ocean - occurrence, geochemistry and palaeoceanographic applications. Sedimentology 59 (6), 1817–1835.

Grossman, E. L., Ku, T.-L., 1986. Oxygen and carbon isotope fractionation in biogenic aragonite: Temperature effects. Chemical Geology: Isotope Geoscience section 59, 59–74.

Guay, C., Falkner, K., 1997. Barium as a tracer of Arctic halocline and river waters. Deep Sea Research Part II: Topical Studies in Oceanography 44 (8), 1543–1569.

Gussone, N., Bohm, F., Eisenhauer, A., Dietzel, M., Heuser, A., Teichert, B. M., Reitner, J., WÃ¶rheide, G., Dullo, W.-C., 2005. Calcium isotope fractionation in calcite and aragonite. Geochimica et Cosmochimica Acta 69 (18), 4485–4494.

Gussone, N., Eisenhauer, A., Heuser, A., Dietzel, M., Bock, B., Bohm, F., Spero, H. J., Lea, D. W., Bijma, J., Nagler, T. F., 2003. Model for kinetic effects on calcium isotope fractionation in inorganic aragonite and cultured planktonic foraminifera. Geochimica et Cosmochimica Acta 67 (7), 1375–1382.

Hardie, L. A., 1967. The gypsum-anhydrite equilibrium at one atmosphere pressure. The American Mineralogist 52, 171–200.

Hardie, L. A., 1991. On the Significance of Evaporites. Annual Review of Earth and Planetary Sciences 19 (1), 131–168.

Hardie, L. A., Eugster, H. P., 1971. The Depositional Environment of Marine Evaporites: a Case for

Shallow, Clastic Accumulation. Sedimentology 16 (3-4), 187–220.

Hardie, L. A., Eugster, H. P., 1980. Evaporation of Seawater: Calculated Mineral Sequences. Science 208 (4443), 498–500.

Harouaka, K., Eisenhauer, A., Fantle, M. S., 2014. Experimental investigation of Ca isotopic fractionation during abiotic gypsum precipitation. Geochimica et Cosmochimica Acta 129, 157–176.

Harrison, T. N., 2012. Experimental VNIR reflectance spectroscopy of gypsum dehydration: Investigating the gypsum to bassanite transition. American Mineralogist 97 (4), 598–609.

Haug, G. H., 2003. Climate and the Collapse of Maya Civilization. Science 299 (5613), 1731–1735.

Hay, W. W., Migdisov, A., Balukhovsky, A. N., Wold, C. N., Flögel, S., Söding, E., 2006. Evaporites and the salinity of the ocean during the Phanerozoic: Implications for climate, ocean circulation and life. Palaeogeography, Palaeoclimatology, Palaeoecology 240 (1-2), 3–46.

Hensley, T. M., 2006. Calcium Isotopic Variation in Marine Evaporites and Carbonates: Applications to Late Miocene Mediterranean Brine Chemistry and Late Cenozoic Calcium Cycling in the Oceans. Ph.D. thesis, University of California.

Hernandez-Molina, F. J., Stow, D. A. V., Alvarez-Zarikian, C. A., Acton, G., Bahr, A., Balestra, B., Ducassou, E., Flood, R., Flores, J.-A., Furota, S., Grunert, P., Hodell, D., Jimenez-Espejo, F., Kim, J. K., Krissek, L., Kuroda, J., Li, B., Llave, E., Lofi, J., Lourens, L., Miller, M., Nanayama, F., Nishida, N., Richter, C., Roque, C., Pereira, H., Goni, M. F. S., Sierro, F. J., Singh, A. D., Sloss, C., Takashimizu, Y., Tzanova, A., Voelker, A., Williams, T., Xuan, C., 2014. Onset of Mediterranean outflow into the North Atlantic. Science 344 (6189), 1244–1250.

Herwartz, D., Surma, J., Voigt, C., Assonov, S., Staubwasser, M., 2017. Triple oxygen isotope systematics of structurally bonded water in gypsum. Geochimica et Cosmochimica Acta 209, 254–266.

Hildyard, R. C., Llana-fúnez, S., Wheeler, J., Faulkner, D. R., Prior, D. J., 2011. Electron backscatter diffraction (EBSD) analysis of bassanite transformation textures and crystal structure produced from experimentally deformed and dehydrated gypsum. Journal of Petrology 52 (5), 839–856.

Hilgen, F., Kuiper, K., Krijgsman, W., Snel, E., Laan, E. V. D., van der Laan, E., 2007. Astronomical tuning as the basis for high resolution chronostratigraphy: The intricate history of the Messinian Salinity Crisis. Stratigraphy 4, 231–238.

Hodell, D. A., Brenner, M., Curtis, J. H., 2005a. Terminal Classic drought in the northern Maya lowlands inferred from multiple sediment cores in Lake Chichancanab (Mexico). Quaternary Science Reviews 24, 1413–1427.

Hodell, D. A., Brenner, M., Curtis, J. H., Guilderson, T., 2001. Solar Forcing of Drought Frequency in the Maya Lowlands. Science 292 (5520), 1367–1370.

Hodell, D. A., Brenner, M., Curtis, J. H., Medina-González, R., Ildefonso-Chan Can, E., Albornaz-

Pat, A., Guilderson, T. P., 2005b. Climate change on the Yucatan Peninsula during the Little Ice Age. Quaternary Research 63, 109–121.

Hodell, D. A., Curtis, J. H., Brenner, M., 1995. Possible role of climate in the collapse of Classic Maya civilization. Nature 375 (6530), 391–394.

Hodell, D. A., Mueller, P. A., McKenzie, J. A., Mead, G. A., 1989. Strontium isotope stratigraphy and geochemistry of the late Neogene ocean. Earth and Planetary Science Letters 92, 165–178.

Hodell, D. A., Turchyn, A. V., Wiseman, C. J., Escobar, J., Curtis, J. H., Brenner, M., Gilli, A., Mueller, A. D., Anselmetti, F., Ariztegui, D., Brown, E. T., 2012. Late Glacial temperature and precipitation changes in the lowland Neotropics by tandem measurement of δ^{18}O in biogenic carbonate and gypsum hydration water. Geochimica et Cosmochimica Acta 77, 352–368.

Hoggarth, J. A., Restall, M., Wood, J. W., Kennett, D. J., 2017. Drought and Its Demographic Effects in the Maya Lowlands. Current Anthropology 58 (1), 82–113.

Holland, H. D., Horita, J., Seyfried, W. E., 1996. On the secular variations in the composition of Phanerozoic marine potash evaporites. Geology 24 (11), 993.

Horita, J., 1989. Stable isotope fractionation factors of water in hydrated saline mineral-brine systems. Earth and Planetary Science Letters 95 (1-2), 173–179.

Horita, J., Wesolowski, D. J., 1994. Liquid-vapor fractionation of oxygen and hydrogen isotopes of water from the freezing to the critical temperature. Geochimica et Cosmochimica Acta 58 (16), 3425–3437.

Horner, T. J., Kinsley, C. W., Nielsen, S. G., 2015. Barium-isotopic fractionation in seawater mediated by barite cycling and oceanic circulation. Earth and Planetary Science Letters 430, 511–522.

Horner, T. J., Pryer, H. V., Nielsen, S. G., Crockford, P. W., Gauglitz, J. M., Wing, B. A., Ricketts, R. D., 2017. Pelagic barite precipitation at micromolar ambient sulfate. Nature Communications 8 (1), 1342.

Hsieh, Y. T., Henderson, G. M., 2017. Barium stable isotopes in the global ocean: Tracer of Ba inputs and utilization. Earth and Planetary Science Letters 473, 269–278.

Hsu, K., Montadert, L., 1978. Initial Reports of the Deep Sea Drilling Project, 42 Pt. 1. Vol. 42 Pt. 1 of Initial Reports of the Deep Sea Drilling Project. U.S. Government Printing Office, Washington.

Hsü, K. J., Montadert, L., Bernoulli, D., Cita, M. B., Erickson, A., Garrison, R. E., Kidd, R. B., Mèlierés, F., Müller, C., Wright, R., 1977. History of the Mediterranean salinity crisis. Nature 267 (5610), 399–403.

Hsü, K. J., Ryan, W. B. F., Cita, M. B., 1973. Late Miocene Desiccation of the Mediterranean. Nature 242 (5395), 240–244.

Husson, J. M., Higgins, J. A., Maloof, A. C., Schoene, B., 2015. Ca and Mg isotope constraints on the origin of Earth's deepest δ^{13}C excursion. Geochimica et Cosmochimica Acta 160, 243–266.

Kasprzyk, A., Jasinska, B., 1998. Isotopic composition of the crystaUization water of gypsum in the Badenian of the northern Carpathian Foredeep: a case study from the cores Przyborow 1 and Strzegom 143. Geological Quarterly 42 (3), 301–310.

Kennett, D. J., Breitenbach, S. F. M., Aquino, V. V., Asmerom, Y., Awe, J., Baldini, J. U. L., Bartlein, P., Culleton, B. J., Ebert, C., Jazwa, C., Macri, M. J., Marwan, N., Polyak, V., Prufer, K. M., Ridley, H. E., Sodemann, H., Winterhalder, B., Haug, G. H., 2012. Development and Disintegration of Maya Political Systems in Response to Climate Change. Science 338 (6108), 788–791.

Khademi, H., Mermut, A., Krouse, H., 1997. Isotopic composition of gypsum hydration water in selected landforms from central Iran. Chemical Geology 138 (3-4), 245–255.

Khalil, A. A. A., 1982. Kinetics of gypsum dehydration. Thermochimica Acta 55 (2), 201–208.

Kluge, T., Affek, H. P., 2012. Quantifying kinetic fractionation in Bunker Cave speleothems using Δ47. Quaternary Science Reviews 49, 82–94.

Knauth, L., Beeunas, M. A., 1986. Isotope geochemistry of fluid inclusions in Permian halite with implications for the isotopic history of ocean water and the origin of saline formation waters. Geochimica et Cosmochimica Acta 50 (3), 419–433.

Krijgsman, W., Capella, W., Simon, D., Hilgen, F. J., Kouwenhoven, T. J., Meijer, P. T., Sierro, F. J., Tulbure, M. A., van den Berg, B. C., van der Schee, M., Flecker, R., 2018. The Gibraltar Corridor: Watergate of the Messinian Salinity Crisis. Marine Geology 403 (March), 238–246.

Krijgsman, W., Fortuin, A. R., Hilgen, F. J., Sierro, F. J., 2001. Astrochronology for the Messinian Sorbas basin (SE Spain) and orbital (precessional) forcing for evaporite cyclicity. Sedimentary Geology 140 (1-2), 43–60.

Krijgsman, W., Hilgen, F. J., Raffi, I., Sierro, F. J., Wilson, D. S., 1999. Chronology, causes and progression of the Messinian salinity crisis. Nature 400 (August), 652–655.

Krijgsman, W., Meijer, P. T., 2008. Depositional environments of the Mediterranean "Lower Evaporites" of the Messinian salinity crisis: Constraints from quantitative analyses. Marine Geology 253 (3-4), 73–81.

Kushnir, J., 1980. The coprecipitation of strontium, magnesium, sodium, potassium and chloride ions with gypsum. An experimental study. Geochimica et Cosmochimica Acta 44 (10), 1471–1482.

Lachniet, M. S., 2009. Climatic and environmental controls on speleothem oxygen-isotope values. Quaternary Science Reviews 28 (5-6), 412–432.

Landais, A., Barkan, E., Luz, B., 2008. Record of δ^{18}O and ^{17}O-excess in ice from Vostok Antarctica during the last 150,000 years. Geophysical Research Letters 35 (2), L02709.

Landais, A., Barkan, E., Yakir, D., Luz, B., 2006. The triple isotopic composition of oxygen in leaf water. Geochimica et Cosmochimica Acta 70 (16), 4105–4115.

Landais, A., Steen-Larsen, H., Guillevic, M., Masson-Delmotte, V., Vinther, B., Winkler, R., 2012.

Triple isotopic composition of oxygen in surface snow and water vapor at NEEM (Greenland). Geochimica et Cosmochimica Acta 77, 304–316.

Laskar, J., Robutel, P., Joutel, F., Gastineau, M., Correia, A. C. M., Levrard, B., 2004. A long-term numerical solution for the insolation quantities of the Earth. Astronomy & Astrophysics 428 (1), 261–285.

Lea, D., Boyle, E., 1989. Barium content of benthic foraminifera controlled by bottom-water composition. Nature 338 (6218), 751–753.

Li, J., Li, M., Fang, X., Zhang, G., Zhang, W., Liu, X., 2017a. Isotopic composition of gypsum hydration water in deep Core SG-1, western Qaidam basin (NE Tibetan Plateau), implications for paleoclimatic evolution. Global and Planetary Change 155, 70–77.

Li, S., Levin, N. E., Soderberg, K., Dennis, K. J., Caylor, K. K., 2017b. Triple oxygen isotope composition of leaf waters in Mpala, central Kenya. Earth and Planetary Science Letters 468, 38–50.

Lin, Y., Clayton, R. N., Gröning, M., 2010. Calibration of δ^{17}O and δ^{18}O of international measurement standards - VSMOW, VSMOW2, SLAP, and SLAP2. Rapid Communications in Mass Spectrometry 24 (6), 773–776.

Lloyd, R. M., 1968. Oxygen isotope behavior in the Sulfate-Water System. Journal of Geophysical Research 73, 6099.

Lofi, J., Sage, F., Deverchere, J., Loncke, L., Maillard, A., Gaullier, V., Thinon, I., Gillet, H., Guennoc, P., Gorini, C., 2011. Refining our knowledge of the Messinian salinity crisis records in the offshore domain through multi-site seismic analysis. Bulletin de la Societe Geologique de France 182 (2), 163–180.

Londeix, L., Benzakour, M., Suc, J.-P., Turon, J.-L., 2007. Messinian palaeoenvironments and hydrology in Sicily (Italy): The dinoflagellate cyst record. Geobios 40 (3), 233–250.

Longinelli, A., 1979. Isotope geochemistry of some Messinian evaporates: Paleoenvironmental implications. Palaeogeography, Palaeoclimatology, Palaeoecology 29, 95–123.

Longinelli, A., Cortecci, G., 1970. Isotopic abundance of oxygen and sulfur in sulfate ions from river water. Earth and Planetary Science Letters 7 (4), 376–380.

Lou, W., Guan, B., Wu, Z., 2011. Dehydration behavior of FGD gypsum by simultaneous TG and DSC analysis. Journal of Thermal Analysis and Calorimetry 104 (2), 661–669.

Lowenstein, T. K., Timofeef, M. N., Brennan, S. T., Hardie, L. A., Demicco, R. V., 2001. Oscillations in phaneroizoic seawater chemisrty: Evidence from fluid inclusions. Science 294, 1086–1088.

Lu, F. H., Meyers, W. J., 2003. Sr, S, and O(SO_4) Isotopes and the Depositional Environments of the Upper Miocene Evaporites, Spain. Journal of Sedimentary Research 73, 444–450.

Lu, F. H., Meyers, W. J., Schoonen, M. A., 1997. Minor and trace element analyses on gypsum: an experimental study. Chemical Geology 142 (1-2), 1–10.

Lu, F. H., Meyers, W. J., Schoonen, M. A., 2001. S and O(SO_4) isotopes, simultaneous modeling, and environmental significance of the Nijar messinian gypsum, Spain. Geochimica et Cosmochimica Acta 65 (18), 3081–3092.

Lugli, S., Bassetti, M. A., Manzi, V., Barbieri, M., Longinelli, A., Roveri, M., 2007. The Messinian 'Vena del Gesso' evaporites revisited: characterization of isotopic composition and organic matter. Geological Society, London, Special Publications 285 (1), 179–190.

Lugli, S., Gennari, R., Gvirtzman, Z., Manzi, V., Roveri, M., Schreiber, B. C., 2013. Evidence of Clastic Evaporites In the Canyons of the Levant Basin (Israel): Implications For the Messinian Salinity Crisis. Journal of Sedimentary Research 83 (11), 942–954.

Lugli, S., Manzi, V., Roveri, M., Schreiber, B. C., 2015. The deep record of the Messinian salinity crisis: Evidence of a non-desiccated Mediterranean Sea. Palaeogeography, Palaeoclimatology, Palaeoecology 433, 201–218.

Lugli, S., Manzi, V., Roveri, M., Schreiber, C. B., 2010. The Primary Lower Gypsum in the Mediterranean: A new facies interpretation for the first stage of the Messinian salinity crisis. Palaeogeography, Palaeoclimatology, Palaeoecology 297 (1), 83–99.

Luz, B., Barkan, E., 2010. Variations of $^{17}O/^{16}O$ and $^{18}O/^{16}O$ in meteoric waters. Geochimica et Cosmochimica Acta 74 (22), 6276–6286.

Luz, B., Barkan, E., Bender, M. L., Thiemens, M. H., Boering, K. A., 1999. Triple-isotope composition of atmospheric oxygen as a tracer of biosphere productivity. Nature 400 (6744), 547–550.

Madsen, I., Scarlett, N., 2008. Quantitative Phase Analysis. In: Dinnabier, R. (Ed.), Powder Diffraction: Theory and Practice. Royal Society of Chemistry, London, pp. 298–331.

Manzi, V., Gennari, R., Hilgen, F., Krijgsman, W., Lugli, S., Roveri, M., Sierro, F. J., 2013. Age refinement of the Messinian salinity crisis onset in the Mediterranean. Terra Nova 25 (4), 315–322.

Manzi, V., Lugli, S., Marco, R., Schreiber, B., 2009. A new facies model for the Upper Gypsum of Sicily (Italy): chronological and palaeoenvironmental constraints for the Messinian salinity crisis in the Mediterranean. Sedimentology 56 (7), 1937–1960.

Marion, G. M., 1997. A theoretical evaluation of mineral stability in Don Juan Pond, Wright Valley, Victoria Land. Antarctic Science 9 (1), 92–99.

Marshall, B., DePaolo, D., 1982. Precise age determinations and petrogenetic studies using the KCa method. Geochimica et Cosmochimica Acta 46 (12), 2537–2545.

Matsubaya, O., 1971. Oxygen isotopic fractionation between the water of crystallization of gypsum and the mother solution. Abstract Paper of Annual Meeting of Geochem. Soc. Japan, 17A01 (in Japanese).

Matsubaya, O., Sakai, H., 1973. Oxygen and hydrogen isotopic study on the water of crystallization

of gypsum from the Kuroko type mineralization. Geochemical Journal 7 (3), 153–165.

Matsuhisa, Y., Goldsmith, J. R., Clayton, R. N., 1978. Mechanisms of hydrothermal crystallization of quartz at 250Â°C and 15 kbar. Geochimica et Cosmochimica Acta 42 (2), 173–182.

McAdie, H., 1964. The effect of water vapor upon the dehydration of $CaSO_4 \cdot 2H_2O$. Canadian Journal of Chemistry 42, 792–801.

McArthur, J., Howarth, R., Bailey, T., 2001. Strontium isotope stratigraphy: LOWESS version 3: best fit to the marine Sr-isotope curve for 0-509 Ma and accompanying look-up table for deriving numerical age. The Journal of Geology 109 (2), 155–170.

McCaffrey, M. A., Lazar, B., Holland, H. D., 1987. The evaporation path of seawater and the coprecipitation of Br^- and K^+ with halite. Journal of sedimentary petrology 57 (5), 928–938.

McConnaughey, T., 1989. ^{13}C and ^{18}O isotopic disequilibrium in biological carbonates: I. Patterns. Geochimica et Cosmochimica Acta 53 (1), 151–162.

McConnell, J. D. C., Astill, D. M., Hall, P. L., 1987. The pressure dependence of the dehydration of gypsum to bassanite. Mineralogical Magazine 51 (361), 453–457.

McCulloch, M., Fallon, S., Wyndham, T., Hendy, E., Lough, J., Barnes, D., 2003. Coral record of increased sediment flux to the inner Great Barrier Reef since European settlement. Nature 421 (6924), 727–730.

McKenzie, J., Jenkyns, H., Bennet, G., 1979. Stable isotope study of the cyclic diatomite - Claystones from the tripoli formation, Sicily: A prelude to the Messenian salinity crisis. Palaeogeography, Palaeoclimatology, Palaeoecology 29 (143), 125–141.

Medina-Elizalde, M., Burns, S. J., Lea, D. W., Asmerom, Y., von Gunten, L., Polyak, V., Vuille, M., Karmalkar, A., 2010. High resolution stalagmite climate record from the Yucatán Peninsula spanning the Maya terminal classic period. Earth and Planetary Science Letters 298 (1-2), 255–262.

Medina-Elizalde, M., Rohling, E. J., 2012. Collapse of Classic Maya Civilization Related to Modest Reduction in Precipitation. Science 335 (6071), 956–959.

Meilijson, A., Steinberg, J., Hilgen, F., Bialik, O. M., Waldmann, N. D., Makovsky, Y., 2018. Deep-basin evidence resolves a 50-year-old debate and demonstrates synchronous onset of Messinian evaporite deposition in a non-desiccated Mediterranean. Geology 46 (3), 243–246.

Merlivat, L., 1978. Molecular diffusivities of $H_2{}^{16}O$, $HD^{16}O$, and $H_2{}^{18}O$ in gases. The Journal of Chemical Physics 69 (6), 2864.

Merlivat, L., Jouzel, J., 1979. Global climatic interpretation of the deuterium-oxygen 18 relationship for precipitation. Journal of Geophysical Research 84 (C8), 5029.

Merlivat, L., Nief, G., 1967. Fractionnement isotopique lors des changements d'état solide-vapeur et liquide-vapeur de l'eau à des températures inférieures à 0Â°C. Tellus 19 (1), 122–127.

Miller, M. F., 2002. Isotopic fractionation and the quantification of ^{17}O anomalies in the oxygen three-isotope system. Geochimica et Cosmochimica Acta 66 (11), 1881–1889.

Misra, S., Owen, R., Kerr, J., Greaves, M., Elderfield, H., 2014. Determination of ^{11}B by HR-ICP-MS from mass limited samples: Application to natural carbonates and water samples. Geochimica et Cosmochimica Acta 140, 531–552.

Modestou, S., Simon, D., Gutjahr, M., Marzocchi, A., Kouwenhoven, T. J., Ellam, R. M., Flecker, R., 2017. Precessional variability of $^{87}Sr/^{86}Sr$ in the late Miocene Sorbas Basin: An interdisciplinary study of drivers of interbasin exchange. Paleoceanography 32 (6), 531–552.

Mook, W. G., 2000. Environmental Isotopes in the Hydrological Cycle: Principles and Applications, Vol. I: Introduction - Theory, Methods, Review. UNESCO, IAEA, Paris.

Muller, D., Mueller, P. a., McKenzie, J. a., 1990. Strontium Isotopic Ratios As Fluid Tracers in Messinian Evaporites of the Tyrrhenian Sea (Western Mediterranean Sea). Proceedings of the Ocean Drilling Program, Scientific Results, Vol. 107 107, 603–614.

Müller, D. W., Mueller, P. A., 1991. Origin and age of the Mediterranean Messinian evaporites: implications from Sr isotopes. Earth and Planetary Science Letters 107 (1), 1–12.

Natalicchio, M., Dela Pierre, F., Lugli, S., Lowenstein, T. K., Feiner, S. J., Ferrando, S., Manzi, V., Roveri, M., Clari, P., 2014. Did Late Miocene (Messinian) gypsum precipitate from evaporated marine brines? Insights from the Piedmont Basin (Italy). Geology 42 (3), 179–182.

Oi, T., Morimoto, H., 2013. Oxygen and Hydrogen Isotopic Preference in Hydration Spheres of Chloride and Sulfate Ions. Zeitschrift für Physikalische Chemie 227 (6-7), 807–819.

Orszag-Sperber, F., jun 2006. Changing perspectives in the concept of "lago-mare" in mediterranean late miocene evolution. Sedimentary Geology 188-189, 259–277.

Ortí, F., 2011. Selenite facies in marine evaporites: a review. In: Quaternary carbonate and evaporite sedimentary facies and their ancient analogues. John Wiley & Sons Ltd., Chichester, West Sussex, UK, pp. 431–463.

Ortí, F., Pueyo, J. J., Geisler-Cussey, D., Dulau, N., 1984. Evaporitic sedimentation in the coastal salinas of Santa Pola (Alicante, Spain). Revista d'Investigacions Geologiques 38 (39), 169–220.

Ossorio, M., Van Driessche, A. E., Pérez, P., García-Ruiz, J. M., 2014. The gypsum-anhydrite paradox revisited. Chemical Geology 386, 16–21.

Ostroff, A., 1964. Conversion of gypsum to anhydrite in aqueous salt solutions. Geochimica et Cosmochimica Acta 28 (9), 1363–1372.

Pack, A., Herwartz, D., 2014. The triple oxygen isotope composition of the Earth mantle and understanding $\Delta^{17}O$ variations in terrestrial rocks and minerals. Earth and Planetary Science Letters 390, 138–145.

Packter, A., 1974. The precipitation of calcium sulphate dihydrate from aqueous solution. Journal of Crystal Growth 21 (2), 191–194.

Palmer, M., Edmond, J., 1992. Controls over the strontium isotope composition of river water. Geochimica et Cosmochimica Acta 56 (5), 2099–2111.

Panieri, G., Lugli, S., Manzi, V., Roveri, M., Schreiber, B., Palinska, K. A., 2010. Ribosomal RNA gene fragments from fossilized cyanobacteria identified in primary gypsum from the late Miocene, Italy. Geobiology 8 (2), 101–111.

Parkhurst, D. L., Appelo, C. A. J., 2013. Description of input and examples for PHREEQC version 3: a computer program for speciation, batch-reaction, one-dimensional transport, and inverse geochemical calculations. Tech. rep., US Geological Survey.

Passey, B. H., Hu, H., Ji, H., Montanari, S., Li, S., Henkes, G. A., Levin, N. E., 2014. Triple oxygen isotopes in biogenic and sedimentary carbonates. Geochimica et Cosmochimica Acta 141, 1–25.

Paulik, F., Paulik, J., Arnold, M., 1992. Thermal decomposition of gypsum. Thermochimica Acta 200 (C), 195–204.

Paytan, A., 1998. Sulfur Isotopic Composition of Cenozoic Seawater Sulfate. Science 282, 1459–1462.

Perry, E., Velazquez-Oliman, G., Marin, L., 2002. The Hydrogeochemistry of the Karst Aquifer System of the Northern Yucatan Peninsula, Mexico. International Geology Review 44 (3), 191–221.

Pierre, C., 2018. The isotopic record of gypsum diagenesis in diluted solutions: Observations in natural salinas and experiments. Chemical Geology 493, 451–457.

Pierre, C., Fontes, J., 1978. Isotope Composition of Messinian Sediments from the Mediterranean Sea as Indicators of Paleoenvironments and Diagensis. In: Initial Reports of the Deep Sea Drilling Project, 42 Pt. 1. U.S. Government Printing Office.

Pierre, C., Rouchy, J. M., 1990. Sedimentary and diagenetic evolution of Messinian evaporites in the Tyrrhenian Sea (ODP Leg 107, sites 652, 653, and 654); petrographic, mineralogical, and stable isotope records. Proceedings of the Ocean Drilling Program, Tyrrhenian Sea, covering Leg 107 of the cruises of the Drilling Vessel JOIDES Resolution, Malaga, Spain to Marseille, France, sites 650-656, 20 December 1985-18 February 1986. 107, 187–210.

Playà, E., Recio, C., Mitchell, J., 2005. Extraction of gypsum hydration water for oxygen isotopic analysis by the guanidine hydrochloride reaction method. Chemical Geology 217, 89–96.

Prasad, P. S. R., Chaitanya, V. K., Prasad, K. S., Rao, D. N., 2005. Direct formation of the γ-$CaSO_4$ phase in dehydration process of gypsum: In situ FTIR study. American Mineralogist 90 (4), 672–678.

Prasad, P. S. R., Pradhan, A., Gowd, T. N., 2001. In situ micro-Raman investigation of dehydration mechanism in natural gypsum. Current Science 80 (9), 1203–1207.

Pretet, C., van Zuilen, K., Nägler, T. F., Reynaud, S., Böttcher, M. E., Samankassou, E., 2015. Constraints on barium isotope fractionation during aragonite precipitation by corals. The

Depositional Record 1 (2), 118–129.

Prieto-Taboada, N., Gómez-Laserna, O., Martínez-Arkarazo, I., Olazabal, M. Á., Madariaga, J. M., 2014. Raman Spectra of the Different Phases in the $CaSO_4$-H_2O System. Analytical Chemistry 86 (20), 10131–10137.

Putnis, A., Winkler, B., Fernandez-Diaz, L., 1990. In situ IR spectroscopic and thermogravimetric study of the dehydration of gypsum. Mineralogical Magazine 54 (374), 123–128.

Rapin, W., Meslin, P. Y., Maurice, S., Vaniman, D., Nachon, M., Mangold, N., Schroder, S., Gasnault, O., Forni, O., Wiens, R. C., Martinez, G. M., Cousin, A., Sautter, V., Lasue, J., Rampe, E. B., Archer, D., 2016. Hydration state of calcium sulfates in Gale crater, Mars: Identification of bassanite veins. Earth and Planetary Science Letters 452, 197–205.

Reghizzi, M., Gennari, R., Douville, E., Lugli, S., Manzi, V., Montagna, P., Roveri, M., Sierro, F. J., Taviani, M., 2017. Isotope stratigraphy ($^{87}Sr/^{86}Sr$, $\delta^{18}O$, $\delta^{13}C$) of the Sorbas basin (Betic Cordillera, Spain): Paleoceanographic evolution across the onset of the Messinian salinity crisis. Palaeogeography, Palaeoclimatology, Palaeoecology 469, 60–73.

Reghizzi, M., Lugli, S., Manzi, V., Rossi, F. P., Roveri, M., 2018. Orbitally Forced Hydrological Balance During the Messinian Salinity Crisis: Insights From Strontium Isotopes ($^{87}Sr/^{86}Sr$) in the Vena del Gesso Basin (Northern Apennines, Italy). Paleoceanography and Paleoclimatology 33 (7), 716–731.

Rennie, V. C. F., Turchyn, A. V., 2014. Controls on the abiotic exchange between aqueous sulfate and water under laboratory conditions. Limnology and Oceanography: Methods 12 (4), 166–173.

Rigaudier, T., Lécuyer, C., Gardien, V., Suc, J. P., Martineau, F., 2011. The record of temperature, wind velocity and air humidity in the δD and $\delta^{18}O$ of water inclusions in synthetic and Messinian halites. Geochimica et Cosmochimica Acta 75 (16), 4637–4652.

Risi, C., Landais, A., Bony, S., Jouzel, J., Masson-Delmotte, V., Vimeux, F., 2010. Understanding the ^{17}O excess glacial-interglacial variations in Vostok precipitation. Journal of Geophysical Research Atmospheres 115 (10).

Robertson, K., Bish, D., 2013. Constraints on the distribution of $CaSO_4 \cdot nH_2O$ phases on Mars and implications for their contribution to the hydrological cycle. Icarus 223 (1), 407–417.

Rosell, L., Orti, F., Kasprzyk, A., Playa, E., Peryt, T. M., 1998. Strontium geochemistry of Miocene primary gypsum; Messinian of southeastern Spain and Sicily and Badenian of Poland. Journal of Sedimentary Research 68 (1), 63–79.

Rossi, C., Vilas, L., Arias, C., 2015. The Messinian marine to nonmarine gypsums of Jumilla (Northern Betic Cordillera, SE Spain): Isotopic and Sr concentration constraints on the origin of parent brines. Sedimentary Geology 328, 96–114.

Rouchy, J., Orszag-Sperber, F., Blanc-Valleron, M.-M., Pierre, C., Rivière, M., Combourieu-Nebout, N., Panayides, I., 2001. Paleoenvironmental changes at the Messinian–Pliocene boundary in

the eastern Mediterranean (southern Cyprus basins): significance of the Messinian Lago-Mare. Sedimentary Geology 145 (1-2), 93–117.

Rouchy, J. M., Caruso, A., 2006. The Messinian salinity crisis in the Mediterranean basin: A reassessment of the data and an integrated scenario. Sedimentary Geology 188-189, 35–67.

Roveri, M., Bertini, A., Stefano, A. D., Gennari, R., Gliozzi, E., Grossi, F., Iaccarino, S. M., Lugli, S., Manzi, V., Taviani, M., A, V. G. P. U., 2008. A high-resolution stratigraphic framework for the latest Messinian events in the Mediterranean area. Stratigraphy 5, 323–342.

Roveri, M., Flecker, R., Krijgsman, W., Lofi, J., Lugli, S., Manzi, V., Sierro, F. J., Bertini, A., Camerlenghi, A., De Lange, G., Govers, R., Hilgen, F. J., Hübscher, C., Meijer, P. T., Stoica, M., 2014a. The Messinian Salinity Crisis: Past and future of a great challenge for marine sciences. Marine Geology 352, 25–58.

Roveri, M., Gennari, R., Lugli, S., Manzi, V., 2009. The Terminal Carbonate Complex: the record of sea-level changes during the Messinian salinity crisis. GeoActa 8, 63–77.

Roveri, M., Lugli, S., Manzi, V., Gennari, R., Schreiber, B. C., 2014b. High-resolution strontium isotope stratigraphy of the Messinian deep Mediterranean basins: Implications for marginal to central basins correlation. Marine Geology 349, 113–125.

Rudge, J. F., Reynolds, B. C., Bourdon, B., 2009. The double spike toolbox. Chemical Geology 265 (3-4), 420–431.

Ryan, W. B. F., 2009. Decoding the Mediterranean salinity crisis. Sedimentology 56 (1), 95–136.

Saad, N., Hsiao, G., Chapellet-volpini, L., Vu, D., 2013. Two-Pronged Approach to Overcome Spectroscopically Interfering Organic Compounds with Isotopic Water Analysis. Geophysical Research Abstracts (15), EGU2013–13296.

Saha, A., Lee, J., Pancera, S. M., Bräeu, M. F., Kempter, A., Tripathi, A., Bose, A., 2012. New Insights into the Transformation of Calcium Sulfate Hemihydrate to Gypsum Using Time-Resolved Cryogenic Transmission Electron Microscopy. Langmuir 28 (30), 11182–11187.

Sarma, L. P., Prasad, P. S. R., Ravikumar, N., 1998. Raman spectroscopic study of phase transitions in natural gypsum. Journal of Raman Spectroscopy 29 (9), 851–856.

Schoenemann, S. W., Schauer, A. J., Steig, E. J., 2013. Measurement of SLAP2 and GISP δ^{17}O and proposed VSMOW-SLAP normalization for δ^{17}O and ^{17}O excess. Rapid Communications in Mass Spectrometry 27 (5), 582–590.

Schreiber, C., Kingsman, D. J. J., 1975. New Observations on the Pleistocene Evaporites of Montallegro, Sicily and a Modern Analog. SEPM Journal of Sedimentary Research Vol. 45.

Selli, R., 1960. Il Messiniano Mayer-Eymar (1867). Proposta di un neostratotipo. Giornale di Geologia 28, 1–33.

Sheppard, S. M. F., Schwarcz, H. P., 1970. Fractionation of carbon and oxygen isotopes and magnesium between coexisting metamorphic calcite and dolomite. Contributions to Mineralogy

and Petrology 26 (3), 161–198.

Sierro, F., Hilgen, F., Krijgsman, W., Flores, J., 2001. The Abad composite (SE Spain): a Messinian reference section for the Mediterranean and the APTS. Palaeogeography, Palaeoclimatology, Palaeoecology 168 (1-2), 141–169.

Sierro, F. J., Flores, J. A., Zamarreño, I., Vázquez, A., Utrilla, R., Francés, G., Hilgen, F. J., Krijgsman, W., 1999. Messinian pre-evaporite sapropels and precession-induced oscillations in western Mediterranean climate. Marine Geology 153, 137–146.

Simon, D., 2017. Gateway exchange, climatic forcing and circulation of the Mediterranean Sea during the late Miocene: A model perspective. No. 129.

Simon, D., Marzocchi, A., Flecker, R., Lunt, D. J., Hilgen, F. J., Meijer, P. T., 2017. Quantifying the Mediterranean freshwater budget throughout the late Miocene: New implications for sapropel formation and the Messinian Salinity Crisis. Earth and Planetary Science Letters 472, 25–37.

Simon, D., Meijer, P. T., 2017. Salinity stratification of the Mediterranean Sea during the Messinian crisis: A first model analysis. Earth and Planetary Science Letters 479, 366–376.

Sofer, Z., 1975. Isotopic Compositions of Hydration Water in Gypsum. Ph.D. thesis, The Feinberg Graduate School, Rehovot, Israel (in Hebrew).

Sofer, Z., 1978. Isotopic composition of hydration water in gypsum. Geochimica et Cosmochimica Acta 42, 1141–1149.

Sofer, Z., Gat, J., 1972. Activities and concentrations of oxygen-18 in concentrated aqueous salt solutions: Analytical and geophysical implications. Earth and Planetary Science Letters 15 (3), 232–238.

Soler-Bientz, R., Watson, S., Infield, D., 2010. Wind characteristics on the Yucatan Peninsula based on short term data from meteorological stations. Energy Conversion and Management 51 (4), 754–764.

Speranza, G., Cosentino, D., Tecce, F., Faccenna, C., 2013. Paleoclimate reconstruction during the Messinian evaporative drawdown of the Mediterranean Basin: Insights from microthermometry on halite fluid inclusions. Geochemistry, Geophysics, Geosystems 14, 5054–5077.

Spötl, C., Vennemann, T. W., 2003. Continuous-flow isotope ratio mass spectrometric analysis of carbonate minerals. Rapid communications in mass spectrometry : RCM 17, 1004–1006.

Stark, S. C., O'Grady, B. V., Burton, H. R., Carpenter, D., 2003. Frigidly concentrated seawater and the evolution of Antarctic saline lakes. Australian Journal of Chemistry 56 (2-3), 181–186.

Stawski, T. M., Van Driessche, A. E., Ossorio, M., Diego Rodriguez-Blanco, J., Besselink, R., Benning, L. G., 2016. Formation of calcium sulfate through the aggregation of sub-3 nanometre primary species. Nature Communications 7, 1–9.

Steig, E. J., Gkinis, V., Schauer, A. J., Schoenemann, S. W., Samek, K., Hoffnagle, J., Dennis, K. J., Tan, S. M., 2014. Calibrated high-precision ^{17}O-excess measurements using cavity ring-down

spectroscopy with laser-current-tuned cavity resonance. Atmospheric Measurement Techniques 7 (8), 2421–2435.

Stoica, M., Krijgsman, W., Fortuin, A., Gliozzi, E., 2016. Paratethyan ostracods in the Spanish Lago-Mare: More evidence for interbasinal exchange at high Mediterranean sea level. Palaeogeography, Palaeoclimatology, Palaeoecology 441, 854–870.

Strydom, C. A., Hudson-Lamb, D. L., Potgieter, J. H., Dagg, E., 1995. The thermal dehydration of synthetic gypsum. Thermochimica Acta 269-270 (C), 631–638.

Surma, J., Assonov, S., Bolourchi, M. J., Staubwasser, M., 2015. Triple oxygen isotope signatures in evaporated water bodies from the Sistan Oasis, Iran. Geophysical Research Letters 42 (20), 8456–8462.

Surma, J., Assonov, S., Herwartz, D., Voigt, C., Staubwasser, M., 2018. The evolution of ^{17}O-excess in surface water of the arid environment during recharge and evaporation. Scientific Reports 8 (1), 4972.

Tan, H.-B., Huang, J.-Z., Zhang, W.-J., Liu, X.-Q., Zhang, Y.-F., Kong, N., Zhang, Q., 2014. Fractionation of hydrogen and oxygen isotopes of gypsum hydration water and assessment of its geochemical indications. Australian Journal of Earth Sciences 61 (6), 793–801.

Tarutani, T., Clayton, R. N., Mayeda, T. K., 1969. The effect of polymorphism and magnesium substitution on oxygen isotope fractionation between calcium carbonate and water. Geochimica et Cosmochimica Acta 33 (8), 987–996.

Taube, H., 1954. Use of Oxygen Isotope Effects in Study of Hydration of Ions. The Journal of Physical Chemistry 58 (7), 523–528.

Thode, H., Monster, J., 1965. Sulfur isotope geochemistry of petroleum, evaporites and ancient seas. American Association of Petroleum Geologists Memoir 4, 367–377.

Thompson, J. B., Ferris, F. G., 1990. Cyanobacterial precipitation of gypsum, calcite, and magnesite from natural alkaline lake water. Geology 18 (10), 995.

Tipper, E. T., Gaillardet, J., Galy, A., Louvat, P., Bickle, M. J., Capmas, F., 2010. Calcium isotope ratios in the world's largest rivers: A constraint on the maximum imbalance of oceanic calcium fluxes. Global Biogeochemical Cycles 24 (3).

Tipper, E. T., Galy, A., Bickle, M. J., 2008. Calcium and magnesium isotope systematics in rivers draining the Himalaya-Tibetan-Plateau region: Lithological or fractionation control? Geochimica et Cosmochimica Acta 72 (4), 1057–1075.

Topper, R. P. M., Lugli, S., Manzi, V., Roveri, M., Meijer, P. T., 2014. Precessional control of Sr ratios in marginal basins during the Messinian Salinity Crisis? Geochemistry, Geophysics, Geosystems 15 (5), 1926–1944.

Topper, R. P. M., Meijer, P. T., 2013. A modeling perspective on spatial and temporal variations in Messinian evaporite deposits. Marine Geology 336, 44–60.

Torfstein, A., Turchyn, A. V., 2017. Rates and Cycles of Microbial Sulfate Reduction in the Hyper-Saline Dead Sea over the Last 200 kyrs from Sedimentary $\delta^{34}S$ and $\delta^{18}O_{(SO_4)}$. Frontiers in Earth Science 5, 1–14.

Turchyn, A. V., Schrag, D. P., 2004. Oxygen isotope constraints on the sulfur cycle over the past 10 million years. Science (New York, N.Y.) 303 (5666), 2004–2007.

Uemura, R., Barkan, E., Abe, O., Luz, B., 2010. Triple isotope composition of oxygen in atmospheric water vapor. Geophysical Research Letters 37 (4), 1–4.

Urey, H., Lowenstam, H., Epstein, S., McKinney, C., 1951. Measurement of Paleotemperatures and Temperatures and the Southeastern United States. Bulletin of the geological society of America 62 (4), 399–416.

Urey, H. C., 1947. The thermodynamic properties of isotopic substances. Journal of the Chemical Society (Resumed), 562–581.

Usiglio, J., 1849. Analyse de l'eau de la Méditerranée sur les côtes de France. Annales de Chimie et de Physique 3eme ser 27, 92–107.

Van Couvering, J., Castradori, D., Cita, M., Hilgen, F., Rio, D., 2000. The base of the Zanclean Stage and of the Pliocene Series. Episodes 23, 179–187.

van der Heijden, G. H., Pel, L., Huinink, H. P., Kopinga, K., 2011. Moisture transport and dehydration in heated gypsum, an NMR study. Chemical Engineering Science 66 (18), 4241–4250.

van der Laan, E., Gaboardi, S., Hilgen, F. J., Lourens, L. J., 2005. Regional climate and glacial control on high-resolution oxygen isotope records from Ain el Beida (latest Miocene, northwest Morocco): A cyclostratigraphic analysis in the depth and time domain. Paleoceanography 20 (1), 1–22.

Van Der Laan, E., Snel, E., De Kaenel, E., Hilgen, F. J., Krijgsman, W., 2006. No major deglaciation across the Miocene-Pliocene boundary: Integrated stratigraphy and astronomical tuning of the Loulja sections (Bou Regreg area, NW Morocco). Paleoceanography 21 (3), 1–27.

Van Driessche, A. E. S., Benning, L. G., Rodriguez-Blanco, J. D., Ossorio, M., Bots, P., Garcia-Ruiz, J. M., 2012. The Role and Implications of Bassanite as a Stable Precursor Phase to Gypsum Precipitation. Science 336 (6077), 69–72.

van Zuilen, K., Müller, T., Nägler, T. F., Dietzel, M., Küsters, T., 2016. Experimental determination of barium isotope fractionation during diffusion and adsorption processes at low temperatures. Geochimica et Cosmochimica Acta 186, 226–241.

Vasconcelos, C., McKenzie, J., A., Bernasconi, S., Grujic, D., Tiens, A., J., 1995. Microbial mediation as a possible mechanism for natural dolomite formation at low temperatures. Nature 377, 220–222.

Vasconcelos, C., McKenzie, J. A., 1997. Microbial Mediation of Modern Dolomite Precipitation

and Diagenesis Under Anoxic Conditions (Lagoa Vermelha, Rio de Janeiro, Brazil). Journal of Sedimentary Research 67, 378–390.

Vasconcelos, C., McKenzie, J. a., Warthmann, R., Bernasconi, S. M., 2005. Calibration of the δ^{18}O paleothermometer for dolomite precipitated in microbial cultures and natural environments. Geology 33 (4), 317–320.

Vogel, M. B., Des Marais, D. J., Parenteau, M. N., Jahnke, L. L., Turk, K. A., Kubo, M. D., 2010. Biological influences on modern sulfates: Textures and composition of gypsum deposits from Guerrero Negro, Baja California Sur, Mexico. Sedimentary Geology 223 (3-4), 265–280.

Vogel, M. B., Des Marais, D. J., Turk, K. A., Parenteau, M. N., Jahnke, L. L., Kubo, M. D., 2009. The Role of Biofilms in the Sedimentology of Actively Forming Gypsum Deposits at Guerrero Negro, Mexico. Astrobiology 9 (9), 875–893.

von Allmen, K., Böttcher, M. E., Samankassou, E., Nägler, T. F., 2010. Barium isotope fractionation in the global barium cycle: First evidence from barium minerals and precipitation experiments. Chemical Geology 277 (1-2), 70–77.

Wahl, D., Byrne, R., Anderson, L., 2014. An 8700 year paleoclimate reconstruction from the southern Maya lowlands. Quaternary Science Reviews 103, 19–25.

Wahl, D., Estrada-Belli, F., Anderson, L., 2013. A 3400 year paleolimnological record of prehispanic human-environment interactions in the Holmul region of the southern Maya lowlands. Palaeogeography, Palaeoclimatology, Palaeoecology 379-380, 17–31.

Wang, Y.-W., Kim, Y.-Y., Christenson, H. K., Meldrum, F. C., 2012. A new precipitation pathway for calcium sulfate dihydrate (gypsum) via amorphous and hemihydrate intermediates. Chem. Commun. 48 (4), 504–506.

Warren, J. K., 1982. The hydrological setting, occurrence and significance of gypsum in late Quaternary salt lakes in South Australia. Sedimentology 29 (5), 609–637.

Warren, J. K., 2010. Evaporites through time: Tectonic, climatic and eustatic controls in marine and nonmarine deposits. Earth-Science Reviews 98 (3-4), 217–268.

Warren, J. K., 2016. Depositional Chemistry and Hydrology. In: Evaporites. Springer International Publishing, Cham, pp. 85–205.

Wassenaar, L. I., Van Wilgenburg, S. L., Larson, K., Hobson, K. A., 2009. A groundwater isoscape (δD, δ^{18}O) for Mexico. Journal of Geochemical Exploration 102 (3), 123–136.

Webster, J. W., Brook, G. A., Railsback, L. B., Cheng, H., Edwards, R. L., Alexander, C., Reeder, P. P., 2007. Stalagmite evidence from Belize indicating significant droughts at the time of Preclassic Abandonment, the Maya Hiatus, and the Classic Maya collapse. Palaeogeography, Palaeoclimatology, Palaeoecology 250 (1-4), 1–17.

Winkler, R., Landais, A., Risi, C., Baroni, M., Ekaykin, A., Jouzel, J., Petit, J. R., Prie, F., Minster, B., Falourd, S., 2013. Interannual variation of water isotopologues at Vostok indicates

a contribution from stratospheric water vapor. Proceedings of the National Academy of Sciences 110 (44), 17674–17679.

Yaeger, J., Hodell, D. A., 2009. The Collapse of Maya Civilization: Assessing the Interaction of Culture, Climate, and Environment. In: Sandweiss, D. H., Quilter, J. (Eds.), El Niño, Catastrophism, and Culture Change in Ancient America. Harvard University Press, Dumbarton Oaks, Washington, D.C., Ch. 10, pp. 187–242.

Yoshimura, T., Kuroda, J., Lugli, S., Tamenori, Y., Ogawa, N. O., Jiménez-Espejo, F. J., Isaji, Y., Roveri, M., Manzi, V., Kawahata, H., Ohkouchi, N., 2016. An X-ray spectroscopic perspective on Messinian evaporite from Sicily: Sedimentary fabrics, element distributions, and chemical environments of S and Mg. Geochemistry, Geophysics, Geosystems 17 (4), 1383–1400.

Zeebe, R., Wolf-Gladrow, D., 2001. Stable Isotope Fractionation. CO_2 in Seawater: Equilibrium, Kinetics, Isotopes: Equilibrium, Kinetics, Isotopes.

Zimbelman, D., Rye, R., Breit, G., 2005. Origin of secondary sulfate minerals on active andesitic stratovolcanoes. Chemical Geology 215 (1-4), 37–60.

Appendix A

Tables for Section 2.3

Table A.1a. Isotopic analysis (δ^{17}O, δ^{18}O and δD values) of hydration water of a gypsum standard (NEWGYP) extracted using the WASP and analyzed by CRDS and IRMS.

Line/date	Method	$\delta^{17}O$	1σ	$\delta^{18}O$	1σ	δD	1σ	d-excess	1σ	^{17}O−excess	1σ	H_2O
		(‰)		(‰)		(‰)		(‰)		(per meg)	(per meg)	(‰)
L3-28/1/15	CRDS	0.12	0.05	0.21	0.07	-51.23	0.14	-52.3	0.4	21	15	21.3
L4-29/1/15	CRDS	0.2	0.04	0.35	0.04	-50.83	0.12	-52.8	0.3	27	15	20.8
L5-30/1/15	CRDS	0.23	0.04	0.42	0.1	-50.91	0.23	-53.3	0.6	19	11	20.9
L4-30/1/15	IRMS	0.36	0.05	0.67	0.09	-	-	-	-	7	3	20.5
L5-30/1/15	IRMS	0.35	0.01	0.65	0.02	-	-	-	-	10	8	20.6
L2-30/1/15	IRMS	0.29	0.03	0.52	0.05	-	-	-	-	11	3	20.9
L1-30/1/15	IRMS	0.34	0.09	0.62	0.17	-	-	-	-	10	4	20.7
L2-30/1/15	IRMS	0.29	0.1	0.53	0.19	-	-	-	-	9	7	20.6
L3-30/1/15	IRMS	0.17	0.11	0.32	0.2	-	-	-	-	0	8	20.8
L4-30/1/15	IRMS	0.17	0.03	0.31	0.06	-	-	-	-	10	4	20.8
L5-30/1/15	IRMS	0.28	0.06	0.51	0.1	-	-	-	-	9	4	20.4
L6-30/1/15	CRDS	0.16	0.04	0.25	0.07	-50.89	0.52	-54.2	0.5	18	7	20.9
L1-03/2/15	CRDS	0.13	0.05	0.16	0.09	-50.34	0.32	-51.6	0.6	33	8	20.8
L2-03/2/15	CRDS	0.14	0.02	0.25	0.03	-51.28	0.17	-53.3	0.2	8	14	21.9
L4-04/2/15	CRDS	0.17	0.02	0.3	0.05	-51.48	0.29	-53.9	0.4	20	16	20.4
L5-05/2/15	CRDS	0.13	0.02	0.21	0.02	-51.81	0.1	-53.5	0.1	23	14	20.3
L1-09/2/15	CRDS	0.16	0.02	0.27	0.04	-51.59	0.27	-53.8	0.1	13	14	20.7
L2-09/2/15	CRDS	0.12	0.02	0.18	0.03	-51.88	0.09	-53.3	0.2	21	13	20.5
L3-10/2/15	CRDS	0.18	0.03	0.29	0.04	-51.63	0.19	-54	0.2	18	16	20.9
L6-18/2/15	CRDS	0.07	0.03	0.11	0.04	-51.8	0.18	-53.4	0.2	20	12	20.8
L1-22/2/15	CRDS	0.2	0.02	0.33	0.03	-51.24	0.2	-54.7	0.2	32	10	20.7
L3-04/2/15	CRDS	0.17	0.03	0.3	0.04	-50.39	0.23	-52.9	0.1	11	13	20.7
L4-02/3/15	CRDS	0.16	0.02	0.29	0.02	-50.8	0.08	-53.1	0.2	12	11	20.1
L1-03/3/15	CRDS	0.19	0.02	0.32	0.03	-51.27	0.19	-53.8	0.2	17	13	20.9
L2-05/3/15	CRDS	0.23	0.02	0.41	0.02	-50.36	0.35	-53.5	0.5	18	7	20.6
L3-06/3/15	CRDS	0.37	0.04	0.66	0.05	-50.8	0.18	-56.1	0.3	17	15	20.2
L4-08/3/15	CRDS	0.18	0.02	0.32	0.03	-51.74	0.13	-54.3	0.2	12	15	21.9
L5-09/3/15	CRDS	0.28	0.03	0.5	0.05	-50.64	0.19	-54.6	0.2	19	10	19.9
L6-11/3/15	CRDS	0.22	0.01	0.4	0.01	-51.31	0.1	-54.5	0.2	3	11	20.7
L1-12/3/15	CRDS	0.28	0.03	0.52	0.03	-51.16	0.06	-55.3	0.2	12	13	20.8
L6-13/3/15	CRDS	0.18	0.02	0.31	0.05	-50.63	0.36	-53.1	0.2	15	15	20.7
L3-22/3/15	CRDS	0.25	0.02	0.45	0.03	-50.5	0.3	-54.5	0.5	6	16	20.4
L4-23/3/15	CRDS	0.21	0.03	0.39	0.03	-51.29	0.18	-53.2	0.4	9	15	20.5
L6-26/3/15	CRDS	0.22	0.03	0.43	0.03	-50.28	0.21	-53.7	0.2	-5	16	20.8
L6-27/3/15	CRDS	0.24	0.01	0.41	0.02	-50.81	0.22	-54.1	0.1	18	10	20.7
L5-30/3/15	CRDS	0.21	0.03	0.37	0.03	-51.1	0.23	-54	0.2	16	12	21.2
L4-01/4/15	CRDS	0.16	0.03	0.29	0.03	-50.81	0.15	-53.1	0.4	0	12	20.9

Table A.1b. Table A.1a continued. Isotopic analysis (δ^{17}O, δ^{18}O and δD values) of hydration water of a gypsum standard (NEWGYP) extracted using the WASP and analyzed by CRDS and IRMS.

Line/date	**Method**	$\delta^{17}O$ (‰)	**1σ**	$\delta^{18}O$ (‰)	**1σ**	δD (‰)	**1σ**	**d-excess** (‰)	**1σ**	^{17}O−excess (per meg)	**1σ** (per meg)	**H_2O** (‰)
L3-02/4/15	CRDS	0.22	0.02	0.37	0.03	-50.64	0.39	-53.7	0.2	19	15	20.8
L1-20/4/15	CRDS	0.16	0.03	0.29	0.03	-50.01	0.27	-52.4	0.4	5	13	20.5
L2-21/4/15	CRDS	0.04	0.06	0.04	0.12	-50.66	0.65	-50.3	0.4	27	9	20.3
L5-21/4/15	CRDS	0.13	0.04	0.21	0.06	-50.87	0.38	-52.6	0.3	6	13	20.9
L3-22/4/15	CRDS	0.18	0.02	0.32	0.02	-50.59	0.27	-53.1	0.2	13	15	20.9
L4-22/4/15	CRDS	0.07	0.02	0.09	0.02	-51.39	0.18	-52.4	0.2	20	14	20.8
L3-22/4/15	CRDS	0.14	0.03	0.24	0.06	-50.99	0.39	-52.8	0.4	8	13	20.9
L4-22/4/15	CRDS	0.03	0.02	0.03	0.02	-51.24	0.18	-51.7	0.1	17	14	20.7
AVG	CRDS	0.18		0.31		-51.02		-53.4		15		20.7
STD		±0.07		±0.13		±0.49		±1.1		±8		±0.4
AVG	IRMS	0.27		0.49		n/a		n/a		8		20.7
STD		±0.07		±0.14						±4		±0.2

Table A.2. Memory effect tests and experiments of vacuum leakage in the WASP lines during GHW extraction. The term "fresh" refers to a line in which the previous sample analyzed was close in isotopic value to the next sample and memory effects should be minimized.

Sample/Line	**Line status**	$\delta^{17}O$ (‰)	**1σ**	$\delta^{18}O$ (‰)	**1σ**	δD (‰)	**1σ**	^{17}O−excess (per meg)	**1σ**
ENR-gyp L5	"Fresh" line	12.96	0.04	24.93	0.05	34.73	0.19	-126	9
ENR-gyp L6	"Fresh" leaking line	12.78	0.04	24.58	0.05	33.56	0.39	-120	8
ENR-gyp L1	After depleted sample	13.12	0.03	25.24	0.05	35.1	0.38	-125	14
ENR-gyp L2	After depleted sample	13.08	0.03	25.14	0.05	34.66	0.36	-115	13
NEWGYP- L3	"Fresh" line	0.07	0.02	0.09	0.02	-51.39	0.18	20	14
NEWGYP-L4	"Fresh" leaking line	0.03	0.02	0.03	0.02	-51.24	0.18	17	14
DPL-gyp L1	"Fresh" line	-6.79	0.04	-12.83	0.06	-149.66	0.24	1	14
DPL-gyp L2	"Fresh" line	-6.89	0.02	-13.04	0.03	-150.35	0.16	10	9
DPL-gyp L5	After Enriched sample	-6.75	0.03	-12.77	0.03	-150.75	0.04	11	19
DPL-gyp L6	After Enriched sample	-6.78	0.02	-12.79	0.02	-150.8	0.11	-10	21

Table A.3. Isotopic analysis (δ^{17}O, δ^{18}O and δD values) of hydration water of a gypsum standard (NEWGYP) and natural samples. *Samples analyzed in replicate (in these cases, the analytical error refers to the external precision, taking the average of the indicated number of samples).

	CRDS (MCM ON)					CRDS (MCM OFF)					IRMS		
Sample	**δ^{17}O** (‰)	**δ^{18}O** (‰)	**δD** (‰)	**d-excess** (‰)	**^{17}O-excess** (per meg)	**δ^{17}O** (‰)	**δ^{18}O** (‰)	**δD** (‰)	**d-excess** (‰)	**^{17}O-excess** (per meg)	**δ^{17}O** (‰)	**δ^{18}O** (‰)	**^{17}O-excess** (per meg)
BG-10	-1.00	-1.93	-53.36	-37.9	**20**	-0.89	-1.78	-52.9	-38.6	**57**	-1.01	-1.96	**28**
	± 0.02	± 0.02	± 0.21	± 0.2	**± 13**	± 0.01	± 0.03	± 0.14	± 0.2	**± 11**	± 0.02	± 0.04	**± 7**
CRI-01	-0.06	-0.15	-41.91	-40.7	**15**	-0.04	-0.16	-42.3	-42.9	**54**	0.09	0.12	**24**
	± 0.02	± 0.04	± 0.23	± 0.2	**± 7**	± 0.02	± 0.04	± 0.30	± 0.3	**± 12**	± 0.01	± 0.01	**± 5**
NEWGYP (n=36/8)*	0.17	0.3	-51.03	-53.4	**15**	0.12	0.15	-51.23	-53	**42**	0.28	0.51	**8**
	± 0.07	± 0.13	± 0.48	± 1.0	**± 8**	± 0.04	± 0.05	± 0.35	± 0.6	**± 12**	± 0.07	± 0.14	**± 4**
SBL-2.3	1.55	2.92	-27.71	-51.6	**-7**	1.88	3.4	-27.47	-54.7	**77**	1.85	3.52	**-11**
	± 0.01	± 0.03	± 0.27	± 0.3	**± 15**	± 0.02	± 0.02	± 0.11	± 0.1	**± 13**	± 0.01	± 0.02	**± 1**
SBL-8	1.68	3.13	-27.72	-53.2	**7**	1.74	3.17	-28.31	-53.7	**61**	1.9	3.6	**5**
	± 0.02	± 0.02	± 0.07	± 0.1	**± 15**	± 0.02	± 0.02	± 0.07	± 0.2	**± 14**	± 0.01	± 0.03	**± 5**
PI 6A-13H-2 7-8 cm	4.46	8.53	3.76	-64.5	**-26**	5.08	9.41	6.93	-68.4	**123**	4.87	9.3	**-32**
	± 0.01	± 0.02	± 0.14	± 0.2	**± 12**	± 0.04	± 0.05	± 0.20	± 0.4	**± 18**	± 0.00	± 0.01	**± 2**
PI 6C-7H-2 25-26 cm	4.89	9.3	9.76	-64.7	**-17**	5.32	9.74	11.21	-66.8	**190**	4.98	9.51	**-32**
	± 0.03	± 0.05	± 0.26	± 0.3	**± 9**	± 0.02	± 0.02	± 0.06	± 0.2	**± 7**	± 0.02	± 0.03	**± 2**
Salina 1 (n=3)*	5.61	10.74	13.21	-72.7	**-48**	5.74	10.74	13.55	-72.4	**72**	5.88	11.26	**-51**
	± 0.02	± 0.03	± 0.16	± 0.2	**± 8**	± 0.04	± 0.04	± 0.18	± 0.4	**± 16**	± 0.03	± 0.07	**± 5**

Table A.4. Isotopic composition of water samples distilled using the WASP and analysed by CRDS.

Sample	$\delta^{17}O$ (‰)	1σ (‰)	$\delta^{18}O$ (‰)	1σ (‰)	δD (‰)	1σ (‰)	d-excess (‰)	1σ (‰)	^{17}O-excess (per meg)	1σ (per meg)
JRW	-9.99	0.01	-18.85	0.02	-146.01	0.19	**5.6**	**0.2**	**-4**	**13**
JRW-WASP	-10.02	0.03	-18.9	0.05	-146.19	0.2	**5.9**	**0.2**	**2**	**13**
BOTTY	-3.95	0.02	-7.52	0.02	-50.18	0.21	**10.6**	**0.2**	**20**	**13**
BOTTY-WASP	-3.96	0.02	-7.54	0.03	-50.22	0.11	**10.7**	**0.3**	**24**	**10**
SPIT	-0.07	0.02	-0.13	0.03	0.16	0.14	**1.5**	**0.3**	**-6**	**11**
SPIT-WASP	-0.08	0.02	-0.17	0.02	-0.17	0.2	**1.4**	**0.3**	**6**	**13**
ENR	5.64	0.02	10.76	0.01	40.23	0.1	**-46.4**	**0.1**	**-36**	**18**
ENR-WASP	5.55	0.02	10.59	0.02	39.58	0.12	**-45.6**	**0.1**	**-37**	**12**
DEPO-03A	3.03	0.03	5.81	0.02	21.34	0.16	**-25.3**	**0.2**	**-43**	**21**
DEPO-03B	3.03	0.02	5.8	0.02	21.33	0.08	**-25.3**	**0.2**	**-40**	**17**
DEPO-06A	4.15	0.01	7.95	0.01	34.02	0.18	**-29.9**	**0.2**	**-47**	**10**
DEPO-06B	4.2	0.03	8.03	0.03	34.4	0.11	**-30.1**	**0.2**	**-36**	**16**

Appendix B

Tables for Section 2.4

Table B.1a. Fractionation factor between gypsum hydration water and the mother solution in experiments of hydration of anhydrite at different temperatures.

Experiment ID	Temperature (°C)	CRDS analyzer	H_2O %	mother water/GHW	$\delta^{17}O$	1σ	$\delta^{18}O$	1σ	δD	1σ	$\alpha^{17}O$	$\alpha^{18}O$	αD	θ
#32 water 3 °C	3	L2140-*i* Picarro		water	-3.85	0.04	-7.35	0.07	-48.45	0.47	1.00198	1.00373	0.979	**0.5304**
#32 gypsum 3 °C	3	L2140-*i* Picarro	19.7	GHW	-1.88	0.04	-3.65	0.06	-68.86	0.40				
#32 water 3 °C	3	L2140-*i* Picarro		water	-3.93	0.02	-7.33	0.03	-49.69	0.14	1.00204	1.00386	0.979	**0.5298**
#32 gypsum 3 °C	3	L2140-*i* Picarro	20.1	GHW	-1.81	0.12	-3.51	0.21	-68.78	0.27				
#33 water 3 °C	3	L2140-*i* Picarro		water	-3.84	0.04	-7.32	0.08	-47.92	0.29	1.00194	1.00366	0.978	**0.5287**
#33 gypsum 3 °C	3	L2140-*i* Picarro	20.2	GHW	-1.91	0.02	-3.68	0.02	-68.58	0.12				
#33 water 3 °C	3	L2140-*i* Picarro		water	-3.88	0.02	-7.39	0.03	-48.68	0.08	1.00193	1.00364	0.978	**0.5312**
#33 gypsum 3 °C	3	L2140-*i* Picarro	20.5	GHW	-1.92	0.02	-3.71	0.02	-68.89	0.09				
#26 water 8 °C	8	L1102-*i* Picarro		water	-	-	-7.50	0.04	-50.03	0.38	-	1.00375	0.980	-
#26 gypsum 8 °C	8	L1102-*i* Picarro	20.1	GHW	-	-	-3.78	0.05	-68.58	0.31				
#29 water 8 °C	8	L1102-*i* Picarro		water	-	-	-7.49	0.04	-49.11	0.32	-	1.00311	0.980	-
#29 gypsum 8 °C	8	L1102-*i* Picarro	20.6	GHW	-	-	-4.40	0.06	-68.12	0.34				
#30 water 8 °C	8	L2140-*i* Picarro		water	-3.82	0.02	-7.28	0.04	-48.34	0.10	1.00196	1.00371	0.979	**0.5272**
#30 gypsum 8 °C	8	L2140-*i* Picarro	20.6	GHW	-1.87	0.03	-3.59	0.05	-67.85	0.28				
#30 water 8 °C	8	L2140-*i* Picarro		water	-3.86	0.02	-7.36	0.02	-48.27	0.10	1.00191	1.00361	0.979	**0.5299**
#30 gypsum 8 °C	8	L2140-*i* Picarro	20.4	GHW	-1.95	0.01	-3.77	0.01	-67.93	0.17				
#31 water 8 °C	8	L2140-*i* Picarro		water	-3.85	0.03	-7.33	0.05	-48.51	0.10	1.00206	1.00390	0.981	**0.5300**
#31 gypsum 8 °C	8	L2140-*i* Picarro	20.9	GHW	-1.79	0.02	-3.46	0.03	-66.65	0.19				
#31 water 8 °C	8	L2140-*i* Picarro		water	-3.90	0.02	-7.43	0.02	-48.36	0.06	1.00209	1.00396	0.981	**0.5300**
#31 gypsum 8 °C	8	L2140-*i* Picarro	20.8	GHW	-1.81	0.02	-3.50	0.03	-67.02	0.14				
#6 water 20 °C	20	L1102-*i* Picarro		water	-	-	-7.46	0.06	-50.03	0.23	-	1.00354	0.981	-
#6 gypsum 20 °C	20	L1102-*i* Picarro	20.4	GHW	-	-	-3.95	0.03	-68.13	0.30				
#6 water 20 °C	20	L1102-*i* Picarro		water	-	-	-7.48	0.04	-50.24	0.39	-	1.00326	0.980	-
#6 gypsum 20 °C	20	L1102-*i* Picarro	20.6	GHW	-	-	-4.23	0.03	-68.64	0.41				
#7 water 20 °C	20	L1102-*i* Picarro		water	-	-	-7.48	0.04	-50.38	0.26	-	1.00347	0.981	-
#7 gypsum 20 °C	20	L1102-*i* Picarro	20.2	GHW	-	-	-4.04	0.03	-68.82	0.35				
#7 water 20 °C	20	L1102-*i* Picarro		water	-	-	-7.51	0.02	-51.23	0.43	-	1.00342	0.980	-
#7 gypsum 20 °C	20	L1102-*i* Picarro	20.3	GHW	-	-	-4.08	0.05	-68.91	0.42				
#24 water 25°C	25	L1102-*i* Picarro		water	-	-	-7.50	0.05	-49.91	0.23	-	1.00332	0.980	-
#24 gypsum 25 °C	25	L1102-*i* Picarro	20.0	GHW	-	-	-4.21	0.02	-68.72	0.29				
#24 water 25°C	25	L1102-*i* Picarro		water	-	-	-7.54	0.06	-50.52	0.49	-	1.00354	0.981	-
#24 gypsum 25 °C	25	L1102-*i* Picarro	20.1	GHW	-	-	-3.99	0.07	-68.19	0.09				
#25 water 25°C	25	L1102-*i* Picarro		water	-	-	-7.58	0.06	-49.98	0.40	-	1.00344	0.981	-
#25 gypsum 25 °C	25	L1102-*i* Picarro	20.2	GHW	-	-	-4.17	0.04	-67.74	0.29				
#25 water 25°C	25	L1102-*i* Picarro		water	-	-	-7.59	0.04	-49.90	0.43	-	1.00370	0.982	-
#25 gypsum 25 °C	25	L1102-*i* Picarro	20.8	GHW	-	-	-3.92	0.05	-67.17	0.41				
#25 water 25°C	25	L2140-*i* Picarro		water	-3.93	0.03	-7.50	0.03	-49.13	0.15	1.00181	1.00341	0.981	**0.5298**
#25 gypsum 25 °C	25	L2140-*i* Picarro	20.7	GHW	-2.13	0.04	-4.11	0.05	-67.53	0.30				
#23 water 30°C	30	L1102-*i* Picarro		water	-3.91	0.02	-7.48	0.02	-49.18	0.17	1.00174	1.00330	0.981	**0.5279**
#23 gypsum 30 °C	30	L1102-*i* Picarro	20.7	GHW	-2.17	0.03	-4.21	0.05	-67.07	0.15				
#28 water 30°C	30	L2140-*i* Picarro		water	-3.90	0.02	-7.49	0.03	-49.29	0.22	1.00174	1.00328	0.981	**0.5299**
#28 gypsum 30 °C	30	L2140-*i* Picarro	20.1	GHW	-2.17	0.03	-4.23	0.04	-67.05	0.26				

Table B.1b. Table B.1a continued. Fractionation factor between gypsum hydration water and the mother solution in experiments of hydration of anhydrite at different temperatures.

Experiment ID	Temperature (°C)	CRDS analyzer	H_2O %	mother water/GHW	$\delta^{17}O$	1σ	$\delta^{18}O$	1σ	δD	1σ	$\alpha^{17}O$	$\alpha^{18}O$	αD	θ
#12 water 35°C	35	L1102-*i* Picarro		water	-	-	-7.45	0.05	-50.38	0.24	-	1.00343	0.981	-
#12 gypsum 35 °C	35	L1102-*i* Picarro	19.8	GHW	-	-	-4.04	0.02	-68.42	0.09				
#12 water 35°C	35	L1102-*i* Picarro		water	-	-	-7.45	0.01	-50.44	0.09	-	1.00343	0.981	-
#12 gypsum 35 °C	35	L1102-*i* Picarro	20.0	GHW	-	-	-4.04	0.02	-68.56	0.09				
#13 water 35°C	35	L1102-*i* Picarro		water	-	-	-7.44	0.02	-50.36	0.06	-	1.00342	0.981	-
#13 gypsum 35 °C	35	L1102-*i* Picarro	19.9	GHW	-	-	-4.05	0.02	-68.09	0.11				
#13 water 35°C	35	L1102-*i* Picarro		water	-	-	-7.47	0.02	-50.53	0.09	-	1.00341	0.982	-
#13 gypsum 35 °C	35	L1102-*i* Picarro	20.0	GHW	-	-	-4.08	0.02	-67.99	0.11				
#18 water 40 °C	40	L1102-*i* Picarro		water	-	-	-7.47	0.02	-50.44	0.06	-	1.00353	0.982	-
#18 gypsum 40 °C	40	L1102-*i* Picarro	21.1	GHW	-	-	-3.96	0.04	-67.96	0.09				
#18 water 40 °C	40	L1102-*i* Picarro		water	-	-	-7.47	0.02	-50.58	0.07	-	1.00338	0.981	-
#18 gypsum 40 °C	40	L1102-*i* Picarro	20.8	GHW	-	-	-4.11	0.02	-68.42	0.08				
#19 water 40 °C	40	L1102-*i* Picarro		water	-	-	-7.46	0.02	-50.83	0.10	-	1.00349	0.983	-
#19 gypsum 40 °C	40	L1102-*i* Picarro	20.1	GHW	-	-	-4.00	0.08	-66.62	0.37				
#19 water 40 °C	40	L1102-*i* Picarro		water	-	-	-7.36	0.05	-50.30	0.05	-	1.00343	0.982	-
#19 gypsum 40 °C	40	L1102-*i* Picarro	21.0	GHW	-	-	-3.96	0.03	-67.05	0.14				
#19 water 40 °C	40	L2140-*i* Picarro		water	-3.91	0.02	-7.48	0.02	-49.05	0.06	1.00169	1.00318	0.982	**0.5314**
#19 gypsum 40 °C	40	L2140-*i* Picarro	20.9	GHW	-2.23	0.04	-4.32	0.05	-65.85	0.35				
														AVG θ
														SD θ

Table B.2a. Fractionation factor between gypsum hydration water and the mother solution in mixing experiments ($CaCl_2$ and Na_2SO_4) at different temperatures and initial Ca_2^+ and SO_4^{2-} concentrations. Experiment were performed in an oven with no agitation and in a shaking bath.

Experiment ID	Initial Ca^{2+} and SO_4^{2-} concent (mol/L)	Temperature (℃)	Drifting/Shaking	CRDS analyzer	mother water/ GHW	% H_2O	$\delta^{17}O$	1σ	$\delta^{18}O$	1σ	δD	1σ	$\alpha^{18}O$	αD
1A 5 DRF WAT	0.25	5	Drifting	L1102-*i* Picarro	water		-7.35	0.03	-50.25	0.18	1.0036	0.979		
1A 5 DRF GYP	0.25	5	Drifting	L1102-*i* Picarro	GHW	20.7	-3.80	0.04	-70.39	0.34				
1B 5 DRF WAT	0.25	5	Drifting	L1102-*i* Picarro	water		-7.36	0.04	-50.24	0.17	1.0034	0.978		
1B 5 DRF GYP	0.25	5	Drifting	L1102-*i* Picarro	GHW	21	-4.01	0.03	-71.28	0.29				
2A 5 DRF WAT	0.166	5	Drifting	L1102-*i* Picarro	water		-7.34	0.03	-49.97	0.19	1.0036	0.978		
2A 5 DRF GYP	0.166	5	Drifting	L1102-*i* Picarro	GHW	20.6	-3.75	0.06	-71.32	0.28				
2B 5 DRF WAT	0.166	5	Drifting	L1102-*i* Picarro	water		-7.31	0.04	-50.07	0.25	1.0033	0.977		
2B 5 DRF GYP	0.166	5	Drifting	L1102-*i* Picarro	GHW	20.8	-4.01	0.02	-71.94	0.31				
3A 5 DRF WAT	0.065	5	Drifting	L1102-*i* Picarro	water		-7.32	0.03	-49.91	0.21	1.0037	0.976		
3A 5 DRF GYP	0.065	5	Drifting	L1102-*i* Picarro	GHW	20.5	-3.66	0.05	-72.81	0.29				
3B 5 DRF WAT	0.065	5	Drifting	L1102-*i* Picarro	water		-7.24	0.02	-49.94	0.28	1.0033	0.976	**AVG** 1.0035	0.977
3B 5 DRF GYP	0.065	5	Drifting	L1102-*i* Picarro	GHW	19.8	-3.93	0.02	-72.74	0.14			**1σ** 0.0002	0.0011
1A 20 DRF WAT	0.25	20	Drifting	L1102-*i* Picarro	water		-7.22	0.03	-49.19	0.18	1.0039	0.984		
1A 20 DRF GYP	0.25	20	Drifting	L1102-*i* Picarro	GHW	20.4	-3.37	0.04	-64.78	0.34				
1B 20 DRF WAT	0.25	20	Drifting	L1102-*i* Picarro	water		-7.31	0.04	-48.83	0.17	1.0038	0.983		
1B 20 DRF GYP	0.25	20	Drifting	L1102-*i* Picarro	GHW	20.1	-3.58	0.03	-65.19	0.29				
2B 20 DRF WAT	0.166	20	Drifting	L1102-*i* Picarro	water		-7.26	0.04	-49.36	0.25	1.0036	0.980		
2B 20 DRF GYP	0.166	20	Drifting	L1102-*i* Picarro	GHW	20.5	-3.70	0.02	-67.94	0.31				
3A 20 DRF WAT	0.125	20	Drifting	L1102-*i* Picarro	water		-7.31	0.03	-49.17	0.21	1.0036	0.979		
3A 20 DRF GYP	0.125	20	Drifting	L1102-*i* Picarro	GHW	20.8	-3.72	0.05	-68.97	0.29				
3B 20 DRF WAT	0.125	20	Drifting	L1102-*i* Picarro	water		-7.24	0.02	-48.83	0.28	1.0036	0.979	**AVG** 1.0037	0.981
3B 20 DRF GYP	0.125	20	Drifting	L1102-*i* Picarro	GHW	20.7	-3.70	0.02	-68.73	0.14			**1σ** 0.0001	0.0021
1A 25 SH WAT	0.25	25	Shaking	L1102-*i* Picarro	water		-7.40	0.05	-50.52	0.23	1.0036	0.982		
1A 25 SH GYP	0.25	25	Shaking	L1102-*i* Picarro	GHW	20.4	-3.80	0.05	-67.49	0.24				
1B 25 SH WAT	0.25	25	Shaking	L1102-*i* Picarro	water		-7.50	0.04	-50.76	0.36	1.0038	0.982		
1B 25 SH GYP	0.25	25	Shaking	L1102-*i* Picarro	GHW	20.6	-3.74	0.04	-67.86	0.33				
2A 25 SH WAT	0.166	25	Shaking	L1102-*i* Picarro	water		-7.51	0.04	-50.95	0.22	1.0034	0.981		
2A 25 SH GYP	0.166	25	Shaking	L1102-*i* Picarro	GHW	20.5	-4.16	0.06	-68.85	0.26				
2B 25 SH WAT	0.166	25	Shaking	L1102-*i* Picarro	water		-7.51	0.06	-50.50	0.28	1.0034	0.981		
2B 25 SH GYP	0.166	25	Shaking	L1102-*i* Picarro	GHW	20.7	-4.11	0.03	-68.90	0.42				
3A 25 SH WAT	0.125	25	Shaking	L1102-*i* Picarro	water		-7.51	0.05	-50.86	0.23	1.0036	0.980		
3A 25 SH GYP	0.125	25	Shaking	L1102-*i* Picarro	GHW	20.3	-3.93	0.08	-69.48	0.45				
3B 25 SH WAT	0.125	25	Shaking	L1102-*i* Picarro	water		-7.45	0.04	-50.30	0.28	1.0032	0.978	**AVG** 1.0035	0.981
3B 25 SH GYP	0.125	25	Shaking	L1102-*i* Picarro	GHW	20.8	-4.25	0.07	-70.88	0.56			**1σ** 0.0002	0.002
1A 25 DRF WAT	0.25	25	Drifting	L1102-*i* Picarro	water		-7.63	0.09	-51.00	0.42	1.0036	0.983		
1A 25 DRF GYP	0.25	25	Drifting	L1102-*i* Picarro	GHW	20.3	-4.03	0.08	-67.42	0.45				
1B 25 DRF WAT	0.25	25	Drifting	L1102-*i* Picarro	water		-7.54	0.05	-50.67	0.16	1.0034	0.982		
1B 25 DRF GYP	0.25	25	Drifting	L1102-*i* Picarro	GHW	20.5	-4.14	0.07	-67.48	0.58				

Table B.2b. Table B.2a continued. Fractionation factor between gypsum hydration water and the mother solution in mixing experiments ($CaCl_2$ and Na_2SO_4) at different temperatures and initial $Ca_2{}^+$ and $SO_4{}^{2-}$ concentrations. Experiment were performed in an oven with no agitation and in a shaking bath.

Experiment ID	Initial Ca^{2+} and SO_4^{2-} concent (mol/L)	Temperature (°C)	Drifting/Shaking	CRDS analyzer	mother water/ GHW	% H_2O	$\delta^{17}O$	1σ	$\delta^{18}O$	1σ	δD	1σ		$\alpha^{18}O$	αD
2A 25 DRF WAT	0.166	25	Drifting	L1102-*i* Picarro	water		-7.62	0.04	-50.67	0.41	1.0037	0.980			
2A 25 DRF GYP	0.166	25	Drifting	L1102-*i* Picarro	GHW	20.4	-3.98	0.06	-69.37	0.33					
2B 25 DRF WAT	0.166	25	Drifting	L1102-*i* Picarro	water		-7.42	0.05	-50.44	0.24	1.0035	0.981			
2B 25 DRF GYP	0.166	25	Drifting	L1102-*i* Picarro	GHW	20.2	-3.98	0.05	-68.38	0.32					
3A 25 DRF WAT	0.125	25	Drifting	L1102-*i* Picarro	water		-7.47	0.04	-50.39	0.25	1.0036	0.980			
3A 25 DRF GYP	0.125	25	Drifting	L1102-*i* Picarro	GHW	19.8	-3.92	0.06	-69.80	0.39					
3B 25 DRF WAT	0.125	25	Drifting	L1102-*i* Picarro	water		-7.45	0.02	-50.61	0.30	1.0035	0.980	**AVG**	1.0035	0.981
3B 25 DRF GYP	0.125	25	Drifting	L1102-*i* Picarro	GHW	19.8	-3.96	0.04	-69.50	0.20			**1σ**	0.0001	0.001
1A 45 SH WAT	0.25	45	Drifting	L1102-*i* Picarro	water		-7.27	0.02	-49.81	0.21	1.0032	0.984			
1A 45 SH GYP	0.25	45	Drifting	L1102-*i* Picarro	GHW	20.6	-4.07	0.04	-64.71	0.38					
1B 45 SH WAT	0.25	45	Drifting	L1102-*i* Picarro	water		-7.26	0.04	-49.88	0.37	1.0033	0.984			
1B 45 SH GYP	0.25	45	Drifting	L1102-*i* Picarro	GHW	20.6	-4.02	0.03	-65.01	0.29					
2A 45 SH WAT	0.166	45	Drifting	L1102-*i* Picarro	water		-7.18	0.05	-49.43	0.24	1.0029	0.983			
2A 45 SH GYP	0.166	45	Drifting	L1102-*i* Picarro	GHW	20.2	-4.30	0.09	-65.83	0.21					
2B 45 SH WAT	0.166	45	Drifting	L1102-*i* Picarro	water		-7.20	0.04	-49.72	0.20	1.0029	0.983			
2B 45 SH GYP	0.166	45	Drifting	L1102-*i* Picarro	GHW	19.9	-4.30	0.04	-65.76	0.39					
3A 45 SH WAT	0.125	45	Drifting	L1102-*i* Picarro	water		-7.19	0.02	-49.81	0.36	1.0032	0.982	**AVG**	1.0031	0.983
3A 45 SH GYP	0.125	45	Drifting	L1102-*i* Picarro	GHW	20.1	-4.06	0.03	-67.00	0.38			**1σ**	0.0002	0.0010
1A 55 SH WAT	0.25	55	Shaking	L1102-*i* Picarro	water		-7.53	0.02	-50.72	0.22	1.0035	0.984			
1A 55 SH GYP	0.25	55	Shaking	L1102-*i* Picarro	GHW	20.3	-4.09	0.05	-65.90	0.43					
1B 55 SH WAT	0.25	55	Shaking	L1102-*i* Picarro	water		-7.63	0.05	-50.98	0.26	1.0035	0.984			
1B 55 SH GYP	0.25	55	Shaking	L1102-*i* Picarro	GHW	20.7	-4.13	0.06	-66.45	0.24					
2A 55 SH WAT	0.166	55	Shaking	L1102-*i* Picarro	water		-7.55	0.02	-50.22	0.34	1.0032	0.983			
2A 55 SH GYP	0.166	55	Shaking	L1102-*i* Picarro	GHW	20.5	-4.34	0.03	-66.17	0.31					
2B 55 SH WAT	0.166	55	Shaking	L1102-*i* Picarro	water		-7.54	0.04	-50.64	0.21	1.0035	0.984			
2B 55 SH GYP	0.166	55	Shaking	L1102-*i* Picarro	GHW	20.1	-4.11	0.03	-65.63	0.44					
3A 55 SH WAT	0.125	55	Shaking	L1102-*i* Picarro	water		-7.49	0.04	-50.27	0.39	1.0031	0.983			
3A 55 SH GYP	0.125	55	Shaking	L1102-*i* Picarro	GHW	20.4	-4.36	0.05	-66.20	0.25					
3B 55 SH WAT	0.125	55	Shaking	L1102-*i* Picarro	water		-7.59	0.04	-50.30	0.15	1.0032	0.983	**AVG**	1.0033	0.983
3B 55 SH GYP	0.125	55	Shaking	L1102-*i* Picarro	GHW	20.3	-4.39	0.04	-66.84	0.26			**1σ**	0.0002	0.001
1A 55 DRF WAT	0.25	55	Drifting	L1102-*i* Picarro	water		-7.44	0.06	-50.64	0.28	1.0034	0.984			
1A 55 DRF GYP	0.25	55	Drifting	L1102-*i* Picarro	GHW	20.3	-4.03	0.05	-65.85	0.32					
1B 55 DRF WAT	0.25	55	Drifting	L1102-*i* Picarro	water		-7.49	0.08	-49.65	0.62	1.0033	0.985			
1B 55 DRF GYP	0.25	55	Drifting	L1102-*i* Picarro	GHW	20.2	-4.21	0.05	-63.67	0.37					
2A 55 DRF WAT	0.166	55	Drifting	L1102-*i* Picarro	water		-7.41	0.05	-50.70	0.33	1.0032	0.984			
2A 55 DRF GYP	0.166	55	Drifting	L1102-*i* Picarro	GHW	20.1	-4.22	0.05	-66.05	0.19					
2B 55 DRF WAT	0.166	55	Drifting	L1102-*i* Picarro	water		-7.43	0.08	-50.18	0.47	1.0032	0.985			
2B 55 DRF GYP	0.166	55	Drifting	L1102-*i* Picarro	GHW	20.4	-4.23	0.08	-64.64	0.42					
3A 55 DRF WAT	0.125	55	Drifting	L1102-*i* Picarro	water		-7.44	0.03	-49.85	0.20	1.0027	0.982			
3A 55 DRF GYP	0.125	55	Drifting	L1102-*i* Picarro	GHW	20.6	-4.79	0.04	-67.26	0.18					
3B 55 DRF WAT	0.125	55	Drifting	L1102-*i* Picarro	water		-7.44	0.06	-50.37	0.49	1.0035	0.984	**AVG**	1.0032	0.984
3B 55 DRF GYP	0.125	55	Drifting	L1102-*i* Picarro	GHW	20.6	-3.95	0.03	-65.16	0.34			**1σ**	0.0003	0.001

Table B.3. Fractionation factor between gypsum hydration water and the mother solution in experiments of hydration of anhydrite adding different concentrations of NaCl.

Experiment ID	NaCl (g/L)	αH_2O	Mother water/GHW	H_2O %	CRDS analyzer	$\delta^{18}O$	±σ	δD	±σ	$\alpha^{18}O$	αD	$\alpha^{18}Oavg$	±σ	$\alpha Davg$	±σ
	0	1	data in table SI 1		L1102-I and L2140-I Picarro										
NaCl1	30	0.98	water		L1102-I Picarro	-7.32	0.02	-49.01	0.14						
NaCl1	30		GHW	20.8	L1102-I Picarro	-4.17	0.03	-67.56	0.19	1.0032	0.9805				
NaCl2	30	0.98	water		L1102-I Picarro	-7.34	0.04	-49.38	0.24						
NaCl2	30		GHW	21.0	L1102-I Picarro	-4.07	0.04	-67.54	0.34	1.0033	0.9809	1.0032	0.00008	0.9807	0.0003
NaCl3	80	0.942	water		L1102-I Picarro	-7.28	0.04	-49.84	0.32						
NaCl3	80		GHW	20.7	L1102-I Picarro	-4.10	0.02	-66.80	0.19	1.0032	0.9821				
NaCl5	80	0.942	water		L1102-I Picarro	-7.33	0.02	-49.40	0.12						
NaCl5	80		GHW	21.0	L1102-I Picarro	-3.80	0.02	-65.88	0.22	1.0036	0.9827	1.0034	0.00025	0.9824	0.0004
NaCl6	150	0.88	water		L1102-I Picarro	-7.12	0.05	-48.83	0.15						
NaCl6	150		GHW	20.9	L1102-I Picarro	-3.78	0.02	-63.55	0.26	1.0034	0.9845				
NaCl7	150	0.88	water		L1102-I Picarro	-7.26	0.04	-49.29	0.29						
NaCl7	150		GHW	20.2	L1102-I Picarro	-3.99	0.03	-63.85	0.37	1.0033	0.9847				
NaCl8	150	0.88	water		L1102-I Picarro	-7.24	0.06	-49.66	0.16						
NaCl8	150		GHW	20.4	L1102-I Picarro	-4.09	0.06	-64.26	0.28	1.0032	0.9846	1.0033	0.00009	0.9846	0.0001
NaCl9	200	0.829	water		L1102-I Picarro	-7.58	0.03	-51.11	0.25						
NaCl9	200		GHW	19.8	L1102-I Picarro	-3.64	0.07	-61.66	0.31	1.0040	0.9889				
NaCl10	200	0.829	water		L1102-I Picarro	-7.54	0.06	-51.24	0.67						
NaCl10	200		GHW	19.6	L1102-I Picarro	-3.89	0.04	-62.38	0.20	1.0037	0.9883	1.0038	0.00021	0.9886	0.0004
NaCl11	300	0.699	water		L1102-I Picarro	-7.21	0.04	-50.15	0.28						
NaCl11	300		GHW	19.8	L1102-I Picarro	-2.70	0.08	-59.17	0.18	1.0045	0.9905				
NaCl12	300	0.699	water		L1102-I Picarro	-7.35	0.11	-49.04	0.41						
NaCl12	300		GHW	19.7	L1102-I Picarro	-2.46	0.06	-60.35	0.16	1.0049	0.9881	1.0047	0.00027	0.9893	0.0017

Table B.4. XRD analysis of solid recovered in experiments of mixing Ca_2^+ and SO_4^{2-} solutions (mixing experiments), hydration of anhydrous $CaSO_4$ in low salinity solutions (hydration of anhydrite) and hydration of anhydrous in NaCl brines.

Mixing Experiments Experiment ID	Initial SI_{gyp}	Temperature (°C)	Gypsum (%)	Bassanite (%)	Anhydrite (%)
EXP #1A-5°C	1.5	5	99	0.6	0.1
EXP #2A-5°C	1.26	5	99.4	0.6	0
EXP #3A-5°C	0.75	5	99	0.7	0.3
EXP #1A-25°C	1.42	25	99	0.8	0.2
EXP #2A-25°C	1.18	25	98.9	0.7	0.3
EXP #3A-25°C	0.68	25	99.4	0.6	0
EXP #1A-55°C	1.39	55	99.1	0.9	0.1
EXP #2A-55°C	1.15	55	99.1	0.7	0.3
EXP #3A-55°C	0.66	55	99.2	0.8	0

Hydration of Anhydrite Experiment ID	Temperature (°C)	Gypsum (%)	Bassanite (%)	Anhydrite (%)
#32-3°C	3	99	0.3	0.7
#24-25°C	25	99.2	0.6	0.6
#13-35°C	35	98.1	0.5	0.3

Hydration of Anhydrite in brine Experiment ID	NaCl (g/l)	Temperature (°C)	Gypsum (%)	Bassanite (%)	Anhydrite (%)
NaCl 30 g/L Exp2	30	20	99.2	0.2	0.8
NaCl 150 g/L Exp7	150	20	98.6	1.2	0.2
NaCl 200 g/L A Exp9	200	20	97.7	1.5	0.8
NaCl 300 g/L A Exp12	300	20	92.9	2.5	4.6

Table B.5. **A**. Stable isotopes in hydration water of gypsum precipitated from brines in a natural salt factory in Cabo de Gata (Almeria, SE Spain) (Evans et al., 2015)[1]. Mother water is calculated using published fractionation factors of Gonfiantini and Fontes (1963)[2] and Sofer (1978)[3] and those proposed in this study, at 20°C and salinity of 150 gl^{-1} of NaCl. **B**. Isotopic compositions of brines from the same salt factory.

A. Gypsum

	Gypsum hydration water[1]				Mother water (1.004, 0.980)[2,3]				Mother water (1.0033, 0.985)			
Sample	$\delta^{18}O$	1σ	δD	1σ	$\delta^{18}O$	1σ	d-excess	1σ	$\delta^{18}O$	1σ	d-excess	1σ
#1SALINA	10.56	0.17	12.94	0.35	6.53	33.62	**-18.6**	0.3	7.23	28.37	**-29.5**	0.3
#2SALINA	10.25	0.13	9.57	0.45	6.23	30.17	**-19.7**	0.2	6.93	24.94	**-30.5**	0.2
#3SALINA	11.37	0.07	15.94	0.30	7.34	36.67	**-22.1**	0.1	8.05	31.41	**-33.0**	0.1
#4SALINA	11.60	0.10	18.62	0.24	7.57	39.41	**-21.1**	0.3	8.27	34.13	**-32.0**	0.3
#5SALINA	10.86	0.04	16.69	0.31	6.83	37.44	**-17.2**	0.2	7.53	32.17	**-28.1**	0.2

B. Brines

	Mother water				
Sample	$\delta^{18}O$	1σ	d-excess	1σ	Residue (mg/L)
Brine 1	2.35	0.04	10.61	0.44	51.2
Brine 2	1.99	0.12	6.06	0.44	109.3
Brine 3	1.17	0.07	7.98	0.42	40.6
Brine 4	6.83	0.07	31.59	0.54	88.6
Brine 5	8.45	0.02	36.50	0.29	162.0
Brine 6	8.60	0.09	33.46	0.45	227.7
Brine 7	9.81	0.07	34.17	0.37	306.7
Brine 8	2.46	0.06	13.86	0.47	49.6
Brine 9	3.51	0.06	7.62	0.29	302.6
Brine 10	4.15	0.09	12.81	0.31	265.7

Appendix C

Tables for Chapter 3

Table C.1. Isotopic composition of measured gypsum hydration water (GHW) and calculated lake mother water (MW) from samples recovered from core CH1 7-III-04, Lake Chichancanab.

Sample name	Depth (cm)	Age (C.E.)	$\delta^{17}O$ (GHW)	$\delta^{18}O$ (GHW)	δD (GHW)	$\delta^{17}O$ (MW)	$\delta^{18}O$ (MW)	δD (MW)	^{17}O-excess (MW)	d-excess (MW)
A										
CHI 07-III-04 128.0-128.5 cm	128	1092	4.08	7.81	-2.66	2.24	4.33	17.0	-46	-17.7
CHI 07-III-04 129.0-129.5 cm	129	1085	3.83	7.33	-4.58	1.99	3.85	15.0	-38	-15.8
CHI 07-III-04 130.5-131.0 cm	130.5	1073	3.70	7.08	-5.86	1.87	3.60	13.7	-33	-15.1
CHI 07-III-04 131.0-131.5 cm	131	1069	3.91	7.46	-4.57	2.07	3.99	15.0	-31	-16.9
CHI 07-III-04 132.0-132.5 cm	132	1059	4.21	8.04	-1.35	2.37	4.57	18.3	-35	-18.2
CHI 07-III-04 133.0-133.5 cm	133	1050	3.73	7.12	-3.90	1.90	3.65	15.7	-30	-13.5
CHI 07-III-04 133.5-134.0 cm	133.5	1046	3.84	7.34	-4.41	2.01	3.87	15.2	-34	-15.8
CHI 07-III-04 134.0-134.5 cm	134	1041	4.11	7.85	-2.99	2.27	4.37	16.6	-31	-18.3
CHI 07-III-04 135.5-136.0 cm	135.5	1026	3.90	7.45	-3.74	2.06	3.98	15.9	-36	-15.9
CHI 07-III-04 136.0-136.5 cm	136.5	1013	4.01	7.65	-2.63	2.17	4.17	17.0	-31	-16.4
CHI 07-III-04 136.5-137.0 cm	137.5	1000	4.04	7.71	-3.20	2.20	4.24	16.4	-36	-17.5
CHI 07-III-04 137.0-137.5 cm	138	993	3.83	7.34	-4.14	2.00	3.87	15.5	-42	-15.5
CHI 07-III-04 139.5-140.0 cm	139.5	973	3.77	7.21	-4.19	1.93	3.73	15.4	-40	-14.5
CHI 07-III-04 140.0-140.5 cm	140	967	3.89	7.45	-3.27	2.05	3.98	16.3	-47	-15.5
CHI 07-III-04 140.5-141.5 cm	140.5	960	3.83	7.31	-4.04	1.99	3.84	15.6	-32	-15.1
CHI 07-III-04 142.0-142.5 cm	142	939	4.36	8.33	-1.27	2.52	4.85	18.4	-36	-20.4
B										
CHI 07-III-04 148.0-148.5 cm	148	849	3.95	7.54	-3.18	2.11	4.07	16.4	-33	-16.1
CHI 07-III-04 149.0-149.5 cm	149	833	4.00	7.65	-3.72	2.16	4.18	15.9	-43	-17.5
CHI 07-III-04 150.0-151.0 cm	150	817	4.21	8.04	-1.92	2.37	4.56	17.7	-36	-18.8
CHI 07-III-04 151.0-151.5 cm	151	801	4.13	7.89	-2.62	2.29	4.42	17.0	-36	-18.3
CHI 07-III-04 151.5-152.0 cm	151.5	793	4.31	8.24	-1.40	2.47	4.77	18.2	-43	-19.9
CHI 07-III-04 153.0-153.5 cm	153	768	3.75	7.17	-3.70	1.91	3.69	15.9	-33	-13.6
CHI 07-III-04 153.5-154.0 cm	153.5	760	4.05	7.74	-2.34	2.22	4.26	17.3	-32	-16.8
CHI 07-III-04 154.0-154.5 cm	154	752	4.28	8.18	-0.88	2.44	4.70	18.8	-35	-18.8
CHI 07-III-04 154.5-155.0 cm	154.5	744	3.98	7.60	-3.69	2.14	4.12	15.9	-33	-17.1
CHI 07-III-04 154.5-155.0 cm	154.5	744	4.11	7.84	-3.01	2.27	4.37	16.6	-32	-18.3
CHI 07-III-04 155.0-155.5 cm	155	736	4.12	7.89	-2.76	2.28	4.42	16.9	-45	-18.5
CHI 07-III-04 155.5-156.0 cm	155.5	728	3.90	7.48	-3.44	2.07	4.01	16.2	-45	-15.9
CHI 07-III-04 156.0-156.5 cm	156	720	4.08	7.81	-3.47	2.24	4.34	16.1	-48	-18.6
C										
CHI 07-III-04 166.0-166.5 cm	166	611	3.84	7.32	-4.48	2.00	3.85	15.1	-26	-15.7
CHI 07-III-04 167.0-167.5 cm	167	605	4.15	7.93	-1.91	2.31	4.46	17.7	-43	-17.9
CHI 07-III-04 167.5-168.0 cm	167.5	602	3.86	7.34	-4.59	2.02	3.86	15.0	-19	-15.9

Table C.2. Paleo-lake temperature calculations. The equation of Grossman and Ku (1986) was used to calculate the temperature at which the aragonitic shells of *Pyrgophorus coronatus* formed.

Sample	$\delta^{18}O$ (Carbonate)	$\delta^{18}O$ (GHW)	Temperature (°C)
CHI 07-III-04 133.0-133.5 cm	2.96	3.65	25.0
CHI 07-III-04 133.5-134.0 cm	3.46	3.87	23.7
CHI 07-III-04 139.5-140.0 cm	3.40	4.07	24.9
CHI 07-III-04 140.5-141.0 cm	3.23	3.99	25.3
CHI 07-III-04 153.0-153.5 cm	3.06	4.07	26.4
CHI 07-III-04 154.0-154.5 cm	3.26	4.70	28.4
CHI 07-III-04 166.0-166.5 cm	2.59	3.85	27.6
Mean			**25.9**
1σ			**1.7**

Table C.3a. Output table of Bayesian age-depth analysis. Mean ages display single 'best' model based on the weighted mean age for each depth. Positive and negative age errors represent 95% confidence intervals.

Depth (cm)	Positive Age Error (C.E.)	Negative Age Error (C.E.)	Mean Age (C.E.)
0	2025.6	1953.5	2004
1	2021.3	1948.7	2000.8
2	2019.6	1938.9	1993.6
3	2018.6	1920.1	1986.5
4	2018.5	1897.6	1979.7
5	2018.7	1874.6	1972.9
6	2014.2	1867.4	1965.4
7	2011.8	1859.3	1958
8	2010	1846.3	1950.5
9	2008.4	1831.4	1943
10	2006.6	1814	1935.6
11	2001.4	1805.9	1928.4
12	1997.7	1796.8	1921
13	1995.4	1787.2	1913.7
14	1993.2	1773.1	1906.5
15	1991.6	1758.2	1899.2
16	1985.5	1751.1	1891.9
17	1981.2	1744	1884.4
18	1978	1731.8	1877.2
19	1975.3	1719	1869.9
20	1973.4	1705	1862.8
21	1967.1	1698.7	1855.6
22	1961.7	1692.4	1848.4
23	1957.2	1684.3	1841.2
24	1953.8	1673.3	1833.9
25	1950.8	1661.2	1826.7
26	1942.6	1654.2	1819.5
27	1937.1	1648.5	1812.4
28	1932.8	1640.3	1805.3
29	1928.9	1630.3	1798.2
30	1925.5	1619.9	1791.1
31	1917.6	1612.2	1783.7
32	1911.4	1605	1776.4
33	1907.3	1597.2	1769.1
34	1902.1	1588.6	1761.7
35	1899.1	1576.3	1754.3
36	1889.9	1569.6	1747.2
37	1884.8	1562.5	1740
38	1878.6	1555.9	1732.8
39	1874.2	1546.3	1725.6
40	1870.9	1535.3	1718.4
41	1863.1	1530	1711.1
42	1856.5	1524.1	1703.8
43	1851	1515.5	1696.5
44	1846.6	1506.5	1689.3
45	1843	1499.4	1682
46	1836	1494.1	1674.9
47	1829.3	1488	1667.6
48	1824.2	1480.7	1660.4
49	1820	1471.6	1653.1
50	1817.4	1463.2	1646
51	1808.4	1457.4	1638.8
52	1801.1	1450.9	1631.7
53	1794.7	1443.7	1624.5
54	1788.8	1433.9	1617.5
55	1783.3	1424	1610.6
56	1774.4	1418.9	1603.3
57	1767.7	1411.9	1596
58	1761.3	1404.7	1588.7
59	1756.1	1395.4	1581.3
60	1752.8	1386.9	1574.3
61	1742.5	1382.3	1567
62	1735.3	1377.7	1559.7
63	1730	1370.6	1552.4
64	1722.8	1363.1	1544.9
65	1716.8	1353.5	1537.5
66	1706.5	1349.3	1530.2
67	1698.3	1344.9	1522.8
68	1692.2	1338.1	1515.2
69	1687.9	1331.8	1507.7
70	1683	1323.9	1500.3
71	1671.5	1319.3	1493.2
72	1664.5	1313.4	1486.2
73	1658	1305.6	1479.2
74	1653.6	1297.6	1472
75	1648.5	1290.1	1465
76	1638.8	1285.7	1457.7
77	1631.8	1280.5	1450.5
78	1625.4	1273.7	1443.2
79	1620.4	1267.4	1435.9
80	1614	1258.6	1428.6
81	1604.9	1253.8	1421.8
82	1595.6	1248.3	1415.1
83	1588.2	1241.6	1408.2
84	1581.9	1234.6	1401.5
85	1576.8	1225.3	1394.6
86	1567.5	1221.4	1387.7
87	1557.7	1216.6	1380.6
88	1549.7	1211.5	1373.7
89	1543	1204.8	1366.7
90	1537.7	1195.6	1359.8
91	1529.9	1191.4	1352.9
92	1522	1186.4	1345.8
93	1517.1	1180.5	1338.8
94	1510.2	1174.9	1331.8
95	1505	1167.6	1324.8
96	1494.9	1164	1317.7
97	1483.8	1159.3	1310.6
98	1476.3	1153.2	1303.4
99	1469.1	1146.4	1296.2
100	1464.9	1138.6	1288.9
101	1452.1	1135.1	1281.8
102	1440.8	1130.8	1274.5
103	1432.4	1124.8	1267.4
104	1426.3	1118.1	1260.1
105	1419.7	1110.5	1252.9
106	1407.6	1107.3	1245.3
107	1397.7	1103.1	1237.8
108	1389.7	1098.2	1230.2
109	1383.5	1092.9	1222.7
110	1376.9	1085.2	1215.1
111	1365.3	1082.2	1208.3
112	1354.9	1078.7	1201.6
113	1345.4	1074.8	1194.9
114	1337	1070.4	1188.2
115	1329.3	1064.3	1181.5
116	1318.1	1061.3	1174.6
117	1308.8	1058.7	1167.8
118	1300.9	1055.5	1160.8
119	1293.2	1050.4	1154

Table C.3b. Table C.2a continued. Output table of Bayesian age-depth analysis. Mean ages display single 'best' model based on the weighted mean age for each depth. Positive and negative age errors represent 95% confidence intervals.

Depth (cm)	Positive Age Error (C.E.)	Negative Age Error (C.E.)	Mean Age (C.E.)
120	1288.3	1044	1147
121	1274.1	1042.7	1140.1
122	1262.6	1040.7	1133.3
123	1252.7	1038	1126.3
124	1244.4	1034.8	1119.2
125	1237.9	1029	1112.2
126	1224.3	1027.2	1105.6
127	1211.8	1025.1	1098.6
128	1203	1021.4	1091.7
129	1195.7	1016.6	1084.8
130	1190.9	1010.3	1078.1
131	1175.8	1005.6	1068.7
132	1165.4	997.3	1059.4
133	1157.9	985	1050.2
134	1151.4	967.4	1041
135	1146.8	948	1032.2
136	1127.1	940.2	1019.3
137	1110.5	925.7	1006.2
138	1099.2	902.2	992.9
139	1092	874.6	979.7
140	1087	847.5	966.9
141	1056.6	838.5	953.1
142	1029.7	828.4	939.1
143	1011.1	814.5	925
144	997.8	795.5	911.1
145	989.4	770.4	897.2
146	965.8	761	881.1
147	954.1	749.2	865
148	946	733.4	848.9
149	940.7	710.8	832.9
150	936.9	681	817
151	915.2	676.2	801
152	901.2	670.8	784.7
153	891.6	663.9	768.4
154	882.9	654.6	752.2
155	876.9	636.7	736.1
156	835.6	635.2	720.2
157	800.2	632.2	704.1
158	772.6	628.7	687.7
159	753.8	622.7	671.2
160	741.2	610	654.8
161	729.3	605.5	647
162	722.7	597.6	639.3
163	717.3	586.6	631.9
164	712.6	573.6	624.3
165	706.5	557.8	616.7
166	695.1	552.1	610.7
167	685.3	543.5	604.5
168	676.1	531.9	598.5
169	668.6	517.4	592.4
170	664.3	501	586.5
171	652.7	493.8	579.4
172	644.9	485.1	572.3
173	636.9	475.4	565.4
174	632.7	462.1	558.6
175	629.9	446.8	551.8
176	620.8	439.9	543.2
177	614.5	432.8	534.4
178	610	421.9	525.5
179	605.7	408.1	516.8
180	602.3	393.1	508.2
181	591.9	386.2	499.2
182	584	379.1	490.1
183	577.8	372	481.2
184	573.4	359.3	472.3
185	569.9	345.3	463.6
186	556.8	339.1	453
187	547.3	333.1	442.5
188	541.6	321.9	432
189	535.7	307.6	421.3
190	531.3	291.9	410.7
191	510.2	284.1	397.5
192	497.5	274.8	384.3
193	487.3	260.9	371.1
194	480.5	243.4	357.9
195	474.6	220.4	344.7
196	445.6	214.7	331.6
197	418.9	207.4	318.4
198	400.5	198.4	305.3
199	387.3	187.3	292.3
200	377.2	170.3	279.3
201	362.3	165.8	269.7
202	351.9	158.6	260
203	344	148.5	250.1
204	338.9	133.1	240.1
205	334.5	116.1	230.2
206	325.9	110.1	222
207	318.2	101.8	213.7
208	312.6	92.2	205.4
209	308.2	81.8	197.3
210	304.2	67.6	189.2
211	292.6	61.5	180.9
212	284.1	54.1	172.5
213	277.8	44.4	164.3
214	273.3	33.5	155.9
215	269.3	21.1	147.7
216	258.6	13.7	138.5
217	250.6	4.4	129.4
218	243.8	-8.6	120.3
219	239	-23.7	111.1
220	233	-42.4	102.2
221	223.8	-52.3	92.1
222	216.4	-67	82.2
223	210.5	-82.4	72.5
224	206	-101.8	62.7
225	202.7	-127.1	52.9
226	192.2	-136.3	42.9
227	185.8	-147	32.8
228	179.4	-160.1	22.8
229	174.2	-176	12.7
230	169.9	-196.4	2.6
231	160.7	-207.1	-7.1
232	153.4	-217	-16.7
233	145.9	-228.7	-26.6
234	141	-243.2	-36.3
235	136.8	-264.2	-45.6
236	126.2	-271.6	-55.4
237	116.9	-281.5	-65.1
238	108.7	-292	-74.8
239	103	-306.6	-84.6

Table C.4a. The BACON function 'Events' was used to quantify the probability of arid conditions at any calendar age. Fifty-year window widths were used, with the windows moving at 10-year steps from the core's bottom ages to its top.

Cal Year (BP)	Age (C.E.)	Probability of Drought	Cal Year (BP)	Age (C.E.)	Probability of Drought	Cal Year (BP)	Age (C.E.)	Probability of Drought
105.1	1844.9	0	705.1	1244.9	0.0034	1305.1	644.9	0.49422
115.1	1834.9	0	715.1	1234.9	0.0068	1315.1	634.9	0.529752
125.1	1824.9	0	725.1	1224.9	0.012581	1325.1	624.9	0.586535
135.1	1814.9	0	735.1	1214.9	0.024991	1335.1	614.9	0.654029
145.1	1804.9	0	745.1	1204.9	0.040972	1345.1	604.9	0.681231
155.1	1794.9	0	755.1	1194.9	0.064264	1355.1	594.9	0.650119
165.1	1784.9	0	765.1	1184.9	0.090275	1365.1	584.9	0.556273
175.1	1774.9	0	775.1	1174.9	0.121047	1375.1	574.9	0.426726
185.1	1764.9	0	785.1	1164.9	0.153859	1385.1	564.9	0.314519
195.1	1754.9	0	795.1	1154.9	0.189221	1395.1	554.9	0.212853
205.1	1744.9	0	805.1	1144.9	0.223563	1405.1	544.9	0.134988
215.1	1734.9	0	815.1	1134.9	0.252975	1415.1	534.9	0.080755
225.1	1724.9	0	825.1	1124.9	0.289527	1425.1	524.9	0.046073
235.1	1714.9	0	835.1	1114.9	0.33526	1435.1	514.9	0.025842
245.1	1704.9	0	845.1	1104.9	0.394594	1445.1	504.9	0.015471
255.1	1694.9	0	855.1	1094.9	0.465148	1455.1	494.9	0.009011
265.1	1684.9	0	865.1	1084.9	0.551513	1465.1	484.9	0.00561
275.1	1674.9	0	875.1	1074.9	0.67069	1475.1	474.9	0.0034
285.1	1664.9	0	885.1	1064.9	0.794798	1485.1	464.9	0.00289
295.1	1654.9	0	895.1	1054.9	0.890513	1495.1	454.9	0.0017
305.1	1644.9	0	905.1	1044.9	0.949677	1505.1	444.9	0.00119
315.1	1634.9	0	915.1	1034.9	0.976029	1515.1	434.9	0.00068
325.1	1624.9	0	925.1	1024.9	0.985379	1525.1	424.9	0.00085
335.1	1614.9	0	935.1	1014.9	0.985889	1535.1	414.9	0.00051
345.1	1604.9	0	945.1	1004.9	0.984189	1545.1	404.9	0.00051
355.1	1594.9	0	955.1	994.9	0.980279	1555.1	394.9	0.00085
365.1	1584.9	0	965.1	984.9	0.970758	1565.1	384.9	0.00221
375.1	1574.9	0	975.1	974.9	0.958007	1575.1	374.9	0.00476
385.1	1564.9	0	985.1	964.9	0.939646	1585.1	364.9	0.011051
395.1	1554.9	0	995.1	954.9	0.908535	1595.1	354.9	0.019211
405.1	1544.9	0	1005.1	944.9	0.870962	1605.1	344.9	0.033152
415.1	1534.9	0	1015.1	934.9	0.824549	1615.1	334.9	0.048453
425.1	1524.9	0	1025.1	924.9	0.777967	1625.1	324.9	0.067834
435.1	1514.9	0	1035.1	914.9	0.735124	1635.1	314.9	0.097756
445.1	1504.9	0	1045.1	904.9	0.694492	1645.1	304.9	0.138728
455.1	1494.9	0	1055.1	894.9	0.66763	1655.1	294.9	0.198742
465.1	1484.9	0	1065.1	884.9	0.653859	1665.1	284.9	0.266576
475.1	1474.9	0	1075.1	874.9	0.658279	1675.1	274.9	0.319279
485.1	1464.9	0	1085.1	864.9	0.6695	1685.1	264.9	0.356681
495.1	1454.9	0	1095.1	854.9	0.693472	1695.1	254.9	0.374192
505.1	1444.9	0	1105.1	844.9	0.717613	1705.1	244.9	0.374532
515.1	1434.9	0	1115.1	834.9	0.746855	1715.1	234.9	0.359572
525.1	1424.9	0	1125.1	824.9	0.779667	1725.1	224.9	0.345291
535.1	1414.9	0	1135.1	814.9	0.807038	1735.1	214.9	0.33543
545.1	1404.9	0	1145.1	804.9	0.83288	1745.1	204.9	0.32897
555.1	1394.9	0	1155.1	794.9	0.859572	1755.1	194.9	0.316389
565.1	1384.9	0	1165.1	784.9	0.883203	1765.1	184.9	0.287657
575.1	1374.9	0	1175.1	774.9	0.900374	1775.1	174.9	0.246515
585.1	1364.9	0	1185.1	764.9	0.916865	1785.1	164.9	0.212173
595.1	1354.9	0	1195.1	754.9	0.920945	1795.1	154.9	0.17494
605.1	1344.9	0	1205.1	744.9	0.914655	1805.1	144.9	0.135668
615.1	1334.9	0	1215.1	734.9	0.897314	1815.1	134.9	0.109657
625.1	1324.9	0	1225.1	724.9	0.870622	1825.1	124.9	0.088575
635.1	1314.9	0	1235.1	714.9	0.83662	1835.1	114.9	0.070724
645.1	1304.9	0	1245.1	704.9	0.792758	1845.1	104.9	0.054573
655.1	1294.9	0	1255.1	694.9	0.739544	1855.1	94.9	0.046753
665.1	1284.9	0	1265.1	684.9	0.680551	1865.1	84.9	0.042333
675.1	1274.9	0.00017	1275.1	674.9	0.620707	1875.1	74.9	0.040292
685.1	1264.9	0.00017	1285.1	664.9	0.554403	1885.1	64.9	0.040802
695.1	1254.9	0.0017	1295.1	654.9	0.49966	1895.1	54.9	0.041823

Table C.4b. Table C.4a continued. The BACON function 'Events' was used to quantify the probability of arid conditions at any calendar age. Fifty-year window widths were used, with the windows moving at 10-year steps from the core's bottom ages to its top.

Cal Year (BP)	Age (C.E.)	Probability of Drought	Cal BP	Age (C.E.)	Probability of Drought
1905.1	44.9	0.048113	1905.1	44.9	0.048113
1915.1	34.9	0.058824	1915.1	34.9	0.058824
1925.1	24.9	0.072934	1925.1	24.9	0.072934
1935.1	14.9	0.087385	1935.1	14.9	0.087385
1945.1	4.9	0.102006	1945.1	4.9	0.102006
1955.1	-5.1	0.122407	1955.1	-5.1	0.122407
1965.1	-15.1	0.142809	1965.1	-15.1	0.142809
1975.1	-25.1	0.16627	1975.1	-25.1	0.16627
1985.1	-35.1	0.186331	1985.1	-35.1	0.186331
1995.1	-45.1	0.207242	1995.1	-45.1	0.207242
2005.1	-55.1	0.231554	2005.1	-55.1	0.231554
2015.1	-65.1	0.253655	2015.1	-65.1	0.253655
2025.1	-75.1	0.285957	2025.1	-75.1	0.285957
2035.1	-85.1	0.305338	2035.1	-85.1	0.305338
2045.1	-95.1	0.32812	2045.1	-95.1	0.32812
2055.1	-105.1	0.348011	2055.1	-105.1	0.348011
2065.1	-115.1	0.361102	2065.1	-115.1	0.361102
2075.1	-125.1	0.377083	2075.1	-125.1	0.377083
2085.1	-135.1	0.397144	2085.1	-135.1	0.397144
2095.1	-145.1	0.410405	2095.1	-145.1	0.410405
2105.1	-155.1	0.421285	2105.1	-155.1	0.421285
2115.1	-165.1	0.428936	2115.1	-165.1	0.428936
2125.1	-175.1	0.437946	2125.1	-175.1	0.437946
2135.1	-185.1	0.450697	2135.1	-185.1	0.450697
2145.1	-195.1	0.458348	2145.1	-195.1	0.458348
2155.1	-205.1	0.464298	2155.1	-205.1	0.464298
2165.1	-215.1	0.463618	2165.1	-215.1	0.463618
2175.1	-225.1	0.469228	2175.1	-225.1	0.469228
2185.1	-235.1	0.470928	2185.1	-235.1	0.470928
2195.1	-245.1	0.468038	2195.1	-245.1	0.468038
2205.1	-255.1	0.455457	2205.1	-255.1	0.455457
2215.1	-265.1	0.450867	2215.1	-265.1	0.450867
2225.1	-275.1	0.429106	2225.1	-275.1	0.429106
2235.1	-285.1	0.410745	2235.1	-285.1	0.410745
2245.1	-295.1	0.381843	2245.1	-295.1	0.381843
2255.1	-305.1	0.359062	2255.1	-305.1	0.359062
2265.1	-315.1	0.33322	2265.1	-315.1	0.33322
2275.1	-325.1	0.314349	2275.1	-325.1	0.314349
2285.1	-335.1	0.286297	2285.1	-335.1	0.286297
2295.1	-345.1	0.259436	2295.1	-345.1	0.259436
2305.1	-355.1	0.233594	2305.1	-355.1	0.233594
2315.1	-365.1	0.202992	2315.1	-365.1	0.202992
2325.1	-375.1	0.195682	2325.1	-375.1	0.195682
2335.1	-385.1	0.186161	2335.1	-385.1	0.186161
2345.1	-395.1	0.175281	2345.1	-395.1	0.175281
2355.1	-405.1	0.17103	2355.1	-405.1	0.17103
2365.1	-415.1	0.156239	2365.1	-415.1	0.156239
2375.1	-425.1	0.141789	2375.1	-425.1	0.141789
2385.1	-435.1	0.124277	2385.1	-435.1	0.124277
2395.1	-445.1	0.106426	2395.1	-445.1	0.106426
2405.1	-455.1	0.092146	2405.1	-455.1	0.092146
2415.1	-465.1	0.081605	2415.1	-465.1	0.081605
2425.1	-475.1	0.070044	2425.1	-475.1	0.070044
2435.1	-485.1	0.062394	2435.1	-485.1	0.062394
2445.1	-495.1	0.051853	2445.1	-495.1	0.051853
2455.1	-505.1	0.047603	2455.1	-505.1	0.047603
2465.1	-515.1	0.041313	2465.1	-515.1	0.041313
2475.1	-525.1	0.037062	2475.1	-525.1	0.037062
2485.1	-535.1	0.033152	2485.1	-535.1	0.033152
2495.1	-545.1	0.026692	2495.1	-545.1	0.026692

Table C.5a. Stable isotope ratios of lake waters from the Yucatán Peninsula.

Sample - Lakewater	$\delta^{17}O$	(1σ)	$\delta^{18}O$	(1σ)	δD	(1σ)	d-excess	^{17}O-excess	Latitude (N)	Longitude (W)
Lake Chichancanab										
Chichancanab 09-XI-04 2 m	1.55	0.04	2.98	0.04	13.34	0.25	-10.5	-20	19° 52.771'	88° 46.026'
Chichancanab 09-XI-04 3 m	1.40	0.01	2.70	0.02	10.39	0.11	-11.2	-25	19° 52.771'	88° 46.026'
Chichancanab 09-XI-04 12 m	1.43	0.02	2.76	0.03	11.18	0.16	-10.9	-29	19° 52.771'	88° 46.026'
Chichancanab 27-II-05 A	1.76	0.03	3.41	0.04	13.08	0.32	-14.2	-41	19° 52.771'	88° 46.026'
Chichancanab 27-II-05	1.90	0.02	3.68	0.03	15.31	0.16	-14.2	-40	19° 52.771'	88° 46.026'
Chichancanab #1 B SURF	1.78	0.03	3.44	0.04	14.67	0.19	-12.8	-32	19° 52.771'	88° 46.026'
Chichancanab DEEP #2 A	1.76	0.02	3.39	0.02	14.59	0.11	-12.5	-28	19° 52.771'	88° 46.026'
Chichancanab DEEP #2B	1.76	0.01	3.40	0.04	14.47	0.14	-12.7	-31	19° 52.771'	88° 46.026'
Chichancanab DEEP #5 B	1.76	0.02	3.38	0.02	14.31	0.15	-12.8	-25	19° 52.771'	88° 46.026'
Chichancanab DEEP 13 #5	1.76	0.02	3.41	0.03	14.30	0.09	-13.0	-36	19° 52.771'	88° 46.026'
Chichancanab 22-V-00 A	1.97	0.03	3.82	0.04	17.21	0.09	-13.4	-42	19° 52.771'	88° 46.026'
Chichancanab 22-V-00 B	1.65	0.03	3.20	0.03	13.37	0.15	-12.7	-36	19° 52.771'	88° 46.026'
Chichancanab 19-VI-96	1.32	0.03	2.56	0.04	10.13	0.17	-10.5	-30	19° 52.771'	88° 46.026'
CH Lake water surface #1A	1.79	0.03	3.45	0.02	14.86	0.12	-12.7	-28	19° 52.771'	88° 46.026'
CH 8-III-04 0m	1.55	0.04	2.98	0.06	11.95	0.29	-11.6	-23	19° 52.771'	88° 46.026'
CH 8-III-04 1m	1.54	0.02	2.95	0.03	12.16	0.19	-11.1	-21	19° 52.771'	88° 46.026'
CH 8-III-04 2m	1.49	0.02	2.86	0.03	11.73	0.10	-10.8	-24	19° 52.771'	88° 46.026'
CH 8-III-04 3m	1.38	0.03	2.67	0.04	10.39	0.16	-11.0	-32	19° 52.771'	88° 46.026'
CH 8-III-04 4m	1.36	0.03	2.62	0.04	10.08	0.17	-10.9	-23	19° 52.771'	88° 46.026'
CH 8-III-04 5m	1.49	0.03	2.87	0.04	11.73	0.17	-11.2	-19	19° 52.771'	88° 46.026'
CH 8-III-04 6m	1.49	0.03	2.86	0.04	11.80	0.23	-11.1	-19	19° 52.771'	88° 46.026'
CH 8-III-04 8m	1.51	0.04	2.91	0.06	12.04	0.35	-11.2	-21	19° 52.771'	88° 46.026'
CH 8-III-04 10m	1.50	0.03	2.89	0.05	11.80	0.18	-11.3	-25	19° 52.771'	88° 46.026'
CH 8-III-04 12m	1.38	0.03	2.67	0.03	10.37	0.23	-11.0	-26	19° 52.771'	88° 46.026'
CH 8-III-04 14m	1.44	0.02	2.77	0.03	11.47	0.21	-10.7	-21	19° 52.771'	88° 46.026'
Peten Itza Lake										
PI 13-VIII-02 0 m	1.53	0.03	2.94	0.03	16.05	0.21	-7.5	-23	17° 0.170'	89° 47.956'
PI 13-VIII-02 0 m II	1.54	0.03	2.95	0.04	15.34	0.15	-8.3	-21	17° 0.170'	89° 47.956'
PI 13-VIII-02 10 m	1.54	0.03	2.95	0.03	16.31	0.16	-7.3	-16	17° 0.170'	89° 47.956'
PI 13-VIII-02 10 m II	1.56	0.03	3.00	0.05	15.56	0.10	-8.4	-25	17° 0.170'	89° 47.956'
PI 13-VIII-02 20 m	1.50	0.06	2.85	0.10	15.50	0.52	-7.3	-8	17° 0.170'	89° 47.956'
PI 13-VIII-02 20 m II	1.54	0.03	2.95	0.03	15.47	0.10	-8.2	-18	17° 0.170'	89° 47.956'
PI 13-VIII-02 30 m	1.45	0.03	2.78	0.07	15.51	0.38	-6.7	-14	17° 0.170'	89° 47.956'
PI 13-VIII-02 30 m II	1.42	0.03	2.73	0.03	14.21	0.17	-7.6	-19	17° 0.170'	89° 47.956'
PI 13-VIII-02 40 m	1.43	0.04	2.75	0.04	14.98	0.29	-7.0	-24	17° 0.170'	89° 47.956'
PI 13-VIII-02 40 m II	1.44	0.03	2.79	0.03	14.50	0.09	-7.8	-32	17° 0.170'	89° 47.956'
PI 13-VIII-02 60 m	1.42	0.04	2.74	0.05	15.19	0.27	-6.7	-24	17° 0.170'	89° 47.956'
PI 13-VIII-02 60 m II	1.43	0.02	2.75	0.04	14.45	0.11	-7.6	-19	17° 0.170'	89° 47.956'
PI 13-VIII-02 90 m	1.34	0.03	2.59	0.07	14.28	0.54	-6.4	-29	17° 0.170'	89° 47.956'
PI 13-VIII-02 90 m II	1.38	0.04	2.65	0.04	13.17	0.14	-8.1	-22	17° 0.170'	89° 47.956'
PI 13-VIII-02 120 m	1.41	0.05	2.72	0.08	15.01	0.49	-6.8	-27	17° 0.170'	89° 47.956'
PI 13-VIII-02 120 m II	1.34	0.01	2.58	0.02	12.85	0.10	-7.8	-26	17° 0.170'	89° 47.956'
PI 13-VIII-02 150 m	1.40	0.04	2.68	0.05	14.68	0.31	-6.8	-17	17° 0.170'	89° 47.956'
PI 13-VIII-02 150 m II	1.41	0.03	2.71	0.04	14.01	0.17	-7.7	-22	17° 0.170'	89° 47.956'
PI1 06-VIII-02-0m	1.58	0.03	3.01	0.04	15.74	0.14	-8.3	-10	17° 0.170'	89° 47.956'
PI1 06-VIII-02-5m	1.48	0.02	2.83	0.02	15.04	0.10	-7.6	-15	17° 0.170'	89° 47.956'
PI1 06-VIII-02-10m	1.47	0.03	2.81	0.03	14.90	0.11	-7.6	-14	17° 0.170'	89° 47.956'
PI1 06-VIII-02-15m	1.16	0.02	2.23	0.02	12.62	0.16	-5.2	-11	17° 0.170'	89° 47.956'
PI1 06-VIII-02-20m	1.10	0.02	2.10	0.02	11.79	0.11	-5.0	-14	17° 0.170'	89° 47.956'
PI5 06-VIII-02-0m	1.44	0.02	2.77	0.02	15.00	0.08	-7.2	-23	17° 0.170'	89° 47.956'
PI5 06-VIII-02-5m	1.51	0.01	2.90	0.03	15.46	0.17	-7.7	-17	17° 0.170'	89° 47.956'
PI5 06-VIII-02-10m	1.49	0.02	2.85	0.02	15.62	0.05	-7.2	-18	17° 0.170'	89° 47.956'
PI2-06-VIII-02-0m	1.45	0.02	2.79	0.03	14.95	0.12	-7.4	-20	17° 0.170'	89° 47.956'
PI17-06-VIII-02-0m	1.50	0.03	2.85	0.03	15.22	0.10	-7.6	0	17° 0.170'	89° 47.956'
PI17-06-VIII-02-7m	1.47	0.03	2.81	0.03	14.97	0.08	-7.5	-13	17° 0.170'	89° 47.956'
PI13-06-VIII-02-150m	1.45	0.01	2.74	0.03	15.01	0.14	-6.9	-1	17° 0.170'	89° 47.956'
PI07-06-VIII-02-0m	1.24	0.02	2.39	0.02	11.91	0.08	-7.2	-22	17° 0.170'	89° 47.956'
PI07-06-VIII-02-7m	1.39	0.03	2.66	0.02	14.00	0.18	-7.3	-18	17° 0.170'	89° 47.956'
Lake Peten #193 B 12-VIII-2005	1.53	0.02	2.94	0.04	15.56	0.14	-7.9	-19	17° 0.170'	89° 47.956'
Peten Itza Lake 6-VII-1995 core site surface	1.39	0.03	2.69	0.07	13.86	0.38	-8.1	-31	17° 0.170'	89° 47.956'
Peten Itza Remate PI-22-VIII-99 core site	1.51	0.04	2.95	0.04	14.89	0.24	-8.7	-41	17° 0.170'	89° 47.956'
Peten Itza Central 29-VIII-99 surf	1.57	0.03	3.02	0.02	15.86	0.42	-8.9	-25	17° 0.170'	89° 47.956'

Table C.5b. Table C.5a continued. Stable isotope ratios of lake waters from the Yucatán Peninsula.

Sample - Lakewater	$\delta^{17}O$	(1σ)	$\delta^{18}O$	(1σ)	δD	(1σ)	d-excess	^{17}O-excess	Latitude (N)	Longitude (W)
Salpeten Lake										
SP-13-VI-02 0m ST1 A A	2.22	0.03	4.23	0.04	20.13	0.32	-13.7	-13	16°58.8'	89°40.0'
SP-13-VI-02 2m ST1 A B	2.23	0.02	4.26	0.02	20.62	0.14	-13.5	-22	16°58.8'	89°40.0'
SP 13-07-02 5 m STIA	2.24	0.05	4.31	0.10	20.23	0.41	-14.3	-36	16°58.8'	89°40.0'
SP-13-VI-02 10m ST1 A A	2.23	0.04	4.27	0.08	21.28	0.45	-12.9	-19	16°58.8'	89°40.0'
SP-13-VI-02 15m ST1 A B	2.09	0.04	4.01	0.06	19.99	0.44	-12.1	-19	16°58.8'	89°40.0'
SP-13-VI-02 20m ST1 A B	2.07	0.02	3.97	0.03	19.95	0.15	-11.8	-27	16°58.8'	89°40.0'
SP-13-VI-02 30m ST1 A A	1.87	0.03	3.59	0.04	16.67	0.21	-12.1	-25	16°58.8'	89°40.0'
SP shore 10-VIII- 2005	2.16	0.02	4.18	0.02	18.32	0.40	-14.9	-44	16°58.8'	89°40.0'
Salpeten 20-I-2006 #210	2.45	0.02	4.70	0.03	23.06	0.37	-14.5	-31	16°58.8'	89°40.0'
SP2 19-VIII-99 bottom 16 m	1.93	0.03	3.70	0.03	16.23	0.11	-13.3	-27	16°58.8'	89°40.0'
Xcaamal Lake										
XCA 30-VIII-2 0m	1.08	0.03	2.06	0.05	3.36	0.30	-13.1	-8	20° 36.599'	89° 42.907'
XCA 30-VIII-2 2m	0.89	0.04	1.68	0.04	1.87	0.33	-11.6	-3	20° 36.599'	89° 42.907'
XCA 30-VIII-2 4m	0.93	0.02	1.80	0.03	3.20	0.19	-11.2	-17	20° 36.599'	89° 42.907'
XCA 30-VIII-2 6m	0.90	0.04	1.73	0.07	3.19	0.32	-10.7	-13	20° 36.599'	89° 42.907'
XCA 30-VIII-2 8m	0.91	0.02	1.74	0.04	3.52	0.13	-10.4	-8	20° 36.599'	89° 42.907'
XCA 30-VIII-02 10 m	1.01	0.03	1.90	0.02	4.59	0.13	-10.6	7	20° 36.599'	89° 42.907'
XCA 30-VIII-02	1.02	0.02	1.95	0.02	5.08	0.07	-10.5	-9	20° 36.599'	89° 42.907'
XCA 5-III-04 0m	0.87	0.03	1.67	0.05	3.14	0.29	-10.2	-11	20° 36.599'	89° 42.907'
XCA 5-III-04 1m	0.52	0.02	1.03	0.04	-2.53	0.15	-10.8	-19	20° 36.599'	89° 42.907'
XCA 5-III-04 2m	0.38	0.03	0.74	0.04	-5.56	0.25	-11.5	-16	20° 36.599'	89° 42.907'
XCA 5-III-04 3m	0.46	0.04	0.88	0.07	-1.78	0.36	-8.8	-4	20° 36.599'	89° 42.907'
XCA 5-III-04 4m	0.41	0.04	0.78	0.07	-1.81	0.18	-8.0	0	20° 36.599'	89° 42.907'
XCA 5-III-04 5m	0.78	0.03	1.48	0.06	2.20	0.32	-9.6	-3	20° 36.599'	89° 42.907'
XCA 5-III-04 6m	0.19	0.02	0.38	0.01	-5.13	0.07	-8.2	-15	20° 36.599'	89° 42.907'
XCA 5-III-04 7m	0.43	0.01	0.86	0.01	-4.36	0.14	-11.2	-26	20° 36.599'	89° 42.907'
XCA 5-III-04 8m	0.36	0.02	0.70	0.04	-2.47	0.24	-8.0	-7	20° 36.599'	89° 42.907'
XCA 5-III-04 9m	0.21	0.05	0.43	0.06	-5.53	0.30	-9.0	-15	20° 36.599'	89° 42.907'
XCA 5-III-04 10m	0.46	0.03	0.87	0.04	-0.99	0.27	-8.0	-6	20° 36.599'	89° 42.907'
XCA 5-III-04 11m	0.46	0.03	0.88	0.06	-1.25	0.27	-8.3	-9	20° 36.599'	89° 42.907'
CXCA 5III 04 Cladium H2O	0.64	0.03	1.27	0.04	1.11	0.34	-9.1	-29	20° 36.599'	89° 42.907'
Xcaamal A 26-II-05	1.03	0.03	1.99	0.06	4.58	0.51	-11.3	-15	20° 36.599'	89° 42.907'
Xcaamal 08-VIII-01 used to cond	1.28	0.03	2.51	0.06	7.39	0.27	-12.6	-39	20° 36.599'	89° 42.907'
San Jose Lake										
SJ 4-III-04 0m	-0.41	0.02	-0.75	0.02	-8.06	0.18	-2.1	-10	20° 52.316'	90° 8.252'
SJ 4-III-04 1m	-0.45	0.02	-0.86	0.03	-8.94	0.07	-2.0	4	20° 52.316'	90° 8.252'
SJ 4-III-04 2m	-0.16	0.02	-0.33	0.03	-4.60	0.13	-1.9	17	20° 52.316'	90° 8.252'
SJ 4-III-04 3m	-0.31	0.03	-0.63	0.03	-6.91	0.16	-1.9	19	20° 52.316'	90° 8.252'
SJ 4-III-04 4m	-0.37	0.03	-0.72	0.04	-7.08	0.14	-1.3	15	20° 52.316'	90° 8.252'
SJ 4-III-04 5m	-0.28	0.02	-0.55	0.02	-5.71	0.22	-1.3	10	20° 52.316'	90° 8.252'
SJ 4-III-04 6m	-0.25	0.02	-0.50	0.03	-5.41	0.08	-1.4	10	20° 52.316'	90° 8.252'
SJ 04-II-04 7 m	-0.35	0.01	-0.65	0.03	-6.31	0.17	-1.1	-5	20° 52.316'	90° 8.252'
SJ 4-III-04 8m	-0.23	0.02	-0.46	0.02	-5.07	0.07	-1.4	8	20° 52.316'	90° 8.252'
SJ 4-III-04 9m	-0.18	0.02	-0.37	0.02	-4.73	0.08	-1.8	11	20° 52.316'	90° 8.252'
SJ 4-III-04 10m	-0.29	0.03	-0.58	0.03	-6.57	0.14	-2.0	15	20° 52.316'	90° 8.252'
San Jose B surface #5	0.09	0.03	0.17	0.03	-3.87	0.09	-5.3	1	20° 52.316'	90° 8.252'

Table C.5c. Table C.5b continued. Stable isotope ratios of lake waters from the Yucatán Peninsula.

Sample - Lakewater	$\delta^{17}O$	(1σ)	$\delta^{18}O$	(1σ)	δD	(1σ)	d-excess	^{17}O-excess	Latitude (N)	Longitude (W)
Punta Laguna										
Punta Laguna 3-IV-05	1.32	0.03	2.58	0.04	11.42	0.09	-9.4	-41	20° 38.888'	87° 38.128'
Punta Laguna 26-V-00 mid basin	0.76	0.02	1.45	0.03	5.83	0.17	-5.8	-6	20° 38.888'	87° 38.128'
Punta Laguna 26-V-00 east basin	1.05	0.03	2.00	0.05	8.40	0.17	-7.6	-8	20° 38.888'	87° 38.128'
Punta Laguna 3-VI-95	0.88	0.03	1.69	0.03	5.64	0.28	-8.9	-12	20° 38.888'	87° 38.128'
Punta Laguna 20-I-96 end of the dock	0.20	0.03	0.41	0.04	0.40	0.16	-3.9	-16	20° 38.888'	87° 38.128'
Punta Laguna 2-5-96	0.22	0.02	0.45	0.05	0.05	0.33	-4.5	-18	20° 38.888'	87° 38.128'
Other lakes										
Sacnab surf water 13-VIII-03	2.16	0.05	4.11	0.06	22.07	0.12	-10.8	-8	17° 03.0'	89° 22.0'
Sacnab west end 31-VIII-99	1.39	0.03	2.68	0.03	12.04	0.13	-9.3	-22	17° 03.0'	89° 22.0'
Lake Petenxil surface 16-VIII-03	2.12	0.02	4.05	0.02	15.03	0.17	-17.4	-16	17° 0.170'	89° 47.956'
Sayacil # 2 deep	2.28	0.02	4.38	0.03	16.29	0.17	-18.8	-26	20° 41.037'	88° 48.73'
Sayaucil surface A #6	2.70	0.02	5.18	0.04	19.79	0.19	-21.6	-28	20° 41.037'	88° 48.73'
Sayaucil #2 deep	2.35	0.03	4.54	0.04	17.14	0.31	-19.2	-47	20° 41.037'	88° 48.73'
Sayaucil #6 surface	2.65	0.02	5.11	0.05	19.73	0.15	-21.1	-41	20° 41.037'	88° 48.73'
Yalahau #5	1.66	0.03	3.21	0.03	14.30	0.16	-11.3	-29	20° 39.4'	89° 13.1'
Lake Sacpuy Surface	1.46	0.02	2.84	0.03	9.68	0.28	-13.0	-39	16° 59.4'	90° 3.1'
Lake Sacpuy Surface 16-VIII-03	2.43	0.02	4.69	0.02	22.07	0.38	-15.5	-39	16° 59.4'	90° 3.1'
Lake Yaxha 13-8-03 4.2 m	1.72	0.04	3.29	0.04	16.31	0.21	-10.0	-12	17° 3.5'	89°24.5'
Tikal Aguada 13-VIII-01	2.68	0.02	5.14	0.03	19.46	0.15	-21.6	-30	17° 13.741'	89° 36.131'
Lake Quexil 16-VIII-03 surface	2.16	0.02	4.16	0.03	17.95	0.14	-15.3	-32	16° 55.5'	89° 48.1'
Uaxactun Aguada 13-VIII-01	0.57	0.03	1.10	0.04	-1.43	0.13	-10.2	-12	17° 23.643'	89° 38.077'
Santa Ana Vieja Aguada 14-VIII-01	-0.36	0.02	-0.66	0.04	-4.87	0.21	0.4	-8	16° 38.6'	89° 45.0'
Aguada Zacpeten 30-I-2006	2.64	0.03	5.08	0.03	21.87	0.40	-18.8	-36	16° 59.255'	89° 39.602'
Laguna Milagros 15-V-02	1.23	0.03	2.34	0.04	11.42	0.34	-7.3	-6	18° 30.2'	88° 25.5'
Sayil little basin 4-III-05	1.92	0.02	3.69	0.04	14.29	0.21	-15.2	-21	20° 10.684'	89° 39.128'
Laguna near Xcaamal A 31-III-05	1.39	0.03	2.67	0.04	15.17	0.34	-6.5	-20	20° 36.599'	89° 42.907'
Laguna near Xcaamal B 31-III-05	1.40	0.03	2.71	0.04	15.66	0.16	-13.8	-35	20° 36.599'	89° 42.907'
Cenote 05-III-04 261B 0m	2.42	0.01	4.65	0.02	18.69	0.16	-18.5	-29	20° 35.707'	89° 42.70'
Cenote 261 A Surf	3.01	0.02	5.82	0.05	23.21	0.32	-23.3	-57	20° 35.707'	89° 42.70'
Cenote 261 95B 2-VIII-2005	1.69	0.02	3.26	0.02	9.98	0.17	-16.1	-27	20° 35.707'	89° 42.70'
Cenote 261 B 26-II-05	2.59	0.01	4.98	0.03	20.23	0.23	-19.6	-37	20° 35.707'	89° 42.70'
Cenote 261 26-II-05	2.35	0.04	4.55	0.05	18.19	0.11	-18.3	-48	20° 35.707'	89° 42.70'
Cenote 261 21-VIII-05	1.23	0.02	2.43	0.03	4.78	0.06	-14.6	-47	20° 35.707'	89° 42.70'
Quexil shore 7-III-2005	2.03	0.05	3.93	0.07	17.57	0.49	-13.8	-36	20° 35.707'	89° 42.70'
Cenote X'caamal #96B 2-VIII-2005	0.63	0.02	1.22	0.03	-0.55	0.09	-10.3	-13	20° 35.707'	89° 42.70'
Monifata 7-VIII-97	0.79	0.02	1.52	0.05	2.66	0.25	-9.5	-10	16° 55.343'	89° 50.247'
La Gloria 21-VIII-09	0.87	0.02	1.72	0.05	3.80	0.33	-10.0	-36	16° 56.745'	90° 22.495'
Uxmal Fountain	0.10	0.03	0.20	0.03	-1.45	0.18	-3.0	-3	20° 21.672'	89° 46.091'
Yalahau surface #3 B	1.62	0.05	3.10	0.06	12.74	0.52	-12.1	-20	20° 39.447'	89° 12.979'
Yalahau deep #1 A	1.62	0.04	3.13	0.04	13.22	0.28	-11.8	-37	20° 39.447'	89° 12.979'
Well Macanche 28-VIII-99	1.46	0.02	2.80	0.03	13.31	0.25	-9.1	-23	16° 58.0'	89° 38.5'
Macanche surface 28-VIII-99	1.62	0.04	3.12	0.06	14.28	0.45	-10.7	-30	16° 58.0'	89° 38.5'
Amatitlan 13-III-2000 1m	-2.57	0.03	-4.91	0.03	-39.95	0.12	-0.7	28	14° 28.908'	90° 36.103'
Amatitlan 14-III-2000 core site	-1.63	0.03	-3.09	0.05	-29.25	0.26	-4.5	4	14° 28.908'	90° 36.103'
Amatitlan 15-III-2000 core site	-2.77	0.04	-5.28	0.09	-42.11	0.51	0.1	23	14° 28.908'	90° 36.103'
Amatitlan 14-III-2000 hot spring	-2.98	0.05	-5.66	0.08	-48.06	0.65	-3.1	14	14° 28.908'	90° 36.103'
Coba deep #5	1.31	0.03	2.51	0.04	11.41	0.23	-8.6	-14	20° 29.652'	87° 44.308'
Coba deep #2	1.27	0.01	2.43	0.02	11.22	0.17	-8.3	-11	20° 29.652'	87° 44.308'
Coba surface #1A	1.30	0.03	2.47	0.04	10.86	0.16	-8.9	-8	20° 29.652'	87° 44.308'
Coba surface #1	1.26	0.01	2.41	0.02	10.81	0.15	-8.5	-9	20° 29.652'	87° 44.308'
Lake Coba 2-V-96	-0.15	0.02	-0.25	0.04	-3.69	0.17	-2.6	-16	20° 29.652'	87° 44.308'
L. Coba 2-VI-96	0.54	0.02	1.03	0.02	2.75	0.14	-5.5	0	20° 29.652'	87° 44.308'

Table C.6a. Stable isotope ratios of river and freshwaters from the Yucatán Peninsula.

Sample - Groundwater	$\delta^{17}O$	(1σ)	$\delta^{18}O$	(1σ)	δD	(1σ)	d-excess	^{17}O-excess	Latitude (N)	Longitude (W)
Bladen River, Toledo, 13-I-02	-2.18	0.03	-4.14	0.02	-21.31	0.08	11.8	7	16° 28.290'	88° 38.766'
Rio Blanco, Toledo, BZ, 11-I-02	-2.09	0.03	-3.96	0.05	-21.07	0.15	10.6	5	15° 19.941'	91° 0.104'
Sibun River, Cayo, BZ 14-I-02	-2.19	0.04	-4.15	0.06	-19.47	0.27	13.7	2	17° 6.566'	88° 39.601'
South Stann Creek, BZ, 13-1I-02	-2.07	0.03	-3.93	0.02	-19.20	0.12	12.3	5	16° 43.449'	88° 25.820'
Rio Sibun 21-VIII-01	-1.64	0.02	-3.10	0.03	-16.67	0.12	8.2	-1	17° 6.566'	88° 39.601'
Rio Dolores 21-VIII-01	-2.35	0.02	-4.47	0.04	-21.20	0.34	14.6	11	15° 41.012'	90° 24.513'
San Simon V 21-VIII-01	-2.59	0.03	-4.93	0.05	-26.00	0.39	13.4	14	15° 50.078'	90° 17.245'
Uspantan 20-VIII-01	-4.68	0.03	-8.90	0.03	-58.81	0.25	12.4	32	15° 19.684'	90° 57.355'
Arroyo 21-VIII-01	-1.80	0.03	-3.45	0.04	-18.74	0.31	8.9	20	16° 24.445'	90° 6.651'
Rio Candelaria 21-VIII-01	-2.10	0.04	-4.00	0.05	-20.30	0.23	11.7	16	15° 53.068'	90° 11.245'
Seasonal wetland Peten 21-VIII-01	-1.23	0.02	-2.36	0.02	-9.20	0.13	9.7	20	16° 8.675'	90° 10.833'
Rio Passion 21-VIII-01	-1.83	0.04	-3.50	0.04	-16.41	0.22	11.6	19	16° 31.868'	90° 11.313'
Coban Rio Cahabon 21-VIII-01	-3.56	0.04	-6.76	0.07	-41.11	0.18	13.0	19	15° 27.926'	90° 22.339'
Rio Ixlu 13-VIII-01	-2.00	0.04	-3.81	0.05	-24.09	0.24	6.4	11	16° 58.460'	89° 41.199'
Rio Dulce 14-VIII-01	-1.70	0.04	-3.26	0.07	-17.37	0.21	8.7	25	15° 39.438'	89° 0.014'
Rio Ixbobo 14-VIII-01	-1.83	0.04	-3.48	0.04	-16.94	0.20	10.9	6	16° 8.866'	89° 24.167'
Town of Copan Rio Aguas Calientes 15-VIII-01	-2.92	0.03	-5.50	0.04	-31.20	0.23	12.8	-9	14° 50.434'	89° 9.212'
Rio Copan at site 15-VIII-01	-3.09	0.02	-5.87	0.04	-33.42	0.30	13.6	12	14° 50.011'	89° 8.487'
Rio Machaquila 14-VIII-01	-1.78	0.03	-3.34	0.04	-18.66	0.18	8.1	-8	16° 23.612'	89° 26.615'
Rio Cienega 15-VIII-01	-1.49	0.02	-2.81	0.02	-11.84	0.06	10.6	-1	15° 44.074'	89° 4.626'
Rio San Pedro 14-VIII-01	-1.68	0.02	-3.18	0.02	-13.79	0.26	11.7	-4	15° 56.833'	89° 14.697'
Rio San Juan 14-VIII-01	-2.06	0.01	-3.90	0.03	-19.93	0.34	11.3	7	16° 37.871'	89° 36.251'
Rio Camotan 15-VIII-01	-3.14	0.03	-5.95	0.03	-36.06	0.25	11.6	13	14° 51.300'	89° 19.424'
Rio Matagun 15-VIII-01	-3.90	0.04	-7.38	0.05	-48.48	0.26	10.6	1	14° 58.6'	89° 31.45'
Cenote Cristal 11-VIII-01	-2.23	0.02	-4.27	0.03	-25.04	0.30	9.1	25	20° 35.707'	89° 42.70'
Cenote Aktun Ha	-2.14	0.02	-4.08	0.05	-23.60	0.25	9.0	19	20° 35.707'	89° 42.70'
Cenote Ik Kil near Chichen 12-VIII-01	-2.06	0.03	-3.90	0.04	-21.87	0.19	9.4	0	20° 35.707'	89° 42.70'
Celestun Cenote 18-VIII-94	-0.59	0.02	-1.13	0.02	-6.01	0.22	3.0	7	20° 35.707'	89° 42.70'
Rio Grande 15-VIII-01	-3.01	0.02	-5.73	0.04	-36.49	0.39	9.4	18	14° 57.278'	89° 32.231'
Kikil 21-VI-94	-1.30	0.03	-2.49	0.06	-13.56	0.22	6.4	14	21° 11.511'	88° 10.117'
Bacalar surface 12-VI-02	-1.27	0.04	-2.46	0.06	-15.16	0.15	4.5	35	18° 39.100'	88° 24.522'
Cenote Azul Bacalar 12-VI-02	-2.04	0.03	-3.89	0.05	-24.26	0.15	6.9	16	18° 39.100'	88° 24.522'
E of Paxcaman #142 Source 1-XIII-2005	-1.55	0.05	-2.97	0.07	-15.91	0.40	8.0	12	16° 56.7'	89° 46.3'
Xcambo water sample paso B 3-III-05	-2.05	0.04	-3.90	0.07	-22.71	0.46	8.5	6	21° 18.54'	89° 21.11'
Xcambo 2nd pool A 3-III-05	-1.11	0.02	-2.16	0.03	-14.69	0.25	2.6	28	21° 18.54'	89° 21.11'
Xcambo, paso 3-III-05	-2.09	0.02	-3.98	0.04	-23.85	0.36	8.0	7	21° 18.54'	89° 21.11'
Rio Lagartos Cenote	-1.49	0.03	-2.83	0.05	-15.21	0.18	7.4	6	21° 35.759'	88° 8.745'
Telchaquillo Cenote 29-III-05	-2.18	0.04	-4.18	0.04	-24.54	0.15	8.9	26	20° 38.58'	89° 27.29'
Mayapan drip 3-4-5 29-III-05	-2.15	0.02	-4.11	0.03	-25.06	0.26	7.8	18	20° 37.751'	89° 27.631'
Cenote Chi-Huan Holca 30-III-05	-2.25	0.02	-4.27	0.05	-26.76	0.07	7.4	8	20° 45.46'	88° 55.52'
Mayapan pool watertable A 2-III-05	-2.32	0.02	-4.42	0.04	-25.88	0.15	9.5	19	20° 28.564'	89° 11.864'
Mayapan dripwater2 29-II-05	-1.81	0.02	-3.47	0.02	-22.35	0.31	5.4	23	20° 37.751'	89° 27.631'
Mayapan dripwater2 29-II-05	-1.81	0.02	-3.47	0.02	-22.35	0.31	5.4	23	20° 37.751'	89° 27.631'
Calcehtok 2 25-II-05	-1.32	0.03	-2.49	0.02	-9.86	0.26	9.9	-1	20° 33.052'	89° 54.733'
Calcehtok 3 pool	-1.42	0.02	-2.70	0.02	-14.36	0.12	6.9	10	20° 33.052'	89° 54.733'
Rio Ixtul 7-VIII-2005 #146	-1.94	0.03	-3.69	0.05	-20.74	0.19	8.5	13	20° 55.37	87° 7.39
Rio Ixtul 7-VIII-2005 #146	-1.95	0.03	-3.68	0.05	-20.60	0.12	9.0	-5	20° 55.38	87° 7.40
Calcehtok 4 cascada	-1.58	0.02	-3.00	0.03	-14.40	0.11	9.8	9	20° 33.041'	89° 54.740'
Calcehtok 3 pool	-1.43	0.02	-2.69	0.02	-14.02	0.13	7.4	-7	20° 33.041'	89° 54.740'
Calcehtok drip 3	-1.87	0.03	-3.54	0.04	-19.64	0.26	8.7	-3	20° 33.041'	89° 54.740'
Rio Madre Vieja 18-VIII-01	-3.21	0.03	-6.08	0.04	-43.25	0.37	5.5	6	16° 41.818'	89° 44.859'
Rio Benque Viejo 16-VIII-01	-3.67	0.04	-6.96	0.05	-51.06	0.18	4.6	7	17° 4.264'	89° 8.374'
Rio Asuchillo 17-VIII-01	-3.06	0.02	-5.82	0.02	-36.58	0.12	10.1	15	15° 19.941'	91° 0.104'
Rio Blanco 20-VIII-01	-4.77	0.02	-9.05	0.03	-62.84	0.07	9.7	10	15° 19.941'	91° 0.104'
Rio Hato 16-VIII-01	-4.10	0.02	-7.79	0.03	-52.61	0.08	9.9	12	15° 19.941'	91° 0.104'
L Catemaco, MX 21-V-03 01F2	-1.06	0.01	-2.03	0.03	-7.50	0.17	8.8	13	18° 25.44'	95° 7.54'
L. Izabal 3-VI-02	-1.51	0.04	-2.90	0.02	-14.98	0.40	8.0	8	15° 38.052'	88° 59.491'
Edzna water bath #105 2-VIII-05	-2.04	0.02	-3.90	0.03	-24.26	0.28	6.9	17	19° 35.51'	90° 13.42'
Uxmal Fountain	0.12	0.04	0.20	0.08	-1.57	0.19	-3.2	15	20° 21.39'	89° 45.58'
Jalacte Creek 08-I-02 Toledo District	-1.78	0.03	-3.40	0.06	-17.44	0.38	9.8	18	16° 10.1'	89° 4.5'
Rio Cunen El Molino 20-VIII-01	-4.70	0.03	-8.94	0.05	-61.18	0.37	10.3	24	15°17.48	91° 4.14'
Madre Vieja Trib 18-VIII-01	-2.98	0.02	-5.67	0.03	-42.81	0.36	2.5	15	16° 41.818'	89° 44.859'
CA-2 Km 90 Rio 18-VIII-01	-3.17	0.02	-6.05	0.02	-37.94	0.11	10.5	32	16° 41.818'	89° 44.859'
Rio Chixoy 20-VIII-01	-4.73	0.02	-9.00	0.02	-64.21	0.35	7.8	30	15° 21.283'	90° 39.361'
Xbuya Ha 10-VI-94 13:53	-1.34	0.03	-2.53	0.03	-14.15	0.19	6.0	-4	21° 23.41'	88° 53.42
Xbuya Ha 940614 10:30 3m VOCAL	-2.04	0.05	-3.86	0.08	-22.39	0.33	8.4	-4	21° 23.41'	88° 53.43
Noc Ac 10:30 sup 940614	-2.05	0.03	-3.87	0.07	-22.18	0.21	8.7	-6	21° 23.41'	88° 53.44
Dzibilchaltun 28-5-94 sample 1	-2.10	0.05	-3.97	0.06	-22.98	0.21	8.7	2	21° 5.30'	89° 35.48'
Dzitya cenote 18-5-96	-2.08	0.02	-3.90	0.05	-22.97	0.25	8.2	-13	21° 3.09	89° 40.53'53
Rio Lagartos Chiquila cenote 11-VI-1994	-1.49	0.04	-2.87	0.04	-17.19	0.53	5.7	24	21° 35.759'	88° 8.745'
Rio Lagartos Chiquila cenote 30-VI-1994	-1.47	0.02	-2.83	0.02	-16.56	0.23	6.1	24	21° 35.759'	88° 8.745'
Celestun Cenote 18-6-94	-0.46	0.03	-0.90	0.03	-6.08	0.06	1.1	14	20° 51.37'	90° 23.43'
Dzitnup (Xkeken) 14-VI-96	-1.94	0.05	-3.69	0.09	-21.38	0.41	8.2	16	20° 39.4'	88° 14.34'
Cenote Dziuche 25-V-96	-2.00	0.03	-3.83	0.03	-22.21	0.23	8.4	19	19° 53.57	88° 48.28

Table C.6b. Table C.6a continued. Stable isotope ratios of river and freshwaters from the Yucatán Peninsula.

Sample - Groundwater	$\delta^{17}O$	(1σ)	$\delta^{18}O$	(1σ)	δD	(1σ)	d-excess	^{17}O-excess	Latitude (N)	Longitude (W)
Peten Itza 31-X-99	-2.26	0.03	-4.30	0.04	-24.76	0.47	9.6	14	17° 0.170'	89° 47.956'
Cave Actuum Caan 1 #194 15-Aug-2005	-1.33	0.04	-2.51	0.04	-17.21	0.24	2.9	-5	17° 7.47'	88° 51.00'
Cave Actuum Caan 1B #194 15-Aug-2005	-1.37	0.02	-2.58	0.02	-18.30	0.16	2.3	-10	17° 7.47'	88° 51.00'
Cave Actuum Caan 2 #195 15-Aug-2005	-1.83	0.02	-3.47	0.02	-19.47	0.05	8.3	4	17° 7.47'	88° 51.00'
Cave Actuum Caan 3 B 15-Aug-05	-1.90	0.02	-3.58	0.03	-18.57	0.15	10.1	-6	17° 7.47'	88° 51.00'
Cave Tiki Tiki drip (1-2-3) 28-02-05	-0.38	0.03	-0.73	0.04	-2.65	0.16	3.2	0	19° 58.04'	88° 59.642'
Cave Tikitiki pool 28-III-14	-2.64	0.04	-5.00	0.06	-32.48	0.21	7.8	-4	19° 58.04'	88° 59.642'
Cave Tikitiki pool B 28-III-14	-2.65	0.04	-5.05	0.05	-32.73	0.51	7.6	19	19° 58.04'	88° 59.642'
Cave Ixinche water pool 1-III-05	-2.07	0.04	-3.95	0.05	-25.41	0.27	6.2	21	20° 9.608'	88° 47.624'
Cave Ixinche 2nd water sample 1-II-05	-2.40	0.02	-4.54	0.03	-26.61	0.09	9.8	0	20° 9.608'	88° 47.624'
Cave Ixinche water pool B 1-III-05	-2.05	0.02	-3.86	0.03	-26.35	0.15	4.6	-7	20° 9.608'	88° 47.624'
Cave Ixinche 2nd water sample B 1-II-05	-2.36	0.05	-4.46	0.09	-26.94	0.31	8.8	3	20° 9.608'	88° 47.624'
Loltun Cave 21-V-94 Site 1	-1.72	0.04	-3.26	0.06	-16.68	0.25	9.3	-3	20° 15.183'	89° 27.397'
Loltun Cave 21-V-94 Site 2	-2.17	0.03	-4.11	0.04	-22.68	0.31	10.2	0	20° 15.183'	89° 27.397'
Loltun Cave 21-V-94 Site 2 B	-2.14	0.02	-4.06	0.03	-23.25	0.32	9.1	9	20° 15.183'	89° 27.397'
Loltun Cave 26-V-96	-1.94	0.02	-3.67	0.04	-19.85	0.16	9.4	-1	20° 15.183'	89° 27.397'
Loltun Cave 26-II-05	-0.60	0.03	-1.13	0.03	-1.86	0.12	7.2	2	20° 15.183'	89° 27.397'
Loltun Cave B 26-II-05	-0.63	0.03	-1.20	0.02	-3.29	0.25	6.3	-2	20° 15.183'	89° 27.397'

Table C.7. Stable isotope ratios of rainwater from the Yucatán Peninsula.

Sample - Rainwater	$\delta^{17}O$	(1σ)	$\delta^{18}O$	(1σ)	δD	(1σ)	d-excess	^{17}O-excess	Latitude (N)	Longitude (W)
RAIN Chichancanab 7-3-94	-1.44	0.04	-2.74	0.04	-14.22	0.54	7.7	14	19° 52.771'	88° 46.026'
RAIN Chichancanab 7-3-94 B	-1.20	0.25	-2.29	0.47	-13.38	1.52	7.3	11	19° 52.771'	88° 46.026'
RAIN-9-I-2007 3:30 PM	-0.09	0.02	-0.18	0.05	13.73	0.17	15.2	6	20° 0.993'	89° 1.218'
RAIN-30-III 3:00 PM	-1.50	0.03	-2.84	0.04	-18.16	0.36	4.6	-1	20° 0.993'	89° 1.218'
RAIN-25-I-2007 7:00 PM	0.26	0.05	0.47	0.07	15.40	0.41	11.6	6	20° 0.993'	89° 1.218'
RAIN 23-II-2007 8:00 PM	-0.08	0.04	-0.15	0.06	8.66	0.26	9.9	3	20° 0.993'	89° 1.218'
RAIN 8-III-2007 8:00	-0.96	0.02	-1.84	0.01	6.51	0.10	21.2	14	20° 0.993'	89° 1.218'
RAIN 15-I-2007 9:00	0.11	0.02	0.20	0.02	13.77	0.21	12.1	2	20° 0.993'	89° 1.218'
RAIN 5-VIII-2007 8:00	-2.80	0.02	-5.33	0.04	-30.52	0.29	12.2	16	20° 0.993'	89° 1.218'
RAIN 23-VI-2007 2:40PM	-1.29	0.03	-2.45	0.02	-14.16	0.25	5.5	1	20° 0.993'	89° 1.218'
RAIN 11-V-2007 9:30 PM	0.23	0.03	0.45	0.02	12.61	0.26	9.0	-4	20° 0.993'	89° 1.218'
RAIN 08-II-2017 1:00PM	-0.02	0.02	-0.05	0.04	11.26	0.37	11.7	3	20° 0.993'	89° 1.218'
RAIN 13-I-2007 2:15AM	0.43	0.02	0.80	0.03	16.43	0.32	10.0	5	20° 0.993'	89° 1.218'
RAIN 11-V-2007 9:30 PM	0.22	0.02	0.36	0.03	11.02	0.78	8.1	8	20° 0.993'	89° 1.218'
RAIN 08-II-2017 1:00PM	-0.03	0.02	-0.11	0.04	10.50	0.28	11.4	11	20° 0.993'	89° 1.218'
RAIN 13-I-2007 2:15AM	0.46	0.03	0.83	0.06	16.37	0.28	9.7	10	20° 0.993'	89° 1.218'
RAIN 06-II-2007 6:00PM	-0.42	0.05	-0.84	0.08	9.55	0.45	16.3	16	20° 0.993'	89° 1.218'
RAIN 12-I-2007 2:30PM	0.10	0.05	0.13	0.07	14.37	0.36	13.4	13	20° 0.993'	89° 1.218'
RAIN 6-II-2007 6.00 pm	-0.38	0.02	-0.78	0.03	10.11	0.12	16.3	29	20° 0.993'	89° 1.218'
RAIN 11-II-2007 5:00 PM	-1.09	0.02	-2.10	0.02	0.79	0.09	17.6	22	20° 0.993'	89° 1.218'
RAIN 12-I-2017 2:30PM	0.08	0.02	0.12	0.04	14.23	0.12	13.3	18	20° 0.993'	89° 1.218'
RAIN 29-IV-2007	0.10	0.02	0.18	0.02	15.12	0.29	13.7	4	20° 0.993'	89° 1.218'
RAIN 31-V-2017 6:00	-3.90	0.05	-7.37	0.07	-46.60	0.61	12.4	-2	20° 0.993'	89° 1.218'
RAIN 31-VII-2005	-0.60	0.03	-1.13	0.03	4.94	0.18	13.8	-1	20° 0.993'	89° 1.218'
RAIN Roof drain 31-VII- 2005	-0.60	0.03	-1.16	0.03	4.33	0.31	13.3	16	20° 0.993'	89° 1.218'
RAIN Punta Laguna 2-VI-96	0.23	0.05	0.42	0.06	11.63	0.16	8.2	7	20° 38.888'	87° 38.128'
RAIN Calcehtok 25-II-05	-0.48	0.03	-0.92	0.03	3.04	0.05	9.9	5	20° 33.041'	89° 54.740'
RAIN Peten Itza 21-I-96	-0.74	0.03	-1.41	0.03	1.50	0.16	12.8	4	17° 0.170'	89° 47.956'
RAIN Merida 16-VI-94	-0.63	0.03	-1.16	0.05	-3.03	0.08	6.2	-17	20° 58.654'	89° 37.407'
RAIN X'Caamal 8-VIII-01	0.20	0.02	0.39	0.03	4.97	0.20	1.8	-4	20° 36.599'	89° 42.907'
RAIN Piste 9-VI-96	-3.24	0.02	-6.15	0.03	-39.02	0.50	10.2	10	20° 41.53	88° 35.22

Table C.8. Monte Carlo modelling solutions. n defines number of successful simulations.

Data Input					Assumed Freshwater input			Modeled Lakewater			Derived Parameters			RH Uncertainty		Lakewater Uncertainty				
Age (years C.E.)	$\delta^{18}O$	δD	d-excess	^{17}O-excess	Mean $\delta^{18}O$	Mean δD	Mean ^{17}O-ex	Mean $\delta^{18}O$	Mean δD	Mean ^{17}O-ex	Mean RH	Mean T	Mean Xe	min RH	Max RH	min d-excess	Max d-excess	Min ^{17}O-ex	Max ^{17}O-ex	n
Modern	2.98	13.34	-10.47	-20	-4.35	-22.02	7	2.98	13.34	-21	0.80	24.4	0.85	0.76	0.85	-11.44	-9.56	-26	-14	3338
Modern	2.70	10.39	-11.19	-25	-4.45	-23.58	2	2.70	10.38	-25	0.81	24.8	0.85	0.75	0.86	-12.15	-10.30	-31	-19	5379
Modern	2.76	11.18	-10.87	-29	-4.46	-23.14	-1	2.76	11.16	-29	0.80	24.7	0.85	0.75	0.86	-11.84	-9.98	-35	-23	4305
Modern	3.41	13.08	-14.20	-41	-4.53	-22.95	-4	3.42	13.06	-39	0.76	24.8	0.85	0.71	0.81	-15.12	-13.30	-45	-35	2019
Modern	3.42	14.71	-12.68	-31	-4.37	-21.95	1	3.42	14.69	-31	0.78	24.3	0.85	0.73	0.83	-13.59	-11.72	-37	-25	3476
Modern	3.49	15.00	-12.69	-26	-4.35	-21.90	6	3.49	15.00	-26	0.77	24.3	0.85	0.72	0.83	-13.84	-12.00	-32	-20	3373
Modern	3.44	14.46	-13.08	-30	-4.38	-22.14	2	3.44	14.45	-30	0.77	24.5	0.85	0.72	0.83	-13.99	-12.13	-36	-24	3770
Modern	3.43	14.88	-12.56	-35	-4.39	-21.76	-2	3.43	14.86	-35	0.77	24.3	0.85	0.73	0.83	-13.48	-11.65	-41	-29	2828
Modern	3.38	14.50	-12.52	-29	-4.37	-21.99	3	3.38	14.49	-29	0.78	24.4	0.85	0.73	0.83	-13.48	-11.61	-35	-23	3596
Modern	3.41	14.68	-12.57	-27	-4.37	-21.95	5	3.41	14.67	-27	0.78	24.4	0.85	0.73	0.83	-13.53	-11.70	-33	-21	3432
Modern	3.39	14.56	-12.55	-38	-4.43	-21.91	-4	3.40	14.53	-37	0.77	24.4	0.85	0.73	0.82	-13.49	-11.64	-42	-32	2075
Modern	3.40	14.38	-12.83	-25	-4.37	-22.13	6	3.40	14.37	-25	0.78	24.5	0.85	0.73	0.83	-13.75	-11.89	-31	-19	3489
Modern	3.40	14.34	-12.86	-20	-4.31	-22.27	9	3.40	14.33	-22	0.78	24.4	0.85	0.73	0.83	-13.79	-11.93	-26	-15	2018
Modern	3.36	14.27	-12.65	-30	-4.38	-22.09	2	3.36	14.26	-30	0.78	24.5	0.85	0.73	0.83	-13.54	-11.68	-36	-24	3813
Modern	3.68	15.31	-14.18	-40	-4.43	-21.98	-4	3.69	15.29	-39	0.76	24.5	0.85	0.71	0.81	-15.06	-13.23	-45	-34	2368
Modern	2.98	11.98	-11.28	-31	-4.45	-22.97	-1	2.98	11.98	-31	0.79	24.7	0.85	0.74	0.85	-12.79	-10.93	-37	-25	4283
Modern	2.92	11.94	-10.75	-24	-4.41	-22.93	4	2.92	11.93	-24	0.80	24.6	0.85	0.75	0.85	-12.35	-10.49	-30	-18	4700
Modern	2.88	11.63	-10.81	-24	-4.42	-23.10	4	2.88	11.63	-24	0.80	24.6	0.85	0.75	0.85	-12.35	-10.48	-30	-18	4805
Modern	2.69	10.18	-11.36	-32	-4.52	-23.62	-3	2.69	10.17	-31	0.80	24.9	0.85	0.75	0.85	-12.27	-10.41	-38	-26	3635
Modern	2.62	9.59	-11.37	-27	-4.48	-24.06	0	2.62	9.59	-27	0.81	24.8	0.85	0.75	0.87	-12.31	-10.44	-33	-21	5323
Modern	2.88	11.49	-11.52	-23	-4.42	-23.21	5	2.88	11.49	-23	0.80	24.6	0.85	0.75	0.85	-12.46	-10.62	-29	-17	4742
Modern	2.85	11.47	-11.36	-26	-4.43	-23.13	2	2.85	11.46	-26	0.80	24.6	0.85	0.75	0.86	-12.26	-10.39	-32	-20	4745
Modern	2.90	11.61	-11.55	-24	-4.42	-23.17	4	2.90	11.61	-24	0.80	24.6	0.85	0.75	0.85	-12.51	-10.66	-30	-18	4837
Modern	2.91	11.54	-11.74	-33	-4.49	-23.11	-3	2.91	11.53	-32	0.79	24.8	0.85	0.74	0.85	-12.68	-10.81	-39	-27	3656
Modern	2.65	10.02	-11.19	-25	-4.46	-23.82	2	2.65	10.02	-25	0.81	24.8	0.85	0.75	0.86	-12.10	-10.26	-31	-19	5425
Modern	2.79	11.39	-10.93	-33	-4.49	-22.94	-3	2.80	11.37	-32	0.80	24.7	0.85	0.75	0.85	-11.86	-10.01	-39	-27	3062
Modern	3.82	17.21	-13.37	-42	-4.37	-21.01	-5	3.83	17.17	-40	0.76	23.9	0.85	0.71	0.80	-14.26	-12.50	-44	-36	903
Modern	3.13	13.05	-12.96	-36	-4.47	-22.45	-4	3.13	13.03	-35	0.78	24.6	0.85	0.73	0.83	-12.92	-11.07	-41	-30	2617
Modern	3.27	13.69	-12.48	-36	-4.44	-22.29	-3	3.27	13.68	-35	0.78	24.5	0.85	0.73	0.83	-13.40	-11.54	-41	-30	2902
Modern	2.50	9.92	-10.10	-28	-4.48	-23.43	-2	2.50	9.92	-28	0.81	24.8	0.85	0.76	0.87	-10.99	-9.16	-34	-22	4495
Modern	2.62	10.33	-10.87	-31	-4.50	-23.35	-3	2.62	10.32	-30	0.81	24.8	0.85	0.75	0.85	-11.55	-9.70	-37	-25	3618
Modern	3.41	14.30	-12.95	-36	-4.42	-22.17	-3	3.41	14.29	-35	0.77	24.5	0.85	0.72	0.83	-13.91	-12.06	-42	-30	3113
1040.10	4.33	16.97	-17.68	-46	-4.44	-22.19	-4	4.34	16.95	-44	0.72	24.5	0.85	0.67	0.79	-18.58	-16.74	-51	-40	2473
1032.30	3.85	15.01	-15.82	-38	-4.43	-22.66	-1	3.86	15.00	-38	0.75	24.6	0.85	0.69	0.80	-16.76	-14.91	-44	-32	4148
1019.90	3.60	13.70	-15.13	-33	-4.43	-23.12	1	3.61	13.69	-33	0.76	24.6	0.85	0.70	0.82	-16.04	-14.21	-39	-28	4896
1015.30	3.99	15.02	-16.89	-31	-4.40	-23.00	6	3.99	15.01	-31	0.74	24.6	0.85	0.68	0.80	-17.82	-15.96	-37	-25	4586
1006.00	4.57	18.31	-18.22	-35	-4.35	-21.82	6	4.57	18.28	-35	0.72	24.3	0.85	0.66	0.77	-19.14	-17.29	-41	-29	3295
1001.40	4.37	16.48	-18.47		-4.41	-22.73	3	4.37	16.47	-38	0.72	24.5	0.85	0.65	0.79	-19.41	-17.53	-53	-19	11064
996.80	3.65	15.71	-13.50	-30	-4.36	-21.79	4	3.65	15.69	-30	0.77	24.2	0.85	0.71	0.82	-14.41	-12.56	-36	-24	3296
992.20	3.87	15.18	-15.78	-34	-4.40	-22.59	2	3.87	15.17	-34	0.75	24.5	0.85	0.69	0.81	-16.71	-14.85	-40	-28	4563
987.60	4.37	16.63	-18.34	-31	-4.37	-22.60	8	4.37	16.62	-32	0.72	24.5	0.85	0.66	0.78	-19.27	-17.40	-37	-26	3557
973.10	3.98	15.87	-15.94	-36	-4.40	-22.28	1	3.98	15.86	-36	0.75	24.4	0.85	0.69	0.80	-16.86	-15.02	-42	-31	3969
962.40	4.17	17.00	-16.37	-31	-4.35	-21.89	6	4.17	16.99	-32	0.74	24.4	0.85	0.68	0.79	-17.29	-15.44	-37	-25	3437
951.60	4.24	16.41	-17.48	-36	-4.40	-22.50	3	4.24	16.41	-36	0.73	24.5	0.85	0.67	0.79	-18.41	-16.55	-42	-30	4427
946.30	3.87	15.46	-15.49	-42	-4.46	-22.30	-4	3.87	15.44	-41	0.75	24.5	0.85	0.69	0.80	-16.41	-14.58	-47	-36	2401
930.20	3.73	15.41	-14.46	-40	-4.43	-22.05	-3	3.74	15.39	-39	0.76	24.5	0.85	0.70	0.81	-15.39	-13.53	-45	-34	2637
924.90	3.98	16.35	-15.48	-47	-4.49	-21.91	-5	3.99	16.31	-44	0.74	24.3	0.85	0.69	0.78	-16.35	-14.57	-48	-41	694
919.50	3.84	15.56	-15.13	-32	-4.38	-22.23	3	3.84	15.55	-32	0.75	24.4	0.85	0.70	0.81	-16.07	-14.20	-38	-26	4018
903.10	4.85	18.38	-20.42	-36	-4.37	-22.44	7	4.85	18.38	-36	0.70	24.4	0.85	0.63	0.76	-21.36	-19.49	-42	-30	3638
835.30	4.07	16.44	-16.10	-33	-4.37	-22.07	4	4.07	16.43	-33	0.74	24.4	0.85	0.68	0.80	-17.03	-15.17	-39	-28	3741
823.70	4.18	15.88	-17.52	-43	-4.44	-22.64	-3	4.18	15.87	-42	0.73	24.6	0.85	0.67	0.79	-18.45	-16.62	-48	-37	3760
812.10	4.56	17.72	-18.77	-36	-4.38	-22.22	5	4.56	17.71	-36	0.72	24.4	0.85	0.65	0.77	-19.71	-17.85	-42	-30	3969
800.40	4.42	17.01	-18.33	-36	-4.39	-22.46	4	4.42	16.99	-36	0.72	24.5	0.85	0.66	0.78	-19.26	-17.39	-42	-30	4324
794.50	4.77	18.25	-19.89	-43	-4.38	-22.21	0	4.77	18.23	-43	0.70	24.4	0.85	0.64	0.76	-20.82	-18.96	-49	-37	4039
776.90	3.69	15.91	-13.62	-33	-4.35	-21.70	1	3.69	15.90	-33	0.76	24.2	0.85	0.70	0.82	-14.56	-12.70	-39	-27	3277
771.00	4.26	17.30	-16.80	-32	-4.35	-21.91	6	4.26	17.28	-32	0.73	24.3	0.85	0.68	0.79	-17.74	-15.88	-38	-26	3378
765.20	4.70	18.78	-18.81	-35	-4.34	-21.74	6	4.70	18.77	-35	0.71	24.3	0.85	0.64	0.77	-19.74	-17.89	-41	-29	3206
759.30	4.12	15.92	-17.07	-33	-4.40	-22.61	5	4.13	15.91	-33	0.74	24.5	0.85	0.68	0.79	-18.01	-16.15	-39	-27	4217
759.30	4.37	16.61	-18.31	-32	-4.37	-22.61	7	4.37	16.61	-32	0.72	24.5	0.85	0.66	0.78	-19.24	-17.37	-37	-26	3658
753.40	4.42	16.86	-18.46	-45	-4.44	-22.46	-3	4.42	16.85	-44	0.72	24.6	0.85	0.66	0.77	-19.40	-17.56	-51	-39	3330
747.40	4.01	16.17	-15.88	-45	-4.47	-22.08	-5	4.01	16.13	-43	0.74	24.4	0.85	0.69	0.78	-16.81	-14.97	-48	-40	1354
741.50	4.34	16.14	-18.57	-48	-4.51	-22.80	-4	4.34	16.12	-46	0.72	24.7	0.85	0.66	0.77	-19.49	-17.64	-52	-42	2273
634.30	3.85	15.11	-15.67	-26	-4.35	-22.70	8	3.85	15.11	-27	0.75	24.4	0.85	0.69	0.81	-16.58	-14.73	-32	-20	3045
625.30	4.46	17.73	-17.93	-43	-4.39	-21.92	-2	4.46	17.71	-43	0.72	24.4	0.85	0.66	0.78	-18.86	-17.01	-49	-37	3296
620.70	3.86	15.00	-15.91	-19	-4.21	-23.35	10	3.86	15.00	-22	0.77	24.0	0.85	0.72	0.81	-16.74	-15.05	-25	-17	461

Appendix D

Tables for Chapters 5, 6 and 7

Table D.1a. Isotopic composition of measured gypsum hydration water and calculated mother water values (d-excess and ^{17}O-excess) from samples obtained from PLG units, SE Spain.

			GYPSUM HYDRATION WATER						MOTHER WATER	
Sample Name	**Height in cycle (m)**	**Age**	**δ^{17}O**	**σ**	**δ^{18}O**	**σ**	**δD**	**σ**	**^{17}O-Excess**	**d-excess**
Cycle 1										
CdA C1 10 cm	0.1	5969	3.31	0.03	6.34	0.05	-8.40	0.15	-38	-11.9
CdA C1 40 cm	0.4	5969	2.89	0.03	5.56	0.03	-14.19	0.15	-50	-11.5
CdA C1 70 cm	0.7	5969	2.14	0.04	4.13	0.04	-21.90	0.17	-45	-8.0
Cycle 2										
Q1	0.4	5951	2.26	0.00	4.31	0.01	-17.78	0.12	-19	-5.2
Q2	0.8	5951	2.16	0.02	4.11	0.02	-19.46	0.01	-10	-5.3
Q3	1.29	5951	2.06	0.01	3.95	0.01	-19.37	0.31	-26	-3.9
Q4	1.64	5951	2.32	0.01	4.44	0.02	-15.60	0.10	-23	-4.0
Q5	2.32	5951	1.82	0.01	3.47	0.03	-23.31	0.30	-19	-4.1
Q6	3.15	5951	1.85	0.04	3.50	0.05	-20.31	0.44	-5	-1.3
Q7	4.41	5951	1.59	0.01	3.03	0.02	-24.94	0.11	-8	-2.3
Q8	5.1	5951	1.50	0.04	2.86	0.04	-26.32	0.19	-17	-2.4
Q9	5.3	5951	3.34	0.02	6.35	0.03	-3.34	0.11	-15	-6.8
Q10	5.84	5951	2.02	0.03	3.82	0.05	-20.19	0.11	-1	-3.8
Q11	6.65	5951	1.41	0.03	2.65	0.06	-27.03	0.42	3	-1.4
Q12	7.59	5951	1.97	0.02	3.72	0.05	-20.83	0.32	-1	-3.6
Q13	8.64	5951	2.30	0.02	4.39	0.02	-16.48	0.11	-20	-4.6
Q14	9.57	5951	0.84	0.03	1.58	0.03	-32.94	0.20	-7	1.1
Q15	10.32	5951	2.09	0.04	3.97	0.06	-18.45	0.40	-6	-3.2
Q16	11.78	5951	3.09	0.02	5.88	0.02	-6.09	0.22	-16	-5.8
Q17	12.63	5951	1.60	0.04	3.07	0.04	-23.86	0.10	-23	-1.6
Q18	13.51	5951	1.77	0.03	3.37	0.03	-22.32	0.05	-12	-2.4
Q19	14.7	5951	3.39	0.02	6.45	0.02	-3.89	0.14	-17	-8.1
Q20	15.24	5951	2.23	0.03	4.23	0.03	-17.18	0.25	-9	-4.0
Q21	15.54	5951	3.31	0.03	6.28	0.04	-4.26	0.13	-9	-7.2
Q22	16.81	5951	2.04	0.02	3.89	0.02	-19.24	0.03	-12	-3.3
Q23	17.87	5951	1.91	0.03	3.64	0.05	-20.63	0.12	-15	-2.8
Cycle 3										
G.6.1	18.2	5931			4.46	0.03	-16.39	0.34		-5.0
Cycle 4										
G.5.3	0	5910	2.30	0.04	4.38	0.06	-17.88	0.23	-19	-5.9
G.5.2	6	5910	2.99	0.05	5.69	0.05	-10.97	0.30	-17	-9.3
G.5.1	15.5	5910			5.65	0.11	-11.61	0.46		-9.6
Cycle 5										
G.4.2	0	5887	1.92	0.02	3.65	0.04	-25.45	0.21	-14	-7.8
G.4.1	10.7	5887	0.58	0.02	1.10	0.04	-38.55	0.38	-6	-0.8
Cycle 6										
G.3.2	0	5867	3.03	0.03	5.79	0.04	-8.22	0.18	-28	-7.2
G.3.1	9.1	5867	2.59	0.03	4.95	0.04	-14.61	0.20	-24	-7.1
Cycle 7										
G.2.1	8.9		2.35	0.02	4.52	0.03	-16.89	0.16	-37	-6.0
BOSQUE 00	8.82	5837	1.21	0.03	2.31	0.03	-33.62	0.29	-18	-5.4
BOSQUE 01	8.4	5837	1.51	0.03	2.88	0.05	-29.54	0.10	-15	-5.8
BOSQUE 02	7.98	5837	2.13	0.03	4.06	0.04	-22.59	0.16	-23	-8.2
BOSQUE 03	7.56	5837	1.84	0.02	3.52	0.02	-25.24	0.10	-19	-6.5
BOSQUE 04	7.14	5837	1.72	0.01	3.30	0.02	-26.45	0.15	-21	-6.0
BOSQUE 05	6.72	5837	1.28	0.03	2.44	0.04	-31.71	0.19	-15	-4.5
BOSQUE 06	6.3	5837	0.85	0.03	1.61	0.02	-36.81	0.14	-5	-3.1
BOSQUE 07	5.88	5837	1.98	0.03	3.80	0.04	-23.90	0.12	-25	-7.4
BOSQUE 08	5.46	5837	2.24	0.02	4.28	0.04	-19.94	0.19	-24	-7.2
BOSQUE 09	5.04	5837	2.60	0.02	4.94	0.03	-16.52	0.06	-15	-8.9
BOSQUE 10	4.62	5837	3.21	0.04	6.12	0.05	-10.07	0.26	-23	-11.8
BOSQUE 11	4.2	5837	2.69	0.02	5.15	0.03	-14.25	0.06	-30	-8.3
BOSQUE 12	3.78	5837	3.03	0.05	5.78	0.10	-11.42	0.61	-19	-10.4
BOSQUE 13	3.36	5837	2.83	0.03	5.41	0.04	-13.60	0.07	-24	-9.7
BOSQUE 14	2.94	5837	3.37	0.03	6.42	0.02	-6.97	0.06	-14	-11.0
BOSQUE 15	2.52	5837	2.99	0.02	5.70	0.01	-11.08	0.08	-18	-9.5
BOSQUE 16	2.1	5837	3.36	0.02	6.42	0.02	-5.46	0.10	-32	-9.4
BOSQUE 17	1.68	5837	3.36	0.03	6.40	0.02	-6.36	0.12	-21	-10.2
BOSQUE 18	1.26	5837	3.64	0.03	6.95	0.05	-2.86	0.26	-27	-11.1
BOSQUE 19	0.84	5837	3.43	0.04	6.55	0.04	-5.18	0.30	-35	-10.3
BOSQUE 20	0.42	5837	3.32	0.03	6.33	0.06	-5.36	0.15	-25	-8.6
BOSQUE 21	0.2	5837	2.87	0.04	5.49	0.04	-10.97	0.20	-26	-7.7
G.2.2	0	5837			4.77	0.04	-13.54	0.37		-4.6
Cycle 8										
G.1.1	5.55	5816	2.92	0.03	5.54	0.04	-10.48	0.32	-10	-7.6
G.1.2	0	5816	2.97	0.03	5.68	0.03	-9.84	0.38	-33	-8.0

Table D.1b. Table D.1a continued. Isotopic composition of measured gypsum hydration water and calculated mother water values (d-excess and ^{17}O-excess) from samples obtained from PLG units, SE Spain.

			GYPSUM HYDRATION WATER						MOTHER WATER	
Sample Name	**Height in cycle (m)**	**Age**	**δ^{17}O**	**σ**	**δ^{18}O**	**σ**	**δD**	**σ**	**^{17}O-Excess**	**d-excess**
Cycle 10										
RdA -35 cm nuc cone	-0.35	5774			2.02	0.05	-32.71	0.33	-13	-2.2
0cm 5cm	0	5774			4.95	0.06	-15.44	0.22		-7.9
10cm 11cm 12cm	0.1	5774			5.19	0.05	-14.14	0.27	-16	-8.5
50 cm	0.5	5774			4.93	0.03	-14.33	0.20		-6.6
56cm 57cm	0.55	5774			6.32	0.06	-6.23	0.15	-15	-9.5
87cm 91cm	0.87	5774			5.39	0.06	-11.62	0.28		-7.5
102cm 105cm	1.02	5774			4.43	0.04	-18.82	0.29		-7.2
107cm	1.07	5774			5.67	0.04	-12.98	0.26		-11.2
117cm	1.17	5774			4.63	0.04	-19.11	0.24		-9.1
137cm	1.37	5774			3.68	0.04	-24.22	0.49		-6.8
153cm	1.53	5774			5.25	0.05	-13.63	0.20	-29	-8.4
161cm	1.61	5774			3.65	0.04	-23.85	0.27		-6.1
192cm	1.92	5774			4.39	0.02	-17.82	0.28	-37	-5.9
231cm	2.31	5774			3.30	0.04	-23.98	0.28	-25	-3.5
272cm	2.72	5774			5.24	0.04	-12.55	0.15	-32	-7.3
306cm	3.06	5774			3.29	0.01	-24.12	0.30	-30	-3.6
SC50A&B	4.5	5774			4.31	0.03	-19.90	0.30		-7.4
SC100A	5	5774			3.34	0.04	-25.71	0.25		-5.6
SCTOP	6	5774			2.83	0.02	-30.26	0.28	-10	-6.1
Cycle 11										
C7-01	4.0	5754	1.42	0.02	2.69	0.05	-29.65	0.28	-3	-4.4
C7-02	4.0	5754	2.15	0.03	4.10	0.06	-21.27	0.26	-23	-7.1
C7-04	4.0	5754	1.21	0.04	2.31	0.05	-29.36	0.17	-19	-1.1
C7-05	3.0	5754	1.43	0.04	2.72	0.04	-29.83	0.19	-7	-4.8
C7-06	1.0	5754	2.24	0.01	4.30	0.01	-19.82	0.38	-29	-7.2
C7-07	0.0	5754	2.21	0.02	4.20	0.03	-20.36	0.14	-12	-7.0
Cycle 12										
BdI C15 -5 cm	-0.05	5721	2.92	0.04	5.58	0.06	-14.41	0.40	-24	-11.9
BdI C15 10 cm	0.1	5721	3.29	0.02	6.29	0.07	-7.25	0.29	-29	-10.3
BdI C15 46 cm	0.46	5721	3.16	0.05	6.03	0.09	-9.73	0.27	-30	-10.8
BdI C15 130 cm	1.3	5721	3.04	0.18	5.82	0.34	-11.62	0.99	-34	-11.0
BdI C15 200 cm	2	5721	2.38	0.04	4.59	0.06	-17.23	0.30	-44	-6.9
BdI C15 400 cm	4	5721	0.98	0.04	1.89	0.08	-33.86	0.34	-20	-2.3
BdI C15 450 cm	4.5	5721	0.87	0.04	1.72	0.07	-36.28	0.44	-41	-3.4
BdI C15 480 cm	4.8	5721	1.89	0.03	3.63	0.06	-25.41	0.28	-29	-7.6
BdI C15 520 cm	5.2	5721	2.30	0.05	4.46	0.07	-23.99	0.41	-55	-12.7
BdI C15 550 cm	5.5	5721	1.94	0.05	3.75	0.12	-21.54	1.24	-42	-4.6
BdI C15 600 cm	6	5721	1.12	0.03	2.15	0.07	-34.07	0.25	-23	-4.6
Cycle 13										
BdI C16 0m	0	5702	2.64	0.02	5.08	0.05	-15.05	0.18	-43	-8.6
BdI C16 10m	0.1	5702	0.97	0.03	1.84	0.06	-34.74	0.44	-7	-2.8
BdI C16 25m	0.25	5702	3.54	0.05	6.81	0.06	-5.37	0.50	-53	-12.5
BdI C16 35m	0.35	5702	1.55	0.02	2.99	0.06	-27.17	0.48	-34	-4.2
BdI C16 55m	0.55	5702	2.91	0.03	5.61	0.05	-10.74	0.24	-57	-8.4
BdI C16 75 cm	0.75	5702	1.83	0.04	3.52	0.05	-23.09	0.46	-35	-4.3
BdI C16 95 cm	0.95	5702	2.79	0.03	5.36	0.06	-12.92	0.18	-43	-8.7
BdI C16 120 cm	1.2	5702	3.60	0.06	6.87	0.17	-1.79	0.51	-33	-9.3
BdI C16 140 cm	1.4	5702	3.82	0.03	7.33	0.02	0.31	0.27	-48	-10.8
BdI C16 160 cm	1.6	5702	3.16	0.04	6.08	0.07	-6.39	0.16	-49	-7.7
BdI C16 240 cm	2.4	5702	4.13	0.02	7.90	0.04	4.04	0.12	-43	-11.6
Cycle 15										
RdA C16 -35 cm	-0.35	5663	2.37	0.05	4.58	0.08	-18.81	0.38	-49	-8.4
RdA C16 5 cm	0.05	5663	0.14	0.05	0.26	0.09	-45.27	0.86	-5	-0.9
RdA C16 45 cm	0.45	5663	2.37	0.02	4.55	0.05	-19.15	0.38	-40	-8.6
RdA C16 85 cm	0.85	5663	3.36	0.04	6.45	0.08	-7.27	0.71	-44	-11.6
RdA C16 200 cm	2	5663	3.40	0.05	6.50	0.06	-5.81	0.15	-35	-10.5
RdA C16 270 cm	2.7	5663	2.13	0.04	4.11	0.06	-20.45	0.24	-38	-6.3
RdA C16 320 cm	3.2	5663	3.12	0.03	6.00	0.06	-9.35	0.18	-53	-10.1
Nijar Basin										
GY-NIJAR-01			-1.21	0.02	-2.34	0.02	-62.86	0.21	25	1.9
GY-NIJAR-02			1.84	0.02	3.49	0.03	-22.05	0.18	-11	-3.1
GY-NIJAR-03			2.89	0.03	5.51	0.03	-10.80	0.18	-18	-7.7
GY-NIJAR-04			-1.21	0.03	-2.38	0.04	-58.48	0.58	36	6.6
GY-NIJAR-05			-0.53	0.01	-1.05	0.02	-58.82	0.17	15	-4.3
GY-NIJAR-06			-0.76	0.02	-1.47	0.04	-57.94	0.59	8	-0.1
GY-NIJAR-07			2.63	0.03	5.00	0.04	-15.43	0.34	-20	-8.4

Table D.1c. Table D.1b continued. Isotopic composition of measured gypsum hydration water and calculated mother water values (d-excess and ^{17}O-excess) from samples obtained from PLG units, Sicily.

			GYPSUM HYDRATION WATER						MOTHER WATER	
Sample Name	**Height in cycle (m)**	**Age**	**δ^{17}O**	**σ**	**δ^{18}O**	**σ**	**δD**	**σ**	**^{17}O-Excess**	**d-excess**
Resedimented Lower Gypsum, Sicily										
EM MS massive selenite A		5579	3.94	0.04	7.55	0.06	0.74	0.27	-38	-12.1
EM MS massive selenite B		5579	3.38	0.04	6.49	0.05	-8.77	0.22	-43	-13.4
EM lower gypsum banded in place 2B		5579	3.04	0.01	5.79	0.01	-10.19	0.14	-20	-9.3
EM lower banded gypsum hard bit location 2A		5579	2.95	0.02	5.65	0.03	-10.80	0.22	-34	-8.8
Primary Lower Gypsum, Sicily										
Cycle 3										
MG-C3 22m	22	5929			7.35	0.09	0.68	0.51		-10.7
MG-C3 28m	28	5929			7.84	0.07	3.37	0.33		-11.8
MG-C3 44m recrys?	44	5929			5.86	0.03	-9.83	0.48		-9.5
Cycle 4										
MG-C4 BASE	0	5910	2.46	0.03	4.74	0.05	-19.20	0.22	-48	-10.1
MG-C4-3m	3	5910			7.26	0.08	-1.36	0.38		-12.0
MG-C4 6m	6	5910	3.10	0.03	5.95	0.07	-14.20	0.22	-44	-14.7
MG-C4 8m	8	5910			5.95	0.07	-14.11	0.24		-14.5
MG-C4-15m banded	15	5910			7.16	0.06	-2.61	0.33		-12.5
MG-C4 15m	15	5910	3.70	0.04	7.11	0.04	-2.52	0.14	-58	-12.0
MG-C4-19m	19	5910			6.65	0.05	-5.62	0.17		-11.5
MG-C4 24m (rep)	24	5910	3.45	0.05	6.61	0.10	-3.57	0.33	-38	-9.0
MG-C4-24m	24	5910			6.93	0.06	-3.35	0.22		-11.4
MG-C4-28m	28	5910			6.38	0.05	-8.81	0.35		-12.5
Cycle 5										
MG-C5 1m selen espagetti	1	5887			6.02	0.08	-10.42	0.19		-11.3
Cycle 6										
MG-C6 1m selenite 10cm	1	5867			6.63	0.06	-6.56	0.21		-12.3
Monte Banco Cycles 1 to 6										
MBC1 bottom good crystal					7.28	0.05	-5.47	0.18		-16.3
MBC1 middle drilled pieces					6.24	0.03	-8.57	0.13		-11.2
MB-C2 middle drilled pieces					7.90	0.11	4.48	0.38		-11.2
MBC3 Selenite surface					7.10	0.06	-2.32	0.31		-11.7
MBC3 Selenite surface (rep)			3.83	0.01	7.30	0.02	-2.03	0.12	-29	-13.0
MBC4 middle bulk					6.62	0.05	-6.90	0.24		-12.5
MBC4 middle bulk (rep)			3.39	0.02	6.47	0.02	-7.22	0.10	-29	-11.6
MBC6 30 cm drilled pieces					6.26	0.08	-9.80	0.15		-12.6
MBC6 30 cm drilled pieces (rep)			3.45	0.07	6.58	0.13	-7.71	0.76	-27	-13.1
Rocca d'Entella										
RdE massive selenite by the road					7.48	0.03	0.36	0.27		-12.0
RdE selenite photo					6.11	0.03	-8.93	0.27		-10.6
RdE banded photo					7.04	0.06	-2.61	0.36		-11.5
RdE banded cones above observatory					6.26	0.06	-9.54	0.35		-12.3
RdE upper part of mountain road					4.33	0.01	-20.20	0.08		-7.9
Santa Ninfa										
SN banded gypsum					6.39	0.04	-4.40	0.19		-8.2
SN well preserved selenite					7.21	0.07	0.20	0.28		-10.0
SN well preserved selenite (rep)			3.82	0.04	7.27	0.06	0.27	0.15	-17	-10.4
SN massive selenite					6.39	0.04	-4.58	0.32		-8.4
MGU										
MGU marl-gyp top C1					6.27	0.07	-9.13	0.37		-12.0
MGU selenite bottom C1					7.72	0.08	-0.94	0.44		-15.3
MGU selenite bottom C1 (rep)			3.85	0.01	7.34	0.02	-1.31	0.06	-27	-12.6
MGU massive selenite C2					8.56	0.06	5.70	0.25		-15.1

Table D.2a. Isotopic composition of measured gypsum hydration water and calculated mother water values (d-excess and ^{17}O-excess) from samples obtained from UG units, Sicily.

			GYPSUM HYDRATION WATER						MOTHER WATER	
Sample Name	**Height in cycle (m)**	**Age**	**δ^{17}O**	**σ**	**δ^{18}O**	**σ**	**δD**	**σ**	**^{17}O-Excess**	**d-excess**
Eraclea Minoa										
Cycle 2										
EM2-6		5511								
EM2-2		5511								
Cycle 3										
EM3-12		5482								
EM3-7		5482								
EM3 0 cm	0	5482			8.33	0.05	4.78	0.38		-14.3
EM3 -30 c	-0.3	5482			8.81	0.04	8.74	0.34		-14.1
EM3 -60 cm	-0.6	5482			9.12	0.12	9.97	0.33		-15.3
EM3 -150 cm	-1.5	5482			9.18	0.05	13.42	0.26		-12.3
EM3 -200 cm	-2	5482			9.02	0.04	9.75	0.22		-14.7
EM3 -205 cm	-2.05	5482			8.48	0.06	7.22	0.26		-13.0
EM3 -220 cm	-2.2	5482			9.34	0.03	12.32	0.25		-14.6
EM3 -230	-2.3	5482			7.09	0.02	-2.61	0.15		-11.9
EM3 -260	-2.6	5482			8.10	0.04	3.31	0.38		-13.9
EM3 -290 cm	-2.9	5482			7.58	0.06	1.67	0.29		-11.5
EM3 -320 cm	-3.2	5482			8.20	0.07	5.23	0.27		-12.7
EM3 -360 cm	-3.6	5482			8.63	0.06	6.02	0.24		-15.4
EM3 -400	-4	5482			6.93	0.07	-2.20	0.21		-10.3
Cycle 4										
EM4-20		5459								
EM4-13		5459								
EM 4 dome top	9	5459	4.86	0.02	9.29	0.04	7.93	0.20	-40	-18.7
EM 4 dome 0-26cm	8.76	5459	2.60	0.04	4.98	0.04	-21.86	0.35	-29	-14.7
EM 4 dome 30 cm	8.7	5459	4.48	0.04	8.55	0.06	3.90	0.17	-29	-16.9
EM 4 dome 39-60 cm	8.4	5459	2.69	0.03	5.13	0.06	-20.61	0.40	-24	-14.7
EM4 dome 60-81	8.29	5459	4.43	0.02	8.51	0.02	5.91	0.10	-55	-14.5
EM 4 dome 81-98 cm	8.02	5459	4.90	0.03	9.36	0.02	9.64	0.36	-43	-17.5
EM4 dome-119-146cm	7.54	5459	4.62	0.03	8.88	0.05	5.03	0.32	-63	-18.4
EM4 dome 300 cm	6	5459	5.20	0.04	9.98	0.06	17.54	0.30	-63	-14.4
EM4 palisade A	5.25	5459	5.13	0.03	9.82	0.05	14.12	0.20	-48	-16.6
EM4 palisade B	5	5459	4.78	0.03	9.16	0.03	9.85	0.41	-54	-15.7
EM4 palisade C	4.75	5459	4.77	0.02	9.11	0.03	8.88	0.13	-36	-16.3
EM4 palisade D	4.5	5459	3.76	0.05	7.21	0.08	-1.45	0.17	-43	-11.7
EM4 palisade E	4.25	5459	4.72	0.02	9.02	0.03	8.37	0.11	-45	-16.1
EM4 palisade F	4	5459	5.11	0.03	9.79	0.04	12.58	0.36	-53	-18.0
EM4 palisade G	3.75	5459	4.46	0.04	8.53	0.06	3.44	0.13	-37	-17.2
EM4 palisade H	3.5	5459	4.05	0.04	7.80	0.05	3.71	0.26	-64	-11.1
EM4 palisade I	3.25	5459	4.85	0.03	9.30	0.06	11.27	0.31	-50	-15.4
EM4 palisade K	3	5459	4.94	0.05	9.43	0.08	12.86	0.35	-40	-14.8
EM4 UGF 4B 1-01-20 cm	2.92	5459	3.99	0.04	7.62	0.07	-2.00	0.24	-30	-15.5
EM laminated gypsum 40 cm below unit K	2.6	5459	4.01	0.05	7.68	0.08	-0.83	0.34	-40	-14.8
EM4 UGF 4-01-130 cm	2.48	5459	3.41	0.02	6.52	0.05	-9.77	0.07	-34	-14.7
EM4 UGF 4-02-200cm	2.2	5459	3.43	0.03	6.57	0.06	-8.90	0.40	-40	-14.2
EM4 3A-02-190 cm	0.94	5459	3.22	0.04	6.14	0.09	-11.71	0.27	-19	-13.6
EM4 Gypsorudite	0	5459	2.76	0.04	5.26	0.05	-18.63	0.18	-20	-13.6
EM4 veins 60 cm		5459			5.72	0.03	-14.70	0.56		-13.3
EM4 UGF 3a VEINS 120 cm		5459			5.76	0.02	-13.24	0.21		-12.1
Cycle 5										
EM5-31		5436								
EM5-22		5436								
EM5 A	4.5	5436			3.34	0.05	-32.01	0.36		-12.0
EM5 B	4	5436			5.30	0.01	-18.95	0.29		-14.3
EM5 C	3.5	5436			8.84	0.06	6.39	0.29		-16.7
EM5 D	3	5436			10.48	0.05	18.26	0.20		-17.7
EM5 E	2.5	5436			8.62	0.07	4.65	0.26		-16.7
EM5 F	2	5436			9.33	0.03	10.41	0.18		-16.5
EM5 G	1.5	5436			8.72	0.07	6.44	0.32		-15.7
EM5 H	1	5436			8.60	0.05	3.40	0.16		-17.8
EM5 I	0.5	5436			8.94	0.04	7.67	0.33		-16.2
EM5 BASE	0	5436			8.75	0.05	5.28	0.27		-17.1
Cycle 6										
EM6-39		5416								
EM6-33		5416								
Cycle 7										
EM7-44		5343								
EM7-43		5343								
EM7-42		5343								
EM7-41		5343								
EM Aren -21 to -17 cm	-0.17	5343	4.31	0.02	8.30	0.04	8.05	0.25	-69	-10.7
EM AREN upper 0-6 cm	0.06	5343	4.18	0.01	8.02	0.01	2.03	0.24	-51	-14.6
EM AREN 76-83 cm	0.83	5343	3.59	0.03	6.89	0.06	-3.71	0.53	-53	-11.5
EM Aren 112-122 cm	1.12	5343	3.70	0.03	7.13	0.04	-1.89	0.20	-60	-11.5
EM Aren 143-148 cm	1.48	5343	4.25	0.01	8.18	0.02	5.93	0.27	-65	-11.9
EM Aren 191-211 cm	2.11	5343	4.50	0.04	8.65	0.09	7.84	0.57	-60	-13.7

Table D.2b. Table D.2a continued. Isotopic composition of measured gypsum hydration water and calculated mother water values (d-excess and ^{17}O-excess) from samples obtained from deep basin units.

			GYPSUM HYDRATION WATER						MOTHER WATER	
Sample Name	Height in cycle (m)	Age	δ^{17}O	σ	δ^{18}O	σ	δD	σ	^{17}O-Excess	d-excess
Leg 42A Site 372										
42 372Z8RW 30.5-33.5cm	0.305	5325			6.05	0.02	-9.65	0.46		-10.8
42 372Z8RW 30.5-33.5cm	0.305	5325	3.11	0.03	5.98	0.02	-9.82	0.09	-48	-10.4
42 372Z8R1W 46-48.5cm	0.46	5325			5.74	0.10	-10.96	0.20		-9.7
42 372Z8R1W 46-48.5cm	0.46	5325	3.16	0.06	6.04	0.08	-10.78	0.19	-26	-11.9
42 372Z8RW 91-94cm	0.91	5325			6.07	0.11	-8.95	0.47		-10.3
43 372Z8RW 91-94cm	0.91	5325	3.33	0.04	6.37	0.07	-8.47	0.21	-36	-12.2
42 372 Z8 R1 W 96-99cm	0.96	5325			5.47	0.07	-11.65	0.53		-8.2
42 372 Z8 R1 W 96-99cm	0.96	5325	3.16	0.05	6.04	0.06	-10.48	0.28	-30	-11.6
42 372 Z8 R2 W 98-100 cm	0.98	5325			6.51	0.04	-7.04	0.28		-11.8
42 372 Z8 R2 W 98-100 cm	0.98	5325	3.11	0.03	5.92	0.09	-9.17	0.25	-14	-9.2
42 372Z8R1 W 126-128.5	1.26	5325			6.37	0.09	-8.37	0.32		-12.0
42 372Z8R1 W 126-128.5	1.26	5325	3.22	0.03	6.20	0.02	-7.28	0.13	-57	-9.6
42 372 Z8 R2 W 146-149 cm	1.46	5325			6.08	0.04	-8.88	0.33		-10.2
42 372 Z8 R2 W 146-149 cm	1.46	5325	2.61	0.01	5.06	0.02	-11.34	0.16	-70	-4.7
Leg 42A Site 374										
42 374 Z11 R2 58.0-59cm	0.58	5315			3.65	0.03	-19.32	0.29		-1.5
42 374Z12R1W 125-127cm	1.25	5315			3.99	0.05	-19.19	0.20		-4.1
42 374Z12R2W 127-130 cm	1.27	5315			3.98	0.06	-19.48	0.23		-4.3
42 374 Z12 R2 W 112-114 cm	1.12	5315			4.11	0.12	-17.15	0.30		-3.0
42 374 Z16 R1 W 89-90cm	0.89	5315	2.30	0.03	4.34	0.04	-13.26	0.16	7	-0.9
42 374Z16R1W 130-135cm	1.3	5315			4.30	0.03	-15.42	0.32		-2.7
42 374Z16R1W 136-135cm	1.36	5315			4.62	0.04	-17.24	0.21		-7.1
42 374Z17R1W 37-39cm	0.37	5315			4.45	0.08	-11.46	0.52		0.1
42 374Z17R1W 58-59cm	0.58	5315			4.22	0.06	-13.08	0.48		0.3
42 374Z17R1W 82-86cm	0.82	5315			4.08	0.03	-14.89	0.21		-0.4
42 374 Z17 R1 W 110-115 cm	1.1	5315			4.38	0.04	-14.00	0.47		-1.9
42 374Z17R1W 115-119cm	1.15	5315			4.85	0.07	-15.23	0.59		-6.9
42 374 Z19 R1 W 19-21 cm	0.19	5315	2.27	0.01	4.32	0.03	-9.94	0.23	-13	2.7
42 374 Z19 R1 W 25-27cm	0.25	5315			3.94	0.07	-14.01	0.33		1.6
42374Z19R1W 77-80cm	0.77	5315			4.57	0.06	-11.23	0.48		-0.6
42374Z19R1W 83-84cm	0.83	5315			4.82	0.07	-18.11	0.33		-9.6
42 374 Z19 R1 W 103-104 cm	1.03	5315			4.65	0.05	-16.82	0.44		-6.9
42 374Z19R1W 124-126cm	1.24	5315			4.31	0.05	-13.31	0.32		-0.7
42 374Z19R1W 136-138cm	1.36	5315			4.44	0.07	-14.04	0.23		-2.5
42 374 Z20 R1 W 51-55 cm	0.51	5315	2.35	0.05	4.47	0.07	-10.73	0.36	-10	0.7
42 374 Z20 R1W 33-36cm	0.33	5315			4.37	0.06	-14.13	0.41		-1.9
42 374Z20R1W 77-81cm	0.77	5315			4.81	0.08	-15.27	0.33		-6.7
42 374Z20R1W 100-104cm	1	5315			4.79	0.05	-17.97	0.29		-9.3

Table D.2c. Table D.2b continued. Isotopic composition of measured gypsum hydration water and calculated mother water values (d-excess and ^{17}O-excess) from samples obtained from deep basin units.

			GYPSUM HYDRATION WATER						MOTHER WATER	
Sample Name	**Height in cycle (m)**	**Age**	**δ^{17}O**	**σ**	**δ^{18}O**	**σ**	**δD**	**σ**	**^{17}O-Excess**	**d-excess**
Leg 107 Site 654										
107 654 A 27 R1w 6-9 cm	0.06	5310	2.44	0.04	4.67	0.07	-13.33	0.21	-27	-3.6
107 654A 27R1 w 12-15	0.12	5310	2.65	0.04	5.07	0.06	-13.15	0.15	-28	-6.6
107-654 A 27-R1w 19-23cm	0.19	5310	2.62	0.04	5.01	0.06	-11.86	0.17	-31	-4.8
107-654 A 27-R1w 20cm	0.2	5310	2.65	0.04	5.09	0.04	-10.74	0.16	-45	-4.3
107-651 A 27-R1w 26cm	0.26	5310	2.88	0.03	5.53	0.04	-8.95	0.28	-37	-5.9
107 654A 27 R1 w 30-33cm	0.3	5310	2.47	0.04	4.69	0.08	-14.56	0.58	-8	-5.0
107 654 A 27 R1w 34-36 cm	0.34	5310	2.48	0.05	4.76	0.11	-14.50	0.23	-33	-5.4
107 654A 27R1 w 43-45	0.43	5310	2.82	0.03	5.36	0.03	-10.80	0.10	-12	-6.5
107-654 A 27R CC W 10cm	1	5310	2.57	0.03	4.92	0.03	-12.56	0.21	-29	-4.8
107-654 A 28-R1w 8cm	0.08	5310	2.81	0.06	5.37	0.13	-10.22	0.41	-29	-6.0
107-654-A28-R1W-25-28 cm	0.25	5310	2.16	0.04	4.15	0.07	-16.05	0.30	-35	-2.2
107-654-A28-R1W-33-34 cm	0.33	5310	2.02	0.02	3.86	0.04	-18.65	0.47	-24	-2.5
107-654-A28-R1W-51-54 cm	0.51	5310	2.14	0.08	4.11	0.14	-16.46	0.47	-30	-2.3
107 654 A 29 R2 21-22 cm	0.21	5310	2.41	0.05	4.60	0.07	-15.47	0.14	-17	-5.2
107 654 30 R1 w 75-76 cm	0.75	5310	2.23	0.04	4.22	0.06	-15.62	0.22	-8	-2.3
107 654 A 30 R1 121-123 cm	1.21	5310	2.30	0.06	4.41	0.07	-15.00	0.23	-30	-3.2
107 654 A 30 R1 135-137 cm	1.35	5310	2.44	0.02	4.65	0.06	-14.73	0.19	-13	-4.8
107 654 A 30 R1 135-137 cm	1.35	5310	1.82	0.05	3.48	0.09	-19.40	0.29	-21	-0.2
107 654 31 R1 w 2-3 cm	0.02	5310	4.18	0.03	8.01	0.05	6.43	0.35	-44	-10.0
107 654A 31R1 w 105-107 cm	1.05	5310	2.50	0.03	4.76	0.03	-16.22	0.29	-14	-7.2
107 654A 31R1 w 89-90 cm	0.89	5310	2.18	0.03	4.17	0.06	-15.35	0.28	-27	-1.6
107 654A 31R1 w 127-129 cm	1.27	5310	2.33	0.04	4.45	0.05	-13.53	0.09	-23	-2.0
107 654A 31R1 w 134-135 cm	1.34	5310	2.11	0.02	4.05	0.03	-15.73	0.04	-32	-1.0
107 654 A 32 R1 3-5 cm	0.03	5310	2.07	0.03	3.95	0.05	-17.16	0.19	-23	-1.7
107 654 32 R1 w 107-110 cm	1.07	5310	2.06	0.02	3.93	0.02	-17.24	0.13	-19	-1.7
107 654 32 R1 w 144-145 cm	1.44	5310	2.35	0.04	4.45	0.08	-14.43	0.48	-4	-2.9
107 654 32 R1 w 27-28.5 cm	0.27	5310	2.21	0.04	4.24	0.04	-15.77	0.12	-32	-2.6
107 654 32 R2 w 9-10 cm	0.09	5310	2.30	0.03	4.34	0.04	-11.23	0.13	0	1.2
107 654 32 R2 w 9-10 cm	0.09	5310	2.16	0.01	4.14	0.03	-16.41	0.11	-27	-2.5
107 654 32 R2 w 41-43 cm	0.41	5310	2.25	0.04	4.30	0.05	-16.33	0.20	-23	-3.7
107 654 3 2R2 w 144-145 cm	1.44	5310	2.30	0.02	4.37	0.02	-15.71	0.12	-13	-3.6
107 634 A 33 R1 w 72-74 cm	0.72	5310	3.53	0.05	6.74	0.05	-2.78	0.33	-33	-9.3
107 634 A 33 R1 w 63-66 cm	0.63	5310	3.16	0.02	6.03	0.03	-7.75	0.10	-24	-8.7
107 654 34 R1 w 30-37 cm	0.3	5310	2.30	0.05	4.38	0.07	-16.49	0.22	-9	-4.4
107 634 A 34 R1 w 35-37 cm	0.35	5310	1.88	0.02	3.58	0.02	-18.07	0.18	-15	0.3
107 654 34R1 w 51-53 cm	0.51	5310	2.51	0.02	4.79	0.04	-14.09	0.11	-24	-5.3
107 654 A 34R1w 99-106 cm	0.99	5310	2.40	0.02	4.56	0.02	-14.13	0.12	-10	-3.5
107 654 34R1 w 101-102.5 cm	1.01	5310	2.06	0.04	3.93	0.06	-16.26	0.31	-19	-0.6
107 654 A 34 R1 119-122 cm	1.19	5310	2.20	0.05	4.21	0.07	-15.75	0.16	-23	-2.4
107 654 34 R2 w 2-3 cm	0.02	5310	2.60	0.02	4.97	0.02	-12.61	0.45	-23	-5.2
107 634 A 34 R2 w 18-20 cm	0.18	5310	2.28	0.03	4.38	0.04	-14.21	0.19	-32	-2.2
107 654 A 34R2w 32-33 cm	0.32	5310	2.18	0.04	4.16	0.08	-16.58	0.52	-17	-2.8
107 654 A 34R2w 75-76 cm	0.75	5310	2.22	0.04	4.24	0.06	-15.68	0.36	-20	-2.5
107 634 A 34 R2 w 90-94 cm	0.9	5310	2.24	0.03	4.27	0.05	-14.70	0.33	-13	-1.7
107 634 A 34 R2 w 144-145 cm	1.44	5310	2.19	0.03	4.19	0.06	-15.52	0.22	-21	-2.0
107 634 A 34 R3 w 2-3 cm	0.02	5310	2.27	0.02	4.34	0.04	-13.47	0.17	-24	-1.0
107 634 A 34 R3 w 27-28 cm	0.27	5310	2.23	0.03	4.27	0.05	-14.99	0.16	-23	-2.0
107 654 A 34R3w 44-48 cm	0.44	5310	2.20	0.06	4.17	0.10	-16.56	0.26	-10	-2.9
107 634 A 34 R3 w 62-63 cm	0.62	5310	2.02	0.03	3.86	0.04	-16.19	0.21	-18	0.0
107 654A 34R3 w 90-91	0.9	5310	2.06	0.05	3.95	0.08	-18.31	0.57	-22	-2.8
107 634 A 34 R3 w 120-123 cm	1.2	5310	2.18	0.03	4.16	0.05	-15.83	0.18	-21	-2.0
107 654 A 34R3w 146-147 cm	1.46	5310	2.29	0.03	4.36	0.05	-15.14	0.19	-14	-3.0
107-654-A35-R1W-58-59 cm	0.58	5310	1.06	0.03	2.01	0.05	-33.59	0.32	-5	-3.0

Table D.3. Isotopic composition of measured gypsum hydration water and calculated mother water values (d-excess and ^{17}O-excess) from samples obtained from the Cabo de Gata Salinas, SE Spain.

			GYPSUM HYDRATION WATER						MOTHER WATER	
Sample Name	**Height in cycle (m)**	**Age**	**δ^{17}O**	**σ**	**δ^{18}O**	**σ**	**δD**	**σ**	**^{17}O-Excess**	**d-excess**
Modern Marine Gypsum										
#1SALINA					10.56	0.17	12.94	0.35		-24.4
#2SALINA					10.25	0.13	9.57	0.45		-25.4
#3SALINA					11.37	0.07	15.94	0.30		-27.9
#4SALINA					11.60	0.10	18.62	0.24		-26.9
#5SALINA					10.86	0.04	16.69	0.31		-23.0
Salina 1					10.49	0.02	12.39	0.24		-24.5
Salina 4 2015					12.00	0.02	19.71	0.08		-29.0
Salina gypsum on water wheel					11.81	0.09	18.97	0.47		-28.2
DEPO2 beside wheel					11.61	0.02	17.73	0.09		-27.9
DEPO3					11.25	0.04	15.87	0.12		-27.0
DEPO10					12.05	0.01	19.46	0.12		-29.7
Modern marine gypsum (IRMS)										
Salina5-1			5.75	0.07	11.01	0.12			-59	
Salina 5-3			5.80	0.36	11.09	0.69			-51	
Salina 5-4			6.08	0.39	11.66	0.74			-70	
Salina 5-5			5.90	0.12	11.31	0.25			-66	
Depot1			6.27	0.10	12.03	0.20			-74	
desert roses_2_Depot 1			5.89	0.07	11.30	0.12			-71	
Depot_3			6.00	0.13	11.53	0.24			-82	
lost pond-6			5.50	0.01	10.56	0.01			-72	
Calentador2			6.12	0.09	11.72	0.17			-62	
Noria2015			6.05	0.03	11.61	0.04			-74	
BRINES CABO DE GATA SALINAS										
D5-26/03			1.04	0.06	1.99	0.12	6.06	0.44	-6	-9.9
C-23/07			0.62	0.05	1.17	0.07	7.98	0.42	8	-1.3
D1-23/07			1.24	0.04	2.35	0.04	10.61	0.44	14	-9.2
D3-23/07			3.57	0.03	6.83	0.07	31.59	0.54	-31	-23.1
D4-23/07			4.40	0.01	8.45	0.02	36.50	0.29	-58	-31.1
D5-23/07			4.12	0.95	7.94	1.82	30.43	8.47	-60	-33.1
D6-23/7			5.10	0.05	9.81	0.07	34.17	0.37	-64	-44.3
D1-10/09			1.28	0.04	2.46	0.06	13.86	0.47	-15	-5.8
D5-10/09			1.83	0.04	3.51	0.06	7.62	0.29	-20	-20.4
D6-10/9			2.16	0.05	4.15	0.09	12.81	0.31	-30	-20.4

Table D.4a. Results of strontium, calcium and barium isotope analysis on PLG units, SE Spain.

Sample Name	Height in cycle (m)	Age (ka)	$^{87}Sr/^{86}Sr$	2σ (E-6)	$\delta^{44/40}Ca$	2σ	$\delta^{138/134}Ba$
Cycle 1							
CdA C1 10 cm	0.1	5969	0.708974	10	0.34	0.03	0.00
CdA C1 40 cm	0.4	5969	0.708975	8	0.40	0.03	
CdA C1 70 cm	0.7	5969	0.708971	6	0.45	0.03	
Cycle 2							
Q1	0.4	5951	0.708974	10	0.39	0.02	
Q2	0.8	5951	0.708968	10			
Q3	1.29	5951					
Q4	1.64	5951	0.708961	10			
Q5	2.32	5951					
Q6	3.15	5951					
Q7	4.41	5951					
Q8	5.1	5951					
Q9	5.3	5951	0.708972	10	0.44	0.03	
Q10	5.84	5951			0.76	0.02	
Q11	6.65	5951					
Q12	7.59	5951					
Q13	8.64	5951	0.708973	6	0.54	0.03	
Q14	9.57	5951					
Q15	10.32	5951					
Q16	11.78	5951	0.708979	6	0.64	0.03	0.02
Q17	12.63	5951					
Q18	13.51	5951			0.35	0.03	
Q19	14.7	5951					
Q20	15.24	5951					
Q21	15.54	5951	0.70897	8			
Q22	16.81	5951			0.67	0.03	
Q23	17.87	5951	0.708953	7	0.38	0.02	0.14
Cycle 3							
G.6.1	18.2	5931	0.708965	6	0.86	0.03	0.08
Cycle 4							
G.5.3	0	5910	0.708955	9	0.30	0.03	0.06
G.5.2	6	5910			0.80	0.03	
G.5.1	15.5	5910	0.708935	9	0.78	0.03	0.18
Cycle 5							
G.4.2	0	5887	0.70894	6	0.42	0.03	
G.4.1	10.7	5887	0.708957	7	0.71		0.12
Cycle 6							
G.3.2	0	5867	0.708933	7	0.36		
G.3.1	9.1	5867	0.708958	6	0.56	0.02	
Cycle 7							
G.2.1							
BOSQUE 00	8.82	5837	0.708964	7	0.77	0.02	
BOSQUE 01	8.4	5837	0.708959	7	0.85	0.03	0.14
BOSQUE 02	7.98	5837	0.708971	6	0.77	0.02	
BOSQUE 03	7.56	5837	0.708957	5	0.82	0.03	
BOSQUE 04	7.14	5837	0.708959	6	0.90	0.03	
BOSQUE 05	6.72	5837	0.708963	5	0.86	0.02	0.11
BOSQUE 06	6.3	5837	0.708961	6	0.86	0.03	
BOSQUE 07	5.88	5837	0.708957	6	0.79	0.02	
BOSQUE 08	5.46	5837	0.708956	5	0.81	0.03	
BOSQUE 09	5.04	5837	0.70896	6	0.72	0.02	
BOSQUE 10	4.62	5837	0.70896	6	0.83	0.03	0.14
BOSQUE 11	4.2	5837	0.708962	6	0.95	0.02	
BOSQUE 12	3.78	5837	0.708961	6	0.95	0.02	
BOSQUE 13	3.36	5837	0.708955	6	0.91	0.02	
BOSQUE 14	2.94	5837	0.70896	6	0.87	0.03	
BOSQUE 15	2.52	5837	0.708958	6	0.79	0.02	0.09
BOSQUE 16	2.1	5837	0.708951	7	0.92	0.03	
BOSQUE 17	1.68	5837	0.708954	7	0.84	0.02	
BOSQUE 18	1.26	5837	0.708955	6	0.81	0.03	
BOSQUE 19	0.84	5837	0.708952	6	0.80	0.02	
BOSQUE 20	0.42	5837	0.708963	7	0.89	0.03	0.14
BOSQUE 21	0.2	5837	0.708951	6	0.66	0.03	
G.2.2	0	5837					
Cycle 8							
G.1.1	5.55	5816	0.70896	6	0.82	0.03	
G.1.2	0	5816	0.708945	6	0.67	0.03	

Table D.4b. Table D.4a continued. Results of strontium, calcium and barium isotope analysis on PLG units, SE Spain.

Sample Name	Height in cycle (m)	Age (ka)	$^{87}Sr/^{86}Sr$	2σ (E-6)	$\delta^{44/40}Ca$	2σ	$\delta^{138/134}Ba$
Cycle 10							
RdA -35 cm nuc cone	-0.35	5774	0.708926	10	0.53	0.02	
0cm 5cm	0	5774					
10cm 11cm 12cm	0.1	5774			0.75	0.03	
50 cm	0.5	5774					
56cm 57cm	0.55	5774	0.708938	10	0.70	0.03	
87cm 91cm	0.87	5774	0.708934	10	0.71	0.03	
102cm 105cm	1.02	5774	0.708938	9	0.71	0.03	
107cm	1.07	5774					
117cm	1.17	5774	0.708933	10			
137cm	1.37	5774					
153cm	1.53	5774	0.70894	10	0.70	0.03	
161cm	1.61	5774	0.708942	9	0.73	0.03	
192cm	1.92	5774			0.85	0.03	
231cm	2.31	5774			0.56	0.03	
272cm	2.72	5774					
306cm	3.06	5774	0.708945	6	0.74	0.02	
SC50A&B	4.5	5774	0.70896	5	0.88	0.03	
SC100A	5	5774	0.708955	14	0.85	0.03	
SCTOP	6	5774	0.708954	10	0.81	0.03	0.05
Cycle 11							
C7-01	4.0	5754	0.708947	5	0.67	0.02	
C7-02	4.0	5754					
C7-04	4.0	5754					
C7-05	3.0	5754	0.708942	5			
C7-06	1.0	5754					
C7-07	0.0	5754	0.708916	6	0.63	0.02	
Cycle 12							
BdI C15 -5 cm	-0.05	5721	0.708962	9	0.91	0.03	0.23
BdI C15 10 cm	0.1	5721					
BdI C15 46 cm	0.46	5721	0.708966	8	1.16	0.03	
BdI C15 130 cm	1.3	5721					
BdI C15 200 cm	2	5721	0.70895	10	1.00	0.02	
BdI C15 400 cm	4	5721	0.708971	10	0.87	0.02	
BdI C15 450 cm	4.5	5721	0.708966	10	1.10	0.03	0.07
BdI C15 480 cm	4.8	5721	0.708972	11	1.02	0.03	
BdI C15 520 cm	5.2	5721	0.708954	9	0.94	0.03	
BdI C15 550 cm	5.5	5721					
BdI C15 600 cm	6	5721	0.708959	9	1.06	0.03	0.01
Cycle 13							
BdI C16 0m	0	5702	0.70896	6	0.58	0.02	
BdI C16 10m	0.1	5702					
BdI C16 25m	0.25	5702					
BdI C16 35m	0.35	5702					
BdI C16 55m	0.55	5702					
BdI C16 75 cm	0.75	5702					
BdI C16 95 cm	0.95	5702	0.708978	7	0.62	0.02	
BdI C16 120 cm	1.2	5702					
BdI C16 140 cm	1.4	5702					
BdI C16 160 cm	1.6	5702					
BdI C16 240 cm	2.4	5702	0.708949	6	0.71	0.02	
Cycle 15							
RdA C16 -35 cm	-0.35	5663	0.708944	7	0.48	0.03	
RdA C16 5 cm	0.05	5663					
RdA C16 45 cm	0.45	5663			0.78	0.03	
RdA C16 85 cm	0.85	5663	0.708944	7	0.66	0.03	
RdA C16 200 cm	2	5663	0.708952	10	0.71	0.03	
RdA C16 270 cm	2.7	5663	0.70896	9	0.77	0.03	
RdA C16 320 cm	3.2	5663	0.708958	10	0.80	0.03	
Nijar Basin							
GY-NIJAR-01			0.708987	10			
GY-NIJAR-02							
GY-NIJAR-03							
GY-NIJAR-04							
GY-NIJAR-05							
GY-NIJAR-06							
GY-NIJAR-07							

Table D.4c. Table D.4b continued. Results of strontium, calcium and barium isotope analysis on PLG units, Sicily.

Sample Name	Height in cycle (m)	Age (ka)	$^{87}Sr/^{86}Sr$	2σ (E-6)	$\delta^{44/40}Ca$	2σ	$\delta^{138/134}Ba$
Resedimented Lower Gypsum, Sicily							
EM MS massive selenite A		5579	0.708953	10			
EM MS massive selenite B		5579	0.708982	10			
EM lower gypsum banded in place 2B		5579	0.70895	10			
EM lower banded gypsum hard bit location 2A		5579	0.708949	11			
Primary Lower Gypsum, Sicily							
Cycle 3							
MG-C3 22m	22	5929					
MG-C3 28m	28	5929					
MG-C3 44m recrys?	44	5929					
Cycle 4							
MG-C4 BASE	0	5910					
MG-C4-3m	3	5910			0.55	0.03	
MG-C4 6m	6	5910					
MG-C4 8m	8	5910					
MG-C4-15m banded	15	5910					
MG-C4 15m	15	5910			0.74	0.04	
MG-C4-19m	19	5910					
MG-C4 24m (rep)	24	5910			0.85	0.03	
MG-C4-24m	24	5910					
MG-C4-28m	28	5910					
Cycle 5							
MG-C5 1m selen espagetti	1	5887					
Cycle 6							
MG-C6 1m selenite 10cm	1	5867					

Table D.5a. Results of strontium, calcium and barium isotope analysis on UG units, Sicily.

Sample Name	Height in cycle (m)	Age (ka)	$^{87}Sr/^{86}Sr$	2σ (E-6)	$\delta^{44/40}Ca$	2σ	$\delta^{138/134}Ba$
Eraclea Minoa							
Cycle 2							
EM2-6		**5511**	0.708785	14			
EM2-2		**5511**	0.708780	14			
Cycle 3							
EM3-12		5482	0.708778	14			
EM3-7		5482	0.708782	14			
EM3 0 cm	0	5482					
EM3 -30 c	-0.3	5482					
EM3 -60 cm	-0.6	5482					
EM3 -150 cm	-1.5	5482					
EM3 -200 cm	-2	5482					
EM3 -205 cm	-2.05	5482					
EM3 -220 cm	-2.2	5482					
EM3 -230	-2.3	5482					
EM3 -260	-2.6	5482					
EM3 -290 cm	-2.9	5482					
EM3 -320 cm	-3.2	5482					
EM3 -360 cm	-3.6	5482					
EM3 -400	-4	5482					
Cycle 4							
EM4-20		5459	0.708774	14			
EM4-13		5459	0.708788	14			
EM 4 dome top	9	5459	0.708762	11			
EM 4 dome 0-26cm	8.76	5459					
EM 4 dome 30 cm	8.7	5459	0.708766	10	0.03	0.03	0.01
EM 4 dome 39-60 cm	8.4	5459					
EM4 dome 60-81	8.29	5459	0.708777	11	0.54	0.03	0.00
EM 4 dome 81-98 cm	8.02	5459	0.708795	10			
EM4 dome-119-146cm	7.54	5459					
EM4 dome 300 cm	6	5459	0.708775	10			
EM4 palisade A	5.25	5459	0.708779	10			
EM4 palisade B	5	5459					
EM4 palisade C	4.75	5459	0.708777	8	0.35	0.03	-0.06
EM4 palisade D	4.5	5459	0.708769	10			
EM4 palisade E	4.25	5459	0.708788	10	0.43	0.03	-0.01
EM4 palisade F	4	5459	0.708769	10			
EM4 palisade G	3.75	5459	0.708782	10			
EM4 palisade H	3.5	5459					
EM4 palisade I	3.25	5459	0.708779	10			
EM4 palisade K	3	5459	0.708779	10			
EM4 UGF 4B 1-01-20 cm	2.92	5459	0.708779	10	0.25	0.03	0.09
EM laminated gypsum 40 cm below unit K	2.6	5459					
EM4 UGF 4-01-130 cm	2.48	5459					
EM4 UGF 4-02-200cm	2.2	5459					
EM4 3A-02-190 cm	0.94	5459	0.708775	10	0.14	0.02	
EM4 Gypsorudite	0	5459					
EM4 veins 60 cm		5459					
EM4 UGF 3a VEINS 120 cm		5459					
Cycle 5							
EM5-31		5436	0.708756	14			
EM5-22		5436	0.708752	14			
EM5 A	4.5	5436					
EM5 B	4	5436					
EM5 C	3.5	5436					
EM5 D	3	5436					
EM5 E	2.5	5436					
EM5 F	2	5436					
EM5 G	1.5	5436					
EM5 H	1	5436					
EM5 I	0.5	5436					
EM5 BASE	0	5436					
Cycle 6							
EM6-39		5416	0.708729	14			
EM6-33		5416	0.708724	14			
Cycle 7							
EM7-44		5343	0.708737	14			
EM7-43		5343					
EM7-42		5343					
EM7-41		5343	0.708734	14			
EM Aren -21 to -17 cm	-0.17	5343					
EM AREN upper 0-6 cm	0.06	5343	0.708719	10			
EM AREN 76-83 cm	0.83	5343					
EM Aren 112-122 cm	1.12	5343					
EM Aren 143-148 cm	1.48	5343					
EM Aren 191-211 cm	2.11	5343	0.708730	10			

Table D.5b. Table D.5a continued. Results of strontium, calcium and barium isotope analysis on beep basin units.

Sample Name	Height in cycle (m)	Age (ka)	$^{87}Sr/^{86}Sr$	2σ (E-6)	$\delta^{44/40}Ca$	2σ	$\delta^{138/134}Ba$
Leg 107 Site 654							
107 654 A 27 R1w 6-9 cm	0.06	5310					
107 654A 27R1 w 12-15	0.12	5310					
107-654 A 27-R1w 19-23cm	0.19	5310					
107-654 A 27-R1w 20cm	0.2	5310					
107-651 A 27-R1w 26cm	0.26	5310					
107 654A 27 R1 w 30-33cm	0.3	5310	0.708772	8	-0.10		
107 654 A 27 R1w 34-36 cm	0.34	5310					
107 654A 27R1 w 43-45	0.43	5310					
107-654 A 27R CC W 10cm	1	5310					
107-654 A 28-R1w 8cm	0.08	5310	0.70874	7	-0.33		
107-654-A28-R1W-25-28 cm	0.25	5310					
107-654-A28-R1W-33-34 cm	0.33	5310					
107-654-A28-R1W-51-54 cm	0.51	5310					
107 654 A 29 R2 21-22 cm	0.21	5310			-0.39		
107 654 30 R1 w 75-76 cm	0.75	5310	0.708789	8	-0.21		
107 654 A 30 R1 121-123 cm	1.21	5310					
107 654 A 30 R1 135-137 cm	1.35	5310					
107 654 A 30 R1 135-137 cm	1.35	5310					
107 654 31 R1 w 2-3 cm	0.02	5310			-0.10		
107 654A 31R1 w 105-107 cm	1.05	5310					
107 654A 31R1 w 89-90 cm	0.89	5310					
107 654A 31R1 w 127-129 cm	1.27	5310					
107 654A 31R1 w 134-135 cm	1.34	5310	0.708784	8	-0.03		
107 654 A 32 R1 3-5 cm	0.03	5310					
107 654 32 R1 w 107-110 cm	1.07	5310					
107 654 32 R1 w 144-145 cm	1.44	5310			-0.17		
107 654 32 R1 w 27-28.5 cm	0.27	5310					
107 654 32 R2 w 9-10 cm	0.09	5310					
107 654 32 R2 w 9-10 cm	0.09	5310					
107 654 32 R2 w 41-43 cm	0.41	5310					
107 654 3 2R2 w 144-145 cm	1.44	5310					
107 634 A 33 R1 w 72-74 cm	0.72	5310	0.708802	8			
107 634 A 33 R1 w 63-66 cm	0.63	5310			0.03		
107 654 34 R1 w 30-37 cm	0.3	5310					
107 634 A 34 R1 w 35-37 cm	0.35	5310					
107 654 34R1 w 51-53 cm	0.51	5310			0.19		
107 654 A 34R1w 99-106 cm	0.99	5310					
107 654 34R1 w 101-102.5 cm	1.01	5310					
107 654 A 34 R1 119-122 cm	1.19	5310					
107 654 34 R2 w 2-3 cm	0.02	5310					
107 634 A 34 R2 w 18-20 cm	0.18	5310					
107 654 A 34R2w 32-33 cm	0.32	5310	0.708804	9	0.21		
107 654 A 34R2w 75-76 cm	0.75	5310					
107 634 A 34 R2 w 90-94 cm	0.9	5310					
107 634 A 34 R2 w 144-145 cm	1.44	5310					
107 634 A 34 R3 w 2-3 cm	0.02	5310					
107 634 A 34 R3 w 27-28 cm	0.27	5310					
107 654 A 34R3w 44-48 cm	0.44	5310					
107 634 A 34 R3 w 62-63 cm	0.62	5310	0.70879	8	0.09		
107 654A 34R3 w 90-91	0.9	5310					
107 634 A 34 R3 w 120-123 cm	1.2	5310					
107 654 A 34R3w 146-147 cm	1.46	5310					
107-654-A35-R1W-58-59 cm	0.58	5310					
Modern Marine Gypsum							
#1SALINA					0.92	0.03	

Table D.6a. Fluid inclusion salinity estimates, Sr/Ca and sulfur isotope results obtained from PLG units, SE Spain.

Sample Name	Height in cycle (m)	Age (ka)	$\delta^{34}S$	$\delta^{18}O_{SO4}$	Sr/Ca	Tm_{ice}	wt % NaCl	ppt	σ
Cycle 1									
CdA C1 10 cm	0.1	5969			1.35	-3.05	5.00	61	20
CdA C1 40 cm	0.4	5969	22.5	12.1	1.33				
CdA C1 70 cm	0.7	5969			1.51				
Cycle 2									
Q1	0.4	5951	22.1	14.9	1.64	-3.60	5.85	73	12
Q2	0.8	5951	22.9	13.9	1.53				
Q3	1.29	5951			1.50	-4.24	6.78	92	21
Q4	1.64	5951			1.75				
Q5	2.32	5951			1.44	-3.25	5.33	64	10
Q6	3.15	5951			1.44				
Q7	4.41	5951			1.56	-3.74	6.07	77	7
Q8	5.1	5951			1.47				
Q9	5.3	5951	22.1	13.4	1.75	-4.33	6.91	94	19
Q10	5.84	5951			1.59				
Q11	6.65	5951			1.50	-2.36	3.96	45	10
Q12	7.59	5951	22.5	13.1	1.60				
Q13	8.64	5951			1.51				
Q14	9.57	5951			1.42				
Q15	10.32	5951			1.82				
Q16	11.78	5951			1.63				
Q17	12.63	5951			1.59	-2.86	4.71	57	24
Q18	13.51	5951			1.93				
Q19	14.7	5951			1.67	-3.73	6.04	77	17
Q20	15.24	5951			1.74				
Q21	15.54	5951	22.2	13.2	1.85				
Q22	16.81	5951	22.8	12.0	1.55				
Q23	17.87	5951			1.20	-2.07	3.49	39	10
Cycle 3									
G.6.1	18.2	5931	22.4	14.0	1.47				
Cycle 4									
G.5.3	0	5910	22.6	14.0	1.31				
G.5.2	6	5910	22.2	11.0	1.89				
G.5.1	15.5	5910	21.9	13.1	1.51				
Cycle 5									
G.4.2	0	5887	22.6	12.8	1.36				
G.4.1	10.7	5887	22.2	12.5	2.47				
Cycle 6									
G.3.2	0	5867	22.6	13.1	1.42				
G.3.1	9.1	5867	22.1	13.3	1.74				
Cycle 7									
G.2.1			22.2	13.0	2.52				
BOSQUE 00	8.82	5837			2.29				
BOSQUE 01	8.4	5837	21.9	12.5	1.97	-3.94	6.34	84	23
BOSQUE 02	7.98	5837			1.60				
BOSQUE 03	7.56	5837			1.91				
BOSQUE 04	7.14	5837			1.86				
BOSQUE 05	6.72	5837			1.94				
BOSQUE 06	6.3	5837	22.6	12.5	2.23				
BOSQUE 07	5.88	5837		13.0	1.60				
BOSQUE 08	5.46	5837	21.9	11.8	1.52				
BOSQUE 09	5.04	5837		14.1	1.36				
BOSQUE 10	4.62	5837			1.61	-3.94	6.34	84	21
BOSQUE 11	4.2	5837			1.54				
BOSQUE 12	3.78	5837			1.49				
BOSQUE 13	3.36	5837			1.52				
BOSQUE 14	2.94	5837			1.47				
BOSQUE 15	2.52	5837			1.42				
BOSQUE 16	2.1	5837			1.68				
BOSQUE 17	1.68	5837			1.49				
BOSQUE 18	1.26	5837			1.42	-3.69	5.98	76	17
BOSQUE 19	0.84	5837	22.5	14.5	1.47				
BOSQUE 20	0.42	5837			1.55				
BOSQUE 21	0.2	5837	22.3	12.5	1.31	-2.31	3.85	45	21
G.2.2	0	5837	22.6	14.1					
Cycle 8									
G.1.1	5.55	5816	22.4	12.3	1.48				
G.1.2	0	5816	22.4	12.8	1.72				

Table D.6b. Table D.6a continued. Fluid inclusion salinity estimates, Sr/Ca and sulfur isotope results obtained from PLG units, SE Spain.

Sample Name	Height in cycle (m)	Age (ka)	$\delta^{34}S$	$\delta^{18}O_{SO4}$	Sr/Ca	Tm_{ice}	wt % NaCl	ppt	σ
Cycle 10									
RdA -35 cm nuc cone	-0.35	5774	22.5	13.0	1.11	-1.71	2.87	32	19
0cm 5cm	0	5774	23.3	14.5					
10cm 11cm 12cm	0.1	5774	22.7	12.9	1.46	-2.44	4.06	47	20
50 cm	0.5	5774	22.4	13.3	1.73				
56cm 57cm	0.55	5774	22.3	12.6	1.72	-3.58	5.76	77	36
87cm 91cm	0.87	5774	22.6	12.4	1.91	-3.31	5.36	69	33
102cm 105cm	1.02	5774	22.5	12.4	1.82	-2.94	4.83	59	22
107cm	1.07	5774	22.7	13.2					
117cm	1.17	5774	22.5	11.5					
137cm	1.37	5774	22.6	13.2					
153cm	1.53	5774			1.72				
161cm	1.61	5774	22.5	11.9	2.17	-2.68	4.42	53	21
192cm	1.92	5774			1.58	-2.46	4.08	48	24
231cm	2.31	5774	22.7	13.6	1.23				
272cm	2.72	5774			1.57				
306cm	3.06	5774			1.70	-2.83	4.58	60	40
SC50A&B	4.5	5774	22.3	11.3	1.89	-2.77	4.54	57	36
SC100A	5	5774			1.93	-2.30	3.81	45	26
SCTOP	6	5774			1.55				
Cycle 11									
C7-01	4.0	5754			1.54				
C7-02	4.0	5754			1.51				
C7-04	4.0	5754			1.58				
C7-05	3.0	5754			1.36				
C7-06	1.0	5754			1.33				
C7-07	0.0	5754			1.45				
Cycle 12									
BdI C15 -5 cm	-0.05	5721			1.584	-3.66	5.93	75	17
BdI C15 10 cm	0.1	5721	22.3	10.4	2.092				
BdI C15 46 cm	0.46	5721			1.874				
BdI C15 130 cm	1.3	5721	22.4	12.8	3.335				
BdI C15 200 cm	2	5721	22.1	13.0	2.158	-4.54	7.21	101	16
BdI C15 400 cm	4	5721			2.529				
BdI C15 450 cm	4.5	5721			2.875				
BdI C15 480 cm	4.8	5721			2.650				
BdI C15 520 cm	5.2	5721			2.874	-5.46	8.49	134	19
BdI C15 550 cm	5.5	5721	21.2	13.1	2.144				
BdI C15 600 cm	6	5721			2.261				
Cycle 13									
BdI C16 0m	0	5702	21.1	13.4	1.27				
BdI C16 10m	0.1	5702			1.39				
BdI C16 25m	0.25	5702			1.43				
BdI C16 35m	0.35	5702			1.54				
BdI C16 55m	0.55	5702			1.59				
BdI C16 75 cm	0.75	5702			1.59				
BdI C16 95 cm	0.95	5702	22.7	12.5	1.63				
BdI C16 120 cm	1.2	5702			1.64				
BdI C16 140 cm	1.4	5702	22.5	12.1	2.28				
BdI C16 160 cm	1.6	5702			1.72				
BdI C16 240 cm	2.4	5702	22.2	10.9	2.01				
Cycle 15									
RdA C16 -35 cm	-0.35	5663	22.7	14.6	1.19				
RdA C16 5 cm	0.05	5663			1.40				
RdA C16 45 cm	0.45	5663			0.68				
RdA C16 85 cm	0.85	5663	22.6	14.0	1.27				
RdA C16 200 cm	2	5663	22.5	13.3	2.01				
RdA C16 270 cm	2.7	5663	22.2	13.5	2.02				
RdA C16 320 cm	3.2	5663	22.4	13.9	2.20				
Nijar Basin									
GY-NIJAR-01			8.7	10.2	0.48				
GY-NIJAR-02			21.9	10.6	2.95				
GY-NIJAR-03			21.8	10.6					
GY-NIJAR-04			21.2	15.1	1.11				
GY-NIJAR-05			6.7	9.0	0.45				
GY-NIJAR-06			-18.3	7.1					
GY-NIJAR-07			20.5	10.8					

Table D.6c. Table D.6b continued. Fluid inclusion salinity estimates, Sr/Ca and sulfur isotope results obtained from PLG units, SE Spain.

Sample Name	Height in cycle (m)	Age (ka)	$\delta^{34}S$	$\delta^{18}O_{SO4}$	Sr/Ca	Tm_{ice}	wt % NaCl	ppt	σ
Resedimented Lower Gypsum, Sicily									
EM MS massive selenite A		5579	22.5	12.9					
EM MS massive selenite B		5579	22.7	12.3					
EM lower gypsum banded in place 2B		5579	21.6	12.6					
EM lower banded gypsum hard bit location 2A		5579	22.4	13.3					
Primary Lower Gypsum, Sicily									
Cycle 3									
MG-C3 22m	22	5929				-4.31	6.87	95	29
MG-C3 28m	28	5929				-4.26	6.79	93	28
MG-C3 44m recrys?	44	5929							
Cycle 4									
MG-C4 BASE	0	5910							
MG-C4-3m	3	5910	22.8	13.0	1.47	-3.80	6.13	80	21
MG-C4 6m	6	5910	22.9	13.4					
MG-C4 8m	8	5910							
MG-C4-15m banded	15	5910	22.7	13.2					
MG-C4 15m	15	5910			2.13	-4.63	7.34	103	13
MG-C4-19m	19	5910	22.8	14.0					
MG-C4 24m (rep)	24	5910			1.92				
MG-C4-24m	24	5910	22.8	13.0					
MG-C4-28m	28	5910	22.6	12.7					
Cycle 5									
MG-C5 1m selen espagetti	1	5887	22.9	14.6					
Cycle 6									
MG-C6 1m selenite 10cm	1	5867							
Monte Banco Cycles 1 to 6									
MBC1 bottom good crystal			22.4						
MBC1 middle drilled pieces			22.6						
MB-C2 middle drilled pieces			23.1						
MBC3 Selenite surface									
MBC3 Selenite surface (rep)									
MBC4 middle bulk			22.9						
MBC4 middle bulk (rep)			23.2						
MBC6 30 cm drilled pieces									
MBC6 30 cm drilled pieces (rep)									

Table D.7a. Fluid inclusion salinity estimates, Sr/Ca and sulfur isotope results obtained from UG units, Sicily.

Sample Name	Height in cycle (m)	Age (ka)	$\delta^{34}S$	$\delta^{18}O_{SO4}$	Sr/Ca	Tm_{ice}	wt % NaCl	ppt	σ
Eraclea Minoa									
Cycle 2									
EM2-6		5511							
EM2-2		5511							
Cycle 3									
EM3-12		5482							
EM3-7		5482							
EM3 0 cm	0	5482							
EM3 -30 c	-0.3	5482							
EM3 -60 cm	-0.6	5482							
EM3 -150 cm	-1.5	5482	22.1	18.2					
EM3 -200 cm	-2	5482							
EM3 -205 cm	-2.05	5482							
EM3 -220 cm	-2.2	5482							
EM3 -230	-2.3	5482	22.6	18.8					
EM3 -260	-2.6	5482							
EM3 -290 cm	-2.9	5482							
EM3 -320 cm	-3.2	5482							
EM3 -360 cm	-3.6	5482	22.4	18.6					
EM3 -400	-4	5482							
Cycle 4									
EM4-20		5459							
EM4-13		5459							
EM 4 dome top	9	5459	21.6	14.5		-3.74	6.07	77	3
EM 4 dome 0-26cm	8.76	5459							
EM 4 dome 30 cm	8.7	5459			1.49				
EM 4 dome 39-60 cm	8.4	5459	20.9	14.9					
EM4 dome 60-81	8.29	5459			2.93	-5.23	8.15	126	30
EM 4 dome 81-98 cm	8.02	5459	20.8	13.7					
EM4 dome-119-146cm	7.54	5459							
EM4 dome 300 cm	6	5459	20.9	13.9		-5.88	8.99	158	63
EM4 palisade A	5.25	5459	21.2	13.2					
EM4 palisade B	5	5459	21.9	16.5					
EM4 palisade C	4.75	5459	21.3	13.9	1.87	-4.00	6.44	84	11
EM4 palisade D	4.5	5459							
EM4 palisade E	4.25	5459	21.3	13.9	2.02	-4.50	7.16	99	16
EM4 palisade F	4	5459							
EM4 palisade G	3.75	5459	21.4	13.6					
EM4 palisade H	3.5	5459				-3.52	5.74	71	9
EM4 palisade I	3.25	5459							
EM4 palisade K	3	5459	21.7	13.7					
EM4 UGF 4B 1-01-20 cm	2.92	5459	22.0	16.4	1.48				
EM laminated gypsum 40 cm below unit K	2.6	5459	21.4	14.9					
EM4 UGF 4-01-130 cm	2.48	5459	22.0	16.5					
EM4 UGF 4-02-200cm	2.2	5459	22.1	17.1					
EM4 3A-02-190 cm	0.94	5459	21.4	17.9	1.31				
EM4 Gypsorudite	0	5459	22.3	17.5					
EM4 veins 60 cm		5459	22.2	17.9					
EM4 UGF 3a VEINS 120 cm		5459							
Cycle 5									
EM5-31		5436							
EM5-22		5436							
EM5 A	4.5	5436							
EM5 B	4	5436							
EM5 C	3.5	5436							
EM5 D	3	5436							
EM5 E	2.5	5436							
EM5 F	2	5436	22.0	16.3					
EM5 G	1.5	5436							
EM5 H	1	5436	22.1	16.9					
EM5 I	0.5	5436							
EM5 BASE	0	5436							
Cycle 6									
EM6-39		5416							
EM6-33		5416							
Cycle 7									
EM7-44		5343							
EM7-43		5343							
EM7-42		5343							
EM7-41		5343							
EM Aren -21 to -17 cm	-0.17	5343							
EM AREN upper 0-6 cm	0.06	5343	21.1	14.8					
EM AREN 76-83 cm	0.83	5343							
EM Aren 112-122 cm	1.12	5343							
EM Aren 143-148 cm	1.48	5343	21.2						
EM Aren 191-211 cm	2.11	5343	21.0	17.1					

Table D.7b. Table D.7a continued. Sulfur isotope results obtained from deep basin units.

Sample Name	Height in cycle (m)	Age (ka)	$\delta^{34}S$	$\delta^{18}O_{SO4}$	Sr/Ca	Tm_{ice}	wt % NaCl	ppt	σ
Leg 42A Site 372									
42 372Z8RW 30.5-33.5cm	0.305	5325							
42 372Z8RW 30.5-33.5cm	0.305	5325	21.4	16.3					
42 372Z8R1W 46-48.5cm	0.46	5325							
42 372Z8R1W 46-48.5cm	0.46	5325	21.0	15.8					
42 372Z8RW 91-94cm	0.91	5325							
43 372Z8RW 91-94cm	0.91	5325	19.5	16.6					
42 372 Z8 R1 W 96-99cm	0.96	5325							
42 372 Z8 R1 W 96-99cm	0.96	5325	21.1	15.5					
42 372 Z8 R2 W 98-100 cm	0.98	5325							
42 372 Z8 R2 W 98-100 cm	0.98	5325	21.8	17.9					
42 372Z8R1 W 126-128.5	1.26	5325							
42 372Z8R1 W 126-128.5	1.26	5325	21.1	15.3					
42 372 Z8 R2 W 146-149 cm	1.46	5325							
42 372 Z8 R2 W 146-149 cm	1.46	5325	21.9	18.2					
Leg 42A Site 374									
42 374 Z11 R2 58.0-59cm	0.58	5315	20.6	12.9					
42 374Z12R1W 125-127cm	1.25	5315		11.8					
42 374Z12R2W 127-130 cm	1.27	5315	20.2	12.3					
42 374 Z12 R2 W 112-114 cm	1.12	5315							
42 374 Z16 R1 W 89-90cm	0.89	5315	22.0	15.7					
42 374Z16R1W 130-135cm	1.3	5315	23.4	15.4					
42 374Z16R1W 136-135cm	1.36	5315							
42 374Z17R1W 37-39cm	0.37	5315							
42 374Z17R1W 58-59cm	0.58	5315	22.2	11.2					
42 374Z17R1W 82-86cm	0.82	5315							
42 374 Z17 R1 W 110-115 cm	1.1	5315							
42 374Z17R1W 115-119cm	1.15	5315	20.1	14.6					
42 374 Z19 R1 W 19-21 cm	0.19	5315	22.2	13.0					
42 374 Z19 R1 W 25-27cm	0.25	5315							
42374Z19R1W 77-80cm	0.77	5315	22.9	15.4					
42374Z19R1W 83-84cm	0.83	5315	21.1	15.4					
42 374 Z19 R1 W 103-104 cm	1.03	5315	21.1	15.9					
42 374Z19R1W 124-126cm	1.24	5315							
42 374Z19R1W 136-138cm	1.36	5315							
42 374 Z20 R1 W 51-55 cm	0.51	5315	22.0	17.0					
42 374 Z20 R1W 33-36cm	0.33	5315							
42 374Z20R1W 77-81cm	0.77	5315							
42 374Z20R1W 100-104cm	1	5315	22.3	14.7					

Table D.7c. Table D.7b continued. Sulfur isotope results obtained from deep basin units.

Sample Name	Height in cycle (m)	Age (ka)	$\delta^{34}S$	$\delta^{18}O_{SO4}$	Sr/Ca	Tm_{ice}	wt % NaCl	ppt	σ
Leg 107 Site 654									
107 654 A 27 R1w 6-9 cm	0.06	5310							
107 654A 27R1 w 12-15	0.12	5310							
107-654 A 27-R1w 19-23cm	0.19	5310							
107-654 A 27-R1w 20cm	0.2	5310							
107-651 A 27-R1w 26cm	0.26	5310			1.53				
107 654A 27 R1 w 30-33cm	0.3	5310	22.4	18.1					
107 654 A 27 R1w 34-36 cm	0.34	5310							
107 654A 27R1 w 43-45	0.43	5310							
107-654 A 27R CC W 10cm	1	5310							
107-654 A 28-R1w 8cm	0.08	5310			1.42				
107-654-A28-R1W-25-28 cm	0.25	5310	22.4	17.7					
107-654-A28-R1W-33-34 cm	0.33	5310							
107-654-A28-R1W-51-54 cm	0.51	5310	22.1	18.3					
107 654 A 29 R2 21-22 cm	0.21	5310	22.9	20.3	1.20				
107 654 30 R1 w 75-76 cm	0.75	5310	22.1	18.2	1.07				
107 654 A 30 R1 121-123 cm	1.21	5310							
107 654 A 30 R1 135-137 cm	1.35	5310	22.1	18.3					
107 654 A 30 R1 135-137 cm	1.35	5310							
107 654 31 R1 w 2-3 cm	0.02	5310			2.01				
107 654A 31R1 w 105-107 cm	1.05	5310							
107 654A 31R1 w 89-90 cm	0.89	5310							
107 654A 31R1 w 127-129 cm	1.27	5310							
107 654A 31R1 w 134-135 cm	1.34	5310	22.1	18	1.28				
107 654 A 32 R1 3-5 cm	0.03	5310							
107 654 32 R1 w 107-110 cm	1.07	5310							
107 654 32 R1 w 144-145 cm	1.44	5310	22.2	18.7	1.60				
107 654 32 R1 w 27-28.5 cm	0.27	5310							
107 654 32 R2 w 9-10 cm	0.09	5310							
107 654 32 R2 w 9-10 cm	0.09	5310							
107 654 32 R2 w 41-43 cm	0.41	5310	22.1	18.8					
107 654 3 2R2 w 144-145 cm	1.44	5310							
107 634 A 33 R1 w 72-74 cm	0.72	5310	21.3	17.8					
107 634 A 33 R1 w 63-66 cm	0.63	5310			1.53				
107 654 34 R1 w 30-37 cm	0.3	5310	22.9	18.3					
107 634 A 34 R1 w 35-37 cm	0.35	5310							
107 654 34R1 w 51-53 cm	0.51	5310			1.34				
107 654 A 34R1w 99-106 cm	0.99	5310							
107 654 34R1 w 101-102.5 cm	1.01	5310							
107 654 A 34 R1 119-122 cm	1.19	5310							
107 654 34 R2 w 2-3 cm	0.02	5310							
107 634 A 34 R2 w 18-20 cm	0.18	5310							
107 654 A 34R2w 32-33 cm	0.32	5310			1.53				
107 654 A 34R2w 75-76 cm	0.75	5310							
107 634 A 34 R2 w 90-94 cm	0.9	5310							
107 634 A 34 R2 w 144-145 cm	1.44	5310							
107 634 A 34 R3 w 2-3 cm	0.02	5310							
107 634 A 34 R3 w 27-28 cm	0.27	5310							
107 654 A 34R3w 44-48 cm	0.44	5310							
107 634 A 34 R3 w 62-63 cm	0.62	5310			3.57				
107 654A 34R3 w 90-91	0.9	5310							
107 634 A 34 R3 w 120-123 cm	1.2	5310							
107 654 A 34R3w 146-147 cm	1.46	5310							
107-654-A35-R1W-58-59 cm	0.58	5310							

Table D.8a. Oxygen, carbon, strontium, calcium and XRD data of PLG carbonates

Sample Name	Depth from base of gypsum (m)	$\delta^{18}O$	$\delta^{13}C$	$^{87}Sr/^{86}Sr$	2σ (E-6)	$\delta^{44/40}Ca$	2σ	% Calcite	% Dolomite	% Aragonite	Cal:Dol
Base of PLG											
CdA C1 -10 cm	-0.1	-6.8	-3.7								100%
Sorbas Cycle 2-3											
Q24	-0.2	-8.2	-2.0								100%
Q25	-0.1	-8.3	-2.3								100%
Sorbas Cycle 3-4											
M5.1	-0.5	-4.2	1.6					61	0	29.8	100%
M5.2	-1.1	-4.5	1.5					65	0.2	27.3	100%
M5.3	-1.6	-6.5	0.1			0.39	0.03	91.8	0.1	1.1	100%
Sorbas Cycle 4-5											
M4.1b	-0.3	-7.9	-3.1			0.25		60.7	1	0	98%
Sorbas Cycle 5-6											
M3.1	-0.75	-7.6	-2.0			0.15		55	0.4	5.8	99%
M3.2	-1.5	-7.2	-2.7					57.1	2.6	1	96%
Sorbas Cycle 6-7											
M2.1	-0.35	-6.3	-1.4	0.70872	6	0.34	0.02	89	0.3	1.9	100%
M2.2	-0.6	-4.9	0.2	0.70877	6	0.06	0.02				
M2.3	-1	-4.0	1.5	0.708802	7	-0.02	0.03	22.1	0.8	50.2	97%
M2.4	-1.2	-3.4	-1.8					16.6	0.2	8.3	99%
M2.5	-1.5	-3.7	1.6	0.708803	9	-0.10	0.03	20.6	0.3	53.6	99%
M2.6	-1.95	-5.9	-1.3					86	0.3	1.6	100%
M2.7	-2.5	-6.3	-1.2	0.708936	9	0.46	0.02	87.6	0.4	0.8	100%
Sorbas Cycle 7-8											
HIGUERA MARL 0	0	-4.9	-1.3								
HIGUERA MARL 5	-0.05	-5.8	-0.8								
HIGUERA MARL 10	-0.1	-6.6	-1.6								
HIGUERA MARL 15	-0.15	-7.0	-1.2								
M1.1	-0.18	-7.3	-1.1	0.708423	6	0.26	0.02	64.1	0.8	4.1	99%
HIGUERA MARL 20	-0.2	-7.6	-1.1								
HIGUERA MARL 25	-0.25	-7.6	-1.1								
HIGUERA MARL 30	-0.3	-7.6	-1.0								
HIGUERA MARL 35	-0.35	-7.1	-0.8								
HIGUERA MARL 40	-0.4	-5.8	0.1								
HIGUERA MARL 45	-0.45	-5.3	0.5								
M1.2	-0.48	-5.3	-0.3	0.708645	6	0.20	0.02	34	0.1	23.3	100%
HIGUERA MARL 50	-0.5	-4.1	1.7								
HIGUERA MARL 55	-0.55	-5.4	0.3								
M1.3	-1.2	-6.2	-1.4	0.70855	10	0.26	0.02	29.1	0.4	5.8	99%
Sorbas Cycle 9-10											
RdA M5 0	0	-2.5	0.5			0.00	0.02	0	42.6	0.0	0%
RdA M5 -2	-0.02	-1.1	0.2					10.8	20.2	0.0	35%
RdA M5 -4	-0.04	0.2	0.6					1.9	12.4	0.0	13%
RdA M5 -6	-0.06	1.3	0.9					9.5	13.1	0.0	42%
RdA M5 -8	-0.08	1.5	0.8					9.7	15.5	0.0	38%
RdA M5 -10	-0.1	1.9	1.5					9.5	14.0	0.0	40%
RdA M5 -12	-0.12	1.4	1.3					18.7	33.9	0.0	36%
RdA M5 -14	-0.14	-1.2	1.1					19.1	30.9	0.0	38%
RdA M5 -16	-0.16	-1.3	1.1			-0.02	0.02	36.4	25.8	0.0	59%
RdA M5 -18	-0.18	-1.2	0.5					39.9	25.7	0.0	61%
RdA M5 -20	-0.2	-2.1	0.4					20.6	12.2	0.0	63%
RdA M5 -22	-0.22	-3.7	-0.1					35.9	16.1	0.0	69%
RdA M5 -24	-0.24	-3.0	-0.1					40.0	10.1	0.0	80%
RdA M5 -26	-0.26	-3.1	-0.1					44.5	12.8	0.0	78%
RdA M5 -28	-0.28	-3.5	-0.1	0.708832	7	-0.13	0.02	37.8	10.7	0.0	78%
RdA M5 -30	-0.3	-3.0	0.3					40.4	7.4	0.0	84%
RdA M5 BULK		0.0	0.6					44.1	11.8	0.0	79%
Sorbas Cycle 10 SC											
RdA C6 SC 130	1.3	3.3	-3.8					0.3	24.4	0.0	1%
RdA C6 SC 120	1.2	3.4	-4.0					0.5	15.7	0.0	3%
RdA C6 SC 110	1.1	3.1	-3.9					0.3	20.4	0.0	2%
RdA C6 SC 100	1	3.3	-4.3					0.1	30.0	0.0	0%
RdA C6 SC 90	0.9	2.9	-4.2					0.2	22.6	0.0	1%
RdA C6 SC 80	0.8	3.2	-4.3					0.2	33.7	0.0	1%
RdA C6 SC 70	0.7	3.0	-4.6					0.0	46.9	0.0	0%
RdA C6 SC 60	0.6	3.0	-4.8					0.0	69.3	0.0	0%
RdA C6 SC 50	0.5	3.0	-4.6	0.708986	12	0.21	0.02	0.0	42.1	0.0	0%
RdA C6 SC 40	0.4	3.1	-4.7					0.1	41.8	0.0	0%
RdA C6 SC 30	0.3	2.9	-4.4					0.1	30.5	0.0	0%
RdA C6 SC 20	0.2	3.2	-4.0					0.0	24.0	0.0	0%
RdA C6 SC 10	0.1	3.0	-3.8					0.2	31.9	0.0	0%
RdA C6 SC 50-80	0.5	3.5	-4.3			0.18	0.02	0.2	52.2	0.0	0%
RdA C6 SC 50-70	0.5	2.9	-4.3								
RdA C6 SC 50-60	0.5	3.2	-4.8								
RdA C6 SC 50-50	0.5	3.2	-4.8								
RdA C6 SC 50-40	0.5	3.0	-4.9								
RdA C6 SC 50-30	0.5	2.8	-4.9								
RdA C6 SC 50-20	0.5	2.9	-4.9								
RdA C6 SC 50-10	0.5	3.1	-4.8	0.709025	6	0.16	0.03	0.0	42.6	0.0	0%

Table D.8b. Table D.8a continued. Oxygen, carbon, strontium, calcium and XRD data of PLG and UG carbonates

Sample Name	Depth from base of gypsum (m)	$\delta^{18}O$	$\delta^{13}C$	$^{87}Sr/^{86}Sr$	2σ (E-6)	$\delta^{44/40}Ca$	2σ	% Calcite	% Dolomite	% Aragonit	Cal:Dol
Sorbas Cycle 9-10											
RdA M7 0	-1.8	4.5	-3.4					0	73.6	1.7	0%
RdA M7 5	-1.75	4.9	-3.3					0.4	41.6	4.3	1%
RdA M7 10	-1.7	5.0	-3.6					0.4	41.8	5.7	1%
RdA M7 15	-1.65	4.7	-3.8					0.7	54	1.2	1%
RdA M7 20	-1.6	4.2	-4.0					0.3	73.7	1.4	0%
RdA M7 25	-1.55	4.0	-3.9					0.3	36.5	3.6	1%
RdA M7 30	-1.5	4.0	-3.9					0.5	70.6	2.4	1%
RdA M7 35	-1.45	3.4	-3.9			-0.19	0.03	0.3	54.5	5.1	1%
RdA M7 40	-1.4	4.5	-3.7					0.8	39.4	4.2	2%
RdA M7 45	-1.35	3.9	-3.2					1.7	18.6	2.4	8%
RdA M7 50	-1.3	5.1	-3.4					0.3	61.1	2.4	0%
RdA M7 55	-1.25	4.3	-3.3					0.3	53.5	1.7	1%
RdA M7 57.5	-1.225	5.0	-3.3					0.4	51.5	4.1	1%
RdA M7 60	-1.2	4.0	-3.2					0.5	28.5	2.4	2%
RdA M7 65	-1.15	4.5	-3.2					0.3	40.7	3	1%
RdA M7 70	-1.1	4.3	-3.3					0.4	57.9	5.3	1%
RdA M7 75	-1.05	2.0	-3.2					16.8	44.2	3.1	28%
RdA M7 80	-1	1.2	-3.1					18.5	33.4	3.4	36%
RdA M7 85	-0.95	0.1	-2.7			0.16	0.02	22.1	18.6	2.8	54%
RdA M7 90	-0.9	5.0	-2.5					0.3	47.2	5.1	1%
RdA M7 95	-0.85	4.7	-2.1					1.6	39.1	4.2	4%
RdA M7 100	-0.8	4.9	1.2					0.7	66.6	1.5	1%
RdA M7 105	-0.75	0.8	0.9					28.7	34.7	0.5	45%
RdA M7 110	-0.7	0.2	1.1					39.6	56	0.5	41%
RdA M7 115	-0.65	3.8	2.0					7.8	64.8	0.8	11%
RdA M7 120	-0.6	3.9	1.7					0.6	33.5	1.2	2%
RdA M7 125	-0.55	4.5	1.2					0.1	83.8	1.1	0%
RdA M7 130	-0.5	3.4	0.9					0.5	26.3	1.1	2%
RdA M7 135	-0.45	5.0	1.2					0	82.3	1.2	0%
RdA M7 140	-0.4	5.3	1.3	0.708894	6	-0.4	0.02	0.1	81.2	2.1	0%
RdA M7 145	-0.35	5.3	1.2					0	71.9	2.9	0%
RdA M7 150	-0.3	4.6	0.5					0.3	16	1.6	2%
RdA M7 155	-0.25	5.8	0.4					0.1	74.6	2.9	0%
RdA M7 160	-0.2	5.4	-0.1					0.3	59.3	3	1%
RdA M7 165	-0.15	5.1	-0.1					0.2	22.8	1.4	1%
RdA M7 170	-0.1	5.2	-0.8					0.3	44.1	6.2	1%
RdA M7 175	-0.05	5.2	-0.8					0.1	59.1	5.4	0%
RdA M7 180	0	5.4	-0.9			-0.25	0.02	0	71.8	4	0%
Sorbas Cycle 10 SC											
SC7-M1	4	4.0	-3.8								
SC7-M2	4	3.5	-4.8								
SC7-M3	4	4.0	-3.9								
SC7-M4	4	5.8	-2.6								
Sorbas Cycle 12-13											
BdI C16 -25	-0.25	-7.3	-0.6								
BdI C16 -20	-0.2	-7.2	-0.6								
BdI C16 -15	-0.15	-7.2	-0.9								
Sorbas Cycle 13-14											
BdI C16 +100	1	-7.3	-1.0								
BdI C16 +100 Bulk	1	-5.3	0.8								
Sorbas Cycle 14-15											
RdA C16 -5	-0.05	-5.3	-3.3								
RdA C16 -10	-0.1	-5.5	-2.7								
RdA C16 -15	-0.15	-5.2	-2.3								
RdA C16 -23	-0.23	-5.7	-1.4								
RdA C16 -25	-0.25	-5.3	-1.5								
RdA C16 -30	-0.3	-4.8	-1.9								
RdA C16 -42	-0.41	-5.3	-2.2								
RdA C16 -60	-0.6	-5.2	-1.8								
RdA C16 -65	-0.65	-5.4	-1.2								
RdA C16 -75	-0.75	-5.6	0.3								
RdA C16 -80	-0.8	-5.7	0.0								
RdA C16 -90	-0.9	-5.5	0.6								
Sorbas within Cycle 15											
RdA C16 37	0.37	-5.4	-2.7								
Sorbas Cycle 15+											
RdA C16 +100	1	-5.5	0.6								
Upper Gypsum											
EM Cycle 4											
EM4 dome 60cm		-0.5	-1.3								
EM4 dome 125 cm		-1.2	-1.3								
EM4 dome 148 cm		-2.0	-1.6								
EM4 pal G-H		0.1	-0.9								
EM4 pal I-J		0.0	-0.9								
EM4 pal J-K		1.1	-1.6								
EM Cycle 7											
EM Aren 86-87 cm		0.3	-0.3								
EM Aren 148-157 cm		-0.3	-0.7								

Table D.9a. Oxygen and hydrogen isotope data of Mediterranean freshwaters

Rainwaters, Sicily			Groundwaters, Sorbas Basin, SE Spain				
$\delta^{18}O$	δD	d-excess	Sample Name	$\delta^{18}O$	δD	^{17}O-ex	d-excess
-5.92	-34.21	13.14	rain 6	-1.81	-7.09	23	7.43
-7.83	-55.42	7.23	rain 7	-4.18	-25.10	16	8.31
-8.17	-53.73	11.62	rain 9	-4.93	-29.17	21	10.29
-5.46	-39.20	4.47	rain 18	-4.97	-35.07	15	4.68
-4.50	-24.22	11.81	rain 20	-2.96	-16.10	16	7.62
-5.22	-34.95	6.79	rain 26	-4.40	-25.59	10	9.62
-2.22	-8.09	9.66	MOLINOS 01-03-2012	-5.86	-36.54	12	10.30
-4.40	-27.23	7.94	MOLINOS 18-03-2012	-5.77	-36.27	4	9.92
-7.22	-38.35	19.42	MOLINOS 24-03-2012	-5.06	-34.10	0	6.35
-7.76	-46.16	15.92	MOLINOS 07-04-2012	-5.80	-35.49	12	10.94
-3.49	-9.93	17.96	MOLINOS 10-08-2012	-5.99	-36.75	6	11.15
-5.27	-33.86	8.32	MOLINOS 10-08-2012	-5.40	-34.74	18	8.44
-3.04	-11.05	13.29	APAS 11-05-2011	-4.21	-27.21	11	6.48
-4.97	-31.94	7.81	APAS 10-08-2011	-5.09	-29.84	28	10.86
-4.71	-27.39	10.29	APAS 01-03-2012	-5.33	-30.59	28	12.06
-6.09	-30.48	18.27	APAS 06-06-2012	-5.26	-30.17	18	11.92
-4.61	-12.52	24.35	PERAL 11-05-2011	-4.94	-31.46	19	8.03
-11.12	-73.92	15.03	PERAL 01-03-2012	-5.33	-30.59	28	12.06
-4.51	-13.05	23.01	PERAL 06-06-2012	-5.26	-30.17	18	11.92
-6.40	-39.10	12.12	PERAL 11-05-2011	-4.94	-31.46	19	8.03
-2.50	-17.63	2.35	PERAL 10-08-11	-5.04	-32.70	20	7.64
-1.89	-7.55	7.54	PERAL 01-3-12	-5.81	-34.98	23	11.49
-4.97	-29.89	9.84	PERAL 06-06-12	-5.66	-34.48	26	10.78
-5.03	-35.81	4.40	VINICA 1-3-12	-5.18	-30.09	24	11.36
-4.26	-26.13	7.94	VINICA 7-4-12	-4.86	-28.91	18	9.97
-3.11	-17.08	7.83	RAIN-01	-5.9	-34.2		13.00
-4.29	-25.81	8.48	RAIN-02	-7.8	-55.4		7.00
-5.55	-30.03	14.35	RAIN-03	-8.2	-53.7		11.90
-5.29	-29.10	13.22	RAIN-04	-5.5	-39.2		4.80
-5.38	-29.50	13.52	RAIN-05	-4.5	-24.2		11.80
-5.23	-28.60	13.21	RAIN-06	-5.2	-35		6.60
-5.39	-30.30	12.79	RAIN-07	-2.2	-8.1		9.50
-5.36	-29.30	13.55	RAIN-08	-4.4	-27.2		8.00
-5.36	-29.99	12.89	RAIN-09	-7.2	-38.4		19.20
-5.55	-30.00	14.40	RAIN-10	-7.8	-46.2		16.20
-5.55	-30.68	13.75	RAIN-11	-3.5	-9.9		18.10
-5.39	-28.86	14.26	RAIN-12	-5.3	-33.9		8.50
-5.36	-29.16	13.71	RAIN-13	-3	-11.1		12.90
-6.20	-33.66	15.90	RAIN-14	-5	-31.9		8.10
-6.26	-35.21	14.85	RAIN-15	-4.7	-27.4		10.20
-6.23	-34.98	14.84	RAIN-16	-6.1	-30.5		18.30
-6.30	-35.55	14.87	RAIN-17	-4.6	-12.5		24.30
-6.33	-35.21	15.42	RAIN-18	-11.1	-73.9		14.90
-5.42	-30.59	12.79	RAIN-19	-1.81	-7.09	23	7.39
-6.29	-36.21	14.08	RAIN-20	-4.18	-25.1	16	8.34
-6.23	-36.84	13.01	RAIN-21	-4.93	-29.17	21	10.27
-6.31	-36.10	14.36	RAIN-22	-4.97	-35.07	15	4.69
-6.01	-35.66	12.41	RAIN-23	-2.96	-16.1	16	7.58
-5.91	-33.45	13.83	RAIN-24	-4.4	-25.59	10	9.61
-6.13	-35.05	14.01					
-6.27	-36.69	13.46					
-5.76	-33.69	12.38					
-5.77	-33.05	13.12					
-5.66	-31.56	13.73					
-5.57	-31.95	12.64					
-5.64	-32.21	12.93					
-5.72	-31.06	14.67					
-4.4	-26	9.20					
-5.2	-23	18.60					

Table D.9b. Table D.9a continued. Oxygen and hydrogen isotope data of Mediterranean freshwaters

Rainwaters, Ancona, Central Apennines			Freshwater, South Appenines			Freshwater, Central Anatolia			
$\delta^{18}O$	δD	d-excess	$\delta^{18}O$	δD	d-excess	$\delta^{18}O$	δD	$\delta^{18}O$	δD
-5.29	-32.5	9.82	-10.8	-71	15.40	-7.83	-66.4	-10.02	
-6.32	-36.6	13.96	-4.1	-24	8.80	-4.76	-36	-12.49	-90.7
-7.62	-51.2	9.76	-3.8	-27	3.40	-8.45	-71.3	-11.85	-84.6
-8.99	-56.9	15.02	-5	-24	16.00	-3.25	-31.6	-8.76	-59.3
-8.94	-52.5	19.02	-6.1	-37	11.80	-0.89	-10.6	-4.83	-27.3
-7.5	-45.8	14.20	-6.8	-39	15.40	-3.03	-27.3	-4.95	-32.1
-6.05	-33.4	15.00	-7.1	-39	17.80	-3.38	-19.9	-5.16	-34.7
-4.22	-17.9	15.86	-5.2	-29	12.60	-7.07	-51.8	-2.33	-13
-6.94	-40	15.52	-11.7	-77	16.60	-6.26	-31	-5.05	-28.4
-9.47	-55	20.76	-10	-59	21.00	-10.38	-66.4	-4.88	-24.3
-10.4	-67.1	16.10	-11.2	-69	20.60	-10.72	-74.5	-7.26	-45.5
-9.4	-62.4	12.80	-9.5	-55	21.00	-14.03	-104.2	-7.32	-44.4
-3.6	-17.1	11.70	-6.8	-36	18.40	-8.95	-51.4	-11.46	-84
-2.9	-9	14.20	-6.9	-39	16.20	-9.43	-58.7	-10.86	-75.1
			-3.3	-17	9.40	-4.05	-28.9	-7	-44
			-7	-44	12.00	-0.46	-7.1	-8.37	-53.1
			-5.1	-30	10.80	-0.46	-4.5	-7.38	-50.7
			-6.9	-39	16.20	-0.52	-7.8	-5.08	-35.3
			-7.4	-44	15.20	-3.93	-11.8	-7.61	-54.3
			-7.1	-37	19.80	-12.11	-89.4	-3.7	-27.3
			-11.1	-66	22.80	-12.76	-84.4	-2.04	-17.7
			-11	-68	20.00	-10.51	-70.7	-4.71	-31.2
			-9.1	-53	19.80	-7.8	-50.1	-1.6	-17.2
			-8.1	-53	11.80	-7.77	-46.9	-9.09	-61
			-10.3	-72	10.40	-3.91	-19.4	-9.08	-54.9
			-5.1	-37	3.80	-5.32	-26.9	-13.69	-113.1
			-5.3	-38	4.40	-8.12	-59.4	-7.98	-50.9
			-5.9	-36	11.20	-4.35	-28.8	-7.06	-45.3
			-6.6	-41	11.80	-7.04	-40.7	-6.15	-39.7
			-7.2	-40	17.60	-16.44	-113.5	-9.48	-61.7
			-4.1	-24	8.80	-11.27	-79.4	-4.99	-30.6
			-11.4	-78	13.20	-9.63	-65.1	-5.53	-32
			-9.6	-63	13.80	-8.92	-64.8	-5.49	-29.7
			-10.7	-69	16.60	-6.56	-46.7	-5.32	-31.1
			-7.7	-45	16.60	-4.5	-37.8	-5.37	-36.6
			-6.4	-31	20.20	-3.3	-26.9	-5.52	-27.6
			-5.7	-38	7.60	-3.07	-22.3	-13.4	-88.8
			-4	-23	9.00	-2.99	-22.9	-4.93	-32.9
			-4.1	-25	7.80	-10.84	-73.3	-4.35	-22.4
			-3.7	-25	4.60	-9.8	-64.7	-6.46	-33.5
			-5.8	-38	8.40	-10.55	-76.4	-11.75	-78
			-7.4	-44	15.20	-10.62	-70.2	-11.58	-71.5
			-7.4	-44	15.20	-6.74	-42.1	-9.59	-66.8
			-10.6	-64	20.80	-0.01	-1.1	-9.37	-60.1
			-9.8	-61	17.40	-5.08	-39.64	-3.63	-28.3
			-9.8	-57	21.40	-4.17	-33.5	-3.72	-28.3
			-8.2	-54	11.60	-3.95	-23.9	-3.52	
						-4.2	-25	-2.55	-17.2
						-5.47	-32.2	-4.88	-38.6
						-6.62	-39.3	-8.14	-51.3
						-5.06	-33.42	-9.41	-73.8
						-1.95	-21.22	-9.26	-61.4
						-7.94	-46.39	-6.25	-37.1
						-11.35	-73.79	-4.7	-28.2
						-11.3	-72.16	-11.81	-82.5
						-15.21	-107.89	-7.08	-44.6
						-15.77	-113.9	-6.29	-40.2
						-16.88	-120.64	-0.28	-6
						-12.62	-99.08	-6.19	-47.8
						-4.63	-38.36	-6.19	-38.3
						-5.76	-38.04	-7.87	-50.8
						-3.6	-42.38	-13.2	-92.5
						5.36	13.89	-6.72	-36.92